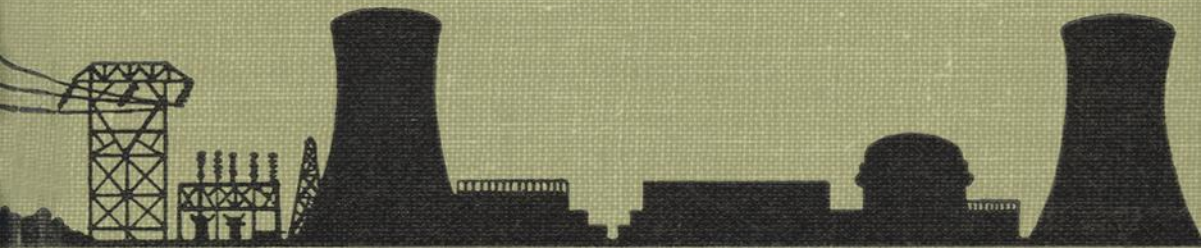


IRRADIATION EFFECTS ON STRUCTURAL ALLOYS FOR NUCLEAR REACTOR APPLICATIONS



STP 484



AMERICAN SOCIETY FOR TESTING AND MATERIALS

Copyright by ASTM Int'l (all rights reserved); Thu Aug 27 10:12:15 EDT 2020

Downloaded/printed by

(USP) Universidade de Sao Paulo ((USP) Universidade de Sao Paulo) pursuant to License Agreement. No further reproductions authorized.

IRRADIATION EFFECTS ON STRUCTURAL ALLOYS FOR NUCLEAR REACTOR APPLICATIONS

A symposium
sponsored by the
AMERICAN SOCIETY FOR
TESTING AND MATERIALS
Toronto, Ontario, Canada, 29 June–1 July 1970

ASTM SPECIAL TECHNICAL PUBLICATION 484
A. L. Bement, symposium chairman

List price \$49.25



AMERICAN SOCIETY FOR TESTING AND MATERIALS
1916 Race Street, Philadelphia, Pa. 19103

© BY AMERICAN SOCIETY FOR TESTING AND MATERIALS 1970
Library of Congress Catalog Card Number: 79-137454
ISBN 0-8031-0069-8

NOTE

The Society is not responsible, as a body,
for the statements and opinions
advanced in this publication

Printed in Baltimore, Md.
March 1971

Foreword

The Symposium on Irradiation Effects on Structural Alloys for Nuclear Reactor Applications was presented at Niagara Falls, Canada, 29 June–1 July 1970, in conjunction with the Seventy-third Annual Meeting of the American Society for Testing and Materials held in Toronto, Ontario, Canada, 22–26 June 1970. The symposium was sponsored by ASTM Committee E-10 on Radiosotopes and Radiation Effects. A. L. Bement, Jr., Battelle Memorial Institute, Pacific Northwest Laboratory, served as chairman of the symposium committee, which consisted of J. Moteff, cochairman, and K. M. Zwilsky, C. J. Baroch, E. Landerman, and L. E. Steele. The six sessions were presided over by L. J. Chockie, D. R. Harries, W. R. Thomas, R. Bullough, J. Moteff, and H. Böhm. Two agenda discussion sessions also were presented to survey the status of two contemporary problem areas.

Related ASTM Publications

**Chemical and Physical Effects of High-Energy Radiation
on Inorganic Substances, STP 400 (1966), \$5.25**

**Irradiation Effects in Structural Alloys for Thermal and
Fast Reactors, STP 457 (1969), \$36.00**

**Analysis of Reactor Vessel Radiation Effects Surveillance
Programs, STP 481 (1970), \$26.00**

Contents

Introduction	1
Pressure Vessel Steels—Fracture Behavior—Session I	
Neutron Dosimetry for Reactor Pressure Vessel Applications—C. Z. SERPAN, JR., AND W. C. MORGAN	3
Discussion	17
Radiation Effects on the Metallurgical Fracture Parameters and Fracture Toughness of Pressure Vessel Steels—R. A. WULLAERT, D. R. IRELAND, AND A. S. TETELMAN	20
Discussion	40
The Effect of Hydrogen on the Ductile Properties of Irradiated Pressure Vessel Steels—C. R. BRINKMAN AND J. M. BEESTON	42
Discussion	73
Evaluation of the Embrittlement of Pressure Vessel Steels Irradiated in JPDR—MASAYUKI KAWASAKI, T. FUJIMURA, K. SUZUKI, H. NAMATAME, AND MINORU KAWASAKI	74
Discussion	95
Pressure Vessel Steels—Structural and Impurity Effects—Session II	
Demonstration of Improved Radiation Embrittlement Resistance of A533B Steel Through Control of Selected Residual Elements—J. R. HAWTHORNE	96
Discussion	127
Neutron Irradiation Effects on Iron Containing Aluminum and Nitrogen— N. IGATA, R. R. HASIGUTI, E. YAGI, U. NISHIIKE, AND K. WATANABE	128
Discussion	140
The Effect of Fast Neutron Irradiation on the Mechanical Properties of Some Quenched and Tempered Steels—R. R. HOSBONS AND B. L. WOTTON	142
Discussion	163
Agenda Discussion Session	
Structure and Composition Effects on Irradiation Sensitivity of Pressure Vessel Steels—L. E. STEELE	164
Thermal Reactor Materials—Session III	
Effects of Irradiation in a Thermal Reactor on the Tensile Properties of Zircaloy 2 and 4 and Borated Stainless Steel—C. J. BAROCH, A. V. MUNIM, AND E. N. HARBINSON	176
Discussion	193
Influence of Irradiation Temperature on the Tensile Properties of Stainless Steel—M. KANGLASKI, J. W. SPRETNAK, A. A. BAUER, AND R. A. WULLAERT	194
The Effect of Neutron Irradiation on the Mechanical Properties of Zirconium Alloy Fuel Cladding in Uniaxial and Biaxial Tests—D. G. HARDY	215
Discussion	258
Metallurgical Properties of Cold-Worked Zircaloy 2 Pressure Tubes Irradiated Under CANDU-PHW Power Reactor Conditions—W. J. LANGFORD	259
Discussion	286

The Temperature and Neutron Dose Dependence of Irradiation Growth in Zircaloy 2—J. E. HARBOTTE	287
Discussion	298
Fast Reactor Materials—Damage Mechanisms—Session IV	
Quantitative Transmission Electron Microscopy of Bubbles in Al and Al-Al ₂ O ₃ Alloys—E. RUEDL	300
Discussion	316
The Mechanism and Kinetics of Void Growth During Neutron Irradiation—R. BULLOUGH AND R. C. PERRIN	317
Discussion	330
Void Formation in Proton Irradiated Stainless Steel—D. W. KEEFER, H. H. NEELY, J. C. ROBINSON, A. G. PARD, AND D. KRAMER	332
Discussion	345
Considerations of Metal Swelling and Related Phenomena Caused by Fast Neutron Irradiation—CHE-YU LI, D. G. FRANKLIN, AND S. D. HARKNESS	347
Discussion	361
Some Observations on the Structure and Tensile Properties of AISI Type 316 Steel as a Function of Fast Reactor Irradiation Temperature—P. J. BARTON AND P. R. B. HIGGINS	362
Fast Reactor Materials—Swelling Behavior—Session V	
Neutron Dosimetry for Fast Reactor Applications—W. N. MCELROY AND R. E. DAHL, JR.	375
Agenda Discussion Session	
How Do We Solve the Void Problem?	400
Fast Reactor Materials—Properties—Session VI	
Neutron Fluence Limit Determinations for Some Fast Flux Test Facility Components—R. A. MOEN, J. C. TOBIN, AND K. C. THOMAS	409
Axial Fatigue of Irradiated Stainless Steels Tested at Elevated Temperatures—J. M. BEESTON AND C. R. BRINKMAN	419
Discussion	449
Effect of Fast Neutron Irradiation on the Creep Rupture Properties of Type 304 Stainless Steel at 600 C—E. E. BLOOM AND J. O. STIEGLER	451
Discussion	467
Uniaxial and Biaxial Creep Rupture of Type 316 Stainless Steel After Fast Reactor Irradiation—A. J. LOVELL AND R. W. BARKER	468
Effect of Irradiation on the Mechanical Properties of 19-9DL Alloy—A. L. LOWE, JR., AND C. J. BAROCH	484
Discussion	494
Influence of Neutron Irradiation on the Creep Rupture Properties of a 16Cr-13Ni Steel—K. EHRLICH, H. BÖHM, AND C. WASSILEW	495
The Effects of Helium on the High-Temperature Ductility of Sandvik 12R72HV and Inco IN-744X—D. KRAMER, K. R. GARR, C. G. RHODES, AND A. G. PARD	509
Discussion	520
Correlation Between the Mechanical Properties and Microstructure of Irradiated Iron and Low-Carbon Steel—V. M. STEFANOVIĆ AND N. LJ. MILAŠIN	521
Irradiation Effects at Cryogenic Temperature on Tensile Properties of Titanium and Titanium-Base Alloys—C. L. YOUNGER AND F. A. HALEY	537

Introduction

The 1970 Symposium on Radiation Effects on Structural Metals was the fifth in a series of related international conferences that have been held biennially. The symposium, sponsored by ASTM Committee E-10 on Radiosotopes and Radiation Effects, had the primary objective of providing a comprehensive review of current technology in the development and evaluation of metallic materials for thermal and fast nuclear reactors. This was accomplished by bringing together the world's experts in nuclear radiation effects on structural metals, utilizing as a focal point a selected group of papers and providing a forum for discussion of new techniques for applying structural metals to various nuclear environments.

This is an expanding field of technology of vital interest to research and development investigators, reactor design, nuclear utilities, the nuclear industry, and government. While efforts to minimize the detrimental aspects of radiation induced property changes in thermal reactor materials are continuing, the development of superior materials that will withstand void swelling in fast breeder reactors is presently the focus of technological effort. Furthermore, experimental and analytical methods for correlating property changes with neutron flux and energy parameters have achieved a promising stage of development. In order to cover the important aspects of the general topic, approximately forty papers contributed by recognized experts from many countries were carefully selected by the symposium committee and were arranged into six sessions. This volume is accordingly divided by session topic to facilitate the reader's review in terms of his preferred interest. The topics include (1) pressure vessel steels—fracture behavior, (2) pressure vessel steels—structural and impurity effects, (3) thermal reactor materials, (4) fast reactor materials—damage mechanisms, (5) fast reactor materials—swelling behavior, and (6) fast reactor materials—properties. Recent advances in neutron dosimetry for thermal and fast reactor applications were reviewed in three invited papers, two of which are included in the proceedings; namely, "Neutron Dosimetry for Reactor Pressure Vessel Applications," by C. Z. Serpan, Jr., and W. C. Morgan and "Neutron Dosimetry for Fast Reactor Applications," by W. N. McElroy and R. E. Dahl, Jr.

Two agenda discussion sessions stimulated plenary discussions of subjects of technical interest. Scientists eminent in the field were selected as

discussion leaders and were given the responsibility for outlining critical points and developing the discussion of each point. These leaders were assisted by rapporteurs who prepared a more or less literal transcription of the discussion. The two sessions were "Structural and Composition Effects on Irradiation Sensitivity of Pressure Vessel Steels," L. E. Steele, chairman, and C. W. Hunter, rapporteur, and "How Do We Solve the Void Problem?" K. Zwilsky, chairman, and T. T. Claudson, rapporteur. The agenda discussion chairmen have condensed, rearranged, organized, added commentary to, and interpreted these discussions, each at his own discretion, in order to contribute a compendium of current thought on each topic. These agenda discussions are included in these proceedings following the formal papers to which they refer. In addition, a rapporteur session, "Swelling of Austenitic Stainless Steels in Fast Reactors—Experimental Evidence and Design Considerations," was presented by J. R. Weir but is not included in this publication.

Scheduling this symposium in Canada not only enhanced the international focus on the symposium topic but also attracted a broader international representation. In addition to the host country, Canada, authors and attendees from Australia, Belgium, Czechoslovakia, France, Germany, India, Italy, Japan, the Netherlands, the United Kingdom, the United States, and Yugoslavia discussed recent work being conducted in their homelands.

Rapid advances in nuclear materials technology along several fronts were evident from this symposium. They suggest the importance of both these proceedings and future symposia to the further development of an international exchange of information encouraged by this and preceding symposia of this series. The authors and discussers are commended for their excellent presentation of both the problems and some solutions in the field of nuclear radiation damage of materials.

The members of the symposium committee were Arden L. Bement, chairman, John Moteff, cochairman, Klaus Zwilsky, Charles J. Baroch, E. Landerman, and Lendell E. Steele. The symposium committee gratefully acknowledges the substantial assistance of Rebecca R. Martin, Pacific Northwest Laboratory, for secretarial services and of Duane N. Sunderman, chairman, ASTM Committee E-10, for his leadership and encouragement.

A. L. Bement

manager, Fuels and Materials Dept.,
Battelle-Northwest, Richland, Wash. 99352;
currently, visiting professor of nuclear materials,
Department of Nuclear Engineering,
Massachusetts Institute of Technology,
Cambridge, Mass. 02139.

C. Z. Serpan, Jr.,¹ and W. C. Morgan²

Neutron Dosimetry for Reactor Pressure Vessel Applications

REFERENCE: Serpan, C. Z., Jr., and Morgan, W. C., "Neutron Dosimetry for Reactor Pressure Vessel Applications," *Irradiation Effects on Structural Alloys for Nuclear Reactor Applications, ASTM STP 484*, American Society for Testing and Materials, 1970, pp. 3-19.

ABSTRACT: The neutron dosimetry analysis effort discussed is aimed solely at obtaining the most accurate projections of neutron fluence and future radiation embrittlement in the pressure vessel of an operating commercial power reactor. The mechanical property changes in materials for reactor pressure vessel applications are caused by neutron/atomic lattice interactions that are highly sensitive to material composition, irradiation temperature, and population and energy of the damage causing neutrons. Of these, the neutron fluence and spectra are most difficult to define accurately for a given irradiation condition since neither can be measured directly. Nevertheless, if radiation induced changes are to be understood and subsequently used as a basis for projecting changes in real reactor components, the neutron dosimetry analysis must be as precise as possible; the ultimate results of any such projections are highly dependent upon the accuracy of the neutron spectrum and neutron fluence used as input. Improvements in both of these areas, as well as in standardization of approaches, are needed for accurate projection of radiation induced changes in reactor pressure vessels. The current status of neutron dosimetry in power reactors is reviewed, and guidelines are provided for improving future dosimetry of reactor pressure vessel surveillance programs.

KEY WORDS: irradiation, particle beams, neutron irradiation, neutron flux, spectra, radiation effects, dosimetry, mechanical properties, microstructure, crystal lattices, embrittlement, power reactors (nuclear), nuclear fuel cladding, pressure vessels, alloy steels, alloy stainless steels

The primary pressure containment vessels of the present generation of light water moderated power reactors are fabricated of heavy-section low-

¹ Research chemist, Reactor Materials Branch, Metallurgy Division, Naval Research Laboratory, Washington, D.C. 20390.

² Senior research scientist, Irradiation Effects Section, Metallurgy and Ceramics Department, Battelle Memorial Institute, Pacific Northwest Laboratory, Richland, Wash. 99352.

alloy ferritic steel [1].³ Economic design considerations dictate that the vessel diameters be kept as small as possible. This results in the vessel wall being close to the nuclear fuel core and causes a corresponding increase in the neutron flux intensity incident on the vessel wall. It is the bombardment of ferritic steel in reactor pressure vessel walls by reactor core neutrons that causes alterations in the steel atomic lattice, with resulting changes in mechanical properties.

These mechanical property changes are highly sensitive to material composition, microstructure, irradiation temperature, and the population and energy of impinging neutrons. Certain changes such as increases in yield and tensile strength are not generally considered detrimental; however, neutron induced increases in the brittle-to-ductile transition temperature of ferritic steels are of significant importance to the overall operational safety of a pressurized reactor vessel.

Embrittlement Analysis

The basic embrittlement analysis problem of reactor pressure vessels arises from the fact that nondestructive measurements of mechanical property changes cannot be made for the precise location of primary interest, the interface between the stainless steel cladding and the alloy steel inside the vessel wall. With present technology, the best alternative is to make mechanical property measurements on specimens irradiated at nearby accessible locations in the same reactor and extrapolate the mechanical property changes to the location of interest.

The Analysis of a Reactor in Use

For example, this technique was used for analysis of the Yankee-Rowe reactor; Fig. 1 is a schematic representation of the reactor, including a section through the vessel core at midplane, showing the positions of the surveillance capsules in relation to the reactor [2]. The magnitude of the extrapolation required for this kind of reactor is given by the neutron flux measurements from "accelerated" and "vessel wall" surveillance location capsules. These show that the measured flux, $n/cm^2\cdot s$, for $E > 0.5$ MeV at the vessel wall location decreased to about 0.001 of the accelerated location fluxes.

Because of the different types and thicknesses of moderating materials between the location at which the specimens were irradiated and the pressure vessel wall, the neutron population as a function of energy can change significantly, and the resulting neutron spectrum will have greater or lesser capabilities for creating damage. Therefore, the damage produced per unit neutron fluence must be taken into account if meaningful projections are to be made of damage in a component and of the resulting service

³ Italic numbers in brackets refer to the list of references at the end of this paper.

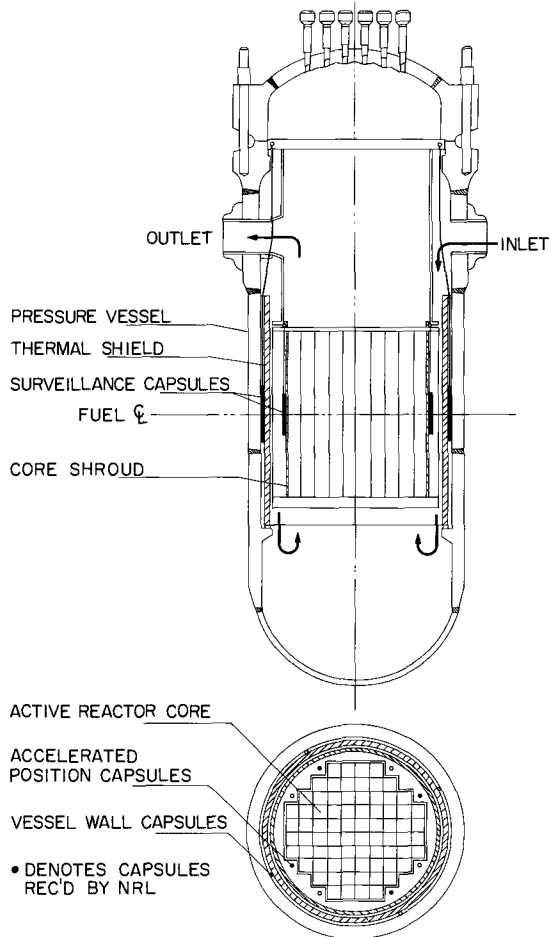


FIG. 1—Schematic representation of the Yankee reactor showing the relative location of accelerated and vessel wall surveillance capsules.

capabilities. Figure 2 shows, as an example of the neutron spectrum changes with position, the neutron spectra for the near-core accelerated surveillance irradiation location and the near-vessel vessel wall surveillance irradiation location of the Big Rock Point reactor (BRPR) as histograms [3]. The smooth curve for the Watt form of the fission spectrum is included for reference. It is clear that the fission spectrum is not a good approximation for the spectrum at either of the BRPR locations.

A closer inspection of Fig. 2 reveals the effects of moderating materials upon neutron distributions in reactors. The spectrum for the accelerated location, which is quite near the reactor fuel core, more closely reflects a

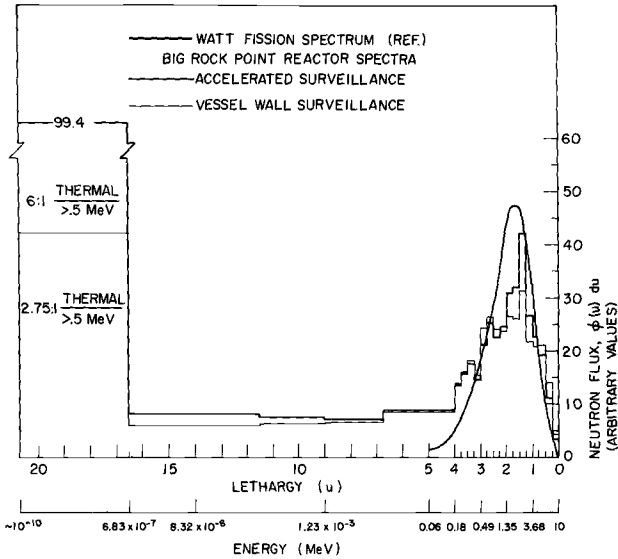
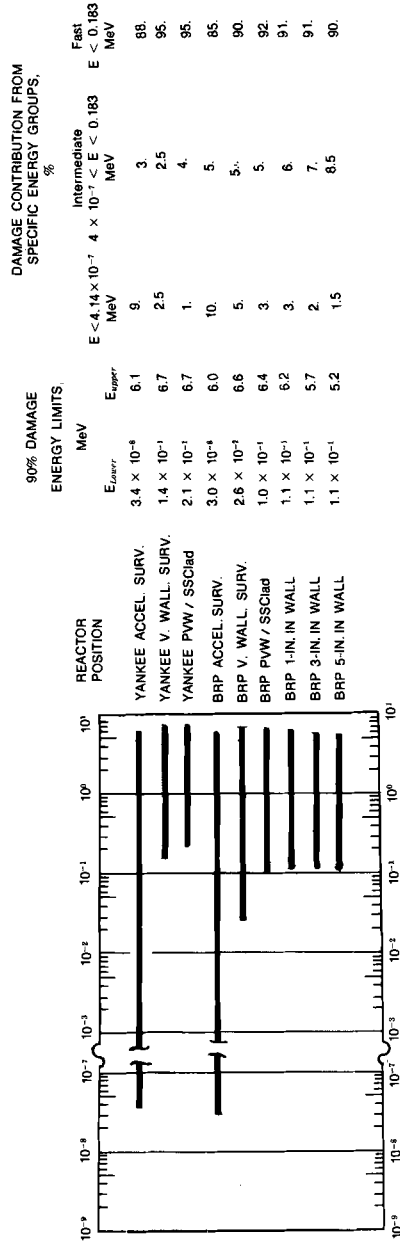


FIG. 2—Theoretical neutron spectra for surveillance locations in the Big Rock Point reactor. The spectra were calculated with the transport theory reactor physics code, Program S, and validated with flux detector measurements. The spectral emphasis is seen to shift from lower to higher energies between the near-core accelerated location and the near-vessel vessel wall location.

fission-spectrum shape than does the spectrum at the vessel wall surveillance location, which is only an inch or two from the internal wall of the reactor vessel. The thermal flux population decreases significantly at the vessel wall location as a result of removal processes occurring in the steel. The neutron spectrum within the vessel wall is again somewhat different than either of these spectra. As a general comment, the average neutron energy increases as a result of the removal processes in the steel and water layers. (Only the relative spectral group intensities are being discussed here. The overall intensity of the vessel wall spectrum is several orders of magnitude lower than the overall intensity of the accelerated location spectrum.) An indication of the importance of these spectral changes can be gained from Table 1; as can be seen, by far the most important radiation effects in the pressure vessel are caused by high-energy neutrons. The intermediate-energy neutrons, of energies greater than thermal but less than about 0.1 MeV, have enough energy to create some damage but are relatively unimportant; thermal neutrons, on the other hand, do contribute to the damage at the accelerated surveillance position but not at the vessel wall position.

The details of this comparison have been presented previously [4]; the most important points to be emphasized here are that (1) the spectrum

TABLE 1—Energy range of neutrons causing 90 percent of a 200 F transition temperature increase in A302B steel irradiated at <450 F.



REACTOR POSITION	90% DAMAGE ENERGY LIMITS		DAMAGE CONTRIBUTION FROM SPECIFIC ENERGY GROUPS, %			
	E_{Lower} MeV	E_{Upper} MeV	$E < 4.14 \times 10^{-7}$ MeV	$4 \times 10^{-7} < E < 0.183$ MeV	Intermediate MeV	Fast $E < 0.183$ MeV
YANKEE ACCEL. SURV.	3.4×10^{-8}	6.1	9.	10.	3.	88.
YANKEE V. WALL. SURV.	1.4×10^{-1}	6.7	2.5	1.	2.5	95.
YANKEE PVW / SSCladi	2.1×10^{-1}	6.7	1.	10.	4.	95.
BRP ACCEL. SURV.	3.0×10^{-4}	6.0	10.	5.	5.	85.
BRP V. WALL. SURV.	2.6×10^{-1}	6.6	5.	3.	5.	90.
BRP PVW / SSCladi	1.0×10^{-1}	6.4	3.	3.	5.	92.
BRP 1-IN. IN WALL	1.1×10^{-1}	6.2	3.	2.	6.	91.
BRP 3-IN. IN WALL	1.1×10^{-1}	5.7	2.	1.5	7.	91.
BRP 5-IN. IN WALL	1.1×10^{-1}	5.2	1.5		8.5	90.

changes with position in the reactor and (2) the damage produced by a given neutron fluence is a function of the neutron spectrum.

Determination of Neutron Spectra

Having described the value of knowing a specific neutron spectrum, it is important to consider how it can be obtained. However, for this particular application, it should be emphasized that uncertainties in spectral definition are only important where, and to the degree that, they result in subsequent uncertainties in the integral of the damage cross section over the total spectrum. The two principal methods for obtaining neutron spectra are (1) calculations using reactor physics codes and (2) computer iterative techniques using activation data from many different flux detector materials simultaneously irradiated in the reactor at the location of interest. Both methods have associated advantages and disadvantages and require considerable professional judgment by the user to assure meaningful results. Either method can be used to obtain neutron spectra at the surveillance locations; however, projections into the pressure vessel can only be made by use of the reactor physics code.

Reactor Physics Codes

The mathematical methods for the most widely used codes for reactor vessel spectrum calculations are diffusion theory, transport theory, and a combination of these two. This does not exhaust the possible methods, but few other applications have been made for power reactors. The diffusion codes are very convenient as they permit calculations to be performed with relatively short computer times. Transport theory codes usually take more computer time because of the nature of the mathematical process involved. A typical transport code in use is DTF-IV [5]; another transport code used for several reactor vessel analyses is Program S [6]. The P3MG code [7] has found use for reactor vessel analyses, because it combines some of the rapid analysis features of diffusion theory while also retaining such desirable features of transport theory as considerations of anisotropic scattering.

The idealized model of the reactor, which is chosen for use in the code, can have a significant effect on the calculated spectrum. The mathematical operations of reactor physics codes and the library of microscopic cross sections used in the calculation can also affect the resultant tabulated neutron spectra. There is no universal set of these cross section values for reactor physics calculations, and, therefore, each computational result will reflect the differences inherent in each set to a greater or lesser degree. Without careful comparison of results from several codes and libraries, it is nearly impossible to discern the cause of differences between sets of results.

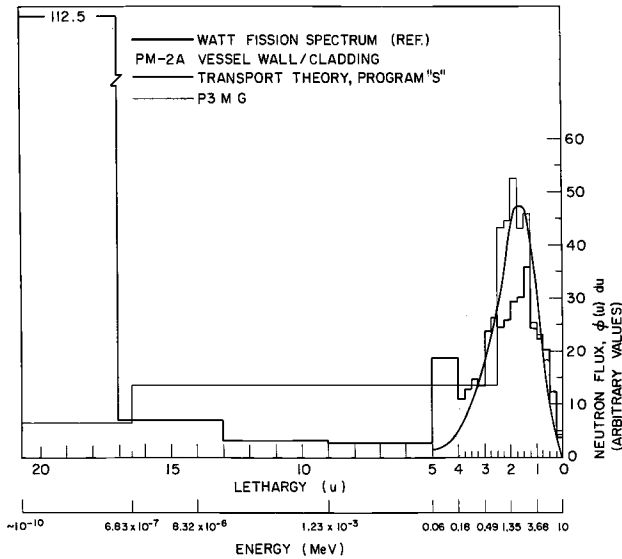


FIG. 3—Theoretical neutron spectra for the alloy steel/stainless steel cladding interface of the PM-2A reactor vessel wall as derived by the transport theory code, Program S, and the P3MG code.

An example of the differences that can arise from use of two different reactor physics codes and cross section libraries is shown in Fig. 3 for the interface of the alloy steel vessel wall and stainless steel cladding of the PM-2A reactor. The heavy line histogram is from a transport theory Program S calculation [8] performed at Battelle-Northwest; the light line histogram is from a P3MG calculation reported by Shure and Oberg [9]. Normalization of the spectra is accomplished on the basis that calculated activation rates of a ^{54}Fe monitor would be the same in each spectrum. The most significant difference is the variation in the relative intensities at different energies; the relative fluences calculated using the two spectra and any one activation monitor would depend on the energy response of the monitor. Thus it is apparent that spectra, calculated by use of a reactor physics code, should be checked by activation of monitors having different energy responses and may require adjustment on the basis of the activation results.

Computer Iterative Analysis

Multiple-foil techniques [10] provide an effective means of adjusting calculated spectra; moreover, if sufficient monitoring data are available, computer iterative analysis techniques can be used to derive neutron spectra directly from the activation data. The multiple-foil technique is, theoretically, capable of yielding very accurate spectra. The method does

require that, unless good estimates of the spectra are available, a large number of monitor materials be irradiated simultaneously for use as input data. A second limitation is that the energy dependent cross sections must be known for all of the monitors; an associated problem is the scarcity of cross section data for monitors which are primarily activated by intermediate-energy neutrons. The second limitation has generally been overcome, as in the case of the SAND-II computer code [11], by the compilation and evaluation of an extensive library of consistent cross sections [12].

Large differences do not always exist between the results obtained by different methods. A recent study by Jenkins [13] shows excellent agreement between the calculated spectrum and the neutron activation results; and, by using the SAND-II code, to adjust the calculated spectrum, even better agreement was obtained. These results show the degree of precision which can be obtained through careful choice of techniques; however, the choice of techniques requires the exercise of professional judgment and considerable experience with the use of different codes under various conditions.

Damage and Fluence

Comparisons of irradiation effects data have been made on the basis of the Radiation Damage Unit (RDU) introduced by Rossin [14] and the Dt unit introduced by Shure [15]. Both approaches are similar in that they use theoretically derived atomic displacement cross sections which are integrated over the neutron flux spectrum with the resultant sum taken as a measure of the relative damaging potential of the spectrum. The damaging potential could then be multiplied by the neutron fluence, and this product used in place of the fluence for comparing radiation damage data. Such a procedure is far more realistic than simply assuming that the damage is directly proportional to the fluence; however, both methods suffer from the defect that they are closely tied to a particular set of theoretical displacement cross sections and they require the introduction of a damage unit scale in addition to the fluence scale.

Dahl and Yoshikawa [16] found that an energy could be determined such that the integral of the displacement cross section over the neutron spectrum was proportional to the flux above that energy for a number of different spectra. This method does not require the introduction of an arbitrary damage unit; however, it does retain the assumption that the damage is proportional to the calculated number of displacements produced during the irradiation.

Various improvements have been made in the models used to derive theoretical displacement cross sections [17], and other models have been developed which are more realistic in that they are based on the formation of vacancy clusters [18] rather than just displacement production. These studies clearly point the direction for future developments in damage cor-

relation work; however, additional improvements and validation studies are required to obtain the accuracy required for pressure vessel surveillance programs.

In addition to the theoretical work, macroscopic damage cross sections have been derived [19] directly from physical property change data by use of computer iterative analysis techniques. Although this approach requires that a fairly substantial body of radiation effects data be compiled on a specific steel irradiated in several different known spectra, the resultant damage cross sections have been shown to be much more precise than currently available theoretical cross sections.

Recently a large-scale effort has been under way with the joint sponsorship of NRL, Battelle-Northwest, and Westinghouse Nuclear Energy Systems to evaluate the accuracy of several reactor physics codes for prediction of the neutron spectrum and flux intensity at different locations associated with a simulated reactor pressure vessel wall and thermal shield. The experimental arrangement provides for the irradiation of neutron flux detectors at seven locations simulating (1) an accelerated surveillance location between the reactor core and a 1-in.-thick "thermal" shield, (2) a vessel wall surveillance location, and (3) five additional locations within an 8-in.-thick steel test block that simulates the pressure vessel wall. Spectra will be calculated for all seven irradiation locations with the DTF-IV transport code, the P1MG code [20], and the 2DB diffusion code [21] and compared with those obtained from multiple foils using the SAND-II computer iterative technique. The results of this series of tests should provide a valuable basis for selection of codes and techniques to be used for pressure vessel surveillance programs.

In addition, mechanical property changes will be measured on test specimens included at the seven locations for comparison with the changes predicted by the various methods. These data will also be used as input to the SAND-II program to improve the damage cross sections for pressure vessel steels, thus increasing the precision obtainable in projections of damage for future surveillance programs.

Spectral Detectors

The selection of neutron detector materials [22] must be considered on the basis of the relationship of their cross sections and the spectrum. The goal is to select materials that will provide coverage of all segments of a neutron spectrum plus some small amount of redundancy to preclude errors arising from a single inconsistent datum. Where possible, a short-term irradiation should be employed to activate the detectors used for spectral determination or adjustment. The optimum set of detectors will be different for different irradiation conditions and spectra; therefore, the following discussion of specific detector materials is included as a general guide rather than as a specific recommendation. Shown in Fig. 4 is a differential

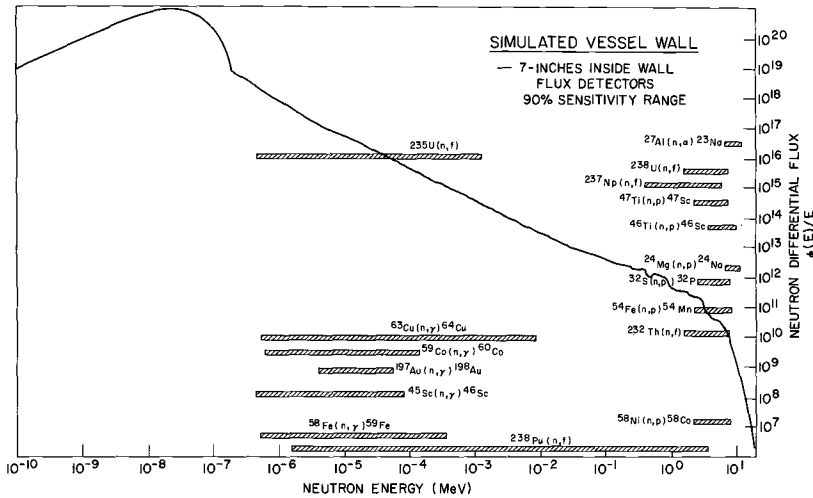


FIG. 4—Schematic representation of the energy range of neutrons effective in causing 90 percent of the activation of a series of materials used for neutron flux detection. The reference spectrum represents deep penetration into a pressure vessel wall.

plot of a neutron spectrum representing deep penetration into a pressure vessel wall [23]. Superimposed are the energy response ranges for a number of different reactions of general use in neutron dosimetry. The shaded regions represent the energy range of neutrons causing 90 percent of the indicated reactions.

For thermal neutron detection [24], cadmium covered cobalt can be used with bare cobalt to obtain the thermal flux by the “difference” method. Resonance detectors include cadmium covered cobalt (from the cadmium difference thermal flux determination above). Additionally, the reaction $^{109}\text{Ag}(n, \gamma)^{110\text{m}}\text{Ag}$ is of significant value as a resonance detector because, like the cadmium covered cobalt, it will be activated by the intermediate-energy neutrons, but the silver does not require the cadmium to be effective. Bare silver and cobalt detectors can thus be used for the “two-foil” method for thermal flux determinations [25–27] as a check against the bare and cadmium covered cobalt difference method.

Resonance activity for the $^{58}\text{Fe}(n, \gamma)^{59}\text{Fe}$ reaction is very useful, because, unlike most n, γ reactions, it has a broad response range, thus providing a valuable contribution to establishing the flux intensity level in the intermediate energy range. The two fission detectors, ^{235}U and ^{238}Pu , are valuable because they cover the energy range between the thermal and fast neutrons. This is particularly so for the ^{238}Pu materials as it covers a broad range reaching the 1-MeV level. Fast neutron detectors should be included to help preclude errors in this important energy range; ^{237}Np , ^{238}U , nickel, iron, and titanium are commonly used [28] for this purpose.

Fluence Monitoring

The overall accuracy of neutron fluence measurements is of course dependent on knowledge of the neutron spectrum. However, if the fluence is derived from a single detector material, or even several if their cross sections cover only a narrow energy response range, a possible source for error is introduced. It is thus valuable to include a variety of neutron detector materials in any experiment to be irradiated for long time periods corresponding to requirements of reactor vessel dosimetry. The selection of materials is severely hampered, however, by the very nature of the irradiation environment.

Irradiations associated with the vessel wall of a reactor must be compatible with the elevated temperature (usually near 550 F (288 C)) and long irradiation periods, ranging over several years, that are common for reactor vessel surveillance programs. Reactor vessel research in general requires detector materials that will be sensitive to activation for these long periods and will retain to the time of analysis some degree of activity from early exposures. It is thus important in vessel surveillance of monitoring to have flux detectors of long half-lives so that the induced activity from early segments of power operations have not significantly decayed or been overcome by new activation from more recent power operations. It is especially important that the reactor operating history be carefully retained and utilized in the fluence analysis. Direct correlation between neutron flux and reactor operating power can be of significant value if no significant changes are made throughout the monitoring period; some changes, for example the type or enrichment of fuel elements, however, can invalidate such correlations.

To help minimize the possibility of errors arising from use of spectrum calculations for extrapolations, the distance between the measurement location and the extrapolation location should be kept as small as possible [29]. For extrapolations to the reactor vessel wall, it is convenient to have a flux value from a detector irradiated in a vessel wall surveillance capsule or from a flux detector wire enclosed inside a tube placed adjacent to the reactor vessel wall. A flux detector tube alongside a reactor vessel wall was used for analysis of the SM-1A reactor [30] with great success.

Summary and Conclusions

For an accurate analysis of a reactor vessel condition, four factors are needed.

1. The neutron spectrum must be well established for each surveillance location. Reactor physics codes are generally used for determining neutron spectra in reactor locations outside the core, although the codes now available were not intended for deep penetration problems such as pressure vessels. Therefore, it is important that spectra obtained from reactor phys-

ics calculations be validated or adjusted with data from flux detector measurements. Spectrum determinations can also be made by computer iterative analysis of a series of many neutron flux detector materials simultaneously exposed to the reactor flux at a specific location. These results should be considerably more accurate, but only if an appropriate set of detectors is selected.

2. Accurate neutron fluence monitoring must be accomplished for surveillance irradiation periods to obtain a thorough knowledge of the trends in radiation induced damage in the reactor vessel steel as a function of fluence. Monitors which have long half-lives and provide coverage of the entire reactor spectrum should be selected.

3. Reactor physics calculations must be used to extrapolate the spectrum and fluence from the closest measurement position to the pressure vessel. Additional research is required to assure the accuracy of such extrapolations for deep penetration problems such as at a reactor vessel wall. It may be necessary to recommend in the future that a large-scale effort be undertaken to write a new code that will properly extrapolate spectra and fluence for this type of situation. Research studies are now under way that may well provide the basis for judging the merits of such an effort.

4. Finally, the materials property change must be calculated at the position of interest; if a macroscopic damage cross section has been obtained for the steel, the property change can be calculated from the above data. Although theoretical displacement cross sections or damage models could be used in lieu of the semiempirical damage cross sections, one should not expect the same degree of accuracy from such a substitution.

The procedure outlined above is believed to result in the highest accuracy obtainable at the present time; however, the degree of accuracy will depend on the particular circumstances and procedures used at each step. Additional research is required before the accuracy limits can be specified.

Acknowledgments

This paper was prepared, in part, as a contribution from ASTM Committee E-10 Subcommittee V on Neutron Dosimetry. Many of the research results discussed were taken from cooperative studies between the Naval Research Laboratory and Battelle-Northwest. The long-term support provided for these studies by the Fuels and Materials Branch, U.S. Atomic Energy Commission, the Army Nuclear Power Field Office, and the Office of Naval Research is acknowledged with appreciation.

References

- [1] Sterne, R. H., Jr., and Steele, L. E., *Nuclear Engineering and Design*, NEDEA, Vol. 10, 1969, pp. 259-307.
- [2] Serpan, C. Z., Jr., and Hawthorne, J. R., "Yankee Reactor Pressure-Vessel Surveillance: Notch Ductility Performance of Vessel Steel and Maximum Service Fluence Determined from Exposures During Cores II, III, and IV," NRL Report 6616, Naval Research Laboratory, 29 Sept. 1967.

- [3] Serpan, C. Z., Jr., and Watson, H. E., *Nuclear Engineering and Design*, NEDEA, Vol. 11, 1969, pp. 393-415.
- [4] Serpan, C. Z., Jr., and McElroy, W. N. in *Radiation Damage in Reactor Materials*, STI/PUB/230, International Atomic Energy Agency, Vienna, 1969.
- [5] Lathrop, K. D., "DTF-IV, A Fortran-IV Program for Solving the Multigroup Transport Equation with Anisotropic Scattering," USAEC Report LA-3373, Los Alamos Scientific Laboratory, Los Alamos, N.M., 1965.
- [6] Duane, B. H., "Neutron and Photon Transport Plane-Cylinder-Sphere (GE-ANPD) Program S Variational Optimum Formulation," XDC-9-118, General Electric Co., Cincinnati, Ohio, 1959.
- [7] Bohl, H. et al, "P3MG—A One-Dimensional Multigroup P-3 Program for the Philco-2000 Computer," WAPD-TM-272, Bettis Atomic Power Laboratory, Pittsburgh, Pa., 1963.
- [8] Serpan, C. Z., Jr., "Notch Ductility and Tensile Property Evaluation of the PM-2A Reactor Pressure Vessel," NRL Report 6739, Naval Research Laboratory, 19 June, 1968; also in *Irradiation Effects in Structural Alloys for Thermal and Fast Reactors*, ASTM STP 457, American Society for Testing and Materials, 1969, pp. 135-155.
- [9] Shure, K. and Oberg, C. T., *Nuclear Science and Engineering*, NSENA, Vol. 27, 1967, pp. 348-359.
- [10] "Discussion of Computer Codes for Determining Neutron Flux Spectra by Multiple Foil Measurements," Tentative Computer Code Information Document, American Society for Testing and Materials, to be published in 1970.
- [11] McElroy, W. N. et al, "A Computer-Automated Iterative Method for Neutron Flux Spectra Determination by Foil Activation," AFWL-TR-67-41, Vols. I, II, III, and IV, Air Force Weapons Laboratory, Albuquerque, N.M., Sept. 1967.
- [12] Simons, R. L. and McElroy, W. N., "Evaluated Reference Cross Section Library for SAND-II," Battelle-Northwest Laboratory report (pending publication).
- [13] Jenkins, J. D., *Transactions of the American Nuclear Society*, TANSA, Vol. 13, No. 1, 1970, p. 251.
- [14] Rossin, A. D., "Dosimetry for Radiation Damage Studies," ANL-6826, Argonne National Laboratory, Argonne, Ill., March 1964.
- [15] Shure, K., "Radiation Damage Exposure and Embrittlement of Reactor Pressure Vessels," WAPD-TM-471, Bettis Atomic Power Laboratory, Pittsburgh, Pa., Nov. 1964.
- [16] Dahl, R. E. and Yoshikawa, H. H., *Nuclear Science and Engineering*, NSENA, Vol. 21, 1965, p. 312.
- [17] Sheely, W. F., *Nuclear Science and Engineering*, NSENA, Vol. 29, 1967, pp. 165-176.
- [18] Russcher, G. E., "Calculated Damage Functions for Determining Irradiation Effectiveness," BNWL-1093, Battelle-Northwest, Richland, Wash., Sept. 1969.
- [19] McElroy, W. N., Dahl, R. E., Jr., and Serpan, C. Z., Jr., *Nuclear Applications and Technology*, NUATA, Vol. 7, Dec. 1969, pp. 561-571.
- [20] Bohl, H. et al, "PIMG—A One-Dimensional Multigroup P-1 Code for the IBM 704," WAPD-TM-135, Bettis Atomic Power Laboratory, Pittsburgh, Pa., July 1969.
- [21] Little, W. W., Jr., and Hardie, R. W., "2DB, A Two Dimensional Diffusion-Burnup Code for Fast Reactor Analysis," BNWL-640, Battelle-Northwest, Richland, Wash., 1968.
- [22] ASTM Tentative Method for Measuring Neutron Flux by Radioactivation (E 261 - 65 T), *Annual Book of ASTM Standards*, Part 30.
- [23] Private communication with R. L. Simons and W. N. McElroy, Battelle-Northwest, Richland, Wash., May 1970.
- [24] ASTM Tentative Method for Measuring Thermal Neutron Flux by Radioactivation Techniques (E 262 - 65 T), *Annual Book of ASTM Standards*, Part 30.
- [25] Hart, R. G., Bigham, C. B., and Miller, F. C., "Silver 109 as an Epithermal Index Monitor for Use with Cobalt Flux Monitors," CRDC-1083, Atomic Energy of Canada, Ltd., Chalk River, Ontario, April 1962.

- [26] Cabell, M. J. and Wilkins, M., "Routine Use of Silver Cobalt Activity Ratio Method to Determine Epithermal Indices for Large Neutron Dose Irradiation," AERE-5122, United Kingdom Atomic Energy Authority, Harwell, Feb. 1966.
- [27] Cabell, M. J. and Wilkins, M., "A Comparison of Pu-240 and Ag-109 as Epithermal Index Monitors for Long Irradiation," AERE-R-4866, United Kingdom Atomic Energy Authority, Harwell, April 1965.
- [28] Barry, K. M. and Corbett, J. A., *Transactions of the American Nuclear Society*, TANSAS, Vol. 13, No. 1, 1970, p. 431.
- [29] ASTM Recommended Practice for Surveillance Tests on Structural Materials in Nuclear Reactors (E 185 - 66), *Annual Book of ASTM Standards*, Parts 30 and 31.
- [30] Serpan, C. Z., Jr., and Steele, L. E., "Neutron Spectral Considerations Affecting Projected Estimates of Radiation Embrittlement of the Army SM-1A Reactor Pressure Vessel," NRL Report 6474, Naval Research Laboratory, 20 Sept. 1966.

DISCUSSION

*E. Landerman*¹—In the list of dosimeters, ^{237}Np and ^{238}U were not suggested for use in surveillance programs. Westinghouse has been using them successfully; K. M. Barry and J. A. Corbett have described their use in a recent ANS paper, "Measurement of Neutron Fluence by ^{237}Np and ^{238}U Fission Dosimeters."² Their results show that from test performance in dissimilar reactors such as the Saxton reactor and the Babcock and Wilcox test reactor (BAWTR), the combination of fission dosimeters, with the P₁MG Code to predict the neutron energy spectrum, yields fast neutron fluences in good agreement with values obtained from the ^{54}Fe monitors.

The data below are from the Saxton reactor:

Reaction	Fast Neutron Fluence, n/cm ² , $E > 1$ MeV
$^{237}\text{Np}(n,f)^{137}\text{Cs}$	1.18×10^{20}
$^{238}\text{U}(n,f)^{137}\text{Cs}$	1.17×10^{20}
$^{54}\text{Fe}(n,p)^{54}\text{Mn}$	1.15×10^{20}

Noting these good relationships, why were they not included and considered in this paper?

*A. D. Rossin*³—I wish to take exception to the statement in the third paragraph of this paper: "With present technology, the best alternative is to make mechanical property measurements on specimens irradiated at nearby accessible locations in the same reactor and extrapolate the mechanical property changes to the location of interest."

This statement is certainly not correct and is misleading to the reader. Any technique that extrapolates to another position in a reactor system could work equally well with any position in any materials testing reactor. The advantages of ease of handling, temperature control, better dosimetry, and factors of 10 to 1000 less irradiation time required because of higher flux levels available far outweigh the problems that go with surveillance.

¹ Fellow engineer, Westinghouse Nuclear Energy Systems, Pittsburgh, Pa. 15230.

² June 1970 Annual Meeting, *Transactions of the American Nuclear Society*, TANSAs, Vol. 13, No. 1, pp. 431-432.

³ Center for Environmental Studies, Argonne National Laboratory, Argonne, Ill. 60439.

Moreover, in order to design reactors there must be experimental evidence on the behavior of irradiated pressure vessel steel throughout the reactor lifetime. To date, designs have met requirements for safety analysis by substantial overdesign. The surveillance approach was accepted by review bodies several years ago as a backup to the limited experimental evidence. Unfortunately, there was no real basis for believing that surveillance would prove worthwhile. This paper notwithstanding, there is still no valid reason to believe that surveillance is either necessary or desirable. Surveillance offers evidence of good intentions on the part of the vendor and has the distinct short-term advantage of giving nothing to evaluate for many years. Hopefully, the design will turn out to have been conservative enough regardless of the findings.

What is still missing is adequate experimental evidence to support design calculations. Because the industry has accepted overdesign, neither it nor government has seen fit to support sufficient research to put this problem to bed.

Two additional points:

1. I might defend the RDU or Dt approach to this extent: the concepts work with any set of displacement cross sections, and results can easily be updated if a new and better set of cross sections is developed. As for a "damage unit scale in addition to the fluence scale," since the fluence scale fails to give the correlation required, who needs it?

The problem with use of an effective energy cutoff [16] is that to validate it for specific cases one must go through the whole damage model approach first, and then the effective energy cutoff limits the usefulness to the cases tested. Unfortunately, to those not familiar with radiation damage, the energy cutoff model gives the impression that only the neutrons with energy above that value cause the damage. This impression has led to much confusion in the past.

2. In practice, determination of neutron spectra turns out to be an experiment that takes substantial effort to perform and skill to interpret. It can be done in special locations, in test reactors, or in mockups, as described in the paper. For power reactors, for long-term irradiations, knowledge of flux and spectra at points of interest, whatever methods are used to determine it, can best be used along with operating history to determine fluence and damage.

What is needed by the power reactor industry at this stage is to get rid of surveillance. Specimens in reactors have broken loose creating potential safety problems. They add to cost, complicate flow patterns, and do not add to safety. Even with accelerated locations, they beg the question. If surveillance specimens predict vessel damage, a \$100 million operating plant is in a lot of trouble. The knowledge is needed early, not later on.

C. Z. Serpan, Jr. (authors' closure)—The discussion by Mr. Landerman is in reference to presentation of this paper which was a condensation of

papers by Serpan and by Odette and Ziebold. In the presentation, ^{237}Np and ^{238}U were omitted from the list of neutron flux detectors on the basis of a rather difficult analysis procedure required, in particular for ^{237}Np . It should be noted, however, that in this final version of the paper these two fission detectors are included.

The discussion by Dr. Rossin permits the continued airing of important divergent views on dosimetry, spectrum, and surveillance. The first comment refers to extrapolation of surveillance results and is not withdrawn by the authors. The statement has been refined in the text, however, to clarify the intent: surveillance irradiations should be made as close as practicable to the location of interest, as this effectively minimizes spectrum, temperature, and flux differences, hence, a significant reduction in potential errors. As this was the original intent of the statement, it was reemphasized in the paragraph preceding the summary and conclusions section. Damage models, trends, approximations, error bands are not needed to evaluate data that have been obtained from irradiation at, or virtually at, the location of interest. As Dr. Rossin says, "there must be experimental evidence on the behavior of irradiated pressure vessel steel through the reactor lifetime." Where better to obtain such *realistic*, not accelerated nor test reactor, data? If surveillance is no good, what alternative does the responsible reactor operator have *today* to assess the future potentially frangible condition of his reactor vessel? Research has been and is continuing to be conducted on this very topic. If the past ten or twelve years of research have provided as little useful information as suggested by Dr. Rossin, then what will come from ten or twelve more years of research?

The question of an energy "cutoff" such as " $>1\text{ MeV}$ " is one that has been with us since the onset of radiation effects testing. Dr. Rossin was one of the first to point out the shortcomings of the concept and, in general, these are recognized and accepted. Nevertheless, no agreement has yet been reached regarding what to use in place of a threshold. The fact is that research data must be placed into terms that can be understood and used by design and operating personnel. Elegant and complicated analysis techniques simply will not be used on a daily working level basis. Thus, it is the obligation of those working in this field not only to mold their techniques for simple use but also to provide reference marks along the way in old, familiar terms to help guide the uninitiated.

It is felt that great progress has been made toward understanding the radiation embrittlement problem and toward solving it. I need only point to the paper by Hawthorne in this volume showing the dramatically reduced embrittlement potential demonstrated on a 30-ton heat of A533B pressure vessel steel produced by composition control. This shows what kind of experimental evidence can and is being developed to support the future design of reactors.

R. A. Wullaert,¹ D. R. Ireland,² and A. S. Tetelman³

Radiation Effects on the Metallurgical Fracture Parameters and Fracture Toughness of Pressure Vessel Steels

REFERENCE: Wullaert, R. A., Ireland, D. R., and Tetelman, A. S., “Radiation Effects on the Metallurgical Fracture Parameters and Fracture Toughness of Pressure Vessel Steels,” *Irradiation Effects on Structural Alloys for Nuclear Reactor Applications, ASTM STP 484*, American Society for Testing and Materials, 1970, pp. 20–41.

ABSTRACT: The effect of radiation on tensile properties, notch bend properties, and fracture toughness was determined on A212B steel from the Pathfinder reactor surveillance program and on A533B steel from the U.S. AEC Heavy Section Technology program. Impact tests were performed on an instrumented Charpy machine which provided load-deflection data in addition to energy absorption data. Valid fracture toughness values were obtained from precracked Charpy specimens.

The results of the notch bend tests on the irradiated steels indicated that the radiation induced increase in the ductile-brittle transition temperature was mainly due to the large radiation induced increase in the friction stress. Radiation reduced the strain rate sensitivity of the yield stress but did not change the temperature dependence of the yield stress. The microscopic cleavage strength was essentially unaffected by irradiation. The relationships between the metallurgical fracture parameters (Cottrell-Petch) and the ductile-brittle transition temperature (*DBTT*) and fracture toughness (K_{Ic}) were established. These relationships were used to predict the radiation induced change in fracture toughness (both *DBTT* and K_{Ic}) from a knowledge of the effect of radiation on metallurgical fracture parameters.

KEY WORDS: irradiation, neutron irradiation, radiation effects, impact tests, tension tests, fracture properties, fracture strength, notch strength, tensile properties, yield strength, brittle fracturing, ductility, pressure vessels, structural steels

There are two approaches to determining the effect of radiation on the fracture toughness of pressure vessel steels: (1) the shift in the ductile-

¹ Director, Materials Engineering, Effects Technology, Inc., Santa Barbara, Calif. 93105.

² Associate chief, Mechanical Metallurgy Division, Battelle Memorial Institute, Columbus, Ohio 43201.

³ Professor and chairman, Materials Department, University of California, Los Angeles, Calif. 90053.

brittle transition temperature *DBTT* and (2) the change in the fracture toughness K_{Ic} . The modern theories of fracture (Cottrell-Petch) define key metallurgical fracture parameters such as friction stress σ_i , grain size d , grain size dependence of the yield stress, k_y , and surface energy or plastic work of microcrack propagation, γ . The effect of radiation on most of these metallurgical fracture parameters has been previously studied, but the results have not been directly linked with the radiation induced change in fracture toughness. The purpose of this paper is to establish the relationships between the key metallurgical fracture parameters and the *DBTT* and K_{Ic} . These relationships are used to predict the radiation induced change in fracture toughness (both *DBTT* and K_{Ic}) from a knowledge of the effect of radiation on metallurgical fracture parameters.

Fracture Theory

Metallurgical Fracture Parameters

To understand how radiation affects the ductile-brittle transition temperature (*DBTT*), it is first necessary to define the metallurgical fracture parameters that are sensitive to radiation and then establish a link between these fracture parameters and the *DBTT*. Hall [1]⁴ and later Petch [2] proposed a relationship between the yield stress σ_y and grain size d of the form

$$\sigma_y = \sigma_i + k_y d^{-1/2} \dots \dots \dots (1)$$

where σ_i is the friction stress and k_y is a constant which determines the grain size dependence of the yield stress. Using the Petch equation for yielding, and assuming that initial crack growth is the critical fracture step, Cottrell [3] predicted that unstable crack growth will occur when

$$\sigma_f = \frac{\beta G \gamma}{k_y} d^{-1/2} \dots \dots \dots (2)$$

where σ_f is the fracture stress when the critical event in the fracture of a tension specimen is microcrack propagation, β is a geometrical factor that depends on stress state, G is the shear modulus, and γ is the effective surface energy for fracture, or the plastic work term. Equations 1 and 2 encompass what is generally referred to as the Cottrell-Petch theory of fracture. The two key metallurgical fracture parameters are σ_y and σ_f , which are functions of the parameters σ_i , k_y , d , and γ . Changes in the shear modulus are usually very small, so this term will not be considered.

Radiation can influence the fracture behavior through the changes it produces in the parameters σ_i , k_y , and γ . The primary effect of fast neutron damage on iron and mild steels is to produce a large increase in the athermal

⁴ Italic numbers in brackets refer to the list of references at the end of this paper.

component of the friction stress σ_i [4-10]. The temperature dependence of the yield stress $d\sigma_y/dT$ is not altered by neutron irradiation [4,5,6]. For mild steels [4,5,7,8] and silicon iron [10], k_y has been found to be insensitive to radiation. Some workers [9] have noted for pure iron that k_y is unchanged by irradiation, but others [5,6] have observed that irradiation produces a substantial decrease in k_y . Johnson et al [11] have reviewed the effect of radiation on k_y for pure iron, mild steel, silicon iron, and molybdenum and conclude that the most reliable observations indicate that radiation decreases k_y . Another possible explanation [12] of this effect is that σ_i is changed more by irradiation in coarse-grained rather than fine-grained material (owing perhaps to differences in substructure or defect annealing at grain boundaries in a fine-grained material). This would cause the slope of a σ_y versus $d^{-1/2}$ plot to decrease and give the impression that k_y was lowered by irradiation. Although the situation in pure iron and molybdenum remains ambiguous at the moment, there is little doubt that in low-carbon and low-alloy steels all changes in σ_y upon irradiation are due to changes in σ_i .

Very little is known about the effect of radiation on γ . Tetelman [12] has shown that γ depends on the temperature dependence of the dislocation velocity, the initial density of mobile dislocations, and the dislocation multiplication process. In general, γ will decrease if the ability for homogeneous plastic deformation is reduced. Since radiation damage is known to produce restricted slip or channeling [13], it would appear that radiation should decrease γ .

From the above discussion it is apparent that radiation damage can affect more than one parameter in the equations for yielding and fracture. To understand the effect of radiation on the *DBTT*, the effect of radiation on σ_y and σ_f (and thus σ_i , k_y , and γ) as a function of temperature must be known.

Ductile-Brittle Transition Temperature in Tension

The *DBTT* in an unnotched tension specimen of mild steel is determined by the yield stress σ_y , the microcleavage fracture stress σ_f , and their dependence on the above fracture parameters. Figure 1a gives a schematic diagram of the temperature dependence of σ_y and σ_f for an unnotched tension specimen of mild steel: σ_y shows the strong temperature dependence typical of body centered cubic metals, and σ_f is only slightly temperature dependent; σ_f' is the true stress at which ductile fracture occurs. The highest temperature at which $\sigma_y = \sigma_f$ is the brittleness transition temperature T_D . At $T \leq T_D$, $\sigma_f = \sigma_y$ since yielding is a prerequisite for fracture. Thus fracture occurs when the stress level reaches σ_y for temperatures below T_D .

Above T_D fracture occurs when the stress level in the material reaches σ_f (a critical stress criterion for fracture). Strain hardening, $\Delta\sigma$, is required

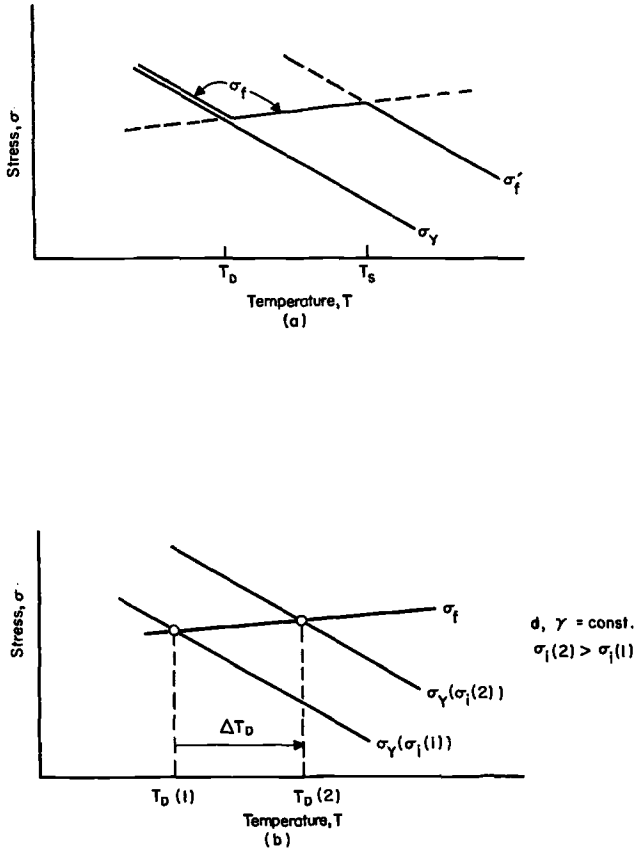


FIG. 1—Effect of temperature on the yield stress σ_y , cleavage fracture stress σ_f , and ductile fracture stress σ_f' : (a) schematic of tension data for mild steel, (b) schematic of the increase in T_D produced by an increase in friction stress σ_i .

to raise the stress level from σ_y to σ_f :

$$\sigma_f = \sigma_y + \Delta\sigma$$

or

$$\sigma_f = \sigma_y + \epsilon_f \frac{d\sigma}{d\epsilon} \quad \text{at } T > T_D \dots \dots \dots (3)$$

where ϵ_f is the cleavage fracture strain and $d\sigma/d\epsilon$ is the strain hardening rate. As the temperature is raised above T_D , σ_y decreases and increasing strain is required to raise σ_y to σ_f by strain hardening. At a temperature T_s , the initiation transition temperature, the ductile fracture strain ϵ_s is reached before the cleavage fracture strain ϵ_f and the material fractures in a ductile manner at σ_f' . T_s is the highest temperature at which cleavage cracks can be nucleated before fracture begins.

Since at T_D

$$\sigma_f = \sigma_y \dots \dots \dots (4)$$

or at T_s

$$\sigma_f = \sigma_y + \epsilon_f \frac{d\sigma}{d\epsilon} \dots \dots \dots (3)$$

a change in the value of σ_y or σ_f will change the *DBTT*. Changes in σ_f and σ_y are brought about by changes in the parameters σ_i , k_y , d , G , γ , $d\sigma/d\epsilon$, and ϵ_f (Eqs 1, 2, and 3). For example, if radiation increases σ_i and the other fracture parameters are unaffected, then σ_y will increase and σ_f will not change. This will result in an increase in the *DBTT* (T_D), as shown in Figure 1b.

Ductile-Brittle Transition Temperature in Notched Bending

A notch produces an embrittling effect by raising the tensile stress level below the notch by increasing the effective strain rate, by concentrating the strain, and primarily by introducing a triaxial stress state below the root of the notch. The effect of a notch on the *DBTT* is shown in Fig. 2. Strain rate and strain hardening effects raise σ_y to σ_y^* and plastic constraint raises σ_y^* to $K_{\sigma(p)}\sigma_y^*$, where $K_{\sigma(p)}$ is the plastic stress concentration factor. $K_{\sigma(p)}$ is a function of the plastic zone size R below a notch and the root radius ρ only and, according to Hill [14], is given by

$$K_{\sigma(p)} = 1 + \ln(1 + R/\rho) \dots \dots \dots (5)$$

The effect of a notch is to increase the *DBTT* from T_D to $T_{D(N)}$.

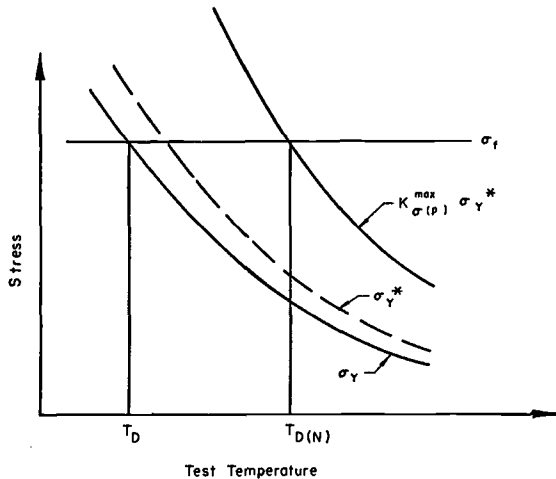


FIG. 2—The effect of increased strain rate and a triaxial stress state on the brittleness transition temperature T_D .

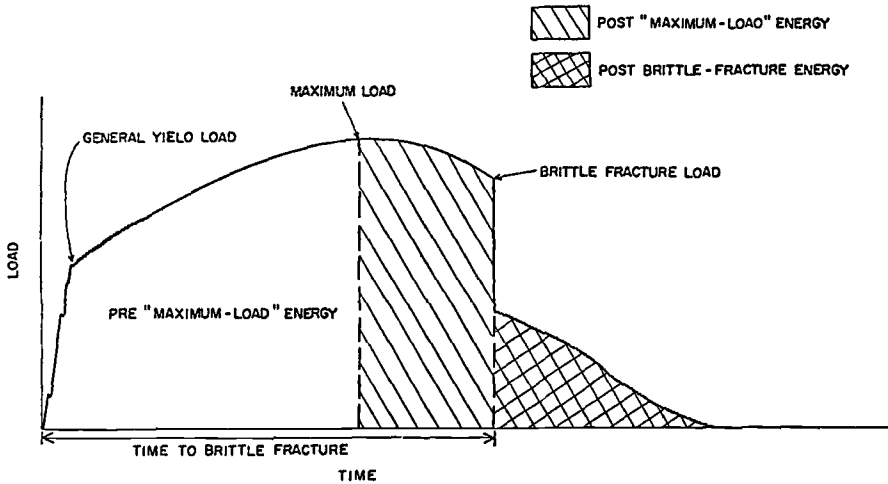


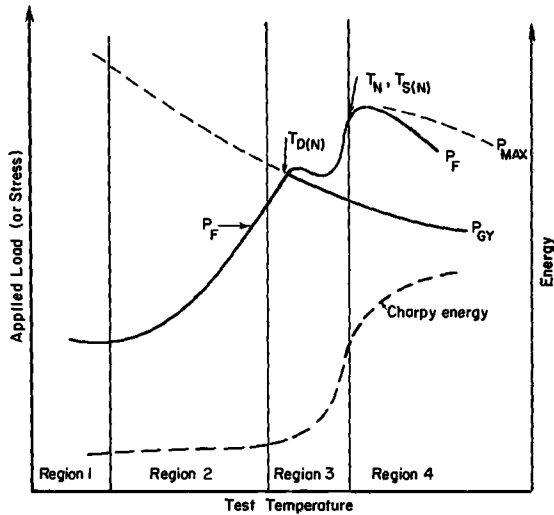
FIG. 3—An idealized load-time trace for an impacted Charpy V notch specimen.

Instrumented Charpy Test

To relate the metallurgical fracture parameters and fracture criteria that have been discussed to the standard Charpy energy curves and the *DBTT* determined from these curves, the yield stress and cleavage fracture stress must be measured in the Charpy test. The loads involved during impact can be obtained by instrumenting the Charpy hammer with strain gages so that the hammer is essentially a load cell. The details of this technique have been reported previously [15].

The additional information obtained from the instrumented Charpy test is general yield load P_{GY} (plastic yielding across the entire cross section of the Charpy specimen), the maximum load P_{max} , the brittle fracture load P_F , and the time to brittle fracture, see Fig. 3. Also, the area under the load-time curve corresponds to the total energy absorbed, which is the only data obtained in a normal uninstrumented Charpy test. The instrumented test, however, allows one to separate the energy absorbed into (1) the energy required to initiate ductile or brittle fracture (pre-maximum load energy), (2) the energy required for ductile tearing (post-maximum load energy), and (3) the energy associated with shear lip formation (post-brittle fracture energy), as shown in Fig. 3.

In a normal Charpy impact study, the energy absorbed is determined as a function of temperature to obtain the Charpy impact curve and the ductile-brittle transition temperature. The instrumented Charpy test also gives the information shown in Fig. 3 as a function of temperature. An example of this type of information is shown in Fig. 4. Various investigators [16–20] have developed theories which permit a detailed analysis of the load-temperature diagram.



Region 1 - Local yielding ($\sigma_y^* > \sigma_f^*$)
 $\sigma_F = \frac{\sigma_y^*}{K_\sigma}$

Region 2 - Plastic constraint ($\sigma_y^* < \sigma_f^*$)
 $\sigma_{yy}^{max} = K_{\sigma(p)} \sigma_y^* \quad \sigma_y^* = \sigma_f^*$

Region 3 - Plastic constraint plus strain hardening
 $[K_{\sigma(p)}^{max} \sigma_y^* < \sigma_f^* \text{ FOR } \frac{P}{P_{GY}} > 0.8]$
 $K_{\sigma(p)}^{max} (\sigma_y^* + \epsilon_f \frac{d\sigma}{d\epsilon}) = \sigma_f^*$
 $\epsilon_f = \frac{\sigma_f^* - K_{\sigma(p)}^{max} \sigma_y^*}{K_{\sigma(p)} \frac{d\sigma}{d\epsilon}}$

Region 4 - Fibrous initiation
 $\epsilon_f > \epsilon_s$

FIG. 4—The variation in general yield load P_{GY} , fracture load P_F , and energy absorbed with temperature for a Charpy specimen in three-point bending.

This diagram can be divided into four regions of fracture behavior where different fracture parameters are involved. The approach used to define the fracture criteria for each region is similar to that presented for the smooth bar tension test. The equations developed are similar to Eqs 3 and 4 except for the effects of a notch (σ_y^* , $K_{\sigma(p)}$). The fracture criterion for each region is shown in Fig. 4, and a detailed development of these equations is given in Ref 15.

For the purposes of this paper, regions 2 and 3 are of most interest. In region 2, $\sigma_y^* < \sigma_f^*$, where σ_f^* is the microcleavage fracture stress below the notch. Plastic deformation is required to raise σ_y^* to σ_f^* . This additional deformation, accomplished through the growth of a plastic zone, increases the maximum tensile stress below the notch (σ_{yy}^{max}) through plastic constraint ($K_{\sigma(p)}$, Eq 5) until fracture occurs at σ_f^* , that is

$$\sigma_{yy}^{max} = K_{\sigma(p)} \sigma_y^* = \sigma_f^* \dots \dots \dots (6)$$

Wilshaw and Pratt [16] found that in mild steel Charpy V notch specimens $K_{\sigma(p)}$ increased until $P/P_{GY}=0.8$, where $K_{\sigma(p)}^{max}=2.18$ and remained constant.

When the temperature is increased further, σ_y^* decreases to such an extent that plastic constraint is no longer able to raise σ_y^* to σ_f^* . This is the beginning of region 3, where strain hardening in addition to plastic constraint is required to produce cleavage fracture. Thus

$$K_{\sigma(p)}^{max}\sigma_y^* < \sigma_f^* \quad \text{for } P/P_{GY} > 0.8$$

and

$$K_{\sigma(p)}^{max}(\sigma_y^* + \Delta\sigma) = \sigma_f^*$$

or, since

$$\Delta\sigma \sim \epsilon_f \frac{d\sigma}{d\epsilon}$$

$$K_{\sigma(p)}^{max} \left(\sigma_y^* + \epsilon_f \frac{d\sigma}{d\epsilon} \right) = \sigma_f^* \dots \dots \dots (7)$$

A technique for calculating the cleavage strength below a notch (σ_f^*) has been developed by Tetelman [17] and summarized by Wullaert [15]. The temperature at which $P/P_{GY}=0.8$ represents the highest temperature at which plastic constraint alone can produce fracture, and $K_{\sigma(p)} = K_{\sigma(p)}^{max} = 2.18$. Using the fracture criterion for region 2,

$$\sigma_f^* = K_{\sigma(p)}\sigma_y^*$$

or

$$\sigma_f^* = 2.18\sigma_y^* \text{ at } P/P_{GY} = 0.8 \dots \dots \dots (8)$$

Green and Hundy [21] have calculated the relationship between σ_y^* and P_{GY} for the case of a Charpy V notch specimen loaded in three-point bending. They assumed plane strain conditions and an ideal plastic material and showed that

$$\sigma_y^* = 33.3P_{GY} \dots \dots \dots (9)$$

where σ_y is in psi and P_{GY} is in pounds. Combining Eqs 8 and 9, the cleavage fracture stress is given by

$$\sigma_f^* = 72.5P_{GY} \text{ at } P/P_{GY} = 0.8 \dots \dots \dots (10)$$

and σ_f^* is considered independent of temperature and strain rate.

Thus, by the use of the instrumented Charpy impact test plus the use of modern notch bend theories, the effect of radiation on the key metallurgical fracture parameters σ_y^* and σ_f^* can be measured. The radiation induced change in these parameters can in turn be related to the effect of radiation on the Cottrell-Petch fracture parameters. A distinct advantage of this approach is the fact that changes in the above parameters can be

related to service performance through the well established correlation between service failures and Charpy energy values.

Results and Discussion

The reactor pressure vessel steels studied in this investigation were A212B from a reactor surveillance program and A533B from the U.S. AEC Heavy Section Steel Technology program. The effect of radiation on tensile properties, Charpy V notch bend properties, and fracture toughness was determined. The interrelationship between the effect of radiation on tensile properties (σ_v , σ_f), notch bend properties ($DBTT$), and fracture toughness (K_{Ic}) was established.

Radiation Effects on the DBTT

Instrumented Charpy impact tests were performed on A212B steel irradiated to fluences of 5.8×10^{16} and 9.4×10^{18} n/cm², $E > 1$ MeV, at approximately 260 C. The Charpy V notch specimens were irradiated in the Pathfinder reactor as part of a surveillance study [22]. Unirradiated material from the same heat of A212B steel as the irradiated material was not available for instrumented Charpy testing, so unirradiated Charpy specimens from an ASTM correlation heat of A212B were tested. A preliminary comparison of the unirradiated material with the material irradiated to a fluence of 9.4×10^{18} n/cm² has been reported [15].

Recently, additional irradiated specimens of A212B steel from the Pathfinder surveillance capsules were tested on the instrumented Charpy impact machine. The Charpy energy curves and the load-temperature information

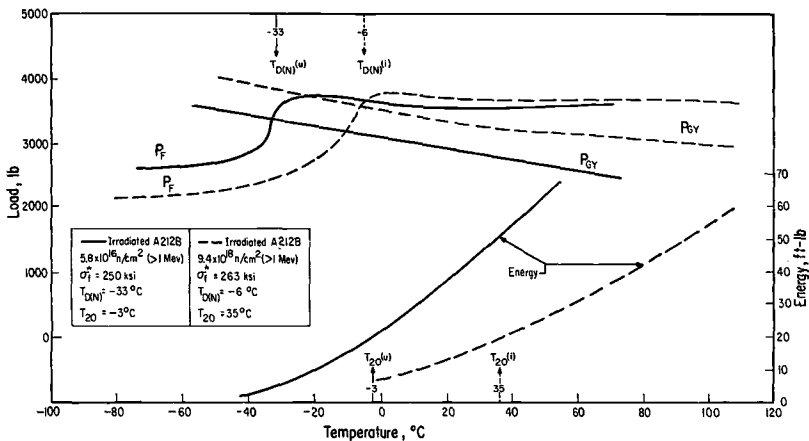


FIG. 5—Comparison of unirradiated and irradiated A212B showing the increase in the brittleness transition temperature T_{DN} , the 20-ft-lb transition temperature T_{20} , and the general yield load produced by irradiation.

TABLE 1—Summary of the effect of radiation on the yield stress (σ_y), microcleavage fracture stress (σ_f^*), and ductile-brittle transition temperature (DBTT) of A212B steel irradiated at ~ 260 C.

Fluence, n/cm ² , $E > 1$ MeV	σ_y , ksi (25 C)		σ_y (Dynamic)	σ_f^* , ksi
	Static ($\sim 10^{-2}$ s ⁻¹)	Dynamic ($\sim 10^3$ s ⁻¹)	σ_y (Static)	
5.8×10^{16}	43.1	94.3	2.18	250
9.4×10^{18}	67.0	108.0	1.61	263

Fluence, n/cm ² , $E > 1$ MeV	DBTT (20 ft·lb), T_{20} , deg C		Brittleness, $T_{D(N)}$, deg C	$\Delta T_{D(N)}$.
		ΔT_{20}		
5.8×10^{16}	-3	...	-33	...
9.4×10^{18}	35	38	-6	27

obtained from the instrumented Charpy tests are shown in Fig. 5. The specimens irradiated to the low fluence of 5.8×10^{16} n/cm² can essentially be considered unirradiated material; these Charpy results are considered base line data for this particular heat of A212B steel. Figure 5 then gives a reasonable indication of the effect of radiation on a given heat of A212B steel.

Table 1 is a summary of the results on irradiated A212B steel. The static yield stress values were obtained from tension tests, and the dynamic values were calculated from the general yield load using Eq 9. The microcleavage fracture stress was calculated (Eq 10) from P_F and P_{GY} values obtained at the temperature where $P/P_{GY} = 0.8$. The calculated value of σ_f^* is assumed to be independent of temperature. The radiation induced increase in the DBTT was determined using both the brittleness transition temperature ($T_{D(N)}$) and the 20-ft·lb temperature (T_{20}). The results of the study are as follows:

1. Radiation increased the yield stress as measured in tension and notched bending.
2. Radiation reduced the strain rate sensitivity of the yield stress but did not significantly change the temperature dependence of the yield stress.
3. Radiation did not change the microcleavage fracture stress significantly.
4. Radiation increased $T_{D(N)}$ and T_{20} but not by the same amount.

Since the temperature dependence of the yield stress and the grain size d are not changed by radiation, the increase in the DBTT ($T_{D(N)}$) must be due to changes in k_y , γ , and the athermal component of σ_i . It has

already been shown that radiation increases σ_i and does not affect k_y in mild steels. The slight increase in σ_f^* produced by irradiation of A212B is consistent with the small increase in σ_f obtained from tension tests on irradiated A212B by Wechsler et al [25]. Chow et al [24] observed no change in σ_f for tension tests on irradiated iron.

The effect of radiation on γ has not been established. The γ of interest here is the plastic work associated with cleavage fracture in regions 2 and 3 of the load-temperature diagram. Thus the γ indirectly measured by this approach is for temperatures well below the upper shelf of the Charpy energy curve and should not be associated with the ability to absorb energy during ductile fracture on the upper shelf (region 4). The fact that σ_f^* is only slightly dependent on radiation indicates that the ratio γ/k_y is not very radiation sensitive (Eq 2). Since radiation does not change k_y in mild steels, γ must be unaffected by radiation. This indicates that the channeling or restricted slip observed in irradiated steels is of such a nature that it does not affect γ/k_y and does not produce less homogeneous deformation on a scale that affects the fracture process.

The fact that $\Delta T_{D(N)}$ and ΔT_{20} were not the same is evidence that the use of a foot-pound fix for determining the *DBTT* of irradiated materials may not be satisfactory. The particular foot-pound fix value used varies with the yield strength of a material [19]. The $T_{D(N)}$ temperature determined by notch bar bend (that is, instrumented Charpy) tests is sensitive to radiation induced changes in yield strength, whereas the foot-pound fix is based on the initial yield strength and does not take into account these changes. For example, the unirradiated A212B has a 20-ft·lb fix value associated with its yield strength of approximately 40,000 psi. The irradiated A212B has a yield strength of approximately 70,000 psi, and the appropriate *DBTT* fix value should be 30 ft·lb. However, the current methods for determining *DBTT* values from Charpy impact results do not consider the obvious change in the yield strength, and the 20-ft·lb value is used for irradiated material. The *DBTT* determined by instrumented Charpy techniques ($T_{D(N)}$) is a well defined measure of the actual fracture transition properties of the material. In addition, the values of σ_y^* and σ_f^* obtained from the instrumented Charpy test can be used to predict accurately the effect of radiation on the *DBTT* and fracture toughness K_{Ic} of pressure vessel steels.

Calculation of the Radiation Induced Shift in the DBTT

A relationship between the *DBTT* and σ_y^* , σ_f^* , and $d\sigma_y^*/dT$ had been derived [18] which accurately predicted the change in the *DBTT* of ferritic steels produced by changes in composition (carbon, nickel), microstructure (grain size, grain boundary carbides) and strain rate. The derivation of this equation is given in the Appendix. Calculations and experi-

ments were performed to determine if Eq 21 could be used to predict the radiation induced shift in the *DBTT*. For this purpose, the relationship is of the form

$$T_D(i) = T_D(u) + \frac{\sigma_f^*(u) - \sigma_f^*(i) - K_{\sigma(p)}[\sigma_y^*(u) - \sigma_y^*(i)]_{T_D(i)}}{K_{\sigma(p)} \left[\frac{d\sigma_y^*(u)}{dT} \right]_{\Delta T_D}} \quad (11)$$

where (u) refers to the unirradiated condition (condition 2, Eq 21) and (i) to the irradiation condition (condition 1, Eq 21). This equation was used to predict the change in the *DBTT* measured in tension, slow bend, and impact (instrumented Charpy).

Equation 11 was used to calculate the change in the *DBTT* for the A212B steel irradiated in the Pathfinder reactor. From Table 1, considering the material irradiated at 5.8×10^{16} n/cm² to be unirradiated, $T_D(u) = -33$ C, $T_D(i) = -6$ C, $\sigma_f^*(u) = 250,000$ psi, and $\sigma_f^*(i) = 263,000$ psi. The difference in the yield stress should be determined at $T_D(i)$. The P_{GY} values for the unirradiated and irradiated materials were determined at $T_D(i) = -6$ C from Fig. 5. These values were converted to σ_y^* values by use of Eq 9, and the values obtained were $\sigma_y^*(u) = 103,000$ psi and $\sigma_y^*(i) = 118,000$ psi. The temperature dependence of the unirradiated material should be determined in the range $T_D(u)$ to $T_D(i)$ (-33 to -6 C). From Fig. 5, $[d\sigma_y^*(u)/dT]_{\Delta T_D} = 292$ psi/deg C. Substituting the above values into Eq 11,

$$T_D(i) = -33 + \frac{(250,000 - 263,000) - 2.18(103,000 - 118,000)}{2.18(292)}$$

$$T_D(i) \text{ (calculated)} = -2 \text{ C}$$

The measured value of $T_D(i)$ was -6 C and the agreement between the calculated value and the measured value is considered quite good.

Equation 11 was also used to predict the radiation induced increase in the *DBTT* as measured by others in tension and notch bending (instrumented Charpy). The results of Chow et al [24] on irradiated Ferrovac E iron and Wechsler et al [25] on irradiated A212B steel were used to determine the usefulness of Eq 11 in predicting the radiation induced change in the *DBTT* measured in tension. The tensile properties of unirradiated and irradiated A212B steel obtained by Wechsler et al are shown in Fig. 6. Irradiation at 60 C to a fluence of 1×10^{19} n/cm² increased T_D from 56 K to 78 K (-217 C to -195 C) and increased σ_f from 150,000 psi to 165,000 psi. The yield strength increase at $T_D(i)$ is 41,000 psi, $d\sigma_y(u)/dT = 1210$ psi/deg C in the temperature region ΔT_D , and $K_{\sigma(p)} = 1$ for tension. It should be noted that for the case of radiation effects on the *DBTT* it is not necessary to measure $\sigma_y(u) - \sigma_y(i)$ at $T_D(i)$, since $d\sigma_y/dT$

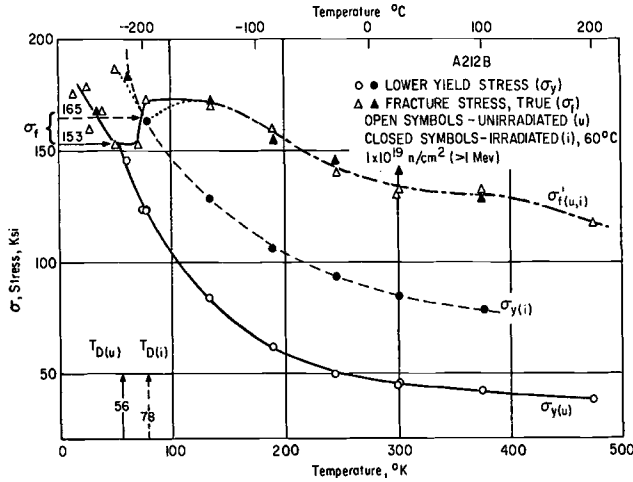


FIG. 6—Comparison of variations in yield stress and fracture stress for unirradiated and irradiated A212B evaluated by conventional tension testing techniques [25].

is not affected by radiation. Using the above values in Eq 11, a calculated value of $T_D = -193$ C is obtained and is very close to the measured value of $T_D = -195$ C. The radiation induced changes in the parameters used in Eq 11 are given in Table 2 for the previously discussed calculations on A212B steel. Also included in Table 2 are values for these parameters for irradiated Ferrovac E iron and A533B steel. Table 3 compares the calculated values of $T_D(i)$ with the experimentally determined values. It is clear that the change in the DBTT due to irradiation can be accurately

TABLE 2—Effect of radiation on the metallurgical fracture parameters used in Eq 11.

Steel	Fluence, n/cm ² , E > 1 MeV	$\Delta\sigma_f^*$, psi	$\Delta\sigma_y^*$, psi	$\frac{d\sigma_y^*(u)}{dT}$, psi/deg C
<i>Tension</i>				
Ferrovac E iron [24]				
0.016-mm grain size...	1×10^{19}	0	63 000	825
0.110-mm grain size...	1	0	54 000	940
A212B [25].....	1	12 000	41 000	1210
<i>Notch Bend</i>				
A212B.....	9.4×10^{18}	13 000	15 000	292
A533B [26].....	~ 9.5	0	14 000	318
	6	~ 18 000	41 500	318

TABLE 3—Calculated and measured radiation induced increases in the DBTT of various steels.

Steel	Fluence, n/cm ² , E > 1 MeV	Irradiation Temperature, deg C	T _D (u), deg C	T _D (i), deg C (calculated)	T _D (i), deg C (measured)
<i>Tension</i>					
Ferrovac E iron [24]					
0.016-mm grain size.....	1 × 10 ¹⁹	60 to 90	-263	-187	-183
0.010-mm grain size.....	1	60 to 90	-235	-177	-169
A212B [25].....	1	60	-217	-193	-195
<i>Notch Bend</i>					
A212B.....	9.4 × 10 ¹⁸	260	-33	-2	-6
A533B [26].....	~9.5	293	-44	0	0
	~6	68	-44	60	59

predicted for Ferravac E iron [24] and A212B steel [25] tested in tension and A212B and A533B [26] steel tested in notch bending.

The above comparison of calculated and measured radiation induced changes in the DBTT has served to establish the validity of Eq 11. However, the real value of Eq 11 is evident when all of the measured values are not available. For example, since radiation does not generally change σ_f^* significantly, $\Delta\sigma_f^* \simeq 0$ and

$$\Delta T_D = \frac{\Delta\sigma_y^*}{d\sigma_y^*(u)/dT} = A \Delta\sigma_y \dots \dots \dots (12)$$

which illustrates the importance of $d\sigma_y^*(u)/dT$ in the constant A for the empirical relationships that have been found between the radiation induced increase in the DBTT and the radiation induced increase in σ_y .

Since radiation does not change the temperature dependence of the yield stress, the radiation induced increase in σ_y can be measured at any temperature. A room temperature measurement of $\sigma_y^*(i)$ can be obtained by an instrumented Charpy or a dynamic tension test. A static tension test can also be used to measure $\sigma_y(i)$ (static), and $\sigma_y^*(i)$ can be calculated from a knowledge of the strain rate sensitivity of the irradiated material. The temperature dependence of the unirradiated material $d\sigma_y^*(u)/dT$ can be determined by performing any of the above tests as a function of temperature. Thus, from a knowledge of $d\sigma_y^*(u)/dT$ before irradiation, and a single measurement of $\sigma_y^*(i)$ after irradiation, the radiation induced shift in the DBTT can be predicted if $\Delta\sigma_f^* \simeq 0$.

If $\Delta\sigma_f^* \neq 0$, then $\sigma_f^*(i)$ can be determined from notch bend tests or tension tests at $T \simeq T_D(i)$. The usefulness of Eq 11 to predict ΔT_D is rather limited if $\Delta\sigma_f^* \neq 0$, since a measured value of ΔT_D can be obtained in the process of determining $\sigma_f^*(i)$. However, Eq 11 is still very useful in determining the contribution of each metallurgical fracture parameter to the shift in the *DBTT*. Also, the equation can be solved for one of the other parameters if ΔT_D is known. The usefulness of $\sigma_y^*(i)$ and $\sigma_f^*(i)$ can be extended beyond a calculation of the shift in the *DBTT* to a calculation of the fracture toughness K_{Ic} , as discussed in the next section.

Calculation of K_{Ic}

A simple model has been developed to calculate the plane strain fracture toughness K_{Ic} from a knowledge of the metallurgical fracture parameters σ_y^* and σ_f^* [27]. The equation can be expressed in the following form

$$K_{Ic} = 2.89\sigma_y^* \{ \exp[(\sigma_f^*/\sigma_y^*) - 1] - 1 \}^{1/2} \rho_0^{1/2} \dots \dots \dots (13)$$

where ρ_0 is the minimum effective root radius below which K_{Ic} is independent of ρ . Tetelman [27] found that a reasonable assumption was $\rho_0 = 0.002$ in. for A302B and A533B steels. This reduces Eq 13 to the form

$$K_{Ic} = 0.13\sigma_y^* \{ \exp[(\sigma_f^*/\sigma_y^*) - 1] - 1 \}^{1/2} \dots \dots \dots (14)$$

Equation 14 appears to be valid at sufficiently low temperatures or in irradiated steels where $\sigma_f^* \leq 3.4\sigma_y^*$. These are the conditions under which a critical stress criterion for fracture applies. At temperatures above that at which $\sigma_f^* \leq 3.4\sigma_y^*$, unstable fracture initiates when a critical plastic strain ϵ_s is achieved near the crack tip ($T_{S(N)}$ or region 4 in Fig. 4).

σ_y^* and σ_f^* were calculated from instrumented Charpy tests on unirradiated A212B steel from the ASTM surveillance correlation heat. Equation 14 was used to calculate K_{Ic} as a function of temperature. Dynamic fracture toughness is used because dynamic yield stress values are obtained from the Charpy impact test. Figure 7 shows σ_y^* (measured) and K_{Ic} (calculated) as a function of temperature. The validity of the predicted K_{Ic} curve was determined by performing valid ASTM fracture toughness tests on precracked Charpy specimens from the same heat of A212B steel. The solid points are the valid K_{Ic} values, and they agree quite well with the predicted values.

One of the most promising uses of Eq 14 is the prediction of the effect of radiation on fracture toughness from a knowledge of metallurgical fracture parameters obtained from testing small Charpy specimens. For example, there appear to be no data on the effect of radiation on the fracture toughness of A212B steel. σ_y^* and σ_f^* values for A212B steel irradiated to 9.4×10^{18} n/cm² were calculated from the load-temperature diagram of Fig. 5. These values were then used in Eq 14 to calculate K_{Ic}

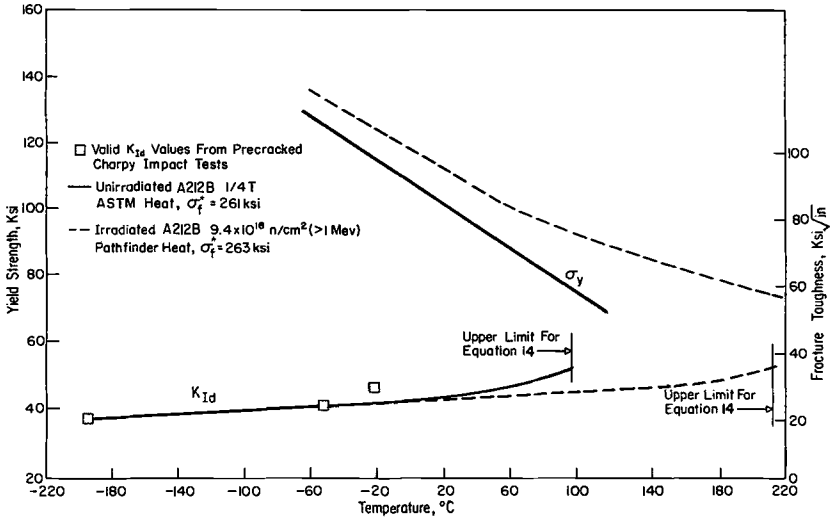


FIG. 7—Comparison of predicted results for unirradiated and irradiated A212B steel with K_{Ia} values from precracked Charpy impact tests of unirradiated A212B steel.

as a function of temperature. The predicted fracture toughness behavior of irradiated A212B is shown in Fig. 7. The model used to calculate K_{Ia} is considered valid only when $\sigma_f^* \leq 3.4\sigma_y^*$. Since σ_y^* decreases with increasing temperature, a temperature limit exists for the predicted K_{Ia} values. The upper limiting temperature is indicated by an arrow in Fig. 7. Since radiation does not change σ_f^* significantly, the predicted decrease in K_{Ia} for irradiated A212B steel is primarily due to the radiation induced increase in σ_y^* .

A great deal of data have been generated on the effects of radiation on A533B steel as part of the AEC Heavy Section Steel Technology (HSST) program. It has been shown previously [22] that K_{Ic} values calculated from Eq 14 or unirradiated A533B steel are in excellent agreement with valid experimental values obtained in the HSST program. The instrumented Charpy data on irradiated A533B steel obtained by Berggren [26] were used to calculate $\sigma_f^* = 309,000$ psi. Mager [28] has reported data for K_{Ic} and σ_y (static) as a function of temperature for A533B irradiated at 540 F (282 C) to a fluence of 4×10^{19} n/cm², $E > 1$ MeV. Equation 14 was used to predict the effect of radiation on K_{Ic} (static) for A533B steel using the σ_f^* and σ_y values obtained above. The measured and predicted values of K_{Ic} for irradiated A533B steel are shown to be in excellent agreement in Fig. 8. Thus a good correlation has been established between K_{Ia} or K_{Ic} and the parameters σ_f^* and σ_y^* for the class of materials studied here. This correlation holds for both the unirradiated and irradiated conditions.

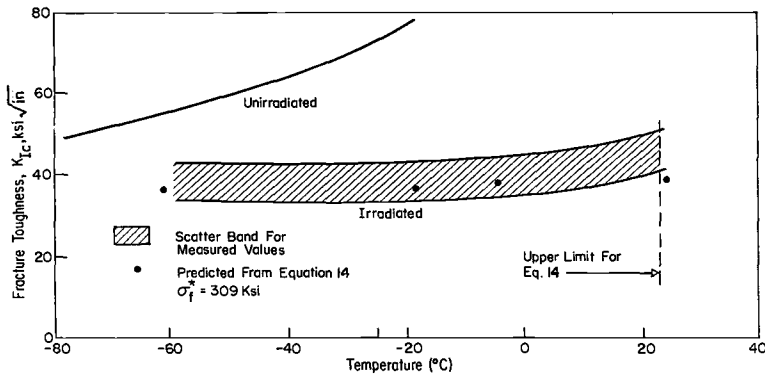


FIG. 8—Comparison of predicted results with postirradiation results of compact K_{Ic} fracture toughness tests for quarter thickness, A533 Grade B Class 1 steel HSST plate 02 [28].

Conclusions

The effect of radiation on the metallurgical fracture parameters defined by the Cottrell-Petch theory of fracture can be linked to the effect of radiation on the fracture toughness as measured by the shift in the ductile-brittle transition temperature or by a change in K_{Ic} . A knowledge of the relationships between key metallurgical fracture parameters and the Charpy energy curve or fracture toughness permits an accurate prediction of the radiation induced embrittlement of pressure vessel steels. The instrumented Charpy test provides a valuable link between the metallurgical and fracture mechanics approaches to fracture toughness. The value of irradiated Charpy specimens, particularly in present surveillance programs, can be considerably enhanced by the use of the instrumented Charpy test.

APPENDIX

Calculation of the Change in the DBTT, $\Delta T_{D(N)}$

Figure 9 is a schematic of the variation of the cleavage fracture stress and yield stress with temperature for two different conditions (with respect to composition, strain rate, irradiation, etc.). The schematic is similar to that shown in Fig. 1b, except that the stresses and transition temperatures in Fig. 9 are those for notch bending. In the figure $K_{\sigma(p)}\sigma_{f1}^*$ is the value of the yield stress for condition 1, where the triaxiality and strain rate effects of the notch have been taken into account. σ_f^* was assumed to be independent of temperature in Fig. 9. The change in the DBTT is taken as the difference between the brittleness transition temperature for conditions 1 and 2, $\Delta T_{D(N)} = T_{D(N)1} - T_{D(N)2}$. The temperature dependence of the yield stress is given by $K_{\sigma(p)}(d\sigma_y^*/dT)$.

Using the schematic diagram in Fig. 9, an expression can be obtained for length A in the terms of the fracture parameters:

$$A = \Delta\sigma_f^* - K_{\sigma(p)}\Delta\sigma_y^*T_{D(N)1} \dots \dots \dots (15)$$

where $\Delta\sigma_f^*$ is determined at $T_{D(N)1}$, and

$$\Delta\sigma_f^* = \sigma_{f2}^* - \sigma_{f1}^* \dots \dots \dots (16)$$

$$\Delta\sigma_y^* = \sigma_{y2}^* - \sigma_{y1}^* \dots \dots \dots (17)$$

Length A is also given by length B times the slope of line C ,

$$A = B \frac{dC}{dT}$$

or

$$A = \Delta T_{D(N)} K_{\sigma(p)} \left(\frac{d\sigma_y^*}{dT} \right)_{2,\Delta T} \dots \dots \dots (18)$$

where the subscript ΔT for $(d\sigma_y^*/dT)$ means that $d\sigma_y/dT$ is measured in the temperature range $T_{D(N)2}$ to $T_{D(N)1}$. Combining Eqs 15 and 18,

$$\Delta\sigma_f^* - K_{\sigma(p)} \Delta\sigma_y^*_{T_{D(N)1}} = \Delta T_{D(N)} K_{\sigma(p)} \left(\frac{d\sigma_y^*}{dT} \right)_{2,\Delta T} \dots \dots \dots (19)$$

Solving for $\Delta T_{D(N)}$, an expression for the change in the DBTT is derived:

$$\Delta T_{D(N)} = \frac{\Delta\sigma_f^* - K_{\sigma(p)} \Delta\sigma_y^*_{T_{D(N)1}}}{K_{\sigma(p)} \left(\frac{d\sigma_y^*}{dT} \right)_{2,\Delta T}} \dots \dots \dots (20)$$

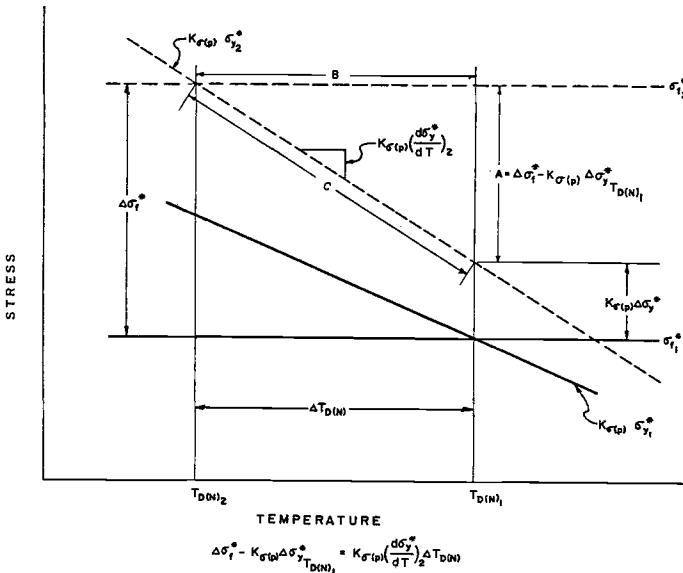


FIG. 9—Schematic of the temperature dependence of the yield stress and cleavage fracture stress for notch bending.

Substituting Eqs 16 and 17 into Eq 20, a more detailed expression is obtained;

$$T_{D(N)_1} - T_{D(N)_2} = \frac{(\sigma_{f_2}^* - \sigma_{f_1}^*) - K_{\sigma(p)}(\sigma_{y_2}^* - \sigma_{y_1}^*)_{T_{D(N)_1}}}{K_{\sigma(p)} \left(\frac{d\sigma_y^*}{dT} \right)_{2, \Delta T}} \dots \dots (21)$$

References

- [1] Hall, E. O., *Proceedings of the Physical Society*, London, PPSBA, Vol. B64, 1951, p. 747.
- [2] Petch, N. J., *Journal of the Iron and Steel Institute*, JISIA, Vol. 174, 1953, p. 25.
- [3] Cottrell, A. H., *Transactions AIME*, TAMMA, Vol. 212, 1958, p. 192.
- [4] Hull, D. and Mogford, I. L., *Philosophical Magazine*, PHMMA, Vol. 3, 1958, p. 1213.
- [5] Campbell, D. B. and Harding, J. in *Response of Metals to High Velocity Deformation*, Interscience, New York, 1961, p. 51.
- [6] Chow, J. G. Y., McRickand, S. B., and Gurinsky, D. H. in *Radiation Damage in Solids*, Vol. 1, International Atomic Energy Agency, Venice, 1962, p. 277.
- [7] Nichols, R. W. and Harries, D. R. in *Radiation Effects on Metals and Neutron Dosimetry*, ASTM STP 341, American Society for Testing and Materials, 1963, p. 162.
- [8] Churchman, A. T., Mogford, I., and Cottrell, A. H., *Philosophical Magazine*, PHMAA, Vol. 2, 1957, p. 1271.
- [9] Mogford, I. L. and Hull, D., *Journal of the Iron and Steel Institute*, JISIA, Vol. 201, 1963, p. 55.
- [10] Hull, D., *Acta Metallurgica*, AMETA, Vol. 9, 1961, p. 191.
- [11] Johnson, A. A., Milasin, N., and Zein, F. N. in *Radiation Damage in Solids*, Vol. 1, International Atomic Energy Agency, Venice, 1962, p. 259.
- [12] Tetelman, A. S. in *Fracture of Solids*, Interscience, New York, 1963, p. 461.
- [13] Eyre, B. L. and Bartlett, A. F., *Philosophical Magazine*, PHMMA, Vol. 12, 1965, p. 261.
- [14] Hill, R., *Mathematical Theory of Plasticity*, Oxford, London, 1950.
- [15] Wullaert, R. A. in *Impact Testing of Metals*, ASTM STP 466, American Society for Testing and Materials, 1970, p. 148.
- [16] Wilshaw, T. R. and Pratt, P. O. in *Proceedings of the First International Conference on Fracture*, Vol. 2, Sendai, Japan, Sept. 1965, p. 973.
- [17] Tetelman, A. S. and McEvily, A. J. R., *Fracture of Structural Materials*, Wiley, New York, 1967.
- [18] Wullaert, R. A., "The Effect of Nickel on the Microstructure and Mechanical Properties of Low Carbon Ferritic Steels," PhD dissertation, Stanford University, Stanford, Calif., May 1969; Technical Report No. 7, Contract DA 31-124ARO-(D) 251, U.S. Army Research Office, Durham.
- [19] Knott, J. F., "Some Effects of Hydrostatic Tension on the Fracture Behavior of Mild Steel," PhD dissertation, University of Cambridge, Cambridge, England, 1962.
- [20] Fearnough, G. D. and Hoy, C. J., *Journal of the Iron and Steel Institute*, JISIA, Vol. 202, Nov. 1964, p. 912.
- [21] Green, A. P. and Hundy, R. B., *Journal of the Mechanics and Physics of Solids*, JMPSA, Vol. 4, 1965, p. 128.
- [22] Ireland, D. R. and Wullaert, R. A., "Influence of Neutron Irradiation on the Properties of Pathfinder Pressure Vessel Steel," Battelle-Columbus Final Report to Northern States Power Co., 18 Nov. 1968.
- [23] Section III, ASME Boiler and Pressure Vessel Code, American Society of Mechanical Engineers.
- [24] Chow, J. G. Y., McRickard, S. B., and Gurinsky, D. H. in *Radiation Damage in Solids*, Vol. 1, International Atomic Energy Agency, Venice, 1962, p. 277.

- [25] Wechsler, M. S., Berggren, R. G., Hinkle, N. E., and Stelzman, W. J. in *Irradiation Effects in Structural Alloys for Thermal and Fast Reactors*, ASTM STP 457, American Society for Testing and Materials, 1969, p. 242.
- [26] Berggren, R. G. et al, "Quarterly Progress Report, Irradiation Effects on Reactor Structural Materials, November 1968-January, 1969," BNWL-1020, Battelle Northwest Laboratory, March 1969, p. 11.22.
- [27] Malkin, J. and Tetelman, A. S., "Relation Between K_{Ic} and Microscopic Strength for Low Alloy Steels," Technical Report No. I, Contract DA4-04-68-C-0008, U.S. Army Research Office, Durham, Aug. 1969.
- [28] Mager, T. R., "Evaluation by Linear Elastic Fracture Mechanics of Radiation Damage of Pressure Vessel Steels," paper 16, 4th Annual Meeting of the Heavy Section Steel Technology Program, Oak Ridge National Laboratory, 31 March-1 April 1970.

DISCUSSION

*J. P. Higgins*¹—The proposed model appears to provide a useful approach for evaluating the effects of radiation on fracture toughness based primarily on mechanical property considerations; however, there are strong indications that certain trace element impurities have a strong effect on the radiation sensitivity of pressure vessel steels. The Naval Research Laboratory has identified copper and phosphorus as being particularly important. Does the proposed model account for minor variations in such trace impurities elements and their potential effect on radiation damage sensitivity?

R. A. Wullaert (authors' closure)—The instrumented Charpy test would be useful in determining whether the large radiation induced shift in the *DBTT* associated with high copper and phosphorous content is related to an enhanced radiation sensitivity of σ_y^* or σ_f^* or both. If the trace impurity elements are inhibiting the recovery of displacement defects, then a large increase in σ_y^* and little change in σ_f^* would be expected. However, if the trace impurities are producing a temper embrittlement type of behavior, a large decrease in σ_f^* would be expected and the increase in σ_y^* would be no greater than that for steels with low impurity element contents. Recent work at the Naval Research Laboratory² has shown that welds with a high copper content show a larger increase in hardness and *DBTT* than low-copper welds irradiated to the same fluence at 288 C. This indicates that at least part of the high radiation sensitivity of high copper content pressure vessel steels is related to the enhanced radiation sensitivity of the yield stress. The effect of trace impurity elements on the radiation sensitivity of σ_f^* remains to be determined.

*A. L. Bement*³—The departure of the fracture load P_F from the maximum load P_{max} in region 4 of your Fig. 4 could result from either macroscopic lateral contraction of the specimen or ductile fracture. Can you distinguish the relative contribution of either process from your load-time traces alone? If so, should not a departure of P_F from P_{max} for lateral contraction prior to brittle fracture initiation be allowed for region 3?

¹ Senior metallurgist, General Electric Co., Nuclear Energy Division, San Jose, Calif.

² Hawthorne, J. R., Fortner, Edward, and Grant, S. P., "Radiation Resistant Experimental Weld Metals for Advanced Reactor Vessel Steels," submitted for publication in *The Welding Journal*, 1 Aug. 1970.

³ Battelle-Northwest, Richland, Wash. 99352.

It is important in interpreting micrographs of ductile fracture surfaces to distinguish between features representing fracture under predominantly biaxial shear stresses and features representing regions subjected to significant hydrostatic tension components due to geometric restraints.

R. A. Wullaert (authors' closure)—For the class of steels studied, lateral contraction is about 1 to 2 percent at $T_{D(N)}$ and 6 to 8 percent at $T_{S(N)}$. This increase in plastic deformation through region 3 is an indication of the additional amount of strain hardening that is required to raise σ_y^* to σ_f^* to produce cleavage fracture. At $T < T_{S(N)}$, cleavage fracture occurs before the load reaches a zero slope, and thus the fracture load is the maximum load ($P_F = P_{\max}$). $T_{S(N)}$ corresponds to the temperature at which ductile tearing first occurs across the root of the notch. This ductile tearing has been observed to occur at the maximum load (zero slope). Figure 3 is a typical load-time (deflection) curve for temperatures above $T_{S(N)}$ where cleavage fracture can still occur. The fibrous crack initiated at P_{\max} will sharpen and accelerate and eventually lead to cleavage fracture at the brittle fracture load P_F . As the temperature is increased above $T_{S(N)}$, the fracture will become 100 percent fibrous and a sharp drop in load will no longer occur. Thus in the initial part of region 4 where cleavage fracture occurs after fibrous initiation at the maximum load, $P_{\max} > P_F$.

C. R. Brinkman¹ and J. M. Beeston¹

The Effect of Hydrogen on the Ductile Properties of Irradiated Pressure Vessel Steels*

REFERENCE: Brinkman, C. R. and Beeston, J. M., "The Effect of Hydrogen on the Ductile Properties of Irradiated Pressure Vessel Steels," *Irradiation Effects on Structural Alloys for Nuclear Reactor Applications, ASTM STP 484*, American Society for Testing and Materials, 1970, pp. 42-73.

ABSTRACT: The influence of hydrogen on the mechanical properties (ductility, fracture strength, and tendency towards delayed failure) was investigated for several irradiated pressure vessel steels. Included were ASTM A302B, A542, and HY-80 steel irradiated at fluences from 8×10^{18} to 4×10^{20} n/cm², $E > 1$ MeV. Specimens from plate sections of these steels which had been quenched and tempered and some from A542 which were given prestrain and heat treatment modifications were prepared and tested. The effects of strength level from irradiation, heat treatment, and microstructure were thus determined. Reductions in ductility and true fracture strength occurred with increasing hydrogen content but were not extensive at strength levels less than 180 ksi in specimens containing 1 to 2 ppm hydrogen. This concentration, however, produced a marked effect on the ductile properties when the strength level was increased by irradiation hardening or heat treatment beyond this threshold range. Irradiation hardening increased the magnitude of the decrease in notched strength resulting from a given hydrogen content in all of the steels and conditions tested. Hydrogen induced delayed failure, however, did not occur to any large extent in HY-80, A302B, and A542 steel in the normal quenched and tempered condition even after irradiation to fluences in excess of 10^{20} n/cm², $E > 1$ MeV, and hydrogen concentrations of up to 4 ppm.

KEY WORDS: hydrogen, hydrogen containing alloys, structural steels, pressurized water reactors, pressure vessels, ductility, fracture strength, mechanical properties, hardening (materials), heat treatment, radiation effects, neutron irradiation, microstructure, tests

Hydrogen in ferritic steels can lead to several deleterious effects including loss of ductility and time-dependent failure at strength levels consider-

¹ Group leader and section chief, respectively, Materials Research, Idaho Nuclear Corp., Idaho Falls, Idaho 83401.

* Work performed under the auspices of the U.S. Atomic Energy Commission, Idaho Operations Office, under Contract AT(10-1)-1230.

ably less than the yield strength. The problems associated with the presence of hydrogen become most acute in high-strength steels where instances of loss of ductility [1]² and delayed failure have been attributed to the presence of hydrogen at the 1 ppm level or less. Further, aqueous environments [2] have been shown to generate sufficient hydrogen at the metal-water interface to embrittle high-strength steel. In lower strength or mild steels, higher hydrogen concentrations are required to effect a decrease in ductility, and the lower critical stress for delayed failure approaches that of the strength obtained from a short-time tension test or is considerably higher than that of high-strength steels at equivalent hydrogen concentrations [3]. The embrittling mechanisms responsible for these effects are still somewhat controversial [4, 5] but are dependent upon temperature, strain rate, applied stress, hydrogen concentration, as well as such material properties as ultimate strength, toughness, residual stress level, and hydrogen diffusivity. The presence of flaws, cracks, voids, and certain microstructural features further serves to accentuate the problem of embrittlement both by increasing the stress intensity factor and by the increased tri-axiality which serves to concentrate hydrogen in the vicinity of a stress riser [6].

Low-alloy carbon steels used in nuclear service for light water reactor (LWR) vessel materials are not expected to be subject to appreciable amounts of hydrogen embrittlement—even in the event of a vessel cladding failure which would allow reactor coolant water to come in contact with the carbon steel and instigate hydrogen generating corrosion reactions [7–10]. It was concluded by Harries and Broomfield [7] that the chief source of diffusible hydrogen would be from these metal-water corrosion reactions, but assuming pessimistic and unacceptable corrosion rates this concentration would not exceed 1 to 2 ppm. Experimental work using irradiated low-strength LWR vessel steels has shown that, whereas hydrogen can embrittle these steels at this concentration level, appreciable amounts of delayed failure, meaning failure below the yield strength, does not occur at room temperature, where the embrittling effect would be a maximum [8, 9]. However, at the onset of this work new steels [11] in the intermediate strength range were being considered for possible use. These steels would be further hardened by irradiation, perhaps to the level where hydrogen embrittlement could be a problem. Potential vessel steel strength plus the fact that cladding failures [12] have occurred indicated a need for the initiation of this work. The objective then was to determine the degree to which the ductility of several of the intermediate-strength steels (namely ASTM A320B, A542 Class II, and HY-80 (A543) in the irradiated condition) was affected by the presence of hydrogen and to determine if hydrogen induced delayed failure were possible.

² Italic numbers in brackets refer to the list of references at the end of this paper.

Experimental

Materials

Low-alloy steel selection at the initiation of this program was based upon current use as a vessel material, possible use as a second generation vessel steel, and availability (1966). The steels were obtained in sections from plates of special reference heats and were identified as indicated in Table 1. Chemical compositions also are given in the table. After allowances were made for flame-cut surfaces, the plates were cut into blanks measuring 11/16 by 11/16 by 5 in., with the long axis in the plate rolling direction. Blanks taken from the approximately two-fifths thicknesses and designated normal quenched and tempered (NQT) material were stamped with identifying lot numbers 31, 51, and 81, corresponding to A302B, A542, and HY-80, respectively. Blanks from other than the two-fifths thickness, as in the case of A542 steel, were used for subsequent cold work and heat treatment modifications. These modifications were made so that comparisons between irradiation strengthened and specially heat-treated or cold-worked material might be made. Further, the heat-treated material would be used to define the effects of these changes on the susceptibility of this steel to hydrogen embrittlement. These modifications were identified by lot numbers and are listed in Table 2, along with the NQT material. Resultant microstructures and grain sizes also are given in the table.

TABLE 1—Material identification and composition.

PLATE IDENTIFICATION									
Steel (ASTM)	Plate Thickness, in.		Identification						
A542 Class II	6¼		Lukens melt slab B427-1 [13]						
HY-80 (A543, Ni-Cr-Mo)	3		U.S.S. heat No. N74L204 [14]						
A302B	4		U.S.S. heat No. N-13438 [15] Plate No. 190784						
CHEMICAL COMPOSITION, wt %									
Steel	C	Mn	P	S	Cu	Ni	Cr	Mo	Si
A542	0.18	0.40	0.013	0.02	0.26	0.23	2.4	0.96	0.32
HY-80	0.14	0.20	0.011	0.015	0.07	3.01	1.6	0.50	0.18
A302B	0.19	1.29	0.02	0.02	0.05	0.02	0.14	0.54	0.3

TABLE 2—*Material processing history.*

Steel	Lot No.	Heat or Cold Working History
A302B.....	31	Placed in a furnace at 500 C and heated 35 C/h to 900 C. Equalized for 3 h and held for an additional 4 h, followed by WQ to a temperature less than 150 C. Tempering: charged into a furnace at 400 C, heated at 35 C/h to 650 C, equalized for 4 h, maintained an additional 4 h and air cooled. Charged into a furnace at 400 C, heated to 675 C, equalized 3 h, maintained an additional 4 h and air cooled. Bainitic microstructure, grain size: ASTM 6 to 7.
HY-80.....	81	Austenitized at 900 C for 3 h, WQ. Tempered at 635 C for 3 h. Tempered martensite microstructure, grain size: ASTM 7 to 8.
A542.....	51	940 C, 1 h/in., WDQ 590 C, 1 h/in., AC 620 C, 12 h, AC Bainitic microstructure, grain size: ASTM 6 to 7.
A542.....	52	Austenitized at 930 C for 1 h, quenched in an ice-brine solution, tempered at 620 C to HRC 24±1. Tempered martensite microstructure.
A542.....	53	Austenitized at 930 C for 1 h, quenched in an ice-brine solution, and tempered at 620 C to HRC 35±1. Martensite microstructure.
A542.....	54	Austenitized at 930 C for 1 h and furnace cooled. Pearlitic microstructure.
A542.....	55	As-received material given a 5 percent reduction in area by rolling.
A542.....	56	10 percent reduction in area.
A542.....	57	25 percent reduction in area.
A542.....	58	Austenitized at 930 C for 1 h and normalized. Bainitic microstructure.

Specimens

Two types of specimens were fabricated, a small tension specimen for low-strain rate tension tests and a notched specimen for static load tests. Specimen configurations are shown in Fig. 1. The notched specimen geometry has been used extensively [9, 16], and the tension specimen was kept small to minimize space required for irradiation. Subsequent to fabrication, all of the specimens except lots 55, 56, and 57 were given a stress relieving anneal of 1 h at 500 C.

Irradiation

Specimens were irradiated in specially designed helium-bonded capsules to several fluences ranging from approximately 7×10^{18} n/cm² to 5×10^{20} n/cm², $E > 1$ MeV. (Henceforth, all fluences reported will be in the above units.) Specimens irradiated to the lower fluence were irradiated in the MTR with the gage center line temperatures less than 300 C, while specimens irradiated to fluences in excess of 10^{20} n/cm² were irradiated in the ETR at temperatures less than 225 C. Considerable amounts of *in situ*

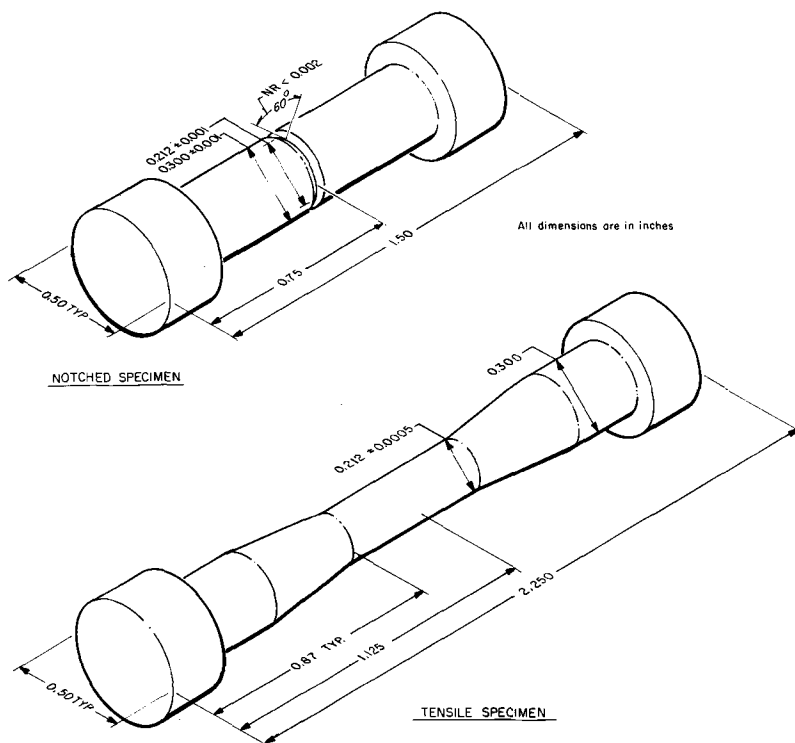


FIG. 1—Notched and tension specimens for hydrogen embrittlement of steel tests.

annealing no doubt occurred at these temperatures, resulting in a decrease in the deleterious effects attributable to irradiation damage; however, these temperatures are within the operating range of most light water reactor vessels.

Cathodic Charging

Postirradiation cathodic charging was the means selected for introducing various amounts of hydrogen into the specimens prior to testing. The solution used was 4 percent sulfuric acid containing 5 mg of sodium arsenate, and a current density of 0.02 A/in.² was applied during charging unless stated otherwise. It was noticed in some of the preliminary work that considerable variation in the hydrogen absorption rates occurred, which was dependent on specimen strength level, chemistry, and whether or not the specimen had been irradiated. These observations were reported elsewhere [17] and by other investigators [2]. Because of this variation in absorption rates a standard charging and aging time was not adopted. For each lot a combination of charging and aging time was sought that would give the desired hydrogen concentration level as determined by posttest gas analy-

sis. Charging times ranged from 2 min to 2 h, and aging was carried out at room temperature for at least $\frac{1}{2}$ h in the case of the plain tension specimens. No visible evidence of permanent damage, that is, blistering or cracking, was seen in specimens charged for times up to 2 h. The notched specimens were given a cadmium plate of approximately 6×10^{-4} in. prior to aging and testing to minimize specimen outgassing. Aging times and temperatures for the notched specimens are given with the data (see section on Static Load Tests).

Testing Procedure

Tension and constant load tests were accomplished using standard tensile and stress rupture equipment. Strain rates of 0.05 to 0.1 min^{-1} gave comparable results; therefore, a strain rate of 0.1 min^{-1} was used. All of the tension and constant load tests reported here were conducted at cell ambient temperatures, 26 ± 3 C.

Gas Analysis

In this investigation, particular emphasis was placed on the analytical technique for accurately determining the postfailure hydrogen concentrations in the gage section of the tested specimens. Immediately after specimen failure the specimen fragments were placed in liquid nitrogen. A single specimen weighing approximately 1.2 g was sheared from each half of the cooled specimen, that is, gage section, adjacent to the fracture surface. These specimens were transferred in liquid nitrogen to the gas analyzer. Hydrogen contents were determined with an EA-1 Exhalograph, (Balzers, Liechtenstein), which has been described elsewhere [17]. A vacuum interlock permitted rapid introduction of the specimens into the analyzer, thus minimizing room temperature outgassing. Hydrogen was extracted at 1000 C and determined quantitatively by thermoconductivity measurements. Occasionally, verification of the hydrogen contents was made using a small mass spectrometer connected in series with the EA-1. Close agreement was obtained.

Specimens from the as-irradiated materials were analyzed and found to contain hydrogen. Hydrogen contents were considerably higher than one would expect based on calculations of n,p production (< 0.1 ppm for the higher fluences). They were as follows:

Approximate Fluence, n/cm^2 , $E > 1$ MeV	Average Hydrogen Content, ppm	Number of Specimens Analyzed	Standard Deviation
Unirradiated.	0 to 0.2
7×10^{18}	0.9	7	0.3
2×10^{20}	1.7	26	0.8
4×10^{20}	2.1	8	1.3

As indicated, these hydrogen concentrations varied considerably; however, there is a trend of increasing hydrogen content with increasing fluence. Prolonged aging (48 h) at temperatures ranging from 100 to 325 C indicated that this hydrogen was essentially trapped or immobile until baking temperatures in excess of 300 C were used. It appears that irradiation damage such as cold work [18, 19] produces a condition which can trap hydrogen. As this hydrogen was nondiffusible at test temperatures and was shown by static load tests to be innocuous to the mechanical properties, it was subtracted as a blank from all concentrations reported herein.

Results

Tensile Properties

Tensile properties of the unirradiated and irradiated steels prior to hydrogenation are given in Tables 3 and 4, respectively. Because of the limited number of irradiated specimens, only one to three specimens were used in obtaining the average values of the properties reported in Table 4. Specimens irradiated to fluences in excess of 10^{20} were probably at or near the point of saturation of irradiation induced hardening [20].

Tension Testing of Hydrogenated Specimens

The effects of increasing hydrogen content on the form of the engineering stress-strain curves of these steels in the irradiated condition are typified by the examples shown for A302B steel in Figs. 2 and 3. As the hydrogen content is increased, the amount of nonuniform elongation and the true fracture strength are decreased. Finally, a concentration is reached where, if the strength level is high enough, the fracture strength drops below the yield (0.2 percent), which, in most cases, is equivalent to the ultimate strength after irradiation to high fluences. Little if any macroplasticity (uniform elongation) occurs prior to failure, and the specimen fails in a brittle manner. The amount of hydrogen required to reach this nil ductility condition apparently is inversely proportional to the strength level assuming a corresponding decrease in toughness. Alternately, if the strength level is not high enough, a point is reached where a further increase in hydrogen content results in little or no change in the ductile properties, and the specimen fails in a predominately ductile manner. This behavior is evident from the effects of hydrogen on the reduction in area (see Figs. 4-6).

The reduction in ductility is demonstrated visually in the photographs of the fractured surfaces (see Figs. 7-9). The photographs show normal cup-cone fracture in the uncharged condition. Increasing the hydrogen content increases the radial zone at the expense of the fibrous and shear-lip zones. Figure 8 shows a definite change in the fracture mode (from ductile to brittle) brought about by the presence of hydrogen, that is, cup-cone to flat with a faceted appearance. Uniform appearance of the fractured

TABLE 3—Tensile properties of unirradiated A542, A302B, and HY-80 steels.

Steel	Lot No.	Hardness	Elastic Limit, ^a ksi	Yield Strength (0.2% offset) ^a	Ultimate Tensile Strength ^a	Reduction of Area, %	Elongation in ½ in., %	Notched Tensile Strength ^a	Notched Reduction of Area, %
A542	51	HRC 25	99.0	109.0	127.0	68.5	27.1	192.3	20.1
	52	25	89.0	105.0	127.0	69.5	28.8	191.7	18.7
	53	36	126.0	148.0	167.0	62.3	22.5	234.7	14.2
	54	HRB 83	45.6	45.0	88.7	61.4	32.4	124.2	12.3
	55	HRC 26	94.0	117.5	129.8	68.1	25.6	193.5	20.4
	56	26	104.6	132.0	138.3	67.6	25.8	192.0	19.4
	57	28	112.6	129.7	139.3	68.0	23.3	195.6	17.5
	58	36	96.0	124.0	174.0	59.8	23.6	201.1	9.3
A302B	31	HRB 93	76.3	78.2	105.3	67.4	30.3	147.4	19.4
HY-80	81	HRC 19	88.0	92.3	108.0	72.4	34.3	163.7	23.8

^a Average values for three specimens, ksi.

TABLE 4—Tensile properties of irradiated A542, A302B, and HY-80 steels.

Steel	Lot No.	Fluence, n/cm ² , E > 1 MeV	Hardness, HRC	Yield Strength 0.2%, ksi	Ultimate Strength, ksi	Reduction of Area, %	Notch Strength, ksi	Notch Strength Ratio
A542.....	51	6 × 10 ¹⁸	27	139	140	66	218	1.5
	51	3 × 10 ²⁰	35	182	182	57	219	1.2
	51	5 × 10 ²⁰	35	206	...
	52	8 × 10 ¹⁸	27	136	140	68	212	1.5
	52	4 × 10 ¹⁸	35	176	176	46	254	1.4
	53	6 × 10 ¹⁸	38	142	188	55	270	1.4
	53	2 × 10 ²⁰	45	251	...
	53	4 × 10 ²⁰	44	227	227	50	192	0.8
	54	8 × 10 ¹⁸	...	90	102	71	143	1.4
	54	2 × 10 ²⁰	29	92	...
	54	3 × 10 ²⁰	28	138	138	...	85	0.6
	55	2 × 10 ²⁰	33	180	180	55	237	1.3
	56	4 × 10 ²⁰	37	182	182	55	236	1.3
	57	2 × 10 ²⁰	36	185	187	55	211	1.1
58	7 × 10 ¹⁸	...	188	188	49	
A302B.....	58	5 × 10 ²⁰	46	235	235	...	84	0.4
	31	8 × 10 ¹⁸	20	109	113	64	176	1.6
	31	2 × 10 ²⁰	29	135	138	48	168	1.2
	31	3 × 10 ²⁰	33	150	150	48	179	1.2
HY-80.....	81	7 × 10 ¹⁸	28	132	134	63	215	1.6
	81	2 × 10 ²⁰	34	173	178	51	260	1.5
	81	4 × 10 ²⁰	34	195	195	55	235	1.2

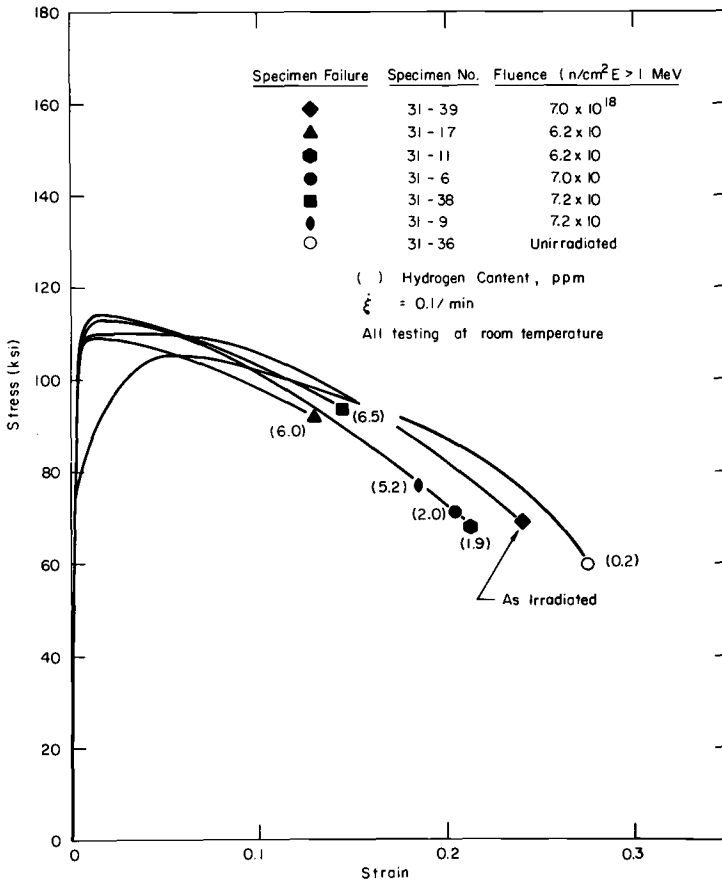


FIG. 2—Engineering stress-strain curves compared for irradiated ($\sim 6.8 \times 10^{18}$ n/cm^2 , $E > 1$ MeV) A302B steel containing various amounts of hydrogen.

surfaces of the hydrogenated specimens (see Fig. 8) was taken as an indication of a fairly homogenous hydrogen distribution produced by the charging and aging treatment applied. Microscopic changes in ductility are apparent from the electron photomicrographs shown in Fig. 9 for irradiated HY-80 steel. Whereas there are no unique features associated with hydrogen embrittlement that distinguish it from any other type of environment induced failure, the transition from dimple rupture to cleavage fracture is apparent.

Figures 10 through 12 are plots of true fracture strength as a function of hydrogen content for the three steels under consideration. To a first approximation, like the reduction in area plots, these figures exhibit a linear decrease in fracture strength with increasing hydrogen content up to approximately 2 ppm. Figure 10 indicates that the fracture strength of A302B

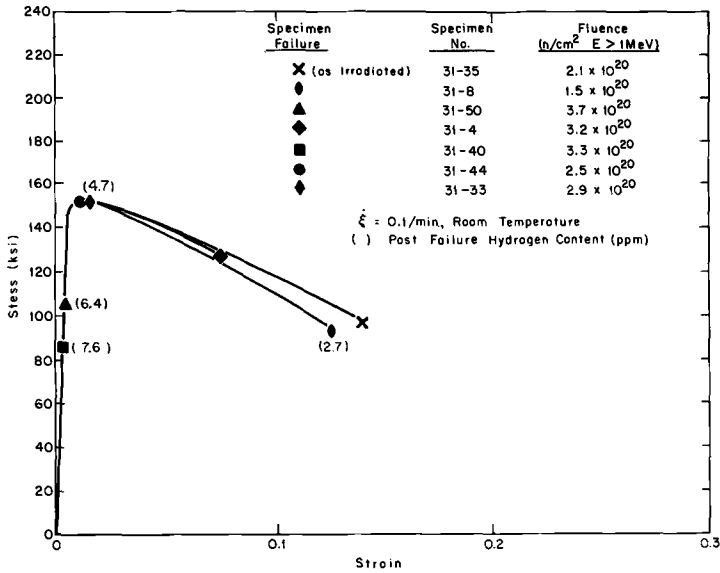


FIG. 3—Engineering stress-strain curves compared for irradiated ($\sim 2.7 \times 10^{20}$ n/cm^2 , $E > 1$ MeV) A302B steel containing various amounts of hydrogen.

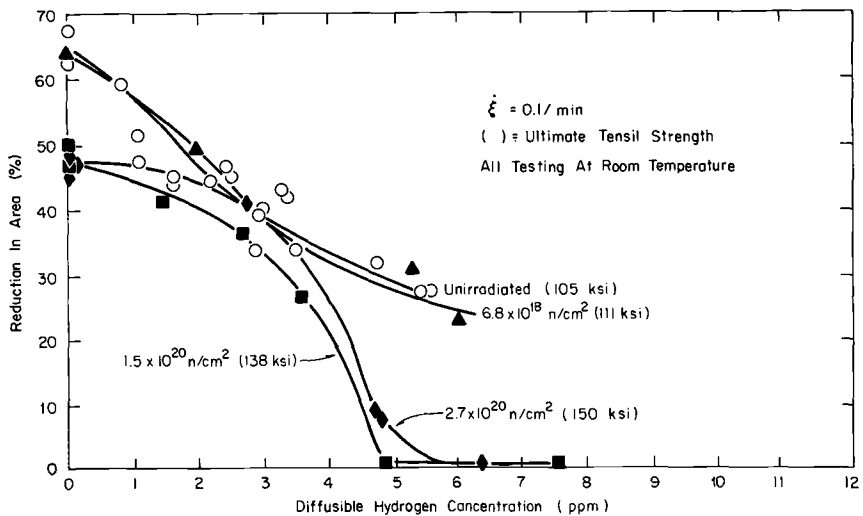


FIG. 4—Effect of hydrogen on the ductility (reduction in area) of A302B steel irradiated to several fluences ($E > 1$ MeV).

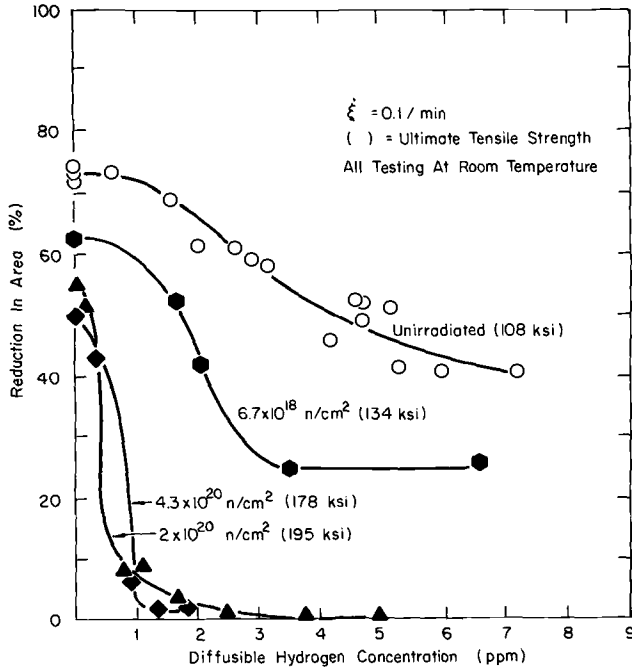


FIG. 5—Effect of hydrogen on the ductility (reduction in area) of HY-80 steel irradiated to several fluences ($E > 1 \text{ MeV}$).

steel is reduced slightly with increasing hydrogen content. However, over the strength level considered (105 to 150 ksi) within the scatter of the data, the extent of this reduction with hydrogen content is nearly insensitive to irradiation induced increases in strength level up to concentrations of 3 to 4 ppm. The fracture strength of HY-80 (see Fig. 11), however, is more adversely affected by the presence of hydrogen; as is indicated, the slope decreases with increasing strength level. The difference appears due to strength level or to a difference in response to a combination of irradiation and hydrogen effects or to both. Figure 12 illustrates the changes in fracture strength due to the presence of hydrogen in irradiated A542 steel heat-treated to various strength levels. Plots of negative slope, $-d\sigma_f/dH_2$, initial linear decrease up to 1 to 2 ppm, are shown in Figs. 13 and 14 as a function of ultimate strength and fracture stress, respectively. A single line fits all of the data, even though material differences are evident, and there are inherent uncertainties in obtaining the slopes from the original curves. The utility of these curves lies in the fact that the ultimate and fracture stress levels are evident at which low diffusible hydrogen concentrations (< 2 ppm) initiate marked changes in the ductile properties of these materials. They also may be useful in predicting the likely response

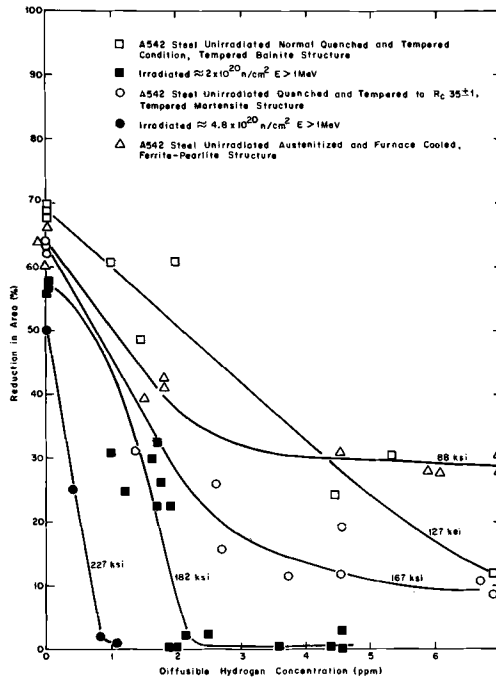


FIG. 6—Reduction in area versus hydrogen content for a number of strength levels (UTS) of A542 steel produced by heat treatment and irradiation.

to hydrogen embrittlement of other low-alloy steels at equivalent strength levels and fluences and similar toughness. Farrell and Quarrell [1] plotted data from similar tests made on unirradiated ultrahigh-strength steel. Their slope versus ultimate strength curve was similar in form to that shown in Fig. 13, thus depicting increased response with increasing strength level; however, their slope versus fracture strength curve was different in that it was initially linear rather than exponential in form. Obviously, individual material chemistry, microstructure, toughness, response to irradiation hardening, as well as strength must be considered in these comparisons.

Static Load Tests

In Figs. 15–20, stress as a function of time to failure is plotted for data obtained from constant load tests. Substantial amounts of delayed failure, defined as a significant difference between the hydrogenated notched tensile strength (NTS) and the lower critical stress for failure (LCS) did not occur in any of the NQT steels tested. Lower critical stress values and hydrogenated notched strengths are given in Table 5.

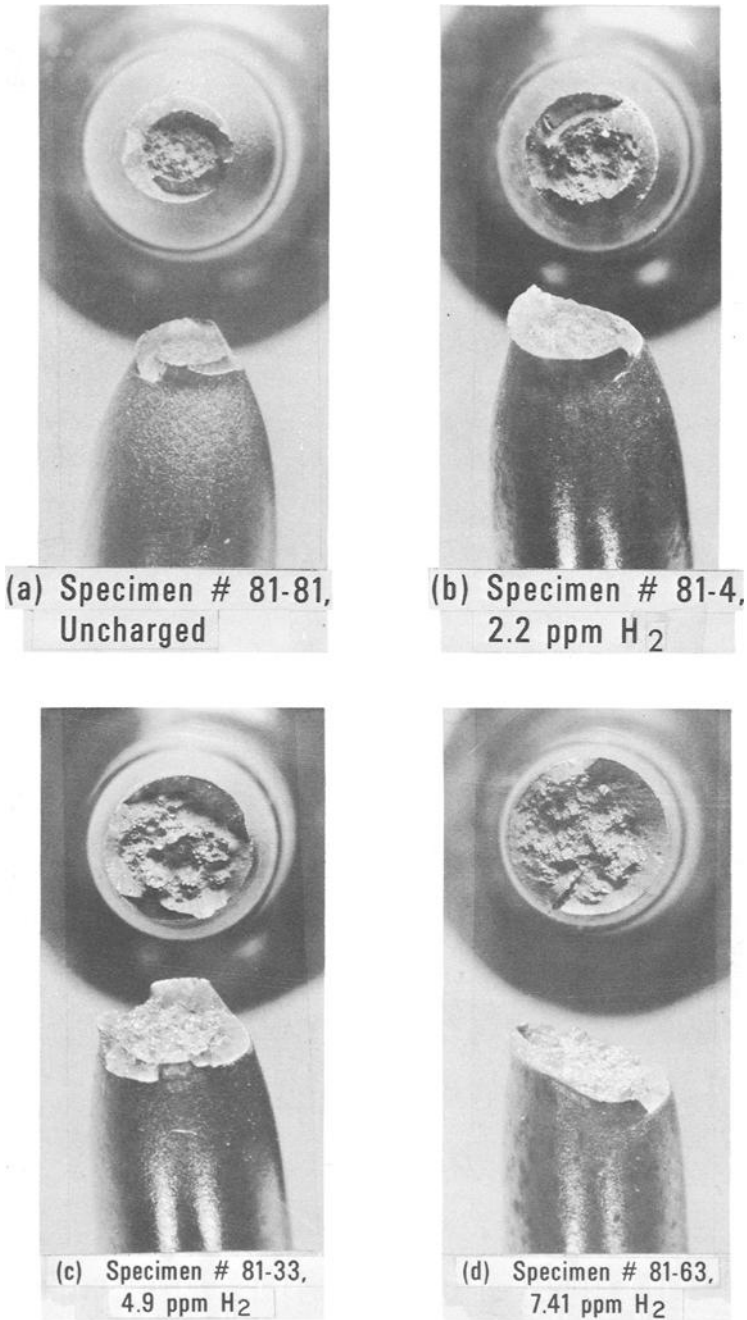


FIG. 7—Fracture of surfaces of hydrogen charged plain tension specimens of HY-80 (unirradiated).

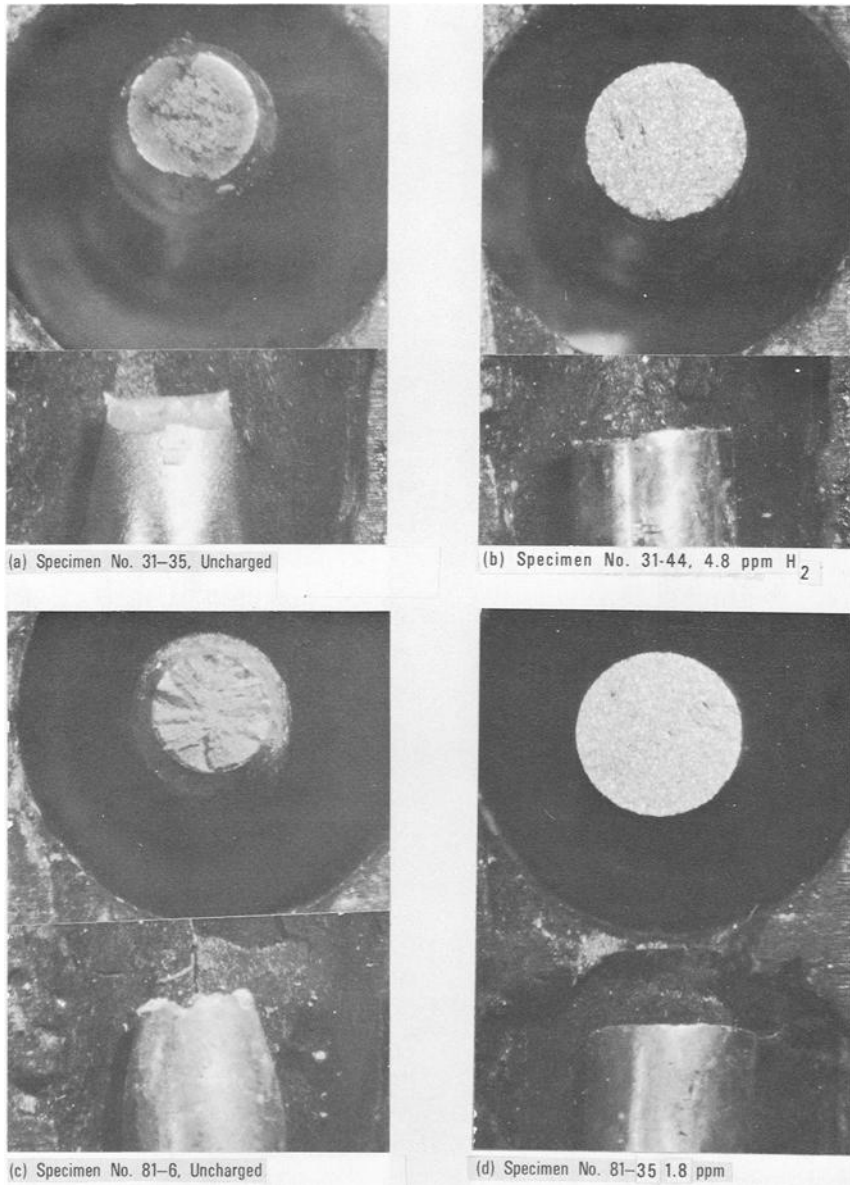


FIG. 8—Fracture surfaces of irradiated plain tension specimens of A302B steel, (a,b) 2.3×10^{20} n/cm², E > 1 MeV, and HY-80 steel; (c,d) 4.9×10^{20} n/cm², E > 1 MeV, showing changes in fracture mode brought about by the presence of hydrogen.

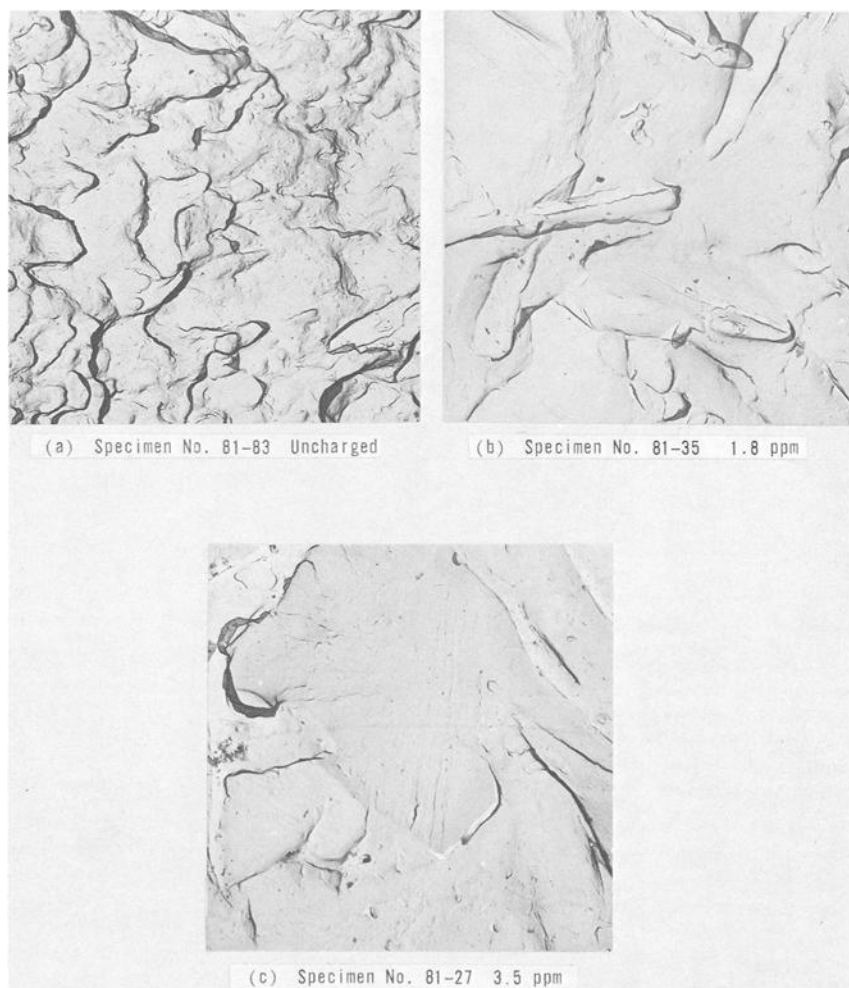


FIG. 9—Embrittlement of HY-80 steel specimens by hydrogen. Specimens initially irradiated to fluences $>10^{20}$ n/cm², $E > 1$ MeV.

Static fatigue data (shown in Fig. 15) for HY-80 steel irradiated to a fluence of 8×10^{18} n/cm² are typical of that found for the normal (NQT) condition of the three steels irradiated to this fluence level. The data show that the steels in the NQT condition containing 2 to 3 ppm hydrogen were not subject to delayed failure.

Comparisons between unirradiated and irradiated (fluences greater than 10^{20} n/cm²) steels in the NQT condition are made in Figs. 16–18. The data show the following: (1) the nondiffusible hydrogen referred to previously has no effect on the static fatigue properties of the irradiated steels, that is,

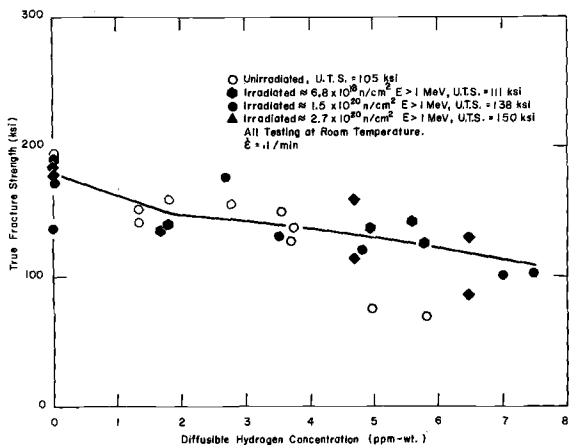


FIG. 10—True fracture strength as a function of hydrogen content for A302B steel irradiated to several fluences.

no indication of a decrease in notched strength in times tested; (2) as the hydrogen content increases the hydrogenated NTS and LCS decrease, with the LCS falling below the unirradiated NTS at about the 2-ppm level; (3) significant amounts of time-dependent failure did not occur even at relatively high hydrogen concentrations. Failure occurred either instantaneously on loading or over a limited stress range, thus giving relatively flat curves rather than the characteristic static fatigue curves found for

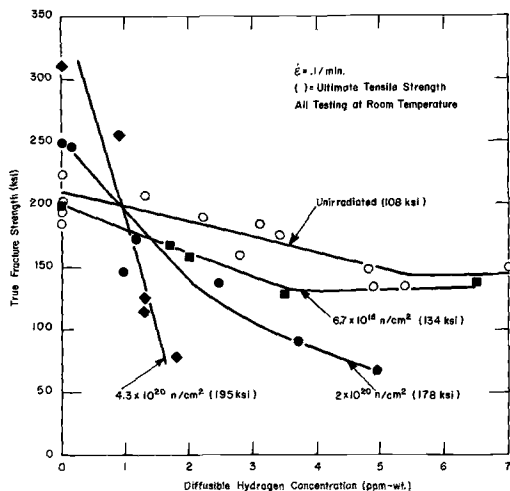


FIG. 11—True fracture strength as a function of hydrogen content for HY-80 steel irradiated to several fluences ($E > 1$ MeV).

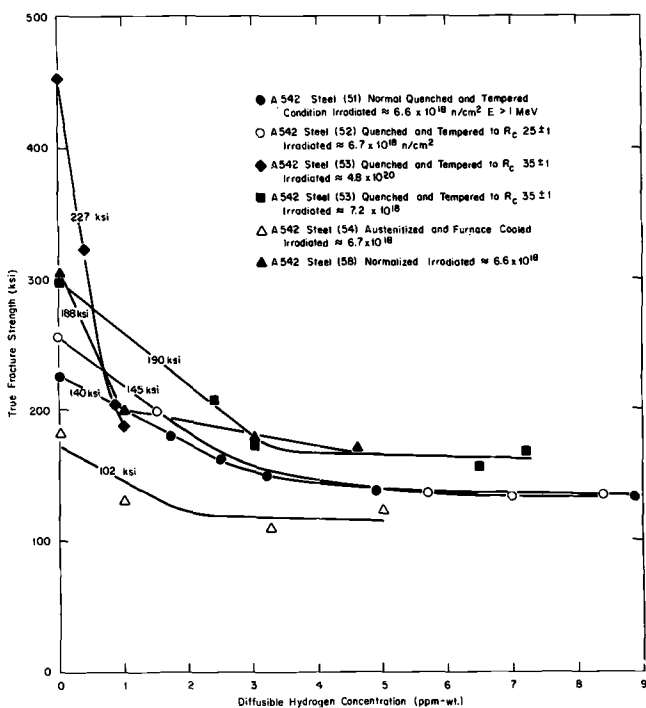


FIG. 12—True fracture strength as a function of diffusible hydrogen concentration for steel heat-treated and irradiated to various strength levels.

high-strength steels tested under similar conditions. The lack of significant amounts of delayed failure is indicative of a sufficient toughness to resist slow stable crack growth except at stress levels approaching the point where instantaneous failure occurs.

Static fatigue curves for specimen blanks of A542 steel receiving heat treatment or cold work modifications prior to specimen machining and irradiation are shown in Figs. 19 and 20. Condition H.T. 52, which was heat-treated to a similar strength level but with a tempered martensite instead of bainite microstructure for the normal quenched and tempered material (H.T. 51), had a similar response to constant loading conditions (see Table 5). The data also indicate that for the unirradiated material increasing the hydrogen content to 5 to 6 ppm will result in increased amounts of delayed failure. Material quenched and tempered to an ultimate tensile strength of 165 ksi prior to irradiation (see Fig. 19), unlike previous conditions, showed considerable amounts of delayed failure at a low concentration level (apparently due to the increased strength level). H.T. 54, the furnace-cooled material with a pearlitic structure, was not prone to delayed failure at the concentration levels studied. LCS values for H.T. 54 are given in Table 5.

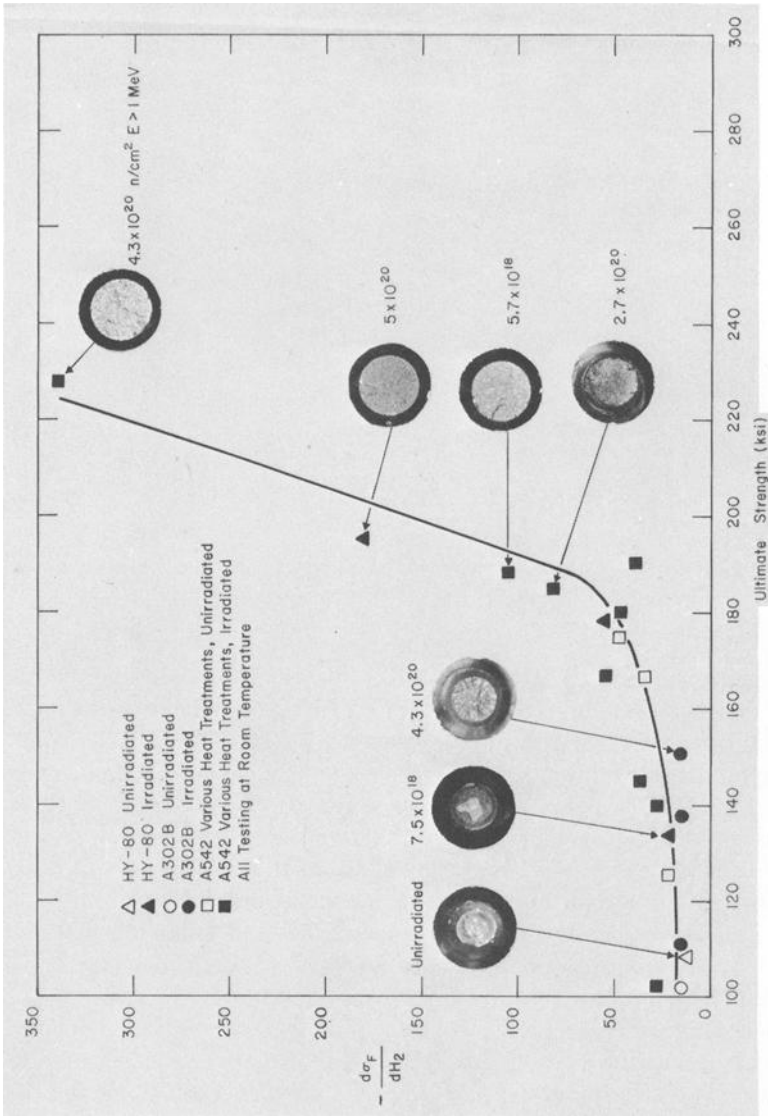


FIG. 13—Susceptibility to hydrogen embrittlement as a function of ultimate strength for A302B, HY-80, and A542 steel containing diffusible hydrogen concentrations (<2 ppm (wt)).

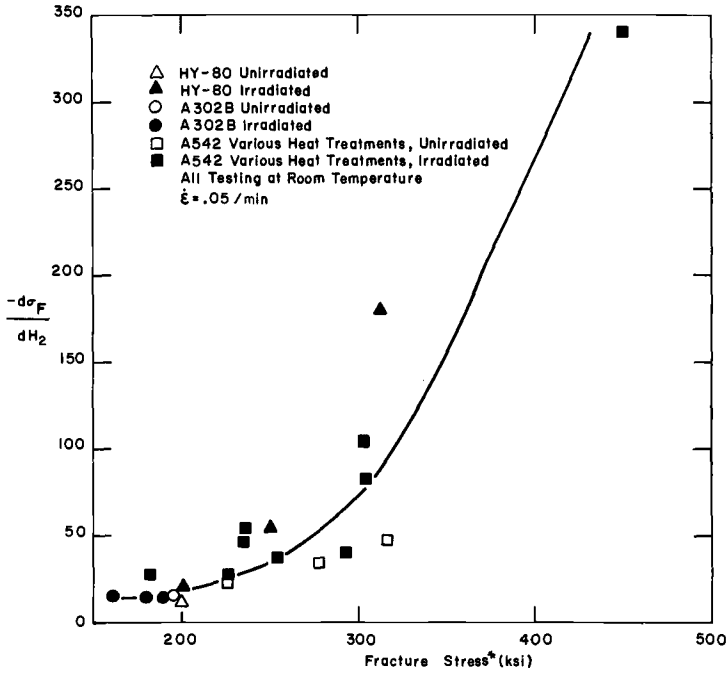


FIG. 14—Susceptibility to hydrogen embrittlement as a function of uncharged fracture stress for A302B, HY-80, and A542 steel containing diffusible hydrogen concentrations (<2 ppm (wt)). Fracture stress: load at failure divided by cross-sectional area at failure.

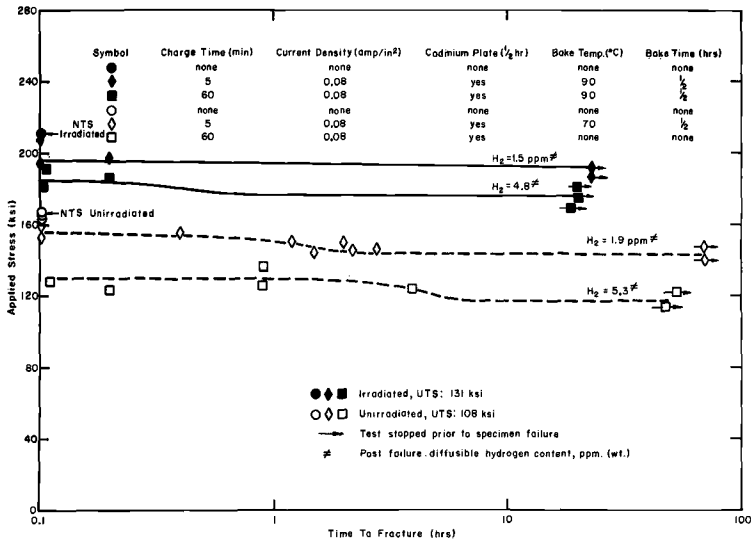


FIG. 15—Constant load rupture curves compared for hydrogenated specimens of unirradiated and irradiated (8×10^{18} n/cm², $E > 1$ MeV) HY-80 steel (H.T. 81).

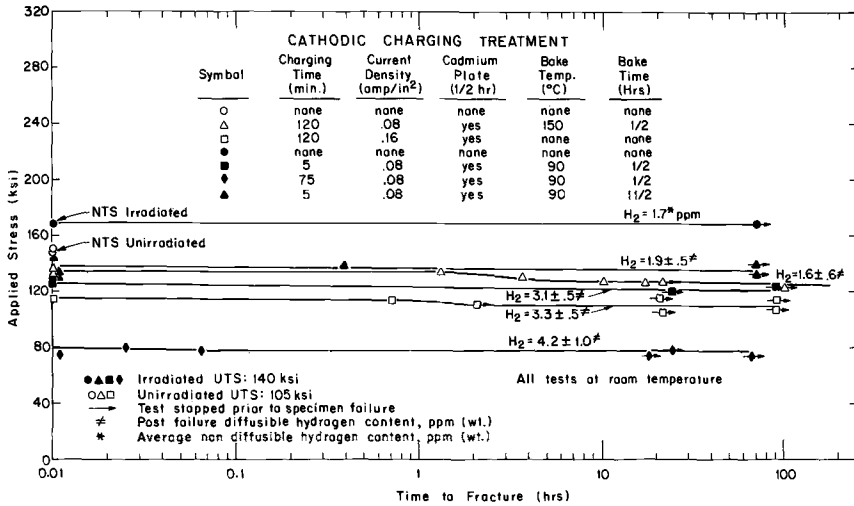


FIG. 16—Constant load rupture curves compared for hydrogenated specimens of unirradiated and irradiated (to 2.5×10^{20} n/cm², $E > 1$ MeV) A302B steel in the normal quenched and tempered condition.

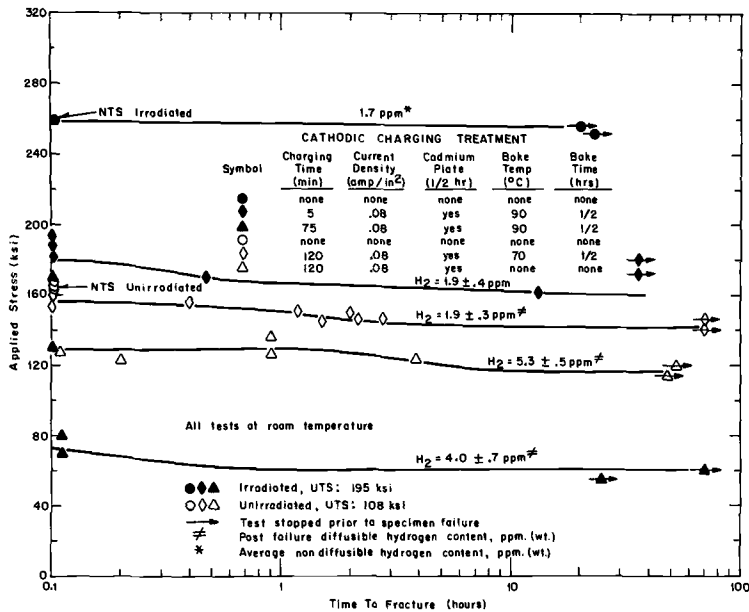


FIG. 17—Constant load rupture curves compared for hydrogenated specimens of unirradiated and irradiated (to 2.2×10^{20} n/cm², $E > 1$ MeV) HY-80 steel (H.T. 81).

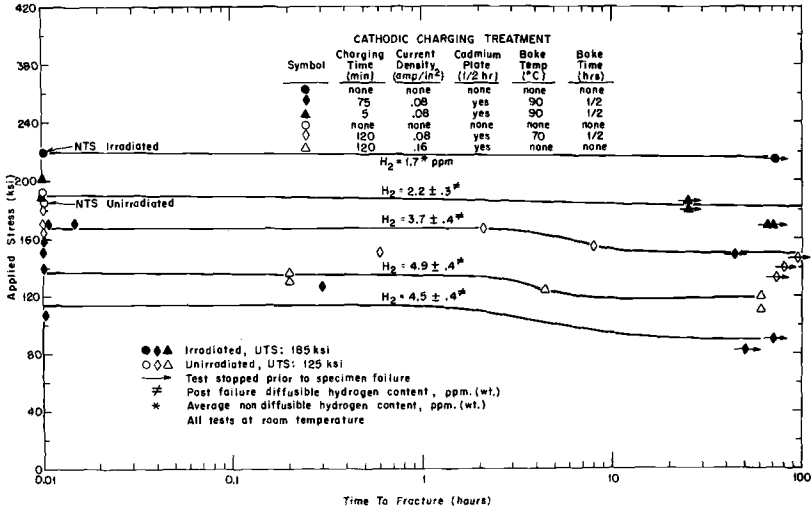


FIG. 18—Constant load rupture curves compared for hydrogenated specimens of unirradiated and irradiated (to 2.4×10^{20} n/cm², E > 1 MeV) A542 steel in the normal quenched and tempered condition (H.T. 51).

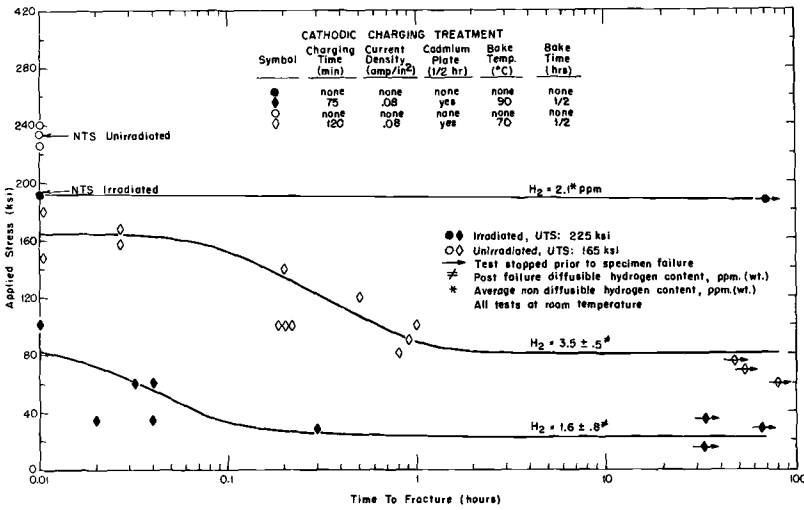


FIG. 19—Constant load rupture curves compared for hydrogenated specimens of unirradiated and irradiated (to 4.2×10^{20} n/cm², E > 1 MeV) A542 steel that had been quenched and tempered to HRC 36 (H.T. 53).

TABLE 5—Constant load properties.

Steel	Lot No.	Fluence, n/cm ² , E > 1 MeV	Ultimate Strength, ^a ksi	Notched Strength, ^a ksi	Hydrogenated Notched Strength, ksi	Notch Strength Ratio ^b	Hydrogen Content, ppm	Approximate Lower Critical Stress, ksi
A542.....	51	Unirradiated	127	192	167	1.3	3.7	149
	51	Unirradiated	127	192	138	1.1	4.9	117
	51	8 × 10 ¹⁸	140	218	200	1.4	1.8	200
	51	2 × 10 ²⁰	185	220	190	1.0	2.2	183
	51	2 × 10 ²⁰	185	220	105	0.6	4.5	90
	51	4 × 10 ²⁰	c	220	170	...	1.6	161
	52	Unirradiated	127	192	162	1.2	3.4	135
	52	Unirradiated	127	192	145	1.1	5.6	95
	52	8 × 10 ¹⁸	141	212	182	1.3	4.0	182
	52	4 × 10 ²⁰	176	255	196	1.1	2.3	196
	53	Unirradiated	167	235	165	1.0	3.5	80
	53	8 × 10 ¹⁸	188	270	250	1.3	0.8	246
	53	4 × 10 ²⁰	277	192	82	0.4	1.6	21
	54	Unirradiated	89	124	105	1.2	5.6	95
	54	8 × 10 ¹⁸	102	143	127	1.2	3.7	114
	54	3 × 10 ²⁰	138	85	75	0.5	5.3	70
	55	2 × 10 ²⁰	180	237	188	1.0	1.2	187
	55	2 × 10 ²⁰	180	237	227	1.3	1.4	227
	56	2 × 10 ²⁰	183	236	203	1.1	1.3	243
	56	2 × 10 ²⁰	183	236	132	0.7	4.3	118
57	2 × 10 ²⁰	185	211	152	0.8	1.4	152	
58	Unirradiated	174	201	130	0.7	3.7	88	
58	5 × 10 ²⁰	235	84	65	0.3	1.0	13	
A302B.....	31	Unirradiated	105	147	140	1.3	0.7	129
	31	Unirradiated	105	147	138	1.3	1.6	122
	31	Unirradiated	105	147	115	1.1	3.3	110
	31	8 × 10 ¹⁸	112	183	154	1.4	3.2	154
	31	3 × 10 ²⁰	150	168	139	0.9	1.9	139

31	3 × 10 ²⁰	150	168	123	0.8	3.1	123
31	3 × 10 ²⁰	150	168	80	0.5	4.2	77
81	Unirradiated	108	164	152	1.4	1.9	143
81	Unirradiated	108	164	128	1.2	5.3	116
81	8 × 10 ¹⁸	131	212	193	1.5	1.5	193
81	8 × 10 ¹⁸	131	212	185	1.4	4.8	174
81	2 × 10 ²⁰	178	260	180	1.0	1.9	160
81	2 × 10 ²⁰	178	260	75	0.4	4.0	60

^a Dynamic tension test conducted on uncharged specimen.

^b Ratio of hydrogenated notched strength to uncharged tensile strength.

^c Test was not conducted.

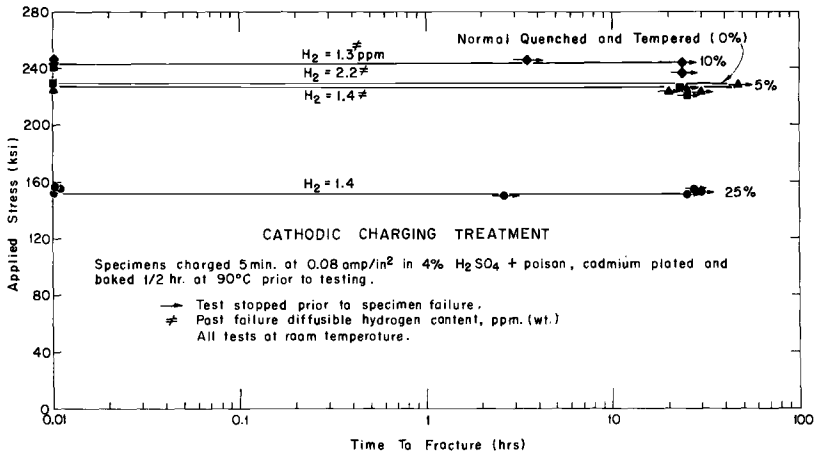


FIG. 20—Constant load rupture curves compared for hydrogenated specimens of irradiated (1.6 to 2.4×10^{20} n/cm², $E > 1$ MeV) A542 steel that had been cold-rolled 5 to 25 percent prior to specimen fabrication.

Figure 20 indicates that, whereas A542 steel cold-worked by rolling is not prone to delayed failure, cold working is deleterious in that a greater decrease in the hydrogenated NTS is found in this steel after being subjected to substantial amounts of cold work. H.T. 58 was very sensitive to the presence of hydrogen even at the 1-ppm level and showed considerable amounts of delayed failure. H.T. 58 was notch sensitive and, therefore, particularly prone to hydrogen embrittlement.

In Figs. 21 and 22, the LCS values as a function of ultimate strength are compared for the NQT and modified heat treatment and cold-worked conditions, respectively. As is shown in Table 5, the hydrogenated NTS was only slightly larger than the LCS in all conditions and hydrogen concentrations except in unirradiated H.T. 52 (5 to 6 ppm), H.T. 53, and H.T. 58, where significant amounts of delayed failure occurred; therefore, conclusions drawn regarding the behavior of LCS values are nearly always applicable to the behavior of the hydrogenated NTS. Figure 21 illustrates the fact that as the strength is increased by irradiation the same amount of hydrogen will produce an increased reduction in the LCS. For example, in the case of HY-80:

Fluence	Hydrogen Content, ppm	Ultimate Strength, ksi	% Decrease in LCS
Unirradiated	1.9	108	13
8×10^{18}	1.5	131	10
2×10^{20}	1.9	178	38

The strength level of HY-80 steel was increased more and to a higher level than were the other NQT steels after irradiation to about 2×10^{20} n/cm². A hydrogen concentration of about 2 ppm resulted in a greater decrease in the LCS of HY-80 than it did in the other steels after a fluence of about 2×10^{20} n/cm²: HY-80 38 percent, A542 16 percent, and A302B 17 percent. Within experimental error, hydrogen concentrations at 1 to 2

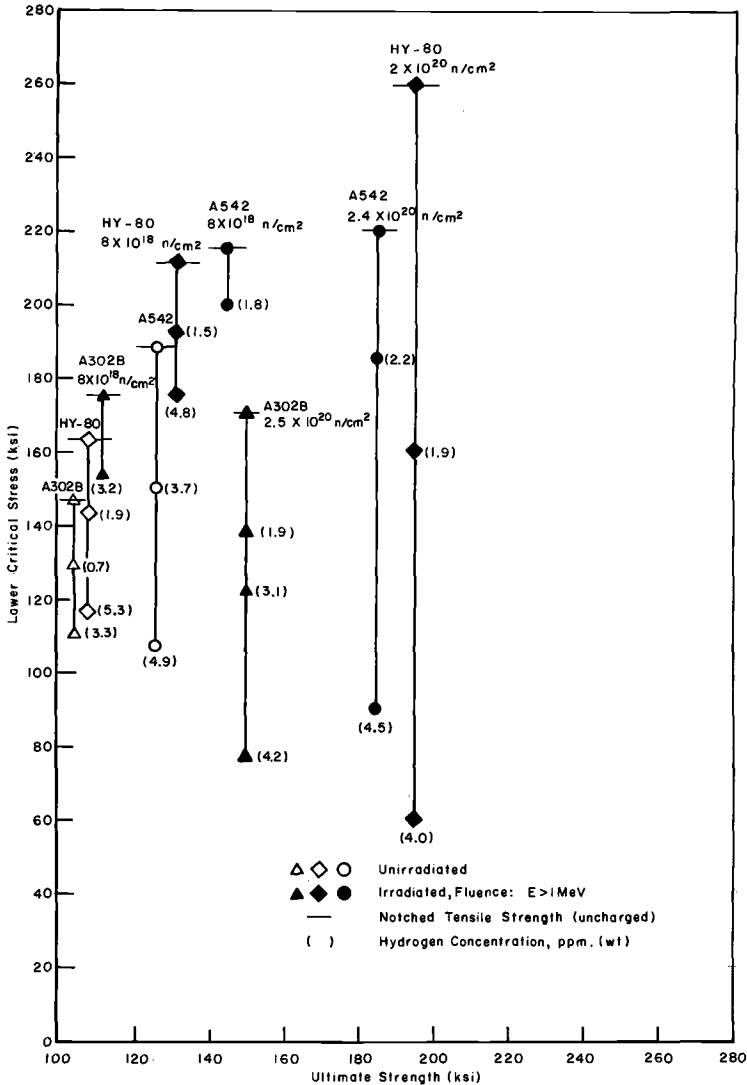


FIG. 21—Lower critical stress levels for failure as a function of ultimate strength at various hydrogen concentrations for steels in normal quenched and tempered condition.

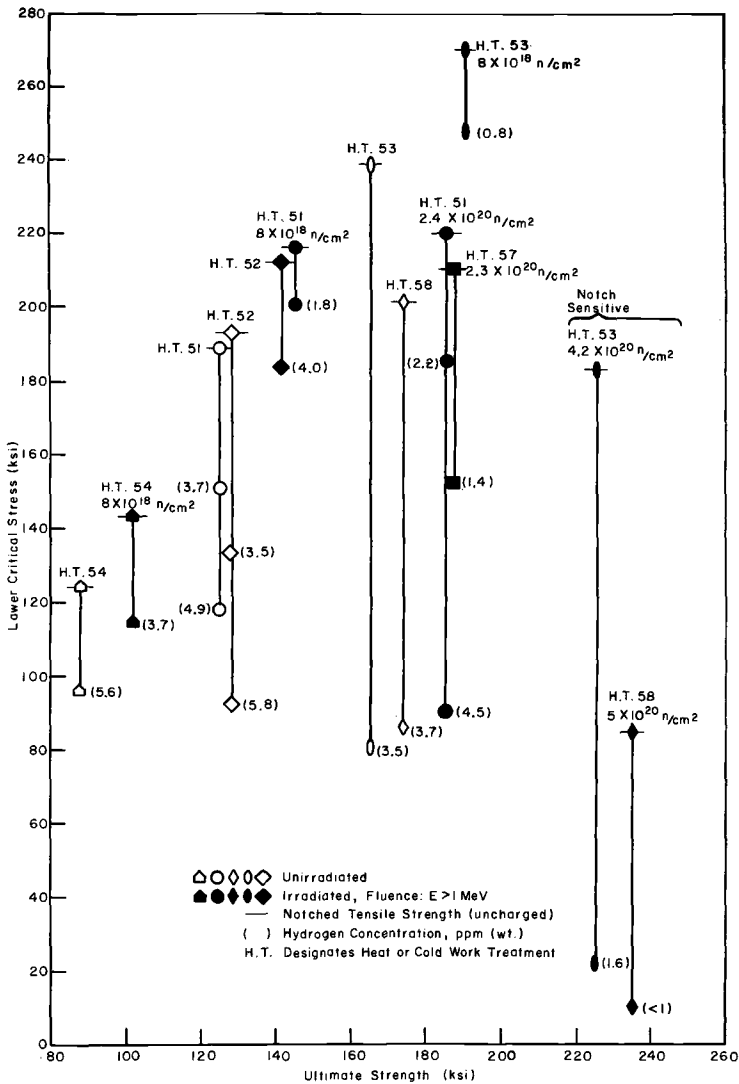


FIG. 22—Lower critical stress levels for failure as a function of ultimate strength at various hydrogen concentrations for A542 steel heat-treated to several levels or cold worked prior to irradiation.

ppm in specimens irradiated to a fluence $> 10^{20} \text{ n/cm}^2$ resulted in an LCS which was nearly equal to the unirradiated NTS. Increasing hydrogen content further decreases the LCS. Figure 22 similarly shows that increasing the strength level by heat treatment (H.T. 53, 58), cold work (H.T. 57), or irradiation results in increased susceptibility to hydrogen embrittlement, that is, larger decrease in the NTS.

Discussion

The tension data showed that hydrogen would begin to have an effect on the ductile properties of these steels in the NQT condition at the 1 to 2-ppm level. The degree to which the ductility, as measured by reduction in area (R.A.), was decreased depended upon the strength level. Increasing the strength level by irradiation increases the susceptibility of these steels to hydrogen embrittlement (ductility change). In the case of A302B, however, this change was minimal at 1 to 2 ppm even after irradiation to high fluences. Concentrations in excess of 4 to 5 ppm were required to reduce R.A. measurements below 10 percent; this occurred only after irradiation to fluences in excess of 10^{20} n/cm². The ductility of HY-80 was much more responsive to increased amounts of hydrogen than A302B. A near nil ductility condition resulted from approximately 1 to 3 ppm hydrogen in the highly irradiated HY-80 steel. This seems to occur at a rather low hydrogen concentration based on comparisons with other unirradiated steels at this same strength level [1] and may be due to irradiation damage which may have introduced other factors than strength elevation, thus enhancing the susceptibility to hydrogen embrittlement. A near nil ductility condition in NQT A542 steel after irradiation to fluences in excess of 10^{20} n/cm² at the 2 to 3-ppm level also occurred. The fact that both of these steels in this condition were still resistant to delayed failure at the 4-ppm level indicates that, even though the ductility of a steel in a given condition may be reduced to a very low level by the presence of hydrogen, it may still possess sufficient toughness to resist crack growth. It is evident that hydrogen can produce a condition of near nil ductility in all three of these steels after irradiation to fluences in excess of 10^{20} n/cm², whereas this was not possible in the unirradiated condition over the concentration range considered.

As far as determined, strength level and not microstructural or cold work variation was the important parameter which determined the degree to which the ductility would be affected by the presence of 1 to 2 ppm hydrogen. Irradiation hardening of these steels to levels in excess of approximately 180 ksi resulted in a condition that was particularly susceptible to hydrogen embrittlement, but not necessarily to delayed failure. H.T. 53 and 58 were susceptible to delayed failure prior to irradiation. Irradiation and hydrogen decreased the notch strength ratio, but even hydrogen concentrations that reduced this ratio to a value less than one (brittle notch) did not result in a condition in which there was an appreciable difference between the notched strength and the LCS.

Hydrogen concentrations of 1 to 2 ppm in these three steels in the NQT condition irradiated to a fluence of about 8×10^{18} n/cm² resulted in a decrease in the NTS; however, irradiation hardening more than compensated for this loss such that the LCS was higher than the unirradiated NTS.

Irradiation to fluences in excess of 10^{20} n/cm² further strengthened these steels but did not fully compensate for the effects of 1 to 2 ppm hydrogen, that is, the LCS was approximately equal to or slightly below the unirradiated NTS. Increasing the hydrogen concentration further reduced the LCS but did not lead to a condition where delayed failure occurred with hold times up to 60 to 70 h.

Practical Implications

Peak design life fluence levels for pressurized water reactors are currently set at 3×10^{19} n/cm². Thus specimens irradiated to fluences in excess of 10^{20} n/cm² and tested were probably at strengths in excess of those likely to be found in LWR steels unless future reactors are designed with the vessel closer to the core. This condition thus represents an advanced state with respect to material property degradation by irradiation and the most susceptible to hydrogen embrittlement. Pressure vessels are subjected to stresses approaching two thirds of the unirradiated yield at reactor operating conditions. In the case of highly irradiated A320B, diffusible hydrogen concentrations of from 4 to 5 ppm were required to initiate failure at stresses approaching the unirradiated yield strength. A542 and particularly HY-80 were more adversely affected by the presence of hydrogen; however, irradiation to fluences of approximately 4×10^{20} n/cm² resulting in a UTS of 195 ksi in the case of HY-80 were required to produce a condition in which 1 to 2 ppm hydrogen could initiate brittle failure at stress levels less than yield. All three of these steels retained considerable notch toughness after irradiation to fluences in excess of 10^{20} n/cm² and were able to resist hydrogen induced stable crack growth at stress levels less than the hydrogenated notch strength despite the probable higher hydrogen concentrations at the notch root, because of stress induced diffusion of hydrogen to the vicinity of the notch. These values indicate that several parts per million of diffusible hydrogen in a reactor vessel concentrated in the region of a flaw, small crack, or other stress riser would not lower the toughness to the point where growth of the flaw to produce crack instability would occur. The fact that operating temperatures for LWR reactors are from 300 to 350 C should serve further to minimize the deleterious effect of hydrogen by increasing intrinsic material toughness.

The data reported herein therefore support the conclusion that medium-strength pressure vessel steels in the normal quenched and tempered condition used for pressurized water and boiling water reactor plants operating under normal conditions will not be embrittled by the presence of 1 to 2 ppm hydrogen to the point where catastrophic failure will occur.

Conclusions

1. The ductility (reduction in area) of A302B steel after irradiation to fluences of nearly 3×10^{20} n/cm², $E > 1$ MeV, was not significantly affected

by the presence of up to 2 ppm hydrogen. Hydrogen concentrations greater than 2 ppm, however, resulted in a marked decrease in ductility with an essentially nil ductility condition reached at the 5 to 6-ppm level.

2. HY-80 and A542 steel in the normal quenched and tempered condition were much more responsive to the presence of 1 to 2 ppm hydrogen. Low-strain rate tests on specimens irradiated to approximately 7×10^{18} n/cm² resulted in a decrease in the reduction of area measurements of about 20 percent (from 65 to 45 percent). Subsequent to irradiation to 2×10^{20} n/cm², $E > 1$ MeV, A542 steel showed essentially nil ductility at the 2 to 3-ppm level, while HY-80 displayed a nil ductility condition at 1 to 2 ppm.

3. Heat treatment or cold working, which increased the strength level (like irradiation), resulted in a condition that was more sensitive to hydrogen induced ductility reductions, particularly after a strength level of approximately 180 ksi had been attained.

4. Hydrogen induced delayed failure did not occur to any large extent in HY-80, A302B, and A542 steel in the normal quenched and tempered condition even after irradiating to fluences in excess of 10^{20} n/cm², $E > 1$ MeV, and hydrogen concentrations of up to 4 ppm.

5. Irradiation hardening increased the magnitude of the decrease in notched strength resulting from a given hydrogen concentration in all of the steels and conditions tested. As irradiation increased the notch strength level, however, this effect was somewhat self-compensating from a design point of view in that at the 1 to 2-ppm level the hydrogenated notch strength or lower critical stress to failure was equal to or only slightly less than that of the unirradiated strength. Increasing the hydrogen concentration beyond this point resulted in a further decrease in the lower critical stress level.

6. Steel (A542) that was heat-treated to a preirradiation hardness of HRC 35 by normalizing, quenching, and tempering treatments was susceptible to hydrogen induced delayed failure in both the pre and postirradiation conditions.

Acknowledgments

We wish to acknowledge the assistance of G. A. Rigby in the accomplishment of much of the experimental work and the Fuels and Materials Branch, RDT, for sponsoring this study.

References

- [1] Farrell, K. and Quarrell, A. G., *Journal of the Iron and Steel Institute*, JISIA, Vol. 202, December 1964, p. 1002.
- [2] Fletcher, E. E. and Elsea, A. R., *Battelle Technical Review*, BATRA, Vol. 16, No. 12, Dec. 1967, p. 10.
- [3] Munse, W. H., *Fracture an Advanced Treatise*, H. Liebowitz, Ed., Vol. IV, Academic Press, 1969, p. 371.

- [4] Tetelman, A. S., "The Mechanism of Hydrogen Embrittlement in Steel," Proceedings of Conference on Fundamental Aspects of Stress Corrosion Cracking, Ohio State University, Sept. 1967, p. 446.
- [5] Johnson, H. H., "On Hydrogen Brittleness in High Strength Steels," Proceedings of Conference on Fundamental Aspects of Stress Corrosion Cracking, Ohio State University, Sept. 1967, p. 439.
- [6] Gilpin, C. B., Paul, D. H., Asunmaa, S. K., and Tiner, N. A. in *Advances in Electron Metallography, ASTM STP 396*, American Society for Testing and Materials, 1966, pp. 7-20.
- [7] Harries, D. R. and Broomfield, G. H., *Journal of Nuclear Materials*, JNUMA, Vol. 9, No. 3, 1963, p. 327.
- [8] Broomfield, G. H., *Journal of Nuclear Materials*, JNUMA, Vol. 16, 1965, pp. 249-259.
- [9] Rossin, A. D., "Hydrogen Embrittlement in Irradiated Steels," ANL-7266, Clearinghouse for Federal Scientific and Technical Information, U.S. Dept. of Commerce, Springfield, Va., Feb. 1967.
- [10] Whitman, G. D., "Technology of Steel Pressure Vessels for Water Cooled Nuclear Reactors," ORNL-NSIC-21, Clearinghouse for Federal Scientific and Technical Information, U.S. Dept. of Commerce, Springfield, Va., Dec. 1967, p. 219.
- [11] Sterne, R. H., *Nucleonics*, NUCLA, Vol. 25, No. 3, March 1967, p. A543.
- [12] Wimunc, E. A., *Power Reactor Technology*, PRETA, Vol. 9, No. 3, Summer 1966, p. 101.
- [13] Personal communication from A. Hoersch, Jr., Luckens Steel Co., Coatesville, Pa., 1 Feb. 1967.
- [14] "Evaluation of Reference Pressure-Vessel Steel for Neutron-Irradiation Studies," Tech. Report, U.S.S., Monroeville, Pa., Project No. 40.002-066 (4).
- [15] Claudson, T. T., "Fabrication History of Alloys Used in the Irradiation Effects on Reactor Structural Materials Program," BNWL-CC-236, Oct. 1963.
- [16] Barnett, W. J. and Troiano, A. R., *Transactions*, American Institute of Mining, Metallurgical and Petroleum Engineers, TAIMA, Vol. 209, April 1957, p. 486.
- [17] Brinkman, C. R. and Beeston, J. M., "Effects of Irradiation on the Surface Activity and Diffusivity of Hydrogen in Steels," IN-1200, Clearinghouse for Federal Scientific and Technical Information, U.S. Dept. of Commerce, Springfield, Va., June 1968.
- [18] Bhat, U. V. and Lloyd, H. K., *Journal of the Iron and Steel Institute*, JISIA, Vol. 188, Aug. 1950, p. 382.
- [19] Hill, M. L. and Johnson, E. W., *Transactions*, American Institute of Mining, Metallurgical and Petroleum Engineers, TAIMA, Vol. 215, Aug. 1959, p. 717.
- [20] Klier, E. P., Hawthorne, J. R., and Steele, L. E., "Tensile Properties of Selected Steels for Use in Nuclear Reactor Pressure Vessels," NRL-6649, Clearinghouse for Federal Scientific and Technical Information, U.S. Dept. of Commerce, Springfield, Va., Sept. 22, 1967.

DISCUSSION

*A. L. Bement*¹—There are important distinctions between the occlusion of hydrogen in cold-worked as compared with irradiated steel. Microtears developed by the cold working of steel create internal surfaces which can trap hydrogen in an absorbed state. This hydrogen would be released at relatively high temperatures. Irradiation induced defects, however, might also trap hydrogen by chemical binding forces, but the hydrogen should be released when the binding energy is overcome by thermal activation or when the defect is annihilated by thermal recovery. Therefore, there could be significant departures from a single hydrogen sensitivity versus ultimate strength correlation for steels representing mixed structural states.

C. R. Brinkman (authors' closure)—Trapping of hydrogen in steel is a complex phenomenon. Indeed, besides microvoids or cracks it is believed that dislocations, grain boundaries, precipitates (interfaces), twins, voids, interstitials, etc., also can be effective in trapping hydrogen. The trapping mechanism is by no means the same and its effectiveness is dependent on the size, density, and binding energy associated with the traps. Thus, microcavities can adsorb monatomic hydrogen at the lattice defect interface or they can absorb hydrogen acting as sites for recombination and collection of molecular hydrogen, or even methane if the temperature is high enough. Similarly, strain fields set up around line or point defects result in atmospheres of atomic hydrogen which can diffuse to the defect cores. Certainly the nature and extent of the structural imperfections introduced by cold working² or irradiation damage will result in differences in the types of traps operative at a given temperature; however, the two conditions could show similar anomalous behavior, as was indicated in this paper, with respect to an apparent increase in hydrogen solubility over that of the unirradiated and strain-free material.

Departure from a simple hydrogen sensitivity versus ultimate strength correlation is indeed a possibility in irradiated materials and it has been shown that this can be accomplished in unirradiated steels by microstructural variations at a given strength level. Additional work needs to be accomplished in order to more closely define the nature of the hydrogen-irradiation induced defect interaction intimated by this work.

¹ Battelle-Northwest, Richland, Wash. 99352.

² Oriani, R. A., *Acta Metallurgica*, AMETA, Vol. 18, Jan. 1970, p. 147.

Masayuki Kawasaki,¹ T. Fujimura,² K. Suzuki,²
H. Namatame,² and Minoru Kawasaki²

Evaluation of the Embrittlement of Pressure Vessel Steels Irradiated in JPDR

REFERENCE: Kawasaki, Masayuki, Fujimura, T., Suzuki, K., Namatame, H., and Kawasaki, Minoru, "Evaluation of the Embrittlement of Pressure Vessel Steels Irradiated in JPDR," *Irradiation Effects on Structural Alloys for Nuclear Reactor Applications, ASTM STP 484*, American Society for Testing and Materials, 1970, pp. 74-95.

ABSTRACT: Three surveillance programs of the JPDR pressure vessel have been performed to date. From the assessment of both the shift of NDT temperature and the reduction of upper shelf energy in the pressure vessel steel due to irradiation, it was concluded that the pressure vessel could be used with safety for about ten years at equivalent full power (45 MWt) operation.

A reference test was also performed on two potential steels for pressure vessel use, namely a Mn-Mo-0.4~0.7Ni steel (A533B Class 1) and a 2¼Cr-1Mo (A542 Class 1) steel, following the completion of the surveillance test. The latter steel was found to be much less sensitive to irradiation than the former. The weld metal and heat affected zone are somewhat more sensitive to irradiation than the base metal for the 2¼Cr-1Mo steel submerged arc weldment.

KEY WORDS: irradiation, neutron irradiation, radiation effects, boiling water reactors, power reactors (nuclear), pressure vessels, dosimetry, embrittlement, heat treatment, fatigue strength, cracking (fracturing), steels, alloy steels, structural steels, tests

The Japan power demonstration reactor (JPDR), which went into operation in 1963, was the first boiling water reactor (BWR) in Japan. The reactor is owned by the Japan Atomic Energy Research Institute (JAERI), which has used it to obtain experience with light-water cooled power reactors. The reactor was constructed by the General Electric Co., but the reactor pressure vessel was fabricated by a Japanese firm using domestic materials. The reactor has operated for a total of 14,096 h

¹ Tokyo Headquarters, Japan Atomic Energy Research Institute, Tokyo, Japan.

² Tokai Research Establishment, Japan Atomic Energy Research Institute, Tokai-mura, Japan.

(18,501 MWD) at an equivalent full power of 45 MWt (12.5 MWe) from 1963 to 1969.³

Findings from the operation have contributed in assuring the integrity of the pressure vessel and its components for the many power reactors that were and are being constructed in Japan. JAERI is proceeding now with a project to double the thermal power of the JPDR (JPDR-II program). In order to confirm the integrity of its pressure vessel with respect to neutron irradiation embrittlement, JAERI has already performed three surveillance programs. In the JPDR, after removal of the surveillance test coupons, positions inside the vessel shroud can be used for a reference test on new vessel steels.

From the results of the surveillance test, it was found that the pressure vessel could be expected to operate for about ten years at an equivalent full power under the existing conditions. In the reference test, interesting behavior concerning the irradiation embrittlement was noted on two domestic steels: one, Mn-Mo-0.4~0.7Ni low-alloy steel (ASTM A533B), has been generally used for light water cooled reactors; the other, $2\frac{1}{4}$ Cr-1Mo low-alloy steel (ASTM A542), is currently being developed for reactor pressure vessel service.

TABLE 1—Specifications of the JPDR pressure vessel and its operating records.

Inner diameter	2083 mm (6.85 ft)		
Inner length	8534 mm (28 ft)		
Wall thickness	67.0 mm (2.5 in.)		
Pressure:			
Normal	61.5 kg/cm ² (G) (875 psi)		
Design	77.34 kg/cm ² (G) (1100 psi)		
Test	116 kg/cm ² (G) (1650 psi)		
Design temperature	343 C (650 F)		
Vessel shell and heads material	ASTM A302B modified steel		
Flange material	ASTM A-336 case 1236		
Term	Reactor Operation Time, h	Integrated Thermal Power, MWD	Electric Generating Time, h
1963.....	659	540	311
1964.....	379	281	176
1965.....	4 043	5 420	3 420
1966.....	3 996	5 535	3 678
1967.....	3 257	4 072	3 059
1968.....	801	1 083	692
1969.....	961	1 570	901
Total.....	14 096	18 501	12 237

³ MWD = megawatt-days, MWt = megawatts thermal, MWe = megawatts electrical.

Results of the Surveillance Test

Specifications of the JPDR and Its Operational Records

Table 1 shows the specifications of the JPDR and its operational records. During operation of this reactor, two kinds of problems concerning pressure vessel integrity were considered: one concerned the reduction of fatigue strength in nozzles, believed to be caused by hair cracks in the stainless steel overlaid welds; and the other was neutron irradiation embrittlement on the pressure vessel steel and its welds near the reactor core. For the former problem, JAERI performed low-cycle fatigue tests with small laboratory specimens and cyclic pressure loading tests with three vessel models. These tests assured that the reactor vessel integrity would be sufficiently maintained. The latter problem was resolved as described below.

Program of Surveillance Test

The surveillance test program for the JPDR pressure vessel is summarized in Table 2. The surveillance test coupons were base metal, weld metal, and heat affected zone specimens. The longitudinal direction of the base metal specimen was that of the rolling of the vessel plate and those of the weld metal and heat affected zone specimens were perpendicular to the welding direction. Each irradiation capsule contained twelve V Charpy test specimens and three tension specimens. Irradiation capsules were located just inside the shroud and inside the vessel wall, as close to the reactor core as possible, and also in the main steam pipe, where the capsules were given equivalent thermal cycles to those of the pressure vessel but without neutron irradiation. Figure 1 shows the locations of the test coupons in the pressure vessel. In the first surveillance test three kinds of test coupons were removed from inside the shroud and from the main steam pipe in June 1966; in the second test specimens were removed from inside the vessel wall in April 1967; and in the third test from inside the shroud again in June 1969.

Dosimetry at the Irradiation Positions

When the JPDR was designed, the fast neutron flux distribution ($E > 0.1$ MeV) in the pressure vessel was calculated by the General Electric Co. (GE) code. However, the results of dosimetry at the irradiation positions differed markedly from the calculated values by the GE code. JAERI made efforts to obtain accurate values both by experiments and calculations using the JAERI code. Figure 2 shows a comparison of the results from the GE code with the experimental values for the fast neutron flux distribution in the JPDR pressure vessel, which were obtained by radiochemical analysis of pure iron wires in irradiation capsules,

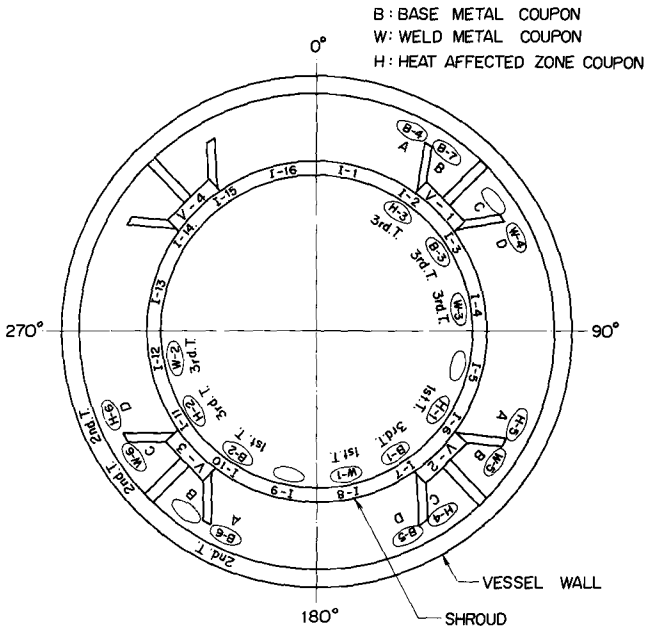


FIG. 1—Location of surveillance coupons.

using the reaction $^{54}\text{Fe}(n,p)^{54}\text{Mn}$. Inside the shroud (position A) the difference between the two calculations was not great, but inside the vessel wall (position B) the difference was fairly large, that is, JAERI's calculated value of the fast neutron flux, 3×10^{10} n/cm²-s, $E > 0.1$ MeV, was about three times as large as that of the GE code, 1.1×10^{10} n/cm²-s. On the other hand, JAERI's experimental value, 6.17 to 8.83×10^{10} n/cm²-s, was about two to three times as large as the value by JAERI code. JAERI considered the experimental values to be correct since the values were obtained by major collaborative works in the JAERI to evaluate accurately the fast neutron flux distribution in the JPDR pressure vessel. Table 3 shows the results of the dosimetry based on the experiment in the surveillance test.

Results of the Surveillance Test

Figure 3 shows the materials for the pressure vessel components and also the nil ductility transition (NDT) temperatures at the preoperational condition of these materials. In Fig. 4 are summarized the results of the whole surveillance test, that is, postirradiation V Charpy tests on the base metal, weld metal, and heat affected zone. The shift of the 30-ft·lb (4.2-kg·m) transition temperature, Tr₃₀, did not differ considerably among the three kinds of test coupon. On the assumption that Tr₃₀ is equivalent

to NDT temperature, as the initial NDT temperature of the base metal is the highest among the test coupons, it was adequate to evaluate the irradiation embrittlement of the JPDR pressure vessel from that of the base metal. Figure 5 shows the shift of Tr30 for the base metal caused by neutron irradiation. The data of the JPDR surveillance test were between Carpenter's sensitive and insensitive curves [7]⁴ and agreed with Steele's data [8] at 260 C, the irradiation temperature. In Fig. 6 the results are compared with those for other light water cooled reactors [9]; the data of the JPDR have the same tendency as the other BWR reactors. Figure 7 shows the influence on the reactor operation due to the neutron irradiation embrittlement of the JPDR pressure vessel. The initial NDT temperature of the vessel wall near the reactor core was about 20 C; the results of surveillance tests showed that, for the assumed reactor life, at full power, of twenty years, the NDT temperature would be about 120 C, assuming

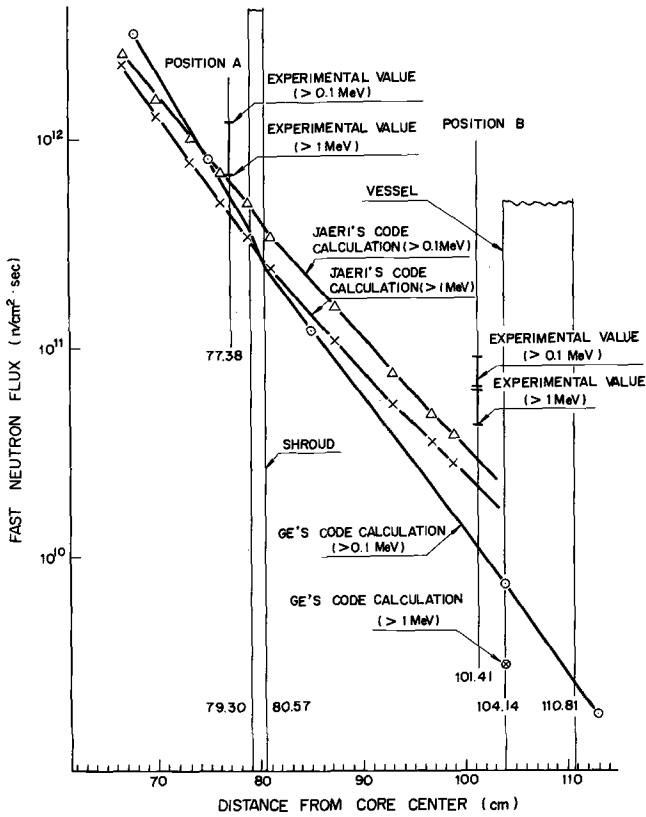
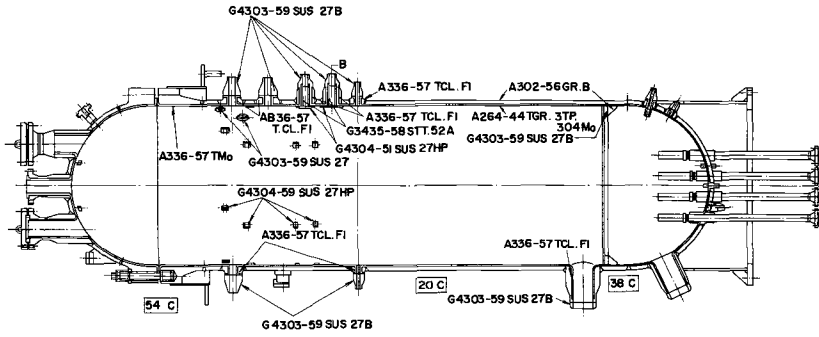


FIG. 2—Radial distribution of fast neutron flux in JPDR pressure vessel.

⁴ Italic numbers in brackets refer to the list of references at the end of this paper.

TABLE 3—Results of dosimetry in surveillance test.

	Fluence of Test Coupons, n/cm ²					
	First Surveillance Test		Second Surveillance Test		Third Surveillance Test	
	<i>E</i> > 0.1 MeV	<i>E</i> > 1 MeV	<i>E</i> > 0.1 MeV	<i>E</i> > 1 MeV	<i>E</i> > 0.1 MeV	<i>E</i> > 1 MeV
Location of test coupons.	Inside of shroud	Inside of shroud	Inside of vessel	Inside of shroud	Inside of shroud	Inside of shroud
Calculated value.	7.11 × 10 ¹⁹	7.83 × 10 ¹⁸	6.61 × 10 ¹⁷	4.96 × 10 ¹⁷
Experimental value.	2.22 to 2.23 × 10 ¹⁹	1.24 to 1.25 × 10 ¹⁹	1.46 to 2.09 × 10 ¹⁸	1.05 to 1.50 × 10 ¹⁸	4.13 to 5.27 × 10 ¹⁸	2.31 to 2.94 × 10 ¹⁸



Remark: Temperature put in squares shows NDT temperature in the component.

FIG. 3—Preoperational NDT temperature in components of JPDR pressure vessel.

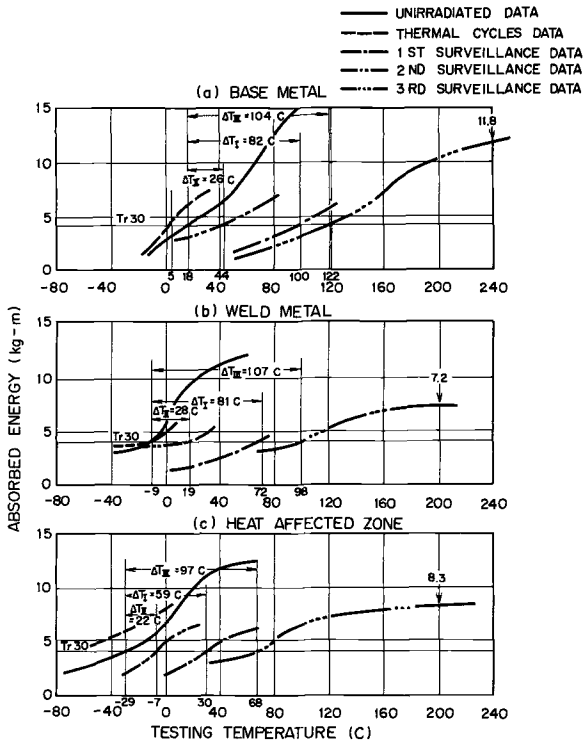


FIG. 4—Results of postirradiation V Charpy test.

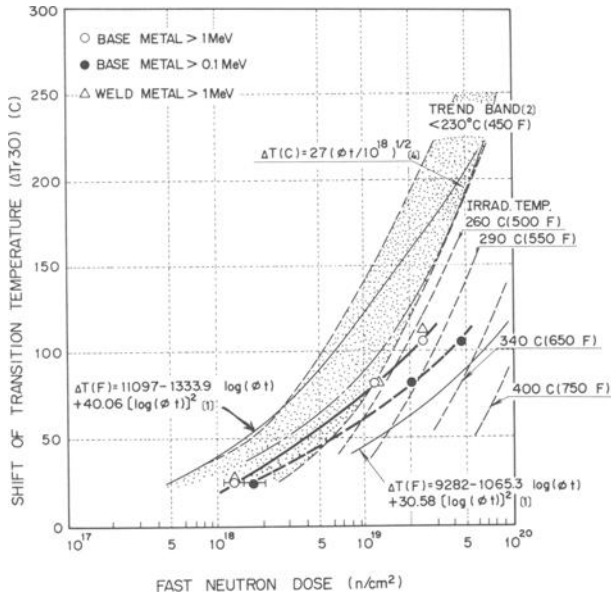


FIG. 5—Irradiation embrittlement of JPDR pressure vessel.

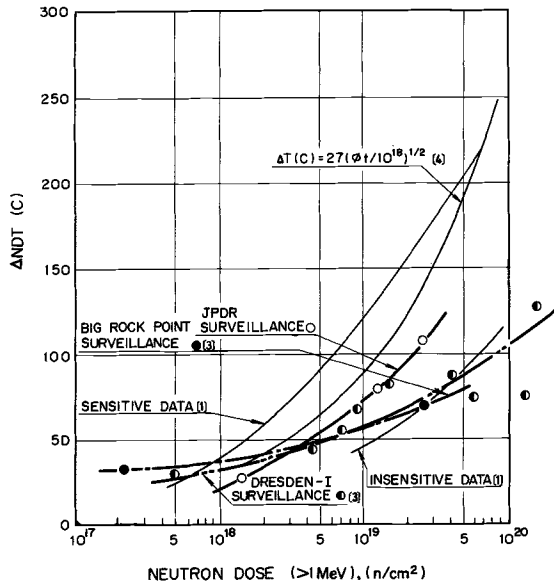


FIG. 6—Comparison of results of surveillance test in several reactors.

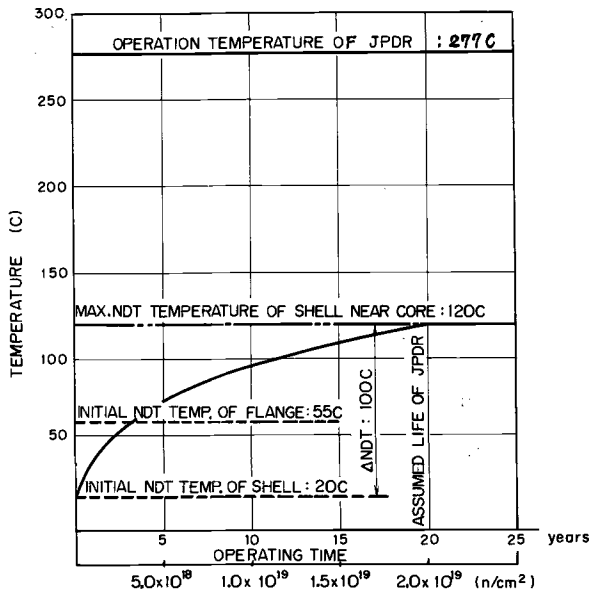


FIG. 7—Shift of NDT temperature in JPDR pressure vessel.

$\Delta T_{r30} = 100$ C for fast neutron fluence, 2×10^{19} n/cm², ($E > 1$ MeV). Therefore, at the end of reactor life, this NDT temperature would be sufficient to avoid a brittle fracture of the pressure vessel at operating temperature. Nevertheless, it is necessary to take precautions if the pressure vessel is to be pressure tested or if the reactor is to be shutdown near the end of reactor life. The shift of NDT temperature is relatively large in the initial stage of operation (the fast neutron dose applied to the vessel wall was approximately 10^{18} to 10^{19} n/cm²); from this fact, the pressure test temperature of the JPDR pressure vessel must be changed to a higher temperature in some cases.

In addition to the shift of transition temperature, the reduction of upper shelf energy due to irradiation should be noticed, since this can also lead to unstable fracture behavior of the pressure vessel. This reduction of upper shelf energy was measured in the third test (Table 4).

According to Burghard et al [5], the reduction of upper shelf energy due to irradiation is formulated as follows:

$$\Delta E/E = -5.70143 - 0.145 \ln \phi t \dots \dots \dots (1)$$

where ΔE is the reduction of upper shelf energy, E is the initial upper shelf energy, and ϕt is the fast neutron fluence ($E > 1$ MeV).

TABLE 4—Upper shelf energy of pressure vessel steels in the JPDR surveillance test.

Metal	Absorbed Energy by V Charpy Test, kg·m (ft·lb)	
	Preirradiation	Postirradiation (2.6×10^{19} n/cm ²)
Base metal.....	9.8 to 14.0 mean 11.9 (86)	9.0 to 12.8 mean 11.2 (81)
Weld metal.....	11.2 to 11.6 mean 11.4 (82)	6.6 to 7.6 mean 7.2 (52)
Heat affected zone.....	11.7 to 12.7 mean 12.2 (88)	7.5 to 9.0 mean 8.3 (60)

NOTE—Tests were performed at 240 C for the base metal specimens and at 200 C for the weld metal and heat affected zone specimens. At these testing temperatures the fracture behaviors showed 100 percent shear mode in all specimens.

However, we found Eq 1 to be incorrect; the correct form is

$$\Delta E/E = -6.0695 + 0.145 \ln \phi t \dots \dots \dots (2)$$

For the base metal specimens of the JPDR pressure vessel steel, the initial upper shelf energy was 11.9 kg·m at 100 C on the average. In the third test (the fast neutron fluence was 2.6×10^{19} n/cm²), the upper shelf energy decreased to 11.2 kg·m at 200 C so that the reduction was extremely small, and this tendency did not agree with the corrected equation (Eq 2). However, this fact is rather common to irradiation data obtained in our country, as shown in Fig. 8, and the tendency for reduction in upper shelf energy for the base metal can be indicated by the following equation:

$$\Delta E/E = -2.63287 + 0.063 \ln \phi t \dots \dots \dots (3)$$

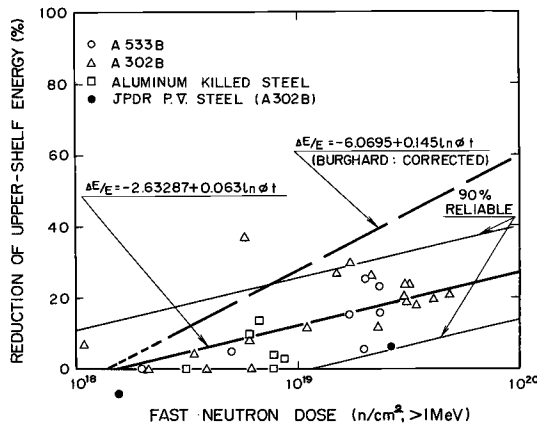


FIG. 8—Reduction of upper shelf energy by irradiation (base metal).

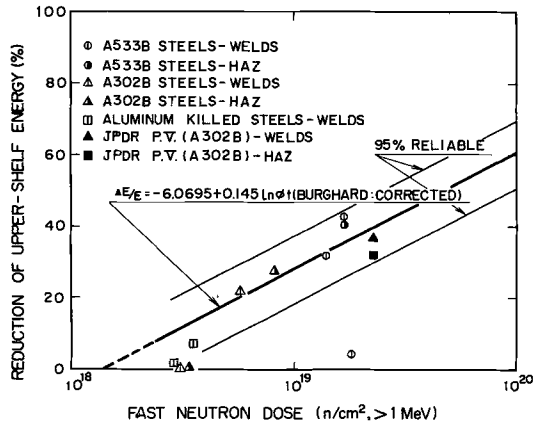


FIG. 9—Reduction of upper shelf energy by irradiation (weldments).

On the contrary, as shown in Fig. 9, the reduction of upper shelf energy in the weld metal and heat affected zones was fairly larger than that of the base metal and fitted Eq 2. Hence, the weld metal becomes the limiting factor in regard to the shelf reduction question.

Concerning the evaluation of the shelf reduction question, we have introduced the judgment, made by the Safety Committee of the Government, that the assessment should be done by taking into account the tentative U.S. Atomic Energy Commission regulation. This regulation means that even in the postirradiation state more than 40 ft·lb of upper shelf energy must be kept in all parts of the vessel components in order to prevent unstable fracture. Furthermore, in actual evaluation, as shown in Fig. 10, we have converted the values obtained from surveillance test plates into ones for production test plates as the most conservative case of weld metal.

Thus, by taking the above considerations into account for the irradiated weld metal, which showed the lowest shelf energy among the three kinds of specimen, we could derive a limiting fluence of about 1×10^{19} n/cm² ($E > 1$ MeV),⁵ from the experimental results as shown in Fig. 10. This limiting fluence corresponds to the usage of the present vessel for ten years.

Finally from the assessment of both the shift of NDT temperature and the reduction of upper shelf energy, it was concluded that the JPDR pressure vessel can be operated with safety for at least ten years at equivalent full power (45 MWt) operation.

⁵ Conservative criterion recommended by the government.

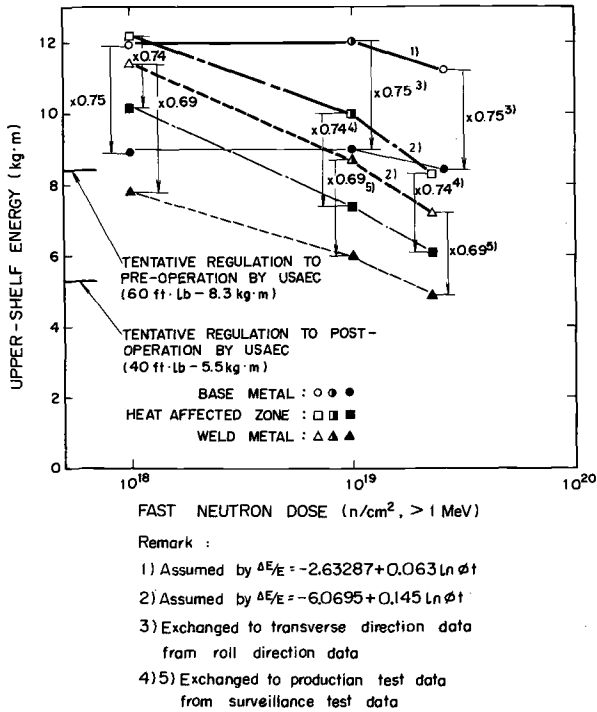


FIG. 10—Evaluation of the reduction of upper shelf energy.

Results of the Reference Test

Testing Purpose

Mn-Mo-Ni steel (A533B Class 1), widely used in the construction of pressure vessels of light water cooled reactors, will be required in thicknesses of 300 mm or greater in the near future with the growing size of reactors. However, properties satisfying some design requirements of pressure vessels, particularly good notch toughness, are hard to obtain in such heavy-section sizes, thus higher strength steels are being considered for future nuclear reactor pressure vessel construction. High-strength steels are also advantageous with respect to the relatively lower total cost for pressure vessel construction.

Cr-Mo steels have been used at temperatures below 550 C for high-pressure piping or vessel construction in steam power electric generation and in the chemical industry. Recently, 2¼Cr-1Mo steel in a thickness of 250 mm has been used for construction of chemical plants in Japan. The heat treatment of quenching and tempering is gradually replacing the customary heat treatment of normalizing and tempering, with the corre-

sponding development of welding procedures. Therefore, the series of Cr-Mo steels is considered to be one of the prime candidate steels for future nuclear structural applications.

On the other hand, pressure vessel steels are required which exhibit lower radiation sensitivity. Steele et al [6] found that the radiation induced increase in transition temperature (ΔNDT) tended to be smaller in the higher strength steel in 306 C irradiation tests of several higher strength steels. Furthermore, in irradiation tests on A302B steels, it was shown that the radiation sensitivity of a steel can be altered appreciably through heat treatment practices and that a tempered martensite structure is generally less radiation sensitive than tempered upper bainite and ferrite structures [7].

From these experimental results it was anticipated that the radiation sensitivity of a steel would depend strongly on the strength level, namely, yield strength, tensile strength, or yield to ultimate strength ratio, although it varies with metallurgical variables other than heat treatment even at the same strength level. In fact, it was found from the latter experimental data that the radiation sensitivity in each single heat of A302B steel becomes smaller with increasing strength level. In this point, at least, Cr-Mo steels with a higher strength level also could be expected to exhibit lower radiation sensitivity.

Thus, as a preliminary study to assess the potential of Cr-Mo steels for future nuclear structural applications, JAERI performed irradiation tests on $2\frac{1}{4}\text{Cr-1Mo}$ steels in the JPDR, following the surveillance test procedure mentioned in the previous section.

Program of Reference Test

The experiments included the comparison of the notch ductilities between the quenched and tempered $2\frac{1}{4}\text{Cr-1Mo}$ steel (A542 Class 1) and the Mn-Mo-Ni steel (A533B Class 1) and also the comparisons of the notch ductility of the weld metal and heat affected zone with that of the base metal for the $2\frac{1}{4}\text{Cr-1Mo}$ (A542 Class 1) submerged arc weldment. Limited investigation results of the influence of nickel content on radiation sensitivity of $2\frac{1}{4}\text{Cr-1Mo}$ steel are also given.

Materials and Condition of Irradiation

Table 5 shows the chemical compositions of the Mn-Mo-Ni steel plate and the $2\frac{1}{4}\text{Cr-1Mo}$ steel plate and weldment in the present reference test together with the heat treatment conditions. The 165-mm Mn-Mo-Ni steel and the 150-mm $2\frac{1}{4}\text{Cr-1Mo}$ steel met ASTM specifications for A533B Class 1 steel and A542 Class 1 steel, respectively. Except for the 25-mm $2\frac{1}{4}\text{Cr-1Mo}$ steels with varying nickel content, all materials were produced commercially.

TABLE 5—Chemical composition and heat treatment condition of Mn-Mo-Ni steel (A533B Class 1) and 2¼Cr-1Mo steel.

Material Identification		Chemical Composition, wt %										Heat Treatment	
Type	Thickness, mm	C	Si	Mn	P	S	Ni	Cr	Cu	Mo	ΣAl	Al _{tot}	
Mn-Mo-Ni (A533B Class 1) ^a	165	0.19	0.27	1.34	0.014	0.008	0.63	0.12	0.22	0.50	0.023	...	908 to 920 C X 10% h → W.Q.; 660 to 670 C X 13 ³ / ₁₂ h → W.Q.; 615 to 625 C X 45 h → F.C.
2¼ Cr-1Mo (A542 Class 1) ^b Base metal	150	0.15	0.31	0.58	0.014	0.006	...	2.10	...	1.06	...	0.033	Base metal: 925 C X 6 h → W.Q.; 640 C X 3 h → W.Q.
Weld metal Heat affected zone		0.12	0.29	0.65	0.020	0.005	...	2.54	...	1.17	...	0.007	Postweld: 620 C X 20 h → F.C.
2¼ Cr-1Mo ^c Standard	25	0.18	0.21	0.50	0.012	0.013	0.05	2.25	...	0.94	0.031	0.022	920 C X 1 h → A.C. (60 C/min); 650 C X 3 h → A.C. (60 C/min); 625 C X 30 h → F.C.
Added 1% Ni		0.16	0.25	0.53	0.015	0.011	1.07	2.27	...	0.98	0.034	0.022	
Added 2% Ni		0.20	0.21	0.53	0.015	0.011	2.00	2.30	...	0.97	0.034	0.024	

^a Plate.

^b Submerged arc weldment.

^c Plate (100-kg laboratory heats).

TABLE 6—Results after preirradiation and postirradiation at 277°C to 3.0×10^{18} n/cm², $E > 1$ MeV, of tension tests and V Charpy impact tests.

Material Identification		Tensile Properties (Room Temperature)						Notch Ductilities										
Type	Plate Thickness, mm	σ_s , kg/mm ²		σ_B , kg/mm ²		δ , %		Tr30, deg C		TrS, deg C		E_{max} , kg·m						
		Unirradiated	Irradiated	Unirradiated	Irradiated	Unirradiated	Irradiated	Unirradiated	Irradiated	Unirradiated	Irradiated	Unirradiated	Irradiated					
		$\Delta\sigma_s$		$\Delta\sigma_B$		Unirradiated	Irradiated	ΔTr_{30}		Unirradiated	Irradiated	ΔE_{max}						
Mn-Mo-Ni (A533B Class1) ^a	165	48.7	54.3	+5.6	62.9	68.7	+5.8	27.7	62.1	-50	6	+56	7	53	+46	19.2
2½Cr-1Mo (A542 Class1) ^b	150	61.9	65.8	+3.9	76.0	78.2	+2.2	26.7	73.3	-64	-64	0	-33	-10	+23	20.9	20.8	-0.1
Weld metal		65.9	72.6	+6.7	77.5	81.9	+4.4	22.9	63.7	12	35	+23	27	52	+25	14.1	10.9	-3.2
Heat affected zone										-84	-70	+14	-27	-15	+12	17.7	18.4	0.7
2½Cr-1Mo ^c	25	51.3	65.9	29.7	77.0	-114	-108	+6	-109	-88	+21	23.4	23.2	-0.2
Standard		53.7	68.5	29.4	73.7	-85	-74	+11	-51	-36	+16	19.7
Added 1% Ni		55.4	71.6	30.2	70.9	-77	-70	+7	-62	-43	+19
Added 2% Ni																		

Note— σ_s = yield strength; σ_B = tensile strength; δ = elongation; ϕ = reduction of area; $\Delta E/E$ = reduction of upper shelf energy; $\Delta E/E$ = reduction of upper shelf energy, %.

^a Plate.
^b Submerged arc weldment.
^c Plate.

Standard V Charpy test specimens and tension specimens of 9-mm diameter were taken in the longitudinal direction from quarter thickness for the Mn-Mo-Ni steel plate and 2¼Cr-1Mo submerged arc weldment, and from half thickness of plates for 25-mm 2¼Cr-1Mo steels with varying nickel content. The weld metal and heat affected zone specimens were oriented with their longitudinal axes perpendicular to the welding direction. V Charpy test specimens were notched perpendicular to the surface of the plates or weldment.

The irradiation test was performed in the JPDR following the third surveillance test previously described. The specimens were irradiated simultaneously in the same operating cycle in the sealed stainless steel capsules, just inside the shroud at 277 C. The fast neutron dose ($E > 1$ MeV) was 3×10^{18} n/cm², measured by the ⁵⁴Fe(n,p)⁵⁴Mn reaction. Irradiation methods used in the present reference test were the same as those used in the surveillance test.

Results

The results of pre and postirradiation tension tests and V Charpy tests are summarized in Table 6. Figure 11 shows the difference in radiation sensitivity between the 2¼Cr-1Mo steel and the Mn-Mo-Ni steel plates of nearly the same thickness (150 mm and 165 mm, respectively). From

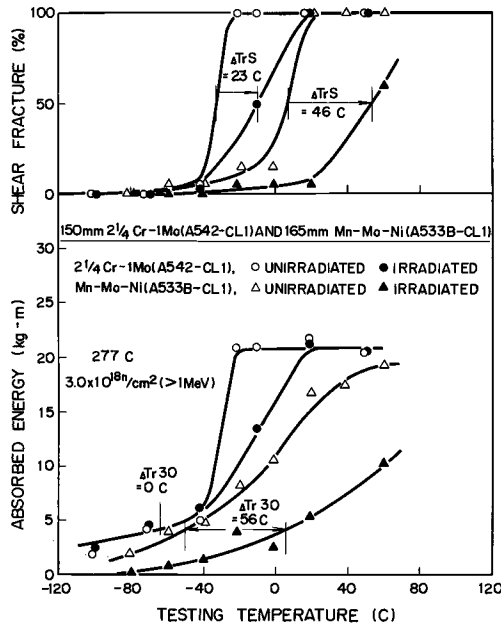


FIG. 11—Comparison of radiation sensitivity of 2¼Cr-1Mo steel and Mn-Mo-Ni steel.

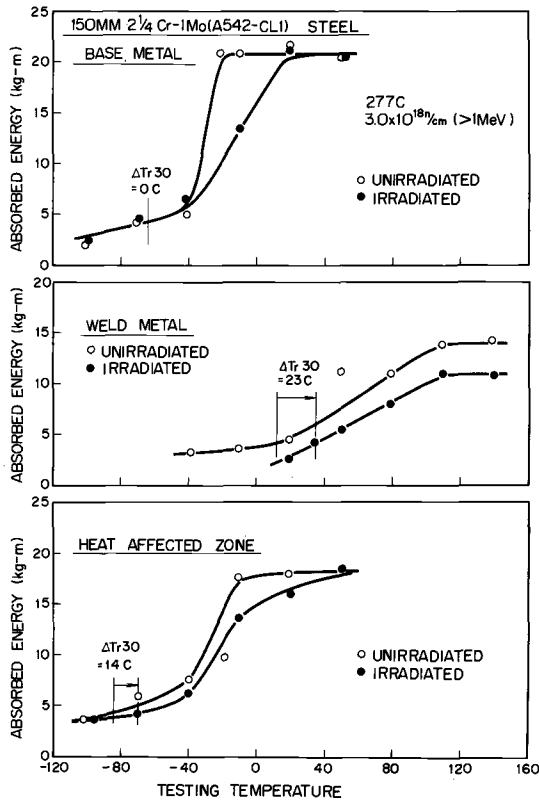


FIG. 12—Notch ductility characteristics of 150-mm $2\frac{1}{4}$ Cr-1Mo submerged arc weldment in response to irradiation.

Fig. 11 it is seen that the $2\frac{1}{4}$ Cr-1Mo steel is much less sensitive to irradiation than the Mn-Mo-Ni steel; on the other hand, Mn-Mo-Ni steel (A302B) and $2\frac{1}{4}$ Cr-1Mo steel (A387) have been reported to show similar ΔTr_{30} values after irradiation at 306 C to 3.8×10^{19} n/cm², $E > 1$ MeV [6]. We consider this discrepancy to be due to the difference in strength level between the $2\frac{1}{4}$ Cr-1Mo steels tested. In order to clarify this point, it is necessary to perform further detailed irradiation tests of $2\frac{1}{4}$ Cr-1Mo steel under various heat treatment conditions.

Figure 12 shows the results for the $2\frac{1}{4}$ Cr-1Mo submerged arc weldment. The weld metal and heat affected zone are rather more sensitive to irradiation than the base metal. These results are similar to those observed on the submerged arc weldments of other steels; for example, Mn-Mo steel (A302B) [8, 9], Mn-Mo-Ni steel (A533) [10], and $3\frac{1}{2}$ Ni-Cr-Mo steel (HY-80) [8, 10].

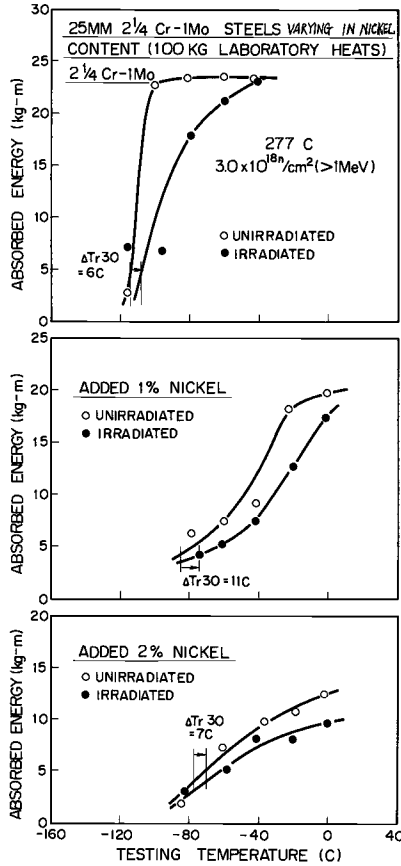


FIG. 13—Notch ductility characteristics of 25-mm 2 1/4Cr-1Mo steels varying in nickel content in response to irradiation.

The effects of nickel content in 2 1/4Cr-1Mo steel on the radiation sensitivity are indicated in Fig. 13. It can be seen that the nickel content, up to 2 weight percent, does not have much influence on the radiation sensitivity of the 2 1/4Cr-1Mo steel, as far as the data in the reference test. However, the increase of nickel content tends to raise the initial transition temperature and to reduce the initial upper shelf energy, thus addition of nickel up to 2 weight percent in 2 1/4Cr-1Mo steel would not be desirable.

Conclusions

From the results of the surveillance test, the following can be concluded.

1. The shift of the NDT temperature of JPDR pressure vessel steel (A302B) due to irradiation is between Carpenter's sensitive and insensitive

curves and agrees with Steele's data at 260 C. After irradiation to 2×10^{19} n/cm², $E > 1$ MeV, the shift would be about 100 C.

2. The reduction of upper shelf energy for the weld metal and heat affected zone follows the relationship derived by Burghard, but for the base metal it becomes extremely small. The upper shelf energy of the JPDR pressure vessel weld metal, whose energy is the lowest, satisfies the assumed limiting energy value, 40 ft·lb (5.5 kg·m), after irradiation to 1×10^{19} n/cm², $E > 1$ MeV.

3. From the assessment of both the shift of NDT temperature and the reduction of upper shelf energy, it was concluded that the pressure vessel could be operated with safety for about ten years at equivalent full power (45 MWt) operation.

The following can be concluded from the results of the reference test.

1. $2\frac{1}{4}$ Cr-1Mo steel (A542 Class 1) is much less sensitive to fast neutron irradiation at 3×10^{18} n/cm², $E > 1$ MeV, than is Mn-Mo-Ni steel (A533B Class 1).

2. The weld metal and heat affected zone are somewhat more sensitive to irradiation than the base metal for a $2\frac{1}{4}$ Cr-1Mo submerged arc weldment.

3. Addition of nickel up to 2 weight percent in $2\frac{1}{4}$ Cr-1Mo steel does not seem to be desirable, because it increases the initial NDT temperature and reduces the initial upper shelf energy.

From the viewpoint of fabrication experience and quality in the pre and postirradiated state, Mn-Mo-Ni steel (A533) has been demonstrated as an excellent pressure vessel material in Japan. From the present preliminary data, $2\frac{1}{4}$ Cr-1Mo steel (A542) was shown to be promising for nuclear pressure vessel steel in the heavy-section range. The steel already has had wide application in non-nuclear industries.

Acknowledgments

We are indebted to M. Hasegawa, professor, Waseda University, for his advice in the reference test program. Thanks are also due to the personnel of the JPDR and Hot Laboratory Divisions for their cooperation. The materials in the reference test were supplied by the Nippon Steel Corp. and the Japan Steel Works, Ltd.

References

- [1] Carpenter, G. F., *Nuclear Science and Engineering*, NSENA, Vol. 19, 1964, p. 18.
- [2] Steele, E. E., *Nuclear Engineering and Design*, NEDEA, Vol. 3, 1966, p. 287.
- [3] Charles, Z. S. et al, *Journal of Basic Engineering*, ASME Transactions, JBAAE, 1967, p. 221.
- [4] Nichols, R. W. and Harries, D. R. in *Radiation Effects on Metals and Neutron Dosimetry*, ASTM STP 341, American Society for Testing and Materials, 1963, p. 162.
- [5] Burghard, H. C., "The Effect of Neutron Irradiation on the Fracture Characteristics of Pressure-Vessel Steels," American Society of Mechanical Engineers, 1967.

- [6] Steele, L. E., Hawthorne, J. R., and Gray, R. A., Jr., "Neutron Irradiation Embrittlement of Several Higher Strength Steels," NRL Report 6419, U.S. Naval Research Laboratory, Sept. 1966.
- [7] Hawthorne, J. R. and Steele, L. E., "Initial Evaluations of Metallurgical Variables as Possible Factors Controlling the Radiation Sensitivity of Structural Steels," NRL Report 6420, U.S. Naval Research Laboratory, Sept. 1966.
- [8] Kawasaki, M. and Fujimura, T., *Transactions*, The Iron and Steel Institute of Japan, Vol. 8, 1968, p. 48.
- [9] Hasegawa, M. in *Irradiation Effects in Structural Alloys for Thermal and Fast Reactors*, ASTM STP 457, American Society for Testing and Materials, 1969, p. 92.
- [10] Hawthorne, J. R. and Potapovs, Uldis, "Initial Assessments of Notch Ductility Behavior of A533 Pressure Vessel Steel with Neutron Irradiation," NRL Report 6772, U.S. Naval Research Laboratory, Nov. 1968.
- [11] Potapovs, Uldis and Hawthorne, J. R., "The Effect of Residual Elements on 550 F Irradiation Response of Selected Pressure Vessel Steels and Weldments," NRL Report 6803, U.S. Naval Research Laboratory, Nov. 1968.

DISCUSSION

*B. Watkins*¹—Could the author please state the location of the notch in the heat affected zone specimens examined. I am particularly interested whether any work has been done where the notch is located near the fusion face in high-input welds. Evidence is accumulating that for many structural steels low toughness values are obtained in this zone. Fracture mechanics considerations would indicate that crack initiation would start at the zone of lowest toughness, provided the stress level and a defect is present of sufficient size to give crack instability. Could the authors please comment.

Masayuki Kawasaki (authors' closure)—In case of surveillance test specimens, the notch root was located at the weld bond line (weld metal-HAZ boundary line), and the notch direction was parallel to the plate surface and normal to the weld beads.

In case of reference test specimens, the notch was located at distance of about 2 mm from the weld bond which was the zone of lowest toughness, and the notch direction was normal both to the plate surface and to the weld beads.

¹ Research manager, Reactor Engineering Laboratory, United Kingdom Atomic Energy Authority, Risley, Warrington, Lancashire.

*J. R. Hawthorne*¹

Demonstration of Improved Radiation Embrittlement Resistance of A533B Steel Through Control of Selected Residual Elements

REFERENCE: Hawthorne, J. R., “**Demonstration of Improved Radiation Embrittlement Resistance of A533B Steel Through Control of Selected Residual Elements,**” *Irradiation Effects on Structural Alloys for Nuclear Reactor Applications, ASTM STP 484*, American Society for Testing and Materials, 1970, pp. 96–127.

ABSTRACT: A successful demonstration test of metallurgically controlled radiation embrittlement sensitivity has been conducted with a large commercial melt of A533B steel. The 30-ton melt represents a scaleup from 300-lb laboratory melts which provided the first evidence of the potential for very low sensitivity to radiation embrittlement at power reactor pressure vessel service temperatures (~550 F, 288 C). The commercial scale demonstration test was sponsored by the U.S. Atomic Energy Commission (AEC), Division of Reactor Development and Technology (DRDT), Fuels and Materials Branch, and depicts the “composition specification approach” to the development of optimum radiation resistance in structural steels.

The primary objective of special melt specifications and melt planning was the reduction of copper and phosphorus contents to the lowest possible level. Restrictions were also imposed on the content of other residual impurity elements with known or suspected influences on radiation embrittlement resistance. For a broad experimental analysis, the melt was split to provide material representing the primary melt analysis (0.03 percent copper) and a melt modification (0.13 percent copper). Plates representing each analysis were also split and sections individually heat-treated to Class 1 or Class 2 strength conditions. All procedures used were standard mill practices.

Radiation assessments showed the primary melt analysis to have very low sensitivity to radiation embrittlement at 550 F (288 C), thereby validating the composition specification approach for future melts. Transition temperature increases measured independently by Charpy V (C_v) and dynamic tear (DT) test methods were 70 F (39 C) or less for fluences up to 3.1×10^{19} n/cm², $E > 1$ MeV. Based upon DT results, the nil ductility transition (NDT) temperature of the Class 1 plate remained below 75 F (24 C) after 550 F (288 C) irradiation.

¹ Metallurgist, Reactor Materials Branch, Metallurgy Division, Naval Research Laboratory, Washington, D.C. 20390.

Results for the 0.13 percent copper melt modification provided direct confirmation of the primary, highly detrimental influence of copper content on radiation embrittlement resistance. The C_v 30 ft·lb transition temperature increases for the Class 1 and Class 2 plates were 140 and 125 F (78 and 69 C), respectively, for a fluence of 2.8×10^{19} n/cm², $E > 1$ MeV. The enhancement of radiation sensitivity by copper content appeared independent of the strength class.

Postirradiation DT characteristics of the primary melt analysis (Class 1 plate) were indicative of excellent fracture resistance at shelf level temperatures.

The A533B scaleup demonstration test fully supports the principles for control of radiation embrittlement sensitivity developed in laboratory research. A summary of 550 F (288 C) radiation data for the ASTM A302B reference plate and A533 standard production plate and weld metals places the results for the special melt in full perspective. The radiation embrittlement sensitivity of the primary melt analysis is shown to be only one-third that of the reference plate and significantly less than that of A533 production materials.

KEY WORDS: irradiation, neutron irradiation, radiation effects, degradation, embrittlement, nuclear reactor materials, power reactors (nuclear), pressure vessels, structural steels, melts, impurities, copper, phosphorus, radiation tolerance, mechanical tests

Variable sensitivity to radiation embrittlement has been revealed for many low-alloy pressure vessel steels [1].² The A533 steel employed extensively in new commercial reactor vessel construction is no exception [2]. Two and threefold differences in brittle-ductile transition temperature increases under equivalent exposure conditions have been documented for both A533 plate and weld metals. As a result, the prediction and possible control of variable sensitivity are of direct interest to reactor vessel operations as well as to future vessel design.

Laboratory studies for the understanding and minimization of steel embrittlement tendencies have revealed the strong influence of residual element content on radiation embrittlement characteristics at elevated service temperatures [3]. As illustrated in Fig. 1, a low residual element content was found essential for low radiation embrittlement sensitivity. Building on this research breakthrough, investigations of specific impurity elements using split laboratory melts subsequently revealed particularly detrimental influences of copper and phosphorus on irradiation resistance [3]. The contributions of other suspect impurity elements, including sulfur, aluminum, vanadium, and nitrogen, have also been assessed experimentally; however, of those elements evaluated, none appear as highly potent as copper and phosphorus.

This report concerns the transfer of laboratory-scale findings to commercial-scale practice. The 30-ton A533B steel melt to be described represents the first large-scale demonstration test of metallurgically controlled

² Italic numbers in brackets refer to the list of references at the end of this paper.

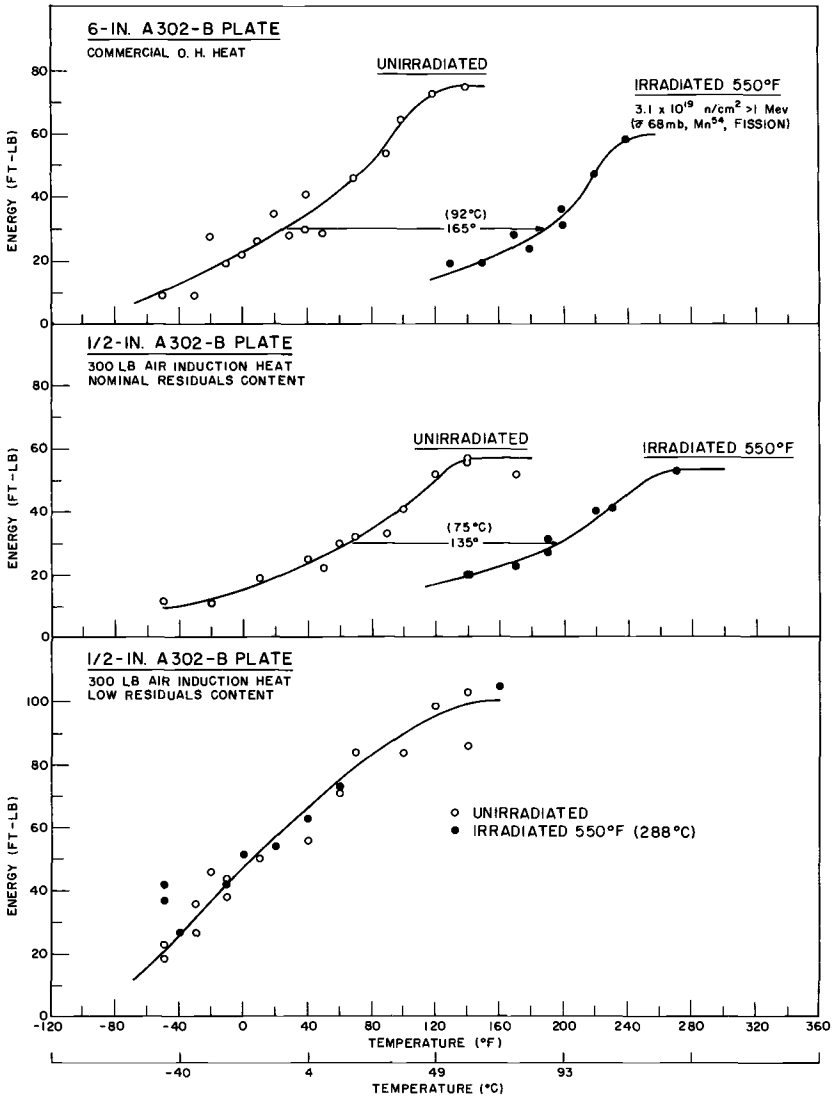


FIG. 1—Comparison of radiation embrittlement sensitivities of one large commercial heat and two air induction heats of A302B steel with nominal and low residual element contents based on Charpy V notch ductility following 550 F (288 C) irradiation [3].

radiation embrittlement behavior. More specifically, the melt was conceived as a major test of industry's capability to provide tonnage quantities of steel with nuclear characteristics matching (or closely approaching) the excellent elevated-temperature radiation resistance shown consistently by high-purity laboratory melts.

The AEC, DRDT, Fuels and Materials Branch, sponsored this scaleup demonstration test. The NRL prime contractor was Lukens Steel Co., Coatesville, Pa. The melt was made to NRL specifications by Latrobe Steel Co., Latrobe, Pa., under subcontract to Lukens Steel. As planned, the melt would not reflect any unusual production techniques or procedures but would be fully representative of conventional (standard) commercial practices.

This report presents initial findings on the radiation performance of 6-in.-thick plates from the 30-ton melt. Detailed specifications and complete mill history (melting, plate fabrication, and heat treatment) are also documented for the highly successful demonstration test.

Melt Specifications and Twin Ingot Processing Plan

General melt requirements on which actual melt specifications were founded are listed in Table 1. A 10-ton melt was considered a minimum for efficient working of the heat. This minimum melt size was also dictated by the limited availability of small-capacity electric furnaces. Plate gage and the desired ingot reduction ratio defined the minimum ingot size. Double slagging and vacuum degassing treatments were consistent with the basic aim of reducing the total impurity content to the lowest possible level.

Composition specifications for the special melt, as given by the purchase order, are summarized in Table 2. Ranges for carbon, manganese, silicon, nickel, and molybdenum contents are those limits specified by the ASTM Standard Specification for A533 Grade B steel. The balance of listed composition restrictions are special purity requirements imposed by NRL on elements with known (or suspect) influences on radiation performance. Maximum allowable values for the two elements of primary concern, copper and phosphorus, served to guide melt shop planning of the furnace charge; however, their reduction was to proceed on a best efforts basis.

In order to ensure a maximum yield of information from this scaleup effort, special steps were added to normal melt handling and plate processing sequences. Special plans included the splitting of the melt between

TABLE 1—General melt and melt processing requirements.

Composition:	A533 Grade B steel
Melt size:	10 ton (minimum)
Melt type:	Electric furnace air melt, fine grain practice
Melt charge:	Selected scrap or hot metal or both
Slag process:	Double slag
Ladle treatment:	Vacuum degas
Ingot size:	18-in.-thick ingot for 3:1 reduction (min)
Plate size:	6.0-in. gage
Rolling ratio:	Approximately 1:1 (aim)

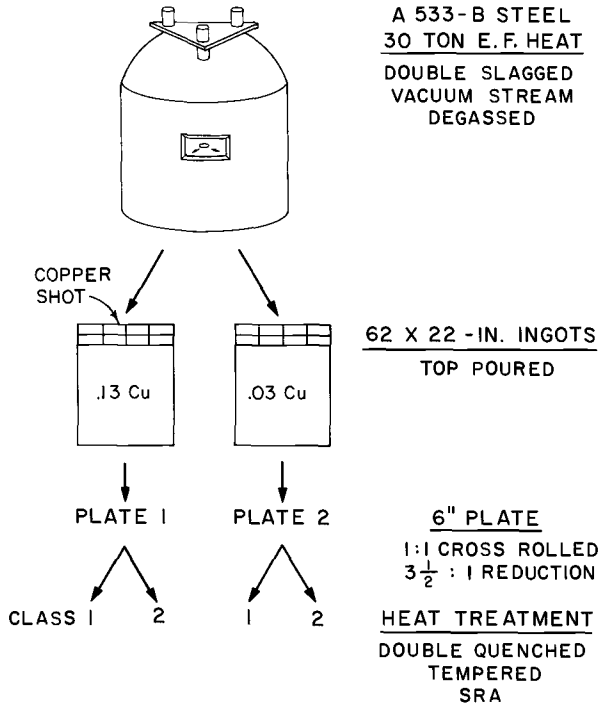


FIG. 2—Schematic plan of processing of special commercial heat of A533B steel for radiation sensitivity studies.

two ingot molds, thereby permitting a study of the effects of two impurity copper contents. The planned copper doping addition to one ingot (0.13 percent Cu) was to represent the approximate copper purity level of "best" current production A533B melts. Plans also called for the splitting of each prime plate into two sections after the final austenitizing treatment, but before tempering, to permit a direct comparison of Class 1 and Class 2 strength conditions. Thus, a total of four plate sections were secured for radiation assessments rather than one large plate representing a single composition and single heat treatment condition. Complete purchase order specifications are given in Appendix I.

The stepwise melt plan and ingot processing sequence through to final tempering treatments are illustrated schematically in Fig. 2. The 3½:1 ingot reduction ratio exceeded the required minimum reduction. Note that pure copper shot was added (gradually) to the first ingot mold³ (during the pour) to take advantage of the higher ladle temperature and head

³ Consistent with purchase specifications, this ingot is identified as ingot 2.

pressure for best mixing. Significant details of melt and ingot processing are given in Appendix II.

Heat Treatment Procedures

Primary heat treatment procedures used for the individual plate sections are outlined in Table 3. The double quench, temper, and thermal stress relief sequence is typical of the heat treatment history of plate forming welded nuclear reactor vessels. Complete heat treatment procedures are given in Appendix III together with a synopsis of mill test results including nondestructive examinations. It should be noted that the heat treatment histories of the Class 1 plate sections from ingots 1 and 2 were identical and that thermal histories of the Class 2 plate sections were also identical. Mill tests of plate sections B and D after the first (1200 F, 649 C) temper indicated that their strengths were below the Class 2 required minimum. These two plates were subsequently re-austenitized, quenched, and tempered at a lower temperature (1150 F, 621 C), whereupon repeat mill tests following a 10-h stress relief indicated acceptable Class 2 properties. Averages of mill tensile property determinations are included in Appendix III.

Drop weight tests by the mill indicated that all plate sections passed the nil ductility transition (NDT) temperature requirement of +10 F (-12 C) maximum.

Preirradiation Properties

Chemical Composition

Individual chemical compositions of ingots 1 and 2 as determined by surveys of plate sections A and B and plate sections C and D are given in Table 2. With the exception of arsenic, antimony, tin, and bismuth, the determinations are based on wet chemistry methods. Values given for As, Sb, Sn, and Bi are approximate limits based on spectrographic comparisons with reference standards. Results for ingot 1 indicate that the melt composition conformed fully to purchase order check analyses requirements (Table 2). Significantly, the copper content of ingot 1 was well below the allowable check test value and met the more stringent ladle analysis maximum as well. Phosphorus and sulfur contents satisfied check test specifications but were above ladle analysis requirements. As expected, the analyses for ingots 1 and 2 were matched except for copper content.

Referring to Appendix II, NRL and Latrobe analyses of dip test specimens (ingot hot top specimens) were in close agreement except for manganese content. Similarly, NRL and Lukens Steel check test results (plate specimens) were in good agreement, although Lukens values for copper and phosphorus were slightly higher.

TABLE 2—Chemical composition: specifications and NRL check analyses.

Determination	Chemical Composition, wt %												
	C	Mn	Si	Ni	Mo	Cu	P	S	As	Sb	Sn	Bi	Other
Melt purchase specifications													
Ladle.....	0.25 max	1.15 1.50	0.15 0.30	0.40 0.70	0.45 0.60	0.08 max	0.007 max	0.007 max	0.01 ^a max	0.01 ^a max	0.02 ^a max	0.02 ^a max	LAP max
Check.....	...	1.10 1.55	0.13 0.32	0.37 0.73	0.41 0.64	0.10 max	0.010 max	^b	0.01 ^a max	0.01 ^a max	0.02 ^a max	0.02 ^a max	...
Ingot 1 (average plates A and B)...	0.17	1.22	0.19	0.58	0.50	0.03	0.008	0.008	<0.03	<0.01	0.02	<0.005	0.02V 0.015Al (0.010-0.012Al ^d)
Ingot 2 (copper modified) (average plates C and D).	0.17	1.21	0.20	0.56	0.50	0.13 ^c	0.008	0.007	<0.03	<0.01	<0.02	<0.005	0.02V 0.015Al (0.010-0.013Al ^d)

^a As+Sb+Sn+Bi ≤ 0.05 max.
^b P+S ≤ 0.022 max.
^c Copper added to ingot 2 during pour.
^d Total aluminum by spectrographic analysis (courtesy Lukens Steel).

TABLE 3—Heat treatment of individual plate sections.

Plate Section	Strength Specification	Heat Treatment
Section A (ingot 1) } Section C (ingot 2) }Class 1 (50-ksi (min) yield strength)	Austenitized 1675 F (913 C)-6 h, water quenched; ^a re-austenitized 1575 F (857 C)-6 h, water quenched; tempered 1250 F (677 C)-6 h, furnace cooled; stress relief annealed 1125 F (607 C)-20 h, furnace cooled.
Section B (ingot 1) } Section D (ingot 2) }Class 2 (70-ksi (min) yield strength)	Same double quench treatment as Class 1 above; tempered 1200 F (649 C)-6 h, furnace cooled; stress relief annealed 1125 F (607 C)-20 h, furnace cooled; re-austenitized 1575 F (857 C)-6 h, water quenched; tempered 1150 F (621 C)-6 h, furnace cooled; stress relief annealed 1100 F (593 C)-10 h, furnace cooled.

^a Dip quenched in agitated water (typical).

Spot checks at two sampling positions in each plate (approximately 3 and 7 ft from the bottom ingot end) and at two test depths through the thickness (surface and $\frac{1}{4}T$ to $\frac{1}{2}T$) did not show composition differences suggestive of marked alloy or trace element segregation. Average copper content values for ingots 1 and 2 were, respectively, $0.03 \pm .01$ percent and $0.13 \pm .01$ percent. The average phosphorus content value for both ingots 1 and 2 was $0.008 \pm .001$ percent. The reported spread in values represents a confidence level of 85 percent or better.



FIG. 3—Microstructures of plate sections A, B, C, and D (quarter thickness location). Structures appear very similar irrespective of the copper content variation. Tempered upper bainite ($\times 500$; nital, picral etchant).

Microstructure

Typical microstructures at the quarter-plate thickness location are shown in Fig. 3. The structures have been classified as tempered upper bainite and give some small evidence of banding. Plate from both ingots 1 and 2 exhibited a duplex prior austenitic grain structure. The grain size of plate section A (0.03 percent Cu) was rated as ASTM No. 7–8 and finer; the grain size of plate section C (0.13 percent Cu) was rated as ASTM No. 8 and finer.

The close similarity of structures of Class 1 plate sections and of Class 2 plate sections has an important bearing on radiation effects comparisons described below.

Tensile Properties

Results of through thickness tension tests of each plate section are summarized in Table 4. The sampling area was located on the plate center line approximately 3 ft above the bottom ingot end. The results confirm that the strength and ductility of all four plate sections were within required ASTM limits for the respective A533B strength classes.

Through thickness properties gradients noted in Table 4 are considered quite small for the type and size of plates involved. Properties at the $\frac{1}{4}T$ and $\frac{3}{4}T$ locations are well matched in all cases. The slight difference in strength levels possibly may be a reflection of the flat quenching procedure used.

Assessments of the longitudinal (RW) and transverse (WR) plate directions also showed only small differences in properties. The observed correspondence between test orientations is indicative of the high degree of cross rolling (1:1 aim) used in plate fabrication.

Noting that the Class 2 plate sections, B and D, were heat-treated together, comparisons of test data for these two sections suggest some influence of copper content on general strength level in this heat treatment condition. Plate section D with 0.13 percent Cu exhibited both a 5 to 10-ksi higher yield strength and a 5 to 10-ksi higher tensile strength than plate section B with 0.03 percent Cu. However, strength differences between the corresponding Class 1 plate sections were insignificant.

Notch Ductility Properties

Drop Weight Test Assessments—Nil ductility transition (NDT) temperatures listed in Table 5 were determined by ASTM Standard Method for Conducting Drop-Weight Test to Determine Nil-Ductility Transition Temperature of Ferritic Steels (E 208 – 69) using type P-3 drop weight test specimens (2 by 5 by $\frac{5}{8}$ in. thick). Through thickness surveys of the Class 1 plate sections revealed very good uniformity throughout. Quarter thickness position NDT temperatures were -20 F (-29 C). Surveys of the Class 2 plate sections also revealed good uniformity with the exception

TABLE 4—Tension test properties of 6-in. plate sections A, B, C, and D.

Plate Section	Nominal Copper Content, wt %	Test Orientations ^a	Yield Strength (0.2% Offset), ^b ksi			Tensile Strength, ^c ksi			Reduction of Area, %			Elongation in 1 in., %							
			Surface	1/4 T	1/2 T	Surface	1/4 T	1/2 T	Surface	1/4 T	1/2 T	Surface	1/4 T	1/2 T					
A (Class 1)	0.03	RW	68.9	66.9	66.8	61.1	88.0	86.3	86.3	85.1	85.1	73.2	70.9	70.4	66.7	28.7	28.7	28.9	28.4
		WR	66.9	66.1	64.5	64.2	88.2	86.5	86.2	85.2 ^d	74.0	71.7	71.7	71.7	71.7	70.7	28.4	29.7	29.1
C (Class 1)	0.13	RW	70.5	68.2 ^e	67.9	67.6	89.7	87.9 ^e	87.8	87.5	87.5	73.2	70.0 ^e	70.4	67.3	27.4	27.7 ^e	28.2	26.7
		WR	70.9	68.3	68.2	68.4	90.6	87.7	87.7	87.7	73.6	71.2	71.3	71.3	70.0	28.5	28.1	28.9	26.9
B (Class 2)	0.03	RW	87.2	79.9	77.1	76.2	103.2	97.1	95.3	95.0	95.0	72.6	66.0	70.0	64.8	25.3	25.8	28.0	27.0
		WR	80.2	78.7	74.7	74.1	103.3	96.4	94.8	94.0	94.0	72.8	68.5	69.4	69.2	25.8	26.8	26.0	27.8
D (Class 2)	0.13	RW	97.8	87.2 ^e	86.2	81.0	113.1	103.9 ^e	103.9	99.2	99.2	69.1	67.9 ^e	65.8	63.1 ^e	23.8	24.9 ^e	24.1	23.2
		WR	91.2	83.3	83.0	78.0	113.4	104.5	104.3	99.7	99.7	69.8	68.2	66.2	64.6	23.8	25.3	25.0	24.8

^a RW = longitudinal; WR = transverse.
^b Average of two specimen tests.
^c 0.252 by 1.750-in.-gage length tension specimens.
^d Slag inclusion visible in failure region.
^e Single determination only.

TABLE 5—Notch ductility characteristics of 8-in. plate sections A, B, C, and D.

Plate Section	Nominal Copper Content, wt. %	Drop Weight Nil Ductility Transition (NDT), deg. F.		Charpy V 30-ft·lb Transition Temperature, ^a deg. F.		Approximate Charpy V Energy Level at NDT, ft·lb		Approximate Charpy V Energy Shelf, ft·lb		Dynamic Tear Test Energy Shelf WR Orientation, ft·lb									
		Surface ^b		Surface		Surface		Surface		Surface									
		Top	Bottom	Top	Bottom	Top	Bottom	Top	Bottom	Top	Bottom								
A (Class 1).....	0.03	-30	-40	-20	-20	-100	-100	-75	-15	95	95	75	30	150	140	120	1260	1130	1020
C (Class 1).....	0.13	-30	-30	-20	-20	-105	-105	-80	-10	95	95	70	25	>145	135	≈115	1180	1060	940
B (Class 2).....	0.03	±0	-90	±0	±0	-85	-85	-15	-15	85	50	75	35	125	125	110	1140	1100	970
D (Class 2).....	0.13	±0	-50	+10	+10	-85	-85	-55	+10	65	55	55	30	110	110	110	1010	1090	870

^a Longitudinal (RW) test orientation.

^b Weld bead on rolled surface.

of the bottom surface layer. The marked differences between top and bottom surface determinations in this case undoubtedly resulted from the flat quenching procedure and the smaller total volume of metal (~ 50 percent less) involved when these particular sections were repeat quenched. Quarter thickness position NDT temperatures of sections B and D were 0 F (-18 C) and 10 F (-12 C), respectively.

Quarter thickness position determinations verified that the maximum NDT temperature requirement ($+10$ F, -12 C) was met in all cases. Copper content did not appear to influence NDT temperature characteristics of either the Class 1 or Class 2 plate sections.

Charpy V Assessments—Charpy V (C_V) notch ductility characteristics of the individual plate sections are summarized and compared to NDT performance in Table 5. As with NDT determinations, relatively good agreement in properties is observed between Class 1 plate sections, between Class 2 plate sections, and between one-quarter and three-quarter thickness locations of a given section. Unlike NDT determinations, however, C_V 30-ft·lb transition temperatures show a distinct gradient from plate surface to plate center with the greater change occurring between the quarter thickness and midthickness positions. Since the NDT temperature did not vary appreciably with test depth while the C_V curve did, the C_V energy level approximating the NDT temperature differed with thickness position. Energy “fix” values (Table 5) vary from as high as 65 to 95 ft·lb (surface locations) to as low as 25 to 30 ft·lb (center location). Radiation effect assessments to be described were indexed to 30-ft·lb transition temperature behavior to allow direct comparisons with the bank of existing data on commercially produced A533 and A302 steels. The choice of a higher index was considered but would not have altered the reported analysis appreciably owing to generally consistent transition temperature characteristics.

Average C_V shelf energy values included in Table 5 attest to the general high purity level of the melt. Shelf levels of the Class 1 plate sections are in good agreement; differences in shelf level of the Class 2 plate sections can be ascribed to the small difference in yield strength. Data scatter at shelf level temperatures as well as in the transition region was somewhat pronounced but did not exceed typical scatter for large commercial melts. Data scatter in the shelf region may have been enhanced by the 1:1 cross rolling practice as well as the better than average melt cleanliness. Photographs of full thickness sections of the Class 1 materials are given in Fig. 4.

Dynamic Tear Test Assessments—Dynamic tear (DT) test shelf level determinations for the transverse (WR) orientation are compared in Table 5. The specimens were of the standard size, $1\frac{5}{8}$ by 7 by $\frac{5}{8}$ in. thick. Differences noted between plate surface and mid thickness locations are considered small. In view of the nominal 1:1 cross rolling ratio and general

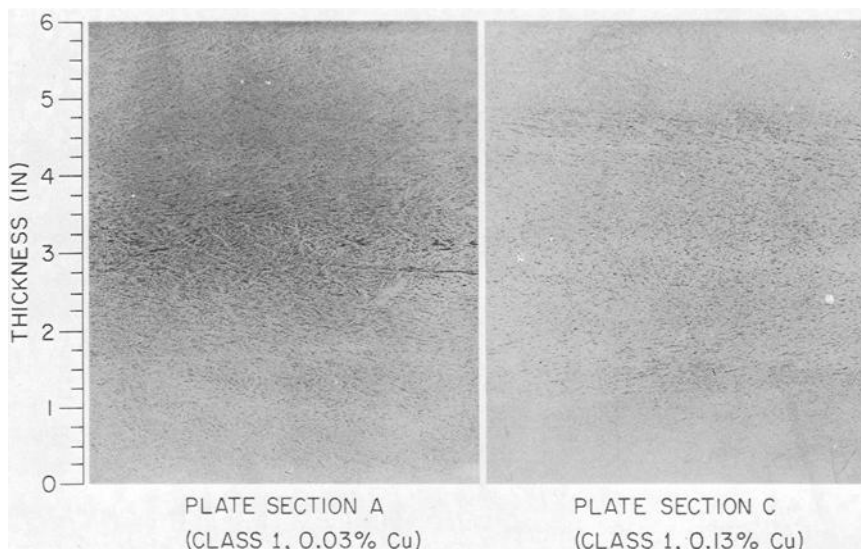


FIG. 4—Macrostructures of Class 1 plate sections from the primary melt analysis and the copper melt modification. The difference in inclusion distributions may reflect the ingot pouring sequence. Plate section C represents the first ingot cast (highest ladle temperature).

melt cleanliness, only slightly higher values would be expected for the longitudinal (RW) test orientation. Shelf values of plate sections A and C significantly exceed values determined for other commercially produced A533B Class 1 plates (~ 1100 ft·lb versus 750 to 850 ft·lb), perhaps for the same reasons.

The DT energy transition curves developed for plate section A are given in Fig. 5. Results are considered representative of through thickness variations observed for the remaining sections. Typically, DT transition curves are displaced to the right of corresponding C_V curves owing to the inherent fracture characteristics of the larger DT specimen. Note that the drop weight NDT indexes the beginning of the temperature range through which DT energy absorption rises to the condition of maximum ductility.

Radiation Investigations

The initial radiation experiment, conducted with C_V specimens of all four plate sections, was designed to compare the effects of copper content and strength class on radiation performance as well as to determine if low radiation embrittlement sensitivity had indeed been secured by the special melt specifications. The experiment was performed at 550 F (288 C) in the Union Carbide research reactor (UCRR) using a fully instrumented assembly.

Subsequent radiation experiments contained DT specimens whereby radiation effects on fracture resistance characteristics could be explored

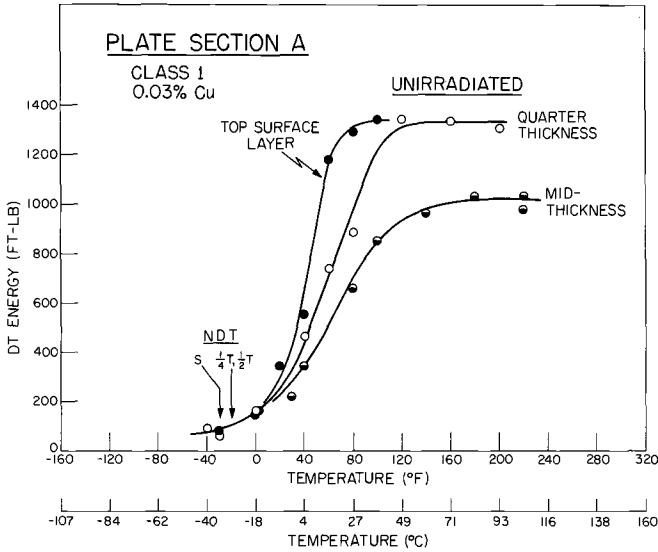


FIG. 5—Dynamic tear (DT) test performance of plate section A at surface, quarter, and mid thickness positions. The $1\frac{1}{2}$ by 7 by $\frac{5}{8}$ -in.-thick specimens were oriented in the transverse (WR) test direction. Corresponding nil ductility transition (NDT) temperatures determined by drop weight tests are also indicated.

quantitatively. By including C_V specimens in each of the reactor units, a partial assessment of the correspondence of C_V and DT test methods for the irradiated case was also achieved. The DT- C_V specimen irradiations were conducted in the UCRR at 550 F (288 C) and in the engineering test reactor (ETR) at <300 F (149 C). The ETR experiments were not instrumented but depended on low-melting point alloys for peak temperature determinations. The DT- C_V assessments have been completed for one plate section, A; systematic assessments of companion sections are still under way.

Neutron fluence values, based on an assumed fission spectrum neutron energy distribution and the $^{54}\text{Fe}(n,p)^{54}\text{Mn}$ reaction, are given for UCRR and ETR experiments. The fission averaged ^{54}Fe cross section was taken as 68 mbarn. Neutron fluence values based on a calculated neutron spectrum and the related ^{54}Fe averaged cross section of 82.6 mbarn are also reported for the UCRR experiments. Spectrum calculations for the ETR facility are not yet available. Detailed techniques for translating fission spectrum fluence values into calculated spectrum fluence values are outlined elsewhere [4, 5].

Initial Determination of Radiation Resistance

Charpy V specimens for this 550 F (288 C) radiation assessment were taken from the quarter thickness location of plate sections A, B, C, and D. Specimens within each material group represented the longitudinal (RW) and transverse (WR) test orientations. The experiment was exposed

in the UCRR F-5 fuel core facility and received a fluence (fission spectrum) of 2.8×10^{19} n/cm², $E > 1$ MeV. The corresponding calculated spectrum fluence value (Φ^{cs} (F-5 facility) = $\Phi^{fs} \times 98.26/114$) was 2.4×10^{19} n/cm², $E > 1$ MeV.

Postirradiation results are shown in Fig. 6. Closed data points refer to the longitudinal orientation; half-filled points refer to the transverse orientation. Results for unirradiated specimens aged at 550 F (288 C) for 700 h, corresponding to the reactor experiment thermal history, are also shown (open points). Thermal control data in each case are indicative of good properties stability at this temperature.

The immediate observation from Fig. 6 is the high radiation embrittlement resistance of the primary melt composition as represented by plate sections A and B. The data also indicate that the radiation resistance of the melt is not dependent upon the heat treatment condition, that is, strength Class 1 or Class 2. The difference in values for sections A and B should be considered insignificant in view of the general level of data scatter for the pre and postirradiation conditions.

Radiation would be expected to have a similarly small effect on drop weight test performance [6]. NDT temperatures below room temperature would thus be projected for this exposure condition⁴. In terms of reactor service, the fluence of 2.8×10^{19} n/cm² equals or exceeds most water reactor vessel lifetime projections. The transition temperature increases recorded for plate sections A and B indicate that a very low 550 F (288 C) radiation embrittlement sensitivity has indeed been achieved by "specification."

Results for plate sections C and D given in Figs. 6c and 6d signify that an elevation in copper content to 0.13 percent appreciably degrades the radiation embrittlement resistance of A533 steel. The average radiation embrittlement sensitivity of the copper modified melt composition, as depicted by these plate sections, appears more than double that of the primary melt analysis. It is reemphasized that, for a given strength class, a direct comparison of results is fully valid owing to the identical melt processing, heat treatment, and irradiation history of the materials. Results of this experiment indicate that the effectiveness of copper content toward enhancing the sensitivity of A533B is not highly dependent on the particular strength class (1 or 2). This observation is supported by data compilations for A533 production plates having a wide range of copper contents [2].

Dynamic Tear Investigations

Primary objectives of DT investigations were (1) the verification of C_v test indications concerning the 550 F (288 C) radiation embrittlement re-

⁴ A direct determination of NDT temperature increase will be possible with drop weight specimens of plate section A currently being irradiated in the Big Rock Point power reactor.

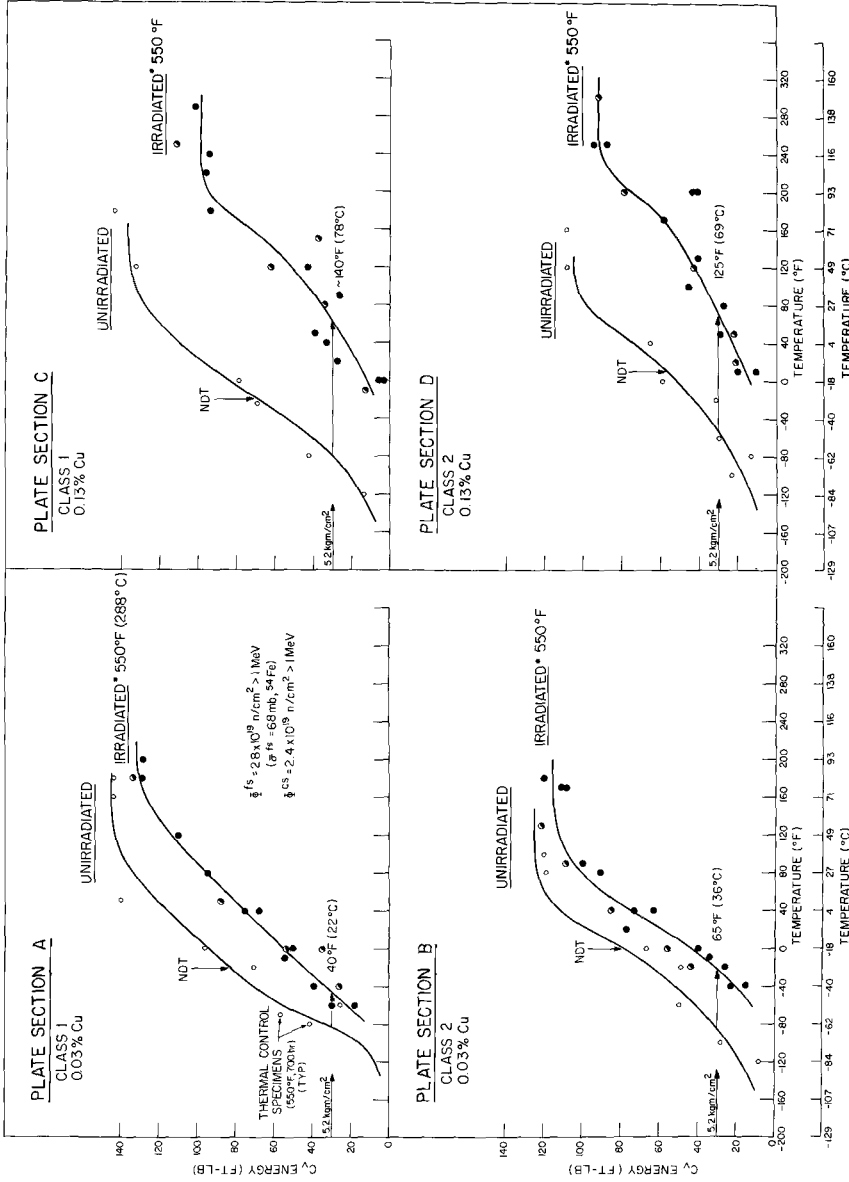


FIG. 6—Charpy V (C_v) assessments of the radiation embrittlement resistance of plate sections A, B, C, and D at 550 F (288 C). Very low sensitivity to radiation embrittlement is indicated for the primary melt analysis represented by plate sections A and B. The melt modification which increased copper content to 0.13 percent is seen to have a strong detrimental effect on radiation performance. Calculated spectrum neutron fluence value, $2.4 \times 10^{19} \text{ n/cm}^2$, $E > 1 \text{ MeV}$, derived from the conversion $\phi^{cs} = \Phi^{1s} \times 98.26/114$.

sistance of the primary melt analysis, (2) the assessment of relative <300 F (149 C) radiation resistance of both the primary melt analysis and the copper modified analysis, and, finally, (3) the assessment of DT shelf level retention with 550 F (288 C) and <300 F (149 C) radiation exposure. Shelf determinations were of particular interest as indications of resistance to fracture for the condition of maximum ductility.

Dynamic tear and C_V specimens for the irradiation series were taken

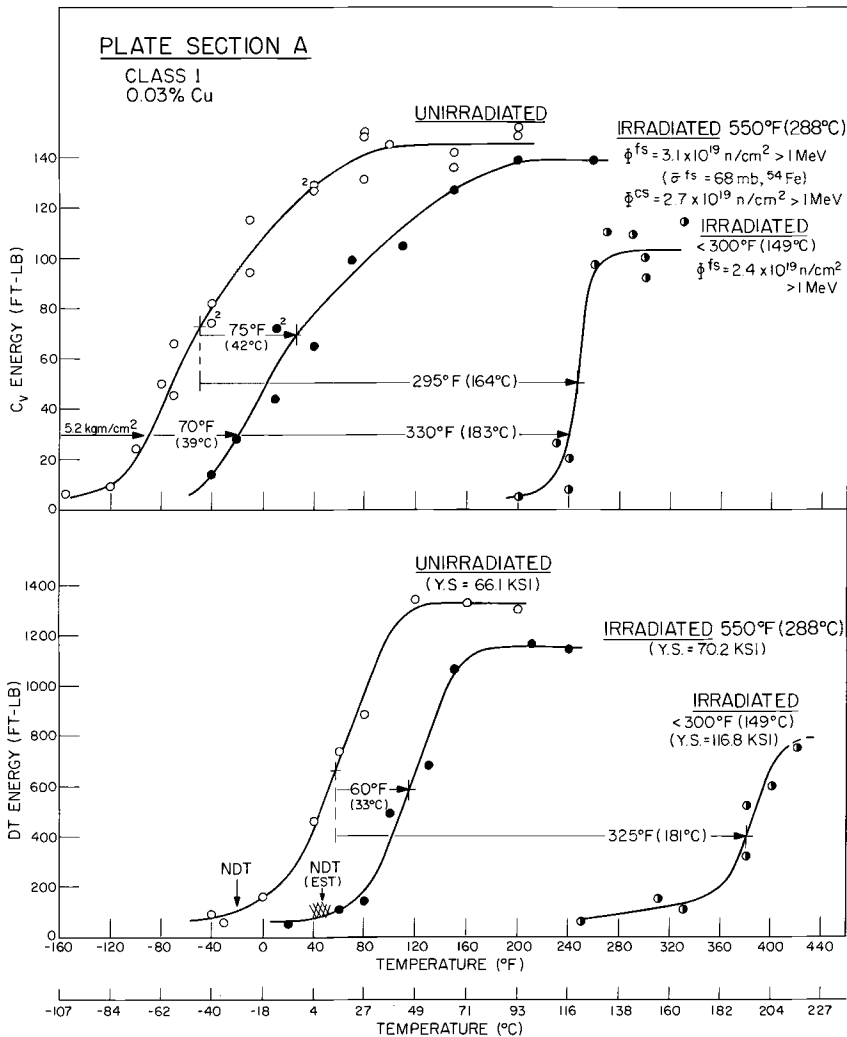


FIG. 7—Comparison of Charpy V and dynamic tear test performance of plate section A at the quarter thickness location. Good agreement of mid energy range transition temperature increases is found for both low-temperature and elevated-temperature radiation assessments.

from the quarter thickness location and were oriented in the transverse (WR) test direction only. Postirradiation assessments of plate section A only have been completed. Combined results for the 550 F (288 C) UCRR irradiation and the <300 F (149 C) ETR irradiation are presented in Fig. 7. The upper graph compares C_V results for the pre and postirradiation conditions; the lower graph gives corresponding DT results. Note that the C_V and DT energy scales are in the ratio of 1:10.

The fluence received by the 550 F (288 C) UCRR DT irradiation was 3.1×10^{19} n/cm², $E > 1$ MeV, slightly higher than the fluence received by the similar experiment. The corresponding calculated spectrum neutron fluence value was 2.7×10^{19} n/cm², $E > 1$ MeV, based on the 0.870 conversion factor for the D-3 core facility. The C_V 30-ft·lb transition temperature increase of 70 F (39 C) agrees well with the initial determination for plate section A (Fig. 6). For comparisons of C_V versus DT results, the mid energy range transition temperature increase was taken as a more appropriate index of irradiation performance. In Fig. 7 the two independent determinations are found in close agreement, 75 F (39 C) C_V versus 60 F (33 C) DT. Noting that the NDT temperature marks the toe of the DT curve, estimates would place the postirradiation NDT temperature between 40 and 50 F (4 to 10 C) for the stated exposure condition. This estimate based on DT performance is in good agreement with the original estimate based on C_V results.

Specimens contained in the <300 F (149 C) ETR experiment received an average fluence (fission spectrum) of 2.4×10^{19} n/cm², $E > 1$ MeV. From Fig. 7, mid energy range transition temperature increases determined by the respective test methods again appear in good agreement. As expected, radiation induced changes with the low exposure temperature were much more pronounced. Consistent with experimental findings for high-purity laboratory heats [3], the primary melt analysis appears about as sensitive to low-temperature irradiation as does the ASTM A302B reference plate. In effect, residual element restrictions serve to optimize elevated temperature radiation embrittlement resistance but have little or no effect on steel embrittlement characteristics at low (below 300 F) exposure temperatures.

Apparent DT shelf and yield strength characteristics of UCRR and ETR exposure conditions are suggestive of excellent fracture resistance at shelf level temperatures. As noted in Fig. 7, changes in shelf level and yield strength with 550 F (288 C) exposure were very small; accordingly, fracture resistance features were not impaired to a significant extent. In the case of the ETR exposure, an exact determination of shelf level was not obtained, but the level clearly exceeded 600 ft·lb. At the measured yield strength of 116.8 ksi, a shelf level of this magnitude according to the Ratio Analysis Diagram (RAD) [7] precludes plane strain fracture in thin or

thick section (up to 12 in.). Overall shelf level performance characteristics of the primary melt analysis thus complement well its transition temperature performance at elevated irradiation temperatures.

Discussion

Experimental results from the individual radiation assessments have confirmed the success of the scaleup effort. The overall yield of significant new information was also gratifying.

To place the radiation embrittlement resistance of the primary melt analysis in full perspective, the results for plate sections A and B have been entered on a summary plot of 550 F (288 C) radiation data for standard production A533 plate and weld metals and the ASTM A302B reference plate (Fig. 8). The potential benefit of low copper and low phosphorus contents in steels for nuclear applications is immediately visible. The radiation embrittlement sensitivity of the primary melt analysis appears to be only one-third that of the ASTM A302B reference plate and significantly less than that of the best A533 production materials. It will be noted that, within the series of production materials, those with the best radiation resistance also had the lowest copper and phosphorus contents [2]. Data points for the 0.13 percent copper melt modification, if added, would fall

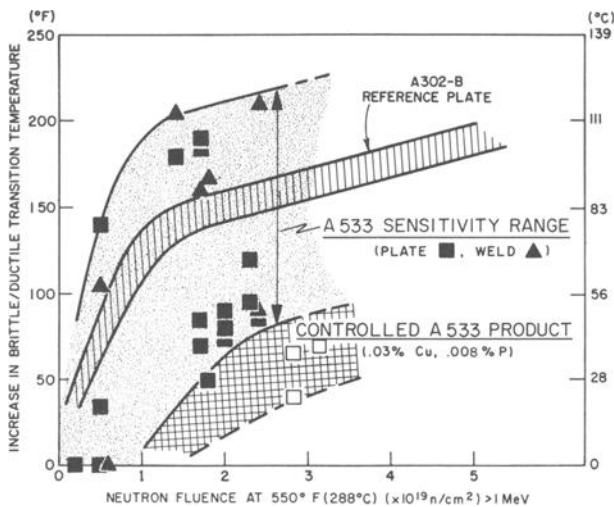


FIG. 8—Increase in Charpy V 30-ft-lb transition temperature with neutron exposure at 550 F (288 C). Performance of plate sections A and B representing the primary melt analysis (open data points) is shown compared to the performance of the ASTM A302B reference plate and conventional A533 materials representative of current reactor vessel construction. The benefit of controlled copper and phosphorus contents is readily apparent.

just below the ASTM A302B reference trend line. Thus, the significance of copper content relative to radiation embrittlement resistance cannot be denied.

Purity specifications used for the scale-up demonstration were proven attainable with conventional melting techniques and good commercial practices. In this regard, it is considered that a reduction of allowable phosphorus content below the 0.010 check test maximum would be beneficial in terms of radiation performance. Surveys of phosphorus content did not reveal appreciable segregation; thus, a tighter check specification may be both realistic as well as beneficial to performance.

To provide material duplicating the primary melt analysis specification in the belt line region of a large reactor vessel, the additional cost to the reactor builder has been estimated at \$35 to 40,000. The cost premium is, by comparison, but a small percentage of the \$2 to 2,500,000 projection of total vessel cost and an even smaller part of the approximately \$100,000,000 overall cost for a large nuclear power plant.

The continuing research effort has undertaken the development of companion weld metals having matching radiation embrittlement resistance characteristics. One study involves the submerged arc welding process and plate from the special melt (low-copper plate section A). Looking toward longer range vessel requirements, other studies are engaged in the improvement of higher strength steels, including A543, A517E, and A542 (plate and weld metals). Simultaneously, studies of radiation effects mechanisms have been initiated to reveal the processes by which copper and other impurity elements alter radiation embrittlement sensitivity. The effort includes a determination of the significance of trace impurities at internal surfaces (particle-matrix interfaces, grain boundaries, etc.) and investigations of heterogeneous nucleation of defect aggregates on impurity solute atoms.

Conclusions

The first large-scale demonstration of metallurgically controlled radiation embrittlement sensitivity has been conducted and has proven highly successful. All research objectives for the 30-ton A533B steel melt were attained. The commercial melt, sponsored by the U.S. Atomic Energy Commission, Division of Reactor Development and Technology, Fuels and Materials Branch, demonstrates industry's capability to produce, in quantity, steel having low radiation embrittlement characteristics approaching the optimum radiation resistance of steel produced in the laboratory.

The 30-ton melt did not require unusual production techniques or procedures to satisfy NRL special specifications to optimize radiation resistance. The NRL specifications were primarily concerned with the maximum

concentrations of certain residual elements having known or suspected influences on radiation performance. The reduction of copper and phosphorus contents to the lowest possible level was stressed. Experimental results have verified this composition approach to the development of maximum radiation embrittlement resistance in reactor structural steels.

According to plan, the A533B melt was split and plates representing the primary melt analysis (0.03 percent Cu, 0.008 percent P) and a melt modification (0.13 percent Cu) were produced. Specific observations from radiation assessments of the 6-in.-thick plates using the C_V and DT test methods were as follows:

1. The primary melt analysis (0.03 percent Cu, 0.008 percent P) exhibited very low sensitivity to radiation embrittlement at 550 F (288 C). Charpy V 30-ft·lb transition temperature increases for Class 1 and Class 2 plates were 40 and 65 F (22 and 36 C), respectively, for a neutron fluence of 2.8×10^{19} n/cm², $E > 1$ MeV. Low radiation embrittlement sensitivity characteristics were confirmed separately by dynamic tear radiation assessments.

2. The melt modification (0.13 percent Cu) appeared about twice as sensitive as the primary melt composition (0.03 percent Cu) to radiation embrittlement at 550 F (288 C): a clear and specific demonstration of the highly detrimental influence of copper content on radiation resistance at elevated temperature. Charpy V 30-ft·lb transition temperature increases for Class 1 and Class 2 plates were 140 and 125 F (78 and 69 C), respectively, for the radiation exposure identified in 1 above.

3. The enhancement of radiation embrittlement sensitivity by copper content is not dependent on Class 1 or Class 2 strength conditions.

4. Residual element restrictions are shown to maximize elevated-temperature radiation embrittlement resistance but have little or no effect on low (less than 300 F, 149 C)-temperature irradiation characteristics. As expected, radiation embrittlement sensitivity of the primary melt analysis (0.03 percent Cu, 0.008 percent P) at <300 F (149 C) was about equal to that of the ASTM A302B reference plate (0.21 percent Cu, 0.013 percent P).

5. The simultaneous exposure of DT and C_V specimens of the primary melt analysis produced comparable increases in mid energy range transition temperature.

6. The DT performance after low- and elevated-temperature exposure suggests excellent retention of fracture resistance at shelf level temperatures for the primary melt analysis Class 1 plate. The DT shelf retention coupled with observed yield strength behavior suggests that the development of plane strain fracture even in thick section components exposed to fluences of at least 2.4×10^{19} n/cm², $E > 1$ MeV, is highly unlikely.

7. The nil ductility transition temperature of the primary melt analysis

Class 1 plate after irradiation at 550 F (288 C) to 3.1×10^{19} n/cm², $E > 1$ MeV, was below 75 F (24 C) according to postirradiation DT test results.

8. The A533B scaleup demonstration fully supports the principles of radiation embrittlement sensitivity control developed in the laboratory.

Acknowledgments

The scaleup demonstration test was sponsored by the U.S. Atomic Energy Commission, Division of Reactor Development and Technology, Fuels and Materials Branch. The advice and support of A. VanEcho, AEC coordinating officer, and the continuing support of this agency are deeply appreciated.

I thank R. H. Sterne, G. Martini, and S. G. Johnson of Lukens Steel Co. and J. V. Alger of the U.S. Steel Corp. for the helpful discussions concerning melt shop options and capabilities in aid of advance melt planning.

I also thank W. S. Pellini and L. E. Steele for their consultation and support through the course of this investigation. Personal efforts and contributions of individual members of the NRL Reactor Materials Branch, which ensured the success of radiation experiment operations, are acknowledged with gratitude.

APPENDIX I

Purchase Specifications for Special 30-ton A533B Steel Melt

General

A single heat of ASTM A533 Grade B steel shall be air melted, vacuum stream degassed, and cast into two 62-in.-wide by 22-in.-thick ingot molds. Each mold will be top poured and filled to a height of approximately 77 in. One ingot shall contain 0.08 percent (maximum) copper; the other ingot shall contain 0.13 percent (aim)⁵ copper. Each ingot shall be cross rolled to 6.0-in.-thick plate using a L/T rolling ratio of approximately 1:1 (aim). Two 96 by 48 by 6.0-in. (thickness) patterns shall be cut from each plate using the pattern layout given in Fig. 9. Primary direction of rolling shall be parallel to the 96-in. pattern dimension. Pattern orientation with respect to the top and center line of the ingot shall be retained with suitable reference markings.

Patterns from ingot 1 (0.08 percent max copper) shall be designated plates A and B; patterns from ingot 2 (0.13 percent copper) shall be designated plates C and D. Pattern size is exclusive of edge allowances. Each plate edge shall be at least $1T$ away from the initial as-quenched plate edge surfaces. Three of the four plate edges shall be at least $1T$ away from initial as-quenched and tempered plate

⁵ Achieved by ingot addition of pure copper shot.

edge surfaces. Edge allowances for plate and test dropouts (Fig. 9) shall not be removed until after the tempering treatment.

Chemical Composition

ASTM A533 Grade B, with following additional special restrictions on melt analysis (weight percent, maximum):

Determination	Cu ^a	P	S	P+S	As	Sb	Sn	Bi	As+Sb+Sn+Bi
Ladle.....	0.08	0.007	0.007	0.012	0.01	0.01	0.02	0.02	0.05
Check.....	0.10	0.010	...	0.022	0.01	0.01	0.02	0.02	0.05

^a Ingot 2 "ladle" maximum: 0.16% copper.

Chemistry and heat treatment shall be in accordance with best fine grain practice.

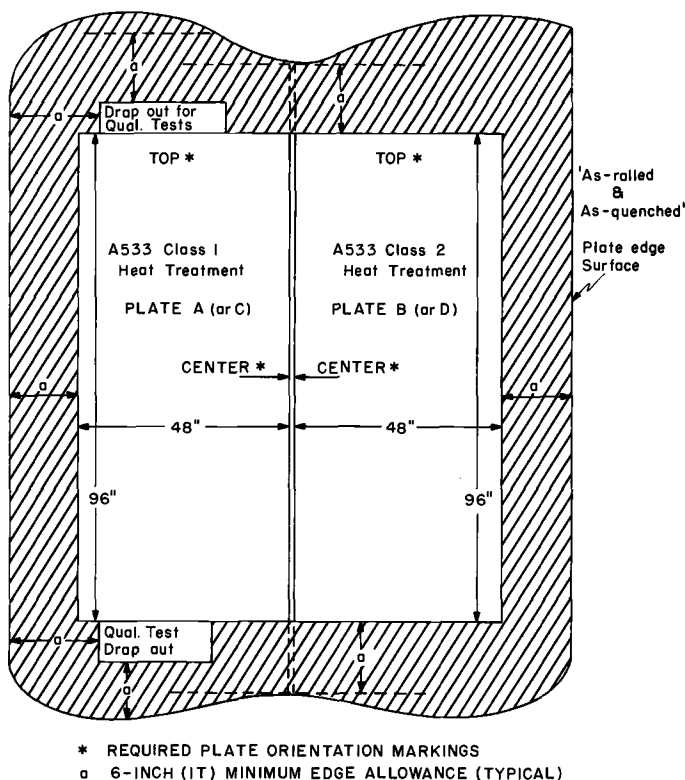


FIG. 9—Layout for cutting two 96 by 48 by 6-in. patterns from ASTM A533B plate.

Heat Treatment

Plates A and C—Heat-treat by double quenching and tempering treatments to meet ASTM A533 Grade B Class 1 specifications: 50,000-psi minimum yield strength, 0.2 percent offset; 80,000 to 100,000-psi tensile strength; 20.0 percent minimum elongation in 2 in.

Plates B and D—Heat-treat by double quenching and tempering treatments to meet ASTM A533 Grade B Class 2 specifications: 70,000-psi minimum yield strength, 0.2 percent offset; 90,000 to 115,000-psi tensile strength; 18.0 percent minimum elongation in 2 in.

Required Qualification Tests

Qualification tests over and above those destructive and nondestructive tests required by ASTM A533 Grade B (firebox quality) steel specifications are

1. Destructive tests: All destructive qualification tests must be a minimum of $1T$ away from the initial quenched and tempered plate edge surfaces.

Drop Weight Tests—Drop weight tests of each plate shall be performed in accordance with ASTM Method E 208 — 69. Each plate shall meet the NDT requirement of +10 F (or lower) at the quarter thickness location. Specimens shall be oriented with their long dimension perpendicular to the primary rolling direction of the plate. Specimens shall be saw cut with the surface on which the weld bead is to be placed parallel to and centered on the quarter thickness plane of the plate. The body of the specimen shall be located toward the center of the plate.

Tension Tests—Tension tests will be performed at the top and bottom of the plate in accordance with the ASTM Specifications for General Requirements for Delivery of Steel Plates for Pressure Vessels (A 20 — 69a).

2. Nondestructive tests

Ultrasonic—The plates shall be sonically sound and inspected in accordance with ASME Code Case 1338-4, Alternate 1, 100 percent.

Certified copies of results of all destructive and nondestructive tests performed for qualification and acceptance of each of the four plates, A, B, C, and D, shall be furnished.

APPENDIX II**Melt and Ingot Processing Details**

Melt Identification: Latrobe Steel Co. heat V22403.
 Melt Type: Basic electric double slag, fine grain practice.
 Furnace: Swindel, 30-ton trunnion type with induction stirrers (17 prior heats on top and bottom linings).
 Furnace Charge: 100 percent scrap, low-phosphorus automobile fender punchings.
 (S, 0.022% maximum; P, 0.007%; Cr, Ni, Mn, <0.02%; Cu, 0.04%).
 Nickel to specifications with electrolytic nickel. Molybdenum to specifications with ferromolybdenum. Manganese to specifications with electrolytic manganese.

Furnace Order Sheet Specifications:

Element	Low, %	High, %	Aim, %	Working Aim, %
C.....	0.18	0.21	0.20	0.19
Si.....	0.15	0.30	0.24	0.24+
Mn.....	1.20	1.40	1.30	1.45
S.....	0.006	LAP	} 0.012 } max	LAP
P.....	0.006	LAP		LAP
Cr.....	0.05	0.10	0.05 max	LAP
V.....	...	0.02	LAP	LAP
Mo.....	0.45	0.60	0.55	0.53
Ni.....	0.40	0.70	0.55	0.55
Cu.....	...	0.08	0.08	LAP
Sn.....	...	0.02	} 0.05 } max	LAP
As.....	...	0.01		LAP
Sb.....	...	0.01		LAP
Bi.....	...	0.01		LAP

Melt Schedule:

Charge	1600	h
Back charge	1730	
First slagging ⁶	1845	
Second slagging ⁶	2000	
Tapped heat	2205	(3070 F furnace, 2960 F ladle)
Commenced vacuum degassing	2210	
Commenced pouring ingot 1	2225	
Completed pouring ingot 2	2240	

⁶ Lanced heat in advance of slagging operation.

Melt Sampling:

Sample Identification	Percentage of Elements									
	C	Si	Mn	S	Cr	Mo	Ni	Cu	V	
After melt in and oxygen (P1).....	0.04	0.017/0.018
After first slagging (P2).....	0.127	0.10	1.02	0.009	0.02	0.37	0.41	0.044	0.01	...
(P3).....	0.120	0.10	1.03	0.006	0.02	0.38	0.41	0.034
After second slagging (P4).....	0.143	0.09	1.04	0.006	0.01	0.38	0.41	0.044	0.01	...
Ladle.....	0.18	0.20	1.37	0.006	0.06	0.53	0.56	0.03/0.12 ^a	0.01	...

^a 28-lb copper shot added to ingot 2 to bring content to approximately 0.13%.

Ingot Type:
 Big end up top poured plug mold (62 by 22 by 77 in. (height to hot top junction)).
 Ingot Sampling:

Sample Identification	Percentage of Elements											Others
	C	Mn	P	S	Ni	Cr	Mo	Si	Cu	Al		
<i>Ingot 1 (28,580 lb)</i>												
Dip test.....	0.176	1.38	0.006	0.006	0.56	0.06	0.53	0.20	0.124	a
Latrobe												
NRL	0.16	1.20	0.007	0.006	0.55	0.07	0.49	0.18	0.12
Ck. top.....	0.20	1.29	0.010	0.010	0.56	0.06	0.51	0.20	0.16	0.016	0.016	...
Lukens												...
Ck. bottom.....	0.19	1.30	0.010	0.009	0.57	0.06	0.52	0.20	0.16	0.016	0.016	...
Lukens												...
<i>Ingot 2 (28,650 lb)</i>												
Dip test.....	0.182	1.37	0.006	0.006	0.56	0.06	0.53	0.20	0.034	a
Latrobe												
NRL	0.16	1.20	0.007	0.006	0.55	0.07	0.51	0.18	0.05
Ck. top.....	0.19	1.26	0.010	0.009	0.56	0.06	0.52	0.20	0.05	0.013	0.016	...
Lukens												...
Ck. bottom.....	0.18	1.26	0.011	0.008	0.54	0.06	0.51	0.20	0.05	0.016	0.016	...
Lukens												...

a As+ Sb + Sn + Bi < 0.05%.

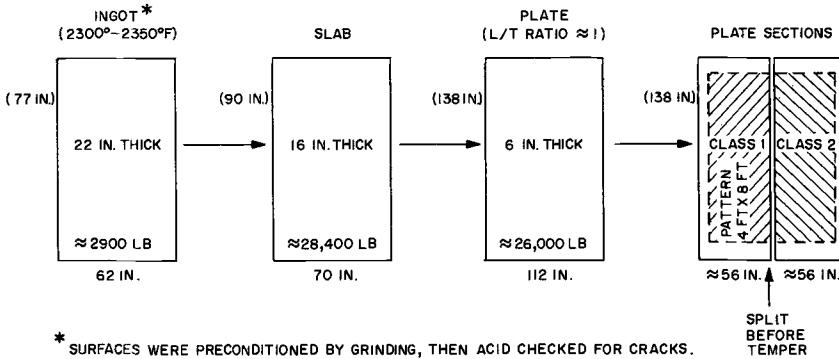


FIG. 10—Ingot processing of 30-ton melt ASTM A533B steel. The schematic shows the ingot-to-plate (6 in.) sequence and, far right, the two final plate sections.

Ingot Processing:

Ingot processing: Ingots were given a full anneal after stripping, then slow cooled to below 600 F. Surfaces were inspected and any major surface defects were removed by grinding. Ingots were heated to 2300 to 2350 F and tandem rolled on Lukens 140/206 mills directly to 6-in. gage following the ingot-to-plate sequence outlined schematically in Fig. 10. The plates finished rolling above 1600 F and were buried in sand. The L/T ratios from ingot to plate were 1.03:1 (plate length/ingot length ÷ plate width/ingot width = 1.03).

APPENDIX III

Plate Heat Treatment, Qualification, and Inspection

Heat Treatment

Both 6-in.-gage plates were heated to 1675 ± 25 F, held 6 h, and water (dip) quenched, then reheated to 1575 ± 25 F, held 6 h and water (dip) quenched. Following stress relief at 1050 ± 25 F for 6 h and air cooling, both plates were split in half longitudinally by gas cutting. (Orientation of each plate section relative to the parent plate was retained by suitable heat-resistant reference markings.) After gas cutting all four plate sections were stress relieved at 1050 ± 25 F for 6 h and air cooled.

Plate section A from ingot 1 (low copper) and plate section C from ingot 2 (high copper) were tempered for Class 1 properties at 1250 ± 25 F. Plate section B from ingot 1 and plate section D from ingot 2 were tempered for Class 2 properties at 1200 ± 25 F. All tempered sections were then stress relieved at 1125 ± 25 F for 20 h. Furnace cooling to 600 F was used consistently with tempering and the final stress relief treatment.

Mechanical tests revealed that Class 2 requirements were not met by plate sections B and D. These sections were requenched from 1575 ± 25 F after 6 h at temperature, tempered at 1150 ± 25 F for 6 h, air cooled, stress relieved at 1100 F for 10 h, and water quenched. After gas cutting to size, plate sections B and D and the test sections received a final stress relief at 1050 ± 25 F for 6 h, followed by furnace cooling to below 600 F.

TABLE 6—Quarter thickness tensile properties of 6-in.-thick plate sections.

Plate Section	Strength Specification	Test Orientation ^a	Ingot Location	Yield Strength (0.2% offset), ^b ksi	Tensile Strength, ^c ksi	Elongation, %	Reduction of Area, %
Section A (ingot 1).....	Class 1	L	Top	66.9	87.7	27	68.5
		L	Bottom	59.2	84.1	27	67.7
		T	Top	67.3	87.3	25	69.2
		T	Bottom	63.6	83.5	27	68.1
Section C (ingot 2).....	Class 1	L	Top	64.9	91.0	27	68.2
		L	Bottom	63.6	85.0	27	68.0
		T	Top	68.2	90.0	27	68.2
		T	Bottom	64.8	85.9	27	68.0
Section B (ingot 1).....	Class 2	L	Top	79.2	98.2	25	65.8
		T	Top	78.9	98.0	25	65.9
		T	Bottom	81.5	98.5	25	66.2
Section D (ingot 2).....	Class 2	L	Top	88.7	107.4	24	64.1
		T	Top	87.1	104.7	24	64.4
		T	Bottom	81.0	96.7	25	65.8

^a L = parallel to ingot and plate long axis.
 T = transverse to ingot and plate long axis.
^b 0.505-in.-diameter tension test specimens.
^c Average of duplicate tests.

Strength Qualification Tests

Tension tests were conducted on specimens oriented with their central axis lying in the plate section top $\frac{3}{4}T$ plane. Properties based on the duplicate tests are given in Table 6.

Ultrasonic Inspection Tests

All four plates were ultrasonically tested to ASME Code Case 1338-4 Alternate #1, 100 percent search after heat treatment but before final cutting. The instrument was calibrated on a $\frac{3}{4}$ -in.-diameter flat bottom hole drilled in a 6-in.-gage calibration block to a depth of 10 percent of the gage. An ingot top end indication of massive size was noted in both parent plates (ingot 1 and 2). A smaller (but slightly above specification) indication was noted about one quarter of the plate length from the ingot bottom end of plate 1. Nondestructive test reports included plots of all indications for evaluation and reference.

References

- [1] Steele, L. E., Hawthorne, J. R., and Gray, R. A., Jr., in *The Effects of Radiation on Structural Metals*, ASTM STP 426, American Society for Testing and Materials, 1967, pp. 346-370.
- [2] Hawthorne, J. R. and Potapovs, U. in *Irradiation Effects in Structural Alloys for Thermal and Fast Reactors*, ASTM STP 457, American Society for Testing and Materials, 1969, pp. 113-134.
- [3] Potapovs, U. and Hawthorne, J. R., *Nuclear Applications*, NUAPA, Vol. 6, No. 1, Jan. 1969, pp. 27-46.
- [4] Serpan, C. Z., Jr., and Steele, L. E., "Neutron Spectral Considerations Affecting Projected Estimates of Radiation Embrittlement of the Army SM-1A Reactor Pressure Vessel," NRL Report 6474, Naval Research Laboratory, 30 Sept. 1966.
- [5] Serpan, C. Z., Jr., and Hawthorne, J. R., *Journal of Basic Engineering*, ASME Transactions, Series D, JBAEA, Vol. 89, Dec. 1967, pp. 897-910.
- [6] Hawthorne, J. R. and Steele, L. E., "The Effect of Neutron Irradiation on the Charpy-V and Drop Weight Test Transition Temperatures of Various Steels and Weld Metals," NRL Report 5479, Naval Research Laboratory, 27 May 1960.
- [7] Pellini, W. S., "Evolution of Engineering Principles for Fracture-Safe Design of Steel Structures," NRL Report 6957, Naval Research Laboratory, 23 Sept. 1969.

DISCUSSION

*E. Landerman*¹—Although the A533B with 0.03 percent Cu shows decreased radiation embrittlement, materials of this copper level are not available to the nuclear industry. Copper levels for currently used heats (using selected scrap) have been lowered in recent years to ~0.10 to 0.15 percent. Special scrap would be required for 0.03 percent Cu heats and are not available for materials required for current reactor vessels within any reasonable schedule and for needed construction planning.

J. R. Hawthorne (author's closure)—Formal disclosure of the research findings of Potapovs and Hawthorne which first provided positive identification and experimental verification of the detrimental effect of copper and phosphorus on radiation embrittlement resistance dates back only to June 1968 (see Ref 3). Understandably, some time would elapse before the industry (reactor vendors and vessel fabricators) would come to realize and seek the marked benefits of reduced copper and phosphorus impurities in reactor vessel steels. Only of late have steel producers had sufficient inquiries for such steel to prompt a reexamination of their technology and capabilities for providing low-copper and -phosphorus melts. Thus, it is fully understandable that steel vendors have not yet established those limits for copper content which can be supplied on a standard or a premium cost basis or which can be supplied on a small or large tonnage basis. In effect, the full circle of indoctrination from laboratory to general practice has not been completed, but, hopefully, the results for the demonstration melt will accelerate the process.

I recognize the current difficulties in obtaining low-copper content melts. It is encouraging that Lukens Steel Co., the prime supplier of thick plate for reactor vessels, is exploring the problems attending routine production of such melts. One major problem presented to a cold metal shop such as Lukens is the quality and availability of low-copper content scrap. Conceivably, this problem can be eased somewhat by the use of a hot metal charge (or alternately, ingot iron) either alone or in conjunction with selected scrap to boost volume and to lower copper contents as well. It is pointed out that a 0.06 percent copper content (maximum) was the research target for the current study and may well be sufficiently low for steel optimization.

¹ Fellow engineer, Westinghouse Nuclear Energy Systems, Pittsburgh, Pa. 15230.

N. Igata,¹ R. R. Hasiguti,¹ E. Yagi,² U. Nishiike,¹ and K. Watanabe³

Neutron Irradiation Effects on Iron Containing Aluminum and Nitrogen

REFERENCE: Igata, N., Hasiguti, R. R., Yagi, E., Nishiike, U., and Watanabe, K., "Neutron Irradiation Effects on Iron Containing Aluminum and Nitrogen," *Irradiation Effects on Structural Alloys for Nuclear Reactor Applications*, ASTM STP 484, American Society for Testing and Materials, 1970, pp. 128–141.

ABSTRACT: Several authors have emphasized that aluminum nitride in iron and iron alloys not only lowers the transition temperature but also suppresses the rise of the transition temperature due to irradiation. To clarify the mechanism of the effect of aluminum nitride, structural changes after irradiation and annealing are observed by means of internal friction and electron microscopy. Materials investigated are iron, containing 0.05 wt% Al and 0.01 wt% N with <1 ppm C and a few ppm O, and iron, containing 0.02 wt% Al and 0.005 wt% N with 10 ppm C and 20 ppm O. The materials are annealed at 750 C before irradiation and irradiated in the JRR-2 at temperatures of 60 C and up to 1.2×10^{19} n/cm², $E > 1$ MeV. Two new peaks in internal friction are found at ~125 C and ~155 C after irradiation. Besides these changes a new type of precipitate is observed by electron microscopy. These precipitates are thin, doughnut shaped disks with a diameter of 0.3 μ m and are considered to be complex defects of irradiation induced point defects, nitrogen, and aluminum atoms. The 125 C peak of internal friction disappears after annealing at 250 C for 30 min; the 150 C peak disappears after annealing at 150 C for 30 min or aging at room temperature for about half a year. Resolution of free nitrogen is observed, but precipitates do not disappear even after annealing at 350 C for 30 min. The precipitates suppress the formation of irradiation induced complex nitrogen defects and irradiation hardening because of the strong effect of aluminum on nitrogen atoms.

KEY WORDS: irradiation, neutron irradiation, radiation effects, water cooled reactors, pressure vessels, structural steels, aluminum, nitrides, iron, transition temperature, point defects, precipitates, annealing, embrittlement, hardening (materials), nitrogen, electron microscopy

¹ Associate professor, professor, and graduate student, respectively, Department of Metallurgy, University of Tokyo, Tokyo, Japan.

² Institute for Physical and Chemical Research, Saitama-ken, Japan.

³ Japan Atomic Energy Research Institute, Ibaragi-ken, Japan.

Many investigators have emphasized the role of aluminum and aluminum nitride in reducing the change in the brittle transition temperature due to irradiation [1, 2].⁴ Investigation of the effect of Al or AlN in iron alloys is thought to be important to the development of pressure vessel steels that will better withstand irradiation embrittlement. Also, it is a very interesting problem from the standpoint of the study of lattice imperfections. The objectives of this study were to clarify the atomistic structural changes due to neutron irradiation and subsequent annealing and also to clarify the mechanism of the effects of Al and AlN in reducing irradiation hardening. We used internal friction and electron microscopy techniques in our investigations.

Previously, we [3] had clarified the behavior of nitrogen or carbon atoms in pure iron, "Puron." In that case the complexes of nitrogen and point defects induced by irradiation were responsible for the irradiation hardening. As these complex defects redissolved in the matrix after annealing the hardening effect recovered. This suggests that the study of changes in these complex defects should clarify the mechanism of irradiation hardening. In this investigation the behavior of nitrogen in iron-aluminum-nitrogen is compared with that in pure iron.

Experimental Procedure

The two kinds of materials used were high-purity iron containing (1) 0.05 weight percent aluminum, 0.01 weight percent nitrogen, with <1 ppm carbon and a few ppm oxygen (specimen A) and (2) 0.02 weight percent aluminum, 0.005 weight percent nitrogen, with 10 ppm carbon and 20 ppm oxygen (specimen B). For specimen A, electrolytic, high-purity iron containing almost no carbon atoms was used; for specimen B, Puron containing 70 ppm nitrogen and 30 ppm carbon was used. Aluminum and nitrogen gas were introduced into both while melting under vacuum. After cold rolling to form more AlN, the sheets were heated under argon atmosphere at 750 C for 60 min (specimen A) and for 10 min (specimen B). The specimens were again heated to 830 C for 10 min under wet hydrogen atmosphere to eliminate excess nitrogen atoms. The final cooling rates were 500 deg C/min for specimen A and 100 deg C/h for specimen B. Both specimens were aged for several months at room temperature before irradiation. Irradiation was performed in the JRR-2 at 60 C to a fluence of 1 to 2×10^{19} n/cm². Since JRR-2 is a water cooled reactor, the specimens were put into an aluminum capsule, which was submerged while being irradiated. Internal friction measurements were made after irradiation. Electrolytic polishing, to produce thin foils, was performed in a semihot cell at the Japan Atomic Energy Research Institute.

Internal friction and Young's modulus were measured under a vacuum of 10^{-3} torr and at ~ 500 cycles using an automatic, digital measuring

⁴ *Italic numbers in brackets refer to the list of references at the end of this paper.*

apparatus. The temperature for the internal friction measurement ranged from room temperature to 180 C, and the heating rate was 1 deg C/min. The postirradiation annealing was also performed at 10^{-3} torr.

For the electron microscopy studies the specimens were cut and annealed after electrolytic polishing by the Bollmann method. Specimens were brought back to the University of Tokyo and observed with a JEM 150 electron microscope from the Japan Electron Optics Laboratory.

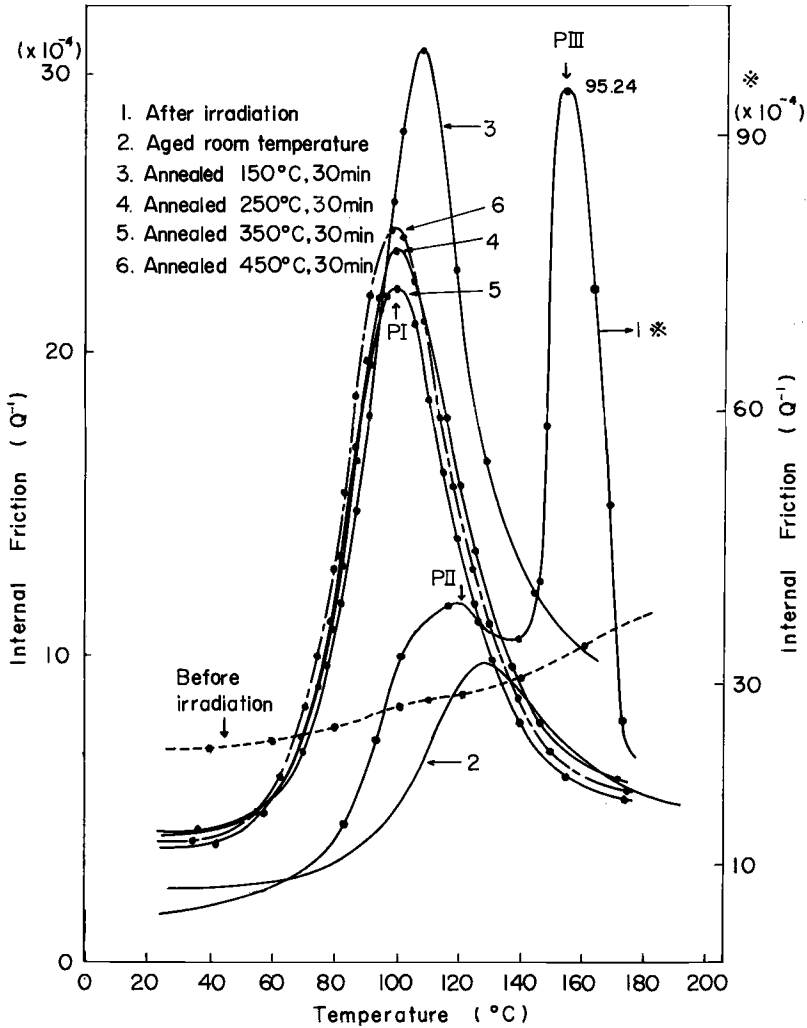


FIG. 1—The behavior of nitrogen before and after irradiation and after postirradiation annealing (specimen A).

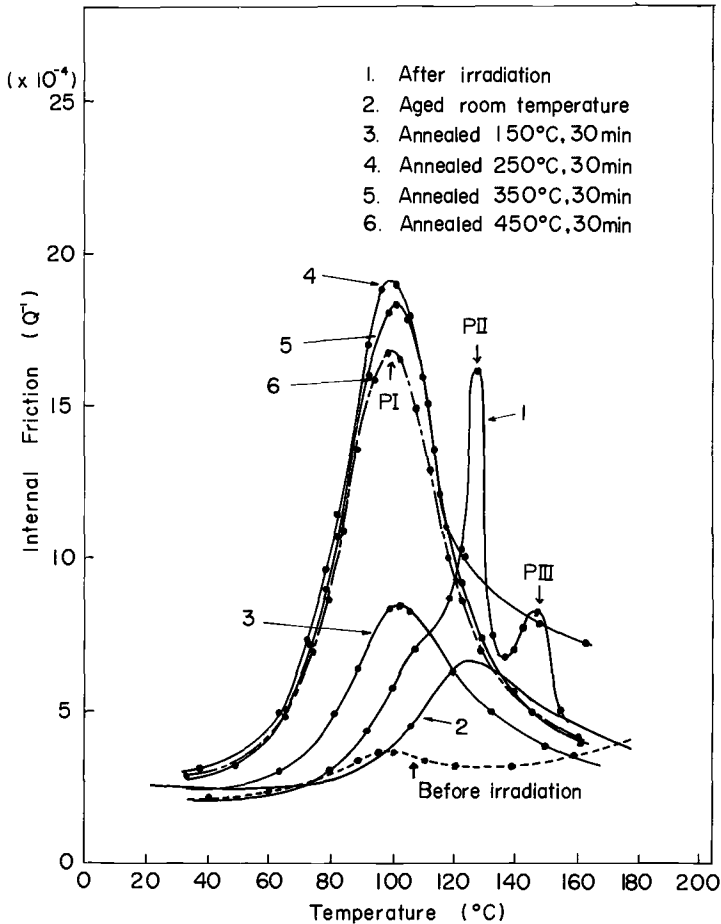


FIG. 2—The behavior of nitrogen before and after irradiation and also after postirradiation annealing (specimen B).

Experimental Results

Internal Friction

Before irradiation only a small nitrogen peak, less than 1×10^{-4} , was observed, as shown in Figs. 1 and 2 for specimens A and B, respectively. After irradiation two new peaks were observed at ~ 125 C and ~ 155 C in both specimens A and B as also shown. The two new peaks for specimen A were much higher than those for B. Hereafter, we shall call the usual

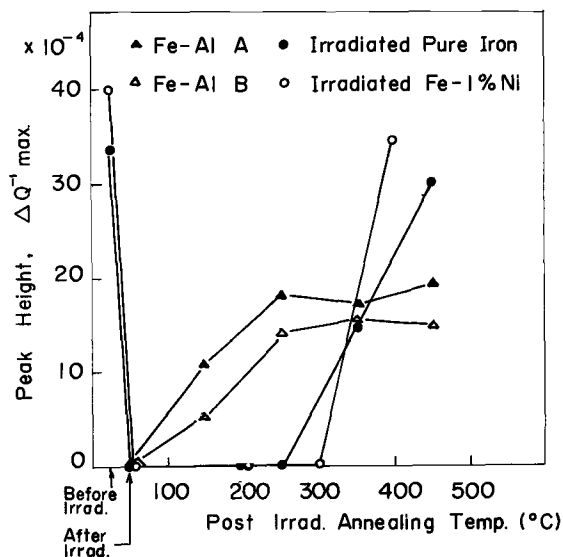


FIG. 3—The comparison of the reversion process in Fe-Al-N, Puron, and Fe-1Ni. Data from Ref 9 also are compared.

nitrogen Snoek peak “PI,” the ~ 125 C peak “PII,” and the ~ 155 C peak “PIII.” After annealing at 150 C for 30 min peak PIII disappeared in both specimens A and B. Peak PIII also disappeared after room temperature aging of both specimens for more than half a year. This shows that these defects are unstable at 150 C. After 350 C and 450 C annealing the peak height for peak PI did not change greatly. The peak height attributed to nitrogen was much lower than was the case for pure iron [3]. The behavior of free nitrogen atoms is shown and compared with pure iron in Fig. 3.

Electron Microscopy

Before irradiation, besides some precipitate of polyhedral AlN, metastable precipitates like Fe_{16}N_2 were observed, which possibly were due to metastable nitrides other than AlN. These are shown in Fig. 4. After irradiation, new doughnut shaped precipitates with a diameter of about $0.3 \mu\text{m}$ were observed as shown in Fig. 5. Since they were not observed in irradiated pure iron or unirradiated Fe-Al-N alloy, they were considered to consist of irradiation induced point defects, nitrogen atoms, and aluminum atoms. After annealing at 150 to 450 C for 30 min, these doughnut

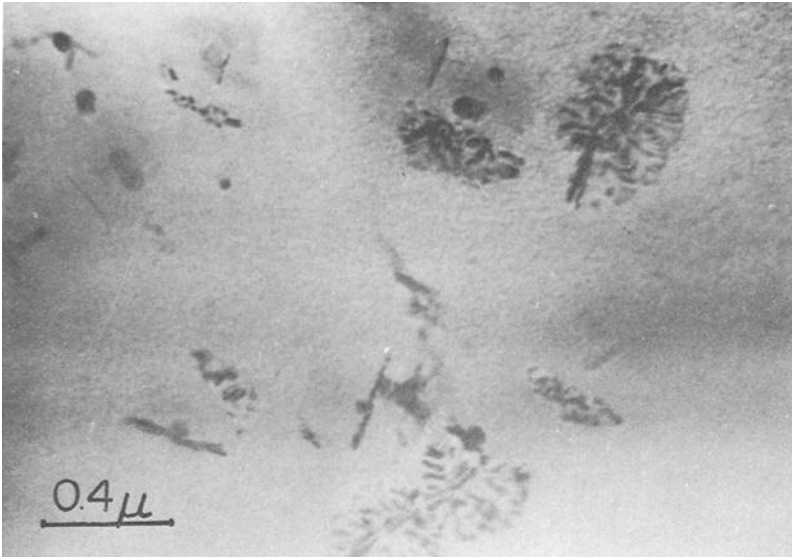


FIG. 4—*Metastable precipitates before irradiation.*



FIG. 5—*Stable precipitates which are formed after irradiation.*

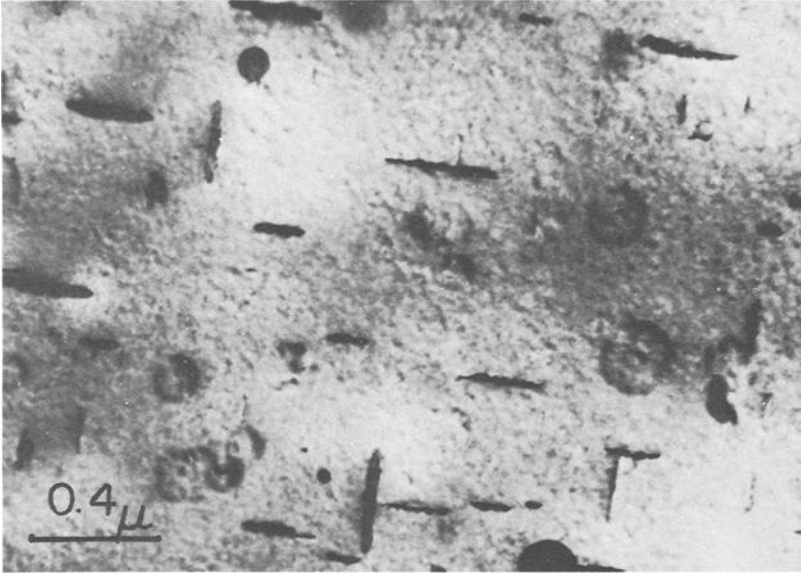


FIG. 6—Stable precipitates after postirradiation annealing at 300 C, 30 min.

shaped precipitates were still evident (see Fig. 6). They were very stable and suppressed the formation of complex defects of nitrogen and point defects. Although both the metastable phase and complex defects were observed in pure iron, only the complex defects were observed in the case of Fe-Al-N (the precipitates were not observed).

Discussion

Before Irradiation

Almost no Snoek peak was observed in the unirradiated specimens, but in electron microscopy studies metastable nitrides like Fe_{16}N_2 in addition to AlN were observed. Resolution of these nitrides by 150 C annealing was observed in the control specimens as it was in the specimens of pure iron [3]. Because the behaviors of the two were similar, we believe that the control specimen contained Fe_{16}N_2 .

The formation of AlN at 850 or 750 C was not complete in Fe-Al-N containing less than 0.01 weight percent carbon; the amount of AlN was 55 percent or less. These results indicate the partial formation of metastable nitrides [4]. If we assume that these precipitates are 10 Å in thick-

ness, the total amount of nitrogen in the metastable phase matches the observed value [5]. In specimen B a lesser quantity of metastable precipitates was observed, probably due to the lower contents of aluminum and nitrogen (the content of aluminum in specimen B was 0.02 weight percent).

After Irradiation

Three peaks were observed in internal friction measurements. Peak PI is the Snoek peak for free nitrogen. Peak PII, at about 125 C, would be the same as the peak which was found in a previous low-frequency experiment [6] and can be attributed to nitrogen trapped by aluminum atoms. This correspondence can be made because the ratio of the temperature for peak PII to that of the Snoek peak is about 1.05 in both this high- and that low-frequency experiment and because the relaxation due to solute nitrogen atoms trapped with some species should not change the ratio of the peak temperature to that of free nitrogen in measurements at different frequencies.

The peak at 155 C, PIII, probably is due to a vacancy-nitrogen complex, since the ratio of the temperature of that peak to that of the Snoek peak is about 1.14, just the same as in the case of irradiated or cold-worked iron containing carbon atoms [7, 8]. Considering the similar or equivalent behavior of carbon and nitrogen atoms [9], peak PIII probably is due to a similar complex consisting of a nitrogen atom and a vacancy.

Since the measurement of internal friction was performed about one month later in specimen B than in specimen A, the relative height of peak PIII to peak PII was less in specimen B than in specimen A, which is consistent with the observation that peak PIII decays much faster than peak PII. After aging at room temperature for more than several months, peak PIII was not observed and peak PII decreased in both specimens A and B. Corresponding to this behavior, a new type of precipitate was observed. These precipitates were thin, doughnut shaped disks with an average diameter of 0.3 μm . Since these new precipitates were observed after peaks PII and PIII had decayed, and since they were not observed in either un-irradiated Fe-Al-N or irradiated Fe-N, they probably consist of nitrogen, aluminum atoms, and irradiation induced defects. Although the diffusion constant of aluminum atoms in iron is small near room temperature [10], the diffusion of aluminum would be very much enhanced by the help of irradiation induced vacancies that form precipitates. If we assume that these precipitates have one atomic layer and account for the concentration of nitrogen atoms, the composition of the precipitates would become $\text{Fe}_3\text{-Al-N}$ accompanied with vacancies. The estimated behavior of these precipitates is shown in Fig. 7. The behaviors of AlN and solute nitrogen atoms are also shown in the same figure. The invisible precipitates might come from the assumption that the new type of precipitate (Fe-Al-N- ϕ)

Behavior of Nitrogen Atoms in Irradiated Fe-Al-N

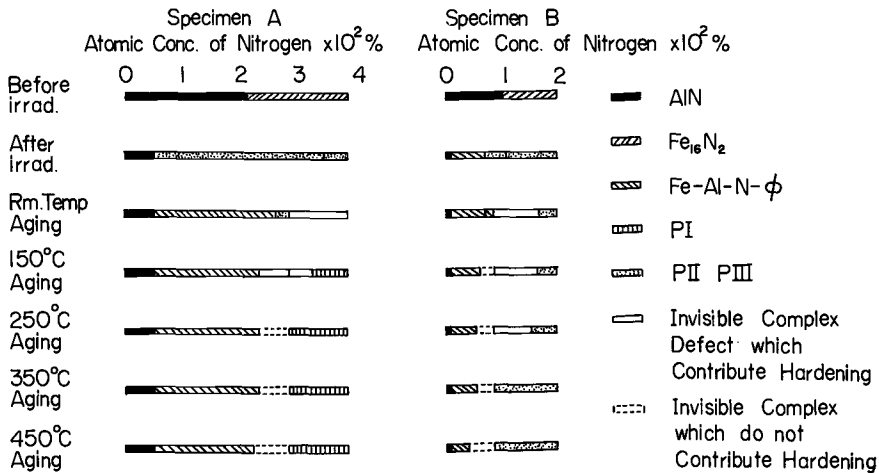


FIG. 7—Schematic representation of the behavior of nitrogen due to irradiation and post-irradiation annealing. (This diagram should be considered schematic due to the assumptions used). For peaks PII and PIII in specimen A, the background is taken higher, considering the decrease of the background at higher temperature.

consists of one atomic layer. The doughnut shaped fringe could be due to either the strong strain field around the circular precipitates or the atomic steps in the precipitates.

A smaller amount of AlN hexagonal precipitate was observed after irradiation, indicating resolution of AlN by irradiation. Data from unpublished research of K. Matsumoto and H. Nakamura have shown about 10 to 20 percent resolution even in thicker AlN precipitates; thus, as was the case here, more of the total would redissolve in a thinner AlN precipitate. However, there also is evidence for the resolution of metastable precipitates in iron [11]. Accordingly, the increase of internal friction would come mainly from the resolution of metastable precipitates but, as in this case, partly from AlN precipitates.

Postirradiation Annealing

The precipitates formed after irradiation were much more stable than those observed before irradiation and remained stable even after 450 C annealing, at which temperature irradiation hardening recovered. However, gradual precipitate resolution due to postirradiation annealing is observed in specimens A and B. The resolution of nitrogen from complexes

of nitrogen and irradiation induced point defects begins with annealing at 150 C, increases at 250 C, and saturates above 350 C. This behavior corresponds to changes in mechanical properties due to postirradiation annealing,⁵ indicating that complexes of nitrogen and irradiation induced point defects are essential in irradiation hardening.

The Role of Aluminum in Irradiation Hardening

As mentioned above, even when AlN is not completely formed, aluminum atoms stabilize irradiation induced point defects and nitrogen by forming a new type of precipitate, thereby reducing the contribution of hardening due to nitrogen-point defect complexes. Assuming that the amount of Snoek peak reversion due to nitrogen corresponds to the amount of complex defects formed, then hardening due to the complex defects can be correlated with the reversion in the Snoek peak as shown in Fig. 7.⁵ In Fig. 8 the results of this investigation are compared with data for zone melted iron [12], Puron, and Fe-1Ni [11]. These results show that irradiation hardening is closely related to the amount of Snoek peak reversion due to reduced nitrogen atom concentration and corresponds to the num-

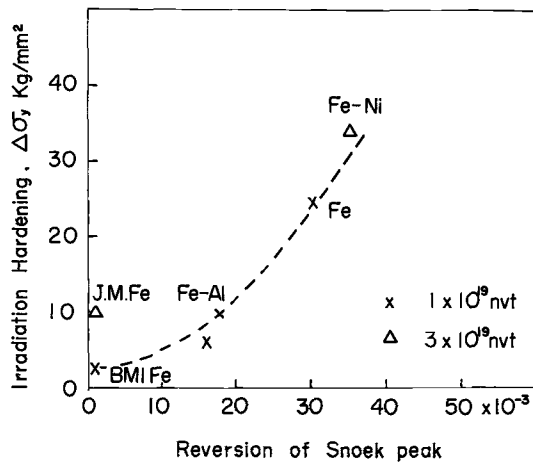


FIG. 8—The relationship between the reversion of nitrogen and the recovery of irradiation induced hardening. The amount of nitrogen reversion is assumed proportional to the concentration of nitrogen-point defect complexes introduced by irradiation. The data J. M. Fe are taken from Hasiguti et al, the hardening data are taken from K. Kitajima, and the BMI Fe data are taken from Ref 12.

⁵ Data from unpublished research of K. Kitajima and also of G. Mima and T. Yamane.

ber of invisible complexes of nitrogen and point defects formed after irradiation. Finally, the effect of aluminum in irradiation hardening would come not only from the formation of aluminum nitride but also from the formation of precipitates that are more stable than complex defects after irradiation.

Conclusions

1. Before irradiation, precipitates of Fe_{16}N_2 in addition to hexagonal AlN were observed. This showed reversion after annealing at 150 C for 30 min.

2. After irradiation, the resolution of nitrogen from a metastable phase and partially from AlN was observed by internal friction measurements. Three peaks were observed at 100 C, ~ 125 C, and ~ 155 C at 550 cps. The 100 C peak, PI, is the Snoek peak; the ~ 125 C peak, PII, and the ~ 155 C peak, PIII, are attributed to nitrogen trapped with an aluminum atom and an irradiation induced vacancy, respectively. Peaks PII and PIII decrease and peak PIII disappears at room temperature or after 150 C annealing. After room temperature aging, a new type of stable precipitate was observed, which seemed to consist of aluminum, nitrogen, and irradiation induced defects.

3. After postirradiation annealing at both 150 C and 250 C, nitrogen resolution was observed. This can be interpreted as the resolution of nitrogen complexed with irradiation induced point defects and correlates with changes in irradiation hardening.

4. The role of aluminum in reducing irradiation hardening or embrittlement consists of the formation not only of AlN but also of stable precipitates that prevent complexes of nitrogen and irradiation induced point defects.

Acknowledgments

This study was sponsored by the Steel Irradiation Subcommittee of the 122nd Committee for Nuclear Materials of the Japan Society for the Promotion of Science. We would like to express our appreciation to the committee members and also for the support from the staffs in the Hot Laboratory of the Japan Atomic Energy Research Institute.

References

- [1] Harries, D. R. and Eyre, B. L. in *Flow and Fracture of Metals and Alloys in Nuclear Environments*, ASTM STP 380, American Society for Testing and Materials, 1965, p. 105.
- [2] Hasegawa, M. in *Irradiation Effects in Structural Alloys for Thermal and Fast Reactors*, ASTM STP 457, American Society for Testing and Materials, 1969, p. 92.

- [3] Igata, N., Hasiguti, R. R., and Seto, S., *Transactions of the Iron and Steel Institute of Japan*, TISJA, Vol. 10, 1970, p. 21.
- [4] Ichiyama, T., Koizumi, M., Yoshida, I., Kunio, K., and Nishiumi, S., *Journal of the Iron and Steel Institute of Japan*, TEHAA, Vol. 55, 1969, p. 1229.
- [5] Hale, K. F. and McLean, *Journal of the Iron and Steel Institute*, JISIA, Vol. 201, 1963, p. 337.
- [6] Private communication with Y. Uchida and T. Sugeno.
- [7] Wagenblast, H. and Swartz, J. C., *Acta Metallurgica*, AMETA, Vol. 13, 1965, p. 42.
- [8] Oren, E. C. and Stephenson, E. T., *Metal Science Journal*, MESJA, Vol. 4, 1970, p. 9.
- [9] Wuttig, M., Stanley, J. T., and Birnbaum, H. K., *Physica Status Solidi*, PHSSA, Vol. 27, 1968, p. 701.
- [10] Sato, K., *Transactions*, Japan Institute for Metals, TJIMA, Vol. 4, 1963, p. 121.
- [11] Hasiguti, R. R., Igata, N., Kaneko, H., Kitajima, K., Koda, S., Mima, G., and Yamane, T., "The Role of Nitrogen and Carbon Atoms in Neutron Irradiation Effects on Iron and Iron Alloy," unpublished research.
- [12] Smidt, F. A. and Bement, A. L., *Dislocation Dynamics*, McGraw-Hill, New York, 1968, p. 409.

DISCUSSION

*J. T. Stanley*¹—This paper is an interesting and timely contribution to our understanding of irradiation effects in steel. However, there are two points concerning interpretation of the data that need to be discussed.

1. It should be noted that separation of the internal friction data shown in Figs. 1 and 2 to determine relative magnitudes of the three different peaks is not without an element of uncertainty. An alternate analysis would assign a value of at least 15.5×10^{-4} to peak PI, the normal Snoek peak, for specimen A immediately following irradiation instead of the value of zero presented by the authors in Fig. 3. The significance of this alternate interpretation of the data is that it presents evidence for breaking up of precipitate particles by neutron irradiation.

2. Consideration of the magnitude of peak PIII makes it unlikely that this peak could be due to a nitrogen vacancy complex. The magnitude of peak PIII in the present case would require a relaxation strength per nitrogen-vacancy complex about 100 times that of the carbon-vacancy complex postulated by Wagenblast and Swartz. It seems unlikely that the nitrogen vacancy could have such a large relaxation strength but still have about the same motion energy as the carbon vacancy complex.

N. Igata (authors' closure)—2. The peak height of PIII was taken as 65×10^{-4} by taking into account of the slope of the background, which was estimated from the shape of peak PII. This value is about 50 times larger than the value of Wagenblast and Swartz. This high peak value shows that the resolution of metastable nitride or thin AlN precipitates is much greater than the resolution of the metastable carbides in Fe-0.2C shown by Wagenblast and Swartz. It does not show, however, that the relaxation strength per unit defect in the case of the nitrogen vacancy is 50 times higher than in the case of carbon vacancy.

1. Since the temperature was measured by a thermocouple directly attached to the specimen, the accuracy of the temperature measurement would be high. Thus, while the peak can be interpreted to be other than the normal Snoek peak, it also provides evidence for the break up of precipitate particles by neutron irradiation.

¹ Associate professor, School of Engineering, Arizona State University, Temple, Ariz. 85281.

*A. L. Bement*²—Have you observed the occurrence of radiation anneal hardening in the specimens exhibiting a PIII peak resulting from the resolution of nitrogen? If so, did the hardening decay with room temperature aging?

N. Igata (authors' closure)—Although we did not measure the hardening as a function of aging time at room temperature, the possibility of a change in hardening corresponding to structural changes must exist.

² Battelle-Northwest, Richland, Wash. 99352.

R. R. Hosbons¹ and B. L. Wotton¹

The Effect of Fast Neutron Irradiation on the Mechanical Properties of Some Quenched and Tempered Steels

REFERENCE: Hosbons, R. R. and Wotton, B. L., "The Effect of Fast Neutron Irradiation on the Mechanical Properties of Some Quenched and Tempered Steels," *Irradiation Effects on Structural Alloys for Nuclear Reactor Applications, ASTM STP 484*, American Society for Testing and Materials, 1970, pp. 142–163.

ABSTRACT: Specimens from seven heats of AISI 403, five heats of A542, and one heat of AISI 431 were irradiated at 300 C in pressurized water to find the effect of chemical composition on their irradiated properties. The change in ductile-brittle transition temperature ΔT after the maximum integrated fast neutron flux of 1×10^{20} n/cm², $E > 1$ MeV, was similar for these steels. Some of the heats were also tested after an integrated flux of 6×10^{19} n/cm², $E > 1$ MeV, and the results showed that the latter flux caused saturation of damage in AISI 403. The total impurity concentration of AISI 403 appeared to control the size of ΔT at saturation, but there was no such correlation in the other steels. Obversely, the nitrogen concentration of A542 did affect its change of transition temperature for a given flux; a titanium concentration of 0.1 weight percent increased the unirradiated transition temperature but not ΔT . AISI 431 is unsuitable for use at 300 C as it is thermally embrittled. Although the ΔT values for AISI 403 and A542 were the same, the latter had a lower initial transition temperature.

KEY WORDS: irradiation; neutron irradiation, radiation tolerance, radiation damage, neutron flux, mechanical properties, chemical composition, grain size, quenching (cooling), tempering, martensitic stainless steels, alloy steels, pressure vessels

Fast neutron irradiation increases the nil ductility temperature (NDT) and yield stress of ferritic and martensitic steels. Much information is available on carbon and low-alloy steels in the normalized and tempered conditions but there is little information on quenched and tempered steels, especially high-alloy martensitic grades.

¹ Research engineers, Fuels and Materials Div., Metallurgical Engineering Branch, Chalk River Nuclear Laboratories, Atomic Energy of Canada Ltd., Chalk River, Ontario.

Two martensitic stainless steels, AISI 403 and AISI 431, and a low-alloy steel, A542, all quenched and tempered, were irradiated at 300 C. The effect of chemical composition and grain size on the changes in NDT and yield stress of AISI 403 and A542 with fast neutron irradiation was investigated. Only one heat of AISI 431 was tested.

Investigations on body centered cubic (bcc) metals [1, 2]² have shown that the change in tensile properties of these metals with irradiation saturates with high neutron fluxes. Beeler [3] has stated that saturation of damage occurs when the number of displacement spikes is so large that they make peripheral contact. Damage in pressure vessel steel has been found to occur below an integrated flux of 5×10^{19} n/cm², $E > 1$ MeV [4]; therefore, specimens have been irradiated to 6×10^{19} n/cm², $E > 1$ MeV, and 1×10^{20} n/cm², $E > 1$ MeV.

Experimental Procedure

Materials

Seven heats of AISI 403, one heat of AISI 431, and 5 heats of A542 were tested. The fabrication, heat treatment, and chemical composition of these steels are shown in Tables 1 and 2. The AISI 403 and AISI 431 stainless steels were obtained as extrusions, and the A542 was obtained as rolled tube according to ASTM Specification P22, bar stock and casting. All heats were quenched and tempered before machining.

Specimens—The tension specimens shown in Fig. 1 were used. Standard Charpy V notch specimens were used for the impact tests, as results from these specimens have been correlated to drop weight tests for both irradiated and unirradiated specimens [5]. All specimens were machined in the transverse direction (Fig. 2).

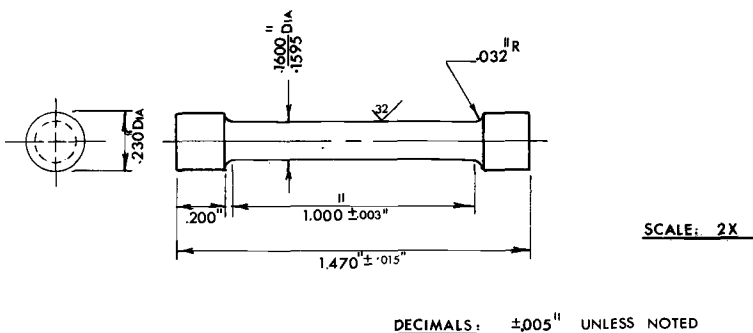


FIG. 1—Details of tension specimen used.

² Italic numbers in brackets refer to the list of references at the end of this paper.

TABLE 1—Chemical compositions of alloys tested.

Alloy	C, %	Mn, %	P, %	S, %	Si, %	Cr, %	Co, %	Mo, %	Ni, %	Ti, %	N, ppm	O, ppm	As, ppm	Sb, ppm	Cu, ppm	Sn, ppm	V, ppm	Fe
403A.....	0.09	0.42	0.016	0.011	0.50	11.92	0.024	...	0.3	...	195	90	<10	<10	1185	60	<10	Bal
403B.....	0.12	0.41	0.010	0.020	0.45	13.44	0.01	...	0.22	...	250	80	<10	<10	1200	110	20	
403C.....	0.13	0.53	0.02	0.018	0.33	12.00	0.027	...	0.20	...	170	80	<10	<10	1200	110	20	
403D.....	0.10	0.25	0.021	0.021	0.45	12.10	0.024	...	0.19	...	230	155	<10	<10	1030	340	<10	
403E.....	0.12	0.64	0.013	0.022	0.36	12.20	0.023	...	0.15	...	260	85	<10	<10	620	60	25	
403F.....	0.08	0.63	0.020	0.020	0.37	12.06	0.025	...	0.22	...	165	100	<10	<10	1010	100	<10	
403G.....	0.09	0.66	0.02	0.020	0.18	11.98	0.021	...	0.21	...	190	150	<10	<10	1110	150	30	
431.....	0.15	0.73	0.027	0.011	0.51	15.58	0.037	...	2.49	...	790	85	<10	<10	1000	160	60	
542A.....	0.11	0.39	0.016	0.014	0.31	2.25	...	0.96	0.24	...	80	30	<10	<10	600	250	40	
542B.....	0.11	0.40	0.010	0.014	0.36	2.27	...	0.97	0.17	0.1	60	40	<10	<10	1825	300	50	
542C.....	0.10	0.47	0.006	0.016	0.36	2.21	...	0.95	0.17	...	135	25	<10	<10	935	220	30	
542D.....	0.13	0.48	0.003	0.010	0.29	2.24	...	0.99	0.26	...	60	20	<10	<10	1300	260	35	
542E.....	0.08	0.35	0.012	0.017	0.31	2.19	...	0.95	0.05	...	70	20	<10	<10	255	240	35	

TABLE 2—Heat treatment and origin of heats.

Identity	Fabrication Details	Heat Treatment
403A.....	Air poured extrusion	Air hardened 1850 F, tempered 4 h 1150 F
403B.....	Vacuum degassed extrusion	Air hardened 1850 F, tempered 4 h 1150 F
403C.....	Air poured extrusion	Air hardened 1800 F, tempered 4 h 1140 F
403D.....	Argon degassed extrusion	Air hardened 1800 F, tempered 1160 F
403E.....	Argon degassed extrusion	Air hardened 1800 F, tempered 4 h 1150 F
403F.....	Air poured extrusion	1800 F 2 h water quenched, tempered 4 h 1160 F
403G.....	Air poured extrusion	1750 F 2 h water quenched tempered 4 h 1150 F
431.....	Air poured forging	1800 F oil quenched, tempered 8 h 1100 F, air cooled, tempered 8 h 1100 F, water quenched
542A.....	Electric arc melted rolled pipe	1775 F for ½ h, water quenched, 1100 to 1125 F 4 h
542B.....	Electric melted rolled pipe	
542C.....	Electric melted rolled pipe	
542D.....	Forged bar	
542E.....	Centrifugally cast bar	

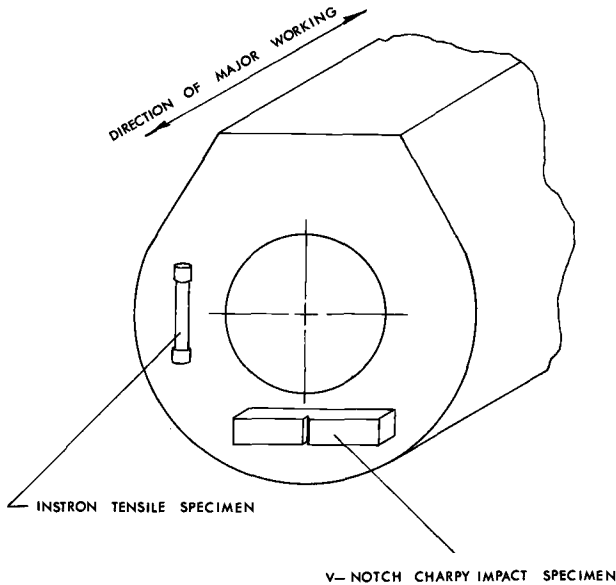


FIG. 2—Specimen orientation relative to extrusion section.

The specimens were tested in three conditions:

1. Control specimens—machined from as-received heat-treated material.
2. Thermal control specimens—heated in pressurized water at 300 C.
3. Irradiated specimens—irradiated at 300 C.

Irradiation—The specimens were irradiated in a reactor insert consisting of a heat-treated Zr-2.5Cb pressure tube closed at the bottom and flanged

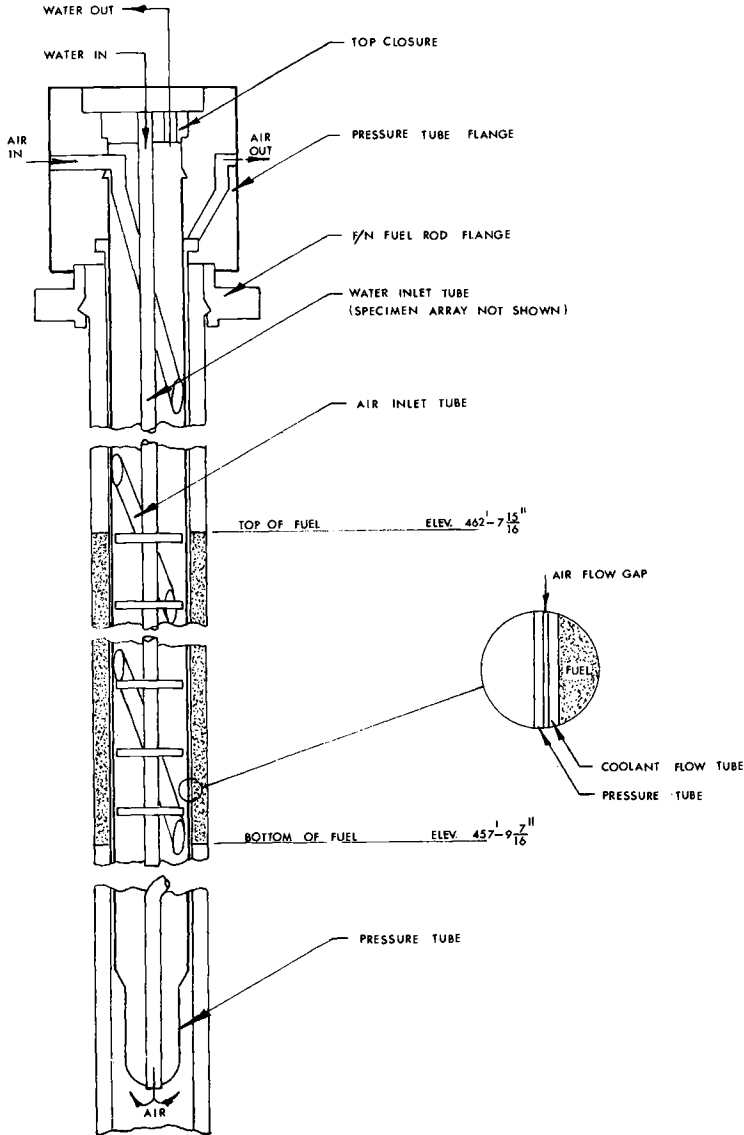


FIG. 3—Mechanical test specimen irradiation insert.

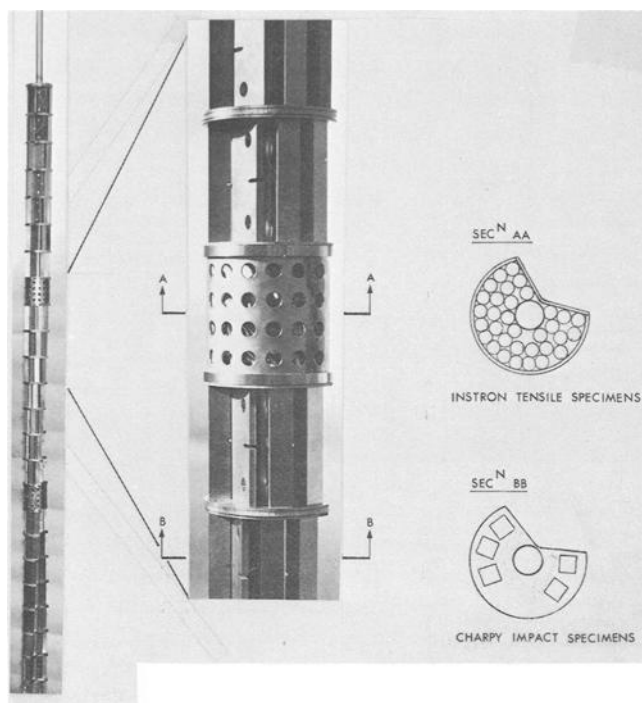


FIG. 4—*Mechanical test specimen array.*

at the top. A 24-ft water inlet tube passed down the center of the pressure tube and the specimen array was suspended around this tube (see Fig. 3).

The specimens were located in trays stacked to form an assembly within the region of fast neutron flux of the insert (see Fig. 4). All specimens were exposed to the flow of hot pressurized water.

An air cooling line passed down the inside of the pressure tube, in a spiral around the specimen stringer, and out through the bottom end. The insert was designed to allow this air to flow up the annulus between the containment tube and the coolant flow tube to provide a good medium by which the excess heat, produced by gamma heating, could be dissipated to the cooling water. In actual operation this cooling proved unnecessary, since the normal loop flow maintained a temperature differential of less than 10 C across the specimen array.

Three irradiations were undertaken, and the irradiation conditions and the integrated fast neutron flux for the steels are shown in Table 3.

TABLE 3—Irradiation conditions.

Irradiation	Materials	Total Time, h	Specimen Temperature, deg C	Integrated Fast Flux, n/cm ² , $E > 1$ MeV
1.....	403A, 403B 403D, 403F 431A, 542A	1352	295 ± 8	6.0 × 10 ¹⁹
2.....	403A, 403C 403E, 403G 431A, 542A	2332	306 ± 5	9.5 × 10 ¹⁹
3.....	542A, 542B 542C, 542D 542E	2288	315 ± 10	1.0 × 10 ²⁰

Fast neutron exposures were determined by analyzing spectra of activated iron wire monitors which had been located in dummy impact specimens, subtracting the ⁶⁰Co⁵⁹Fe mixture and comparing the result with a standard ⁵⁴Mn spectrum. The cross section for the ⁵⁴Fe(n,p)⁵⁴Mn reaction was assumed to be 70 mbarn; this figure is based on experience at Chalk River Nuclear Laboratories and gives the best correlation with reactor neutron fluxes (within 10 percent).

Testing

Tension Testing—Two tension specimens of each material, from each of the control, thermal control, and irradiation groups, were tested at room temperature, 250 C (482 F), and 295 C (563 F). All tests were performed on 30,000-lb-capacity testing machines manufactured by the Tinius Olsen Testing Machine Co., Willow Grove, Pa. One of the machines was installed in a shielded test facility.

All specimens were tested at a range of 6000 lb with a crosshead speed of 0.050 in./min. Uniform and total elongation measurements were made from the load versus time charts by relating crosshead speed to chart speed. The reduced diameter of each specimen was measured using a vernier travelling microscope and the reduction in area was calculated.

Specimens were heated in the test position using a three zone, split element furnace. Tests indicated that specimen temperature could be controlled within ±2.0 C. Specimens were held 5 to 10 min at temperature before testing.

Impact Testing—Unirradiated specimens were tested on a TMI remotely controlled impact tester manufactured by Testing Machines Inc., Mineola, N.Y. Specimens were heated or cooled in constant temperature baths as specified by ASTM Specification for Notched Bar Impact Testing of

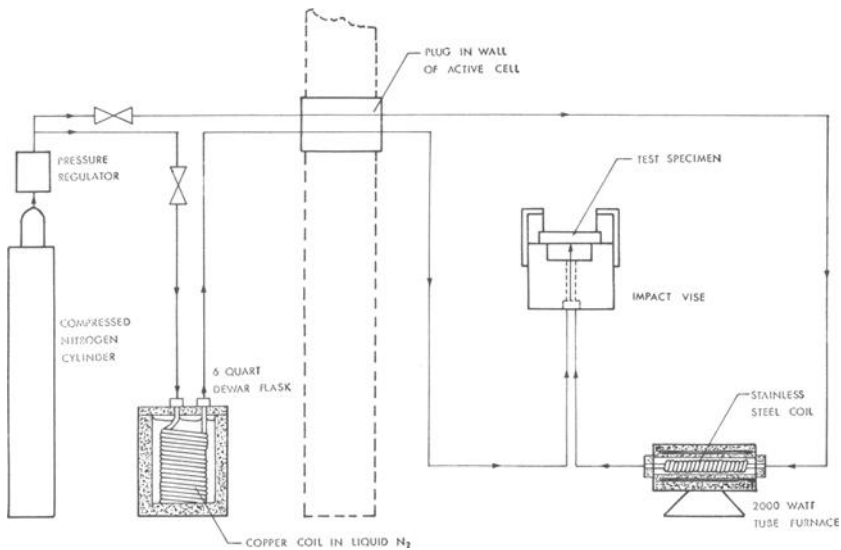


FIG. 5—Flow diagram for heating and cooling system in impact testing cell.

Metallic Materials (E 23 — 66). As this is impractical for testing in-cell irradiated specimens, a method was developed to heat or cool the specimens after they had been centered in the vise. The irradiated specimens were brought to the test temperature by blowing heated or cooled nitrogen gas over the specimen, which was partially contained in a shroud [6]. A schematic diagram of the equipment is shown in Fig. 5. A constant temperature zone (± 1 C) was obtained $\frac{3}{4}$ in. around the notch.

Results

Tension Results

AISI 403—Tension test results are given in Tables 4–6. The thermal control specimens showed that heating at 300 C produced no significant change in tensile properties. All the irradiated specimens showed an increase in 0.2 percent yield strength of 14 to 31 percent at room temperature and 12 to 20 percent at 295 C with some decrease in the reduction of area. The changes in the 250 C tensile properties were similar to those at 295 C. The air cast, water quenched heat, 403G, showed the greatest change, and the argon degassed, air quenched heats, D and E, appeared to be the least radiation sensitive.

Exposure at the higher irradiation level did not produce any pronounced difference in properties. The increase in room temperature yield strength of 403A was about 16 percent after an irradiation of 6.0×10^{19} n/cm², further irradiation producing little further change.

TABLE 4—Room temperature tensile properties of alloys tested.

Heat	0.2% Yield Stress, ksi			UTS, ksi			Total Elongation, %			Reduction in Area, %		
	C	I1	I2	C	I1	I2	C	I1	I2	C	I1	I2
	403A.....	93.8	108.8	110.0	108.2	120.9	121.9	14.5	8.8	9.0	59.0	29.4
403B.....	86.8	106.4	...	108.5	122.1	...	12.0	12.7	...	37.3	22.3	...
403C.....	100.2	...	117.6	118.7	...	129.1	13.9	...	15.1	52.1	...	47.4
403D.....	96.7	112.7	...	112.8	123.2	...	14.7	15.6	...	58.3	53.6	...
403E.....	102.2	...	116.7	122.3	...	129.8	13.7	...	13.4	43.8	...	39.5
403F.....	90.0	107.0	...	107.2	120.0	...	13.1	11.9	...	36.5	29.8	...
403G.....	89.3	...	117.2	107.5	...	125.5	15.2	...	10.7	62.2	...	27.3
431.....	129.0	154.2	168.6	155.0	154.2	179.7	4.9	0	0.8	22.4	0	3.7
542A.....	126.8	133.7	129.0	138.0	137.5	138.0	14.7	11.3	13.5	67.7	59.8	58.0
542B.....	138.9	...	141.9	132.7	...	155.2	13.9	...	12.9	61.7	...	49.7
542C.....	122.2	...	131.0	134.3	...	136.3	14.6	...	13.9	66.6	...	64.0
542D.....	139.3	...	146.9	151.2	...	156.4	13.7	...	11.5	58.2	...	48.6
542E.....	108.5	...	111.9	118.8	...	123.5	16.2	...	12.0	74.3	...	57.6

NOTE—C = control; I1 = 6×10^{19} n/cm², E > MeV; I2 = 1×10^{20} n/cm², E > 1 MeV.

TABLE 5—250 C tensile properties of alloys tested.

Heat	0.2% Yield Stress, ksi			UTS, ksi			Total Elongation, %			Reduction in Area, %		
	C	I1	I2	C	I1	I2	C	I1	I2	C	I1	I2
403A.....	83.2	101.8	97.0	94.9	107.2	106.8	8.8	7.3	7.8	51.3	16.7	25.1
403B.....	75.8	91.2	...	92.5	104.2	...	8.3	8.9	...	37.2	22.8	...
403C.....	90.3	...	103.0	103.7	...	113.4	8.9	...	9.3	50.5	...	33.0
403D.....	85.5	100.7	...	95.5	108.2	...	10.6	10.4	...	60.6	47.9	...
403E.....	89.2	...	104.2	103.3	...	112.8	10.0	...	9.7	48.6	...	39.9
403F.....	79.6	88.9	...	92.5	103.5	...	10.4	9.9	...	48.8	42.3	...
403G.....	80.2	...	99.7	91.7	...	106.5	10.3	...	9.8	57.7	...	38.3
431.....	119.1	137.0	144.1	144.6	163.4	167.7	6.0	4.0	5.1	21.7	9.1	8.7
542A.....	111.6	118.4	118.0	125.2	124.1	124.0	11.7	9.2	11.2	61.4	53.5	64.0
542B.....	124.9	...	134.0	141.9	...	145.5	11.3	...	10.0	56.1	...	46.1
542C.....	109.4	...	118.2	123.1	...	126.2	11.5	...	11.3	61.3	...	58.2
542D.....	123.8	...	135.5	139.0	...	144.0	10.0	...	9.2	50.1	...	36.9
542E.....	95.7	...	101.7	107.0	...	107.7	13.2	...	9.3	75.6	...	44.6

NOTE—C = control; I1 = 6×10^{19} n/cm², E > 1 MeV; I2 = 1×10^{20} n/cm², E > 1 MeV.

TABLE 6—295 C tensile properties of alloys tested.

Heat	0.2% Yield Stress, ksi			UTS, ksi			Total Elongation, %			Reduction in Area, %		
	I1	I2	C	I1	I2	C	I1	I2	C	I1	I2	
	C	I1	I2	C	I1	I2	C	I1	I2	C	I1	I2
403A.....	80.5	91.3	93.7	91.1	101.8	103.9	7.3	8.3	8.1	41.0	24.7	17.7
403B.....	74.9	88.3	...	90.0	100.8	...	7.9	7.6	...	35.3	32.5	...
403C.....	89.0	...	104.1	101.3	...	114.3	9.0	...	8.8	50.4	...	31.4
403D.....	85.1	96.4	...	94.8	103.9	...	10.5	9.4	...	60.9	51.4	...
403E.....	88.3	...	99.8	102.3	...	108.3	8.6	...	7.9	46.4	...	39.5
403F.....	79.4	89.2	...	91.8	100.2	...	9.7	8.6	...	48.3
403G.....	79.1	...	95.2	89.8	...	101.6	8.7	...	10.0	53.3	...	46.1
431.....	119.4	135.2	140.1	145.4	153.2	164.9	4.2	2.0	4.8	13.2	4.3	11.5
542A.....	116.0	116.4	119.7	129.5	125.6	122.0	11.4	8.2	10.8	52.7	44.8	65.0
542B.....	124.9	...	135.8	141.4	...	146.2	11.2	...	10.1	54.4	...	43.7
542C.....	110.0	...	114.8	124.3	...	127.9	12.2	...	12.1	60.2	...	47.4
542D.....	122.3	...	133.7	135.4	...	142.9	9.4	...	7.6	47.9	...	29.4
542E.....	101.6	...	104.7	114.2	...	111.9	12.7	...	12.1	64.8	...	66.9

NOTE—C = control; I1 = 6×10^{19} n/cm², E > 1 MeV; I2 = 1×10^{20} n/cm², E > 1 MeV.

AISI 431—In percentage the increase in yield stress was similar to that in *AISI 403*. After irradiation the room temperature ductility was almost zero, but at 250 and 295 C the loss of ductility was similar to *AISI 403*.

A542—The variation in the initial yield stress at room temperature of these heats was greater than in the heats of *AISI 403*, varying from 108 ksi (heat E) to 139 ksi (heat D). However, all the heats had good ductility (about 14 percent elongation at room temperature) and there was little heat-to-heat variation in elongation to failure at all test temperatures. The increase in tensile strength with fast neutron irradiation was lower than in the heats of *AISI 403*; the increase in yield stress was between 3 and 10 ksi after an integrated fast neutron flux of 1×10^{20} n/cm². Heat C had the lowest overall change in tensile properties after irradiation.

Impact Tests

Two criteria were used to determine the ductile-brittle transition temperature:

1. Temperature corresponding to a 50 percent shear failure.
2. Temperature corresponding to specific energy levels (NDT). These levels were

- a. 15 ft·lb for *AISI 403*.
- b. 30 ft·lb for *AISI 431* and *A542*.

For comparison purposes criterion 1 will be used; criterion 2 is included for design purposes, as it is used in section III of the ASME Boiler and Pressure Vessel Code.

AISI 403—The impact-energy-temperature curves for the 403 heats are shown in Fig. 6. The transition temperatures and their change with irradi-

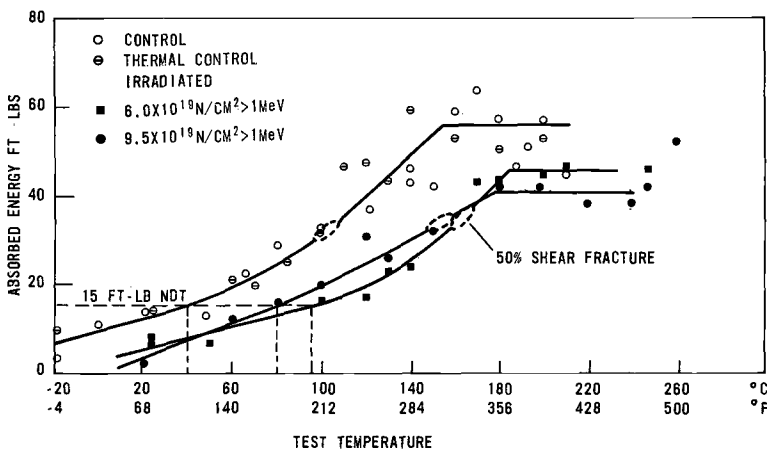


FIG. 6—Effect of fast neutron irradiation on the Charpy V notch impact properties of *AISI 403*, heat A.

TABLE 7—Transition temperatures of materials tested.

Material	Neutron Exposure, n/cm ² , E > 1 MeV	Transition Temperature, deg C					
		NDT			50% Shear		
		C	I	ΔT	C	I	ΔT
403A.....	6.0×10 ¹⁹	40	80	40	96-112	158-168	59
	9.5	40	95	55	96-112	146-160	51
403B.....	6.0	26	78	52	72-82	130-140	58
403C.....	9.5	85	145	60	110-122	194-208	85
403D.....	6.0	16	96	80	96-108	168-178	71
403E.....	9.5	46	86	40	82-94	126-138	44
403F.....	6.0	26	112	86	68-78	150-160	82
403G.....	9.5	-16	84	100	60-66	146-154	87
431.....	6	180-192	290-300	110
		224-234		66
	1×10 ²⁰	180-192	302-308	120
		212-232		88
542A.....	6×10 ¹⁹	-44	-30	14	-16--8	-6-0	10
	1×10 ²⁰	-56	-8	44	-38--28	-2-6	36
542B.....	1	64	120	56	78-90	122-132	43
542C.....	1	0	100	100	30-42	110-120	80
542D.....	1	-6	60	66	8-20	40-48	28
542E.....	1	-4	64	68	42-54	68-78	24

NOTE—C = control

I = irradiation

ΔT = shift in transition temperature

NDT = 15 ft·lb for AISI 403, 30 ft·lb for AISI 431 and A542

ation (ΔT) are shown in Table 7. Although the two criteria give different absolute values for the transition temperatures, they do give similar values of ΔT.

Heat G had the lowest initial transition temperature (60 C) but had the greatest change with irradiation. Air poured, air hardened heat A appeared to have the best impact properties, with an unirradiated transition temperature of about 105 C and a shift of 51 C after exposure at 9.5×10^{19} n/cm², E > 1 MeV. Energy levels in the ductile range were comparatively high at about 60 ft·lb and did not show a large decrease after irradiation. The similarity between the curves for the two irradiation levels (Fig. 6) would again indicate that there was little if any further irradiation damage beyond the 6.0×10^{19} -n/cm² level.

AISI 431—The impact energy temperature curves for this steel are shown in Fig. 7; the transition temperatures are given in Table 7.

The transition temperature of AISI 431 increased by about 40 C after 1352 h at 300 C but did not increase any further after longer times. The increase in transition temperature was 66 C after irradiation at 6×10^{19} n/cm² and changed by an additional 22 C on irradiation to 9.5×10^{19} n/cm².

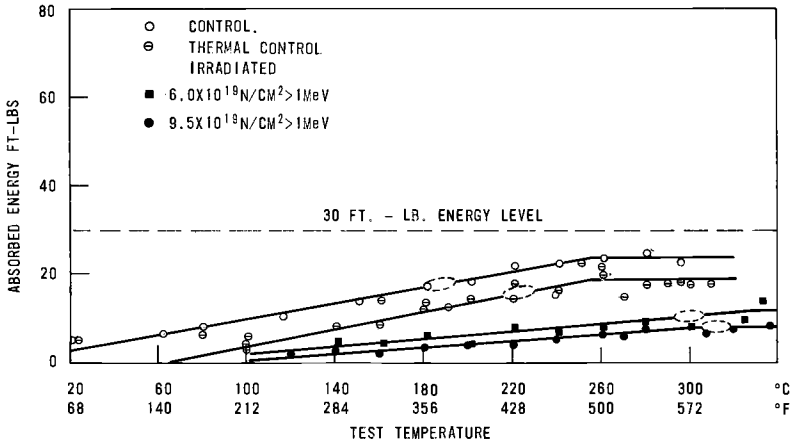


FIG. 7—Effect of fast neutron irradiation on the Charpy V notch impact properties of AISI 431, heat A.

A542—Figures 8 through 10 show the impact energy-temperature curves of these heats. The transition temperatures are shown in Table 7. The variation in unirradiated transition temperatures of the heats of A542 was greater than in the case of AISI 403, but generally the transition temperatures were lower. With the exception of heat C the variation of change in transition temperature of these heats was small (40 C) and was lower than that found in the heats of 403 and 431. Heat C, which came from the same source as heat A, had the greatest change in transition temperature. The

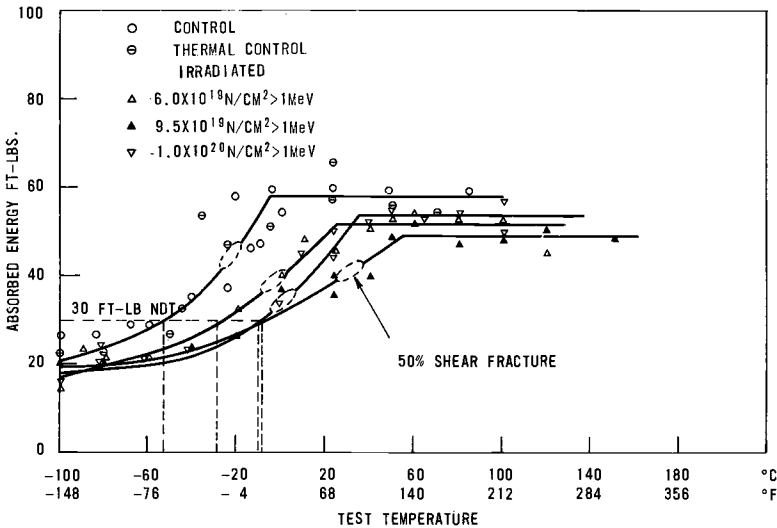


FIG. 8—Effect of fast neutron irradiation on the Charpy V notch impact properties of AISI 543 Grade 2, heat A.

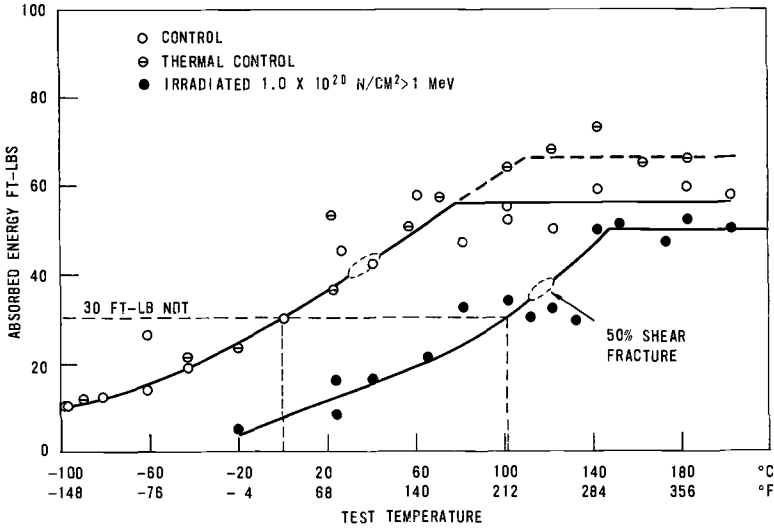


FIG. 9—Effect of fast neutron irradiation on the Charpy V notch impact properties of AISI 543 Grade 2, heat C.

impact properties of heats D and E were similar although they had different fabrication histories.

Metallographic Examination

AISI 403—The polished sections from all specimens revealed large and small globular groups and stringers of inclusions randomly distributed.

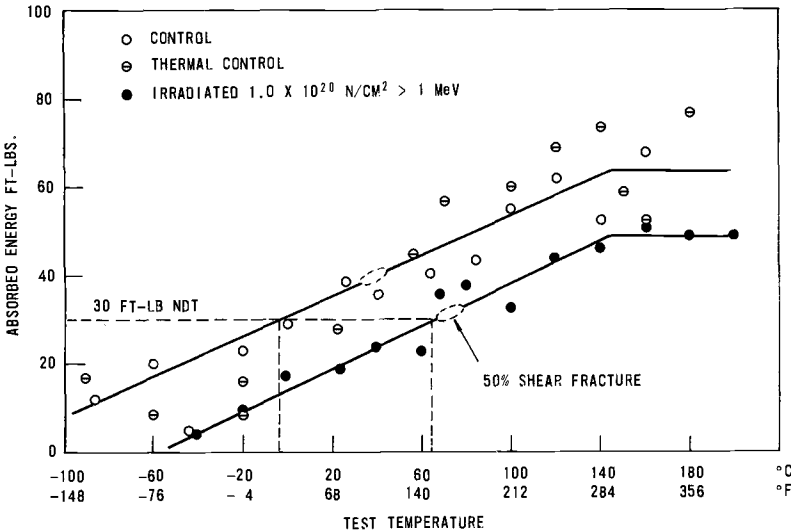


FIG. 10—Effect of fast neutron irradiation on the Charpy V notch impact properties of AISI 543 Grade 2, heat E.

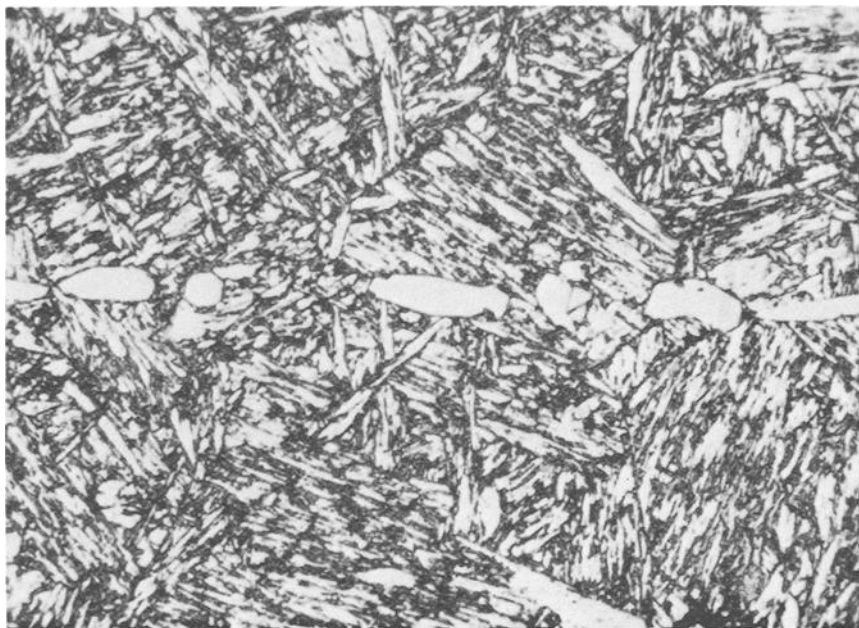


FIG. 11—*Representative microstructure of AISI 403 stainless steel ($\times 500$).*

The specimens were etched in a solution consisting of 1 g of picric acid, 5 parts hydrochloric acid, and 95 parts ethyl alcohol and reexamined. Figure 11 shows the typical microstructure of free ferrite in a matrix of tempered martensite in each of the AISI 403 steels. Ferrite stringers in the 403B specimens were large and were oriented parallel to the extrusion direction. Ferrite in the remaining 403 specimens was randomly distributed. The grain sizes of these heats are shown in Table 8.

TABLE 8—*Grain size of steels tested.*

Material	Grain Size, μm
403A	43
403B	38
403C	33
403D	28
403E	47
403F	46
403G	32
431	40
542A	20
542B	29
542C	33
542D	32
542E	28

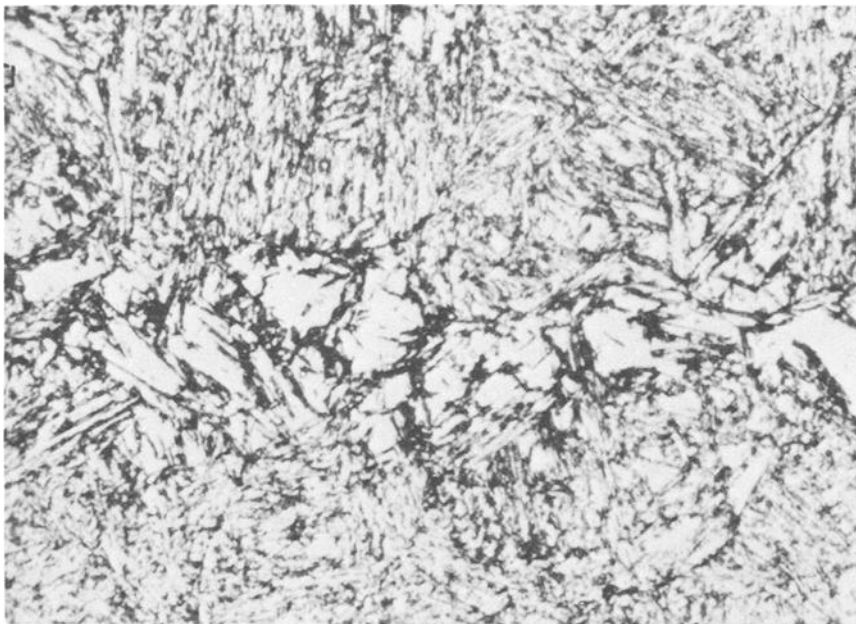


FIG. 12—*Typical microstructure of AISI 431 stainless steel (×500).*

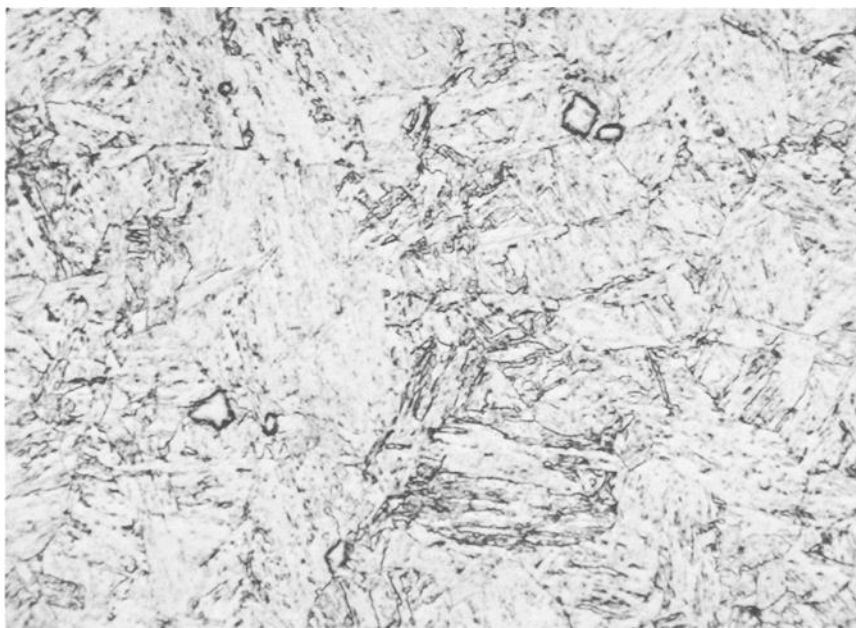


FIG. 13—*Typical microstructure of A543 steel (×500).*

AISI 431—The 431 alloy, as polished, showed randomly distributed inclusions similar to those noted in the 403 heats. A typical microstructure with the picric acid etch is shown in Fig. 12. The material exhibited an acicular tempered martensite structure with a few large areas of free ferrite with a grain size as shown in Table 8.

A542—Very few inclusions were seen in these heats with the exception of heat B, Fig. 13, which had large angular inclusions later identified by electron microprobe analysis as either TiN or TiC. The fine-grained tempered martensite structure was less acicular than the AISI 403 and 431 stainless steels. No free ferrite was observed. The grain sizes of these heats are shown in Table 8.

Discussion

AISI 403

The impact test results of heat 403A, Table 7, show that the change in transition temperature (ΔT) for heat 403A was 59 C after an integrated flux of 6×10^{19} n/cm² but only 51 C after 1×10^{20} n/cm². This indicates that saturation of fast neutron damage may have occurred by a flux of 6×10^{19} n/cm². Saturation is also suggested by the results of heats 403F and 403G. Saturation should be dependent on the composition of the steel, as saturation occurs when the rate of annealing equals the rate of damage formation. The annealing rate depends upon the diffusion rate of the atoms in the matrix; thus, for different steel alloys, different annealing rates would be expected.

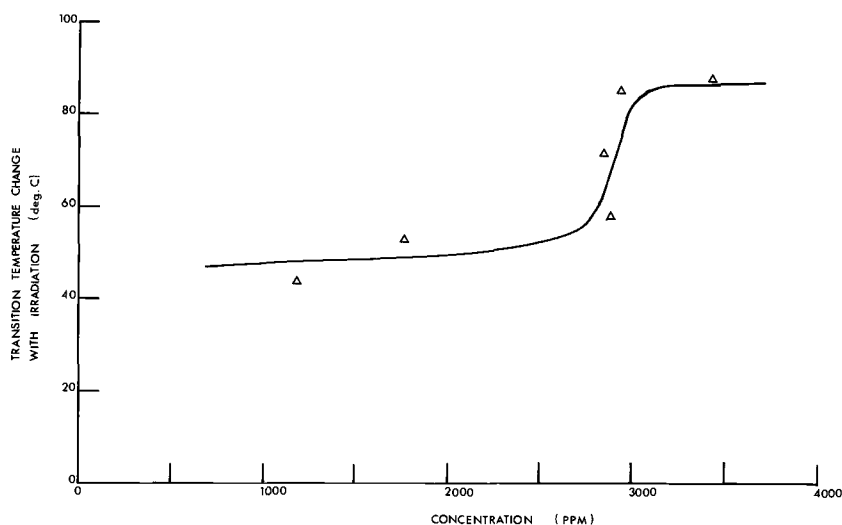


FIG. 14—Effect of impurities on the change of transition temperature of AISI 403 with irradiation.

The concentration of residual elements (copper, vanadium, antimony, arsenic, etc.) also affects the sensitivity of steels to fast neutron damage [7]. Figure 14 shows the total residual impurity concentration plotted against the change of transition temperature at saturation. An S curve is the best fit for the points of the graph, but the general trend is that sensitivity of AISI 403 to fast neutron damage increases as the impurity concentration increases. The impurity elements which changed the sensitivity the most were nickel, copper, and tin. Potopovs and Hawthorne [8] have shown that the copper concentration of steel has a marked effect on its sensitivity to fast neutron damage. The present work shows that other impurity elements may also affect the sensitivity. This possibly explains why argon or vacuum degassing was beneficial. Although little oxygen and nitrogen was removed, the concentrations of some other volatile residual elements could have been reduced. Point defects formed during irradiation will associate with the impurity atoms. The nature of the interaction is not understood, but the point defects produced during irradiation either provide nucleation sites for precipitation of solute atoms and hence increase the precipitation rate [9, 10] or introduce defect clusters which trap the solute atom [11, 12].

Grain size affects the change in NDT of normalized steels with irradiation [13–15]: the change increases as the grain size increases. Grain boundaries act as either barriers to dislocations or as sinks for migrating point defects. Thus the change of transition temperature could depend not only on the grain size but also on the distribution of carbides in the grain. A quenched and tempered steel has a finer carbide distribution than a pearlitic or bainitic steel, and therefore the grain size effect may not be as pronounced. This then could account for the lack of correlation between grain size and change in transition temperature.

AISI 431

Analysis of the results of A431 shows that this alloy has the greatest change in transition temperature after irradiation at 300 C. This is due partly to temper embrittlement that can occur in the absence of irradiation. Grounes [16] has postulated that if a number of factors influence the change in transition temperature then the total change is the sum of the individual factors if they act independently. Steele et al [14] irradiated two heats of a Ni-Cr-Mo steel, one of which had been temper embrittled after a suitable heat treatment. Although the embrittled heat had a higher transition temperature, the change in transition temperature of the two heats on irradiation was the same. The change in transition temperature of a steel which is susceptible to temper embrittlement can be expressed by

$$\Delta T = \Delta T_E + \Delta T_I$$

where

- ΔT = total change in transition temperature,
 ΔT_E = change in transition temperature due to temper embrittlement,
 and
 ΔT_I = change in transition temperature due to irradiation.

The thermal control tests showed that the transition temperature of AISI 431 had increased by about 40 C, which by applying the above rule gives $\Delta T_I \sim 80$ C (average of both irradiations). This figure is consistent with values of ΔT found for the heats of AISI 403.

A542

Analysis of these results by the same method as used for AISI 403 is not as simple. All the heats of 403 were extrusions of the same size; and, apart from water quenching, heats 403F and 403G, the only variable was chemical composition. The A542 material was obtained in a different wall thickness and was made by different fabrication processes. Heat B was found to contain 0.1 percent titanium. Woodfine [17], in an experiment to determine the effect of alloying elements on the occurrence of temper embrittlement in steels, found that titanium increased the transition temperature even without the embrittling heat treatment. Although the titanium concentration of Woodfine's alloys was higher than that of the present investigation, this lower titanium concentration may affect the initial transition temperature. The change in transition temperature of heat B with fast neutron irradiation was slightly greater than those of heats A, D, and E, but the small difference suggests that titanium does not affect the sensitivity of steel to fast neutron damage.

Heat 542C was found to be the most sensitive to damage even though it had the second lowest copper concentration; however, this heat contained the highest nitrogen concentration, which could influence its sensitivity.

Reynolds [15] has tested irradiated, quenched, and tempered A336 F22, which has the same chemical composition as A542. The 30 ft·lb NDT of the alloy tested increased by 22 C after an integrated fast neutron flux of about 3×10^{19} n/cm², $E > 1$ MeV. This is consistent with the results found in the present work when the difference in integrated flux is taken into account [18].

Summary

1. Results of this irradiation indicate that saturation of fast neutron damage may occur in AISI 403 irradiated at 300 C by an integrated fast neutron flux of 6×10^{19} n/cm², $E > 1$ MeV.
2. The sensitivity to fast neutron damage of AISI 403 is thought to depend upon the concentration of impurity elements present, thus degassing the melt is beneficial.

3. A542 is a better steel for reactor use as, even though its change in transition temperature is the same as AISI 403, it has a lower initial NDT.

References

- [1] Hull, D. and Mogford, I. L., *Philosophical Magazine*, PHMAA, Vol. 13, 1958, p. 6.
- [2] Wronski, A. S., Sargent, G. A., and Johnson, A. A. in *Flow and Fracture of Metals and Alloys in Nuclear Environments*, ASTM STP 380, American Society for Testing and Materials, 1965, pp. 69–85.
- [3] Beeler, J. R., *Flow and Fracture of Metals and Alloys in Nuclear Environments*, ASTM STP 380, American Society for Testing and Materials, 1965, pp. 86–104.
- [4] Steele, L. E., Hawthorne, J. R., and Gray, R. A., Jr., NRL Report 6419, Naval Research Laboratories, Washington, D.C., Sept. 1965.
- [5] Pellini, W. S. and Puzak, P. S., NRL Report 6013, Naval Research Laboratories, Washington, D.C., 1963.
- [6] Wotton, B. L. and Hosbons, R. R., to be published in *Materials Research and Standards*.
- [7] Steele, L. E., *Atomic Energy Review*, AERVA, Vol. VII, No. 2, 1969.
- [8] Potoповs, U. and Hawthorne, J. R., *Nuclear Applications*, NUAPA, Vol. 6, 1969, p. 27.
- [9] Stanley, J. T. et al, *Radiation Effects*, Gordon and Breach, New York, 1967, p. 97.
- [10] Hull, D. and Hogford, I. L., *Philosophical Magazine*, PHMAA, Vol. 6, 1961, p. 535.
- [11] Wuttig, M. et al, *Physica Status Solidi*, PHSSA, Vol. 27, 1967, p. 701.
- [12] Wagenblast, H. and Damask, A. C., *Journal of Physics and Chemistry of Solids*, JPCSA, Vol. 23, 1962, p. 221.
- [13] Nichols, R. W. and Harries, D. R. in *Radiation Effects on Metals and Neutron Dosimetry*, ASTM STP 341, American Society for Testing and Materials, 1963 pp. 162–198.
- [14] Steele, L. E., Hawthorne, J. R., Serpan, Jr., C. Z., Klier, E. P., and Watson, H. E., NRL Memo 1593, Naval Research Laboratories, Washington, D.C., Feb. 1965.
- [15] Reynolds, M. B., *Journal of Materials*, JMLSA, Vol. 1, No. 1, March 1966, p. 127.
- [16] Grounes, M., Swedish Atomic Energy Report S-370, Aktiebolaget Atomenergi, Stockholm, Sweden, Sept. 1967.
- [17] Woodfine, B. C., *Journal of the Iron and Steel Institute*, JISIA, Vol. 173, 1953, p. 240.
- [18] Hosbons, R. R. and Wotton, B. L., "The Effect of Fast Neutron Irradiation on the Mechanical Properties of Some Stainless and Low Alloy Steels," AECL-3363, Atomic Energy of Canada Limited, Chalk River, Ontario, Feb. 1969.

DISCUSSION

*A. L. Bement*¹—In your specimens of A431 and A403 steel, which exhibit semicontinuous stringers of delta ferrite, one would expect low-energy absorption in a Charpy test for the transverse direction. In this case there is a weak phase (delta ferrite) surrounded by a strong phase (tempered martensite), and fracture should initiate and propagate along the delta ferrite stringers. Therefore, a systematic correlation of impact properties against bulk structure (grain size, mean carbide separation, etc.) should not be expected unless mechanical anisotropy is taken into account.

R. R. Hosbons (authors' closure)—Only AISI 403 heat B contains semi-continuous stringer orientation which would affect the charpy V notch properties of the steel, and therefore we think that the analysis we have carried out is still valid.

¹ Battelle-Northwest, Richland, Wash. 99352.

AGENDA DISCUSSION SESSION

L. E. Steele¹

Structure and Composition Effects on Irradiation Sensitivity of Pressure Vessel Steels

REFERENCE: Steele, L. E., "Structure and Composition Effects on Irradiation Sensitivity of Pressure Vessel Steels," *Irradiation Effects on Structural Alloys for Nuclear Reactor Applications*, ASTM STP 484, American Society for Testing and Materials, 1970, pp. 164–175.

ABSTRACT: The paper emphasizes engineering implications of the effects of structure and composition on the irradiation sensitivity of steels. Theoretical considerations are discussed and reviewed as they relate to possible explanations for observations on the subject.

The structural aspects include primarily the type of metallurgical microstructure and the grain size and also the steel condition, that is, plate, forging, weld metal, or weld heat affected zone. The compositional factors are never quite separable from structural factors in a microscopic sense. Several interstitial elements, primarily nitrogen, carbon, oxygen, and hydrogen, have been investigated for their relationship to neutron radiation sensitivity. Substitutional elements, including nickel, copper, phosphorus, vanadium, sulfur, and boron, as constituents in steels have also been included. Copper and phosphorus are found particularly detrimental to radiation resistance when present in quantities above certain levels.

KEY WORDS: neutron irradiation, radiation effects, radiation tolerance, nuclear reactor engineering, pressure vessels, steels, structural steels, nuclear reactor components, microstructure, embrittlement, interstitials, grain size, heat treatment, martensite, solid solutions, steel constituents

The technological and scientific importance of structure and composition as these affect the irradiation embrittlement sensitivity of reactor

¹ Head, Reactor Metals Branch, Metallurgy Division, Naval Research Laboratory, Washington, D.C. 20390.

pressure vessel steels led to an agenda discussion session on the subject. The illuminating discussion in turn formed much of the basis for this summary; nonetheless, to assure completeness, this summary is prefaced necessarily by reference to the earlier work in this field and to the papers presented in the first two sessions, Pressure Vessel Steels—Fracture Behavior and Pressure Vessel Steels—Structural and Impurity Effects, of the symposium. In the interest of readability and early publication, direct quotations of discussors are eliminated in favor of a paraphrased condensation. (Individual contributors and discussors are recognized in the acknowledgments.)

For purposes of this review, the critical aspects of structural or compositional influences on radiation sensitivity are correlated with reactor service situation. Thus, for example, while the theoretical aspects of the influence of nitrogen or carbon on the behavior of otherwise pure iron after low-temperature irradiation are of interest, the emphasis is on their role in steel at reactor service temperatures.

While time did not permit a full summary of our understanding of this subject during the symposium, the well developed body of published information provided for the drawing of conclusions which naturally will reflect somewhat my experience and opinions.

Structure and Irradiation Sensitivity

Metallurgical Microstructure

The influence of metallurgical microstructure after irradiation at low temperatures (<300 F, 149 C) has been identified as important by several investigators [1, 2, 3].² In one experiment [4] three laboratory heats of steel meeting the nominal ASTM composition specifications for Type A212B—no uranium and additions of uranium to levels of 0.06 and 1.1 percent—were irradiated simultaneously with a commercial plate. These three were produced in $\frac{1}{2}$ -in. plate with great care (more typical of a vacuum stream degassed steel) and, except for the 1.1 percent uranium version, proved to be far superior to the commercial reference standard in terms of radiation embrittlement after exposure to an irradiation of 1.3×10^{19} n/cm², $E > 1$ MeV, at 240 F (116 C). While variations in residual element contents might partially explain their superior performance, the major difference noted was the microstructure: the uranium bearing steels being essentially martensitic in structure compared to the usual ferrite-pearlite structure of commercial A212B steel. The martensitic structure was attributed to the rapid cooling in air of the very thin plate produced from the heat. Another suggested explanation for the superior radiation resistance of the 0.06 percent uranium steel is that the uranium served as a

² Italic numbers in brackets refer to the list of references at the end of this paper.

“getter” for nitrogen, reducing the amount in solution. Nitrogen in solution has been identified as critical to the irradiation sensitivity of steels and iron in the temperature range of this irradiation (240 F, 116 C). It is unfortunate that the uranium bearing steels and the related superior control version were not available in sufficient quantity to permit irradiation at a variety of temperatures to more fully test the irradiation sensitivity advantages of this steel and their causes.

A more specific test of microstructural effects was provided by an experiment in which two steels—Type A350 forging grade (a C-Ni-Mn steel of high radiation sensitivity) and A543 plate (a Ni-Cr-Mo steel of low sensitivity)—were placed into reverse positions of sensitivity through heat treatment alone [3, 5]. After irradiation at <240 F (116 C), the highest strength versions, characterized in both steels by a tempered martensite structure, proved to be most insensitive to radiation (less than one half the change exhibited in the sensitive state). Since no composition changes occurred, microstructural variations were credited with the reversal of irradiation embrittlement sensitivity in these two steels, which are quite dissimilar in unirradiated properties.

The results published to date suggest that the effect of metallurgical microstructure on radiation embrittlement sensitivity may be quite significant. However, at temperatures of nuclear reactor service no such body of evidence is available.

Grain Size

Several investigators have identified grain size as an important factor in radiation sensitivity of steels [1, 6, 7, 8]. For example, Nichols and Harries [7] irradiated steels having markedly different ferrite grain size but similar microstructures at ~300 F (150 C) to a fluence (fission) of 7×10^{17} n/cm². Their data show a distinct effect, superior radiation resistance, with finer grain size. Similar findings were observed by Klepfer and Gordon [8], though the steels compared contained different microstructural features and were irradiated at a temperature range higher than that used by Nichols and Harries (470 to 545 F, 243 to 285 C). Close examination of the steels studied by Klepfer and Gordon distinguished differences in composition which, at the higher temperatures involved, may be of overriding importance to the relative sensitivity of a given steel. In spite of the doubts raised, however, Klepfer and Gordon have developed an impressive model for the effects of ferrite grain size on steel embrittlement which includes effects of temperature, dose rate, and exposure time.

On the negative side, however, are the important observations by Trudeau [1], which showed an inverse effect, greater embrittlement in a fine-grained 3.25 percent nickel steel than in a coarse-grained product of the same steel. Recent data by Hawthorne [9]³ showing the effects of copper

³ Included in this ASTM Special Technical Publication.

content on sensitivity point to no significant role of grain size in irradiation of a 0.13 percent copper version of A533B steel at 550 F (288 C) and a 0.03 percent copper product. The latter, which was relatively insensitive to radiation, had a grain size which was slightly larger than that of the more sensitive 0.13 percent copper version. Thus, it appears that composition effects may be more important than grain size or microstructural effects in the temperature range of water reactor vessel service (>500 F, 260 C). At lower temperatures grain size is thought to be very important.

Discussion identified the role of the grain boundary (and the advantage of its abundance in fine-grained steel) as a defect trap and as a sink for dislocation pileups. This role is thought to be especially important where free interstitial elements such as nitrogen (and a projected nitrogen defect complex) may be more homogeneously trapped, thereby lessening the effects on macroscopic properties of the irradiated steel. A more homogeneous distribution of nitrogen would also aid the resolution of nitrogen as the temperature is raised, minimizing the possibilities for a "lingering" effect of the nitrogen defect complexes in the lower range of reactor operation, about 500 F (260 C).

Considering the practical case of quenched and tempered steels (current practice) irradiated at normal vessel service temperatures, the ferrite grain size has less meaning because of the finer carbide distribution inherent to the quenched structure. Hosbons and Wotton [10]³ ascribe a lack of correlation between irradiation induced embrittlement of A542 steel and grain size to such a quenched structure. On a similar practical base is the fact that steelmaking practice for current pressure vessel steels aims routinely for a fine grained structure.

Composition or Impurities and Irradiation Sensitivity

More effort has been devoted to the study of compositional effects than to structural effects on the sensitivity of steels to neutron induced changes. The most exciting recent development has been the identification and verification of the role of copper in steel embrittlement at elevated temperatures. The work at the Naval Research Laboratory (NRL) on this subject and the vivid demonstration of copper effects were summarized for A533B steel in a paper by Hawthorne [9].

Studies by Little and Harries [11, 12], Castagna et al [13], and Igata et al [14, 15] have verified nitrogen in solid solution as a major factor in radiation embrittlement of iron and steel when the exposure is at low temperature (less than about 482 F, 250 C). The effect is attributed to nitrogen plus neutron irradiation produced defects in relatively stable complexes. At higher temperatures, between 300 and 750 F (150 and 400 C) [11, 14], nitrogen returns to solution, producing a related reduction of hardness. Igata et al have shown the recovery of hardening and the parallel resolution of nitrogen on annealing to 482 F (250 C), but the presence of uni-

identified stable precipitates was noted even after postirradiation annealing at 572 F (300 C) for 30 min.

It has been suggested that the most important factor in compositional effects is the combination of irradiation produced defects and available interstitial elements and that the role of substitutional elements such as titanium, silicon, and aluminum can best be understood in this context. However, examination of the empirical evidence [9, 16] suggests that at elevated temperatures the presence of substitutional elements, such as copper and phosphorus, controls the level of embrittlement in the Mn-Mo steels currently used in the United States for reactor pressure vessels. Copper has been shown to be especially effective, with the level of embrittlement at an irradiation temperature of 550 F (288 C) paralleling the copper level.

The Effects of Copper on Embrittlement

The important effect of copper was recognized in studies involving very clean laboratory heats of Type A302B steel, prepared by J. V. Alger of the U. S. Steel Applied Research Laboratory, with selected residual element impurities added [16]. Following a vivid demonstration by NRL of copper and phosphorus effects in these laboratory heats, a large (30 ton) heat of ASTM Type A533B steel was procured at the request of the U. S. Atomic Energy Commission. In addition to ASTM specifications, added limits were specified on copper (0.03 percent, with a high-copper version of 0.13 percent), phosphorus (0.009 percent), and other residuals, such as arsenic, antimony, bismuth, and tin (total 0.05 percent maximum) and vanadium (0.02 percent maximum). After irradiation at 550 F (288 C), the increase in transition temperature for the 0.03 percent copper version was only 40 F (22 C) versus 150 F (83 C) for a reference A302B steel which represented a midrange sensitivity for several component heats of A533B steel irradiated to comparable fluences. Other strong evidence of the effects of copper is found through a comparison of the increase in transition temperature with neutron exposure as a function of copper content for A533B steel (plate and welds) irradiated to various fluences [17]. Steels containing copper levels from 0.19 to 0.32 percent showed increases in transition temperature on an average twice those of a group of steels containing from 0.09 to 0.14 percent copper. The latter, in turn, produced shifts twice as great as those for the 0.03 percent copper steel. The welds of A533B studied contained copper at levels >0.19 percent and consequently fell in the high-sensitivity group. In a major effort [18] to produce higher strength pressure vessel steels having high resistance to radiation embrittlement, welds have been studied and special welds prepared in which the copper, nickel, and manganese contents were controlled in a statistical sequence to test any irradiation effects attributable to these elements individually or in various combinations. Copper again proved to be of overriding importance to radiation sensitivity.

How does copper so greatly affect radiation embrittlement? No clear answers are yet in hand, but hypotheses have been advanced and studies are under way. Early observations of effects of copper on sensitivity to steel embrittlement *only* at elevated temperature led to an examination of the possibilities of segregation of copper to interfaces which would become the initiation sites for subsequent fracture. Thus, in a cooperative study between the Naval Research Laboratory and the Massachusetts Institute of Technology, Ziebold [19] examined fracture surfaces of broken Charpy V specimens using a scanning electron microscope. Copper was observed in conjunction with manganese sulfide inclusions in the fracture, but this segregation was not conclusively related to increased sensitivity in the high-copper material. Hunter [20] of the Pacific Northwest Laboratory used scanning electron microscopy to look for possible variations in fracture mode between selected high- and low-copper steels after irradiation. Again, no significant variations attributable to copper segregation were noted, leaving much doubt regarding the hypothesis of copper segregation at points conducive to fracture [21]. Smidt of the Naval Research Laboratory has suggested several alternatives which are being investigated; these include

1. *A more sensitive test of the possibility of copper segregation at interfaces which subsequently become the fracture surface.* This involves examination of the fracture surfaces by Auger spectroscopy to ascertain if segregation has occurred at the 550 F irradiation temperatures and the relative magnitude of the effect in high- and low-copper alloys. It is essential that a fresh fracture surface be examined in high vacuum, and the experiment is being conducted in cooperation with Dale Stein, University of Minnesota, using the techniques and approaches developed for studies of temper embrittlement. An estimate of the vacancy supersaturations necessary to increase the diffusivity of copper in iron in a large enough amount to permit segregation appears to be outside the realm of possibility.

2. *A test of the more likely mechanism, the formation of a copper-vacancy complex which serves as the nucleation site for vacancy aggregates.* Such a defect aggregate would have greater thermal stability than those produced in lower temperature (<300 F, 149 C) irradiations or in low-copper material which undergoes dynamic recovery in the 550 F temperature range. This hypothesis also helps to explain the fact that even low-copper steels show relatively high embrittlement sensitivity when irradiated at low (<300 F, 149 C) temperatures. The mechanism of embrittlement is simply one in which the higher yield strength in the material containing aggregates causes a greater shift in transition temperature [21]. Specimens are presently being irradiated by NRL to verify the higher yield strength in copper bearing alloys and the retardation of the recovery process.

In discussion, a mechanism similar to that in semiconductors, where a silicon interstitial element may change places with an impurity substitu-

tional element converting it into an interstitial impurity atom, was suggested to explain the role of copper [22, 23]. If such a "conversion" mechanism were active, it is suggested that saturation of the deleterious effects of copper might occur with higher temperature as such exchanges are accelerated and essentially completed.

Regardless of the exact mechanism, however, it is abundantly clear that copper plays a major role in the embrittlement of reactor pressure vessel steels and that the more of it that is removed from the steels going into reactors the better.

Embrittlement and Other Elements

Other elements identified as being important in the embrittlement process include boron [24] and nickel [25].³ Harries and Eyre [24] postulated that, in addition to the expected neutron produced displacement damage, boron containing steels may undergo additional damage because of the energetic products from the transmutation reaction $^{10}\text{B} + n \rightarrow ^7\text{Li}$ and ^4He . Embrittlement was indeed more severe in boron containing steels when irradiated at temperatures of 302 F (150 C) but did not show the significant difference between boron and nonboron steels when the irradiation temperature was higher, 482 F (250 C). Further, most steels used or seriously considered for reactor pressure vessel service contain no significant amounts of boron.

Kawasaki et al [25] identify added nickel as a possible factor in changing the embrittlement of a modified $2\frac{1}{4}\text{Cr-1Mo}$ steel. It is noted, however, that the more sensitive nickel bearing version showed very small added shifts in transition temperature, that they contained higher levels of phosphorus, and that no analysis for copper was available for these steels. In an earlier study [26] of nickel effects, Ni-Cr-Mo steel showed no significant effects of nickel on radiation sensitivity. In fact, a patent [27] based on this early study has been granted J. V. Alger of U. S. Steel for a "radiation resistant steel." The role of nickel in radiation sensitivity of welds has been further investigated by Hawthorne, Fortner, and Grant [18], with no significant effect indicated for a base electrode composition of $2\frac{1}{4}\text{Cr-1Mo}$.

The influence of phosphorus has been demonstrated in typical pressure vessel steels but primarily is of academic interest only, since current practice for making pressure vessel steels (including a vacuum stream degassing operation) reduces phosphorus to levels below those found critical to the enhancement of steel embrittlement.

Practical Considerations

The ultimate value of research is validated by its application. In the case of steels for nuclear reactor pressure vessels, close communication between the researcher, the steelmaker, and the steel user generally has as-

sured prompt application of research data. (Nevertheless, there is room for even better communication and cooperation.)

Progressive improvements in the steel for nuclear reactor pressure vessels have resulted from (1) a conscious effort on the part of steelmakers to improve their product for a critical function, (2) advances in technology leading to the demand for higher strength, with a natural move to quenched and tempered low-alloy steels to meet this advance, and (3) the application of lessons learned in irradiation effects research. This pattern of progress, if extended to every vessel component, would eventually assure the optimum in reliability in spite of neutron irradiation effects. Unfortunately, no such idealized sequence has occurred or is likely to occur. Proof of the latter statement rests in the rather extreme differences observed between irradiated plate and weld metal and, in the United Kingdom, between plate, weld, and weld heat affected zone material (unirradiated) in certain steels. Thus, while important progress has been made toward improving vessel plate steels (both before and after irradiation), the weld, with high copper content, becomes the weak link in irradiated welded structures. Similarly, in the United Kingdom, weld heat affected zone cracking has been described as a potential problem without superimposing the added factor of radiation.

In spite of the "weak link" aspects of weld metal in the irradiation sensitivity context, there is abundant evidence that the critical factor is composition, especially copper and phosphorus contents, in the current and projected grades of U. S. reactor pressure vessel steels. Thus, the answer to excessive irradiation embrittlement sensitivity in welds appears to be control of composition. No significant effect of metallurgical microstructure nor grain size in the welds or heat affected zone of current pressure vessel steels has been identified. In fact, the heat affected zone in A302B and A533B steels, which may exhibit grain coarsening, has been identified as relatively insensitive to radiation embrittlement compared to the weld metal. Such favorable behavior on the part of the heat affected zone in higher strength steels is an open question, however; no significant difference between plate and forging response has been noted.

In summary, on a practical basis, a continuing close relationship for communication and cooperation among researchers, steelmakers, and steel users will assure rapid transformation of research data into technological innovation with related advancements of benefit to the whole nuclear industry.

Summary

Progress in both fundamental and applied research on radiation embrittlement of reactor pressure vessel steels has been rapid in recent years; hence, the agenda discussion session was most fruitful. The examination

of the microstructural and compositional aspects of radiation embrittlement of steels permits summary statements of what we now know and implications of what is needed in the way of additional study. (Emphasis is on conditions pertinent to the service environment.)

1. Metallurgical microstructure can affect embrittlement sensitivity. Such effects have been observed especially with low irradiation temperatures. Changing the microstructure by heat treatment in steels otherwise the same has been demonstrated to change the sensitivity. A ferrite-pearlite structure appears to produce embrittlement sensitivity, while tempered bainite and especially tempered martensite tend to coincide with relative radiation embrittlement insensitivity. Of most significance, however, is the fact that studies conducted at elevated (reactor vessel service) temperatures have not identified significant effects of metallurgical microstructure. The accepted explanation for microstructural influences is based on the relative abundance and homogeneity of sinks for radiation produced defects.

2. Grain size in several carbon and low-alloy steels has been identified as paralleling embrittlement sensitivity, coarse grain structure being sensitive and fine grain structure being relatively insensitive. Experimental evidence favors this statement, but it is by no means a unanimous conclusion. The important practical effects of grain size on steels irradiated at reactor vessel service temperatures are not as clear, since the isolation of microstructural effects from composition or impurity effects has not been emphasized. The projected mechanism by which small grain size reduces embrittlement is one of providing for a relatively homogeneous coupling of grain boundaries and neutron defects to reduce the effect on the mechanical properties of the steel when irradiated. Of practical importance is the fact that grain size is believed to be less significant in the quenched and tempered steels because the fine distribution of martensite may serve as defect sinks in the same way that fine grain structures do. Further, current U. S. steelmaking practice for vessel steels routinely produces a fine-grained product.

3. The study of composition or impurity effects on radiation sensitivity has been directed fundamentally at interstitial elements and their effects in pure iron (and in steels) after irradiation at low temperatures, much below vessel service temperatures; on the other hand, a more applied research effort has focused on substitutional elements in steels irradiated at service temperatures. The former effort is enlightening as to the causes of radiation embrittlement, but the latter holds more value for providing an early engineering solution to the question.

In summary, free nitrogen (in solid solution), through a mechanism believed to involve a nitrogen-neutron defect complex, has been shown to have a major effect on the sensitivity of steels when the irradiation temperature is low (less than about 480 F, ~ 250 C). The observation of resolu-

tion of nitrogen on annealing at progressively higher temperatures has aided in understanding the mechanisms involved. On the other hand, the other major contributor to radiation hardening, copper, has been shown to be effective only at elevated temperatures. This effect is not understood fully but is thought to be caused by a retardation of annealing because of a copper-vacancy aggregate which exhibits relatively high thermal stability. Experiments are under way to validate this postulate, but the most important fact is that very low sensitivity to radiation embrittlement parallels low copper (0.03 percent) content. Even copper levels as high as 0.14 percent show superior 550 F (288 C) radiation resistance in comparison to steels containing 0.19 percent copper or greater.

Phosphorus, boron, and vanadium have also been identified as contributors to radiation embrittlement sensitivity, but current steel making practice and the specific U. S. vessel steel compositions dictate low phosphorus, boron, and vanadium levels. These elements are not to be overlooked, however, as higher strength steels are considered for reactor vessel service.

4. Applying the lessons learned in fundamental and applied research efforts dictates care in assuring the production of reactor vessels containing steels (including welds and weld heat affected zones) which exhibit a fine grain structure and are of maximum cleanliness, especially in terms of copper as well as nitrogen, phosphorus, sulfur, vanadium, and certain other trace residual elements including antimony, arsenic, bismuth, and tin. This will not be easy, but, with a concerted effort encompassing, if necessary, revised composition specifications including those for weld electrodes, vessels of relative insensitivity to radiation embrittlement should be possible in the future. At the same time, lessons learned from research on radiation embrittlement should aid the projection of levels of embrittlement to be expected in vessels already constructed, thereby greatly aiding the establishment of procedures for operation of reactors to maximize vessel reliability.

Acknowledgments

Thanks are due all of the authors of papers presented in Sessions I and II of this symposium for providing the stimulating data upon which much of the discussion was based. The contribution of the discussors, N. Igata, B. Watkins, D. R. Harries, L. J. Chockie, E. Landerman, R. G. Berggren, J. R. Hawthorne, R. A. Wullaert, J. V. Alger, A. L. Bement, J. E. Corbett, R. Bullough, C. Baroch, and C. W. Hunter, are acknowledged with gratitude. The assistance of Chairman A. L. Bement and his symposium committee and Chairman D. N. Sunderman of ASTM Committee E-10 are greatly appreciated as well. Special recognition goes to C. W. Hunter, who served as discussion recorder, and to D. R. Harries for so ably assisting the discussion session as comoderator.

References

- [1] Trudeau, L. P., *Radiation Effects on Reactor Structural Materials*, AEC Monograph Series, American Society for Metals, Rowman and Littlefield, New York, 1964.
- [2] Wechsler, M. S., *The Interaction of Radiation with Solids*, North Holland Publishing Co., Amsterdam, 1964, p.642
- [3] Steele, L. E., *Atomic Energy Review*, AERVA, Vol. VII, No. 2, International Atomic Energy Agency, Vienna, 1969, pp. 108-133.
- [4] Steele, L. E. and Hawthorne, J. R., "New Information on Neutron Embrittlement and Embrittlement Relief of Reactor Pressure Vessel Steels," NRL Report 6160, Naval Research Laboratory, 6 Oct. 1964; *ASTM STP 380*, American Society for Testing and Materials, 1965, pp. 283-311.
- [5] Hawthorne, J. R. and Steele, L. E., "Initial Evaluation of Metallurgical Variables as Possible Factors Controlling the Radiation Sensitivity of Structural Steels," NRL Report 6420, Naval Research Laboratory, 29 Sept. 1966; *ASTM STP 426*, American Society for Testing and Materials, 1967, pp. 534-572.
- [6] Mogford, I. L., Churchman, A. T., and Hull, D., "The Effect of Neutron Irradiation on the Impact Properties of En2 Mild Steel," AERE Report M/R 2485, Atomic Energy Research Establishment, Harwell, England, 1958.
- [7] Nichols, R. W. and Harries, D. R. in *Symposium on Radiation Effects on Metals and Neutron Dosimetry*, *ASTM STP 341*, American Society for Testing and Materials, 1963, pp. 162-198.
- [8] Gordon, G. M. and Klepfer, H. H. in *The Effects of Radiation on Structural Metals*, *ASTM STP 426*, American Society for Testing and Materials, 1967, pp. 48-66.
- [9] Hawthorne, J. R., "Demonstration of Improved Radiation Embrittlement Resistance of A533-B Steel Through Control of Selected Residual Elements," NRL Report 7121, Naval Research Laboratory, Aug. 1970; Symposium on Effects of Radiation on Structural Metals, American Society for Testing and Materials, Niagara Falls, Canada, 29 June-4 July 1970.
- [10] Hosbons, R. R. and Wotton, B. L., "The Effect of Fast Neutron Irradiation on the Mechanical Properties of Some Quenched and Tempered Steels," Symposium on Effects of Radiation on Structural Metals, American Society for Testing and Materials, Niagara Falls, Canada, 29 June-4 July 1970.
- [11] Little, E. A. and Harries, D. R. in *Irradiation Effects in Structural Alloys for Thermal and Fast Reactors*, *ASTM STP 457*, American Society for Testing and Materials, 1969, pp. 215-241.
- [12] Little, E. A. and Harries, D. R., "Radiation Hardening and Recovery in Mild Steels and the Effects of Interstitial Nitrogen," AERE-R 6263, Atomic Energy Research Establishment, Harwell, England, 1969.
- [13] Castagna, M. et al in *ASTM STP 426*, American Society for Testing and Materials, 1967, pp. 3-20.
- [14] Igata, N. et al, "Neutron Irradiation Effects on Iron Containing Al and N," Symposium on Effects of Radiation on Structural Metals, American Society for Testing and Materials, Niagara Falls, Canada, 29 June-4 July 1970.
- [15] Igata, N., Hasiguti, R. R., and Seto, S., *Transactions*, Iron and Steel Institute of Japan, Vol. 10, 1970, p. 21.
- [16] Potapovs, U. and Hawthorne, J. R., "The Effect of Residual Elements on 550 F Irradiation Response of Selected Pressure Vessel Steels and Weldments," NRL 6803, Naval Research Laboratory, 22 Nov. 1968; *Nuclear Applications*, NUAPA, Vol. 6, No. 1, Jan. 1969, pp. 27-46.
- [17] Steele, L. E., "Critical Aspects of Neutron Irradiation Embrittlement of Pressure Vessel Steels and Weldments," ASME-AIME Symposium on The Technology of Pressure Retaining Steel Components, Vail Village, Colo., 21-23 Sept. 1970.
- [18] Hawthorne, J. R., Fortner, E., and Grant, S. P., "Radiation Resistant Experimental Weld Metals for Advanced Reactor Vessel Steels," presented at National Fall Meeting, American Welding Society, Baltimore, Md., 8 Oct. 1970; *Welding Journal* (pending publication).

- [19] Steele, L. E. et al, "Irradiation Effects on Reactor Structural Materials, QPR, 1 Aug.-31 Oct. 1968," NRL Memorandum Report 1937, Naval Research Laboratory, 15 Nov. 1968.
- [20] Hellerich, C. L. and Hunter, C. W., "Fractography of Irradiated and Unirradiated Pressure Vessel Steel Impact Specimens," BNWL-SA-2298, Battelle-Northwest Laboratory, 1 Feb. 1969.
- [21] Steele, L. E. et al, "Irradiation Effects on Reactor Structural Materials, QPR, 1 May-31 July 1969," NRL Memorandum Report 2027, Naval Research Laboratory, 15 Aug. 1969.
- [22] Watkins, G. D. in *Radiation Damage in Semiconductors*, P. Baruch, Ed., Dunod, Paris, 1965, p. 97.
- [23] Corbett, J. W. and Watkins, G. D., Eds., *Radiation Effects in Semiconductors*, Gordon and Breach, New York, 1971.
- [24] Harries, D. R. and Eyre, B. L. in *Flow and Fracture Behavior of Metals and Alloys in Nuclear Environment, ASTM STP 380*, American Society for Testing and Materials, 1965, pp. 105-119.
- [25] Kawasaki et al, "Evaluation of the Embrittlement of Pressure Vessel Steels Irradiated in JPDR—Results of Surveillance and Reference Tests," Symposium on Effects of Radiation on Structural Metals, American Society for Testing and Materials, Niagara Falls, Canada, 29 June-4 July 1970.
- [26] Hawthorne, J. R. and Steele, L. E., "Initial Evaluation of Metallurgical Variables as Possible Factors Controlling the Radiation Sensitivity of Structural Steels," NRL Report 6420, Naval Research Laboratory, 29 Sept. 1966; *ASTM STP 426*, American Society for Testing and Materials, 1967, pp. 534-572.
- [27] Alger, J. F. et al, "Steel Resistant to Embrittlement by Neutron Radiation," Patent 3,496,034, 17 Feb. 1970.

C. J. Baroch,¹ A. V. Munim,² and E. N. Harbinson¹

Effects of Irradiation in a Thermal Reactor on the Tensile Properties of Zircaloy 2 and 4 and Borated Stainless Steel

REFERENCE: Baroch, C. J., Munim, A. V., and Harbinson, E. N., "Effects of Irradiation in a Thermal Reactor on the Tensile Properties of Zircaloy 2 and 4 and Borated Stainless Steel," *Irradiation Effects on Structural Alloys for Nuclear Reactor Applications*, ASTM STP 484, American Society for Testing and Materials, 1970, pp. 176–193.

ABSTRACT: Babcock & Wilcox conducted a series of tests to determine the effects of irradiation and thermal aging on the tensile properties of core structural materials used in a PWR. Type 304 stainless steel (containing about 250 ppm boron) and Zircaloy 2 specimens were obtained from the first core of the Consolidated Edison Indian Point reactor, and Zircaloy 4 specimens were irradiated in the Babcock & Wilcox test reactor. The Type 304 stainless steel cladding and the Zircaloy 2 channel from the Indian Point reactor had operated at about 600 and 525 F, respectively, and had achieved peak fluences of about 3×10^{21} n/cm², $E > 1$ MeV. The Zircaloy 4 specimens were irradiated at 130, 650, and 725 F to peak fluences of about 9×10^{20} n/cm², $E > 1$ MeV.

The borated stainless steel specimens were tested at 70, 600, 750, 900, 1050, 1200, 1300, and 1450 F. Some of the specimens were annealed at 1832 F for 1 h to eliminate all displacement-type defects. Irradiation increased the strength of the cladding at test temperatures below 900 F, but it had little effect on the strength at higher test temperatures. At all test temperatures the ductility of the cladding was quite low—often less than 0.5 percent. Postirradiation annealing for 1 h at 1832 F returned the strength to the unirradiated condition but had little effect on the ductility.

Specimens obtained from both the longitudinal and transverse directions of the Zircaloy 2 channel were tested at 70, 525, and 750 F. At all test temperatures the ultimate and yield strengths increased with fluence up to the peak fluence achieved in the program. The uniform elongations were all 1 percent or less, regardless of fast fluence or specimen orientation.

Zircaloy 4 ring specimens were tested at 900, 1100, 1300, 1450, and 1600 F. About half of the tension specimens were in the mill-annealed condition, and the remainder were cold-worked. At 1100 F and above the tensile properties of

¹ Chief, Ceramics and Metallurgy Section, and engineer, Nuclear Metallurgy Group, respectively, Research and Development Div., Babcock & Wilcox Co., Lynchburg, Va. 24505.

² Engineer, Wheelabrator Co., Bombay, India.

cold-worked and mill-annealed Zircaloy 4 were identical. At a test temperature of 900 F, irradiation caused some changes in the tensile properties of both materials. The extent of the effect of irradiation was dependent on the level of cold work and fluence.

KEY WORDS: irradiation, zirconium alloys, reactor cores, stainless steels, Zircalloys, radiation effects, nuclear reactors, thermal reactors, pressurized water reactors, mechanical properties, nuclear energy, helium, cladding, tensile properties, tension tests

Detailed knowledge of core material properties before and after irradiation is required in the design of a nuclear power reactor; the behavior of the materials during normal and accident conditions must be known. The effects of irradiation on the properties of structural materials can be determined from experiments conducted in research or test reactors or by examining core components from operating reactors.

This paper describes two programs concerning the effects of irradiation on core and cladding materials. In one, the tensile properties of Type 304 stainless steel containing 250 ppm boron and Zircaloy 2 were evaluated. These materials were obtained from the first core of the Consolidated Edison Indian Point reactor, Buchanan, N. Y., which had operated for 442 effective full power days and had achieved a peak fluence of 2.6×10^{21} n/cm², $E > 1$ MeV. The work on this program was supported by the U. S. Atomic Energy Commission under contract AT(30-1)-3809.

In the other program, the tensile properties of Zircaloy 4 cladding at 900 to 1600 F were determined before and after irradiation. These data are important to core designers, especially if a loss-of-coolant accident should occur during reactor operation or if there is excessive crud buildup on the fuel cladding. Babcock & Wilcox supported the work on this program.

Tensile Properties of Borated Type 304 Stainless Steel

Program Description

During the past few years it has been theorized that the loss of ductility in irradiated austenitic stainless steel at temperatures above 900 F is caused by the accumulation of helium produced by the n, α reaction in boron-10 and other elements in the stainless steel. Because of the high boron content (250 ± 100 ppm) of the cladding from the first core of the Indian Point reactor, a considerable amount of helium was produced by irradiation. The examination of this cladding provides a unique opportunity to determine whether the loss in high-temperature ductility can, indeed, be related to the helium or is caused by some other fast neutron reaction.

Table 1 outlines the scope of the tension testing program. The tests conducted at 70 and 600 F are of interest to thermal reactor designers. The

TABLE 1—Tension testing of stainless steel cladding.

Fluence	Test Temperature, deg F															
	70		600		750		900		1050		1200		1300		1450	
	BA ^a	AA	BA	AA	BA	AA	AA	BA	AA	BA	AA	BA	AA	BA	AA	AA
Peak.....	2 ^b	2	2	2	2	2	2	2	2	2	2	2	2	2	2	0
Minimum.....	2	2	2	2	0	0	0	0	0	0	2	2	2	2	0	0
As-received.....	2	2	2	2	0	0	0	0	0	0	2	2	2	2	0	0
Aged 3000 h.....	2	2	2	2	2	2	2	0	2	2	2	2	2	2	2	2
Aged 6000 h.....	2	2	2	2	0	0	0	0	0	0	2	2	2	2	2	0

^a BA—before annealing; AA—after annealing.

^b Number of specimens tested.

remaining data were obtained to determine the effects of the high helium content on the elevated-temperature properties of the steel. The data from the unirradiated specimens that were aged in helium at 600 F for 3000 and 6000 h were used to separate the effects of thermal aging in the reactor from the effects of irradiation. Some of the irradiated and unirradiated specimens were annealed at 1832 F for 1 h. The annealing eliminated the displacement-type defects in the irradiated specimens and allowed a more precise determination of the contribution of the helium to the loss in ductility. The unirradiated specimens, both as-received and annealed, provide a base line for interpreting the data. The fabrication history for the cladding and fuel assembly were discarded after the core had been inserted into the reactor; thus, it is assumed that the archive and irradiated materials had similar processing histories.

Semicylindrical pieces of the cladding were obtained by slitting 4-in.-long sections of the fuel rod in the axial direction. The sections of cladding were deburred, and the 1-in. gage length was machined using a Tensile Kut machine. The specimens that were annealed were soaked for 1 h at 1832 F and then water quenched. The specimens were packed in Sen-Pak heat treating containers to minimize oxidation during annealing and quenching. Sen-Pak envelopes, fabricated by the Sentry Co., Foxboro, Mass., use a metal foil container to provide a protective sheath during heat treating that automatically neutralizes the entrapped air. All specimens were tested at a strain rate of 0.02 min^{-1} ; an extensometer was attached to each specimen throughout the test. The yield strength was determined using the 0.2 percent offset method.

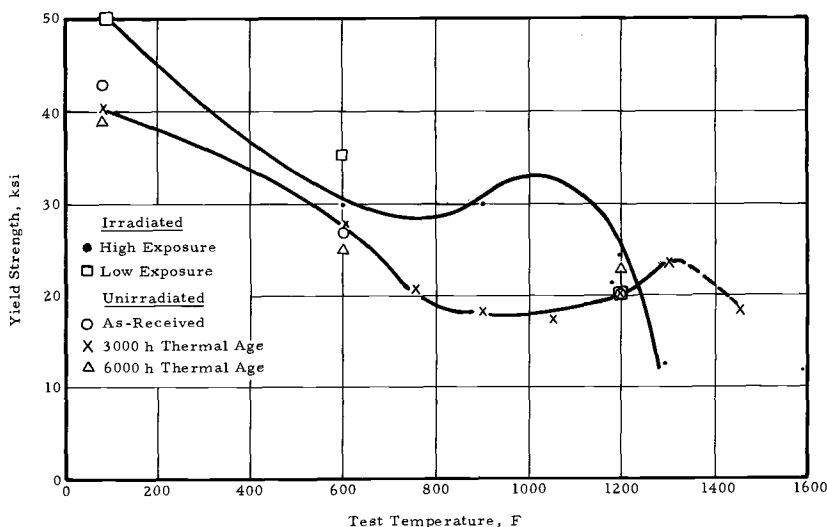


FIG. 1—Yield strength of irradiated and unirradiated stainless steel cladding after annealing.

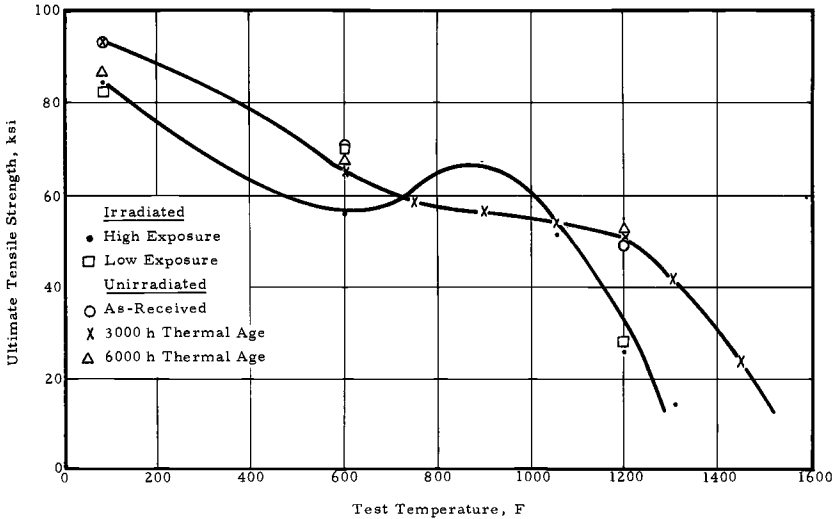


FIG. 2—Ultimate tensile strength of irradiated and unirradiated stainless steel cladding after annealing.

Results

Unirradiated Cladding—The results of the tension tests conducted on unirradiated specimens that were annealed for 1 h at 1832 F are shown graphically in Figs. 1–3. The yield strengths of as-received specimens thermally aged for 3000 and 6000 h decreased as the temperature increased

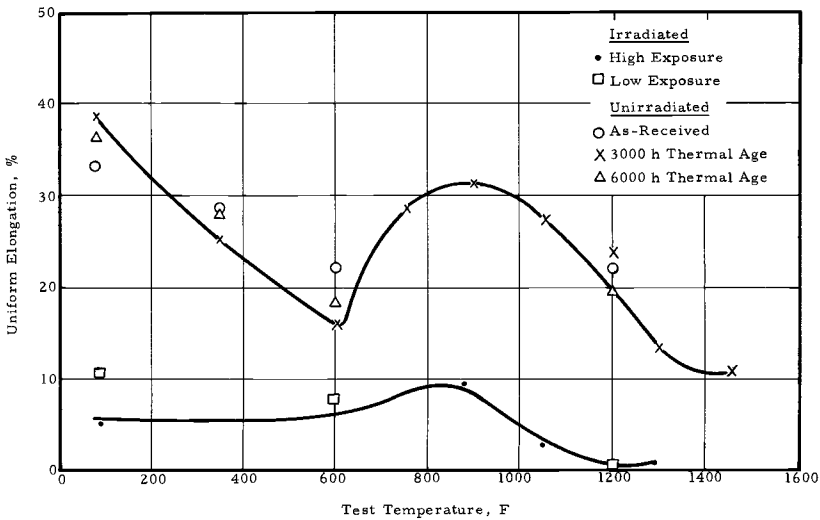


FIG. 3—Uniform elongation of irradiated and unirradiated stainless steel cladding after annealing.

from 70 to 750 F. Little difference was observed in the yield strength of the specimens tested at 750 to 1000 F. The yield strength then increased with increasing temperature from 1000 to 1300 F. The normal softening trend resumed above 1300 F, and at 1450 F the yield strength was approximately the same as it was at 900 F. The ultimate tensile strength generally decreased with increasing temperature.

The uniform elongation of all the materials (Fig. 3) decreased as the test temperature was increased from 70 to 600 F. At 600 F, the uniform elongation began to increase with increasing temperature, until a peak in the total elongation occurred at 850 F. The uniform elongation then decreased as the temperature increased from 850 to 1450 F.

The properties of the as-received, 3000 and 6000-h thermally aged materials that were not annealed were essentially identical to those of the annealed materials. Annealing (1 h at 1832 F) of the unirradiated specimens before testing has essentially no effect on the strength or the ductility of either the as-received or thermally aged cladding.

Irradiated Cladding—Figures 1 through 6 show the results of the tension tests on the irradiated cladding before and after annealing. The data points on these figures represent the average of the two specimens tested at any one condition. The fluence for the irradiated specimens ranged from about 5×10^{20} to 2.5×10^{21} n/cm², $E > 1$ MeV.

The data for the unirradiated and irradiated cladding after annealing are compared in Figs. 1–3. Some minor differences in the strength of the

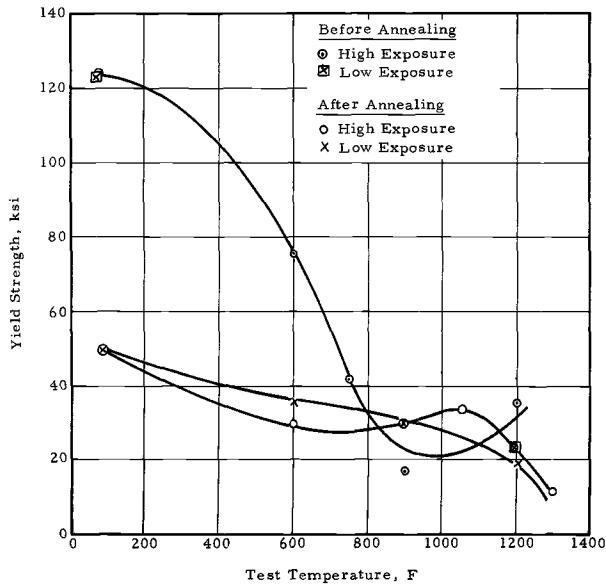


FIG. 4—Yield strength of irradiated stainless steel cladding before and after annealing.

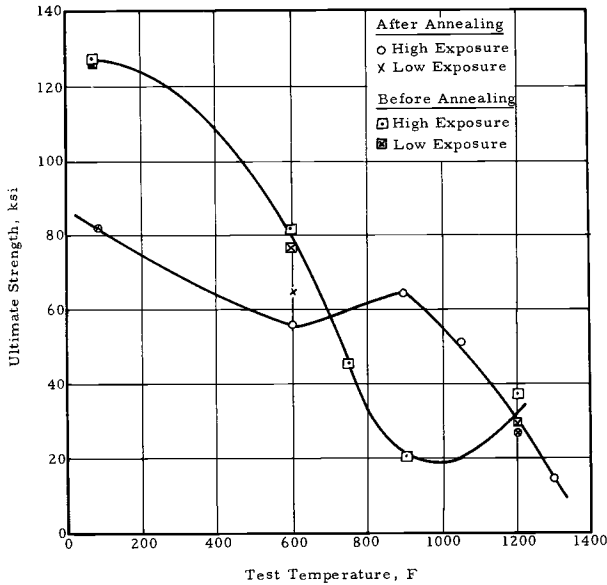


FIG. 5—Ultimate strength of irradiated stainless steel cladding before and after annealing.

unirradiated and irradiated materials were observed, particularly in the shape of the curves above 800 F. It appears that irradiation may have either shifted the start of the secondary hardening process to a slightly lower temperature or altered the process. Because the unirradiated cladding came from a dummy bundle rather than a production bundle and, thus, may not be truly representative of the material irradiated, it is impossible to determine whether these differences were caused by irradiation or by differences in materials.

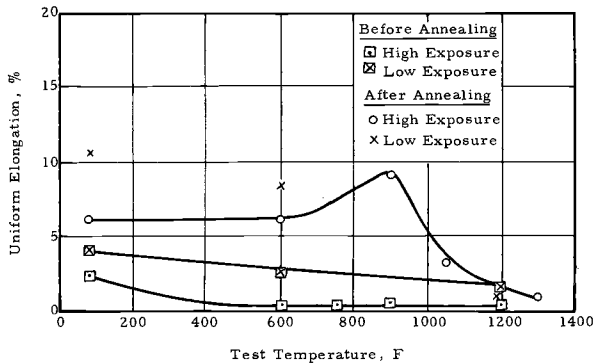


FIG. 6—Uniform elongation of irradiated stainless steel cladding before and after annealing.

The data also indicate that the annealing operation eliminated essentially all of the strengthening produced during irradiation. Even though the strength returned to the unirradiated condition, the elongation of the irradiated cladding after annealing was still considerably less than that for the unirradiated cladding. This would suggest that some factor other than point defects caused the low elongations.

The data for the as-irradiated cladding before and after annealing are compared in Figs. 4–6. Annealing reduced the tensile and ultimate strength of the material significantly at test temperatures below 800 F. At higher test temperatures the strength of the as-irradiated cladding was generally lower than that of the irradiated cladding after annealing. Apparently, the annealing operation produced some secondary hardening that did not occur in the as-irradiated cladding. It is possible also that many of the defects introduced by irradiation began to move rapidly during testing at temperatures above 800 F. The movement of defects led to rupture of the specimens at a lower load than that required to rupture specimens in which there was little defect movement.

Annealing for 1 h at 1832 F restored some of the ductility to the specimens at test temperatures below 1000 F; the restoration of ductility was far from complete however. At test temperatures above 1000 F, there was essentially no difference between the elongation of the as-irradiated cladding and that of the irradiated cladding that had been annealed.

With standard Type 304 stainless steel the irradiation temperature is a fairly significant factor in determining the effect of irradiation on the material's mechanical properties [1, 2].³ Irradiation of the borated Type 304 stainless steel at about 600 F appears to produce a slightly different effect in that

1. It reduces the ductility at temperatures above 900 F; this effect is attributed to helium.
2. It introduces some displacement-type defects and some other product that affects the properties below 900 F.

Annealing the borated stainless steel restores its strength to the unirradiated condition but does not affect the ductility significantly. If displacement defects were the only factor affecting the properties at test temperatures below 900 F, then the annealing operation should restore the strength and ductility. It is possible that helium in sufficient quantities affects not only the elevated-temperature ductility but also the ductility both before and after annealing at test temperatures below 900 F.

Tensile Properties of Zircaloy 2 Channel

Program Description

These tests were conducted to determine the tensile properties of the Zircaloy 2 channel after operation at 525 F for 442 effective full power

³ Italic numbers in brackets refer to the list of references at the end of this paper.

days in the Indian Point reactor. Both longitudinal and transverse specimens were tested at 70, 525, and 750 F. The tensile properties were determined at a strain rate of 0.020 min^{-1} , the yield strength being determined by the 0.2 percent offset method. An Instron extensometer modified to fit these specimens was used at all three test temperatures.

The Zircaloy channel selected for examination was obtained from an element that had received a peak calculated fluence of about $2.5 \times 10^{21} \text{ n/cm}^2$, $E > 1 \text{ MeV}$. The tensile blanks, $4\frac{1}{2}$ in. long, $\frac{1}{2}$ in. wide, and 0.155 in. thick, were obtained by sectioning the channel with an abrasive cutoff wheel and a motorized band saw. A Tensile Kut machine was used to machine the 0.25-in.-wide and 1.0-in.-long gage lengths.

Results

The postirradiation tensile properties for the 70, 525, and 750 F tests are shown graphically as a function of fast fluence in Figs. 7-10. For all test temperatures the ultimate tensile and yield strengths continued to increase with total fluence for fast fluences up to 2.6×10^{21} , $E > 1 \text{ MeV}$. The strength in the longitudinal direction was greater than that in the transverse direction. The channel was fabricated from annealed Zircaloy 4 but the preirradiation tension data were not available. Typical annealed Zircaloy 4 would have a yield strength of about 40,000 psi at 70 F. Thus the strength increased from 40,000 psi in the as-fabricated condition to about 100,000 psi at a fluence of $1.5 \times 10^{20} \text{ n/cm}^2$. Because the preirradiation data were not available, the change in tensile and yield strengths as a function of fast fluence and specimen orientation could not be evaluated. However, the absolute values reported by Irvin [3] for annealed Zircaloy 2 pressure

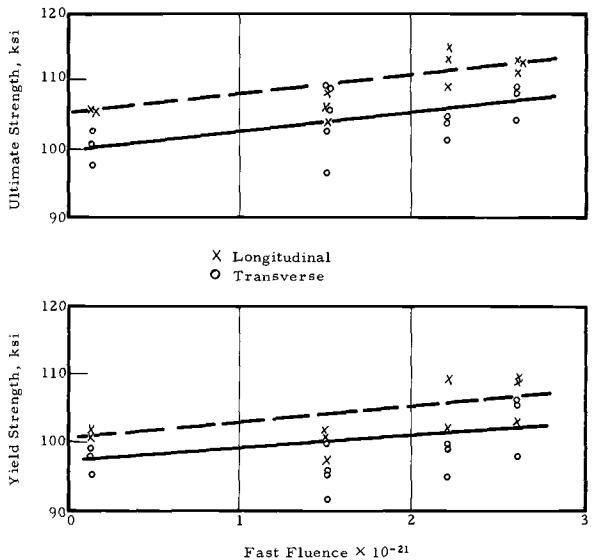


FIG. 7—Effect of irradiation at 525 F on the strength of Zircaloy 2 at 70 F.

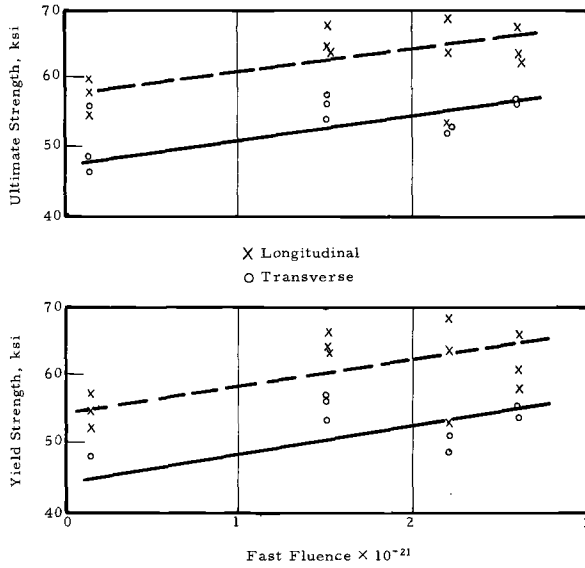


FIG. 8—Effect of irradiation at 525 F on the strength of Zircaloy 2 at 525 F.

tubing irradiated at 540 F to an exposure of 2.2×10^{21} were within the 100,000 to 110,000 psi range obtained from the material in this investigation.

The increases in tensile and yield strengths were accompanied by a decrease in ductility, as shown in Fig. 10. For all three test temperatures the

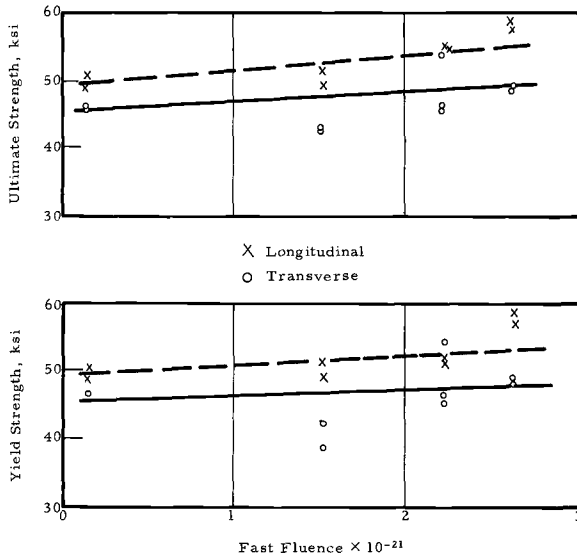


FIG. 9—Effect of irradiation at 525 F on the strength of Zircaloy 2 at 750 F.

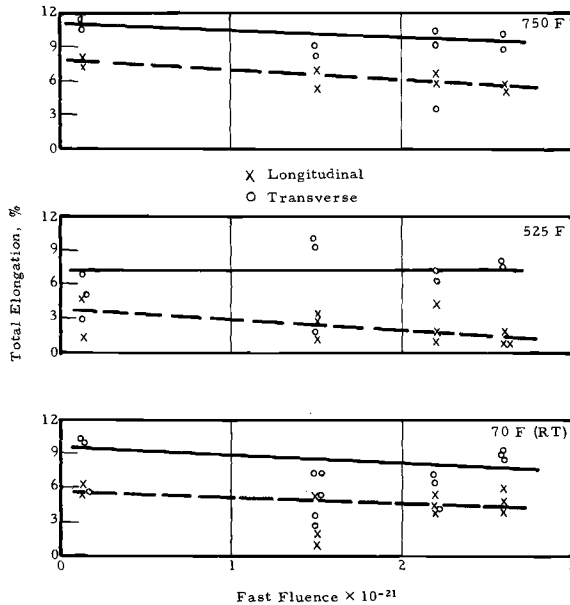


FIG. 10—Effect of irradiation at 525 F on the total elongation of Zircaloy 2.

total elongation in the transverse direction was greater than in the longitudinal direction. The total elongation in both directions was lower at 525 F than at 70 or 750 F. The lower ductility at 525 F is not inconsistent with the results for unirradiated Zircaloy 4 as reported by Scott [4], where the minimum ductility occurred at 500 to 800 F.

Tensile Properties of Zircaloy 4 Cladding

Program Description

Babcock & Wilcox conducted a program to determine the tensile properties of irradiated Zircaloy 4 at test temperatures as high as 1600 F. These data are required to assess the consequences of a loss of primary coolant or of excessive crud buildup in an operating power reactor. About 60 irradiated ring-type specimens were tested at various temperatures; the specimens were obtained from the large program described by Harbinson [5]. Unirradiated ring specimens were also tested at similar temperatures. Table 2 lists specimen descriptions and the temperatures at which they were irradiated and tested. Before testing of the irradiated specimens began, unirradiated specimens were tested at various temperatures after aging for varying lengths of time. During the aging operation, the specimens were sealed in Sen-Pak envelopes to keep them in a relatively inert atmosphere. According to Harbinson hydrogen has little effect on the elevated-temperature properties of unirradiated Zircaloy 4; therefore, none of the unirradiated specimens evaluated in this program were hydrided.

TABLE 2—Test program for irradiated Zircaloy 4 specimens.

Material	Irradiation Temperature, deg F	900 F Test Temperature		1100 F Test Temperature		1300 F Test Temperature		1450 F Test Temperature		1600 F Test Temperature	
		Irradiated and Aged	Irradiated and Aged	Irradiated and Aged	Irradiated and Aged	Irradiated and Aged	Irradiated and Aged	Irradiated and Aged	Irradiated and Aged	Irradiated and Aged	Irradiated and Aged
Annealed	130	1 ^a	1	...	1	1	...	1
	650	1	1	1	1	1	...	1	...	2	...
	775	1	1	1	1	1
Annealed and hydrided .	130	1	1	...	1	1	...	1
	650	1	1	1	1	1	...	2	...	1	1
	775	1	1	1	1	1
Cold worked	130	1	1	...	1	1	...	1	1	1	...
	650	1	1	1	1	1
	775	1	1	1	1	1
Cold worked	130	1	1	...	1	1
	650	1	1	2	1	1	...
	775	1	1	1	1	1

^a Number of specimens tested.

The method used in testing the ring specimens was similar to that described by Sanderson [6] and Fleming [7]. The 0.25-in.-wide ring specimens were obtained from tubing with an outside diameter of about 1.00 in. and an inside diameter of 0.940 in. Both mill-annealed and cold-worked tubing were included in the program. Some of the irradiated ring specimens were hydrided before irradiation. In these hydrided specimens the hydrogen content varied from about 100 to 800 ppm, and the average was about 300 to 400 ppm.

The specimens were strained at the rate of 0.05 in./min. In this program it was assumed that the gage length was equal to the outside diameter of the ring. Load-deflection curves obtained from the crosshead travel provide rather precise information on the ultimate strength of the material; but the yield strength, as determined by the 0.2 percent offset method, and elongations are relative, because the actual gage length was not known.

Results

Effects of Thermal Aging on Tensile Properties—Aging for 4 to 24 h at 900 F resulted in a slight decrease in the yield strength and a minor increase in the total elongation. Most of the changes in properties occurred within the first 4 h of aging. At 900 F there was some difference in the yield strengths, total elongations, and uniform elongations of mill-annealed and cold-worked Zircaloy 4.

Aging at 1100 F caused tensile and yield strengths to decrease, producing increases in uniform and total elongations. After aging for 1 h, however, there were essentially no further changes in the tensile properties. At 1100 F, some minor differences appeared in the properties of mill-annealed and cold-worked Zircaloy 4; however, these differences tended to diminish after aging for 1 h. Aging at 1300 F had essentially no effects on the properties of Zircaloy 4; furthermore, the properties of mill-annealed and cold-worked Zircaloy 4 were essentially identical.

Effects of Irradiation on Tensile Properties—The fluence of these specimens varied from about 8×10^{19} to about 9×10^{20} n/cm², $E > 1$ MeV. Nineteen of the specimens had been irradiated at 775 F, 24 at 650 F, and 17 at 130 F. Twenty-one of the irradiated specimens were aged at 900, 1100, or 1300 F for short periods of time before testing. The aging times were selected as the minimum times that would produce the maximum changes in the properties of unirradiated Zircaloy 4. For example, there were essentially no differences in the properties of unirradiated Zircaloy 4 after aging at 900 F for 4 and 24 h. Consequently, the irradiated specimens were aged for only 4 h. There were not enough irradiated specimens available to prove that the irradiated specimens behaved in the same manner as the unirradiated specimens; nonetheless, the results reported below indicate that aging treatment is not always completely effective in restoring the properties found in the unirradiated condition.

Properties at 900 F—The properties of cold-worked Zircaloy 4 at 900 F are essentially unaffected by irradiation to fluences as high as 9×10^{20} n/cm². Irradiation increased the strength of annealed Zircaloy 4 at 900 F, and the strength increased with fluence to the maximum exposure achieved in this program. Even though irradiation increased the strength of the annealed Zircaloy 4, there was no significant change in the ductility. Neither hydrogen nor irradiation temperature had any significant effect on the properties at 900 F.

The tensile strengths of the cold-worked specimens after aging for 4 h at 900 F were almost identical to the strengths of the as-irradiated specimens; thus, aging had little or no effect on the strength of the irradiated material. The tensile and yield strengths of the irradiated mill-annealed material after aging for 4 h were somewhat lower than the strengths of the as-irradiated annealed material, but they were still higher than the strengths of the unirradiated control specimen. Fluence, however, had little effect on the properties of the aged material. Aging apparently eliminated some of the effects of irradiation. It was not determined whether additional aging would have affected the properties even further.

Properties at 1100 F—The strengths of mill-annealed and cold-worked Zircaloy 4 at 1100 F were not affected by irradiation at any exposure. The elongation of annealed Zircaloy 4 was reduced somewhat by irradiation, whereas the elongation of cold-worked Zircaloy 4 was unaffected by irradiation.

Aging the specimens for 1 h had essentially no effect on the strengths of the specimens that received fluences greater than 3×10^{20} , but it did reduce the strengths of the unirradiated specimens and of the irradiated specimens receiving a fluence of less than 3×10^{20} . The aging operation did not affect the elongation of the irradiated, annealed Zircaloy. While the elongation of the cold-worked Zircaloy 4 was increased by aging when the fluence was less than 3×10^{20} , it was not affected when the fluence was greater than 3×10^{20} n/cm².

Properties at 1300 F, 1450, and 1600 F—At 1300 F there were no significant differences in the properties of cold-worked and annealed material, nor were there any differences between the irradiated, unirradiated, and irradiated and aged specimens. There was considerable scatter in the data obtained at 1450 and 1600 F. Consequently, it is difficult to draw any definite conclusions from these limited data. On the basis of the results at 1300 F one can conclude, however, that irradiation had essentially no effect on the properties at 1450 and 1600 F.

Comparison of Properties of as-Received and Irradiated Zircaloy 4—The yield strength and total elongation of as-received and irradiated Zircaloy 4 are shown in Figs. 11 and 12. The data at 650 and 775 F were taken from the Zircaloy 4 program described by Harbinson [5]. At test temperatures above 900 F, fluence and irradiation temperatures had little effect on the

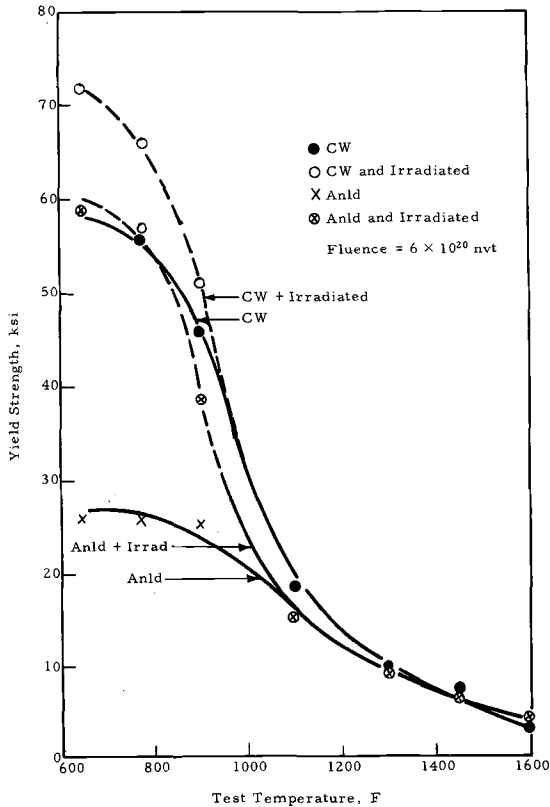


FIG. 11—Yield strength of as-received and as-irradiated Zircaloy 4 as a function of test temperature.

properties of Zircaloy 4. In contrast, however, fluence and irradiation temperature have a relatively important effect on the properties at test temperatures of 650 and 775 F. Consequently, all the data for irradiated specimens shown in Figs. 11 and 12 are from specimens that were irradiated at 650 F to a fluence of 6×10^{20} n/cm².

The data indicate that, at test temperatures above 1100 F, the unirradiated and irradiated properties are essentially identical for both the cold-worked and annealed Zircaloy 4. Below 1100 F there are significant differences. Furthermore, the properties of irradiated material differ from those of as-received material, and these differences in properties increase with decreasing temperature.

Conclusions

1. The ductility of irradiated Type 304 stainless steel containing about 250 ppm boron was generally quite low—often less than 0.5 percent—at

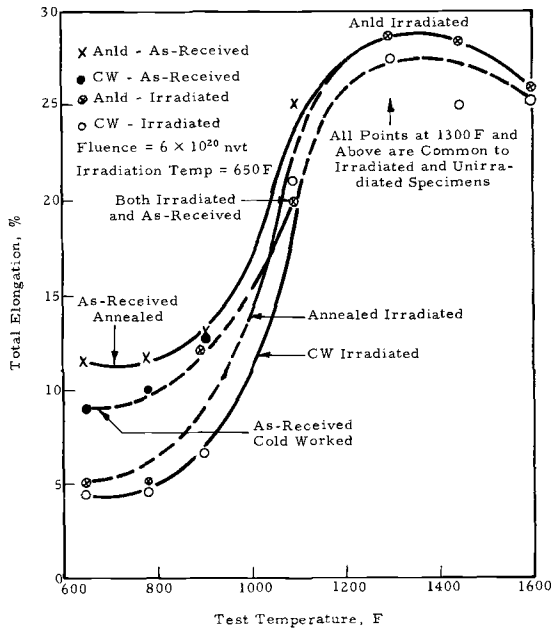


FIG. 12—Total elongation of as-received and as-irradiated Zircaloy 4 as a function of test temperature.

all test temperatures. Postirradiation annealing for 1 h at 1832 F had little effect on the ductility. Irradiation of the borated stainless steel at 600 F apparently introduces enough helium into the steel so that the ductility at test temperatures up to 900 F is reduced significantly, even after a post-irradiation anneal.

2. Irradiation at 525 F to a fluence of 2.5×10^{21} n/cm² increased the strength and reduced the ductility of the Zircaloy 2 obtained from the Indian Point reactor. The properties of the irradiated Zircaloy 2 at 70, 525, and 750 F were consistent with those reported in the literature.

3. Irradiation increased the strength and decreased the ductility of both cold-worked and annealed Zircaloy 4 ring specimens tested at 900 F. These effects became more pronounced with increasing fluence. Annealing the irradiated specimens for 4 h at 900 F before testing removed most of the effects of irradiation but did not restore completely the properties found in the unirradiated condition. Neither the level of cold work nor irradiation had any effect on the properties of Zircaloy 4 at test temperatures of 1100 to 1600 F.

References

- [1] Bement, A. L. et al, "Effects of Irradiation on the Structure and Properties of Stainless Steel," BNWL-SA-1876, Battelle Northwest Laboratory, Richland, Wash. Aug. 1968.

- [2] Conner, J. G. and Porembka, S. W., "A Compendium of Properties and Characteristics for Selected LMFBR Cladding Materials," BMI-1900, Battelle Memorial Institute, Columbus, Ohio, May 1968.
- [3] Irvin, J. E., *Electrochemical Technology*, ECTCA, Vol. 4, No. 5-6, May-June 1966.
- [4] Scott, D. B., "Physical and Mechanical Properties of Zircaloy-2 and -4," WCAP-3269-14, Westinghouse Corp., Pittsburgh, Pa., May 1965.
- [5] Harbinson, E. N. and Baroch, C. J., *Journal of Materials*, JMLSA, Vol. 3, No. 1, March 1968, pp. 107-115.
- [6] Sanderson, C. C., "The Effect of Specimen Geometry on the Tensile Properties of Some Zirconium Alloys," AECL-2207, Atomic Energy of Canada, Ltd., March 1965.
- [7] Fleming, D. C., "Transverse Tensile Tests on Zircaloy-2 from Long-Term Irradiation Fuel Bundles," CRGM-1160, Atomic Energy of Canada, Ltd., Chalk River, Ontario, 1964.

DISCUSSION

*A. L. Bement*¹—Did you observe dimensional changes in the Zircaloy 2 channels from the Indian Point reactor that would indicate the occurrence of radiation induced growth?

C. J. Baroch (authors' closure)—The overall dimensions and shape of the irradiated channel indicated that no gross dimensional changes or distortion had occurred during operation; rather precise measurements are required to detect the volume changes that might occur during irradiation to fluences of $<3 \times 10^{21}$ n/cm². Since the preirradiation dimensions of the channel selected for examination were not available, accurate determination of any radiation induced growth was impossible.

¹ Battelle-Northwest, Richland, Wash. 99352.

*M. Kangilaski,¹ J. W. Spretnak,² A. A. Bauer,¹ and
R. A. Wullaert¹*

Influence of Irradiation Temperature on the Tensile Properties of Stainless Steel*

REFERENCE: Kangilaski, M., Spretnak, J. W., Bauer, A. A., and Wullaert, R. A., "Influence of Irradiation Temperature on the Tensile Properties of Stainless Steel," *Irradiation Effects on Structural Alloys for Nuclear Reactor Applications, ASTM STP 484*, American Society for Testing and Materials, 1970, pp. 194-214.

ABSTRACT: As an initial step in comparing the effects of irradiation in neutron spectrums characteristic of thermal and fast reactors, irradiations to establish the role of temperature on tensile property changes in the thermal reactor spectrum were undertaken. For this purpose specimens of Type 347 stainless steel were irradiated in the ETR at 400 and 650 C to a target fluence of 5×10^{21} n/cm². The results of this irradiation are reported in this paper and are compared with previous results for specimens irradiated to the same fluence at 50 C.

KEY WORDS: irradiation, fast neutrons, radiation damage, radiation effects, fast reactors (nuclear), thermal reactors, mechanical properties, tensile properties, elongation, fractures (materials), dosimetry, helium, bubbles, stainless steels, mechanical tests

Irradiation studies of Type 347 stainless steel were originally undertaken to measure the changes in tensile properties of stainless steel as a result of irradiation to high fast fluences at 50 C in thermal reactors. Results of tests on specimens irradiated in the ETR to fast fluences ranging from 5×10^{21} to 3×10^{22} n/cm² have been previously reported [1, 2].³ Of special

¹ Senior research metallurgist, fellow, and chief, respectively, Materials and Environmental Engineering Div., Battelle Memorial Institute, Columbus, Ohio 43201.

² Professor, Department of Metallurgical Engineering, Ohio State University, Columbus, Ohio 43210.

* Work performed under U. S. Atomic Energy Commission Contract W-7405-eng-92. Submitted by M. Kangilaski to the Graduate School of the Ohio State University as a portion of a thesis in partial fulfillment of the requirements for the degree of Master of Science.

³ Italic numbers in brackets refer to the list of references at the end of this paper.

interest in this study was the irradiation induced embrittlement of stainless steel at elevated testing temperatures [3, 4, 5].

While these irradiations were performed in a thermal reactor, the results are of interest to the LMFBR program because of potential neutron spectrum effects on damage mechanisms and severity of damage, particularly at the high fluence levels to which this material was exposed. Consequently, irradiations were planned in the EBR-II with identical Type 347 stainless steel specimens for the purpose of comparing the effects of irradiation in fast and thermal reactor spectrums. The temperature of irradiation represents an additional variable, with temperatures up to at least 700 C being of interest for LMFBR application.

Materials and Irradiation Conditions

Specimens were taken from the same heat of Type 347 stainless steel that was used for the earlier irradiation studies in ETR [2]. Since only a limited number of the original Type 347 stainless steel specimens were available, additional specimens of Type 348 stainless steel were included in the irradiation experiment. Type 347 stainless steel can be considered as a Type 348 stainless steel (less than 0.10 weight percent tantalum and 0.20 weight percent cobalt). The Type 348 stainless steel rod, from which specimens were machined, was obtained from the stockpile of structural materials kept at Battelle-Northwest for use in experiments to study radiation effects on structural materials. Chemical compositions of both stainless steels are given in Table 1. Grain size of the Type 348 stainless steel was 10 μm while that of the Type 347 stainless steel was 12 μm .

TABLE 1—Chemical analysis of Type 347 and Type 348 stainless steel.

Element	Weight Percent	
	347 SS	348 SS
Chromium.....	17.9	17.5
Nickel.....	10.4	9.67
Manganese.....	1.72	1.67
Silicon.....	0.65	0.51
Columbium.....	0.67	0.58
Copper.....	0.30	0.06
Molybdenum.....	0.20	0.06
Cobalt.....	0.19	0.18
Titanium.....	0.10	Not analyzed
Carbon.....	0.057	0.04
Phosphorus.....	0.024	0.014
Sulfur.....	0.016	0.009
Tantalum.....	0.01	0.03
Boron.....	0.00005	0.0008
Nitrogen.....	0.030	0.037
Iron.....	Balance	Balance

The specimens, contained in NaK to assure better temperature uniformity, were irradiated in a double walled, single gas annulus capsule. For specimens irradiated at 650 C a gas annulus of 12 mil was utilized, while the 400 C temperature was obtained by using a gas annulus of 3 mil. Thermocouples were placed on both sides of the gas gap and the temperatures were continuously monitored. Temperatures could be controlled by changing the conductivity across the gap, effected by varying the helium to nitrogen ratio in the gas which continuously flowed through the gas annulus.

The fast fluence ($E > 1$ MeV) that was received by the specimens was determined with nickel dosimetry wires. These dosimetry wires were placed around the capsule and removed after each cycle. Sections of the wires, which corresponded to specific specimen locations, were counted by gamma spectrometry. The total fast fluence that was received by the specimens ranged from 3.3×10^{21} to 4.6×10^{21} n/cm².

Testing Techniques

Tension Testing

Tension testing was done with an Instron testing machine, at a strain rate of approximately 0.005 in. for all testing temperatures. This was obtained by using a crosshead travel speed of 0.01 in. for specimens with a 2-in. gage length and one of 0.005 in. for specimens with a 1-in. gage length. Strain was measured with an extensometer fastened to the specimen grips; this method was adopted because of the difficulty of remotely fastening an extensometer to the highly radioactive specimens. To check the values for strain, as measured from the stress-strain curve, all specimens were measured after testing. The change in length was divided by the length of the gage section to obtain total elongation values. The measured values showed good agreement with the elongation values obtained from the stress-strain curve. Reduction in area values were obtained by photographing the fractured ends of specimens together with a ruler at $\times 6$.

Fractography

Replicas were taken from the fracture surfaces of selected unirradiated and irradiated specimens after testing. The replicas were prepared by the two-stage cellulose acetate-carbon technique and were shadowed with chromium-carbon from an angle of 45 deg. They were examined by an electron microscope.

Metallography

Specimens for metallography were sectioned and mounted so that the viewing surface was perpendicular to the tension axis. This way the fracture appearance of the specimens could be viewed. The specimens were

ground with 120-grit SiC paper close to midplane of the diameter. The grinding was finished with 240, 400, and 600-grit SiC paper, after which the specimens were polished with diamond paste. Etching was done with oxalic acid.

Helium Analysis

Helium analysis was performed on two of the irradiated specimens by Atomics International, Canoga Park, Calif. Small samples from the irradiated specimens were vaporized in a tungsten helix coil under vacuum. Immediately after the ^4He was released from the sample, a precisely known volume of ^3He was added. Then the ratio of ^4He to ^3He was determined and from this ratio the ^4He content was calculated.

TABLE 2—*Tensile properties of unirradiated and irradiated Type 347 stainless steel.*

Test Temperature, deg C	Fast Fluence, $E > 1$ MeV, n/cm ²	0.2% Offset Yield Strength, psi	Ultimate Strength, psi	Uniform Elongation, %	Total Elongation, %	Reduction in Area, %
Unirradiated						
25	37.0×10^3	90.0×10^3	52.0	64.0	79.0
315	26.8	64.2	31.9	36	72
500	24.0	47.5	22.4	26.6	64
600	23.0	40.5	17.8	22.5	55
750	22.0	33.0	16.0	26	45
Irradiated						
at 50 C						
25	5.5×10^{21}	88.7	111.5	24.7	32.7	70
315	5.5	80.0	84.0	13.2	16.4	60
Irradiated						
at 400 C						
25	4.0	109.0	131.0	12.3	20.6	89
315	4.0	95.6	104.0	4.8	9.5	47
750	4.0	18.0	25.4	2.2	2.3	0.1
Irradiated						
at 650 C						
25	4.2	39.1	95.5	47.5	56.7	88
315	4.2	31.4	63.5	24.0	30.6	65
750	4.2	18.7	21.2	3.1	3.7	5.0
Irradiated						
at 650 C, annealed 1 h						
at 980 C						
25	4.6	32.5	92.2	57.5	69.9	91
315	4.6	22.7	64.5	31.2	37.0	53
750	4.6	14.5	18.2	2.5	3.6	6.0

TABLE 3—Tensile properties of unirradiated and irradiated Type 348 stainless steel.

Test Temperature, deg C	Fast Fluence, $E > 1$ MeV, n/cm ²	0.2% Offset Yield Strength, psi	Ultimate Strength, psi	Uniform Elongation, %	Total Elongation, %	Reduction in Area, %
Unirradiated						
25	...	36.2×10^3	93.0×10^3	58	61.4	82
315	...	27.8	62.8	26.7	29.4	74
440	...	23.2	60.2	22.5	25	70
500	...	23.8	53.2	22.7	25.2	69
600	...	23.4	49.1	21.5	30.3	64
750	...	19.0	27.3	4	35	55
Irradiated at 400 C						
315	3.3×10^{21}	88.1	93.1	3.5	6.6	60
500	3.3	70.6	80.9	2.7	4.9	17
600	3.3	44.9	45.8	1.4	3.2	13
Irradiated at 650 C						
25	4.4	38.0		50		
315	4.4	33.7	63.7	21.0	24.4	69
425	4.4	27.6	55.1	19.7	24.6	46
500	4.4	26.2	48.9	14.8	15.7	15
600	4.4	26.8	38.7	6.5	6.9	6.9
Irradiated at 650 C, annealed 1 h at 980 C						
500	4.6	25.2	58.5	24.5	32.2	48
600	4.6	23.4	42.1	13.1	14.6	29
750	4.6	15.1	17.6	4.6	6.3	14

Experimental Results

Tension Tests

As-Irradiated Specimens—Tension tests were performed on irradiated Type 347 and 348 stainless steel specimens at temperatures ranging from room temperature to 750 C. These specimens had been irradiated at either 400 or 650 C. The tensile properties of unirradiated and irradiated Type 347 stainless steel specimens are given in Table 2; Table 3 gives the tensile properties of the Type 348 stainless steel specimens. Table 2 also includes previously reported test results on Type 347 stainless steel specimens irradiated at 50 C to a fast fluence of 5×10^{21} n/cm² [1]. The yield strength, uniform elongation, total elongation, reduction in area, and ultimate strength of the irradiated specimens of Type 347 and Type 348 stainless steel, as a function of testing temperature, are illustrated in Figs. 1–5.

The tensile properties of both irradiated stainless steels show similar trends. Irradiation at 400 C causes larger increases in yield strength than does irradiation at 650 C. The ultimate strength is also increased to a greater degree by irradiation at 400 C than at 650 C. As the testing temperature is increased, the yield strength and ultimate strength of the irradiated material approaches that of the unirradiated material, and at the higher testing temperatures the strength of the irradiated material is in some cases less than that of the unirradiated stainless steel.

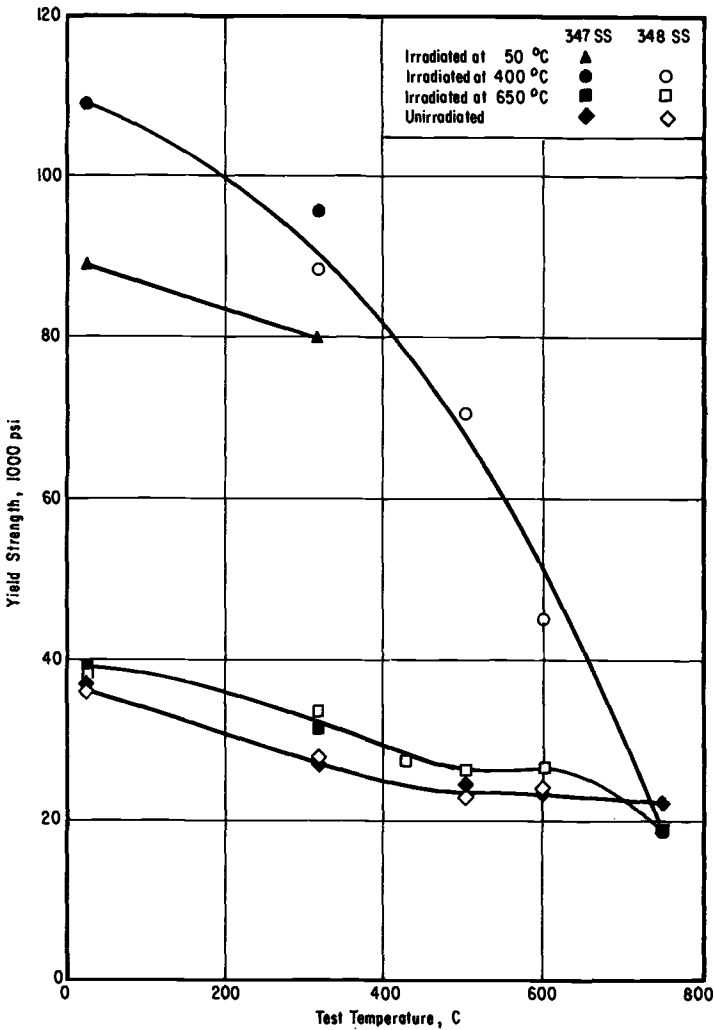


FIG. 1—Yield strength of Types 347 and 348 stainless steel.

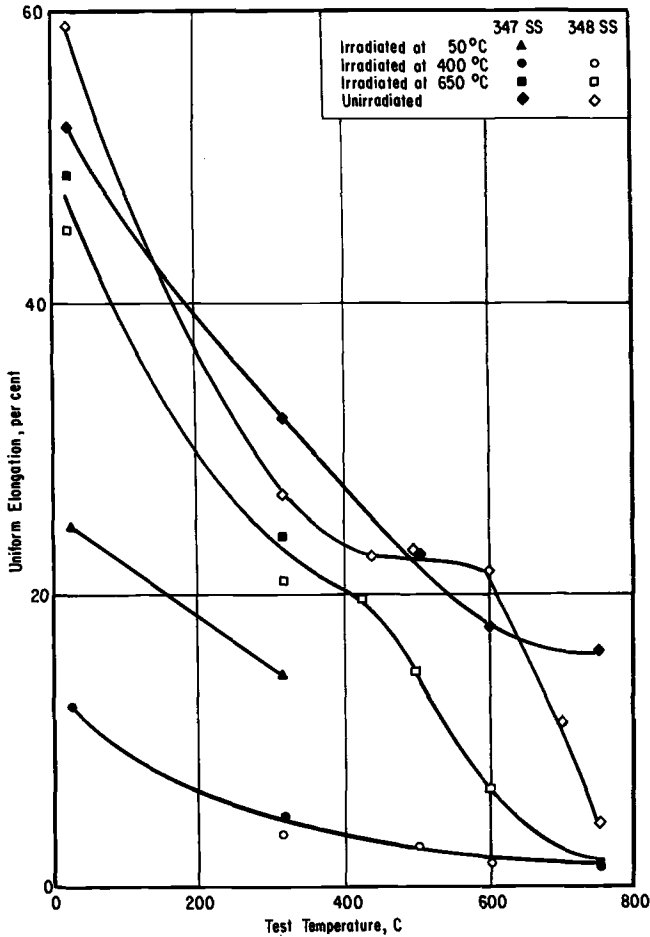


FIG. 2—Uniform elongation of Types 347 and 348 stainless steel.

Both the uniform and total elongations of the stainless steel are reduced by irradiation at all testing temperatures. Irradiation at 400 C causes equal or larger reductions in ductility than irradiation at 650 C for all testing temperatures. Of special note is the rather large reduction in both uniform and total elongation when testing is done above about 500 C. Reduction in area values are slightly reduced by irradiation when tested at 315 C; however, at higher testing temperatures the reduction in area values are drastically reduced by irradiation. Typical stress-strain curves for both the unirradiated and irradiated specimens are illustrated in Figs. 6 and 7.

Irradiated and Annealed Specimens—Selected specimens were annealed after irradiation for 1 h at 980 C to determine whether or not the anneal would restore the preirradiation tensile properties. The anneal restored the preirradiation tensile properties of those specimens tested at 500 C or below. The strength properties of the specimens tested at temperatures above 500 C were reduced, but the annealed irradiated specimens still exhibited significant losses in ductility although some of the ductility was restored by the anneal. Thus, elevated-temperature embrittlement cannot be removed by postirradiation annealing.

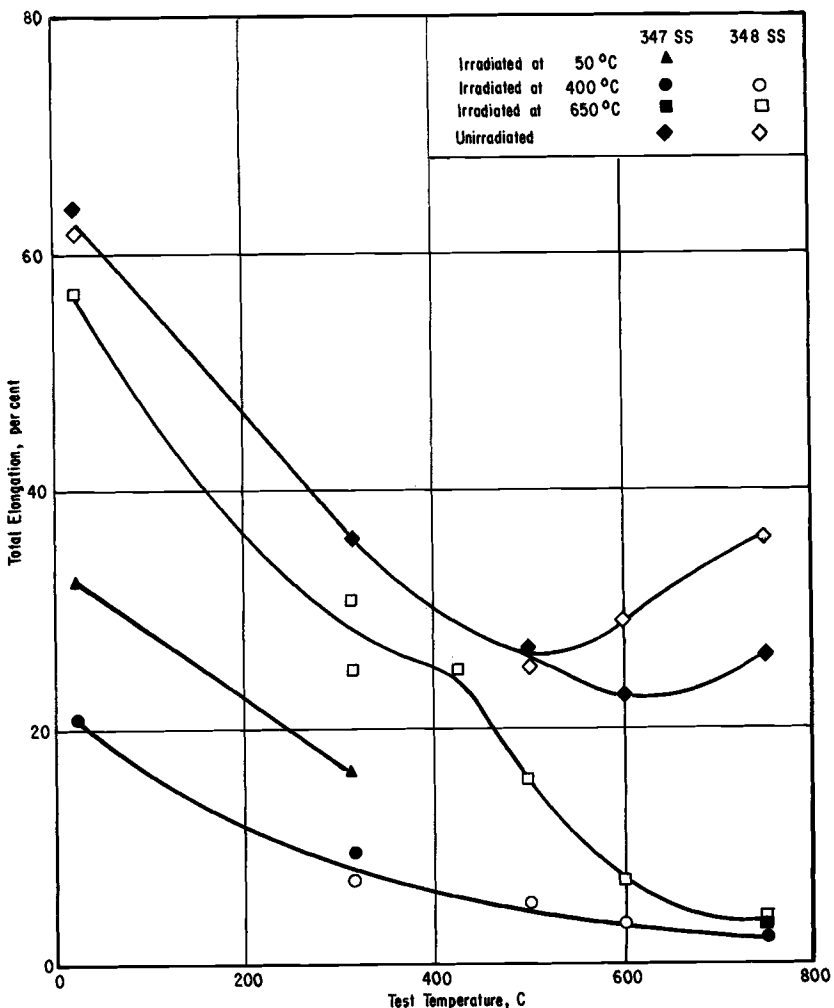


FIG. 3—Total elongation of Types 347 and 348 stainless steel.

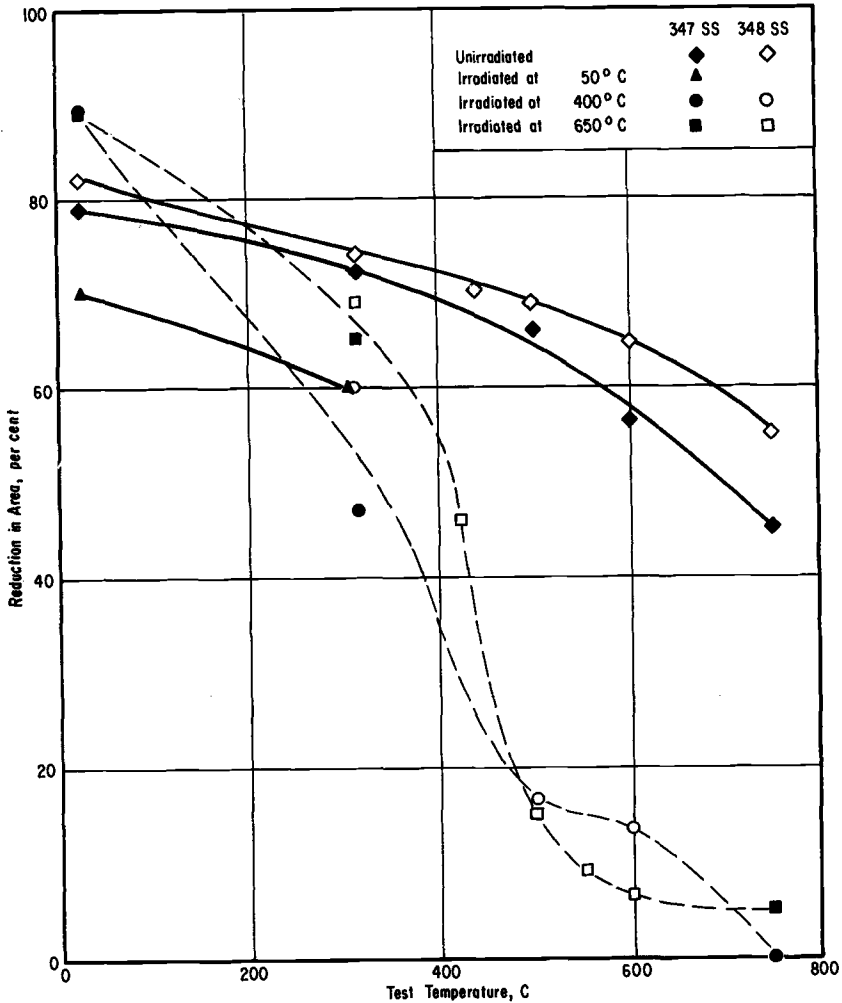


FIG. 4—Reduction in area of Types 347 and 348 stainless steel.

Metallographic Examination

Selected unirradiated and irradiated specimens that were tested in tension were metallographically examined. Of special interest in this examination was the appearance of the fracture area. The irradiation and testing conditions of the specimens that were examined are given in Table 4. Figures 8 through 10 compare the fracture area of an unirradiated specimen of Type 348 stainless steel that was tested at 500 C with those of irradiated specimens that were also tested at 500 C. Figure 8 shows that the unirradiated specimen which was tested at 500 C fractured transgranularly.

This specimen underwent a total elongation of 27 percent, which is evident by considering the large amount of elongation of the grains. Figure 9 shows the fracture area of the specimen that was irradiated at 400 C and tested in tension at 500 C. This specimen exhibited an intergranular fracture. There is very little elongation of the grains and a large number of voids at grain boundaries are visible. Figure 10 shows the fracture area of the specimen that was irradiated at 650 C, annealed for 1 h at 980 C, and then tested at 500 C. The fracture appears to be completely transgranular and

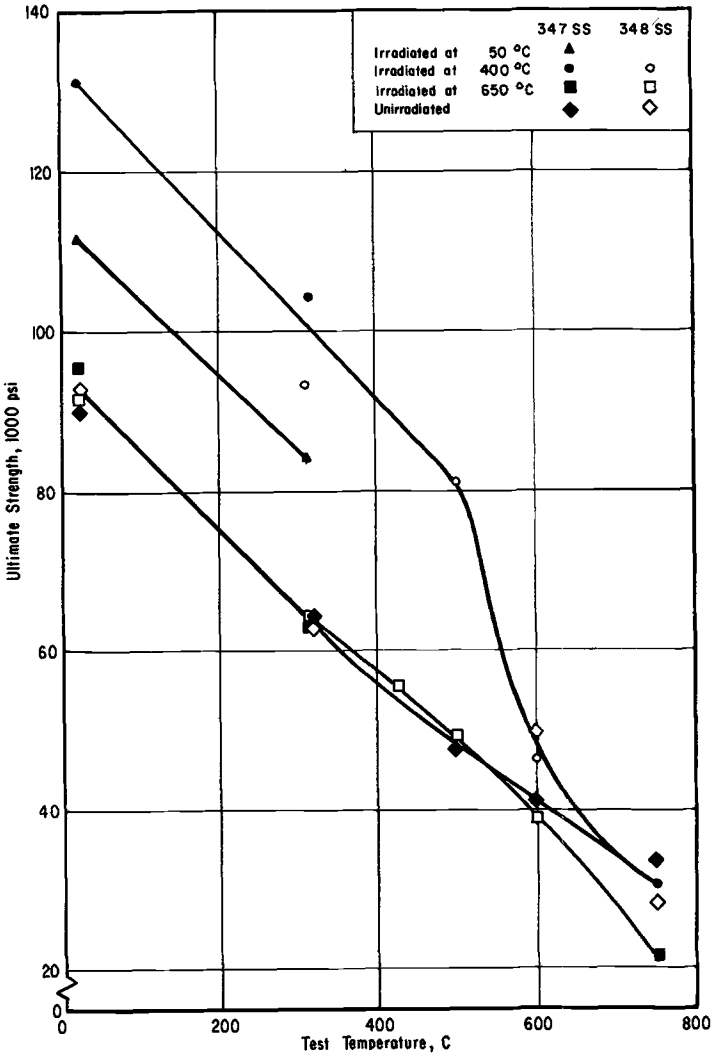


FIG. 5—Ultimate strength of Types 347 and 348 stainless steel.

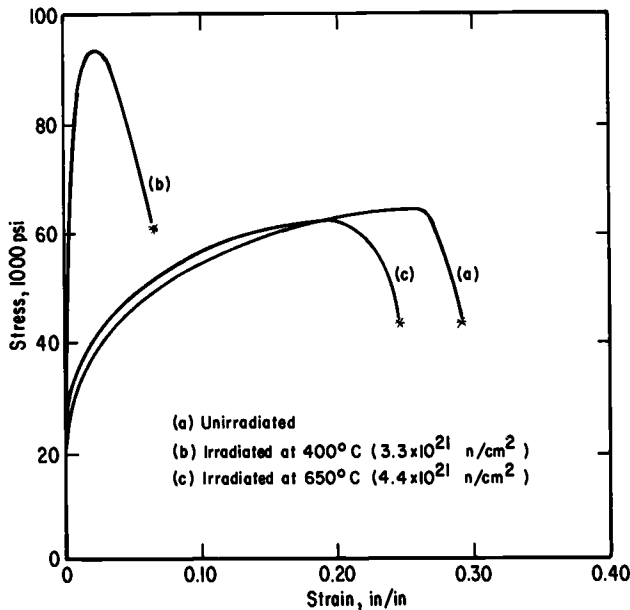


FIG. 6—Engineering stress-stain curves for Type 348 stainless steel tested in tension at 315 C.

is comparable to the unirradiated specimen shown in Fig. 8. This would be expected since the specimen had a total elongation of 32 percent, which is actually more than that of the unirradiated specimen.

Fractography

Replicas were obtained from the fracture surfaces of all the irradiated specimens enumerated in Table 4. For comparison, replicas were also obtained from unirradiated stainless steel specimens which were tested in tension at 500 and 750 C. A typical fracture surface of an unirradiated specimen is illustrated in Fig. 11. The unirradiated specimens fractured transgranularly with considerable plastic flow, as indicated by the presence of dimples.

Both of the irradiated specimens that were tested at 750 C showed completely intergranular fracture. The specimen that was irradiated at 650 C and tested at 750 C shows the possible presence of bubbles at the fracture which occurred at the grain boundaries (Fig. 12a). In the case of the specimen that was irradiated at 650 C, annealed for 1 h at 980 C, and tested at 750 C, there do not appear to be any bubbles (Fig. 12b); however, the specimen does exhibit a large number of dimples on the grain boundaries. It is hypothesized that these dimples are actually helium bubbles that

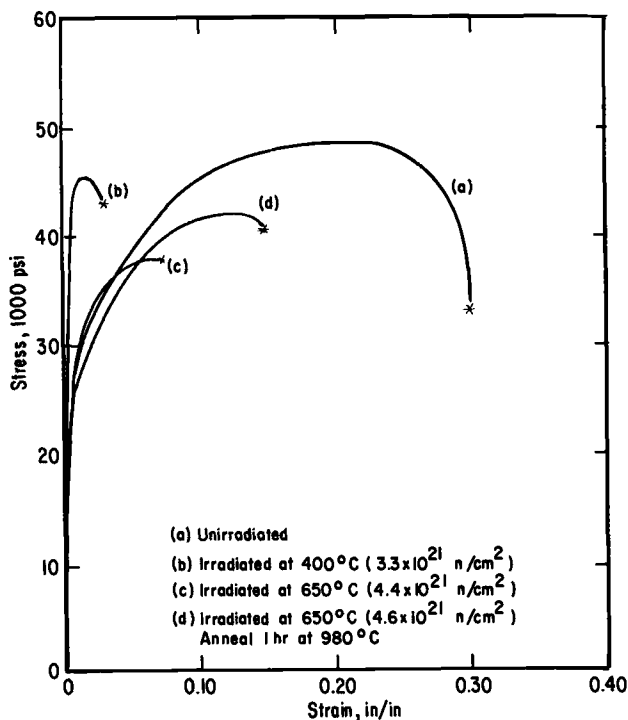


FIG. 7—Engineering stress-strain curves for Type 348 stainless steel tested in tension at 600 C.

were enlarged by the annealing at 980 C and then formed as dimples when they were locally deformed.

The specimen that was irradiated at 400 C and tested at 500 C shows complete intergranular fracture, as shown in Fig. 13. It can also be noticed that there are a large number of small bubbles at the grain boundary. Figure 13*b* illustrates the presence of these bubbles at grain boundaries at a higher magnification.

TABLE 4—Irradiation and testing conditions of specimens examined by light microscopy and fractography.

Material	Irradiation Temperature	Testing Conditions
347 SS.	650 C	Annealed 1 h at 980 C, tested at 750 C
347 SS.	650 C	Tested at 750 C
348 SS.	400 C	Tested at 500 C
348 SS.	650 C	Tested at 500 C
348 SS.	650 C	Annealed 1 h at 980 C, tested at 500 C

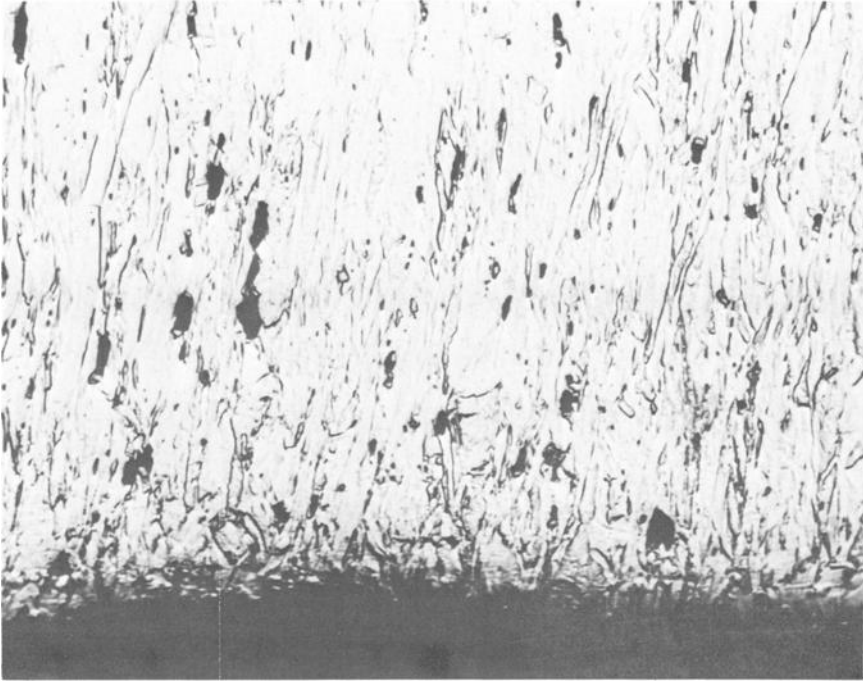


FIG. 8—Fracture appearance of unirradiated Type 348 stainless steel tested in tension at 500 C. Total elongation 27 percent ($\times 250$).

Helium Analysis

Results of the helium analysis, which was performed at Atomic International, are given in Table 5. Along with the analyzed results are the calculated helium results. These calculations were based on n, α cross section data for neutrons with energies > 1 MeV as published by Birrs [6]. The results indicate that the predicted helium content is considerably lower than the analyzed helium content.

It has been suggested by Weitman [7] that considerable amounts of helium are produced from nickel by thermal neutron bombardment. Speci-

TABLE 5—Helium content of irradiated Type 348 stainless steel.

Fast Fluence, n/cm^2	Irradiation Temperature, deg C	Calculated Helium, ppm (atomic)	Analyzed Helium, ppm (atomic)
3.3×10^{21}	400	10.8	23.5
4.4	650	11.7	37.2

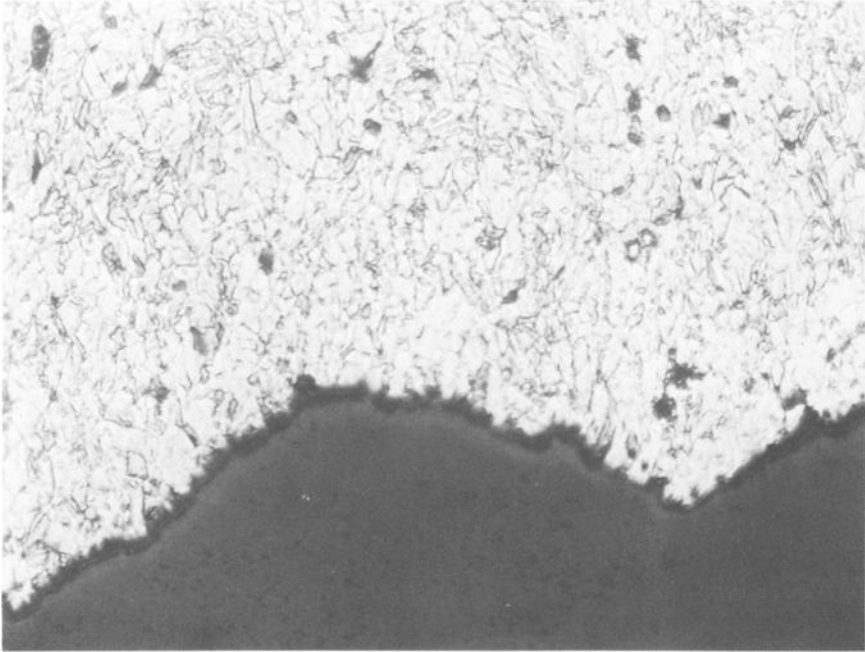


FIG. 9—Fracture appearance of Type 348 stainless steel irradiated at 400 C to a fast fluence of 5×10^{21} n/cm² and tested in tension at 500 C. Total elongation 4.9 percent ($\times 250$).

mens of pure nickel were irradiated in a mixed thermal and fast flux and a pure fast flux (obtained by cadmium shielding). After the irradiation the specimens were analyzed for helium, with the results shown in Fig. 14. These results indicate that considerably more helium is produced by thermal neutrons than by fast neutrons. By extrapolating Weitman's results to a thermal fluence of 5×10^{21} n/cm², it can be seen that the helium content of our irradiated Type 348 stainless steel falls on the predicted line. The source of this helium has not been definitely established, but it is thought to result from nickel-58 being converted to nickel-59 by thermal neutron irradiation, with the nickel-59 having a high cross section to n, α reaction with either thermal or fast neutrons [7].

Discussion

It is quite apparent from Figs. 1–5 that the degree of radiation induced changes in tensile properties is dependent on the irradiation temperature. These are maximum for irradiation at 400 C, intermediate for irradiation at 50 C, and minimum for irradiation at 650 C. Bloom et al [8] have shown that the change in yield strength induced by irradiation is due to the size and distribution of the defect clusters that were produced during irradiation.

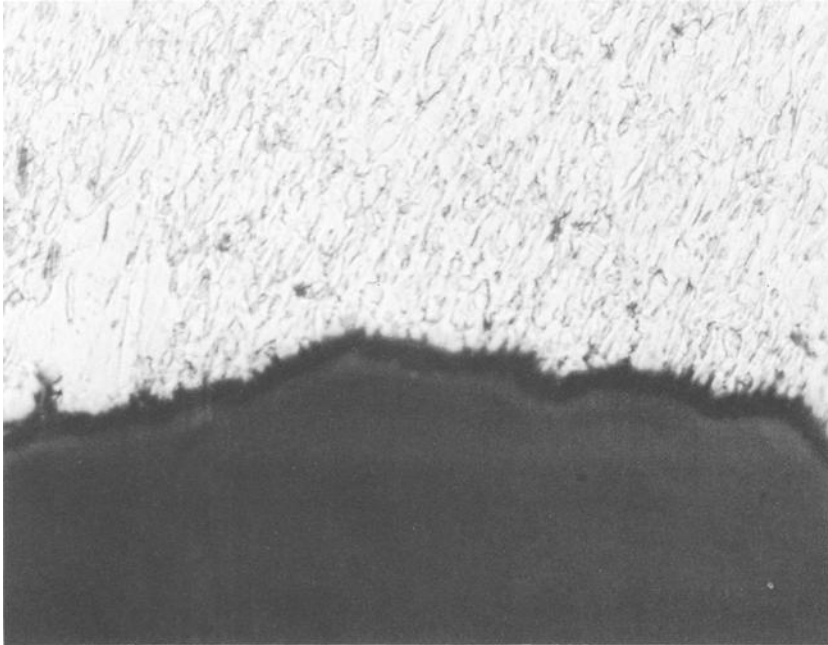


FIG. 10—Fracture appearance of Type 304 stainless steel irradiated at 650 C to a fast fluence of 5×10^{21} n/cm², annealed for 1 h at 980 C, and tested in tension at 500 C. Total elongation 32 percent ($\times 250$).

tion. Irradiation at low temperatures results in a large density of small defects. Irradiation at higher temperatures results in lower defect densities but larger individual defects. The maximum increase in yield strength occurs at about 150 C, and the yield strength decreases slowly from 150 C to 300 C, above which it decreases rapidly. We have concluded that there is an optimum defect size for maximum strengthening but that the amount of strengthening also depends on the defect density. Recent studies have shown that strengthening in irradiated stainless steel is also caused by helium bubbles [9].

At an irradiation temperature of 400 C, defect clusters are expected to be somewhat larger than the optimum size for strengthening and, consequently, the strengthening from defect clusters is not expected to be a maximum. However, at an irradiation temperature of 400 C, it is expected that small helium bubbles will form and make a significant contribution to strength. At an irradiation temperature of 650 C, the defect clusters would be annealed out during irradiation and the helium bubbles would probably be too large to make a significant contribution to yield strength. This is borne out by the fact that irradiation at 650 C does not result in significant increases of yield strength.

As mentioned in the introduction, irradiation affects the tensile elongation of stainless steel by two different mechanisms. At low testing temperatures the presence of defect clusters causes strengthening of the material and also reduces the elongation; at intermediate test temperature (say 400 C) helium bubbles also contribute to these changes in strength and ductility. The reduction in elongation takes place mostly in uniform elongation, with the nonuniform, or necking, elongation remaining about the same. As with the increase in yield strength, the uniform elongation is reduced the most as a result of irradiation at 400 C; irradiation at 650 C does not significantly reduce the uniform elongation in tests below 450 C. At testing temperatures above about 450 C, irradiation causes a drastic reduction in uniform elongation total elongation, and reduction in area (Figs. 3-5).

This reduction in ductility has generally been attributed to helium. Previous transmission electron microscopy studies on the same material [10], irradiated at 50 C to a fast fluence of 2.2×10^{22} n/cm², had shown no visible helium bubbles in the as-irradiated material when it was tested in tension at 600 C. Annealing of the irradiated material at 980 C for 1 h caused the appearance of large helium bubbles accompanied by an in-



FIG. 11—Fracture surface of unirradiated Type 304 stainless steel tested at 750 C. Total elongation 35 percent ($\times 7500$).

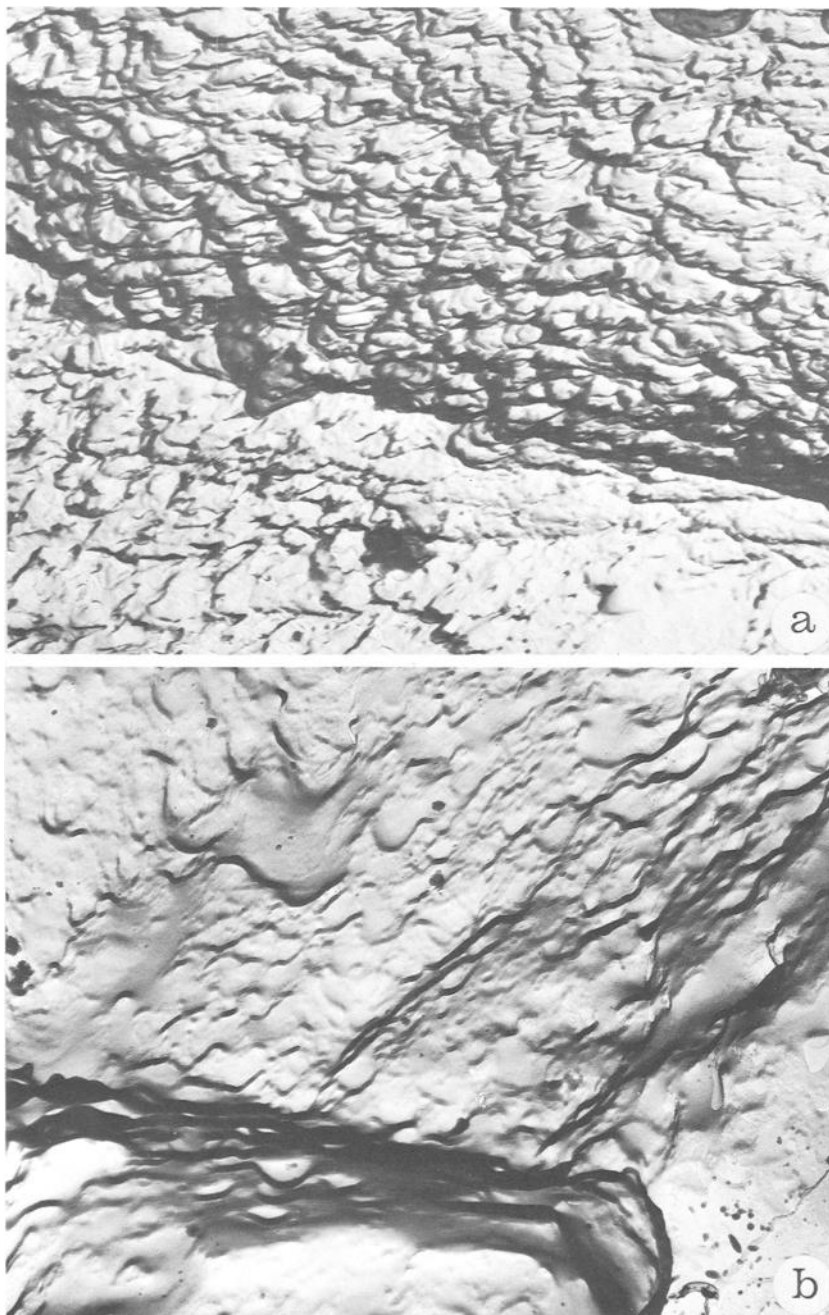


FIG. 12—Fracture surface of Type 347 stainless steel irradiated at 650 C and tested in tension at 750 C ($\times 15,000$): (a) as irradiated, total elongation 3.7 percent; (b) irradiated and annealed 1 h at 980 C before testing, total elongation 3.6 percent.

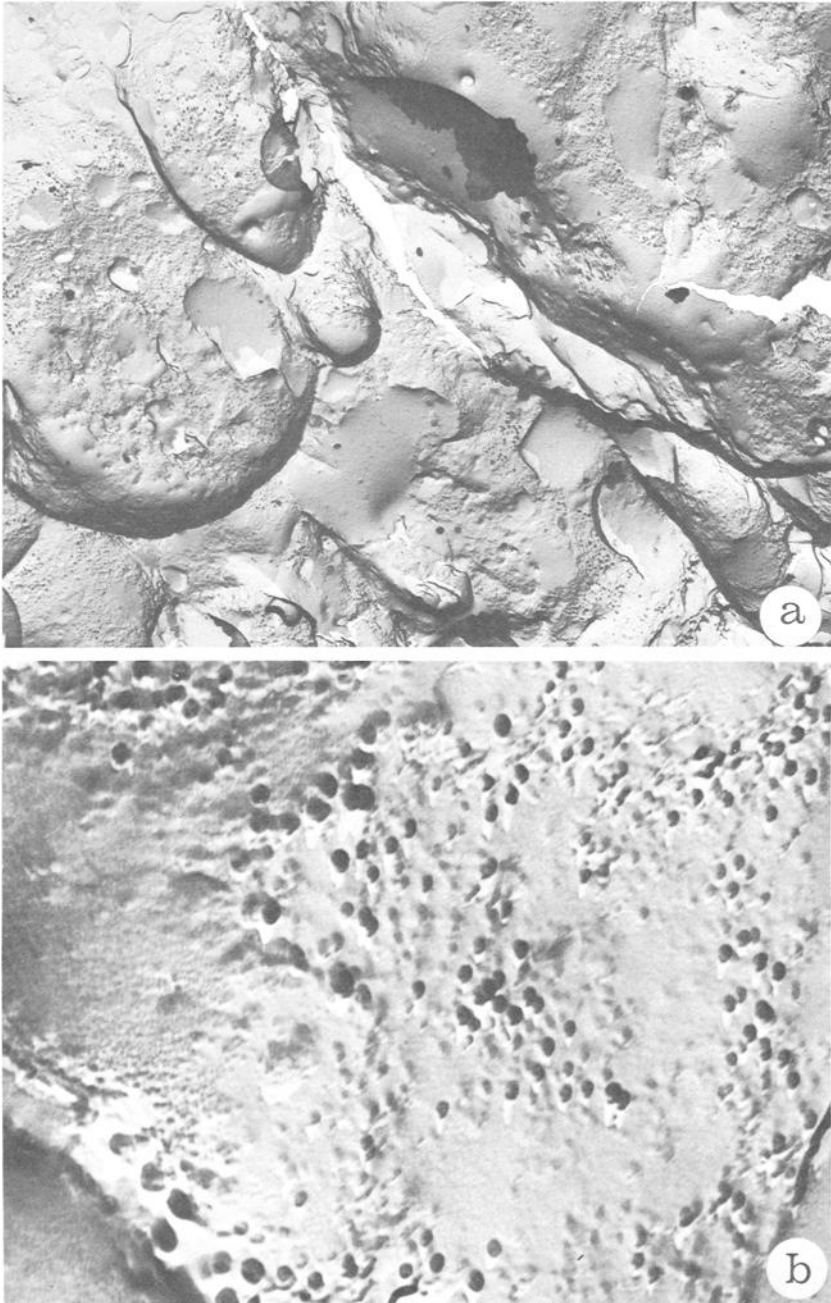


FIG. 13—Fracture surface of Type 348 stainless steel irradiated at 400 C and tested at 500 C ((a) $\times 7500$, (b) $\times 50,000$). Total elongation 4.9 percent.

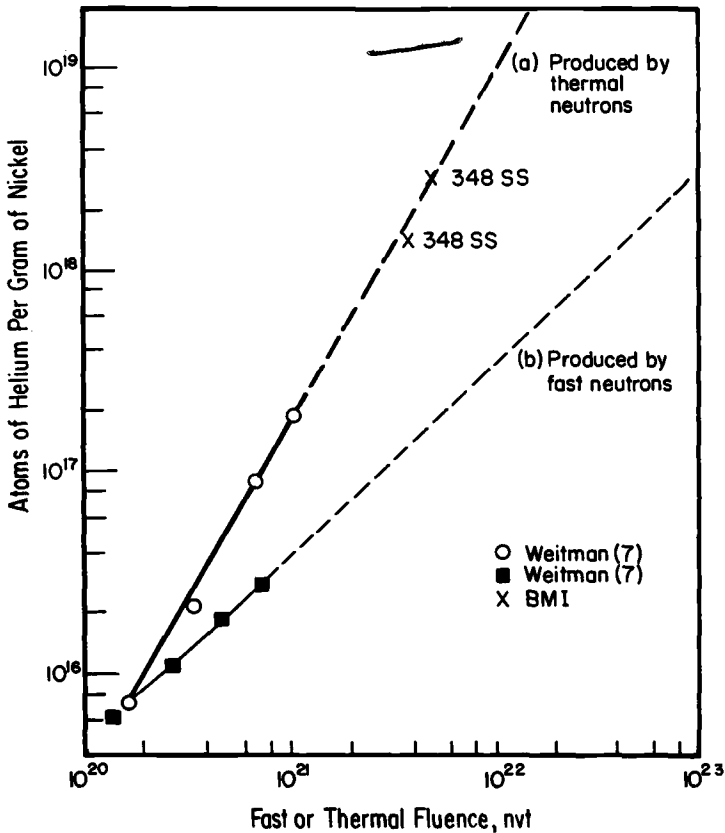


FIG. 14—Helium production in nickel due to fast and thermal fluence, n/cm^2 .

crease in ductility at 600 C. It was concluded that maximum embrittlement was associated with extremely fine helium bubbles and that growth of the helium bubbles produced an overaging effect with some recovery in ductility.

Electron microscopy replicas from the fracture surfaces gave some indications of helium. Figure 13 illustrates the presence of helium bubbles at grain boundary facets of a specimen which fractured intergranularly when tested at 500 C. At the higher testing temperature of 750 C helium bubbles cannot be positively identified although the fracture is intergranular; nevertheless, there is a mottled appearance at the grain boundary facets. It is hypothesized that this mottled appearance represents helium bubbles which were sheared and consequently enlarged during fracture. It is interesting to note that the individual mottles are significantly larger for the specimen that was annealed for 1 h at 980 C before testing at 750 C (Figure 15)—the coarsening of the mottle structure would be expected if the

mottles were sheared helium bubbles, since annealing at 980 C results in enlargement of helium bubbles.

The fracture of specimens which were irradiated at 650 C and then tested at 500 C was an intergranular and transgranular mixture. In areas where the fracture was intergranular there was some indication of the mottle structure at the grain boundary facets. The ductility of the specimen irradiated at 650 C and annealed at 980 C for 1 h was actually comparable to that of the unirradiated specimen that was tested at 500 C.

Figures 6 and 7 compare the engineering stress-strain curves for the unirradiated and irradiated specimens tested at 315 and 600 C. In the case of the stainless steel irradiated at 400 C, the appearance of the curve is significantly changed. The work hardening is reduced and the elongation is drastically reduced. The ultimate strength is significantly increased when tested at 315 C, but the ultimate strength remains about the same when tested at 600 C. Irradiation at 650 C does not change the appearance of the stress-strain curve at low strains, but, since fracture occurs at considerably lower strains for irradiated specimens tested at 600 C, the ultimate strength is reduced. Similar behavior has been observed for other irradiated face centered cubic materials which were tested at elevated temperatures [11]. This behavior has been explained in terms of irradiation induced grain boundary weakening and consequent premature onset of intergranular fracture.

Selected specimens were annealed for 1 h at 980 C after irradiation and then tested in tension at various temperatures (Tables 2 and 3). These included specimens that were irradiated at 400 C as well as 650 C. It was found that the preirradiation tensile properties could be essentially restored for testing temperatures below 500 C; however, tests at 600 and 750 C showed that both ultimate strength and elongation were significantly reduced. Thus it is apparent that the irradiation induced elevated-temperature embrittlement cannot be removed by annealing at high temperatures.

Conclusions

1. Irradiation induced changes of tensile properties are dependent on irradiation temperature. For low-temperature tests (<450 C) the changes in mechanical properties are maximum for irradiation at 400 C, intermediate for irradiation at 50 C, and minimum for irradiation at 650 C.
2. The irradiation induced elevated-temperature embrittlement was found to start at testing temperatures above 450 C and at 750 C was found to be independent of irradiation temperature.
3. Postirradiation annealing resulted in almost complete restoration of preirradiation tensile properties for testing temperatures of 500 C and below. However, it did not remove the effects of elevated-temperature embrittlement as manifested by reductions in ultimate strength and ductility.
4. Testing of as-irradiated specimens at temperatures above 500 C re-

sulted in intergranular fracture with evidence of helium bubbles at grain boundary facets. At 500 C specimens irradiated at 400 C exhibited intergranular fracture while specimens irradiated at 650 C showed mixed intergranular-transgranular fracture.

5. The analyzed helium contents were found to be about 2 to 3 times higher than those predicted from n, α cross section data.

References

- [1] Shober, F. R. and Murr, W. E., *Radiation Effects on Metals and Neutron Dosimetry*, ASTM STP 341, American Society for Testing and Materials, 1963.
- [2] Kangilaski, M. and Shober, F. R., *The Effects of Radiation on Structural Metals*, ASTM STP 426, American Society for Testing and Materials, 1967, pp. 487-511.
- [3] Hughes, A. N. and Caley, J. R., *Journal of Nuclear Materials*, JNUMA, Vol. 10, 1963, pp. 60-62.
- [4] Barnes, R. S., *Nature*, NATUA, Vol. 206, 26 June 1965, pp. 1307-1310.
- [5] Martin, W. R. and Weir, J. R., "Effect of Irradiation Temperature on the Post-irradiation Stress-Strain Behavior of Stainless Steel," ORNL-TM-906, Oak Ridge National Laboratory, Oct. 1964.
- [6] Birss, I. R., *Journal of Nuclear Materials*, JNUMA, Vol. 34, 1970, pp. 241-259.
- [7] Weitman, J., Daverhog, N., and Farvolden, S., "Anomalous Helium Production in Nickel," to be presented at ANS Winter Meeting of 1970.
- [8] Bloom, E. E., Martin, W. R., Stiegler, J. D., and Weir, J. R., *Journal of Nuclear Materials*, JNUMA, Vol. 22, 1967, pp. 68-76.
- [9] Woodford, D. A., Smith, J. P., and Moteff, J., *Journal of the Iron and Steel Institute*, JISIA, Vol. 208, Jan. 1969, pp. 70-76.
- [10] Keller, D. L., "Progress on Development of Materials and Technology for Advanced Reactors During July Through September, 1969," BMI-1872, Battelle Memorial Institute, Oct. 1969.
- [11] Kangilaski, M., Peterson, S. L., Perrin, J. S., and Wullaert, R. A., *Nuclear Applications and Technology*, NUATA, Vol. 9, Oct. 1970, pp. 550-560.

D. G. Hardy¹

The Effect of Neutron Irradiation on the Mechanical Properties of Zirconium Alloy Fuel Cladding in Uniaxial and Biaxial Tests

REFERENCE: Hardy, D. G., "The Effect of Neutron Irradiation on the Mechanical Properties of Zirconium Alloy Fuel Cladding in Uniaxial and Biaxial Tests," *Irradiation Effects on Structural Alloys for Nuclear Reactor Applications*, ASTM STP 484, American Society for Testing and Materials, 1970, pp. 215–258.

ABSTRACT: Short-time axial tension, transverse ring tension, and biaxial closed end burst tests were conducted on sections of fuel cladding from 17 different batches and heat treatments of Zircaloy 2, Zircaloy 4, and Zr-2.5Cb alloy. Specimens were irradiated at 2 to 3×10^{20} n/cm², $E > 1$ MeV, at temperatures of 125 to 250 C and tested at temperatures of 20 and 300 C.

The level of residual cold work was found to have the greatest effect on the mechanical properties of the Zircaloys prior to irradiation, and, although irradiation altered the general level of each property, the effect of cold work was preserved after irradiation for all properties except the uniform elongation. Very low values of uniform elongation (<1 percent) were obtained in the burst test after irradiation at all levels of cold work. In the instances where the texture and grain size influenced the properties, the effect was also preserved after irradiation. For the Zircaloys, the increment in the strength properties due to irradiation was constant at this fluence, independent of cold work, texture, and grain size. The decrements in the uniform and total elongations due to irradiation decreased with increasing cold work. The irradiation hardening of the Zr-2.5Cb alloy was greater than that experienced by the Zircaloys.

Beta heat-treated Zircaloy had higher strength and lower ductility than alpha annealed material in the tension test. Grain size was found to have a much more significant effect on the strength and ductility in the burst and ring tests than in the axial tension test.

KEY WORDS: neutron irradiation, fast neutrons, radiation effects, nuclear fuel cladding, tubing, zirconium alloys, Zircaloys, mechanical properties, ductility, elongation, tensile strength, yield strength, fractures (materials), cold working, heat treatment, texture, zirconium hydrides, axial stress, strains, tension tests

¹ Metallurgist, Applied Materials Research Branch, Chalk River Nuclear Laboratories, Atomic Energy of Canada Limited, Chalk River, Ontario, Canada.

Zirconium alloys can undergo considerable reduction in uniform and total elongation due to fast neutron irradiation at the temperatures encountered in water cooled reactors. The fuel cladding, however, must retain sufficient ductility to enable it to accommodate any strains imposed during the fuel life, such as might occur during fuel power increases, on fuel swelling, or due to buildup of fission gas pressure. Strains caused by expansion of the fuel are of particular importance in collapsible clad, uranium dioxide (UO_2) fuel elements because of the close contact between the cladding and the fuel [1, 2].²

With collapsible cladding, the requirement for adequate ductility must be balanced against the need for some initial strength to resist the formation of longitudinal ridges due to the coolant pressure. Specification of such cladding requires a good knowledge of the relationship between pre and postirradiation mechanical properties and of the factors which can affect these properties. Toward this end, a series of fast neutron irradiations have been conducted at Chalk River Nuclear Laboratories over the past several years on specimens from different cladding batches³ of Zircaloy 2, Zircaloy 4, and zirconium-2½ weight percent columbium alloy. These were selected to cover a wide range of fabrication routes, mechanical properties, textures, heat treatments, and hydride orientations.

The unirradiated properties of six of the Zircaloy 2 batches have been reported previously by Steward and Cheadle [3]. The present paper covers the effect of irradiation on the mechanical properties of all the batches in the unhydrided condition.

Test Program

The axial tube tension test is frequently the only mechanical acceptance test specified for zirconium alloy tubing, even when the tubing is destined for collapsible cladding which experiences most of its strain in the circumferential direction [1]. The actual stress ratio in the cladding may vary over the length of each UO_2 pellet, as suggested by Gittus [4], from essentially hoop stress at the mid pellet position to balanced biaxiality at the pellet ends. Since the stress ratio can have a significant effect on the mechanical properties [3, 5], and because of the anisotropic nature of zirconium alloys, a proper assessment of the mechanical properties of the tubing for this application can best be provided by a test which gives a reasonable simulation of the stress ratio existing in operating fuel cladding [6]. Balanced biaxiality produces the lowest fracture strains, but it is difficult to achieve in a simple tubing test. A closed end burst test, on the other hand, is simple to perform and has a ratio of longitudinal to circum-

² Italic numbers in brackets refer to the list of references at the end of this paper.

³ The term "batch" as applied in this report refers to tubing produced to a particular fabrication schedule from a particular zirconium alloy.

ferential stress of 0.5. Although the fracture strains are not the lowest at this stress ratio, Mehan's [5] data show that they are considerably reduced from the uniaxial values; therefore, this test was adopted to assess the biaxial properties of the tubing.

The results obtained in the burst test were compared with uniaxial longitudinal properties obtained in the conventional tube tension test and with the transverse properties obtained in the ring tension test. The latter test was adopted mainly because of its simplicity, but it was recognized that, because of bending over the edge of the grips [7] and because the actual gage length varies slightly from batch to batch [8], the gage length dependent properties are subject to errors.

Material

Nine different batches of zirconium alloys were selected for this investigation: six Zircaloy 2, one Zircaloy 4, and two Zr-2.5Cb alloy batches. Identification of these batches and their fabrication routes are listed in Table 1.

Three of the Zircaloy 2 batches and the Zircaloy 4 batch were also tested in the alpha annealed and the beta heat-treated condition. The former treatment consisted of heating the tubes in a vacuum for 1 h at 800 C, while the latter involved induction heating the central 1.5 in. of the specimen to 1050 C for 1 min in a vacuum. The latter treatment was intended to determine the effect of the heating cycle used to braze appendages to the fuel cladding.

These particular batches were selected to obtain the widest possible range of mechanical properties, textures, and hydride orientations. Oxygen concentrations varied from 1100 to 1470 ppm.

TABLE 1—Batch identification and fabrication details.

Batch Number	Alloy	Vendor	Method and Amount of Final Cold Reduction	Final Stress Relief Heat Treatment
1.....	Zircaloy 2	Z	15 to 20% cold drawn	None
2.....	Zircaloy 2	Y	~15% cold drawn	None
7.....	Zircaloy 2	Z	60% tube reduced	2 h at 495 C
8.....	Zircaloy 2	X	62% tube reduced	2 h at 427 C
9.....	Zircaloy 2	X	70% tube reduced	2.5 h at 454 C
11.....	Zircaloy 2	V	10% cold drawn ^a	None
16.....	Zircaloy 4	Z	60 to 70% tube reduced	Done, but unknown
17.....	Zr-2.5Cb	X	42% tube reduced	None
18.....	Zr-2.5Cb	Y	40% tube reduced	None

^a Batch 11 was impact extruded at 800 C from small bar stock slugs, then reduced in two draws with an intermediate anneal to finished size. All other batches were conventionally extruded in the high alpha temperature range from prebored or pierced billets, followed by several cold-working and annealing operations to finished size.

The tubes from which the specimens were cut had outside diameters of 0.601 ± 0.0015 in., a wall thickness of 0.0175 ± 0.0015 in., and a length of 19.5 in.

Experimental Details

Specimen Design

The axial tube tension and the closed end burst test specimens were of similar design. A length of 3 in. was chosen after a series of tests had shown this to be the minimum length necessary to avoid end effects.

End plugs were attached to the tubes by magnetic force resistance welding, the process regularly used on production fuel. The very restricted heat affected zone, coupled with the material upset and the mechanical work introduced into the weld zone during the butting operation, were found to prevent the premature tensile and burst failures in the heat affected zone which had previously occurred with fusion welded end plugs. Mechanical end fittings, although satisfactory for testing unirradiated specimens, were too bulky to be considered for the reactor specimens.

The ring tension specimens were 0.25 in. wide.

Specimen Preparation

The tubing was cut to length and air gaged at ten locations for outside diameter and wall thickness. End plugs were welded on and the specimens were pickled to remove 0.0015 in. from the diameter to simulate production practice. The autoclave treatment was simulated by heating in air for 24 h at 400 C. The end plugs were then drilled and tapped so that pressure lines could be attached for burst testing or for extension bars for tension testing.

Some of the early specimens were provided with a 20 line per inch grid pattern using Kodak Photo Resist stabilized by flash pickling prior to the 400 C heat treatment. This practice was later discontinued because of the lack of a satisfactory technique for measuring the grids after irradiation.

Irradiation Facility

Irradiations were conducted in the fast neutron facilities of the NRU reactor at Chalk River. Twelve burst or tension specimens were joined together with screwed connectors, and the ring test specimens, mounted on Zircaloy holders, were screwed into the bottom of each specimen string. Each specimen string was located in an air cooled aluminum flow tube. The irradiation inserts consisted of six such tubes, giving a total capacity of 72 three-inch specimens and 72 ring test specimens.

A surrounding ring of fuel elements provided a flux of about 2×10^{18} n/cm² $E > 1$ MeV, to the central, dry, specimen space containing the aluminum flow tubes. The flux was fairly constant over a length of about 50 in.

Chromel/alumel thermocouples were located at three points in each string. Iron wire flux monitors in small aluminum cans were attached at five points along one string in the first irradiation. Later exposures were estimated from the integrated fuel power output.

Irradiation Conditions

Three separate fast neutron inserts were used to irradiate the specimens described in this paper. Exposure durations varied from 4½ to 5 months and produced the following values of integrated fast flux at the center line:

1. Batches 1, 2, 7, 8, 9, and 11 in the as-received condition: 2.7×10^{20} n/cm², $E > 1$ MeV.

2. Batches 16, 17, and 18 in the as-received condition: 2.9×10^{20} n/cm², $E > 1$ MeV.

3. Batches 1, 7, 11, and 16 in the α annealed and β heat-treated condition: 2.0×10^{20} n/cm², $E > 1$ MeV.

The specimens were air cooled, but due to gamma heating specimen temperatures varied from 125 to 250 C. Control specimens were maintained at 250 C in furnaces for an equivalent exposure time.

Mechanical Testing

Mechanical testing was conducted at 20 and 300 C. Threaded extension bars were used to connect the specimen to the grips of the tension testing machine. Crosshead motion was used to record the specimen strain, and a constant crosshead speed of 0.050 in./min was used, giving a strain rate of 0.017 min⁻¹.

Close separation, double-yoke grips were used to pull the ring tension specimens [9]. A crosshead speed of 0.010 in./min was used to give a strain rate of approximately 0.05 min⁻¹. A gage length of 20 percent of the circumference was assumed for the ring specimens. This represented the average distance over which plastic deformation had been detected on photogridded specimens in earlier tests [9].

Two different hydraulic burst test machines were used to test the specimens of this report. The Mark I machine described in Ref 3 was pressurized with a hand operated pump. Later, an improved version, the Mark II, was built incorporating a motor-driven pump and an X-Y recorder for automatically plotting the pressure and volume increase of the specimen. A schematic diagram of the Mark II machine is shown in Fig. 1. HB-40, a mixture of hydrogenated terphenyl compounds supplied by Monsanto (Canada) Ltd., Montreal, was used as the pressurizing fluid because of its stability at 300 C.

In operation, a closed volume of fluid (*A*) on the specimen side of the differential piston was pressurized by the pumped fluid on the other side of the piston (*B*). The increase in volume of the specimen during pressurization was known by measuring the displacement of the piston with a linear

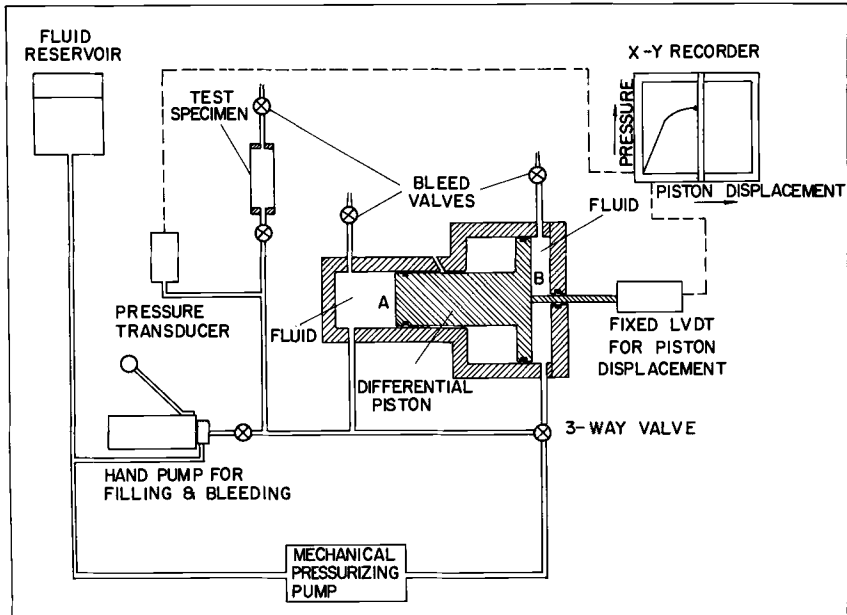


FIG. 1—Schematic arrangement of hydraulic burst test apparatus.

variable differential transformer (LVDT). This output and the output from the pressure transducer were fed to the X-Y recorder. The resulting pressure-displacement curve was treated like a normal load-deflection curve to obtain the proportional limit, the 0.2 percent offset yield strength, the engineering ultimate hoop strength, and the uniform circumferential elongation. The stresses were obtained from the conventional thin-wall formula for hoop stress,

$$\sigma = \frac{Pd_i}{2t_{\min}}$$

where

- σ = the hoop stress,
- P = the internal pressure,
- d_i = the internal diameter, and
- t_{\min} = the minimum wall thickness.

The total circumferential elongation of the unirradiated specimens was measured after testing by wrapping a 0.0015-in.-thick stainless steel scale around the specimen at the location of maximum bulge. This operation proved very difficult to perform on the irradiated specimens in the hot cells, and an estimation of the circumference was obtained by measuring the specimen diameter at right angles to the fracture. This measurement

was related to the circumference by referring to a plot of these two measurements obtained on inactive specimens, as shown in Fig. 2. Since the accuracy of this method was not high, a number of specimens, especially those whose circumferences seemed unreasonable, were sectioned at the maximum bulge, mounted in plastic, and examined metallographically. The circumferences were measured directly on photographs taken at $\times 7.5$.

The circumferential strain rate during the uniform elongation portion of the burst test deformation was approximately 0.03 min^{-1} .

X-ray Diffraction and Line Broadening

The textures of the tubes were determined by X-ray diffraction and plotted as inverse pole figures [10, 11]. A description of the specimen preparation and the inverse pole figures for the first six as-received batches have been published by Steward and Cheadle [3]. The pole figures for batches 17 and 18, the Zr-2.5Cb alloy batches, have also been published by Steward in Refs 9 and 12, respectively.

Because of the varied fabrication histories of the batches, the actual amount of cold work in each was not known. This was estimated by measuring the half height of the $\{10\bar{1}5\}$ diffraction peaks from radial specimens on a texture diffractometer produced by the Siemens and Halske Aktiengesellschaft of West Germany.

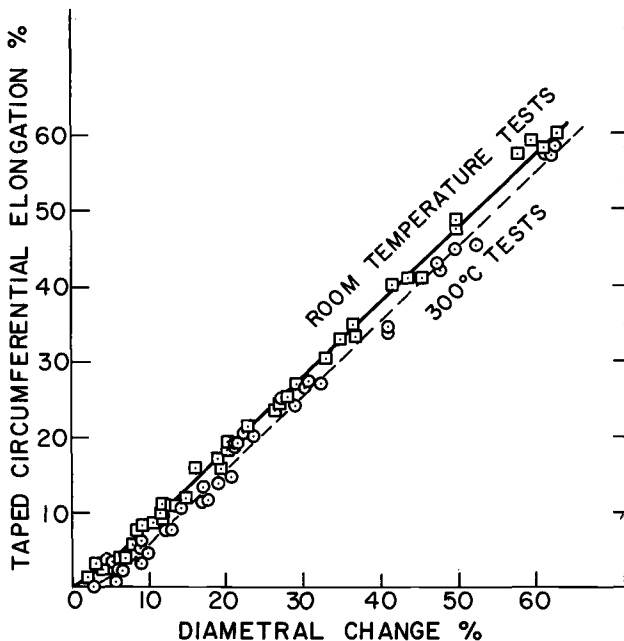


FIG. 2—Total circumferential elongation measured by tape versus diameter increase measured at right angles to burst fracture. Based on unirradiated specimens.

TABLE 2—Axial tube tensile properties (values represent the average of two or three results).

Batch Number and Condition ^a	Test Temperature, deg C	Preirradiation Properties				Postirradiation Properties			
		Yield Strength, ksi, 0.2% Offset	Nominal Ultimate Tensile Strength, ksi	Uniform Elongation, %	Total Elongation in 3 in., %	Yield Strength, ksi, 0.2% Offset	Nominal Ultimate Tensile Strength, ksi	Uniform Elongation, %	Total Elongation in 3 in., %
1-C	20	83.2	95.9	5.3	10.5	102.6	107.7	2.3	5.3
2-C	20	76.3	89.7	4.9	13.3	95.2	99.8	2.5	6.6
7-C	20	79.1	99.9	7.5	16.5	103.4	109.1	2.8	9.8
8-C	20	83.8	104.3	5.6	6.3	108.5	115.2	2.5	2.7
9-C	20	88.9	112.7	6.3	12.1	114.3	123.5	3.6	9.0
11-C	20	59.7	74.8	8.7	19.4	88.8	89.9	2.3	9.5
16-C	20	80.9	106.0	8.2	16.7	107.6	119.4	3.4	8.8
17-C ^b	20	80.5	108.5	9.3	22.0	130.9	144.0	3.0	5.7
18-C ^b	20	79.7	103.0	9.5	18.5	125.9	136.0	0.6	0.8
1-A	20	52.3	77.8	14.8	23.9	78.3	87.7	5.3	15.1
7-A	20	53.9	72.8	15.4	25.7	83.0	85.6	3.6	17.7
11-A	20	48.6	71.9	12.9	17.6	68.7	77.7	4.5	11.0
16-A	20	49.1	72.0	17.4	28.3	74.9	81.9	3.8	15.1
1-B	20	57.6	76.5	10.4	16.5	84.1	95.0	2.0	7.1
7-B	20	57.2	77.7	12.4	18.3	82.5	89.2	2.0	5.3
11-B	20	54.6	72.4	10.6	15.8	80.9	86.6	1.6	5.0
16-B	20	54.5	73.7	9.9	13.8	81.1	87.7	1.8	8.0
1-C	300	48.0	54.2	2.7	7.0	67.1	67.1	0.7	2.2
2-C	300	43.1	48.7	2.3	7.4	53.4	53.8	0.9	5.0
7-C	300	51.7	62.3	4.1	11.8	65.8	67.2	1.3	11.3
8-C	300	50.3	63.3	4.8	5.4	66.4	68.1	1.1	1.4
9-C	300	61.1	73.3	4.0	7.4	74.3	80.2	2.7	7.1
11-C	300	35.3	39.8	6.7	15.3	51.3	51.3	0.3	4.8
16-C	300	54.7	67.5	5.6	11.4	71.6	74.7	1.6	6.2
17-C ^b	300	53.5	73.3	4.4	10.6	90.0	97.2	1.9	3.5

18-C ^b	300	49.0	62.0	6.2	17.2	88.1	91.1	0.6	0.8
1-A.....	300	18.5	32.7	15.3	25.3	46.6	46.6	0.4	7.3
7-A.....	300	18.0	30.3	22.8	38.2	49.2	49.2	0.2	15.5
11-A.....	300	18.4	29.6	12.0	23.9	46.6	46.6	0	6.5
16-A.....	300	18.6	32.3	19.3	32.5	47.8	47.8	0.2	13.8
1-B.....	300	25.0	37.9	10.2	16.7	55.3	56.6	1.0	6.9
7-B.....	300	22.5	38.0	12.2	18.9	55.7	56.0	1.2	6.3
11-B.....	300	25.5	35.7	8.9	13.7	52.2	52.7	0.7	4.5
16-B.....	300	24.4	35.6	8.3	13.4	53.2	54.1	0.9	5.0

^a Metallurgical condition code: C—as received, that is, cold-worked or cold-worked and stress relieved.

A—alpha annealed, 1 h at 800 C.

B—beta heat-treated, 1 min at 1050 C.

^b End plugs pulled off unirradiated specimens, results taken from Refs 9 and 12.

TABLE 3—*Ring tensile properties (values represent the average of two or four results).*

Batch Number and Condition	Test Temperature, deg C	Unirradiated Properties				Postirradiation Properties			
		Yield Strength, ksi, 0.2% Offset	Nominal Ultimate Tensile Strength, ksi	Uniform Elongation, %	Total Elongation in 0.38 in., %	Yield Strength, ksi, 0.2% Offset	Nominal Ultimate Tensile Strength, ksi	Uniform Elongation, %	Total Elongation in 0.38 in., %
1-C.....	20	86.3	103.0	6.6	11.3	113.5	118.5	3.6	8.1
2-C.....	20	72.4	92.2	9.7	23.5	106.5	109.0	3.0	13.9
7-C.....	20	78.2	98.0	9.1	21.9	112.5	116.5	3.1	10.5
8-C.....	20	88.7	109.2	8.4	12.2	111.2	119.5	4.8	11.9
9-C.....	20	89.8	107.5	6.8	11.4	118.5	124.3	3.4	7.7
11-C.....	20	60.4	74.2	9.2	32.9	86.5	94.6	4.9	16.8
16-C.....	20	96.2	108.3	3.7	9.6	130.0	132.0	0.9	3.0
17-C.....	20	90.5	101.9	3.6	11.0	136.5	139.0	0.9	2.8
18-C.....	20	84.5	97.1	3.0	8.8	101.2	106.9	1.1	4.5
1-A.....	20	64.5	76.4	7.9	20.1	87.6	89.0	1.0	9.2
7-A.....	20	60.0	71.6	9.5	26.2	82.0	84.9	1.6	17.3
11-A.....	20	62.0	73.9	9.4	21.5	80.5	82.4	2.0	11.0
16-A.....	20	59.6	72.1	9.2	26.4	83.0	86.0	1.7	15.9
1-B.....	20	58.0	73.1	10.6	12.9	69.8	72.7	1.8	6.1
7-B.....	20	66.2	82.5	8.1	11.4	79.0	83.0	1.9	6.7
11-B.....	20	60.2	75.8	10.7	13.3	79.7	84.1	2.4	6.9
16-B.....	20	60.9	76.4	8.8	12.2	81.8	86.1	2.1	6.9
1-C.....	300	49.4	53.8	3.7	13.3	63.4	66.2	3.0	10.4
2-C.....	300	44.1	49.1	4.1	22.7	56.5	59.0	2.6	16.1
7-C.....	300	50.3	56.6	4.6	19.0	67.2	69.5	2.7	14.9
8-C.....	300	50.6	59.5	5.1	11.6	63.7	67.5	4.0	10.9
9-C.....	300	59.3	68.8	4.9	10.4	76.2	81.0	3.2	9.8
11-C.....	300	29.0	37.4	7.6	43.0	51.7	52.1	2.3	22.1
16-C.....	300	53.0	58.3	1.9	10.0	60.1	61.2	0.7	6.4

17-C.....	300	63.8	70.6	1.7	11.0	86.5	87.1	1.1	3.3
18-C.....	300	59.1	65.4	2.0	9.9	90.8	93.6	0.4	2.8
1-A.....	300	28.6	34.2	11.3	32.3	44.1	45.1	0.7	23.0
7-A.....	300	24.3	30.5	12.8	43.2	40.0	41.1	0.7	24.5
11-A.....	300	24.9	31.0	11.8	30.5	38.0	39.4	2.2	17.3
16-A.....	300	25.0	31.0	12.4	39.8	39.0	40.9	1.0	22.8
1-B.....	300	38.8	39.7	3.5	10.0	46.8	47.6	1.2	5.3
7-B.....	300	31.9	39.1	8.5	11.9	46.6	47.9	1.5	8.0
11-B.....	300	31.2	39.4	9.1	12.7	43.6	45.2	1.6	6.8
16-B.....	300	30.6	37.7	8.1	12.7	44.5	44.9	1.4	6.3

TABLE 4—Closed end burst test properties (values represent the average of two or three results).

Batch Number and Condition	Test Temperature, deg C	Preirradiation Properties				Postirradiation Properties			
		Yield Strength, ksi, 0.2% Offset	Nominal Ultimate Hoop Strength, ksi	Uniform Circumferential Elongation, %	Total Circumferential Elongation in 1.89 in., %	Yield Strength, ksi, 0.2% Offset	Nominal Ultimate Hoop Strength, ksi	Uniform Circumferential Elongation, %	Total Circumferential Elongation in 1.89 in., %
1-C	20	105.5	107.6	2.5	14.3	125.7	125.7	0.2	6.0
2-C	20	91.9	97.7	4.5	12.8	124.0	122.9	0.7	4.0
7-C	20	99.9	109.8	4.2	12.1	129.8	124.2	0.7	10.3
8-C	20	96.5	101.0	3.2	12.3	121.7	121.7	0.	3.5
9-C	20	113.5	119.5	1.5	4.3	129.1	129.1	0.3	1.5
11-C	20	82.0	85.0	4.7	37.5	108.6	108.6	0.3	21.3
16-C	20	105.6	116.8	4.0	9.0	126.7	126.7	0.9	3.1
17-C	20	125.0	139.9	2.0	15.6	163.9	163.9	0.4	0.5
18-C	20	106.4	115.4	4.0	8.1	154.6	154.6	0.2	1.1
1-A	20	77.5	86.0	10.7	32.1	118.4	102.6	1.0	27.2
7-A	20	82.2	94.7	7.8	23.9	118.4	118.4	0.7	16.4
11-A	20	69.0	80.8	12.8	27.7	87.6	88.1	0.5	23.8
16-A	20	78.0	88.2	8.7	37.0	99.1	106.1	1.1	23.3
1-B	20	63.7	74.9	5.0	14.5	92.1	93.5	0.8	9.2
7-B	20	63.8	75.4	5.5	15.8	93.4	94.2	0.7	11.3
11-B	20	60.0	73.3	6.3	14.5	85.7	86.1	0.7	10.0
16-B	20	61.6	72.6	6.2	18.4	87.2	88.0	1.0	12.5
1-C	300	60.1	60.4	0.5	20.0	78.9	78.9	0.3	0.4
2-C	300	56.1	56.9	1.1	18.0	71.1	72.2	0.7	9.8
7-C	300	59.5	65.2	2.2	21.5	85.6	85.8	0.8	2.9
8-C	300	57.8	58.4	1.2	14.8	71.9	72.6	0.7	0.8
9-C	300	69.1	71.6	1.0	1.0	76.2	77.4	1.0	1.0
11-C	300	50.8	51.1	0.7	53.0	...	57.1	0.1	29.0
16-C	300	64.2	69.8	2.0	4.9	79.4	82.4	0.7	2.4

17-C.....	300	82.8	94.2	2.7	8.8	110.8	117.6	0.4	1.0
18-C.....	300	67.8	73.3	2.1	4.5	98.1	99.3	0.3	1.0
1-A.....	300	28.5	31.2	12.9	52.9	55.7	55.7	0.3	37.6
7-A.....	300	28.1	40.8	8.6	58.8	64.9	67.6	1.5	30.2
11-A.....	300	26.2	34.0	13.2	44.9	46.3	46.7	0.3	32.3
16-A.....	300	26.3	37.8	11.3	63.5	59.5	63.2	0.8	38.0
1-B.....	300	27.2	36.1	6.3	23.4	53.4	53.5	0.4	7.7
7-B.....	300	27.8	35.8	6.8	21.4	53.3	55.4	1.0	17.6
11-B.....	300	26.6	35.4	10.3	20.2	51.4	52.9	0.1	17.1
16-B.....	300	26.7	35.9	7.1	26.3	48.2	51.5	0.7	11.0

Results

Mechanical Test Results

Specimens from all batches and heat treatments were tested in the un-irradiated and irradiated conditions at both 20 and 300 C. Two to four specimens were tested under each condition, and the average values for the axial tension tests, the ring tension tests, and the closed end burst tests are presented in Tables 2, 3, and 4, respectively. Typical load-elongation curves obtained in these tests with the six as-received Zircaloy 2

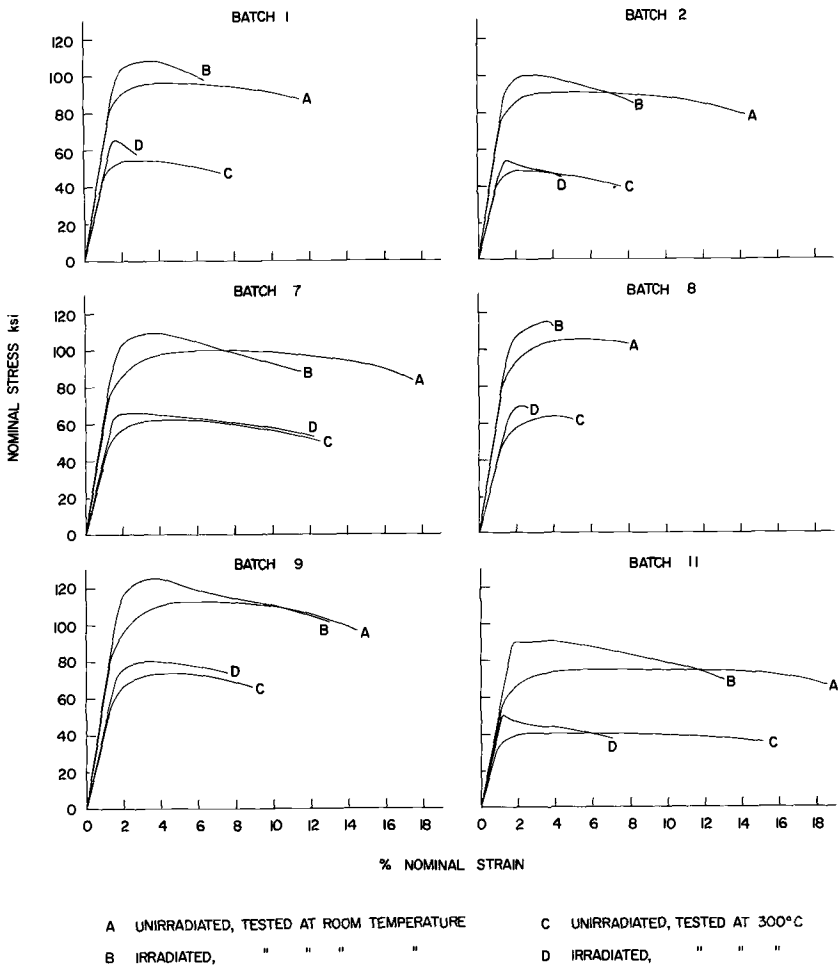


FIG. 3—Typical nominal stress versus nominal strain curves for irradiated and un-irradiated Zircaloy 2 in the axial tension test.

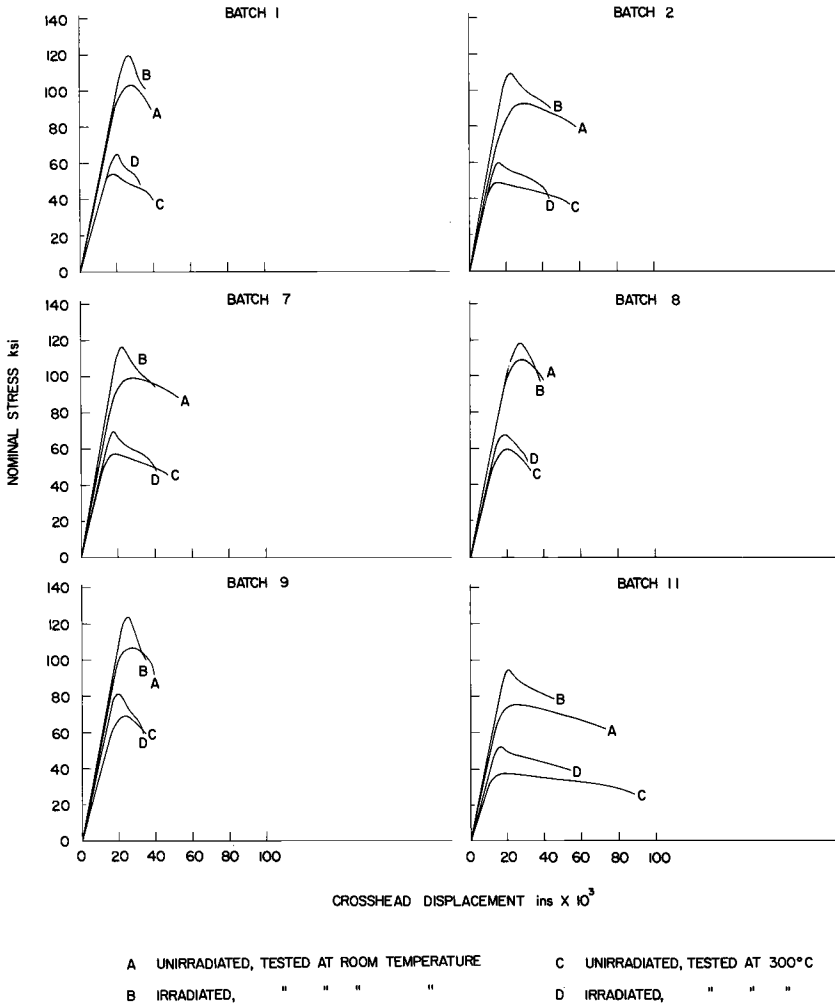


FIG. 4—Typical nominal stress versus crosshead displacement curves obtained for irradiated and unirradiated Zircaloy 2 in the ring tension test.

batches are shown in Figs. 3, 4, and 5. These have been redrawn from the original curves to present them on the same scale.

The appearance of some of the irradiated specimens after tension testing at room temperature is shown in Fig. 6. It is remarkably similar to the appearance of the unirradiated specimens shown previously [3]. Batches 7 and 11 show considerable diameter reduction, while batch 1 shows very little and batch 8 broke in a helical fracture with almost no diameter re-

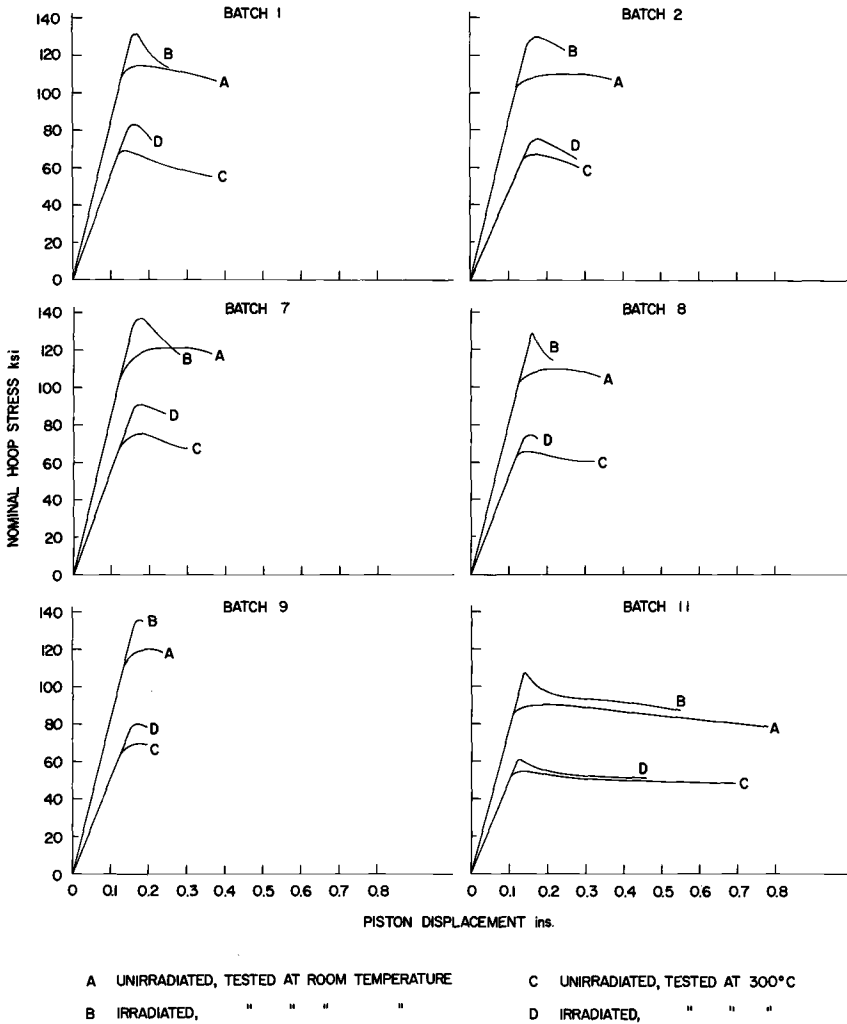


FIG. 5—Typical nominal stress versus piston displacement curves obtained for irradiated and unirradiated Zircaloy 2 in the closed end burst tests.

duction. For the Zr-2.5Cb alloys, a similar helical fracture occurred in batch 18 while some diameter reduction was observed in batch 17.

Irradiated, as-received, ring test specimens, illustrated in Fig. 7, showed less necking in the direction of width than did the unirradiated specimens. Except for the batches with the lowest levels of initial cold work, that is batches 2 and 11, fractures occurred along a single diagonal shear line with very little development of a second intersecting diagonal.

The typical appearance of the as-received batches after burst testing at 20 and 300 C is shown in Fig. 8. At both temperatures, batch 11 exhibited the most bulging, followed by batches 7, 8, and 9 in order of decreasing bulging. The 300 C fractures tended to be shorter and less ragged than those at room temperature. The 300 C batch 11 specimen failed at a pin-hole fracture, a characteristic which it also exhibited in the unirradiated condition.

The appearance of two batches of heat-treated burst test specimens after irradiation is shown in Fig. 9. The alpha annealed specimens exhibited the greatest amount of ductility, with the development of a pronounced banana shape at 300 C, especially in batch 7. Almost all of these specimens developed pinhole fractures at 300 C. Deformation in the beta heat-treated specimens was restricted to the central heat affected zone, with much less circumferential expansion than the alpha annealed specimens. The surface of the heat affected zone developed an orange-peel appearance and the fracture faces were quite irregular. Pinhole failures occurred in a few of the specimens but most developed splits.

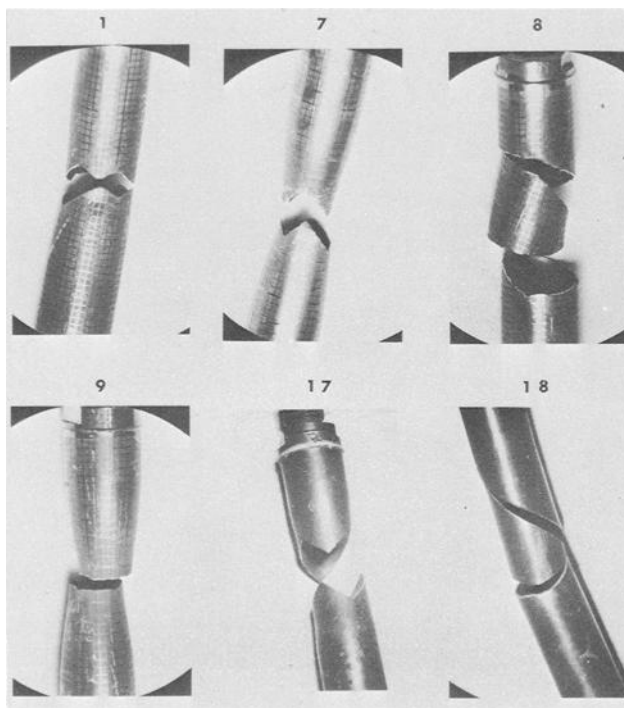


FIG. 6—Typical irradiated axial tension test specimens tested at 20 C.

Texture and Line Broadening

From the inverse pole figures an estimate was made of the proportion of grains in each batch having the idealized orientations *A*, *AB*, *CB*, *C*, and *D* shown in Table 5.

A numerical measure of the texture was obtained by a method due to Cheadle [13]. This involved calculating the fraction of grains that were oriented for twinning in the circumferential (transverse) and radial directions. Ibrahim [14] has provided a sample calculation of this method. The fraction of grains oriented for twinning, as well as the ratio of the proportion of grains which twin in the radial direction to the proportion which twin in the transverse direction, are given in Table 5. The line broadening data are also included in the table.

Metallography

The microstructures of the as-received specimens ranged from almost completely equiaxed to heavily cold-worked, as shown in the longitudinal sections in Fig. 10. Batch 8 had a highly cold-worked structure after being tube reduced 62 percent and stress relieved for $2\frac{1}{2}$ h at 427 C, while that

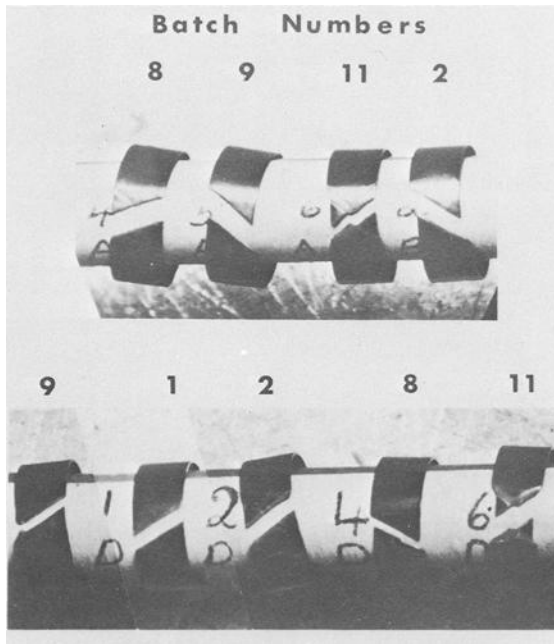


FIG. 7—Appearance of irradiated ring test specimens tested in the as-received condition.

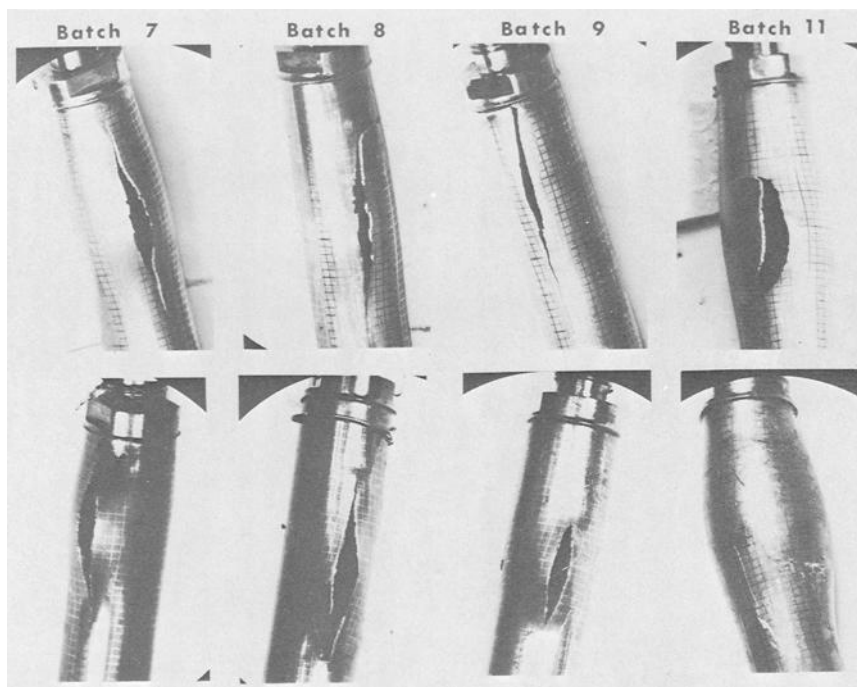


FIG. 8—Typical appearance of irradiated as-received burst test specimens tested at (top) 20 C and (bottom) 300 C.

of batch 11, which was cold drawn about 10 percent, had a more equiaxed grain structure.

Cross sections of the fractured surfaces of unirradiated burst specimens tested at room temperature in the three metallurgical conditions—*as-received*, *alpha annealed*, and *beta heat-treated*—are shown in Fig. 11 for batches 1, 7, and 11. The grain coarsening on annealing can be seen as well as the Widmanstätten structure resulting from the beta heat treatment.

Discussion

The effect of irradiation on these specimens shows the normal response of increasing the strength and decreasing the ductility (elongations) both at room temperature and at 300 C. The yield strength increases to a greater extent than the ultimate strength, increasing the ratio of yield to ultimate strengths. This is also manifest by a drastic reduction in uniform elongation, indicating a reduction in the ability of the material to strain harden after irradiation. The local or necking elongation decreases to a much smaller extent.

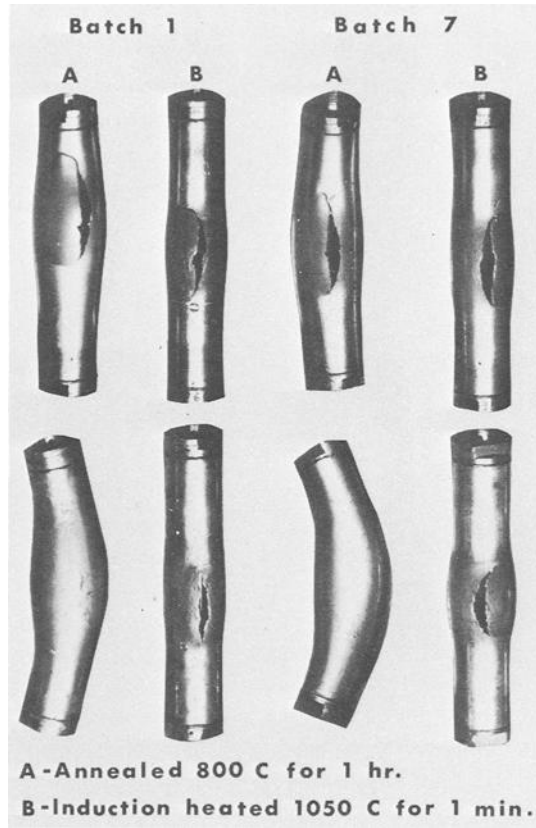


FIG. 9—Typical appearance of heat-treated burst test specimens after irradiation, tested at (top) 20 C and (bottom) 300 C.

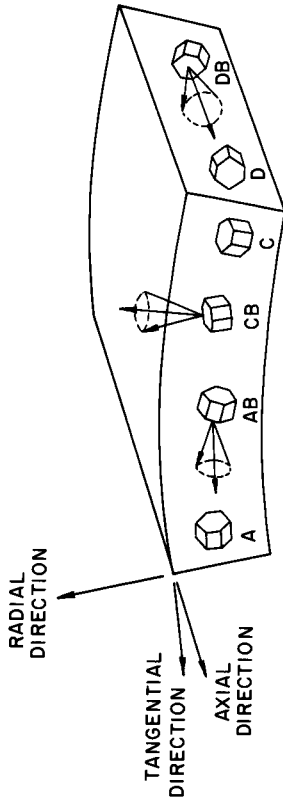
In addition to being affected by fast neutron irradiation, the results are also influenced by a number of other factors, such as type of alloy, level of cold work, texture, stress ratio, heat treatment, and grain size. In the following sections the results will be discussed in terms of these parameters in order to establish overall trends.

Effect of Neutron Irradiation on the Strength Properties

Irradiation hardening has generally been studied by measuring the increment of yield strength. Ells and Fidleris [15] have used an expression proposed by Koppenaal and Kuhlman-Wilsdorf [16] which gives the irradiation induced increment of yield stress, σ_r , as

$$\sigma_r = [(\sigma - \sigma_0)^2 - (\sigma_i - \sigma_0)^2]^{1/2}$$

TABLE 5—Line broadening and texture characteristics of the tubing batches.



THE IDEALISED ORIENTATIONS

Batch Number	Breadth of Half Height of X-ray Reflections from {1015} Planes, arbitrary units	(0002) Pole Texture Coefficients				Resolved Fraction of Grains Which Deform by Twinning		Ratio of Radial Twinning Grains to Tangential Twinning Grains	
		A	AB	CB	C	D	Radial Direction		Tangential Direction
1.....	7.1 to 7.2	2.4	2.7	1.9	3.3	0.1	0.41	0.37	1.1
2.....	7.1	3.4	1.7	2.0	4.1	0.1	0.44	0.35	1.3
7.....	7.3 to 7.4	1.1	1.0	3.7	5.0	0.1	0.69	0.17	4.0
8.....	7.5 to 7.4	8.1	2.4	1.3	1.8	0.3	0.26	0.47	0.5
9.....	7.5	2.6	1.1	3.0	4.5	0.2	0.52	0.24	2.2
11.....	6.9	3.0	1.4	1.4	2.5	0.4	0.46	0.29	1.6
16.....	...	3.8	1.1	2.4	5.6	0.1	0.51	0.29	1.8
17.....	...	1.3	1.2	3.7	2.1	0.2	0.52	0.19	2.7
18.....	...	0.9	1.6	2.0	2.6	0.1	0.41	0.27	1.5

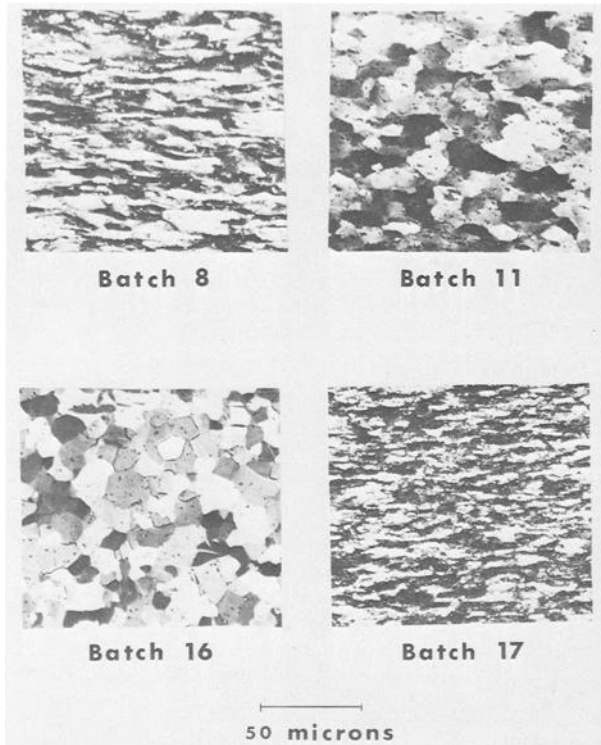


FIG. 10—Variation in grain structure of as-received specimens. Batches 8 and 11 are Zircaloy 2, batch 16 is Zircaloy 4, and Batch 17 is Zr-2.5Cb alloy. Longitudinal section with the tube axis horizontal.

where σ_i is the yield stress before irradiation, σ is the final yield stress, and σ_0 is the temperature-independent component of σ_i . A value of 8000 psi was assigned to σ_0 by Ells and Fidleris and the same value has been used in this paper. Figure 12 plots the values of σ_r at 300 C for the (a) axial tension test, (b) ring tension test, and (c) closed end burst test against the fast fluence. Also included are Ells and Fidleris' [15] curve for Zr-2.5Cb material slow cooled from the $(\alpha+\beta)$ phase and Bement's [17] Zircaloy 2 data for material annealed prior to irradiation. Agreement between these curves and the present results is excellent for the axial tension test: the annealed Zircaloy 2 results fall directly on Bement's curve and the two Zr-2.5Cb results are slightly above the Ells and Fidleris curve, just as for their own cold-worked specimens. This confirms that the increment of yield stress on irradiation is greater in the Zr-2.5Cb alloy than in Zircaloy 2. There was no significant difference in the hardening of Zircaloy 2 and Zircaloy 4.

Agreement is not as good in the case of the ring tension test results. This may reflect the difficulty of obtaining good yield strength values when the gage length is not precisely known. The increments in the closed end burst test show a larger spread. Some of this might be explained by specimen wall thickness variation, but this would hardly account for the factor of two difference between batches 11 and 7, which had σ_r values of 24 and 58 ksi, respectively. On the average the increment in the biaxial tests is higher than in either of the two uniaxial tests, but it is not known if the same σ_0 should apply to the biaxial condition.

Influence of Cold Work on Strength Properties

The strength in the axial tension test provides a good measure of the relative amount of residual cold work present in the various tubing batches. This is explained by the fact that all batches have an absence of basal poles parallel to the tube axis, that is, almost all the poles are concentrated in the transverse plane. The grains therefore are oriented favorably for slip in the axial direction; cross section reduction may occur either by diameter

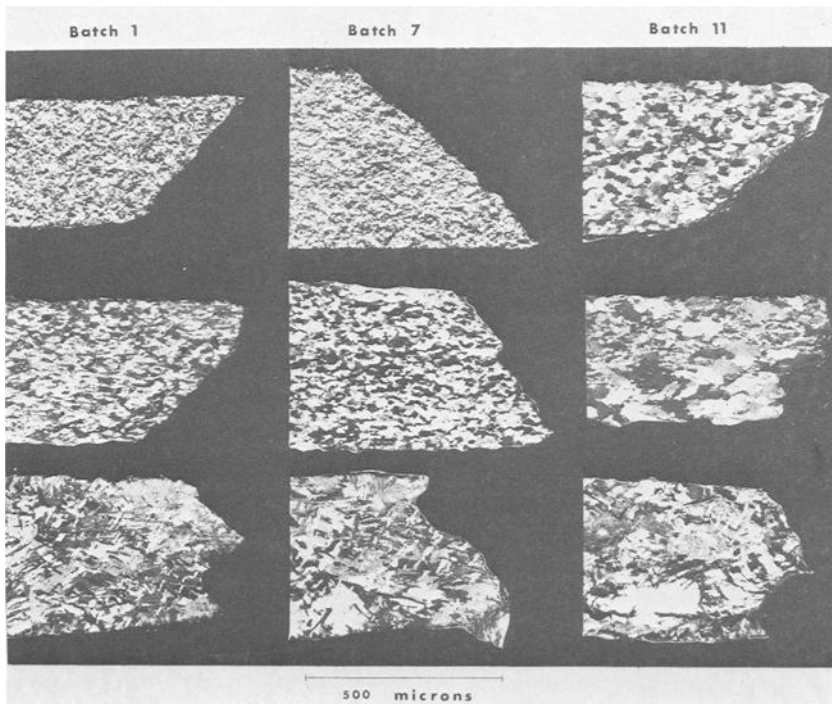
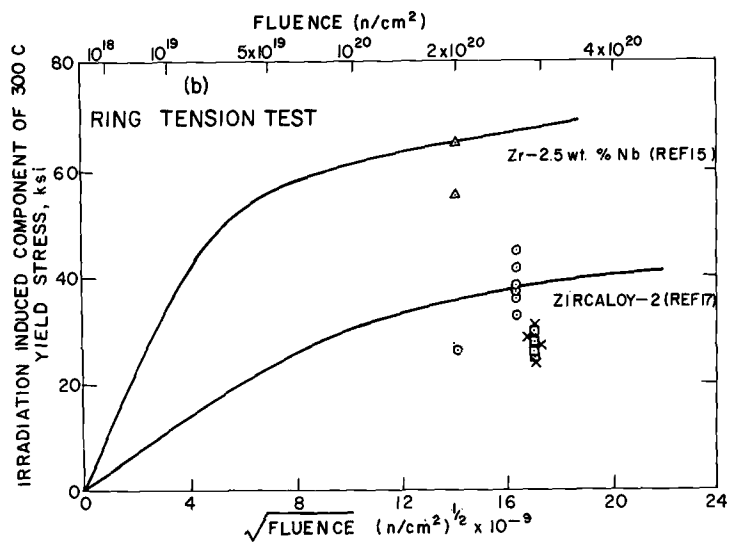
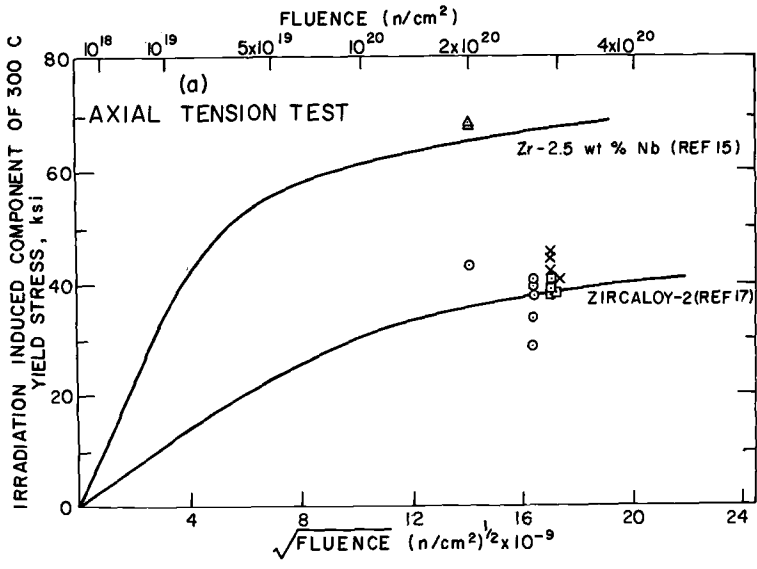


FIG. 11—*Transverse section through fracture of burst test specimens: top, as received; middle, alpha annealed; bottom, beta heat-treated.*



- △ As-received Zr-2.5Cb
- As-received Zircaloy
- Alpha annealed Zircaloy
- × Beta heat-treated Zircaloy

FIG. 12—Irradiation induced component of yield strength at 300 C as a function of fast fluence ($E > 1 \text{ MeV}$).

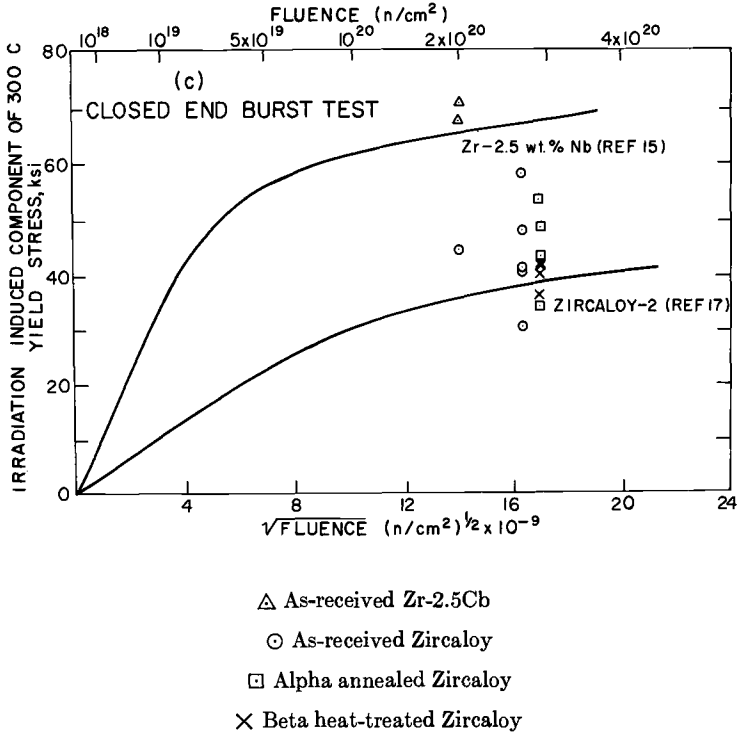


FIG. 12 (Continued)

reduction or wall thickness reduction depending on the relative proportion of radial and tangential basal poles. Thus the strength in the axial direction is largely unaffected by the texture and is more influenced by the level of residual cold work. This is illustrated in Fig. 13, where the axial strengths are plotted against the X-ray line broadening results. Line broadening, which is a measure of the lattice strain or cold work, is proportional to the axial strength, particularly the axial ultimate tensile strength (UTS).

Batch 9 had the highest level of residual cold work despite a stress relieving treatment. Batch 11 had the lowest level, with strength values very close to the annealed condition; but the line broadening data indicate that it had been cold worked. The low strength might indicate that the material was worked preferentially near the outer surface, an effect which could have been removed largely by the three pickling operations given these specimens.

The relative ranking of the as-received batches on a strength basis in the axial tension test is the same after as before irradiation. This is in agreement with the observation that the irradiation induced increment of

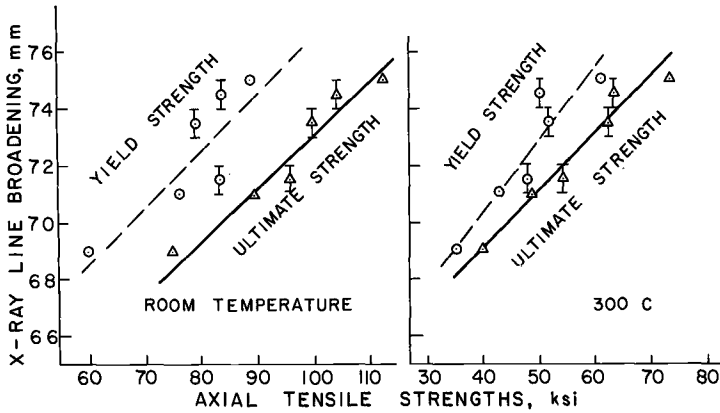


FIG. 13—Breadth of half maximum height for X-ray reflections from the $\{10\bar{1}5\}$ planes compared with axial tensile strength.

yield strength [15], and presumably of the UTS, is independent of prior metallurgical condition.

Influence of Cold Work on Elongation

To determine the combined effects of cold work and irradiation on ductility, the uniform and total elongations have been plotted as a function of the axial ultimate tensile strength, since this was shown to be directly proportional to the amount of residual cold work. The room temperature and 300 C results are presented for the axial tension, ring tension, and closed end burst tests in Figs. 14, 15, and 16. The beta heat-treated results were not included because of the pronounced grain size effect discussed later. The Zr-2.5Cb results were included but they were not considered in drawing the trend lines. They were usually lower in ductility than the Zircaloy specimens after irradiation, probably because of the greater amount of irradiation hardening in the alloy.

Uniform Elongation—In the unirradiated condition, the uniform elongation dropped abruptly from the annealed condition as the amount of cold work increased. In the axial direction a minimum appeared to occur between about 80 and 90 ksi, then the uniform elongation increased slightly with increasing cold work. This agrees with the work of Bement [17], who found a minimum at about 10 percent cold work (~ 82 ksi). Bement also found a minimum in the transverse direction. While his room temperature ring test results showed a constant decrease with increasing cold work, the 300 C ring tests did indicate a minimum. The uniform elongations in the burst test at room temperature also showed the abrupt drop with cold

work and continued to decrease with increasing cold work. At 300 C the values dropped very low, to about 1 percent, and then increased slightly with increasing cold work.

Irradiation caused a large decrease in the uniform elongation, especially in the annealed specimens. The decrement in the uniform elongation due to irradiation was dependent on the level of residual cold work, with the magnitude decreasing with increasing cold work. In the ring test, at both test temperatures, values for the annealed specimens after irradiation were lower than for the cold-worked specimens. The batch 7 300 C value dropped from 22.8 percent before irradiation to 0.2 percent after irradiation. Bement also found this result in the transverse direction at room temperature. In the burst tests, all uniform elongation values but one were reduced to 1 percent or less. None of the parameters, such as cold work, texture, or heat treatment, was effective in increasing the postirradiation uniform elongation in this test.

Total Elongation—In the unirradiated condition the total elongation also showed a decrease with increasing cold work; but, in contrast to the uniform elongation, the initial drop was not as abrupt and no minima were found. At the higher levels of cold work the curve tended to flatten out for the axial specimen, as shown by Bement's results [18], but the burst test curves at 300 C and the ring test curves at both temperatures developed a constant negative slope.

Because of the different gage lengths, the absolute values of total elongation obtained in the three tests cannot be compared directly. For flat tension specimens the shorter the gage length l or the smaller the l/\sqrt{A} ratio [19], where A is the cross-sectional area of gage length, the greater the proportion of local deformation in the gage length and the higher the total elongation. If the three types of specimens used in this investigation were considered to be flattened out, the ring test would have the smallest l/\sqrt{A} ratio (5.9), followed by the burst test (8.5) and the axial tension test (17.3). The results show that on the average the burst test has the highest total elongations and the axial tension test the lowest. Restraint imposed by the edge of the grips probably reduces the local elongation obtained in the ring test.

Although biaxiality and end restraint would also tend to reduce the elongation in the burst test, the mode of deformation in this test may actually increase the elongation as suggested by Swift [20]. He considered that the first effect of unstable strain is to cause a longitudinal region of local swelling. This produces a region of increased curvature connected to a main stable part of the tube by a transition zone of reduced curvature. Since the hoop stress is proportional to the radius of curvature, the hoop stress at the initial swelling will be decreased and increased in the transition zone. The consequence is that unstable straining, in other words wall thinning, or "necking," may develop over a considerable portion of the

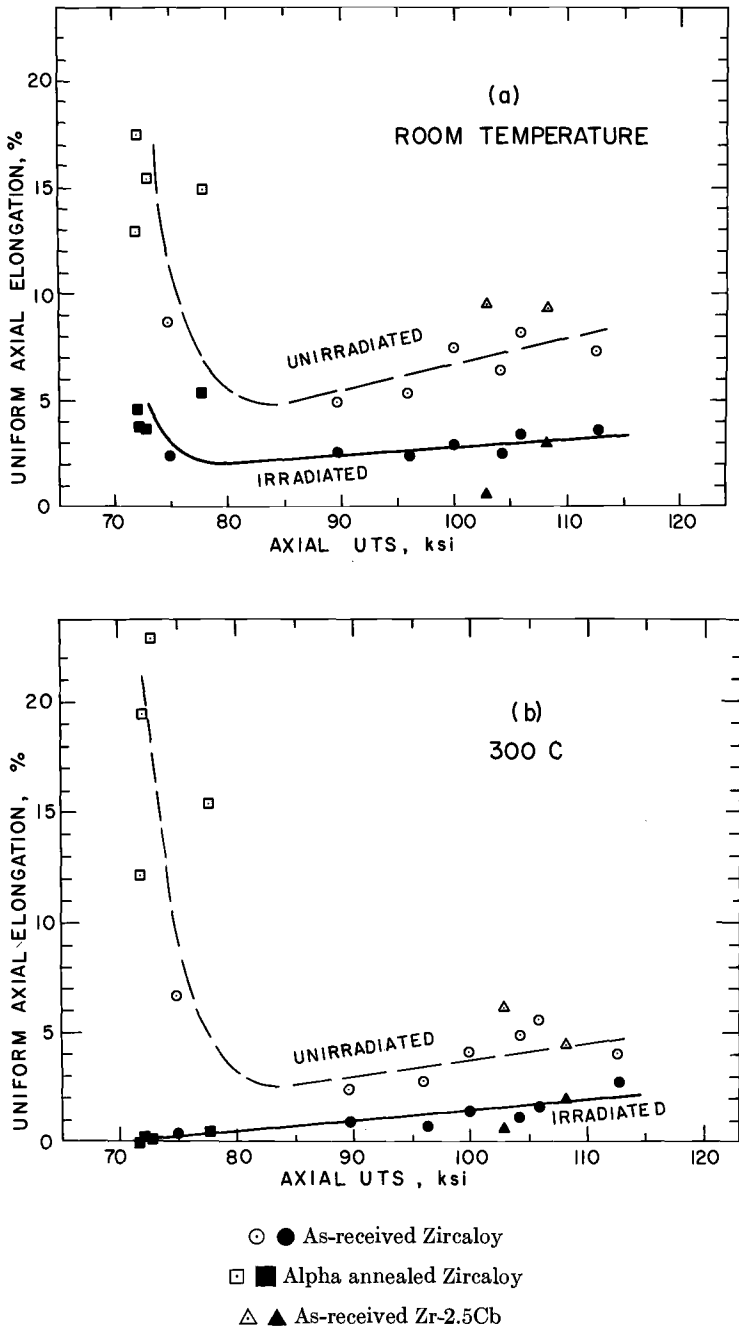
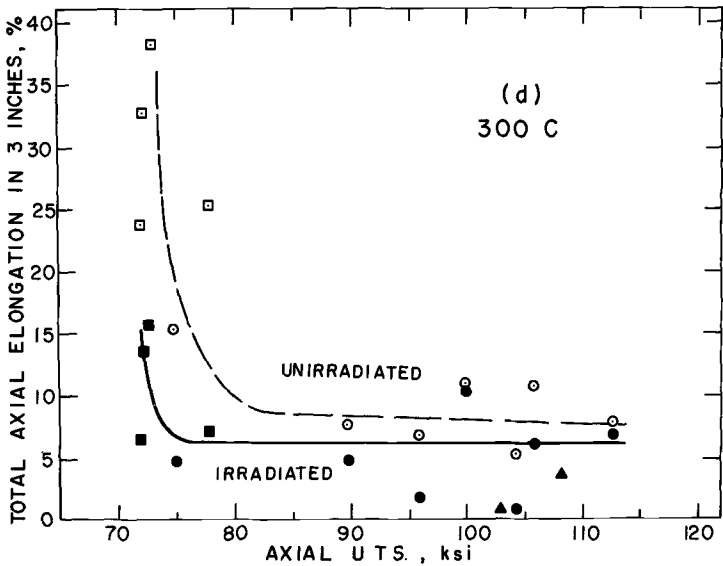
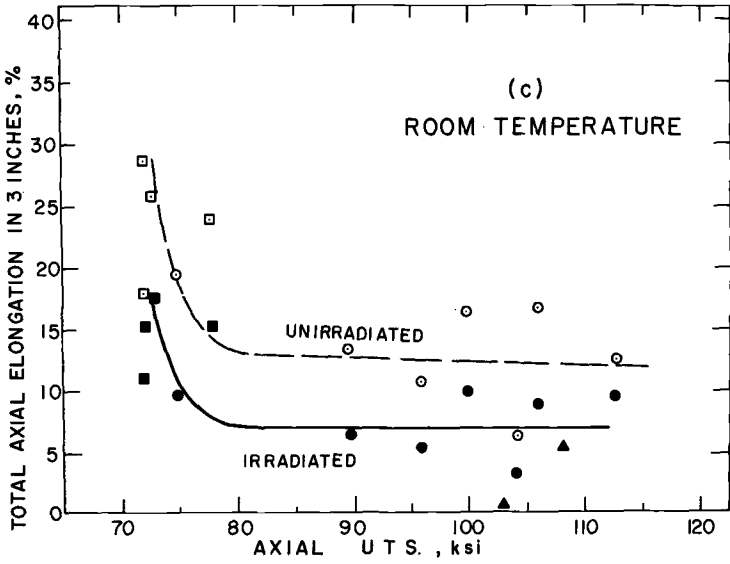


FIG. 14—Influence of cold work, as represented by the axial ultimate tensile strength, on elongation in axial tension test. Open symbols, unirradiated; closed symbols, irradiated.



- ● As-received Zircaloy
- ■ Alpha annealed Zircaloy
- △ ▲ As-received Zr-2.5Cb

FIG. 14 (Continued)

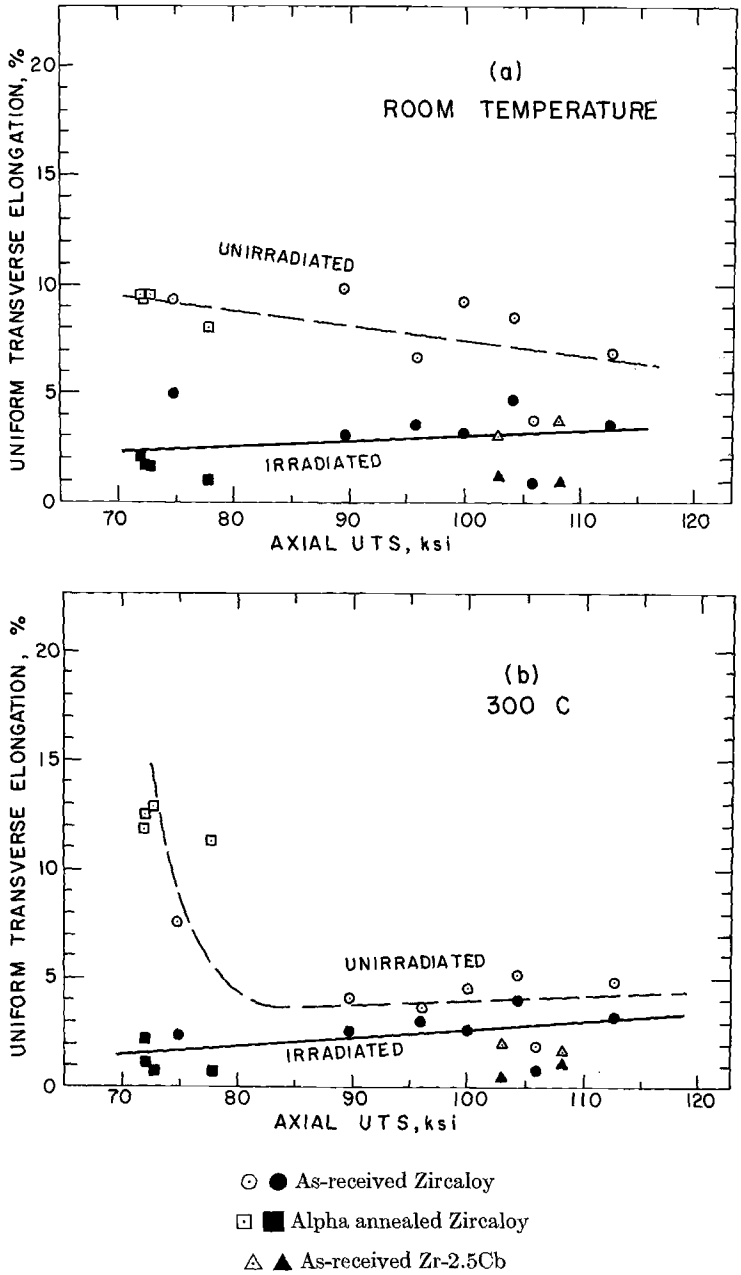
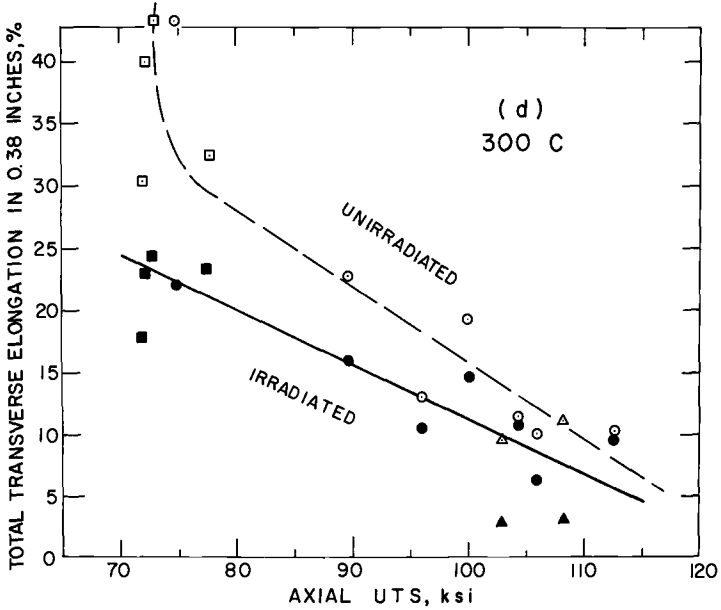
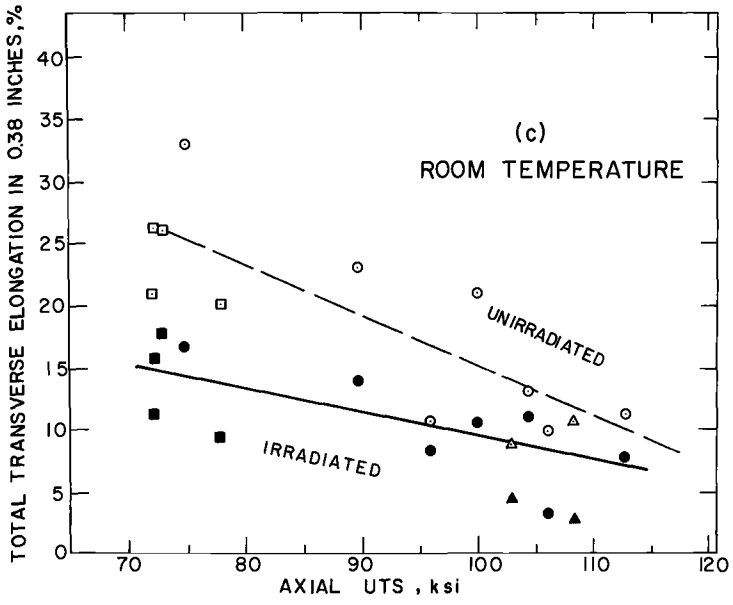


FIG. 15—Influence of cold work, as represented by the axial ultimate tensile strength, on the elongation in the transverse ring tension test. Open symbols, unirradiated; closed symbols, irradiated.



- ● As-received Zircaloy
- ■ Alpha annealed Zircaloy
- △ ▲ As-received Zr-2.5Cb

FIG. 15 (Continued)

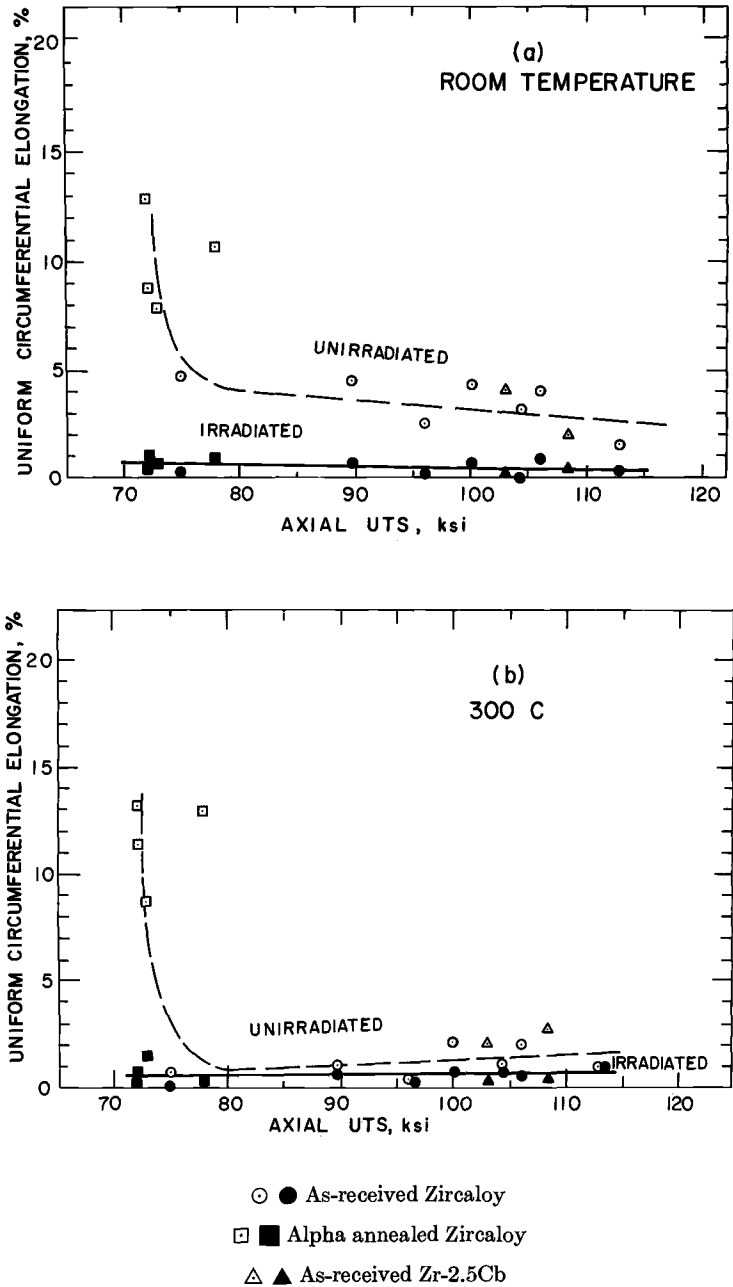
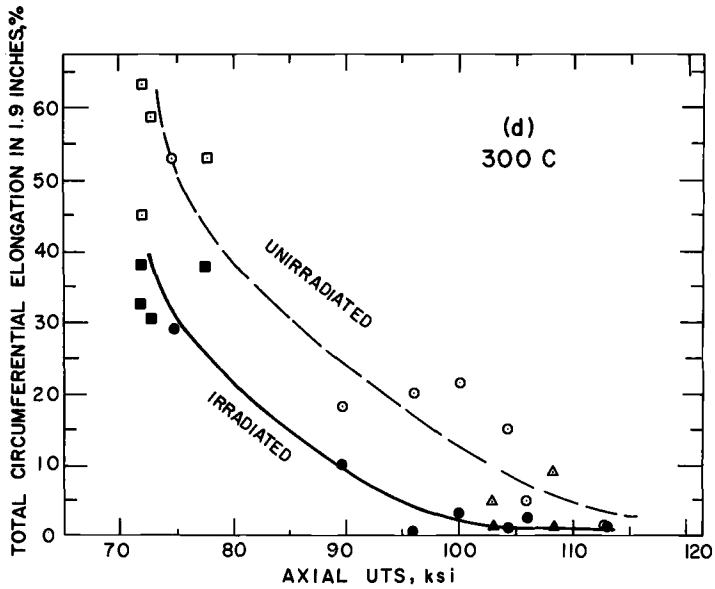
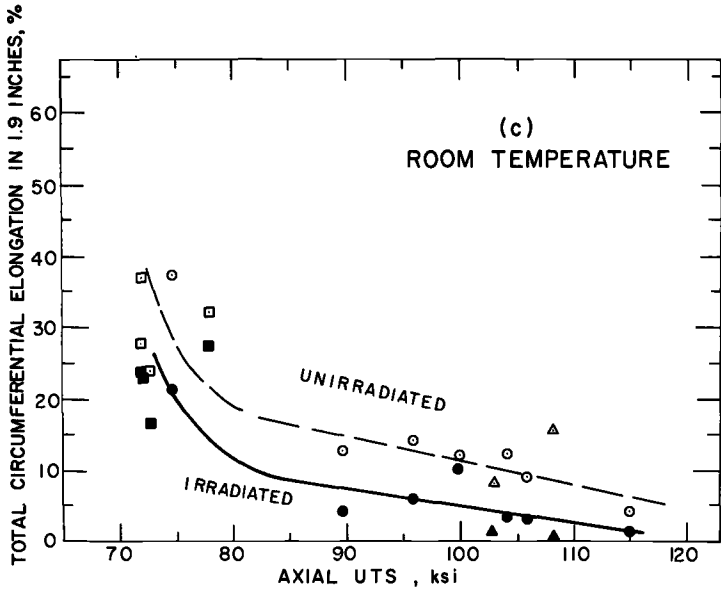


FIG. 16—Influence of cold work, as represented by the axial ultimate tensile strength, on circumferential elongations in the closed end burst test. Open symbols, unirradiated; closed symbols, irradiated.



- ● As-received Zircaloy
- ■ Alpha annealed Zircaloy
- △ ▲ As-received Zr-2.5Cb

FIG. 16 (Continued)

circumference causing larger circumferential elongations than might be expected for this type of specimen.

Irradiation caused a significant decrease in the total elongation, but not as large as that produced in the uniform elongation. The decrement in the total elongation due to irradiation decreased slightly with increasing cold work. This was mostly a reflection of the contribution of the uniform elongation to the total elongation, as the local elongation component exhibited a relatively constant decrease with irradiation. In general, the irradiated specimen curves showing the total elongation as a function of residual cold work appeared displaced below the unirradiated curves by almost a constant amount. In the case of both the axial tension and the ring tension tests, average elongations were generally above 5 percent after irradiation. For the burst test, because of the constant decrease in the total circumferential elongation (TCE) with increasing cold work before irradiation, the TCE values after irradiation at the high levels of cold work were very low. At 300 C, five values with ultimate tensile strengths above 96 ksi had average TCE values of 1 percent or below, and individual values as low as 0.2 percent were obtained. Only two or three burst specimens were tested at each condition, so a wider spread would be expected for a larger sample size. Therefore, on a statistical basis, one would expect that in a large lot of tubes of high tensile strength a certain fraction would have TCE values very close to zero. The use of such tubes would clearly be undesirable for fuel cladding where any strain was possible after it had received fluences of 2 to 3×10^{20} n/cm², $E > 1$ MeV.

Effect of Texture on Strength

The effect of texture on strength is demonstrated in the mechanical properties of batches 7 and 8 in the as-received condition. Although batch 8 had a higher level of cold work, as shown by the line broadening and axial tensile strength results, batch 7 had higher strength in the burst test but lower strength in the ring test.

These results may be explained on the basis of the anisotropy of zirconium caused by the limited deformation systems which may operate. At room temperature slip may occur on the $\{10\bar{1}0\}$ planes in the $\langle 11\bar{2}0 \rangle$ direction, twinning under tension mainly in the $\langle 0002 \rangle$ direction on the $\{10\bar{1}2\}$ planes, and to some extent on the $\{11\bar{2}x\}$ ($x=1, 2, 3$) planes, and twinning under compression along the $\langle 0002 \rangle$ direction on the $\{11\bar{2}3\}$ planes [6]. Tensile yield strengths are lowest when the tension axis is parallel to the $\{10\bar{1}0\}$ planes in the $\langle 11\bar{2}0 \rangle$ direction [21]. Since the critical resolved shear stress is a constant, the applied stress for slip to occur is proportional to the orientation factor $\cos \phi \cos \lambda$, where ϕ is the angle between the tension axis and the normal to the slip plane and λ is the angle between the tension axis and the slip direction of the slip plane. Deformation by slip is favored when the tension axis is parallel to or

within 40 deg of the basal plane, and twinning is favored if the tension axis is parallel to or within 40 deg of the basal plane normal.

Batch 7 had a high proportion of the grains oriented with the basal poles in the radial direction, and batch 8 had a high proportion in the tangential direction. In the ring test batch 7 was oriented so that it could deform easily by slip and therefore had lower strength than batch 8, which deformed mainly by twinning. However, deformation in the burst test was by a different mode: circumferential expansion occurred most easily by wall thinning rather than specimen shortening because of the axial stress. Batch 8 wall could thin easily by slip, whereas batch 7 could do so only by compression twinning and hence exhibited a higher burst strength.

The effect of texture on strength in the absence of variations in the level of cold work is evident in the results of the alpha annealed specimens. Batch 1 with a higher proportion of tangential basal poles had higher strength in the ring test, but batch 7 was stronger in the burst test. These trends hold at both test temperatures before and after irradiation.

Considering the plasticity approach to anisotropy, Hill's theory [21] indicates that increasing anisotropy causes the von Mises yield locus to become more elliptical, requiring higher stress for yielding under biaxial stress than under uniaxial stress. The higher stress required to yield and fracture the closed end burst specimens is illustrated in Fig. 17, where the ratio of the increased strength is plotted against a numerical measure of the texture or anisotropy. The latter is represented by the ratio of the fraction of grains which twin in the radial direction to the fraction which twin in the tangential direction. This plot shows higher strength ratios

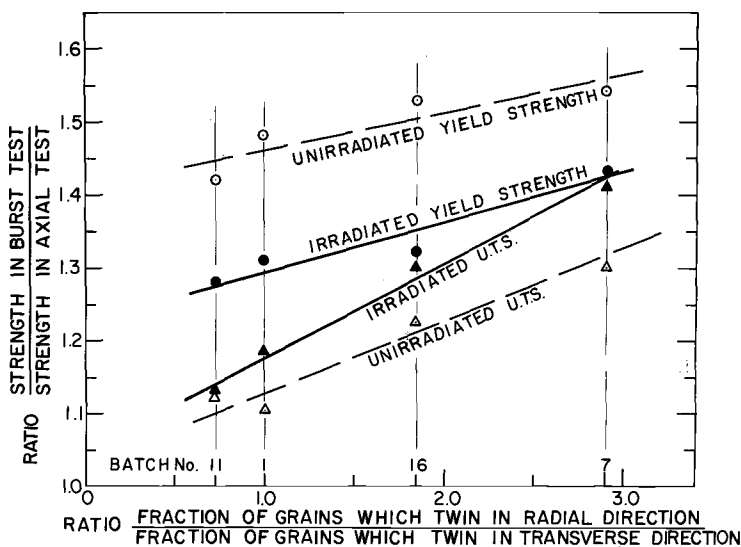


FIG. 17—Effect of texture on strength anisotropy for annealed Zircaloy 2 and 4.

with increasing texture ratios for both the yield and ultimate strengths. This texture effect is preserved after irradiation.

Effect of Texture on Elongation—Texture also has an effect on the ductility of zirconium alloys. This has been observed in the axial tube tension test [3, 22], where tubes with predominantly radial basal poles decreased in diameter but did not decrease in wall thickness whereas tubes with predominantly tangential basal poles decreased in wall thickness but did not decrease in diameter. Figure 6 shows that this effect remains after irradiation. Batch 7 showed more necking and greater elongation than batches 1, 2, and 11, which had lower cold work but fewer radial basal poles. Conversely, batch 8 had the lowest elongation, lower than batch 9 which had more cold work. This trend was also seen in the two high-strength Zr-2.5Cb batches where batch 17 shows more necking than batch 18.

Ductility in the ring tension test seemed to be much more dependent on cold work than on texture. This is illustrated in Fig. 7 where none of the rings show much edge necking, except batches 11 and 2 which have the lowest amounts of residual cold work. There is some indication that in the annealed condition texture hardening limits the ductility because batches 1 and 11, which have a higher proportion of tangential basal poles, always showed lower ductility than batches 7 and 16.

As with the rings, ductility in the closed end burst test was much more dependent on cold work than on texture. Batches with a high proportion of tangential basal poles (batch 8) generally had a low total circumferential elongation (TCE), especially after irradiation, but a very high proportion of radial basal poles (batch 7) was not noticeably better than an equal pole distribution. The extreme banana shape developed by batch 7 in the annealed condition may have reduced its TCE. This batch had a fairly high uniform elongation, and Källström [23] has indicated that the TCE may be increased by providing an internal mandrel to keep the specimen straight during testing.

Steward and Cheadle [3] had found batch 7 to have a high equivalent fracture strain. Although this parameter was not measured after irradiation, it probably did not change much, because Bement showed a relatively small decrease in reduction in area of Zircaloy 2 at this level of irradiation [18, 24]. The results indicate that a high effective strain does not necessarily result in a high TCE. Probably what is needed to achieve a high TCE is the ability of the material to spread its wall thinning around the periphery of the tube. A tube with the basal poles equally distributed between the radial and tangential directions may be best suited to do this.

Effect of Heat Treatment

Alpha annealing of the as-received tubing produced a decrease in strength and an increase in ductility in the axial tension test under all test

conditions. The effect of beta heat treatment compared to the alpha annealing was to increase the strength and decrease the ductility. This agrees with the observations of Goodwin et al [25], who found that Zircaloy 2 slowly cooled from the beta phase showed an increase in yield strength and a decrease in both ductility and UTS. Increases in the UTS have been noted for material quenched from the beta phase [26], so perhaps it is not surprising that the beta heat-treated specimens of this experiment, which were cooled at moderate rates (about 15 to 20 C/s in the 800 to 700 C temperature range), showed a modest increase in the ultimate strength.

The textural changes which occurred on beta heat treatment were not large. The $\langle 0002 \rangle$ pole texture coefficients in the D orientation were essentially zero for the alpha annealed condition and varied from 0.1 to 0.3 for the beta heat-treated condition, not large enough to account for the higher axial strength of the beta heat-treated material.

The response of the properties in the other two tests to heat treatment was somewhat more complicated. In these tests, except for batch 11, alpha annealing produced the expected increase in ductility on annealing. Batch 11, however, showed a large decrease in total elongation, probably due to the critical grain growth which occurred in this batch on alpha annealing, as can be seen in the fracture section of Fig. 11. Grozier [27] determined the critical amount of cold work necessary for grain growth on annealing to be about 9 percent. Batch 11 tubing received about 10 percent, with perhaps the more highly cold-worked outer layers being removed by pickling.

In contrast to the increase in strength produced in the axial tension test by beta heat treatment, little effect on the strength of the ring test and a decrease in strength in the burst test were noted. These effects can be explained by a grain size effect. When zirconium transforms from the beta to the alpha phase, each beta grain transforms into many small alpha platelets which are related in orientation to that of the original beta grain [28]. On plastic deformation this region deforms as though the grain size were that of the original beta grain. The pronounced roughening or orange-peel effect seen on the surface of the burst tested beta heat-treated specimens is evidence of this.

A grain size effect in alpha zirconium was found by Coleman and Hardie [29], in beta heat-treated Zr-2 $\frac{1}{2}$ Cb alloy by Bell and Dicks [30], and in beta heat-treated Zircaloy 2 by Daniel [31]. The results of the present paper suggest that the effect of the prior beta grain size and alpha annealed grain size on the mechanical properties can be related.

The yield strength at room temperature and the total elongation at 300 C have been plotted as functions of the inverse grain size in Figs. 18 and 19, respectively. The yield strength in the axial direction, where there was a relatively large number of grains to support the load, was influenced by the inherent strength of the material, hence the beta heat-treated material

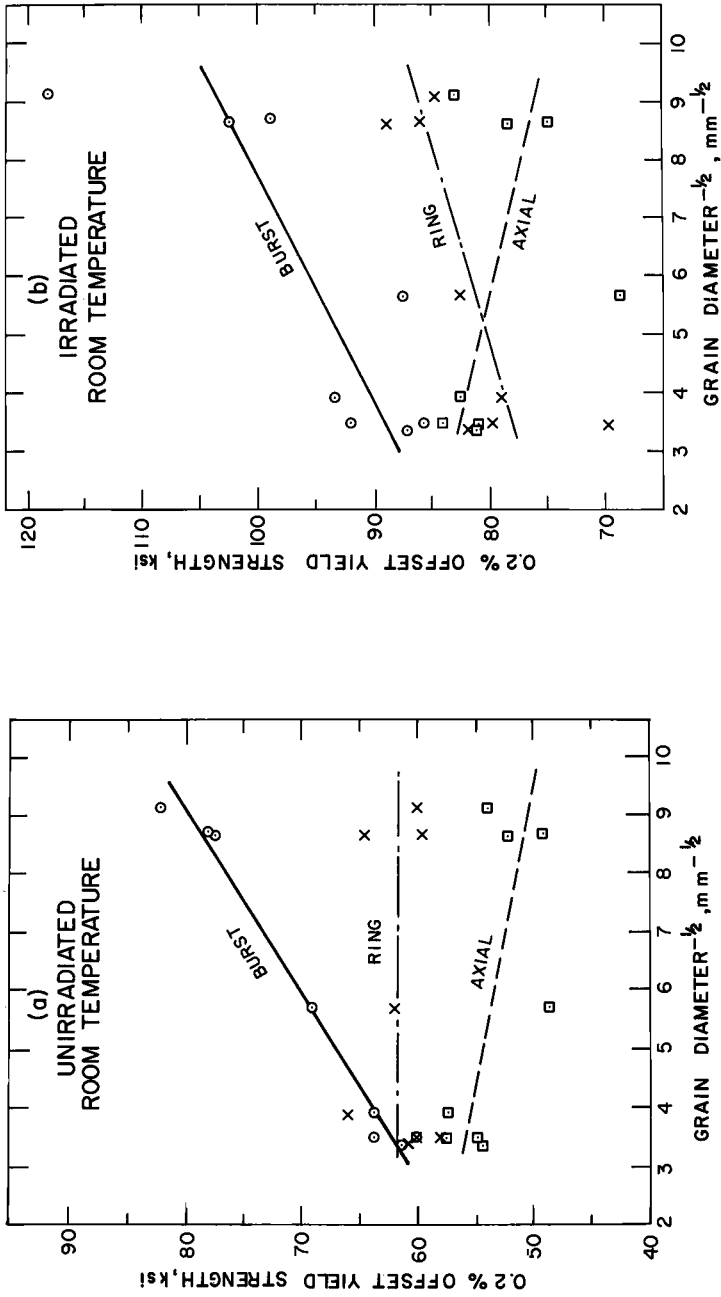


FIG. 18—Effect of grain size on yield strength in heat-treated Zircaloy 2 and 4.

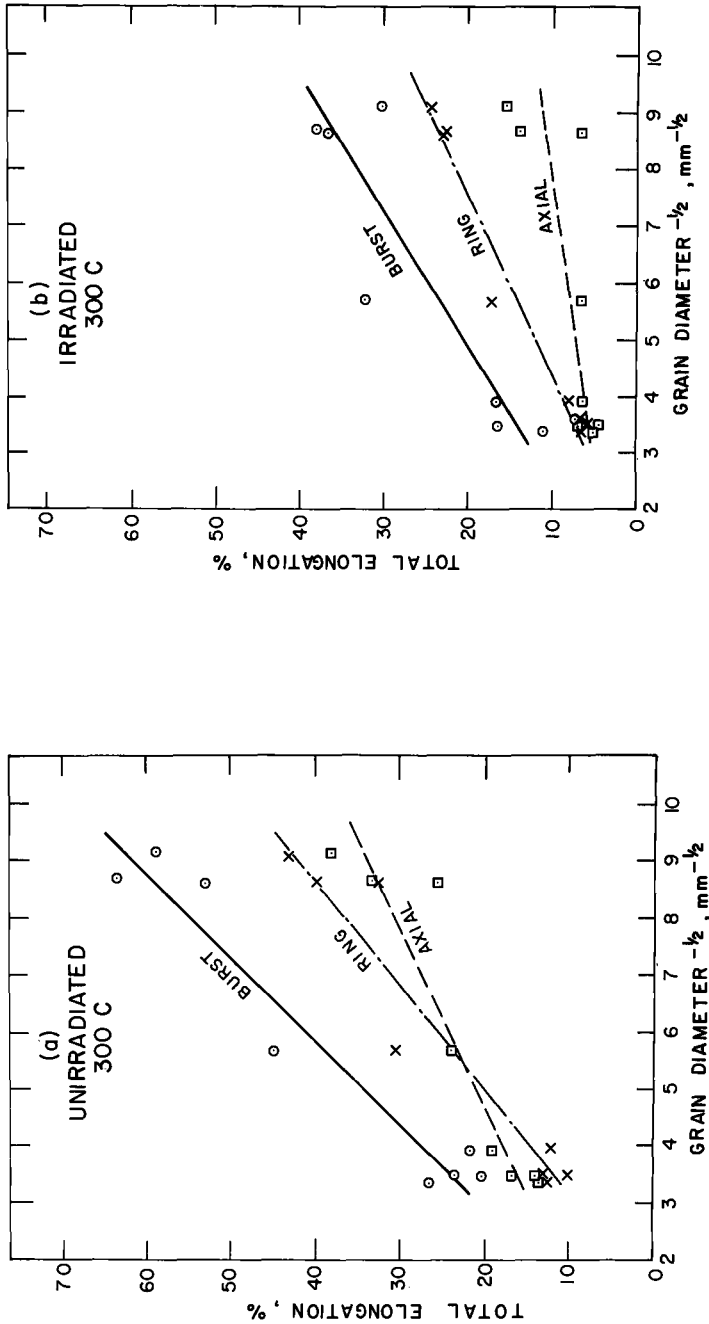


FIG. 19—Effect of grain size on total elongation in heat-treated Zircaloy 2 and 4.

was stronger. In the ring tension test, there were fewer grains to support the load, lessening somewhat the high strength of the beta heat-treated structure, while at 300 C this strength superiority was lost and the grain size effect began to dominate. In the burst test, the stress was concentrated in the grains across the wall thickness and the grain size effect swamped the inherent structural effect both before and after irradiation. The room temperature ultimate strength behaved in the same manner, but at 300 C the structural effect seemed stronger and grain size had less of an effect.

As shown in Fig. 19, grain size had a considerable effect on the total elongation at 300 C, as it had at room temperature in both the unirradiated and irradiated conditions. Again, a larger effect was seen in the closed end burst test, indicating that the grain size effect must be considered in terms of the dimensions of the load supporting member.

The effect of grain size can also be seen in the nature of the burst test fracture surfaces of Fig. 11. The fine-grained, as-received specimens showed a fairly smooth shear-type fracture inclined at about 45 deg to the tube normal. The alpha annealed specimens, with a larger grain size, showed a somewhat irregular fracture, while the beta heat-treated specimens had extremely irregular fractures. It appeared that in the beta heat-treated specimens fracture occurred at the prior beta grain boundaries; the apparent weakness of these grain boundaries has been observed previously [26, 28].

Factors Affecting the Change in Properties on Irradiation

Reference to Fig. 12 shows that there is a variation within the irradiation induced component of yield strength among the batches, particularly in the closed end burst test. The data have therefore been examined to determine whether this variation, or the variation within any of the other mechanical properties, could be related to metallurgical variables.

The effect of alloy composition has been mentioned already: the Zr-2.5 Cb alloy showed significantly greater irradiation hardening than Zircaloy 2; however, the irradiation induced change in the elongation properties was similar to that experienced in Zircaloy 2. There was little detectable difference in the response to irradiation between the properties of Zircaloy 2 and Zircaloy 4.

If the irradiation induced increment of yield strength were dependent on texture, then the increment should be different in individual batches between the axial tension test and the other types of test, or between batches 7 and 8 in the ring and burst tests, but this is not the case. There is no evidence from the present tests that texture has any influence on the irradiation induced component of yield strength, nor does it have any significant effect on the irradiation induced component in any of the other mechanical properties.

The level of cold work has a significant effect on the decrease in uniform

elongation produced by irradiation, a weaker effect on the total elongation, and no effect on the strength properties. At low levels of cold work the decrease in the uniform elongation was considerably larger than at high levels, especially at 300 C as can be seen in Figs. 14, 15, and 16. This could be interpreted as a grain size effect except for the fact that the alpha annealed specimens show a larger decrease than the beta heat-treated specimens. For the total elongation the only definite correlations were found in the axial and ring tension tests at 300 C.

Grain size did not appear to have any effect on the irradiation induced changes in any of the mechanical properties.

Summary and Conclusions

1. Prior to irradiation the relative strengths of the Zircalloys in the axial tension test were determined by the level of cold work. Texture altered this order slightly in the ring and burst tests. Irradiation increased the strength properties, with the yield strength increasing by a larger amount than the ultimate strength. The increment in strength due to irradiation was reasonably constant, independent of cold work, texture, and grain size. Thus the relative ranking of the batches after irradiation was the same as before irradiation with the original effects of cold work and texture being preserved.

2. The irradiation induced increment of yield strength was larger for the Zr-2.5Cb alloy than for the Zircalloys. There was no significant difference in the increment between Zircaloy 2 and Zircaloy 4.

3. For all tests prior to irradiation the uniform elongation of the Zircalloys was primarily influenced by the level of cold work. In general, the uniform elongation decreased abruptly with increasing cold work and then leveled off to small, constant slope.

Irradiation produced a significant decrease in the uniform elongation, especially in low-cold work material. The decrement in the uniform elongation due to irradiation decreased with increasing cold work but was little affected by texture or grain size. In the burst test all values but one were reduced to 1 percent or less regardless of the initial level of cold work, that is, the original effect of cold work was not preserved in all instances after irradiation.

4. The total elongation of the Zircalloys was also primarily influenced by cold work prior to irradiation, although texture had some effect on the deformation behavior in the axial test and a slight effect on deformation in the ring and burst tests. Irradiation decreased the total elongation but not to the same extent as the uniform elongation. The decrement in total elongation due to irradiation decreased slightly with increasing cold work. Largest decrements occurred in the burst test at 300 C, resulting in individual values as low as 0.2 percent. The cold work and texture effects were preserved after irradiation.

5. The Zr-2.5Cb alloy often showed larger decrements in the uniform and total elongation due to irradiation than did Zircalloys of equivalent cold work, probably due to the greater amount of irradiation hardening in this alloy.

6. Compared to the alpha annealed condition, beta heat treatment increased the strength and decreased the ductility of the Zircalloys in the axial tension test. Deformation of the beta heat-treated material was influenced by the large, prior beta grains. Grain size was found to affect the strength, ductility, and fracture behavior in the ring and burst tests. The effect of grain size must be related to the dimensions of the load bearing member.

7. The tests have shown many similarities between the axial tension, ring tension and burst tests, but there are also important differences relating to the effects of stress ratio, texture, and grain size. These differences indicate the desirability of simulating as closely as possible the stress ratio existing in the actual fuel cladding. Of the three tests investigated, the closed end burst simulates this most closely.

Acknowledgments

I gratefully acknowledge the significant contributions made to the earlier phases of this program by K. P. Steward, now with Gulf General Atomics, and R. S. Roberts. Specimen preparation was under the direction of A. R. Daniel, Canadian General Electric Co., Peterborough, Ontario, and D. E. Allen, formerly with the Canadian Westinghouse Co., Port Hope, Ontario. The insert preparation and experimental work was ably done by J. Oliver, W. G. Newell, and D. E. Foote. Thanks are due also to B. A. Cheadle and Miss S. Collins for providing the texture and line broadening results and to G. P. Kiely for the metallography.

References

- [1] Notley, M. J. F., Bain, A. S., and Robertson, J. A. L., "The Longitudinal and Diametral Expansions of UO₂ Fuel Elements," Report AECL-2143, Atomic Energy of Canada Limited, Nov. 1964.
- [2] Kjaerheim, G. and Rolstad, E., *Nuclear Applications and Technology*, NUATA Vol. 7, 1969, p. 347.
- [3] Steward, K. P. and Cheadle, B. A., "The Effect of Preferred Orientation on the Mechanical Properties and Deformation Behaviour of Zircaloy-2 Fuel Sheathing," Report AECL-2627, Atomic Energy of Canada Limited, Aug. 1966.
- [4] Gittus, J. H., "Theoretical Analysis of Some Forces, Stresses, and Strains Produced in Nuclear Fuel Element Cladding by Thermal Expansion of Cracked Fuel Pellets," TRG Report 1547(S), United Kingdom Atomic Energy Authority, The Reactor Group, Springfields, Aug. 1967.
- [5] Mehan, R. L., *Journal of Basic Engineering, ASME Transactions, Series D*, JBAAE, Vol. 83, 1961, p. 499.
- [6] Picklesimer, M. L., *Electrochemical Technology*, ECTCA, Vol. 4, 1966, p. 289.
- [7] Woods, C. R., "Properties of Zircaloy-4 Tubing," U.S. Atomic Energy Commission Report WAPD-TM-585, Westinghouse Electric Corporation, Bettis Atomic Power Laboratory, Dec. 1966.

- [8] Hardy, D. G., unpublished Chalk River results.
- [9] Steward, K. P., "The Properties of Cold Worked Zirconium-2.5 wt% Niobium Fuel Sheathing," Report AECL-2250, Atomic Energy of Canada Limited, March 1965.
- [10] Harris, G. B., *Philosophical Magazine*, PHMAA, Vol. 43, 1952, p. 113.
- [11] Sturcken, E. F. and Duke, W. G., "Measurement of Preferred Orientation of Thin-walled Zircaloy-2 Tubes," U.S. Atomic Energy Commission Report DP-607, I. E. du Pont de Nemours and Co., Savannah River Laboratory, Nov. 1961.
- [12] Steward, K. P., "The Properties of Cold Worked Zirconium-2.5 wt% Niobium Fuel Sheathing—Part II," Report CR-Met-1226, Atomic Energy of Canada Limited, Nov. 1965.
- [13] Cheadle, B. A., unpublished Chalk River results.
- [14] Ibrahim, E. F. in *Applications Related Phenomena in Zirconium and Its Alloys*, ASTM STP 458, American Society for Testing and Materials, 1969, p. 18.
- [15] Ells, C. E. and Fidleris, V., *Electrochemical Technology*, ECTCA, Vol. 4, 1966, p. 268.
- [16] Koppelaar, T. J. and Kuhlmann-Wilsdorf, D., *Applied Physics Letters*, APPLA Vol. 4, 1 Feb. 1964, p. 59.
- [17] Bement, A. L. in *Symposium on Radiation Effects*, Asheville, Sept. 1965, AIME Vol. 37, American Institute of Mining, Metallurgical and Petroleum Engineers, Gordon and Breach, 1967, p. 671.
- [18] Bement, A. L., "Effects of Cold Work and Neutron Irradiation on the Tensile Properties of Zircaloy-2," PhD thesis, University of Michigan, 1963.
- [19] Rudnick, A. and Carlson, R. L., "The Influence of Sheet Thickness on Tensile Properties of Metal Sheet," DMIC Memorandum 5, Defense Metals Information Center, Battelle Memorial Institute, 23 Jan. 1959.
- [20] Swift, H. W., *Journal of the Mechanics and Physics of Solids*, JMPSA, Vol. 1, 1952, p. 1.
- [21] Hill, R., *Proceedings of the Royal Society (London)*, Series A, PRSLA, Vol. 193, 1948, p. 281.
- [22] Rittenhouse, P. L., *Journal of Nuclear Materials*, JNUMA, Vol. 24, 1967, p. 310.
- [23] Källström, O. K., Letter to the Editor, *Journal of Nuclear Materials*, JNUMA, Vol. 31, 1969, p. 111.
- [24] Bement, A. L., Tobin, J. C., and Hoagland, R. G. in *Symposium on Flow and Fracture of Metals in Nuclear Environments*, ASTM STP 380, American Society for Testing and Materials, June 1964, p. 364.
- [25] Goodwin, J. G., Rubenstein, L. S., and Shubert, F. L., in *Symposium on the Newer Metals*, ASTM STP 272, American Society for Testing and Materials, 1959, p. 124.
- [26] Mudge, W. L. and Forscher, F., "Mechanical Properties of Zircaloy-2," U.S. Atomic Energy Commission Report WAPD-101, Westinghouse Electric Corp., Bettis Atomic Power Laboratory, 23 July 1954.
- [27] Grozier, J. D., "Critical Grain Growth in Zircaloy-2," U.S. Atomic Energy Commission Report WAPD-ZH-12, Westinghouse Electric Corp., Bettis Atomic Power Laboratory, Nov. 1958, p. 15.
- [28] Lustman, B. and Kerze, F., *The Metallurgy of Zirconium*, McGraw-Hill, 1955, pp. 505-508.
- [29] Coleman, C. E. and Hardie, D., *Journal of the Institute of Metals*, JIMEA, Vol. 94, 1966, p. 387.
- [30] Bell, L. G. and Dicks, T. S., *Canadian Metallurgical Quarterly*, CAMQA, Vol. 4, 1965, p. 259.
- [31] Daniel, A. R., Canadian General Electric Co., work performed under contract to Atomic Energy of Canada Limited, June 1968.

DISCUSSION

*A. L. Bement*¹—The thermal treatments giving rise to changes in grain size (alpha annealing and beta heat treatment) also cause texture rotation and the redistribution of compositional constituents. Have you eliminated the possible influences of these variables on your grain size correlation of mechanical properties?

D. G. Hardy (author's closure)—The textural differences between the alpha annealed and the beta heat-treated conditions were not large enough to account for the differences in the mechanical properties.

Redistribution of the intermetallic precipitates was observed on beta heat treatment: instead of being randomly distributed as in the alpha annealed structure, they tended to precipitate along the alpha platelet boundaries within each prior beta grain. As reported by Holt² and Ökvist and Källström,³ two different Widmanstätten morphologies have been observed in beta heat-treated Zircaloy depending on the concentration of particles insoluble in the beta phase: a "parallel plate" structure and a "basketweave" structure.

A. R. Daniel of the Canadian General Electric Co., Peterborough, Ontario, working under contract to AECL, found that, although there was a difference in the general level of the total circumferential elongation in the burst test between the two types of structure, in both cases the ductility was proportional to the prior beta grain size. All the specimens reported in this paper developed a basketweave structure. Extrapolating Daniel's TCE versus grain size curve for the basketweave structure to the alpha annealed grain size gives a TCE of 30 percent, approximately the same as the TCE of the alpha annealed specimens reported in Table 4. It therefore appears that the prior beta grain size has a similar effect on the burst properties as the alpha annealed grain size, provided the former has the basketweave structure.

¹ Battelle-Northwest, Richland, Wash. 99352.

² Holt, R. A., *Journal of Nuclear Materials*, JNUMA, Vol. 35, June 1970, p. 322.

³ Ökvist, G. and Källström, K., *Journal of Nuclear Materials*, JNUMA, Vol. 35, June 1970, p. 316.

W. J. Langford¹

Metallurgical Properties of Cold-Worked Zircaloy 2 Pressure Tubes Irradiated Under CANDU-PHW Power Reactor Conditions*

REFERENCE: Langford, W. J., "Metallurgical Properties of Cold-Worked Zircaloy 2 Pressure Tubes Irradiated Under CANDU-PHW Power Reactor Conditions," *Irradiation Effects on Structural Alloys for Nuclear Reactor Applications*, ASTM STP 484, American Society for Testing and Materials, 1970, pp. 259-286.

ABSTRACT: The performance of cold-worked Zircaloy 2 reactor pressure tubes has been assessed by destructive tests of tubes irradiated under CANDU-PHW power reactor conditions of temperature (240 to 280 C), stress (10,500 to 17,200 psi), and neutron irradiation. Reactor service increases biaxial burst strength, accompanied by a change in deformation mode that leads to reduced ductility after irradiation. Crack tolerance of the tubing is virtually unaffected by reactor service, and the critical crack length exceeds 3 in. (75 mm) at 16,000 psi (11.3 kg/mm²) hoop stress and 300 C.

Uniaxial tension tests indicate that operating stress reduces the transverse tensile strength of unirradiated tubing. Irradiation strengthening appears to be direction dependent, suggesting a possible influence of operating stress on the distribution of irradiation damage. Transmission electron microscopy shows the damage to be in the form of discrete dislocation loops.

Oxidation rate in water is enhanced by neutron irradiation but is acceptably low, as is hydrogen/deuterium pickup. Diameter measurements support the evidence from in-pile creep investigations that creep rate partly depends on fast neutron flux.

KEY WORDS: irradiation, neutron irradiation, radiation effects, nuclear reactors, moderators, nuclear reactor engineering, structural members, Zircalloys, uranium, oxides, deuterium, coolants, heavy water reactors, pressurized water reactors, pressure vessels

Zircaloy 2 has several properties which make it an attractive structural material for natural uranium fueled reactors. The effects of neutron irradiation

¹ Fuels and Materials Div., Metallurgical Engineering Branch, Chalk River Nuclear Laboratories, Atomic Energy of Canada Ltd., Chalk River, Ontario, Canada.

* CANDU-PHW denotes the Canadian design of pressurized heavy water cooled reactor utilizing natural uranium fuel and a heavy water moderator.

TABLE 1—Dimensions and metallurgical condition of the Zircaloy 2 pressure tubes.

Tube	History	Inside diameter, in.	Wall thickness, in.	Cold Work, %
289 . . .	Production Douglas Point Tube ^a	3.25	0.154	18
10 . . .	NPD reactor tube	3.25	0.170	17
130 . . .	NPD reactor tube	3.25	0.170	17
391 . . .	Prototype Pickering 1, 2 tube	4.07	0.200	20
425 . . .	NRU reactor loop tube	4.07	0.152	23

^a Rejected for power reactor use because wall thickness was 0.001 in. below specified minimum.

tion on these properties have been widely studied, usually by irradiating prepared test specimens [1, 2],² although some irradiated pressure tubes have been destructively examined [3, 4, 5].

Cold-worked Zircaloy 2 pressure tubes are in service in the Nuclear Power Demonstration (NPD) (25 MWe)³ and Douglas Point (200 MWe) CANDU-PHW power reactors, and are installed in Pickering reactors 1 and 2 (500 MWe each). This paper assesses pressure tube performance based on the destructive examination of two tubes removed from the NPD reactor after 5 years' service, and three tubes irradiated under power reactor conditions as part of test loops in Chalk River's NRU reactor.

Experimental

Material

The Zircaloy 2 pressure tubes were extruded and cold drawn nominally 18 percent, followed by autoclaving in steam for 72 h at 400 C to provide a protective adherent oxide film. Table 1 summarizes pertinent tube data, and Appendix I gives the ingot analyses.

The crystallographic texture of tube 289 was measured using the inverse pole figure technique. The pole figures are shown in Fig. 1 together with the texture coefficients of the idealized orientations. The alpha zirconium crystals (hexagonal close packed symmetry) were oriented predominantly with their basal poles in the tangential direction (orientation A, Fig. 1). Radially oriented basal poles were the next most prevalent. Remaining orientations were between the radial and tangential directions: there were no basal poles in or close to the axial direction. The NPD tubes had a similar texture [6], which is typical of extruded and cold-worked Zircaloy 2 tubes [7].

² Italic numbers in brackets refer to the list of references at the end of this paper.

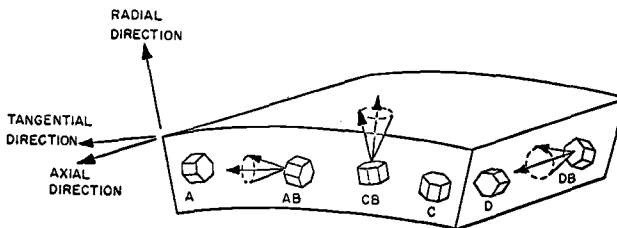
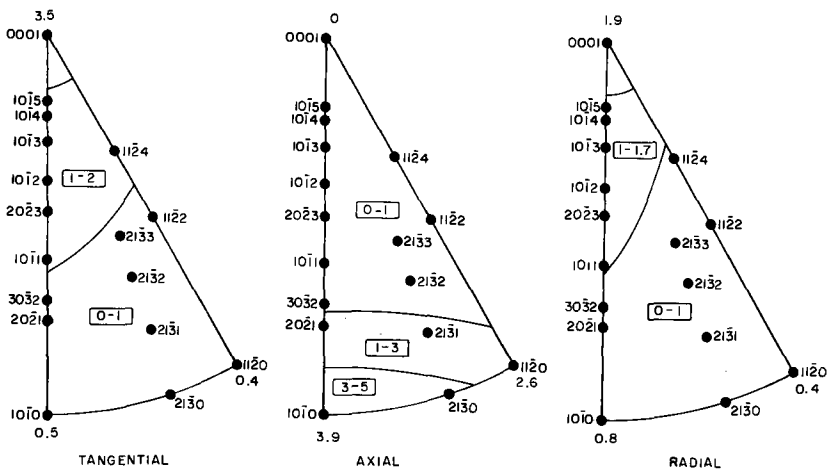
³ MWe, megawatts electrical.

Operating Conditions

The pressure tubes were internally pressurized by light or heavy water coolant at temperatures between 240 and 280 C. Table 2 summarizes operating conditions. Exposure times for the tubes have been normalized to equivalent full power days (EFPD). Energy costs from the CANDU reactor system have been assessed [8] on the basis of the reactor being on line for 7000 h/year, averaged over the reactor's lifetime. A full power year (FPY) is therefore defined in these terms as 292 EFPD.

Experimental Procedures

Appendix II shows the locations of test specimens from each pressure tube relative to neutron dose. All neutron doses in this report are for ener-



A	AB	CB	C	DB	D
3.5	1.6	1.6	1.9	---	---

[A texture coefficient of 1 denotes random orientation]

FIG. 1—Inverse pole figures and texture coefficients of the idealized orientations for Zircaloy 2 tube 289.

TABLE 2—Summary of operating conditions for the pressure tubes.

Tube Exposure (EFPD) ^a	Coolant	Coolant Temperature, deg C	Hoop Stress, psi	pH (pD) (LiOH dosed)	Coolant Chemistry			Maximum Neutron Dose n/cm ² , E>1 MeV	
					H ₂ (D ₂), cm ³ /kg H ₂ O	N ₂ , O ₂ , ppm	F ⁻ , ppm		
289	H ₂ O	280	14 000	9.3 to 10.6	3 to 10	5 to 30	<0.01	<0.1	1.2 × 10 ²¹
10	D ₂ O	252 to 273	10 500	10.2 to 10.9	<1 ^b				1.2
130	D ₂ O	252 to 273	10 500	10.2 to 10.9	1 to 3 ^c				1.2
391	H ₂ O	13 500 and 16 900	13 500 and 16 900	9.5 to 10.5	3 to 10	2 to 20	<0.02	<0.08	2.6 × 10 ²⁰
425	H ₂ O	240 to 270	17 200	9.5 to 10	0.3 to 3	0.2 to 2	<0.02	<0.08	1.6

^a EFPD = equivalent full power days.
^b 57% of exposure time.
^c 16% of exposure time.
^d 27% of exposure time.
^e Not determined.

gies greater than 1 MeV, and were computed from burnup of fuel that had been irradiated within the tubes.

Outside Diameter Measurements—The outside diameter of irradiated tube 289 was measured by a micrometer at several places along its length. At each position, diameters were measured at 30-deg intervals around the tube's circumference. Tube 289 was of particular interest because its inside diameter had been measured at intervals in pile to study the effects of neutron irradiation on creep in Zircaloy 2 pressure tubes [9].

Uniaxial Tension Tests—The tubes' dimensions largely dictate the types of test specimens which may be used. Some flat specimens were obtained, but most uniaxial tension tests were made on simple 0.25-in. (6.3-mm)-wide rings held on semicircular yokes. Miniature cylindrical specimens were obtained from low-flux areas. For future reference these specimen types are labelled F (flat), R (ring), and C (cylindrical); the specimen dimensions are shown in Appendix II.

Biaxial Burst Tests—When a tube with closed ends is internally pressurized, a biaxial stress system results in which the circumferential (hoop) stress is twice the axial stress. In isotropic material the ultimate hoop strength of such a tube, pressurized to failure, is about 15 percent greater than that measured in transverse uniaxial tension tests owing to deformation restraints imposed by the stress system [10]. Cold drawn Zircaloy 2 pressure tubing shows a further 5 percent increase in strength in biaxial tests as a result of the anisotropic deformation of the highly textured material [11]. Biaxial burst tests therefore give a more realistic indication of reactor pressure tube properties than do uniaxial tension tests.

The tests were made on 11-in. (280-mm) and 18-in. (455-mm) tube specimens, the ends of which were sealed with heavy end caps and trapezoidal copper seals. Circumferential and longitudinal strain gages were attached to the outer surface at the thinnest wall section.

Crack Tolerance Tests—An internally pressurized reactor pressure tube operating below its yield stress is unlikely to fail catastrophically; however,

TABLE 3—*Outside diameters of tube 289 before and after irradiation.*

Measurement Position ^a	Original Diameter, in.	Final Diameter, in.	Diameter Increase, in.
466.5	3.5764	3.5788	0.0024
465	3.5766	3.5797	0.0031
463.5	3.5767	3.5825	0.0058
461	3.5772	3.5839	0.0067
460	3.5783	3.5839	0.0056
457.5	3.5760	3.5792	0.0032
456.5	3.5757	3.5782	0.0025
455.5	3.5754	3.5765	0.0011

^a Elevations in NRU reactor are given in feet above sea level.

defects or damage incurred during service could reduce tube strength: a sufficiently large defect will be unstable at operating stress, and consequently the tube could fail rapidly. The length of this "sufficiently large" defect is the critical crack length of the tube for that stress.

The experimental approach used in this evaluation was to burst tubular specimens each containing a thin longitudinal slit of preselected length. The slits were about 0.006 in. (0.15 mm) wide, cut by spark machining, and were sealed with a soft aluminum liner before testing. Further details of this test technique are given in Ref 12.

Metallography and Analysis—Specimens for metallography and hydrogen/deuterium analysis were cut from rings taken from various locations on the tubes, as shown in Appendix II.

Results

Diameter Measurements—The pre and postirradiation diameters of tube 289 are given in Table 3; Fig. 2 compares the tube profiles obtained from measurements of in-pile creep [9] and postirradiation diameters.

Uniaxial Tension Tests—Type R specimens were obtained from tubes 10, 130, and 289; type F specimens from tubes 130 and 289; and type C specimens from tube 289. No tension test specimens were taken from irradiated tubes 391 or 425. Tension tests were carried out at 20, 280, and

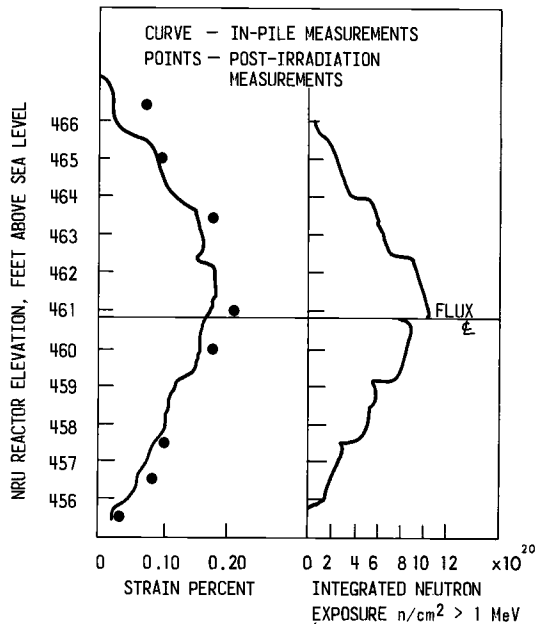


FIG. 2—Diameter profiles of irradiated Zircaloy 2 tube 289.

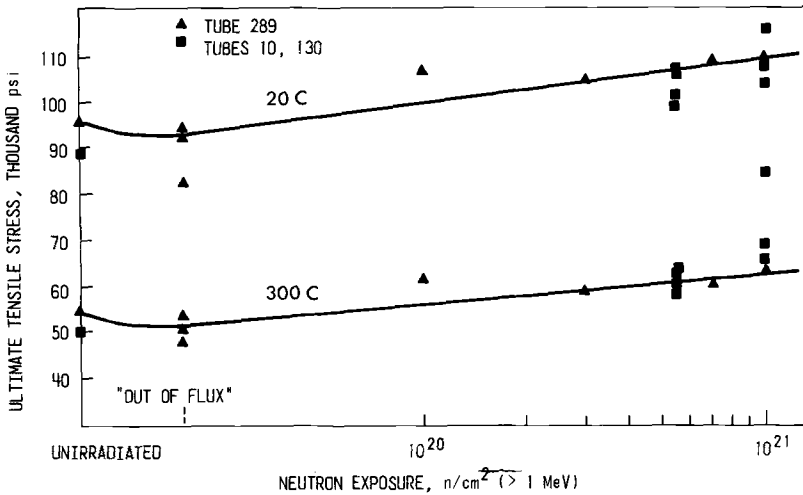


FIG. 3—Ultimate tensile stress versus neutron exposure for cold-worked Zircaloy 2 (transverse).

300 C. Tables 4 and 5 present the test results, and in Fig. 3 ultimate tensile strength (UTS) is plotted as a function of fast neutron dose.

Biaxial Burst Tests—Two specimens from tube 289 and one from tube 130 were burst at 300 C. One of the specimens from tube 289 contained at its midpoint damage caused by a fuel stop or installation tool during service in the experimental loop. The damage is shown in Fig. 4; the maximum depth was 0.016 in. (0.4 mm), measured from the plastic replica. Test results are given in Table 6, which includes data from unirradiated tubes for comparison.

The damaged specimen from tube 289 failed after local thinning of the damaged region. Wall thickness reduction in the remainder of the specimen was only 2 percent. The other two specimens failed at their thinnest wall section. All fractures were completely ductile.

Crack Tolerance (Slit Burst) Tests—Slit burst specimens were prepared from all five tubes. Tests were conducted at 20 and 300 C, and Table 7 gives the results, including data from unirradiated tubes for comparison. Figure 5 shows failure stress plotted as a function of slit length.

Oxide Thickness—Oxide thicknesses on the inside and outside surfaces of tubes 10, 130, and 289 were measured on metallographic sections. The average oxide thickness on the outer tube surfaces (in contact with air during irradiation) was 1 to 3 μm . Patches up to 6 μm and areas free of oxide were also seen. On the inside surface (in contact with pressurized water coolant) oxide thickness varied from 2 to 14 μm , with patches up to 24 μm being seen in tubes 10 and 130. The oxide was frequently cracked and blistered. Table 8 gives the results.

TABLE 4—Tension results: Zircaloy 2 pressure tube 289.

Specimen Type	No	Elevation, ft	Neutron Dose, n/cm ² , E > 1 MeV	Direction	Test Temp., deg C	0.2% YS, kpsi	UTS, kpsi	Elongation, %		Reduction in Area, %
								Uniform	Total	
C.....	1	Archive	0	Tangential	300	50.9	55.0	1.1	6.4	64
	2		0		300	51.3	54.7	1.3	6.0	63
	3		0		20	83.6	94.2	3.3	7.9	48
	4		0		20	88.6	97.5	3.0	7.7	46
	5	454	Out of flux		300	47.7	53.8	3.5	7.4	53
	6				300	47.7	53.8	3.8	8.7	51
	7				20	82.0	95.6	7.4	12.0	37
	8				20	82.0	96.1	6.7	9.7	38
	9				300	47.2	50.6	1.2	6.1	68
	10				300	46.2	50.6	1.1	6.0	74
	11				20	85.5	92.4	3.2	7.3	49
	12				20	86.5	93.7	3.5	8.6	49
R.....	13	467.5			300	Not obtainable on Type R specimens	51.0	Not obtainable on Type R specimens		57
	14				20	obtainable on Type R specimens	94.0			30
	15				20		95.5			34
	16	466	1 × 10 ²⁰		300		60.0			54
	17				300		63.3			48
	18				20		106.0			26
	19				20		108.0			32
	20	457.5	3 × 10 ²⁰		300		60.0			52
	21				300		58.5			57
	22				20		104.0			39
	23				20		106.5			41
	24	462	1 × 10 ²¹		300		65.0			53
	25				20		108.6			33
	26				20		111.5			43

F.....	27	459	7×10^{20}	300	54.2	61.8	2.0	13.0	60
	28			300	51.5	60.2	2.2	12.6	61
	29			20	92.5	109.8	2.6	10.0	28
	30			20	91.5	109.6	3.0	11.2	33

C = cylindrical, R = ring, F = flat.

TABLE 5—Tension results: NPD Zircaloy 2 pressure tubes.

Tube	Specimen Location	Neutron Dose, n/cm ² , E>1 MeV	Direction	Specimen Type	Test Temperature, deg C	0.2% YS, kpsi	UTS, kpsi	Reduction in Area, %	Elongation in 1 in., %
10.....	Coolant Outlet end	5.5×10 ²⁰	Tangential	R	20	^a	102.0	38	^a
				R	280	...	58.5	63	...
	Coolant Inlet end	1.2×10 ²¹	Tangential	R	20	...	107.0	35	...
				R	280	...	63.3	57	...
	≈Flux Center	5.5×10 ²⁰	Tangential	R	20	...	108.3	35	...
				R	280	...	66.1	50	...
130.....	Coolant Outlet end	5.5×10 ²⁰	Tangential	R	20	...	99.8	38	...
				R	280	...	61.3	51	...
	Coolant Inlet end	5.5×10 ²⁰	Tangential	R	20	...	107.4	40	...
				R	280	...	64.7	53	...
	≈Flux Center	1.2×10 ²¹	Tangential	R	20	...	104.5	36	...
				R	280	...	69.5	54	...
≈Flux Center	Unirradiated	5.5×10 ²⁰	Axial	F	20	100.1	117.0	23	5.3
				F	280	79.9	85.2	31	5.7
Production NPD tubes (Ref 13)	Unirradiated	Unirradiated	Tangential	F	20	71.0	89.1	33	20.5
				F	300	44.0	51.9	46	21.4
				^b	20	83.0	87.0	^c	^c
				^b	300	46.7	47.5	^c	^c

^a 0.2% YS and elongation are not normally measured on ring tension specimens.

^b Miniature "Chevenard" tension specimens.

^c Not reported.

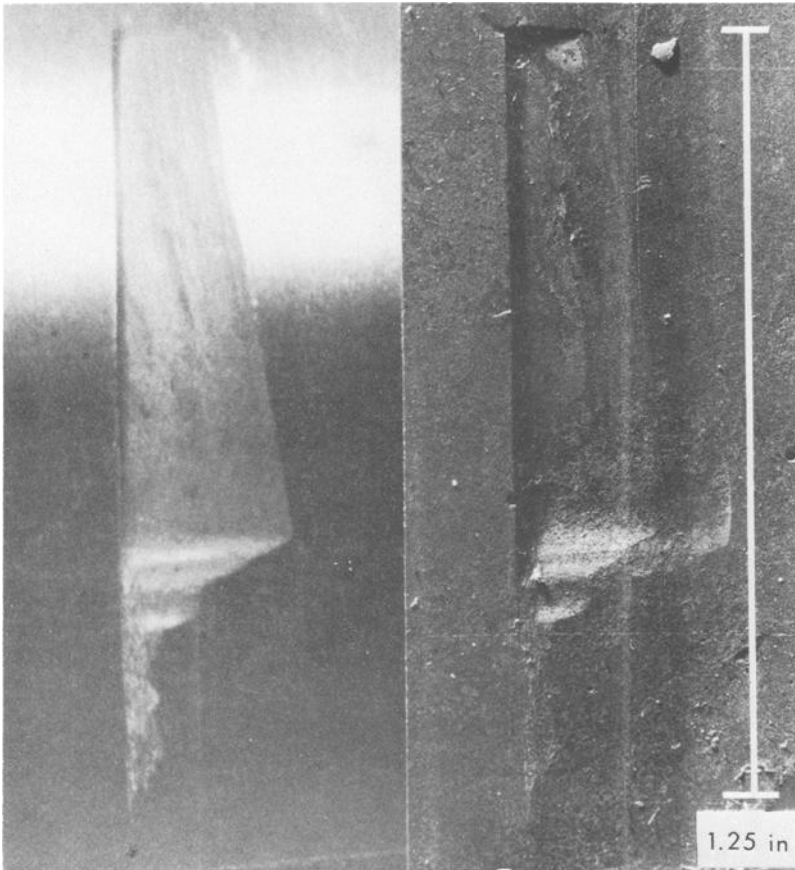


FIG. 4—Defect in tube 289 at an elevation of 464 ft 8 in.: left, viewed from inside the tube through a borescope and, right, epoxy replica. White scale mark is parallel with longitudinal axis of tube.

Hydrogen/Deuterium Analyses—Specimens adjacent to the oxide thickness specimens were analyzed for hydrogen and deuterium (tubes 10 and 130 only) by vacuum fusion techniques. Results can be found in Table 8.

Discussion

Diameter Changes

The postirradiation diameter measurements agree well with the in-pile measurements of Ross-Ross and Hunt [9] but are generally slightly larger. This is probably due to small differences in the techniques used to measure the initial and final diameters. Reference unirradiated tube data recorded

TABLE 6—*Biaxial burst test results on Zircaloy 2 pressure tubes at 300 C.*

Tube	Neutron Dose, n/cm ² , <i>E</i> > 1 MeV	0.2% Yield Stress, psi	Burst Stress, psi	Wall Reduction, %	Circum- ferential Increase, %
130.....	9.0×10 ²⁰	79 000	80 000	12.5 ^a	8
Archive NPD tube.....	0	56 000	61 000	30	20
289.....	1.0×10 ²¹	77 000	77 000	17	7
289 ^b	3.6×10 ²⁰	75 000 ^c	77 000 ^c	20 ^c	10
Archive Douglas Point tube....	0	60 000	63 000	28	30

^a Or higher. Fracture surface damaged during test.

^b Containing 0.016-in.-deep defect at midpoint.

^c Based on minimum wall thickness at defect.

TABLE 7—*Results of slit burst tests: Zircaloy 2 pressure tubes.*

Tube	Neutron Dose, n/cm ² , <i>E</i> > 1 MeV	Specimen Length, in.	Test Temperature, deg C	Slit Length, in.	Failure Stress, psi
10.....	1.2×10 ²¹	18	300	3	17 600
	1.2×10 ²¹	18	20	2	28 600
	8.0×10 ²⁰	18	20	4	16 300
130.....	1.2×10 ²¹	11	20	3	17 200
	1.0×10 ²¹	11	300	2.5	24 000
	8.0×10 ²⁰	11	20	2.5	21 300
	8.0×10 ²⁰	11	300	2	34 200
Archive NPD tubes.....	0	11	300	2	24 800
	0	11	20	2	34 400
	0	11	300	3	19 000
	0	11	20	3	20 400
	0	11	300	2.5	21 100
	0	11	20	2.5	23 000
	0	11	300	3	18 700
289.....	7.0×10 ²⁰	18	300	3.5	16 000 ^a
	2.0×10 ²⁰	18	300	3	16 800
	Out of flux	18	300	3	15 000
391.....	2.6×10 ²⁰	11	300	1.5	44 000
	2.6×10 ²⁰	11	300	3	21 900
	2.6×10 ²⁰	11	300	1.5	38 600
	2.6×10 ²⁰	11	300	3	18 000
	Out of flux	11	300	1.5	39 200
	Out of flux	11	300	3	16 200
425.....	1.6×10 ²⁰	11	300	2.25	25 250

^a Or higher. Seal failed causing slow leakage. Slight crack extension observed.

TABLE 8—Oxide thickness on inside tube surface (pressurized water coolant), hydrogen and deuterium analyses: Zircaloy 2 pressure tubes.

Tube	Neutron Dose, n/cm ² , E > 1 MeV	Oxide Thickness, μm		H ₂ Concentration, ppm	Standard Deviation	D ₂ Concentration, ppm
		Mean	Maximum			
Coolant inlet.....	Out of flux	2	5	34	7.2	...
	3.5×10 ²⁰	4	12	33	1.7	...
	7.0×10 ²⁰	7	14	36	6.8	...
	1.1×10 ²¹	5	10	33	5.8	...
Coolant outlet.....	6.0×10 ²⁰	5	5	34	6.9	...
	2.3×10 ²⁰	4	7	29	3.6	...
	Out of flux	2	5	28	2.7	...
	Archive.....	0		23		
Coolant inlet.....	5.5×10 ²⁰	5	9	23 ^a
	7.0×10 ²⁰	6	14
	1.2×10 ²¹	10	24	19	2.1	17 ^a
Coolant outlet.....	7.0×10 ²⁰	4	8
	5.5×10 ²⁰	4	9	9 ^a
Coolant inlet.....	5.5×10 ²⁰	9	15	31 ^a
	1.2×10 ²¹	11	23	11 ^a
	7.0×10 ²⁰	11	21
Coolant outlet.....	5.5×10 ²⁰	6	10	11 ^a

^a Average of three results; all other analyses are average of twelve results.
NOTE—First eight rows refer to tube 289, next five to 10, and last four to 130.

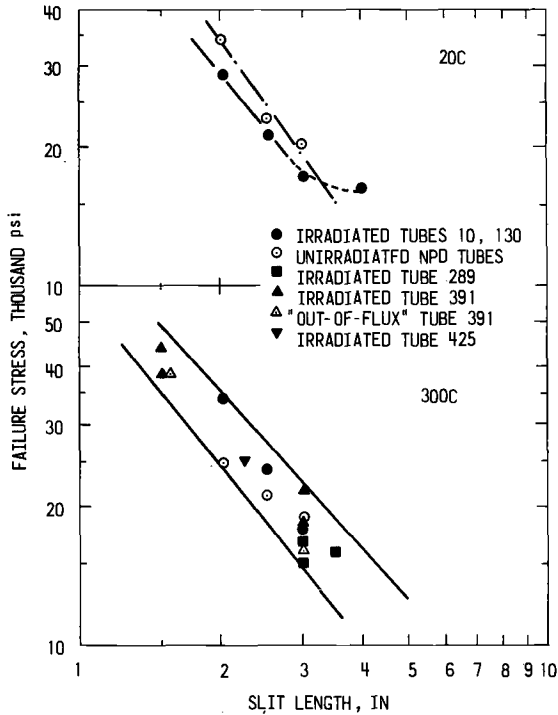


FIG. 5—Failure stress versus slit length for cold-worked Zircaloy 2 pressure tubes.

TABLE 9—Comparison of transverse UTS values of Zircaloy 2 pressure tube material.

Tube	Neutron Dose, n/cm ² , E > 1 MeV	Test Temperature, deg C	UTS, psi
130.....	0	20	87 000
289.....	0	20	95 800
363.....	0	20	94 000
130.....	0	300	47 500
289.....	0	300	54 800
363.....	0	300	50 400
130 ^a	5.5 × 10 ²⁰	20	107 400
289 ^a	3.0	20	105 200
363 ^b	2.3	20	115 700
130 ^a	5.5	300	64 700
289 ^a	3.0	300	59 200
363 ^b	2.3	300	64 700
130 ^a	1.2 × 10 ²¹	20	104 500
	1.2	300	69 500
289 ^a	1.0	20	110 000
	1.0	300	65 000

^a Irradiated as a pressure tube.

^b Irradiated as tension specimens [12].

by Ross-Ross and Hunt were based on measurements of three diameters 60 deg apart, while their in-pile measurements used six diameters at 30-deg intervals. The diameters recorded after irradiation were also averaged from six measurements.

The postirradiation measurements support the conclusions of Ross-Ross and Hunt that the in-reactor creep rate of cold-worked Zircaloy 2 in the temperature range 250 to 300 C depends on fast neutron flux ($E > 1$ MeV), temperature, and hoop stress according to the equation

$$\dot{\epsilon}_t = 4 \times 10^{-27} \sigma_t \phi (T - 160) / h$$

where

$\dot{\epsilon}_t$ = transverse strain rate, h^{-1} ,

σ_t = transverse stress (up to 17,200 psi), and

T = operating temperature, deg C.

Figure 2 shows quite clearly the correspondence between integrated neutron exposure and pressure tube diameter.

Biaxial Burst Properties

Unirradiated Zircaloy 2 pressure tubes show high circumferential and radial strains to failure under burst test conditions when compared with isotropic materials such as steel [6].

Reactor service increased the biaxial burst strength of tubes 130 and 289, with an attendant drop in ductility (Table 6). Irradiation has reduced the initially high circumferential and radial strains: this reduction in ductility can be explained using the following model [14]. Irradiated cold drawn Zircaloy 2 with a texture oriented for $\{10\bar{1}2\}$ twinning in tension generally shows an abrupt yield point in uniaxial tension tests at 300 C. This is attributed to mobile dislocations sweeping channels free of defects: the moving dislocations absorb defects and thus reduce the stress required to move following dislocations. Evidence of such sweeping of defects has been reported by Williams and Gilbert [15]. The situation after yield is unstable, since the stress to initiate plastic flow exceeds the stress required to maintain the flow. In the irradiated tube under biaxial stress, plastic flow commences if a local stress concentration (usually the thinnest wall section) reaches yield, after which it can continue unstably. Failure occurs in this region while the remainder of the tube wall has barely yielded, leading to reduced general deformation. The specimen containing the defect (Fig. 4) provided a good example of highly localized deformation.

Crack Tolerance

In slit burst tests at 20 C, reactor service has slightly reduced failure stress for a given slit length. Aungst and Defferding [3] found little effect

of neutron irradiation on the room temperature failure stress of flawed KER Zircaloy 2 pressure tubing but did not report neutron dose. In both KER and CANDU tubing, pre and postirradiation critical crack lengths were very large in relation to tube wall thickness.

Results at 300 C fall in a fairly well defined band (Fig. 5), but within the band certain trends are evident. Irradiated tubing is stronger than unirradiated tubing with slits below 2.5 in. (65 mm) in length, and even with 3-in. (75-mm) slits irradiated tube 391 is stronger than an out-of-flux specimen. The 20 C results can be superimposed on the 300 C band, indicating that failure stresses are relatively insensitive to test temperature in this temperature range.

In an unirradiated Zircaloy 2 pressure tube containing a sharp defect, extensive plastic deformation can occur at the stress concentration, effectively blunting the tip of the defect. During this deformation the material adjacent to the defect is strain hardened. Extension of the defect, that is, catastrophic failure, is then possible only when the stress concentration reaches the tensile strength of the material adjacent to the tip of the defect. Irradiated tubing on the other hand shows almost no strain hardening, yielding being followed almost immediately by unstable plastic collapse. Failure of irradiated tubes with defects thus occurs when the stress concentration at the tip of the defect reaches yield stress, and the defect extends as the material collapses plastically ahead of it. Since the yield stress of irradiated tubing is slightly higher than the UTS of unirradiated tubing, irradiated tubing fails at similar stresses to unirradiated tubing, accompanied by plastic work and in a high energy absorbing, ductile manner.

The length of defect which will be unstable under reactor design conditions (the "critical crack length") is found by interpolation from Fig. 5. Thus, for Pickering reactors 1 and 2 and for the Douglas Point reactor (all 16,000 psi at 300 C), the critical crack length is about 3 in. (75 mm). Defects this large could not credibly remain undetected. Coolant is expected to leak from a crack longer than about twice the tube wall thickness [16], revealing the presence of the crack before it reaches critical size.

The credibility of "leak before break" as a safety criterion was demonstrated when a Zircaloy 2 pressure tube in a Chalk River reactor loop was damaged during experimental studies of abnormal flow conditions. A three-finned fuel stop came loose and fell to the bottom of the tube, where it fretted three marks into the 0.160-in. (4.1-mm) tube wall in an out-of-flux region. The worst mark was 0.135 in. (3.4 mm) deep and about 1 in. (25 mm) long. Under the operating stress of 17,800 psi (based on original wall thickness) at 300 C, the remaining 0.025-in. (0.63-mm)-thick web cracked through, releasing coolant into the gas annulus surrounding the tube. The leakage was detected and the reactor shut down for inspection. Subsequent examination showed the crack to be about 0.5 in. (13 mm) long at

the outer tube surface. The critical crack length of this tube at 17,800 psi and 300 C predicted from Fig. 5 is about 2.5 in. (65 mm), indicating a substantial safety margin between the crack length at the time of detection and the critical length.

The effects of precipitated hydrides on failure stresses in flawed Zircaloy 2 pressure tubes have been reported earlier [12]: hydrogen (200 ppm by weight) did not affect failure stress at 300 C but reduced it at 20 C; even in this case the critical crack length at 16,000 psi exceeds 2 in. (25 mm). The hydrogen (deuterium) concentrations found in the present work indicate that concentrations in power reactor pressure tubes are unlikely to reach 250 ppm in a 30-year lifetime. The risk of unacceptably short critical crack lengths arising from hydrogen embrittlement is therefore considered to be very low.

Uniaxial Tensile Strength

The main purpose of the uniaxial tests was to show that tube strength continues to be consistent with reactor operating requirements. Irradiation conditions were those of operating pressure tubes rather than a controlled irradiation experiment. Mechanistic interpretation of the effects of reactor service is restricted because the predominant type R (ring) specimens do not permit measurement of yield stress, the usual index of irradiation damage. Within these limitations, some observations were made which indicate that long-term performance of pressure tubes will differ slightly from that predicted by small specimen irradiations, since actual service conditions (temperature variation, biaxial stress, irradiation) are not easily simulated.

In general, the uniaxial tensile strengths of the tubes increased steadily with neutron dose, as shown in Fig. 3, agreeing with the results of small specimen irradiations.

Effect of Temperature—Tubes 10 and 130 showed higher UTS values at the coolant inlet end (252 C) than at coolant outlet (273 C), particularly in tests at 20 C. Neutron dose is the same at each end. The back end of an extruded and cold drawn tube is slightly stronger than the front end [13], probably because the back end of the extrusion billet is cooler at the moment of extrusion, leading to more residual cold work in the back end of the tube. In the NPD reactor the back ends of tubes 10 and 130 were at the coolant outlet end. Assuming that these ends were slightly stronger at the time of installation, the difference in circumferential UTS between inlet and outlet ends of the irradiated tubes may be significant, and possibly suggests differential recovery of irradiation damage and cold work due to the temperature gradient along the pressure tube. Data are limited and some scatter is evident, but the trend seems consistent in the two NPD tubes. The effect is not observed in tube 289, possibly reflecting the considerably shorter exposure of the tube.

Effect of Operating Stress—Tube 289 extended above and below the zone of neutron flux in the NRU reactor test loop: the ends of this tube therefore were exposed to out-of-flux conditions of temperature and biaxial stress. Tension specimens from these areas showed (Table 4) that transverse 0.2 percent YS (yield strength) and UTS had fallen slightly below the unirradiated (archive) values at 20 and 300 C; comparable longitudinal tests were not done. Similar effects had been observed previously in the examination of another irradiated Zircaloy 2 pressure tube [17].

These observations may indicate that stress enhanced recovery of cold work has taken place. Such recovery has been reported for aluminum and iron [18], where the effect of stress is to accelerate dislocation climb, an essential part of the recovery process.

Transverse tension test data from the irradiated portions of the pressure tubes are compared in Table 9 with data from tension test specimens prepared from pressure tubes and irradiated unstressed [12]. At 20 C the irradiated pressure tubes are less strong than the unstressed specimens, even though the pressure tubes received roughly four times as much neutron irradiation; at 300 C the strengths are similar. This tends to support the suggestion that some recovery is occurring under the influence of stress.

In the internally pressurized tube, transverse stress is twice as large as longitudinal stress, so, if stress influences properties, transverse strength might be expected to increase proportionately less than longitudinal strength during neutron irradiation. Table 5 shows this to be true. However, the longitudinal pressure tube specimens show proportionately much larger strength increases than the longitudinal specimens irradiated unstressed (Table 10), which indicates that stress per se does not reduce the extent of irradiation strengthening and, therefore, that directional properties of the tube material may be involved.

TABLE 10—Comparison of longitudinal strengths of Zircaloy 2 pressure tube materials.

Test Temperature, deg C	Tube	0.2% YS, kpsi		UTS, kpsi	
		130	363 ^a	130	363 ^a
20	Unirradiated	71.0	83.0	89.1	96.0
	Irradiated	100.1	109.3	117.0	112.7
	Increase	29.1	26.3	27.9	16.7
	% Increase	40	31	31	18
280 and 300 ^b . . .	Unirradiated	44.0	48.4	51.9	53.5
	Irradiated	79.9	64.6	85.2	64.8
	Increase	35.9	16.2	33.3	11.3
	% Increase	82	33	63	21

^a From Ref 12 (irradiated unstressed).

^b Tube 130 specimens tested at 280 C, tube 363 specimens at 300 C.

Effect of Crystallographic Texture—In cold drawn Zircaloy 2 tubes most basal poles lie in the circumferential direction (see Fig. 1) so that under longitudinal tension the material deforms primarily by $\{10\bar{1}0\} \langle\bar{1}2\bar{1}0\rangle$ slip. When loaded in circumferential tension, a small proportion of the grains will slip, but most grains are oriented for $\{10\bar{1}2\}$ twinning.

Under the biaxial stress system of pressure tube 130, the longitudinal strength increased considerably more than the transverse strength during irradiation (Table 5). This anisotropic irradiation strengthening suggests that, under the influence of the stress field, irradiation damage may become oriented sufficiently so that slip deformation is impeded more effectively than twinning.

Electron Microscopy—Thin foils prepared from irradiated tube 289 were examined by transmission electron microscopy, revealing discrete dislocation loops (Fig. 6) which were not identifiable as either vacancy or interstitial types [15]. The observation may support Bement's [14] suggestion that at neutron doses greater than about 10^{20} n/cm² irradiation hardening is by interstitial loop formation. In common with other results from irradiated zirconium alloys [15], the foils from tube 289 showed no evidence of loop growth or interaction. Although the examination failed to provide positive evidence of an effect of stress on dislocation loop orientation, Williams and Gilbert [15] noted that the larger dislocation loops lay in or near the primary or secondary prismatic planes. This supports the suggestion that irradiation damage in a stressed tube principally impedes the slip system.

Oxidation

Oxidation of the tubes' inside surfaces increased as a result of reactor exposure, the oxide thickness showing some dependence on neutron dose. The increased corrosion in tubes 10 and 130 supports earlier observations from test coupons and fuel sheathing that, for part of the first five years of operation, coolant conditions in the NPD reactor were more oxidizing than was expected, owing to the low dissolved deuterium concentration in the coolant [19]. The maximum oxide thickness on tubes 10 and 130 exposed to coolant at 252 to 273 C is equivalent to an out-of-pile exposure at 345 C for the same length of time. The combined effect of fast neutron flux and low deuterium concentration in the coolant during the early period of reactor operation are thought to have accelerated the corrosion of tubes 10 and 130. The patchy oxide morphology on the irradiated pressure tubes differs from the uniform oxide which characterizes out-of-pile corrosion.

For the coolant chemistry of tube 289's exposure, the posttransition corrosion rate at 280 C is estimated at 0.020 mg/dm² day or less, and a weight gain of about 9 mg/dm² (equivalent to 0.7 μm oxide thickness) would be expected in 458 EFPD, in the absence of neutron irradiation. The original autoclaved film was about 1 μm thick, so the maximum thick-

ness increase in tube 289 is 13 μm , equivalent to a weight gain of 180 mg/dm^2 , or about 20 times the weight gain of unirradiated Zircaloy 2.

A nonautoclaved Zircaloy 2 tube was irradiated earlier in the U-2 loop with similar coolant chemistry to tube 289. Postirradiation examination showed some irradiation enhancement of oxidation [17], but the maximum oxide thickness was only 4 μm after irradiation to 6.5×10^{20} n/cm^2 in 292 EFPD. Since neutron fluxes ($E > 1$ MeV) were closely similar in the irradiation of both tubes, the reduced oxidation is believed to be due to the absence of the autoclaved oxide film. Work by Johnson [20] supports this interpretation: he found that prefilming Zircaloy 2 in 400 C steam increased its susceptibility to irradiation enhancement of oxidation in ammonia dosed coolant.

Assuming linear posttransition oxidation kinetics, the maximum mean oxide thickness increase of 7 μm in tube 289 extrapolates to 115 μm in 30 FPY. In all probability spalling and mechanical damage would prevent such an accumulation. The amount of zirconium metal used in forming this thickness of oxide is equivalent to a uniform thickness loss of 0.0025 in.

A similar extrapolation based on the thickest (14 μm) oxide patches on tube 289 predicts a maximum oxide thickness of 250 μm in 30 FPY, indicating a uniform metal loss of 0.0056 in. There is evidence that these oxide patches do not grow indefinitely but agglomerate prior to the onset of a uniform corrosion rate [21]. The prediction of 0.0056 in. of metal loss therefore seems likely to be unduly pessimistic but would not in any case affect the safe operation of the pressure tubes.

Hydrogen/Deuterium Pickup—The solubility of hydrogen in Zircaloy 2 is about 80 ppm by weight at 280 C [22], decreasing to perhaps less than 1 ppm at 20 C. Hydrogen in excess of solid solubility precipitates as the zirconium hydride $\text{ZrH}_{1.5}$. Deuterium (from heavy water coolant) behaves identically to hydrogen, but because of the different atomic weights twice as much deuterium (in ppm by weight) is required to produce the same amount of precipitate. Since almost all research work has used hydrogen rather than deuterium, it is convenient for the following discussion to use the term “effective hydrogen concentration” for the tubes exposed in heavy water: this is defined as the sum of the hydrogen concentration and half of the deuterium concentration.

The rate of hydrogen pickup from the hot pressurized coolant varies with the rate of oxidation. Initial pickup rate falls rapidly as the oxide thickens. After transition in oxidation kinetics at about 35 mg/dm^2 (2.5 μm of oxide), hydrogen is picked up at a rate which is roughly linear with time. The oxide thicknesses measured on tubes 289, 10, and 130 indicate that the oxidation had progressed beyond transition. Extrapolation of the measured hydrogen and deuterium concentrations at a linear rate therefore provides a reasonable guide to the probable effective hydrogen concentration in a pressure tube at the end of a 30-FPY life.

Tube 130 picked up a maximum of 31 ppm D_2 in 1240 EFPD, which extrapolates to 218 ppm D_2 in 30 FPY. With the initial tube hydrogen concentration of 19 ppm H_2 , this is an effective hydrogen concentration of 128 ppm. Tube 289 picked up a maximum of 13 ppm H_2 in 458 EFPD, which predicts a maximum total concentration of 245 ppm in 30 FPY.

These predicted maximum values of effective hydrogen concentration will have little effect on the tensile properties of Zircaloy 2 pressure tubes at operating temperatures. Sawatzky [23] found virtually no reduction in strength with 200 ppm H_2 at temperatures up to 400 C, although Evans and Parry [24] found that below 150 C ductility was reduced. The combined effect of 200 ppm hydrogen and a neutron dose of 2.3×10^{20} n/cm² on the strength of pressure tube material was indistinguishable from the effect of irradiation alone at 20 and 300 C [12]. Critical crack length was reduced at 20 C but unaffected at 300 C by the hydrogen.

Conclusions

Postirradiation examination of Zircaloy 2 pressure tubes irradiated under power reactor conditions indicates that

1. Critical crack length of the tubing is sufficient to ensure that leakage should give adequate prior warning of an approaching unsafe condition.
2. Anisotropic deformation of biaxially stressed Zircaloy 2 tubes is modified by neutron irradiation.
3. Stress during irradiation reduces the extent of irradiation strengthening, possibly indicating stress enhanced recovery of cold work and irradiation damage.
4. Marked directionality of irradiation strengthening together with evi-

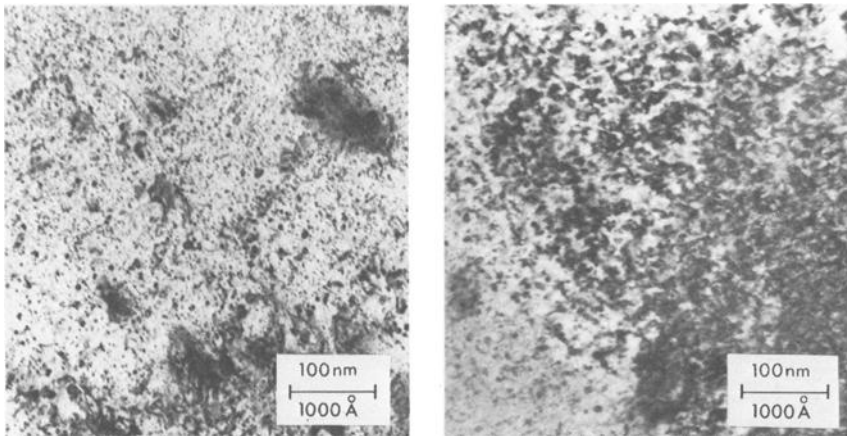


FIG. 6—Transmission electron micrographs showing dislocation loops in irradiated Zircaloy 2 pressure tube 289: left, 2×10^{20} n/cm²; right, 1×10^{21} n/cm².

dence from transmission electron microscopy suggest that the primary irradiation hardening mechanism is impedance of $\{10\bar{1}0\}$ $\langle\bar{1}2\bar{1}0\rangle$ slip by discrete dislocation loops.

5. Neutron irradiation enhances oxidation in LiOH dosed coolant at 280 C. Oxidation rate and hydrogen/deuterium pickup are acceptably low.

These examinations indicate that the strength, ductility, crack tolerance, and corrosion rate of Zircaloy 2 pressure tubes under normal reactor conditions are consistent with requirements for a tube life of 30 years, leaving creep as the factor determining tube life.

Acknowledgments

I wish to thank W. Evans, P. A. Ross-Ross, J. E. LeSurf, B. A. Cheadle, C. E. Ells, and C. D. Williams for their assistance and valuable discussions. The experimental assistance of L. E. J. Mooder, J. G. Bryson, and A. S. Denovan is much appreciated.

APPENDIX I

Ingot analyses of the Zircaloy 2 pressure tube materials. All ingots supplied by Carborundum Metals Co., Akron, N.Y.

Tube Ingot No.	289 K689	10 K223	130 K304	391 K792	425 K791
Al.	<30	28	31	<21	26
B.	<0.2	0.5	<0.2	<0.2	<0.2
C.	<106	130	150	127	141
Cd.	<0.2	<0.5	<0.5	<0.2	<0.2
Co.	<10	<20	<20	<10	<10
Cr.	1000	935	1088	1000	1100
Cu.	<20	<20	21	<20	<20
Fe.	1230	1230	1355	1200	1200
Hf.	<100	83	83	<100	<100
Mg.	<10	<20	<20	<10	<10
Mn.	<20	<20	<20	<20	<20
Mo.	<20	<20	<20	<20	<20
N ₂	48	39	43	45	41
Ni.	600	462	525	500	500
Pb.	<25	<20	<20	<20	<20
Si.	72	51	35	78	74
Sn (%).	1.51	1.41	1.43	1.46	1.49
Ti.	<24	<20	<20	<20	<20
V.	<20	<20	<20	<20	<20
W.	<50	<20	<20	<50	<50
O ₂	1330	^a	^a	1265	1090-1390
H ₂	16	^a	^a	14	6-14

NOTE—Figures are parts per million (ppm) by weight.

^a Not reported.

APPENDIX II

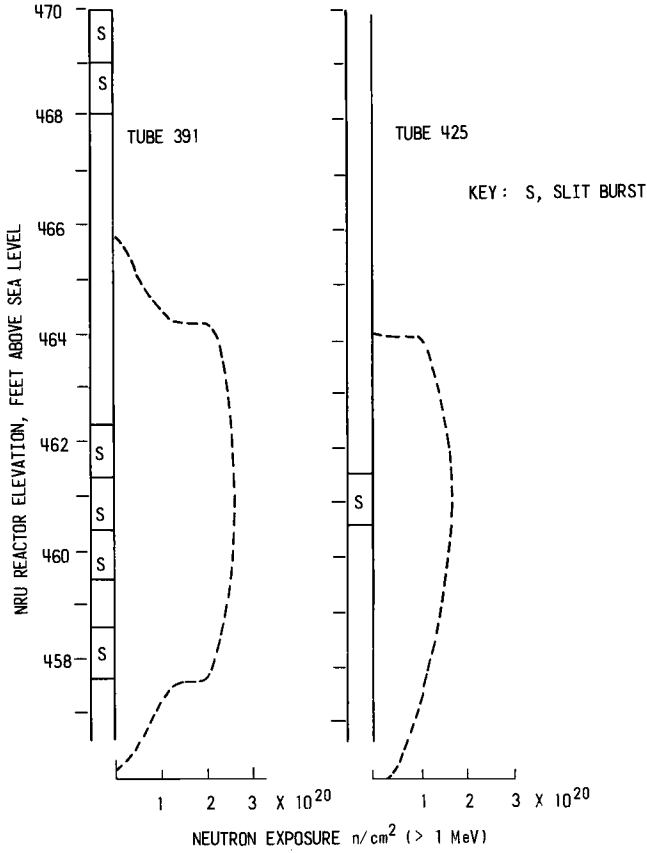


FIG. 7—Test specimen locations of cold-worked Zircaloy 2 pressure tubes 391 and 425.

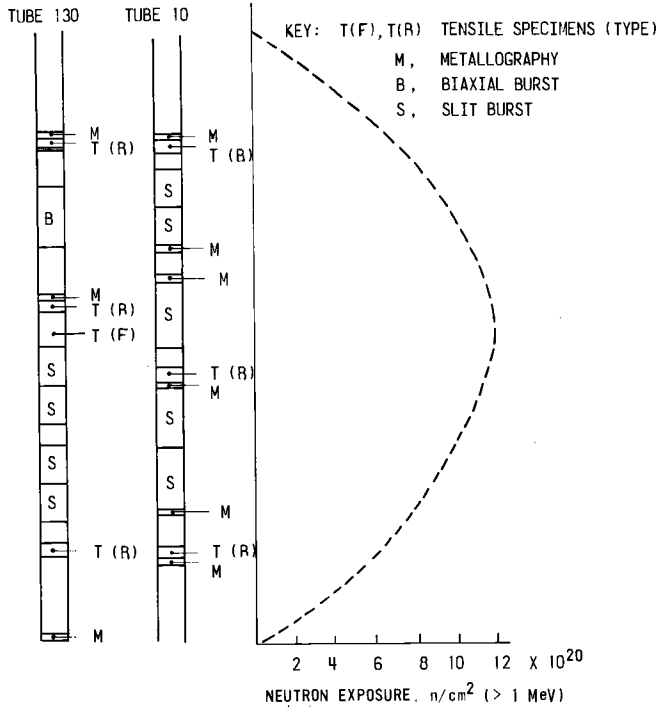


FIG. 8—Test specimen locations of cold-worked Zircaloy 2 pressure tubes 10 and 130.

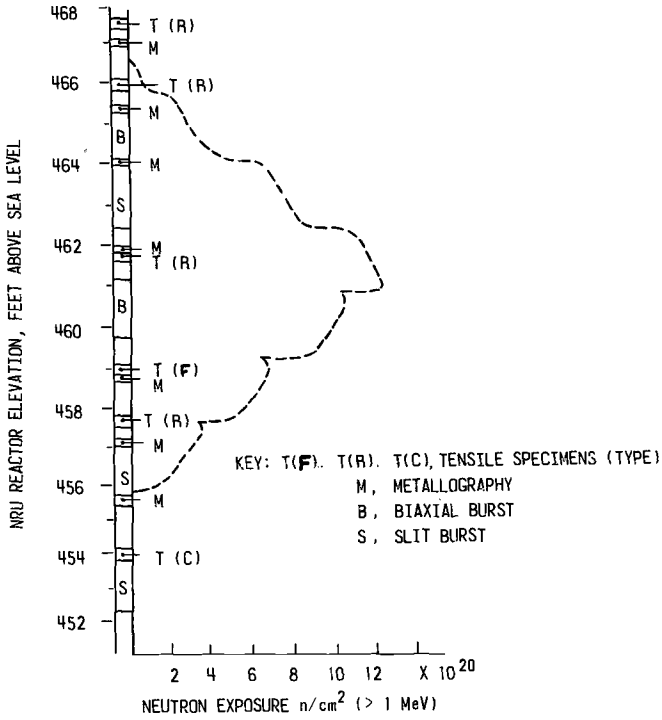


FIG. 9—Test specimen locations of cold-worked Zircaloy 2 pressure tube 289.

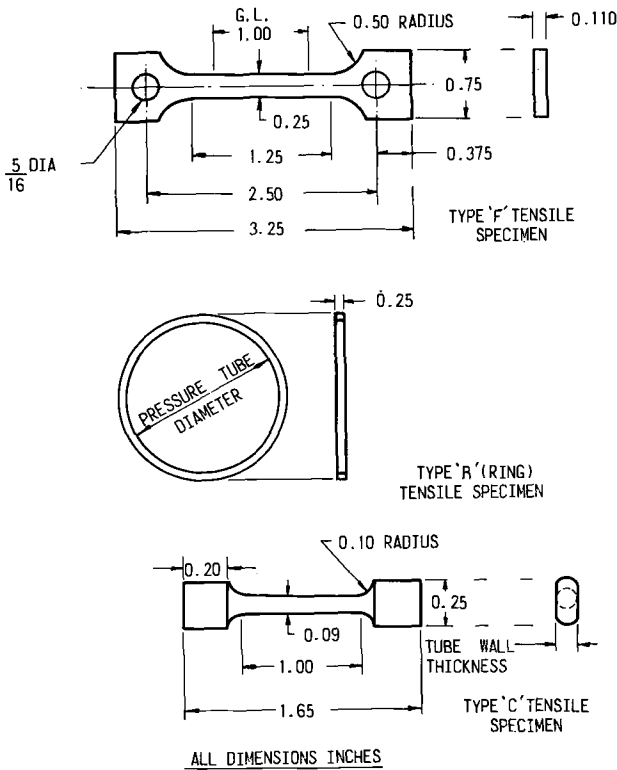


FIG. 10—Tension specimens used in the investigation.

References

- [1] Howe, L. M. and Thomas, W. R., *Journal of Nuclear Materials*, JNUMA, Vol. 2, No. 3, 1960, p. 248.
- [2] Bement, A. L., Tobin, J. C., and Hoagland, R. G. in *Flow and Fracture Behavior of Metals and Alloys in Nuclear Environments*, ASTM STP 380, American Society for Testing and Materials, 1965, p. 364.
- [3] Aungst, R. C. and Defferding, L. J. in *Flow and Fracture Behavior of Metals and Alloys in Nuclear Environments*, ASTM STP 380, American Society for Testing and Materials, 1965, p. 451.
- [4] Kahle, V. E., "Burst Testing of Irradiated Zircaloy Tubing," HW-64168, USAEC Research and Development Report, Richland, Wash., March 1960.
- [5] Fraser, M. C., "Post-Irradiation Evaluation of Zircaloy-2 PRTR Pressure Tubes—Part III," BNWL-5, USAEC Research and Development Report, Richland, Wash., Jan. 1965.
- [6] Cheadle, B. A. and Ells, C. E., *Transactions of the Metallurgical Society*, AIME, TMSAA Vol. 233, 1965, p. 1044.
- [7] Cheadle, B. A., Ells, C. E., and Evans, W., *Journal of Nuclear Materials*, JNUMA, Vol. 23, No. 2, 1967, p. 199.
- [8] Hurst, D. G., "Outlook for CANDU Reactors," presented at the IAEA International Survey Course on Economic and Technical Aspects of Nuclear Power, Vienna, Austria, Sept. 1969; available as AECL-3553, Jan. 1970.
- [9] Ross-Ross, P. A. and Hunt, C. E. L., *Journal of Nuclear Materials*, JNUMA, Vol. 26, 1968, p. 2.

- [10] Hoffman, O. and Sachs, G., *Introduction to Theory of Plasticity for Engineers*, McGraw-Hill, New York, 1953, p. 39.
- [11] Ross-Ross, P. A. and Smith K. L., "Pressure Tube Development for Canada's Power Reactors," Paper 64-WA/NE-5, ASME Winter Annual Meeting, 1964.
- [12] Cowan, A. and Langford, W. J., *Journal of Nuclear Materials*, JNUMA, Vol. 30, No. 3, April 1969, p. 271.
- [13] Veeder, J., "Tensile Properties of NPD-2 Pressure Tubes," AECL-1247, Atomic Energy of Canada Limited, Chalk River, Ontario, April 1961.
- [14] Bement, A. L., AIME Symposium on Irradiation Effects on Metals, Asheville, N.C., Sept. 1965.
- [15] Williams, C. D. and Gilbert, R. W. in *Radiation Damage in Structural Materials*, Vol. 1, International Atomic Energy Agency, Vienna, 1969, p. 235 (also available as AECL-3308).
- [16] Fifth Report of a Special ASTM Committee, *Materials Research and Standards*, MTRSA, Vol. 4, March 1964, p. 107.
- [17] Langford, W. J., "Metallurgical Examination of the U-2 Mk III-1 Pressure Tube," Atomic Energy of Canada Limited, unpublished internal report EDI-147, May 1967.
- [18] Cahn, R. W. in *Physical Metallurgy*, R. W. Cahn, Ed., Wiley, New York, 1965, p. 933.
- [19] Bain, A. S. and Le Surf, J. E., "Oxidation and Hydriding of Zircaloy in NPD Reactor," AECL-3065, Atomic Energy of Canada Limited, Chalk River, Ontario, Jan. 1969.
- [20] Johnson, A. B., BNWL-SA-822, USAEC Research and Development Report, Richland, Wash., May 1967.
- [21] Johnson, A. B. in *Applications Related Phenomena in Zirconium and Its Alloys*, ASTM STP 458, American Society for Testing and Materials, 1969, p. 271.
- [22] Ells, C. E., *Journal of Nuclear Materials*, JNUMA, Vol. 28, 1968, p. 129.
- [23] Sawatzky, A., "Effect of Neutron Irradiation on the Mechanical Properties of Hydrided Zirconium Alloys," AECL-1986, Atomic Energy of Canada Limited, Chalk River, Ontario, June 1964.
- [24] Evans, W. and Parry, G. W., *Electrochemical Technology*, ECTCA, Vol. 4, No. 5-6, May-June 1966.

DISCUSSION

*A. L. Bement*¹—Have you observed a significant effect of notch acuity in your measurements of burst stress versus notch size for your worst cases of neutron fluence and hydride concentration?

W. J. Langford (author's closure)—Notch acuity was not an experimental variable, because early in the development of the test technique the spark machined slit was found to be as equally severe as sharper notch configurations. In the thin wall Zircaloy 2 pressure tubes elastic restraints are almost nonexistent at stress concentrations, and considerable plastic deformation is observed at the slit tips. The observations possibly suggest a limiting notch acuity below which plastic flow at the tip effectively nullifies the effects of increasingly sharp cracks.

¹ Battelle-Northwest, Richland, Wash. 99352.

*J. E. Harbottle*¹

The Temperature and Neutron Dose Dependence of Irradiation Growth in Zircaloy 2

REFERENCE: Harbottle, J. E., "The Temperature and Neutron Dose Dependence of Irradiation Growth in Zircaloy 2," *Irradiation Effects on Structural Alloys for Nuclear Reactor Applications*, ASTM STP 484, American Society for Testing and Materials, 1970, pp. 287-299.

ABSTRACT: Irradiation growth due to fast neutron bombardment has been measured in textured Zircaloy 2 as a function of neutron dose (ϕt) and irradiation temperature. The growth strain ϵ obeys a relationship $\epsilon \propto (\phi t)^n$ over a temperature range -196 to 280 C and for doses up to 10^{21} n/cm². For irradiation temperatures up to 80 C, $n=0.4$; but at 280 C, $n=0.7$. The temperature dependence of irradiation growth in Zircaloy 2 is small, and in the temperature and dose ranges considered the growth strains do not differ by more than a factor of four. The growth rate $G \propto d\epsilon/d(\phi t)$ is initially large at low doses but approaches 1 at high doses ($\sim 10^{21}$ n/cm²).

KEY WORDS: irradiation, neutron irradiation, neutron flux density, temperature, strains, strain rate, crystal lattices, grain structure, interstitials, volume, Zircaloys, nuclear reactor materials, pressurized water reactors, texture, elongation, pressure vessels

A change in shape at constant volume has been observed in some metals following irradiation [*i*]² and is defined as irradiation growth. It can be described further by the instantaneous growth rate G , which may be a function of dose and temperature. For neutron irradiation it is defined as the fractional change of shape of the solid per neutron collision with a lattice atom. If $\epsilon_{1,2,3}$ are the principal strains resulting from a neutron dose

¹ Central Electricity Generating Board, Research and Development Department, Berkeley Nuclear Laboratories, Berkeley, Gloucestershire, England.

² Italic numbers in brackets refer to the list of references at the end of this paper.

$d(\phi t)$, then

$$G = \frac{\sqrt{2}}{3} \frac{1}{\sigma\phi} [(\dot{\epsilon}_1 - \dot{\epsilon}_2)^2 + (\dot{\epsilon}_2 - \dot{\epsilon}_3)^2 + (\dot{\epsilon}_3 - \dot{\epsilon}_1)^2]^{1/2} \dots \dots \dots (1)$$

where σ is the neutron collision cross section (see Appendix I).

Irradiation growth occurs in noncubic metals (such as uranium) having anisotropic physical properties, in particular anisotropic thermal expansion. It also occurs in cold-worked cubic metals, where growth is observed in the direction of plastic strain [2]. In a polycrystal the strain in one direction is the sum of the strains in all the grains present and so depends on the degree of texture. For a random texture there is no macroscopic strain in any direction, though stresses do exist between the grains. For a high degree of texture the macroscopic strains approach those of the single crystal.

Irradiation growth results from the condensation of vacancies and interstitials into loops on different crystal planes. Zircaloy 2 has a hexagonal structure and the anisotropy in lattice vectors causes interstitials to condense onto the close packed prism planes in order to minimize the energy of the defect structure. The collapse of the central multiple vacancy may be influenced by the directional stress produced during the short duration of the thermal spike due to the anisotropic thermal expansion of the material. As the maximum expansion coefficient is in the $\langle 0001 \rangle$ direction, this aids the condensation of vacancies onto the basal planes. The preferential clustering onto nonparallel planes produces extension in the direction of the interstitial loop Burgers vector and an equal contraction of the solid parallel to the vacancy loop vector. Zircaloy 2 has a hexagonal structure with maximum and minimum thermal expansion coefficients in the $\langle 0001 \rangle$ and $\langle 11\bar{2}0 \rangle$ directions, respectively, and should therefore show extension parallel to the basal plane.

Growth of materials under irradiation is particularly important in the design and operation of reactor components. The heavy water reactors SGHW and CANDU both use textured Zircaloy 2 pressure tubing situated in regions of high neutron flux, and this may well exhibit irradiation growth. This would produce elongation of the pressure tube in regions of constant flux and cause the tubes near the core edge to bow owing to the radial flux gradient in this region.

It is clearly important to be able to predict the magnitude of these effects over the lifetime of the reactor, and at present very few experimental data exist on which to base such predictions. The object of the present work is to study the temperature and neutron dose dependence of growth in Zircaloy 2 in order to (1) improve the accuracy of high dose extrapolations, (2) measure the magnitude of irradiation growth as a function of irradiation temperature, and (3) achieve a better understanding of the mechanism involved.

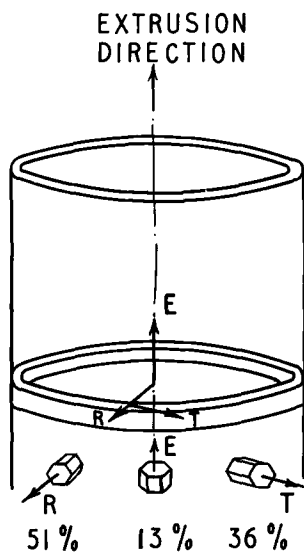


FIG. 1—The basal pole texture of a Zircaloy 2 pressure tube [4].

Experimental

Specimens were cut from Zircaloy pressure tube supplied by United Kingdom Atomic Energy Authority, Culcheth, from their normal production line. These tubes are manufactured by extrusion and are strongly textured [3, 4], having about 87 percent basal pole texture normal to the tube axis (Fig. 1). Strips cut in the longitudinal and transverse directions will therefore exhibit growth strains of an opposite sign, so if welded together at one end to make a bimetal strip they provide a means of measuring the differential growth. The differential extension at the free end is proportional to the specimen length. If both ends of the strips are welded together, irradiation growth causes the specimen to bow, and the central displacement, which is a measure of the growth strain, is now proportional to the square of the specimen length (see Appendix II). The choice of specimen type depends on the anticipated growth strain, the sensitivity required, and the need to remain well within the elastic limit of the material.

Specimens were carefully prepared from Zircaloy 2 strips cut from the tube, heat-treated and machined to final dimensions of 190 by 6 by 1.5 mm. Heat treatment consisted of two stress relieving anneals of 18 h at 500 C between machining and a final anneal of 1 h at 700 C. This treatment had no detectable effect on the texture [4]. The ends were welded in an argon atmosphere, and heat flow along the specimen was minimized by a water bath. The free ends of the linear specimens were spark planed level to give

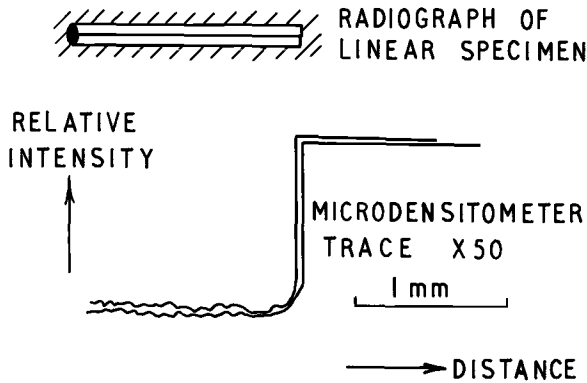


FIG. 2—The measurement of growth in a linear specimen.

a burr-free finish before their relative positions were recorded on fine grain film by exposure to a collimated light beam. This produced a shadowgraph in good focus. A similar technique using an X-ray beam in a radio-graph handling cell is followed for the irradiated specimens. Both films are measured on an optical microdensitometer having a magnification of 50, and two scans are made along the length of each strip; the relative positions of the free ends are thus defined on one piece of paper (Fig. 2), and the growth strain is then the change in relative position between the two films. The differential displacement can be measured to $\pm 10 \mu\text{m}$. Maximum resolution is obtained from the microdensitometer by using an aperture of maximum length and minimum width, thus combining good grain size integration with high resolution during the transition across the image boundary.

Measurement of the bow specimens before and after irradiation was achieved by focusing an optical microscope on a central fiducial mark, as shown in Fig. 3, and comparing it with a flat reference bar. The accuracy of this measurement is $\pm 3 \mu\text{m}$. All irradiations were carried out either in Pluto (fast flux $\sim 1.2 \times 10^{14}$ n/cm²/s) at the Atomic Energy Research Establishment (AERE), Harwell, or in Herald (fast flux $\sim 3 \times 10^{13}$ n/cm²/s) at the Atomic Weapons Research Establishment (AWRE), Aldermaston.

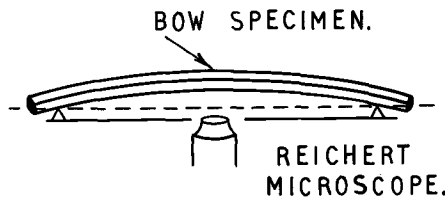


FIG. 3—The measurement of growth in a bow specimen.

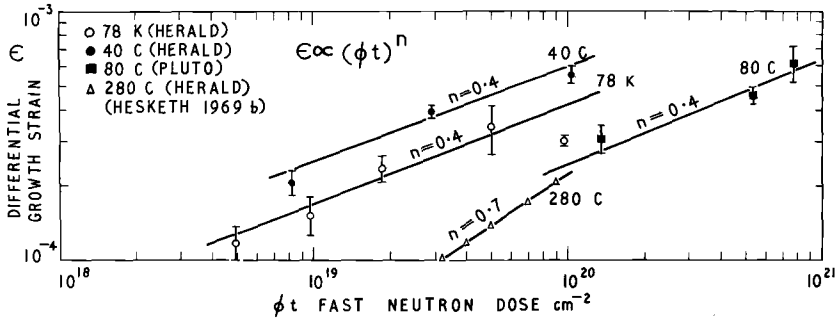


FIG. 4—Differential growth strain as a function of dose at four different irradiation temperatures. The 280 C data are derived from instantaneous growth rate measurements obtained by a transducer technique.

Results

Figures 4 and 5 show the total measured growth strain ϵ and the computed growth rate G plotted as a function of fast neutron doses up to 10^{21} n/cm² and at irradiation temperatures between 78 K and 280 C. Points on Fig. 4 represent an average value from measurements on the number of specimens shown in Table 1, and the indicated error is the standard

TABLE 1—Results of irradiation growth measurements on Zircaloy 2.

Irradiation Temperature	Neutron Dose ($E > 1$ MeV), cm ⁻²	Measured Differential Growth Strain	Growth Coefficient				Number of Specimens	Reactor
			Instantaneous $G_{t_2-t_1}$		Average $G_{t_2-t_0}$			
78 K . . .	4.9 × 10 ¹⁸	1.2 ± 0.2 × 10 ⁻⁴	8.0	± 1.0	18.0	± 4.0	3	Herald
	9.7	1.5 0.3	5.0	1.0	11.6	2.3	4	
	1.9 × 10 ¹⁹	2.3 0.3	3.5	0.5	9.5	1.1	3	
	5.0	3.5 0.5	2.0	0.3	5.2	0.7	3	
	9.8	3.0 0.1	1.5	0.2	2.3	0.1	4	
40 C	8.2 × 10 ¹⁸	2.1 0.2	8.0	1.0	19.0	1.0	7	
	2.9 × 10 ¹⁹	4.0 0.2	3.6	0.3	10.2	0.4	7	
	1.0 × 10 ²⁰	5.6 0.4	1.7	0.2	4.0	0.3	7	
80 C	1.3 × 10 ²⁰	3.1 0.4	0.6	0.1	1.7	0.2	4	Pluto
	5.4	4.7 0.4	0.30	0.03	0.7	0.1	7	
	7.7	6.3 1.0	0.20	0.02	0.6	0.1	4	
280 C	2.2 × 10 ¹⁷	...	9		...		1	Herald
	1.0 × 10 ¹⁸	...	5		...		1	
	1.0 × 10 ¹⁹	...	3		...		1	
	3.0	...	1.5		...		1	

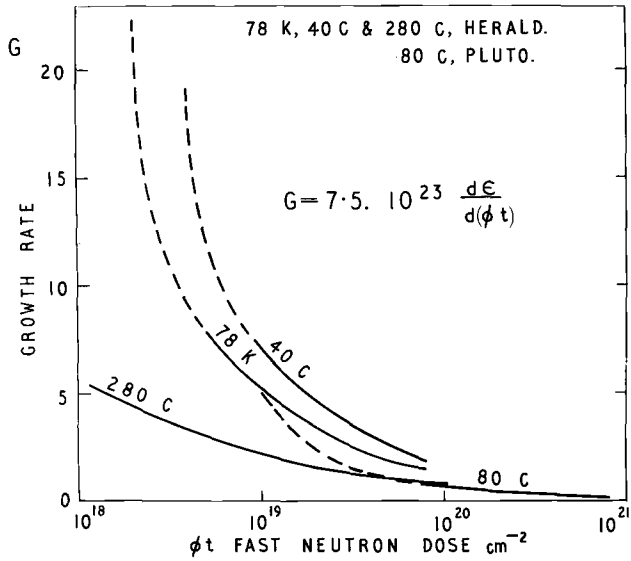


FIG. 5—The growth rate G derived from the strain measurement of Fig. 4.

deviation of each set of results. At 78 K the errors are typically ± 15 percent, for the 40 C points they are ± 8 percent, and for the 80 C measurements, which consist of four linear and four bow specimens, they are ± 12 percent. Each bow specimen provides two strain values by measuring both concave and convex surfaces. The 280 C growth strain curve is derived from instantaneous growth rate data of Hesketh, Harbottle, Waterman, and Lobb [5] shown in Fig. 5. Representing the growth strain by

$$\epsilon \propto (\phi t)^n$$

the points at 78 K, 40 C, and 80 C (Fig. 4) show a reasonable fit to a line of $n = 0.4$, whereas the 280 C line has a slope of 0.7. The specimens yielding the highest dose measurement at 78 K also provided the lowest dose point at $4.9 \times 10^{18} \text{ n/cm}^2$ and were then reirradiated. The specimens thus suffered an intermediate thermal excursion to room temperature for measurement, and this interruption may account for the low strain reading at $9.8 \times 10^{19} \text{ n/cm}^2$ due either to elastic relaxation or a change in the nature of the low-temperature damage. Curves of growth rate G as a function of dose (Fig. 5) were calculated from the straight line data of Fig. 4 using Eq 1 and extrapolated to low doses (dashed line) assuming the same functional dependence on dose.

Discussion

The measurements of total growth strain plotted in Fig. 4 show a non-linear dose dependence at all temperatures, in agreement with Kreyns [6]

results on Zircaloy 4 at 300 C and with the model proposed by Hesketh [7], and in contrast to the linear growth observed in uranium following fission fragment damage [1]. It is quite likely that diffusion is more important in neutron irradiated Zircaloy 2, leading to less localized damage regions. As it has been suggested that only fission fragments produce a sufficiently high defect density to form nuclei for irradiation growth [8], the observation of growth in Zircaloy 2 by fast neutrons suggests that a smaller size nucleus is required for stability or that heterogeneous nucleation at impurities is more important in this material.

The specimens in these experiments all showed elongation of the longitudinal strips and contraction of the transverse strips, corresponding to the formation of interstitial loops on prism planes and vacancy loops on basal planes. Interstitials would be expected, from energy considerations, to favor the close packed prism planes, but the condensation of vacancies onto basal planes may be a result of their generation within the cascade region so that their mode of collapse is conditioned by the anisotropy of the transient spike stresses. Evidence for the importance of the thermal spike can be inferred from the work on growth in α uranium [9, 10], where it has been shown that the growth per Frenkel defect created is much greater following a spike process (with fission fragment and fast neutron damage) than when spikes do not occur (with proton damage). Further evidence for the formation of interstitial loops on prism planes, having $\mathbf{b} = \mathbf{a}/3 \langle 11\bar{2}0 \rangle$, is provided by electron microscope observations of ion bombarded zirconium [11].

Following a damage event the clustering of point defects to form loops is a complex process. It involves both the adiabatic transport of atoms immediately following the event and thermally activated diffusion through the lattice under isothermal conditions. As irradiation growth is a special case of cluster behavior, it is of interest to study its temperature dependence.

Comparison of the growth strains at four different temperatures in the range -196 to 280 C shows an unexpected similarity in magnitude (Fig. 4), differing by not more than a factor of four. In the same temperature range the growth of uranium changes by a factor of 10^4 . The other notable feature is that growth strains are lower at 78 K than at 40 C in the same reactor environment, and this may well be due to the different loop distributions present. Irradiation at 78 K creates a high ambient concentration of isolated point defects, which when raised to room temperature probably nucleate into a fine network of small loops. By contrast, irradiation at 40 C produces mobile defects [12] which on nucleation form a coarse network of larger loops. The small loops (<20 Å in diameter), whose core regions overlap, are unlikely to be fully collapsed³ and will therefore be

³ Private communication with M. O. Tucker, Central Electricity Generating Board, Research and Development Dept., Berkeley Nuclear Laboratories.

less effective in displacing the lattice than the larger loops produced at 40 C.

The reduced growth at 80 C in Pluto compared with that at 40 C in Herald by a factor of 2.5 can be explained by the increased removal of interstitials to sinks at the higher temperature. The efficiency of loop nucleation depends on the ambient concentration of interstitials, which is determined by their rates of production and removal. Balancing the rate of production ($\propto \phi$) with the rate of removal [$\propto \exp(-E_m/kt)$] at the two temperatures and fluxes, where E_m is the interstitial migration energy, we have

$$\phi_1 \exp\left(\frac{E_m}{kT_1}\right) = x\phi_2 \exp\left(\frac{E_m}{kT_2}\right) \dots \dots \dots (2)$$

where $T_1=313$ K, $T_2=353$ K, and x is the ratio of the growth strains at T_1 and T_2 after the same dose. Taking $E_m=0.3$ eV [13] gives $x=2$, in reasonable agreement with the observed value of 2.5.

Irradiation growth at 280 C has a dose dependence different from that at low temperature. At low doses the observed growth rate is less, due to the shorter interaction time available for the migrating defects to form stable nuclei and also perhaps to the larger nucleus required at this temperature. This situation leads to a small concentration of large loops which grow rapidly with increasing dose, in agreement with observed behavior in which $G \propto (\phi t)^{-0.3}$ at 280 C compared with an exponent of -0.6 at lower temperatures. The growth strain, as expected, is lower due to the increased recombination of vacancies and interstitials, the greater probability of thermal dissociation of the clusters, and the annealing of vacancies and interstitials to sinks. If it is assumed that the interstitials are much more mobile than the vacancies, then using a similar approach as before (Eq 2) the annealing kinetics have a reaction order of about 3.5.

Conclusions

1. Growth strain ϵ obeys a relationship

$$\epsilon \propto (\phi t)^n$$

with $n=0.4$ at irradiation temperatures of 78 K, 40 C, and 80 C and $n=0.7$ at 280 C.

2. Dependence of irradiation growth on temperature is not strong. The growth strain at 40 C is greater than the growth strain at 78 K and is explained by the differing dislocation loop distributions following irradiation at 78 and 40 C.

3. Lower initial growth rate at 280 C is probably due to a smaller density of loops and the difficulty in nucleation, but the higher dose exponent ($n=0.7$) is due to the rapid growth of large loops.

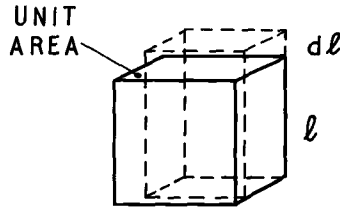


FIG. 6—Irradiation growth produces a shape change in a textured specimen.

4. Growth rate is large ($G > 5$) at low doses ($< 10^{19}$ n/cm²) for irradiation temperatures up to 80 C but approaches 1 at high doses ($\sim 10^{21}$ n/cm²).

Acknowledgments

This paper is published by permission of the Central Electricity Generating Board, Berkeley Nuclear Laboratories, Berkeley, Gloucestershire, England.

APPENDIX I

Growth by Fast Neutron Irradiation

Consider the solid shown in Fig. 6 containing n atoms, that is n/l atoms per unit volume. The number of collisions made by an elemental dose $d(\phi t)$ with cross section σ equals $n\sigma d(\phi t)$. Each collision transfers G atoms from basal planes to prism planes, producing an extension dl in a textured polycrystal. So volume dl contains

$$Gn\sigma d(\phi t) = dl(n/l) \text{ atoms}$$

that is

$$G = \frac{nd\epsilon}{n\sigma d(\phi t)} = \frac{\text{Fractional extension}}{\text{Fraction of lattice atoms suffering neutron collision}}$$

or

$$G = \frac{\sqrt{2}}{3} \frac{1}{\sigma\phi} [(\dot{\epsilon}_1 - \dot{\epsilon}_2)^2 + (\dot{\epsilon}_2 - \dot{\epsilon}_3)^2 + (\dot{\epsilon}_3 - \dot{\epsilon}_1)^2]^{1/2}$$

where ϵ is the generalized strain and $\epsilon_{1,2,3}$ are the principal strains resulting from $d(\phi t)$.

APPENDIX II

Analysis of the Bow Specimens

The equilibrium configuration of the specimen following irradiation growth represents a balance between (1) the external couple exerted on one strip by its

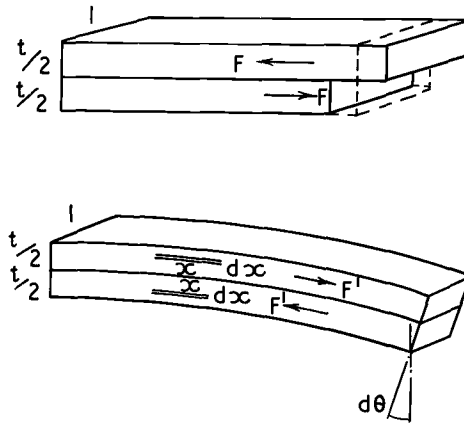


FIG. 7—The equilibrium configuration of a bow specimen is achieved by equating the opposing couples.

partner and (2) the internal couple due to the bowing of the strip. Couple 1, shown in Fig. 7, is derived by allowing a bowed specimen to straighten itself by removing one weld, the growth strain ϵ then being given by the differential extension of the two strips over their original length. To make the ends meet the force F required to be exerted on each strip of thickness t and unit width to respectively extend and contract each by an amount $\epsilon/2$ is given by

$$F = \frac{\epsilon Y t}{4}$$

where Y is the elastic modulus. The resulting couple is then

$$\frac{Y t^2}{16} \epsilon \dots \dots \dots (3)$$

The specimen now is allowed to bow under the bending couple 2 (Fig. 7) producing a radius of curvature R . Consider the force required to produce in a fiber an extension dx at a distance x from the neutral axis:

$$\text{Force} = \frac{x d\theta}{R d\theta} Y dx$$

where the specimen subtends an angle $2d\theta$ at the center. The couple acting on two fibers separated by $2x$ across the neutral axis is then

$$2x \frac{x}{R} Y dx$$

and the total bending couple acting on the specimen is then

$$\int_0^{t/2} \frac{2x^2}{R} Y dx = \frac{Yt^3}{12R} \dots \dots \dots (4)$$

Equating the couples (Eqs 3 and 4) for equilibrium,

$$\epsilon = 4/3 (t/R)$$

As $2Rh \simeq (l/2)^2$, the growth strain is given in terms of the center of bow displacement h and the length l of the specimen by

$$\epsilon = \frac{16}{3} \times \frac{t}{l^2} h$$

References

- [1] Buckley, S. N., International Conference on Properties of Reactor Materials and the effects of Radiation Damage, Berkeley, Butterworths, London, 1962, p. 413.
- [2] Buckley, S. N., AERE—R 5944, Atomic Energy Research Establishment, Harwell, 1968.
- [3] Cheadle, B. and Ells, C., *Transactions AIME*, TAPMA, Vol. 233, 1965, p. 1044.
- [4] Waterman, N. A. and Hesketh, R. V., RD/B/N1240, Research and Development Dept., Berkeley Nuclear Laboratories, 1969.
- [5] Hesketh, R. V., Harbottle, J. E., Waterman, N. A. and Lobb, R. C. in *Radiation Damage in Reactor Materials*, Vol. I, International Atomic Energy Agency, Vienna, 1969b.
- [6] Kreyns, P. H., WAPD-TM-583, Westinghouse Atomic Power Division, 1966.
- [7] Hesketh, R. V., *Journal of Nuclear Materials*, JNUMA, Vol. 30, 1969a, p. 219.
- [8] Thompson, M. W., *Defects and Radiation Damage in Metals*, Cambridge, 1969, p. 336.
- [9] Thompson, M. W., *Journal of Nuclear Materials*, JNUMA, Vol. 3, 1961, p. 354.
- [10] Buckley, S. N., Institute of Metals Spring Meeting, London, April 1966.
- [11] Gulden, T. D. and Bernstein, I. M., *Philosophical Magazine*, PHMAA, Vol. 14 1966, p. 1087.
- [12] Swanson, M. L., *Canadian Journal of Physics*, CJPHA, Vol. 44, 1966, p. 3241.
- [13] Piercy, G. R., *Journal of Nuclear Materials*, JNUMA, Vol. 26, 1968, p. 18.

DISCUSSION

*R. B. Adamson*¹—To date, very little is known about the influence of stress on the growth phenomenon. One of your specimens, the composite specimen which was welded into a unit which bowed under the influence of differential growth, developed a stress during irradiation. Is any difference in the results between that specimen and those irradiated in the stress-free condition? Have you considered the possible effects of irradiation enhanced creep or stress influenced growth on your experiment?

J. E. Harbottle (author's closure)—One of the reasons for having two types of specimen was to examine the effect of stress on the growth strain. No difference was detected in the results from the stressed and the unstressed specimens. The stress developed in the bow specimens is very small and would be unlikely to produce measurable *thermal* creep. The highest temperature at which bow specimens were used was 80 C so the possibility of significant thermal creep is discounted. The stresses are so low that the creep due to *growth* in a polycrystal (radiation enhanced creep) is only a small fraction of the stress-free growth strain.

I have not considered the effect of stress on the growth rate of a single crystal of Zircaloy 2. The experiments of Buckley² on uranium single crystals indicate that stress does not effect their growth rate, but as there are other differences in the growth behavior of the two materials, this observation does not apply necessarily to Zircaloy 2.

*A. L. Bement*³—Both G. R. Piercy and F. A. Nichols have been critical of your past interpretations of growth in Zircaloy 2. G. R. Piercy's⁴ criticism pertained to the difficulty of explaining the in-pile creep data of Fidleris⁴ from the value of the growth coefficient, G , previously reported by Hesketh⁴ (assumed constant with neutron fluence). F. A. Nichols'⁵ criticism pertained to your assumption that Roberts-Cottrell yield creep, which would not be expected to exhibit a reversal in creep strain upon annealing, is controlling. Do the results reported in this paper reconcile these criticisms?

¹ Metallurgist, Knolls Atomic Power Laboratory, Schenectady, N.Y. 12301.

² Buckley, S. N., "Uranium and Graphite," Institute of Metals Spring Meeting, London, 1962.

³ Battelle-Northwest, Richland, Wash. 99352.

⁴ See *Journal of Nuclear Materials*, JNUMA, Vol. 26, 1968.

⁵ See *Journal of Nuclear Materials*, JNUMA, Vol. 26, 1968.

J. E. Harbottle (author's closure)—In a manuscript freely commended by one editor of the *Journal of Nuclear Materials* and firmly rejected by another, R. V. Hesketh has replied to the criticisms of Piercy and of Nichols. There is no difficulty in explaining the in-pile creep data of Fidleris. The initially high value of G explains why steady irradiation creep can be distinguished after about 600 h instead of after about 8000 h, as one would expect if G were to be nearly unity from the beginning of irradiation [5]. There is a confusion in Nichols' work between steady creep and transient creep. The transient probably is not negligible in the relaxation data of the Bettis group. Nichols' criticism rests upon these data.

*E. Ruedl*¹

Quantitative Transmission Electron Microscopy of Bubbles in Al and Al-Al₂O₃ Alloys

REFERENCE: Ruedl, E., "Quantitative Transmission Electron Microscopy of Bubbles in Al and Al-Al₂O₃ Alloys," *Irradiation Effects on Structural Alloys for Nuclear Reactor Applications*, ASTM STP 484, American Society for Testing and Materials, 1970, pp. 300-316.

ABSTRACT: The density and size distribution of small helium bubbles, present in thin foils of Al and Al-Al₂O₃ after alpha particle bombardment and postbombardment annealing, were measured by means of transmission electron microscopy. For making these measurements the conditions for visibility were first established by theoretical calculations of contrast for void sizes similar to those of the observed bubbles. Micrographs were then taken in suitable contrast conditions and the number and size of the bubbles measured on the micrographs. It was found that the density of small bubbles, present in the matrix, can be measured accurately. The density of small bubbles attached to particles, on the other hand, is difficult to measure. Furthermore, the size of very small bubbles is hard to determine with precision since it depends on different parameters. The size and shape of larger bubbles can be established by tilting and stereomicroscopy.

KEY WORDS: irradiation, alpha irradiation, radiation effects, electron microscopy, stereoscopy, heat treatment, deformation, computation, bubbles, voids, helium, aluminum, aluminum alloys, aluminum oxides

The contrast behavior in transmission of empty or gas filled voids in a solid with or without surrounding strain field has been the subject of several theoretical studies [1-4].² The results of these studies showed that a careful examination of the contrast is necessary to obtain detailed information about voids, particularly if the voids are small. Although transmission electron microscopy was very frequently used to examine voids in solids, most of these studies were not made under checked conditions. These investigations, therefore, do not represent suitable tests to

¹ Materials Department, CCR-Euratom, Ispra, Varese, Italy.

² Italic numbers in brackets refer to the list of references at the end of this paper.

evaluate how far quantitative measurements of voids can be made by means of electron microscopy.

Background for the Experiment

During the course of an electron microscopic study of radiation damage effects in aluminum (Al) and aluminum alloys containing dispersed alumina particles (Al–Al₂O₃), thin foils of these materials were bombarded with α particles at 150 ± 50 C (302 F) [5]. After the bombardment finely distributed dots ranging in size from 10 to ~ 40 Å were observed in the Al matrix of the foils; furthermore, features resembling voids were detectable at the interface of the particles. From the annealing behavior at temperatures above 300 C (>570 F) it was concluded that the dots present in the matrix and the features observed at the particle interface were voids filled with helium [5]. The dislocation density in the foils, on the other hand, was low; the contrast behavior of the voids could therefore be studied in detail. The voids were examined in strongly diffracting conditions where, according to Ingram's theoretical calculations [4], the strain contrast becomes the dominant image forming mechanism. Furthermore, high-order reflections were used for the image as recommended by Brown and Mazey [6]. None of these examinations revealed contrast effects at the voids due to a surrounding strain field. If the examined voids had been surrounded by a strain field, this strain field was certainly weak.³ Therefore it is assumed that the He pressure within the voids is approximately balanced by the surface tension; the observed voids will be called He bubbles in this text.

It was of interest to gain insight into the details of the formation and annealing behavior of the bubbles in the Al and Al–Al₂O₃ foils. To obtain such information it is valuable to know the density, the size distribution, and the volume fraction of the bubbles resulting from the various treatments. An attempt was made therefore to measure quantitatively the number and size of the bubbles as observed after α bombardment, and after postbombardment annealing. The measurements were performed such that theoretical contrast calculations were first made for void sizes similar to those of the observed bubbles to establish the conditions for their visibility. Micrographs were then taken in suitable conditions and the number and size of the bubbles imaged on the micrographs were analyzed.

In the present paper the study of the small bubbles is described in greater detail. It will be shown by theory and by experiments that the conditions for good visibility of such bubbles are restricted. In addition,

³ As shown by Lidiard and Nelson in Ref 7, a gas filled void even in thermodynamic equilibrium with a solid has a surrounding strain field. This strain field, however, is presumably only small.

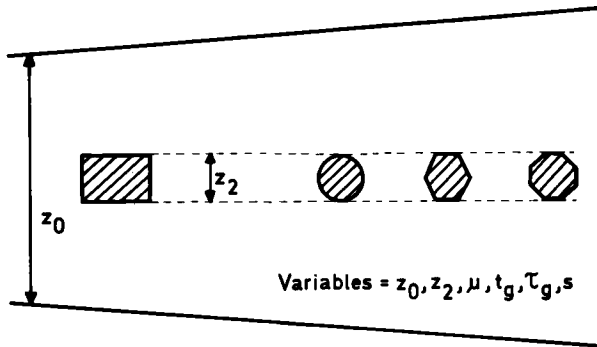


FIG. 1—Schematic representation of voids of various shapes in wedge shaped foil. Variables to be considered for the calculation of contrast at voids are indicated.

some information is also given about larger bubbles which can be more easily examined.

Materials, Specimen Preparation, Irradiation Conditions, and Methods of Observation

The details about (1) the materials used for the present study, (2) the preparation of the specimens, (3) the irradiation conditions, and (4) the methods of observation are given in Ref 5.

Theoretical Considerations

The situation to be considered in the present study for the theoretical calculations of contrast at voids is demonstrated in Fig. 1. Strain-free voids of varying shape and different vertical dimension z_2 are present in a wedge shaped foil at various total foil thicknesses z_0 . The variables to be taken into account for the calculations are indicated in Fig. 1; namely, z_0 and z_2 , the absorption coefficient μ for the matrix, the extinction distance t_g and the absorption distance τ_g in the matrix depending on the reflection used for the image, and s representing the deviation from the Bragg condition.

For the contrast calculations the method developed in Ref 1 was used, which treats the diffraction contrast at voids not surrounded by a strain field. This method was found to be suitable for the present calculations since (1) the bubbles observed in the present work were not surrounded by any detectable strain field and (2) agreement was found previously between the theoretical contrast obtained by this method and experimental observations of contrast at voids in rutile (TiO_2) [1] and at very small bubbles in Al [8].

In the present work detailed calculations of contrast were made only for the exact Bragg condition ($s=0$), since the experimental observations described in Refs 1 and 8 have shown that at deviations ($s \neq 0$) voids

located at particular depths in the foil become invisible. Studies at $s \neq 0$, therefore, are not suitable for a quantitative determination of the density of voids. For this reason, in Fig. 1 the relative distances between the voids and the top and bottom surfaces are not considered as variables.

The thickness-intensity relationships obtained by calculation and used to determine the contrast at voids in bright field (BF) are shown in Fig. 2. The corresponding intensity profiles for $s=0$ in the dark field (DF) can be found in Ref 1. In Fig. 2, one curve corresponds to the transmitted intensity I_T for the case $s=0$ and $\mu=2\pi/\tau_g$ (with $\tau_g/t_g=12$). This curve is suitable for the evaluation of contrast at voids in Al, imaged by a low-order reflection. The second curve in Fig. 2 corresponds to I_T for $s=0$ and $\mu=4\pi/\tau_g$. This curve is suitable for the evaluation of contrast at voids in Al imaged by (1) higher order reflections, due to the drop of τ_g/t_g for higher order reflections [9], or (2) systematic reflections, due to the decrease of t_g for systematic reflections [10]. The third curve in Fig. 2 corresponds to I_T for the case of $st_g=1$ and $\mu=2\pi/\tau_g$. This curve demonstrates the decrease of t_g at $s \neq 0$, leading to an effective extinction distance $t_g^* = t_g \sqrt{1+x^2}$ with $x = st_g$. As mentioned before, a decrease of t_g can also be expected when systematic reflections are used for the image.

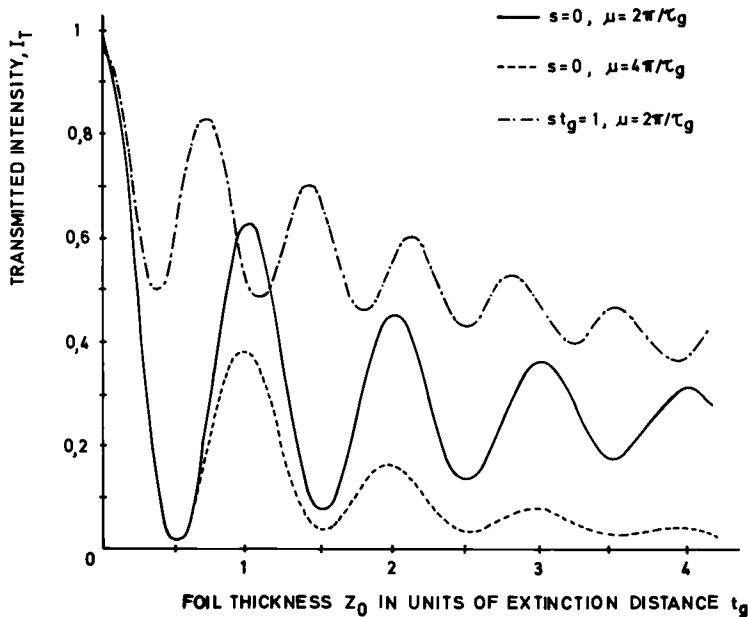


FIG. 2—Intensity-thickness relationships for the bright field. Two curves correspond to the transmitted intensity I_T for $s=0$ and absorption coefficients $\mu=2\pi/\tau_g$ or $\mu=4\pi/\tau_g$. The third curve corresponds to I_T for $st_g=1$ and $\mu=2\pi/\tau_g$.

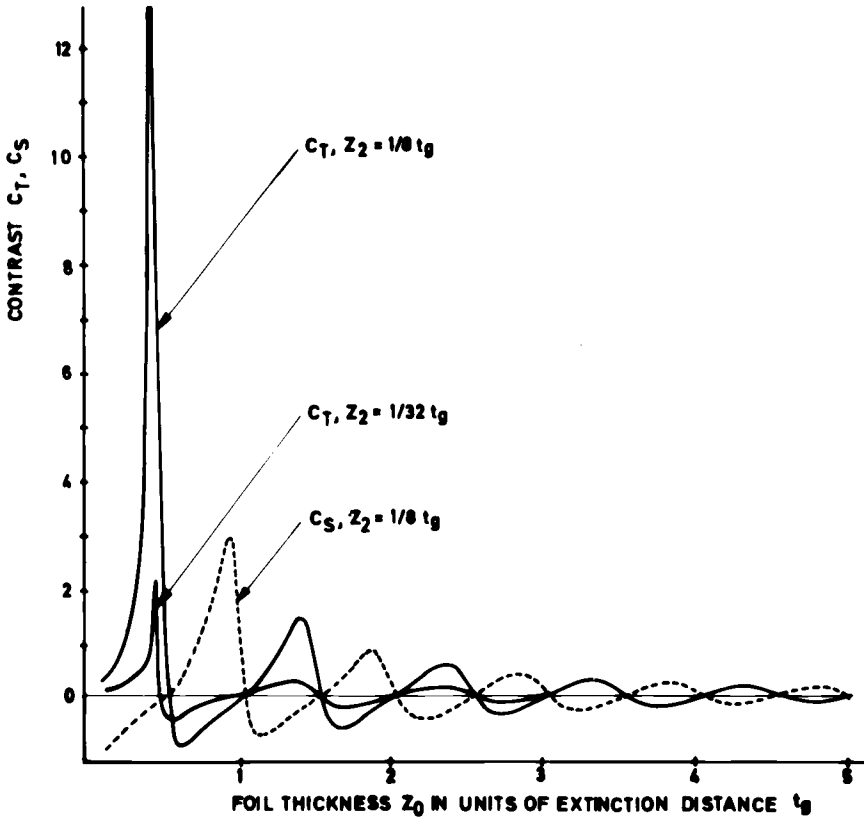


FIG. 3—Variation of contrast in bright field (C_T) and dark field (C_S) with increasing foil thickness z_0 in units of extinction distance t_g , for two void thicknesses z_2 , for $s=0$ and $\mu=2\pi/\tau_g$.

The theoretical contrast at voids in bright field (C_T) and dark field (C_S) was determined from the intensity-thickness relationships as described in Ref 1. The theoretical contrast obtained will now be described separately for small and larger voids, the former corresponding to the bubble sizes observed in the as-bombarded foils and the latter corresponding to the bubble sizes observed in the bombarded and annealed foils.

Contrast at Small Voids

Figure 3 shows the variation of C_T and C_S at increasing total foil thickness z_0 (in units of t_g) for small voids, for $s=0$ and $\mu=2\pi/\tau_g$. Two curves of this figure represent C_T and C_S for a void of thickness $z_2=1/8t_g$, and the third curve, for comparison, represents C_T for a void with $z_2=1/32t_g$.

From Fig. 3 the following contrast behavior can be deduced for small voids: at $s=0$, voids exhibit the strongest contrast within a narrow region

at the front of the first dark thickness fringe in BF. To look for very small voids one should therefore examine this region. However, when using lower order reflections, which gave better contrast than higher order reflections as described later, the region exhibiting the strongest contrast at voids corresponds to a very small foil thickness. Therefore it may be more useful to look for small voids at the front and the rear of the first dark thickness fringe in DF or at the front of the second dark fringe in BF. These regions correspond to a somewhat greater foil thickness and the contrast at small voids within these regions should be strong enough to be visible. It furthermore can be deduced from the profiles that the voids exhibit positive contrast at the front and negative contrast at the rear of the dark fringes in BF and show the opposite contrast behavior in DF. In the thicker part of the foil, where absorption becomes important, smaller voids become invisible because their contrast is too weak.

When a higher order reflection is used for the image, the regions where voids exhibit strong contrast are shifted to greater foil thicknesses. It may then occur that voids become visible at foil thicknesses at which they are invisible when imaged by a low-order reflection, and vice versa. One has to consider also the increased absorption when using a higher order reflection [9]; hence, generally, a somewhat weaker contrast is expected at voids imaged by a higher order reflection.

Contrast at Larger Voids

Figure 4 shows the variation of C_T and C_S at voids of increasing thickness z_2 , for a total foil thickness $z_0 = 2t_0$ and $s = 0$. Two curves in Fig. 4 are for $\mu = 2\pi/\tau_0$, the other two curves are for $\mu = 4\pi/\tau_0$. The figure shows that for the smaller absorption the voids exhibit predominantly negative contrast in BF and predominantly positive contrast in DF. For the larger absorption the voids will become predominantly bright in BF and practically all bright in DF.

When the total foil thickness z_0 is increased, the contrast at voids of various thicknesses z_2 will tend to become predominantly positive for $s = 0$ in BF. Furthermore, the contrast at voids will be only positive in thicker foil parts at very large deviations from the Bragg condition (contrast mainly due to absorption).

Visible Size of Small Voids

Some qualitative statements about the visible size of small voids can be made. Let us consider a void of small constant thickness z_2 such as that shown in Fig. 1 to the left, located in the thin part of a foil (small absorption). Let us assume that at this void just enough contrast arises to make the void visible. Such a void will then show its full size due to its constant thickness. Voids of the same thickness z_2 but of spherical or polygonal

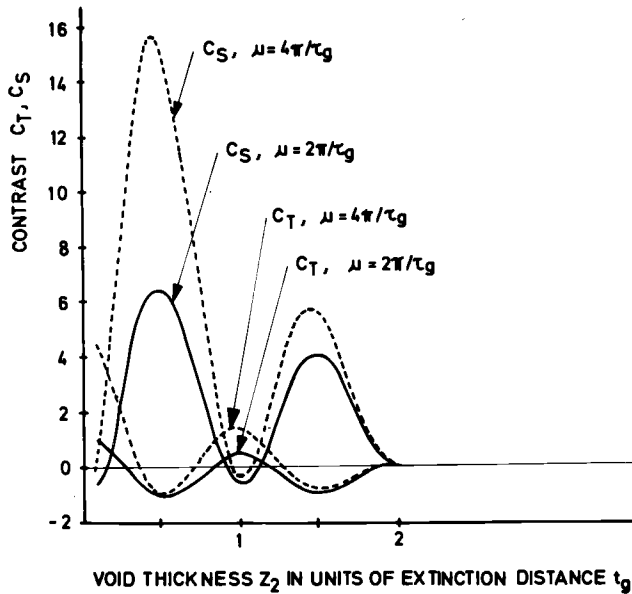


FIG. 4—Variation of contrast C_T and C_S with increasing void thickness z_2 in units of t_g , for a total foil thickness $z_0 = 2t_g$, $s = 0$ and $\mu = 2\pi/\tau_g$ or $\mu = 4\pi/\tau_g$.

shapes such as those shown to the right of Fig. 1, on the other hand, will exhibit enough contrast at void thickness z_2 to be visible but not enough at smaller thicknesses. Therefore, one reasonably can assume that the visible size of very small voids not having a constant thickness will be somewhat smaller than the true size. A somewhat smaller visible size can also be expected for a small void when the absorption becomes larger, as for instance when a higher order reflection is used for the image or the void is located in the thicker foil.

Experimental Results

Measurement of the Number of Bubbles

The examination of the wedge shaped, α bombarded Al and Al-Al₂O₃ foils did not reveal He bubbles up to a thickness of $\sim 600 \text{ \AA}$. Only in foil regions of thicknesses greater than $\sim 600 \text{ \AA}$, were small bubbles observed. Figure 5 shows a BF micrograph of an Al foil, α bombarded for three weeks at $150 \pm 50 \text{ C}$, for a $[200]$ reflection at $s = 0$. The second dark thickness fringe is seen. The bubbles are best revealed at the front and at the rear of this fringe at foil thicknesses predicted by theory. Their contrast is positive at the front and negative at the rear of the fringe as expected.

Figures 6 and 7 demonstrate the effect of increased absorption for a case in which a higher order reflection instead of a low-order reflection is

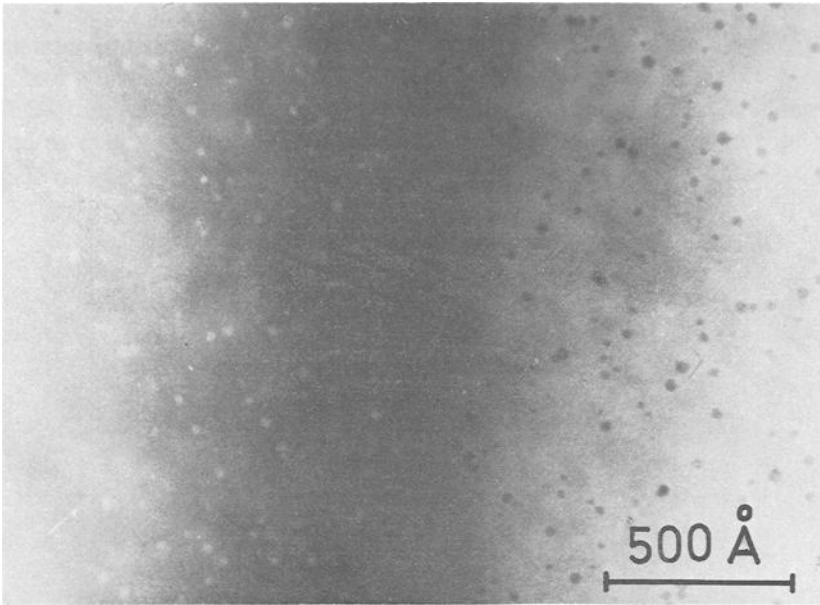


FIG. 5—*BF* micrograph of wedge shaped Al foil after α bombardment. Contrast conditions: $s=0$, $g=[200]$. Second dark thickness fringe visible.

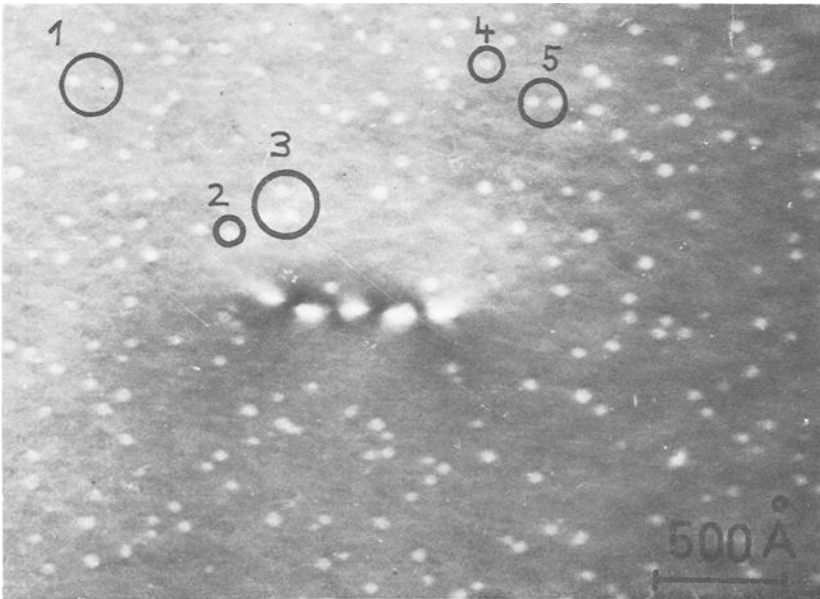


FIG. 6—*BF* micrograph of α bombarded Al foil, imaged at $s=0$ using a $[200]$ reflection. A region at the front of the third dark thickness fringe is shown.

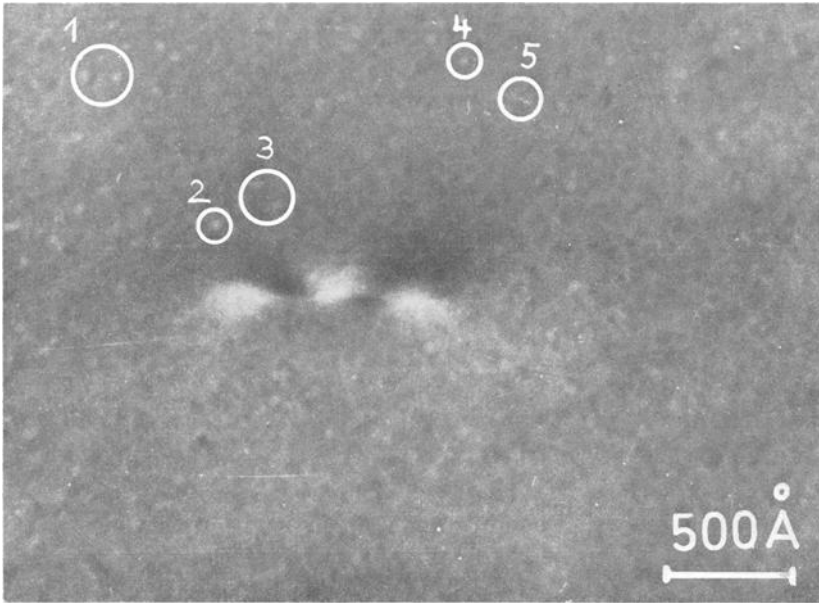


FIG. 7—BF micrograph of the same region as shown in Fig. 6, imaged at $s=0$ by using a $[220]$ reflection. The front of the second dark fringe is now seen. By comparing identical bubbles on Figs. 6 and 7 (examples are encircled and numbered) one notices a strong decrease of contrast and a smaller diameter for bubbles imaged by the higher order reflection.

used for the image. Figure 6 represents an α bombarded Al foil imaged in BF at $s=0$ by a $[200]$ reflection. A region at the front of the third dark thickness fringe is shown. Figure 7 represents the same region (reference point the visible dislocation) imaged at $s=0$ by a $[220]$ reflection. The front side of the second dark thickness fringe can now be seen. In the case of Al, by choosing these two reflections the extinction distances are such that the centers of the third dark thickness fringe due to $\mathbf{g}=[200]$ and of the second dark fringe due to $\mathbf{g}=[220]$ occur at a very similar foil thickness (~ 1600 Å). The regions at the front of these two fringes, where bubbles are best visible, occur at a very similar thickness as well. The results of contrast calculation showed that bubbles present at the front of the second dark fringe corresponding to $\mathbf{g}=[220]$ exhibit a slightly weaker contrast than the bubbles present at the front of the third dark fringe corresponding to $\mathbf{g}=[200]$. This is due to the decrease of the apparent foil and bubble thickness when using the higher order reflection. Comparing the contrast of identical bubbles in Figs. 6 and 7 (examples are encircled and numbered on the two micrographs), a strong decrease of contrast at bubbles in Fig. 7 is found; also a decrease of the bubble diameter is observed. This strong decrease of contrast cannot be explained entirely by a decrease of the ap-

parent foil and bubble thickness. It is suggested that the increase of absorption when using the higher order reflection for the image contributes to the observed decrease of contrast (and bubble diameter). All of these observations are in agreement with the theoretical predictions.

For the measurement of the density of very small bubbles, therefore, a [200] reflection was used for the image and photographs were taken at $s=0$ at the front and rear of the first four dark thickness fringes in BF and DF. The number of the bubbles within these regions was measured on the photographs; thus the number of bubbles was obtained in different regions corresponding to foil thicknesses ranging from 800 to ~ 2600 Å. The results of these measurements are shown in Fig. 8 in the form of a plot of the number of bubbles per unit area against the total foil thickness z_0 .

Figure 9 shows a BF micrograph of an α bombarded Al-1Al₂O₃ foil, imaged by a [200] reflection at $s=0$. Again, the second dark thickness fringe is shown. This micrograph demonstrates that in the thin parts of the foil the contrast behavior of the Al₂O₃ particles (indicated by arrows) is the same as that of the small bubbles.

A detailed description of the contrast occurring at particles in Al was presented by Guyot [11]. As a consequence of the similar contrast, the presence of small bubbles at the particle-matrix interface, therefore, cannot be detected in the thin parts of the foil. To see small bubbles attached to particles one has to choose contrast conditions mainly due to absorption. The bubbles will then appear brighter and the particles darker with respect to the background and thus will be distinguishable from each other. This is demonstrated in Fig. 10, which represents a BF micrograph of an α

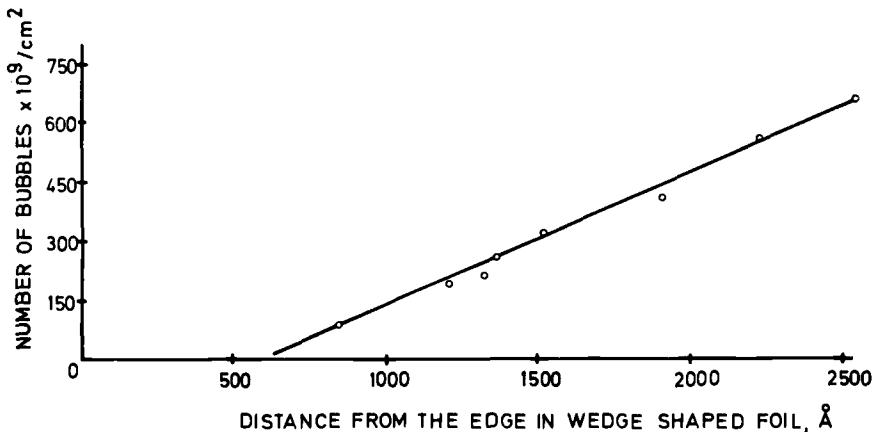


FIG. 8—The variation in number per unit area of He bubbles with increasing distance from the edge of wedge shaped, α bombarded Al foil.

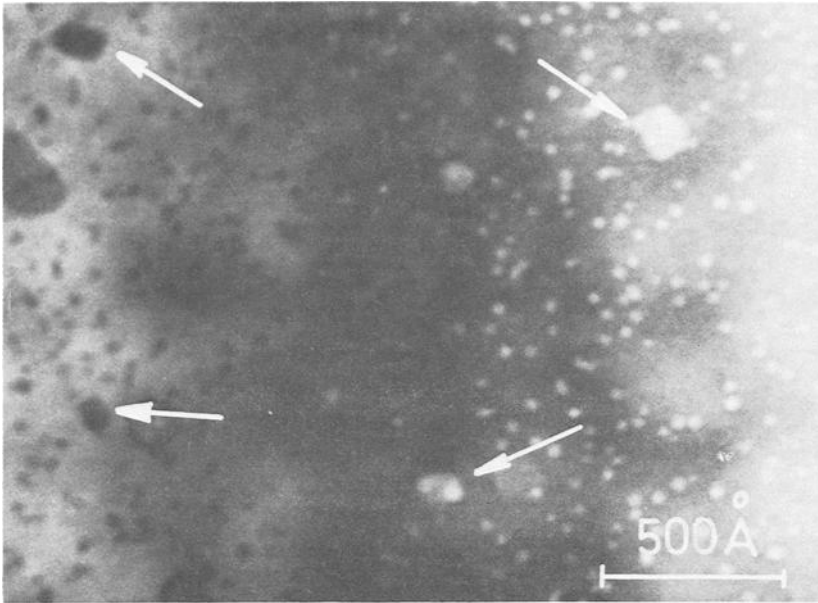


FIG. 9—*BF* micrograph of α bombarded $Al-1Al_2O_3$ foil. Contrast conditions: $s=0$, $g=[200]$. Note similar contrast of bubbles and particles (arrows) at the edges of the dark thickness fringe.

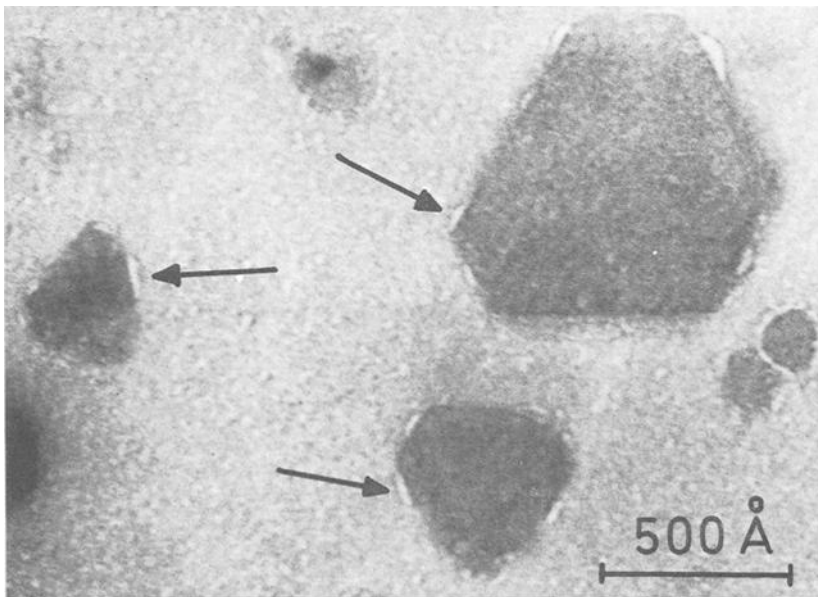


FIG. 10—*BF* micrograph of α bombarded $Al-2.5Al_2O_3$ foil, taken at highest possible resolution. The small bubbles visible at the particle interface (arrows) and the particles themselves are imaged by absorption contrast.

bombarded Al-2.5Al₂O₃ foil. The contrast on this micrograph is mainly due to absorption. The thickness of the shown region was ~ 2500 Å. The micrograph was taken at the highest possible resolution. Small bubbles (indicated by arrows) are now revealed at the interface of the particles. The very small bubbles present in the matrix, on the other hand, are no longer discernible, their contrast due to absorption being too weak.

For the determination of the density of larger bubbles as observed in the α bombarded and annealed foils, contrast conditions mainly due to absorption also were chosen for the image.

Measurement of the Size Distribution of Bubbles

As demonstrated in Fig. 7, the visible diameter of the very small bubbles slightly decreased when using a higher order reflection for the image. For the determination of the size distribution of very small bubbles, only micrographs were therefore analyzed, taken in a [200] reflection. The results of these analyses are shown in the form of histograms of bubble sizes in Figs. 11, 12, and 13. Figures 11 and 12 present the size distribution measured within a region (a) at the front of the second dark thickness fringe in BF, corresponding to a foil thickness ranging from 800 to 900 Å, and (b) at the rear of the second dark fringe corresponding to a foil thickness ranging from 1150 to 1250 Å. Figure 13, on the other hand, represents the size distribution of the bubbles measured within regions at the front (drawn line) and at the rear (dotted line) of the third dark thickness fringe in BF, corresponding to foil thicknesses ranging from 1480 to 1580 Å and 1850 to 1950 Å, respectively. It is seen that the size distribution at the front and at the rear of the third fringe are similar.

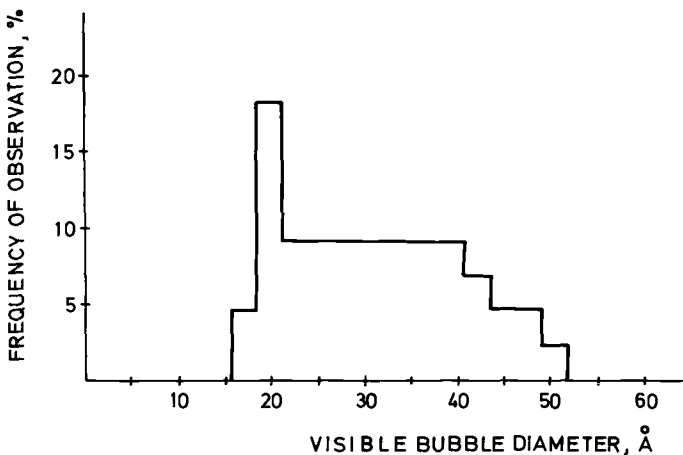


FIG. 11—Histogram of bubble sizes in α bombarded Al foil as measured at the front of the second dark thickness fringe in BF (number of bubbles analyzed=160, in surface area of 2×10^{-9} cm²).

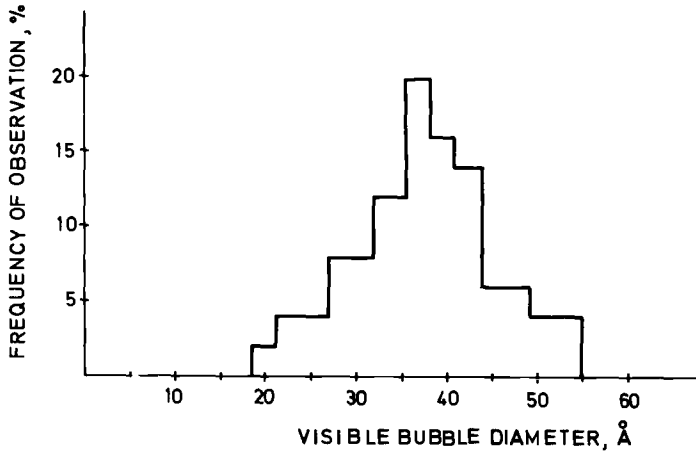


FIG. 12—Histogram of bubble sizes in α bombarded Al foil as measured at the rear of the second dark thickness fringe in BF (number of bubbles analyzed = 160, in surface area of $8.8 \times 10^{-10} \text{ cm}^2$).

Determination of the Shape of Larger Bubbles Present in the Matrix or at Particles

For the measurement of the volume fraction of the larges bubbles formed in the matrix and at particles in the bombarded and annealed foils, the size and shape of these bubbles have to be known. Tilting experiments

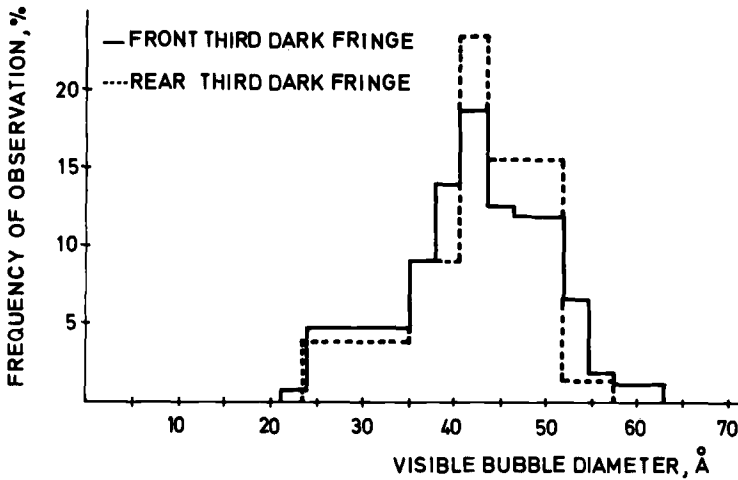


FIG. 13—Histogram of bubble sizes in α bombarded Al foil as measured at the front of the third dark thickness fringe (drawn line) and at the rear of this fringe (dotted line) in BF (number of bubbles analyzed = 160, in surface area of 4.8 and $4 \times 10^{-10} \text{ cm}^2$, respectively).

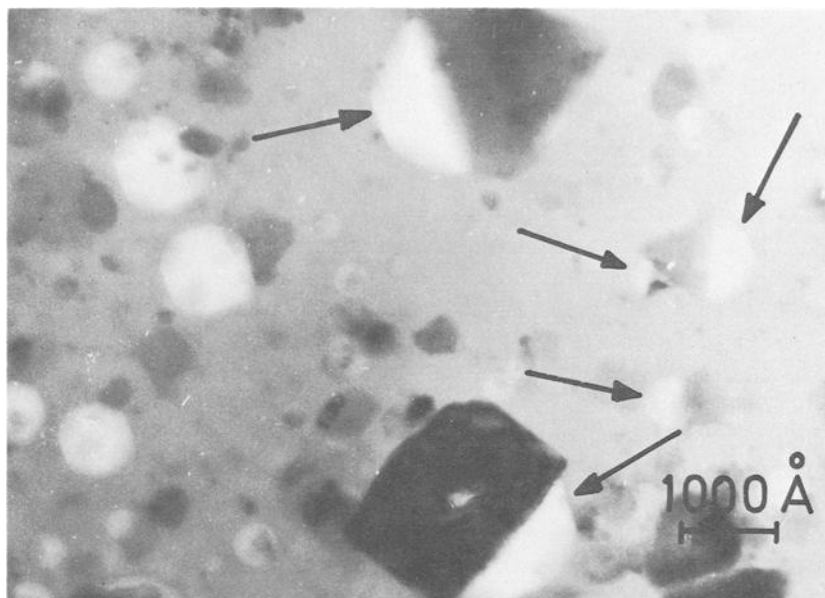


FIG. 14—*BF micrograph of an Al-2.5Al₂O₃ foil α bombarded and subsequently annealed.*

and stereoscopic observations were made to determine the shape and position of the bubbles in contact with particles.

It was found that the bubbles were attached to single faces of the particles and had a configuration similar to that shown in Ref 12 for a bubble attached to a flat, rigid precipitate. Figure 14 demonstrates the configuration of large bubbles (marked by arrows) at particles observed in Al-2.5Al₂O₃ foil which was α bombarded and subsequently annealed for 1 h at 630 C (1162 F).

Discussion

In Fig. 8 the proportionality resulting between the number of bubbles and the foil thickness up to ~ 2600 Å indicates that no relevant overlap of bubbles in projection, leading to a decreased number of bubbles, occurred up to this foil thickness. The interception at ~ 600 Å on the abscissa, on the other hand, shows that below ~ 600 Å foil thickness bubbles either were not formed or were too small to be resolved.

The apparent absence of bubbles in the thinnest parts of the foil can be the result of various conditions. One possible reason could be a radiation induced loss of the injected He from regions near the surface. As shown in Ref 13, He is released from α bombarded Al during postbombardment annealing provided the surface oxide skin is not too thick. Another possible

reason could be the presence of a rather thick oxide film on the surface of the examined specimens. Owing to a presumed lower mobility of the He within the surface oxide, bubbles may not have formed there. Since the dose and dose rate of the α particles, as well as the thickness of the oxide present on the surface of the bombarded specimens, were not precisely known, it is not possible, presently, to draw a conclusion about the apparent absence of bubbles in the thinnest parts of the foil.

The histograms of bubble sizes shown in Figs. 11, 12, and 13 indicate that the mean diameter of the bubbles increased up to a foil thickness of ~ 1500 Å. Only above this thickness does the mean bubble diameter become constant. Overlap of bubble images leading to an apparent increase of the diameter in regions of greater foil thickness can be ruled out on the basis of the proportionality observed in Fig. 8. The theoretical considerations about the visibility of small voids, on the other hand, have shown that the visible size of a very small void should decrease with increasing foil thickness owing to the general decrease of contrast (see Fig. 3). The experimental results, however, indicate an increase of the bubble diameter with increasing foil thickness. Changes in the visible size of bubbles at different foil thicknesses, therefore, cannot be the reason for the observed increase. It is suggested that the previously proposed anomalies in regions near the foil surface are the reason for the observed increase of bubble diameter.

Changes in the density and size distribution of voids with foil thickness (thin-foil effects) have to be considered in all those experiments where voids are produced by bombardment in prethinned specimens. On the other hand, when irradiated specimens containing voids are thinned to electron transparency, the opening of voids or the leaching out of particles has to be considered. Proper corrections then have to be made to obtain quantitative results [14].

Conclusions

1. The density of very small, strain-free bubbles in a solid can be accurately measured by means of transmission electron microscopy, provided the bubbles are all resolvable by the microscope and the chosen contrast conditions are such that all bubbles are revealed.
2. The density of small bubbles attached to particles is difficult to measure. Micrographs have to be taken at the highest resolution, and contrast conditions mainly due to absorption have to be used to detect the bubbles near particles.
3. The size of very small bubbles is hard to determine with precision since the visible size of such bubbles is smaller than the true size, depending on the shape and on the absorption conditions. The size and shape of larger bubbles, on the other hand, can be established by tilting experiments and stereoscopic observations.

4. A determination of the number and size of bubbles at different foil thicknesses is necessary to establish whether thin-foil effects, overlap of bubble images, or opening of bubbles at the specimen surface as a consequence of thinning influences the results of measurement.

References

- [1] Van Landuyt, J., Gevers, R., and Amelineckx, S., *Physica Status Solidi*, PSSAB, Vol. 10, 1965, pp. 319–335.
- [2] Ashby, M. F. and Brown, L. M., *Philosophical Magazine*, PHMAA, Vol. 8, 1963, pp. 1649–1776.
- [3] Rühle, M. in *Proceedings of the Symposium on Radiation Damage in Reactor Materials*, Vol. 1, International Atomic Energy Agency, Vienna, June 1969, pp. 113–158.
- [4] Ingram, J., *Journal of Applied Physics*, JAPIA, Vol. 40, 1969, pp. 5030–5038.
- [5] Ruedl, E. in *Proceedings of the Symposium on Radiation Damage in Reactor Materials*, International Atomic Energy Agency, Vol. 1, Vienna, June 1969, pp. 171–183.
- [6] Brown, L. M. and Mazey, D. J., *Philosophical Magazine*, PHMAA, Vol. 10, 1964, pp. 1081–1085.
- [7] Lidiard, A. B. and Nelson, R. S., *Philosophical Magazine*, PHMAA, Vol. 17, 1968, pp. 425–429.
- [8] Ruedl, E. and Staroste, E. in *Proceedings of the Septième Congrès International de Microscopie Électronique*, Vol. 2, Grenoble, Sept. 1970, p. 343.
- [9] Humphreys, C. J. and Hirsch, P. B., *Philosophical Magazine*, PHMAA, Vol. 18, 1968, pp. 115–122.
- [10] Hirsch, P. B., Howie, A., Nicholson, P. B., Pashley, D. W., and Whelan, M. J., *Electron Microscopy of Thin Crystals*, Chapter 12, Butterworths, London, 1965.
- [11] Guyot, P., *Physica Status Solidi*, PSSAB, Vol. 33, 1969, pp. 201–208.
- [12] Nelson, R. S., *Journal of Nuclear Materials*, JNUMA, Vol. 19, 1966, pp. 149–154.
- [13] Glide, H. R. and Mayne, K. I., *Philosophical Magazine*, PHMAA, Vol. 12, 1965, pp. 997–1003.
- [14] Hilliard, J. E., *Transactions*, Metallurgical Society of AIME, TMSAA, Vol. 224, 1962, pp. 906–917.

DISCUSSION

*K. M. Zwilsky*¹

1. Did you strain the foils and observe what happens to the He bubbles?
2. Did you correlate any mechanical properties of the α injected Al and Al-Al₂O₃ foils with He bubbles?

E. Ruedl (author's closure)

1. We have strained the α bombarded Al and Al-Al₂O₃ foils within the microscope at 20 C by means of a microtensile straining device. As a result of the deformation, the small bubbles showed a tendency to line up in rows in the direction of the maximum applied stress. Some of the larger bubbles contained in the rows exhibited contrast effects due to a surrounding strain field. Such contrast effects were not observed in the as-bombarded foils. A possible interpretation of the strain field observed around some of the bubbles after deformation would be that these bubbles were formed by coalescence of smaller bubbles. Since the deformation experiments were performed at 20 C, the bubbles formed by coalescence would not be able to readjust their radius R by $R^2 = r_1^2 + r_2^2$ to come again in an approximate equilibrium with the He pressure. We intend to study the described phenomena in greater detail.

2. Up to now we have not made a study to correlate the mechanical properties of the α bombarded foils and the He bubbles present in these foils.

¹ U. S. Atomic Energy Commission.

R. Bullough¹ and R. C. Perrin¹

The Mechanism and Kinetics of Void Growth During Neutron Irradiation

REFERENCE: Bullough, R. and Perrin, R. C., "The Mechanism and Kinetics of Void Growth During Neutron Irradiation," *Irradiation Effects on Structural Alloys for Nuclear Reactor Applications, ASTM STP 484*, American Society for Testing and Materials, 1970, pp. 317–331.

ABSTRACT: A theoretical model is presented that is particularly appropriate for a study of void growth kinetics at high neutron doses. These kinetics are presented for peak swelling temperatures where recombination effects can be neglected; their dependence on dislocation density, void density, and dose rate is discussed.

KEY WORDS: irradiation, neutron irradiation, nuclear reactors, dislocations (materials), interstitials, voids, gases, swelling, cold working, stainless steels, structural members, lattices (mathematics)

It is now well established that neutron irradiation of stainless steel and other metals can lead to the formation and growth of extensive voidage. Since the consequent swelling can lead to obvious design problems in the structural reactor components, it is clearly desirable to have a complete understanding of both the mechanism of the void formation and the kinetics of their subsequent growth. Such a theoretical understanding is particularly important if it provides a means for extrapolating the expected swelling beyond total neutron doses than can be achieved in present reactors.

Void Formation and Growth

The basic physical reasons for void formation and growth during neutron irradiation are now reasonably understood and have been discussed in previous papers by us [*1, 2, 3*]² and by other workers [*4, 5*]. Voids are believed to be nucleated as three-dimensional vacancy-inert gas atom

¹Theoretical Physics Division, Atomic Energy Research Establishment, Harwell, Didcot, Berkshire, England.

²Italic numbers in brackets refer to the list of references at the end of this paper.

clusters (small gas bubbles), the presence of gas in these nuclei being essential to ensure their three-dimensional morphology; in the absence of gas the vacancy clusters would adopt a two-dimensional platelet morphology, and this morphology, rather than the spherical void form, would be adopted during any subsequent growth [1]. During this nucleation process, which may continue to quite high neutron doses since inert gas is continually produced, the excess interstitials will aggregate to form numerous interstitial dislocation loops. These interstitial dislocation loops together with the usual deformation induced dislocations have a substantial drift interaction with existing free interstitials but only a small interaction with the vacancies. This means that as the irradiation proceeds the flux of interstitials lost at the dislocation sinks is slightly greater than the corresponding flux of vacancies and, in consequence, a slight excess of vacancies is available to ensure the continuous growth of voids [2, 3]. In a previous calculation [3] we had demonstrated that such a preferential drift process would indeed provide a satisfactory explanation of void growth. In this calculation we used a model in which the actual dislocation distribution was replaced by an idealized set of uniform, parallel straight dislocations. The model had the particular advantage that it enabled the actual spatial form of the interstitial-dislocation drift interaction to be explicitly included in the governing flow equations.

The excess steady state vacancy concentration in the cylindrical regions associated with each dislocation was then calculated and used to estimate the rate of growth of any voids that might be present in such regions. Unfortunately, it was not possible to allow for the cylindrical flow to the dislocations and to simultaneously include the spherical flow in the immediate neighborhood of the voids. Thus by emphasizing the cylindrical flow we certainly profited from accurately including the drift effects but could strictly discuss the void growth rates only when the net loss to the voids was negligible compared with the loss to the dislocations.

This treatment successfully demonstrated that a critical temperature range exists in which the void growth rate³ is a maximum. Furthermore, the predicted temperature ranges for stainless steel and molybdenum are in very good agreement with the observed peak swelling temperature ranges for the corresponding neutron dose rates. The reduction in void growth rate at low temperatures was shown to be due entirely to recombination, and the reduction at high temperatures was identified with the requirement to satisfy the high equilibrium vacancy concentration. A study was also made of the dependence of void growth rate on dislocation density and it was shown that increasing the dislocation density (cold work) leads to an immediate reduction in the growth rate. However it

³ We refer here to the temperature dependence of the growth rate of a single void.

was suggested that this reduction may not be permanently beneficial, since when the dislocation density is high the void radii rapidly increase (as a linear function of dose) and thus could conceivably overtake the slower growing voids in the low dislocation density material. The latter slow growth rate was conjectured and not rigorously established in this previous work; the model was clearly only appropriate to the high dislocation density situation, since only in this case is the net loss to the voids ever relatively negligible. When the dislocation density is small and the loss to the voids is substantial, it clearly is necessary to include the diffusion flow in the spherical region near each void in order to discuss the void growth at high doses.

In the present work we wish to extend this previous calculation into the high dose regime. This extension is achieved by replacing the discrete, idealized dislocation sinks with their associated spatial drift fields by a continuous distribution of *point* sinks. This loss of the discrete nature of the dislocations is unfortunate, but in view of the actual state of the dislocations (a complex combination of dislocation loops and deformation dislocations all tangled up together) the continuous distribution may be argued sensibly to be a more realistic model of the actual dislocation configuration. The presence of preferred drift between the dislocations and the interstitials is included by giving the dislocation elements a slightly larger capture cross section for interstitials than for vacancies. The relative magnitude of the cross sections is obtained by ensuring consistency with the previous explicit drift calculation. The loss to the voids and hence the overall swelling (in the absence of simultaneous void nucleation) is then calculated by considering the point defect diffusion in the neighborhood of each void in the presence of the dislocation sinks. Actually, we also can consider recombination effects, but in the present paper we will omit such nonlinear considerations. This simplification is appropriate to void growth at the peak swelling temperatures [\mathcal{S}] and also will enable us to obtain analytic expressions for the maximum swelling variation with dose. The model is appropriate also for the high dislocation density situation, and we shall see that all our previous conjectures regarding the effects of cold work on the relative swelling are vindicated. Finally, we also shall use this model to discuss the effects of varying dose rate on the peak swelling temperature.

The Model and the Governing Equations

The body is assumed to contain a uniform density ρ_v of spherical voids each of radius $r_v(t)$ and is subjected to continuous neutron irradiation. Each void has an associated spherical volume of radius R where

$$R = 0.68\rho_v^{-1/3} \dots \dots \dots (1)$$

is half the average void separation. If ρ_d is the average dislocation density in the body, then the coupled steady state governing equations for the fractional vacancy and interstitial concentrations, $C_v(r)$ and $C_i(r)$, in the spherical volume around each void are

$$\left. \begin{aligned}
 &D_v \left\{ \frac{d^2}{dr^2} C_v + \frac{2}{r} \frac{d}{dr} C_v \right\} + K - \alpha_R C_v C_i - D_v Z_v \rho_d C_v = 0 \\
 \text{and} & \\
 &D_i \left\{ \frac{d^2}{dr^2} C_i + \frac{2}{r} \frac{d}{dr} C_i \right\} + K - \alpha_R C_v C_i - D_i Z_i \rho_d C_i = 0
 \end{aligned} \right\} \dots\dots\dots (2)$$

where r is the spherical radius measured from the center of a void such that $r_v \leq r \leq R$; D_v and D_i are the vacancy and interstitial diffusion constants, respectively; α_R is the recombination coefficient; Z_v and Z_i are, respectively, the number of sites in an atomic plane crossing each dislocation line from which a vacancy or interstitial can be athermally captured by the dislocation; and K is the dose rate in displacements per atom per second. To allow for the preferential drift of interstitials to the dislocations (compared with the vacancies) we must have $Z_i > Z_v$, and we find, by comparison with our previous explicit spatial drift calculation [2], that Z_i must be about 1 or 2 percent greater than Z_v .

Since $r=R$ is the radius of the spherical volume associated with each void, the boundary conditions on C_v and C_i at $r=R$ are obtained by ensuring that there is zero flux of point defects across this surface; that is, at $r=R$

$$\frac{d}{dr} C_v = 0 \dots\dots\dots (3)$$

$$\frac{d}{dr} C_i = 0 \dots\dots\dots (4)$$

The diffusion controlled net flux of vacancies entering the void must be equal to the kinetically defined net flux of vacancies entering the void and, thus, at $r=r_v$

$$D_v \frac{d}{dr} C_v = K_v [C_v - C_v^e \exp \{F_m b^3 / kT\}] \dots\dots\dots (5)$$

where K_v is the velocity of transfer of a vacancy across the void-matrix interface, C_v^e is the thermal equilibrium vacancy concentration, F_m is the mechanical force tending to shrink the void, and b is a distance on the order of the atomic lattice spacing. Similarly, the interstitial concentration

must satisfy the continuity condition: at $r = r_v$

$$D_i \frac{d}{dr} C_i = K_i C_i \dots \dots \dots (6)$$

where, in the case of interstitials, the probability of interstitial emission from the void is neglected. From the difference of the net fluxes of vacancies and interstitials entering the void, we find that the rate of change of the void radius dr_v/dt must be given by

$$\frac{dr_v}{dt} = D_v \frac{d}{dr} C_v(r_v) - D_i \frac{d}{dr} C_i(r_v) \dots \dots \dots (7)$$

which from Eqs 5 and 6 can be written in the alternative form

$$\frac{dr_v}{dt} = K_v C_v(r_v) - K_i C_i(r_v) - K_v C_v^e \exp [F_m b^3 / kT] \dots \dots \dots (8)$$

If the activation energy for the final defect jump across the void-matrix interface is the same as in the bulk matrix then it can easily be shown that [6]⁴

$$K_v = D_v / b \quad \text{and} \quad K_i = D_i / b \dots \dots \dots (9)$$

Alternatively, if we adopt our previous step model to describe the void-matrix interface, we see that our previous rate equation agrees with Eq 8 if

$$K_v = D_v / 4b \quad \text{and} \quad K_i = D_i / 4b \dots \dots \dots (10)$$

In view of our previous work [1, 3] we have a slight formal preference for Eq 10 over Eq 9, but we shall see that because of the very small absolute magnitude of b the detailed growth kinetics are not sensitive to the choice.

To obtain the void growth rate we have to solve the governing Eqs 2 for C_v and C_i subject to the boundary conditions of Eqs 3 and 4 at $r = R$ and Eqs 5 and 6 at $r = r_v$. These concentrations then can be substituted in either Eq 7 or 8 to provide the void growth rate as a function of r_v . It is necessary then to integrate this differential equation to determine the variation of r_v with time (dose). It is clear that because of the nonlinear recombination terms in Eq 2 this prescription cannot be followed analytically and the general solution must be derived by a complex numerical procedure. We are at present developing such a general procedure, but in the present paper we will restrict the discussion to the situation when the recombination term is zero. Fortunately, as we have shown previously [3], recombination effects are usually small at the peak swelling temperatures and higher, and therefore we feel justified in presenting a detailed solution

⁴ Reference 6 is a detailed discussion of the various physical factors defining such velocity parameters.

appropriate only to such important high-temperature regimes. When the recombination terms are omitted in Eq 2, the two governing equations decouple and can be solved independently, each subject to its two boundary conditions. The general expression for dr_v/dt from Eq 7 or 8 then takes the rather complex form

$$\frac{dr_v}{dt} = \frac{\gamma(K - D_v Z_v \rho_d \bar{C})}{Z_v \rho_d} \times \left\{ \frac{(R - r_v)\beta_v \cosh \beta_v(R - r_v) + (r_v R \beta_v^2 - 1) \sinh \beta_v(R - r_v)}{(R - r_v + r_v R \gamma)\beta_v \cosh \beta_v(R - r_v) + (r_v R \beta_v^2 - 1 - \gamma r_v) \sinh \beta_v(R - r_v)} \right\} - \frac{\gamma K}{Z_i \rho_d} \times \left\{ \frac{(R - r_v)\beta_i \cosh \beta_i(R - r_v) + (r_v R \beta_i^2 - 1) \sinh \beta_i(R - r_v)}{(R - r_v + r_v R \gamma)\beta_i \cosh \beta_i(R - r_v) + (r_v R \beta_i^2 - 1 - \gamma r_v) \sinh \beta_i(R - r_v)} \right\} \tag{11}$$

where

$$\bar{C} = C_v^e \exp [F_m b^3 / kT] \dots \dots \dots \tag{12}$$

$$\beta_v = [Z_v \rho_d]^{1/2} \quad \text{and} \quad \beta_i = [Z_i \rho_d]^{1/2} \dots \dots \dots \tag{13}$$

and

$$\gamma = K_v / D_v = K_i / D_i \dots \dots \dots \tag{14}$$

This nonlinear first-order differential equation has been successfully integrated and some detailed numerical results are presented and discussed in the section on kinetics. However, it is first useful to investigate the analytic form of Eq 11 and its integral in certain limiting situations. This discussion is presented in the next section, where we shall derive approximate analytic criteria which define the various void growth regimes.

Analytic Void Growth Relations

Since we shall be primarily concerned with the kinetics of void growth at high total neutron doses, we may reasonably assume that the minimum void radii we wish to consider are greater than the lattice spacing b . It follows from Eq 9 or 10 that we can therefore legitimately allow γ to become infinite in the rate equation, Eq 11. This limit is equivalent to assuming that the void is, first, an ideal sink for interstitials, since from Eq 6 if $\gamma \rightarrow \infty$

$$C_i(r_v) = 0 \dots \dots \dots \tag{15}$$

and, second, a temperature dependent sink for vacancies, since from Eq

5 if $\gamma \rightarrow \infty$

$$C_v(r_v) = \bar{C} \dots \dots \dots (16)$$

Taking this limit as $\gamma \rightarrow \infty$ in Eq 11 we obtain the somewhat simpler rate equation

$$\begin{aligned} \frac{dr_v}{dt} = & \frac{(K - D_v Z_v \rho_d \bar{C})}{r_v Z_v \rho_d} \\ & \times \left\{ \frac{(R - r_v) \beta_v \cosh \beta_v (R - r_v) + (r_v R \beta_v^2 - 1) \sinh \beta_v (R - r_v)}{R \beta_v \cosh \beta_v (R - r_v) - \sinh \beta_v (R - r_v)} \right\} \\ & - \frac{K}{r_v Z_i \rho_d} \\ & \times \left\{ \frac{(R - r_v) \beta_i \cosh \beta_i (R - r_v) + (r_v R \beta_i^2 - 1) \sinh \beta_i (R - r_v)}{R \beta_i \cosh \beta_i (R - r_v) - \sinh \beta_i (R - r_v)} \right\} \dots (17) \end{aligned}$$

When the void radius r_v is very much less than R , the void growth is not affected by the presence of the neighbouring voids (competition or saturation effects are not then rate controlling) and the right-hand side of Eq 17 can be replaced, when $R\beta_i, R\beta_v \gtrsim 1$, by the much simpler expression

$$\frac{dr_v}{dt} = \frac{(K - D_v Z_v \rho_d \bar{C})}{r_v Z_v \rho_d} \{1 + r_v \beta_v\} - \frac{K}{r_v Z_i \rho_d} \{1 + r_v \beta_i\} \dots \dots \dots (18)$$

There are now two useful limits both of which yield simple analytic expressions for the void growth; the first is

$$r_v \beta_i, r_v \beta_v < 1 \dots \dots \dots (19)$$

Since Z_i is only very slightly greater than Z_v and we may take, without loss of generality,

$$Z_v = 1.00 \dots \dots \dots (20)$$

the condition given by Eq 19 is equivalent to the single inequality

$$\rho_d r_v^2 < 1 \dots \dots \dots (21)$$

Any required explicit deviation of Z_v or Z_i from near unity can be easily accommodated by a suitable modification to ρ_d , since Z_v and Z_i always appear in Eq 17 multiplied by ρ_d . If the $r_v \beta_v$ and $r_v \beta_i$ terms are neglected in Eq 18 in comparison to unity, then the resulting rate equation can be integrated to yield the swelling kinetics:

$$\frac{\Delta V}{V} = \left\{ \left(\frac{1}{Z_v} - \frac{1}{Z_i} \right) \frac{1}{\rho_d} - \frac{D_v s}{K} \right\}^{3/2} 2^{3/2} \frac{[Kt]^{3/2}}{R^3} \dots \dots \dots (22)$$

where the relation used, $\Delta V/V = r_v^3/R^3$, implies the change of volume is due entirely to the growth of the existing voids and that the void nucleation process has finished. The quantity D_v^s is the vacancy self-diffusion constant

$$D_v^s = D_v C_v^e \dots \dots \dots (23)$$

and the mechanical force F_m has been neglected. Also in Eq 22 we have omitted the explicit contribution to the volume change from the distribution of small voids at $t=0$. The inequality, Eq 21, is best satisfied when ρ_d is small, and it therefore follows that in such circumstances we should expect the swelling kinetics to obey a variation like Eq 22 over a substantial dose regime; even when ρ_d is small the kinetics will eventually depart from Eq 22 when r_v approaches R or some analogous saturation condition.

The other limit of physical interest occurs when

$$r_v \beta_i, r_v \beta_v > 1 \dots \dots \dots (24)$$

or, equivalently, when

$$\rho_d r_v^2 > 1 \dots \dots \dots (25)$$

In this case Eq 18 may again be integrated to yield the swelling kinetics:

$$\frac{\Delta V}{V} = \left\{ \left(\frac{1}{Z_v^{1/2}} - \frac{1}{Z_i^{1/2}} \right) \frac{1}{\rho_d^{1/2}} - \frac{D_v^s}{K} [Z_v \rho_d]^{1/2} \right\}^3 \frac{[kt]^3}{R^3} \dots \dots \dots (26)$$

where again we have omitted the initial swelling. The inequality, Eq 25, can, of course, be satisfied over some of the swelling regime when the dislocation density is high. Thus we expect a regime of very rapid swelling to occur when ρ_d is large, in contrast to the slower swelling rate indicated by Eq 22 when ρ_d is small. Both these qualitative features of the dependence of the swelling kinetics on dislocation density will be demonstrated in the next section, where we shall present some accurate numerical solutions of the complete rate equation, Eq 17 (numerically indistinguishable from the solutions of Eq 11 when the explicit γ value is included).

In this model complete mathematical saturation will only occur after 100 percent swelling (when $r_v = R$). The form of the approach to saturation can be deduced by integrating Eq 17 in the limit of small $(R - r_v)$:

$$\frac{\Delta V}{V} \rightarrow \left\{ 1 - \left[\frac{6}{4R^2 K t \rho_d (Z_i - Z_v)} \right]^{1/2} \right\}^3 \dots \dots \dots (27)$$

Thus we expect that the lower ρ_d is the greater will be the dose required to achieve saturation and that the higher the void density ρ_v the greater will be the dose required to achieve saturation. Both these trends will be evident in the accurate kinetics presented in the next section.

Finally, the result of Eq 22 or 26 can be used to expose the approximate dependence of peak swelling temperature on dose rate K . In this section

it is, of course, not possible to actually follow the peak shift with K since we have deliberately omitted the recombination terms. However, we showed in our previous calculation [3] that, at the peak swelling temperature, recombination is not important and also that the swelling is cut off very rapidly at high temperatures by the self-diffusion term in Eq 8:

$$K_v C_v^e = \frac{D_v C_v^e}{4b} = \frac{D_v^s}{4b} \dots \dots \dots (28)$$

It follows that the shift in peak temperature will be very closely correlated to the shift of the point of vanishing $\Delta V/V$. From Eq 22 this occurs at a temperature T given by

$$D_v^s(T) = \frac{K}{\rho_d} \left(\frac{1}{Z_v} - \frac{1}{Z_i} \right) \dots \dots \dots (29)$$

and an almost identical temperature from Eq 26. Thus, from Eq 29 and the known vacancy self-diffusion constant we can estimate the shift in T when K is varied.

Void Growth Kinetics

In the complete void growth rate equation, Eq 11, the term involving \bar{C} is negligible for temperatures at and below the peak swelling temperature. The equation has been integrated numerically, with this term neglected, to give void growth kinetics appropriate to the peak swelling temperature. These kinetics will not depend on the numerical values of the dose rate K or the diffusion constant D_v and D_i . As we have previously commented, these kinetics do not include any possibility of premature saturation effects and it is intended to provide a more complete discussion of saturation effects in a subsequent paper, when the complete numerical solution of the governing equation, Eq 2, should also be available.

The kinetics are presented in Figs. 1, 2, and 3, in each of which we plot the percentage swelling $\Delta V/V$ versus the neutron dose in total displacements per atom. The volume swelling has been deduced directly from the void growth by the relation

$$\frac{\Delta V}{V} = \frac{r_v^3}{R^3} \dots \dots \dots (30)$$

which implies that the volume change is due entirely to the growth of existing voids and not to the continuous nucleation of new voids. It follows that our theoretical kinetics are particularly appropriate to swelling after high neutron doses. Also, if transient changes in the void density are taking place, our present results can be used to predict some of the consequences, as we shall discuss below.

In Figs. 1 and 2 we display sets of kinetics for void densities of $\rho_v = 10^{15}/\text{cm}^3$ and $5 \times 10^{15}/\text{cm}^3$ and various dislocation densities and for $Z_i = 1.02$

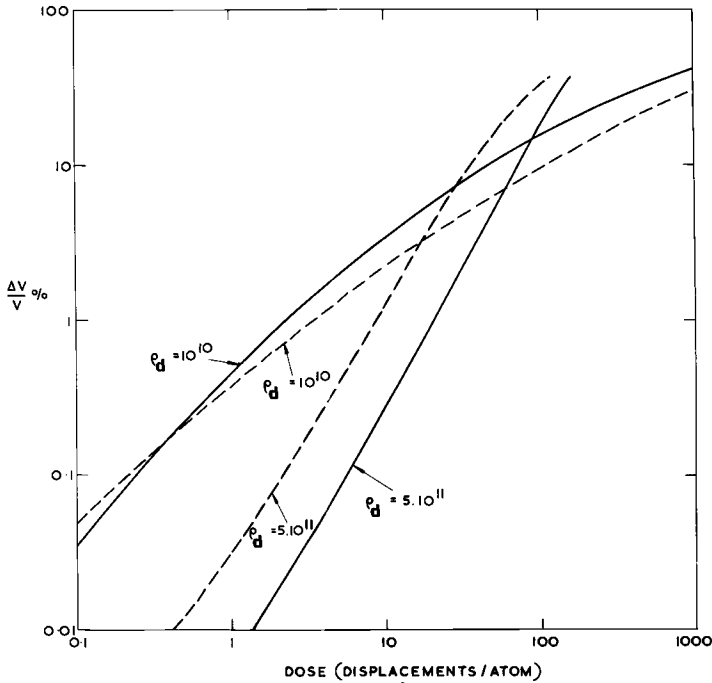


FIG. 1—The kinetics of void swelling when $Z_v=1.00$ and $Z_i=1.02$ for various void and dislocation densities. The solid line denotes a void density $\rho_v=10^{15}/\text{cm}^3$, the dashed line denotes a void density $\rho_v=5 \times 10^{15}/\text{cm}^3$, and ρ_d is the dislocation density in lines/cm².

(Fig. 1) and $Z_i=1.01$ (Fig. 2). All these kinetics have been obtained by starting the numerical integration with $r_v=10 \text{ \AA}$. The 1 percent increase in Z_i causes very little change in the relative form of the various curves but does cause an appreciable increase in the absolute swelling at a given dose. This shift in all the curves is simply a reflection of the essential point that the entire void growth phenomenon is due to the presence of the preferential sinks for the interstitials (the dislocations) and that its magnitude is very sensitive to the difference $Z_i - Z_v$, which defines the relative strength of this preference for interstitials compared with vacancies. This difference is the point sink representation of the spatial drift term discussed in our previous paper [3] and may be estimated by comparing the analytic form of the right-hand side of Eq 11 for very small r_v ($r_v < \gamma^{-1}$) with the previous kinetics [2] based on spatial drift to the dislocations and negligible loss to the voids. When we do this, we find that, if the drift interaction between the dislocations and the interstitials has the magnitude $L/\delta \approx 0.1$ [3] and if $Z_v=1.00$, then the difference

$$Z_i - Z_v = 0.016 \dots \dots \dots (31)$$

Thus we have considered $Z_i=1.01$ and 1.02 to be reasonable physical representations of the interstitial dislocation interaction.

There are several important features indicated by these theoretical kinetics:

1. The kinetics are very sensitive to dislocation density, as we might have expected from the analytic results in the previous section. At low dislocation densities, $\rho_d = 10^{10}$ lines/cm², the kinetics are approximately linear with dose (until saturation effects appear), whereas as at high dislocation densities, $\rho_d = 5 \times 10^{11}$ lines/cm², the kinetics rise very rapidly with (dose)² after an initially reduced swelling rate. This result confirms our previous [3], rather speculative, predictions concerning the high dose effects of cold work.

In fact when $\rho_v = 5 \times 10^{15}$ /cm³ the swelling in the higher ρ_d material becomes equal to and then subsequently exceeds the lower ρ_d swelling at a dose of about 30 displacements per atom. The initially beneficial effect of cold work and its eventual unfortunate consequences are further highlighted in Fig. 3, where the volume swelling is plotted on a linear scale.

2. When the dislocation density is low, the kinetics are not very sensitive to the fivefold change in void density; but, when the dislocation density

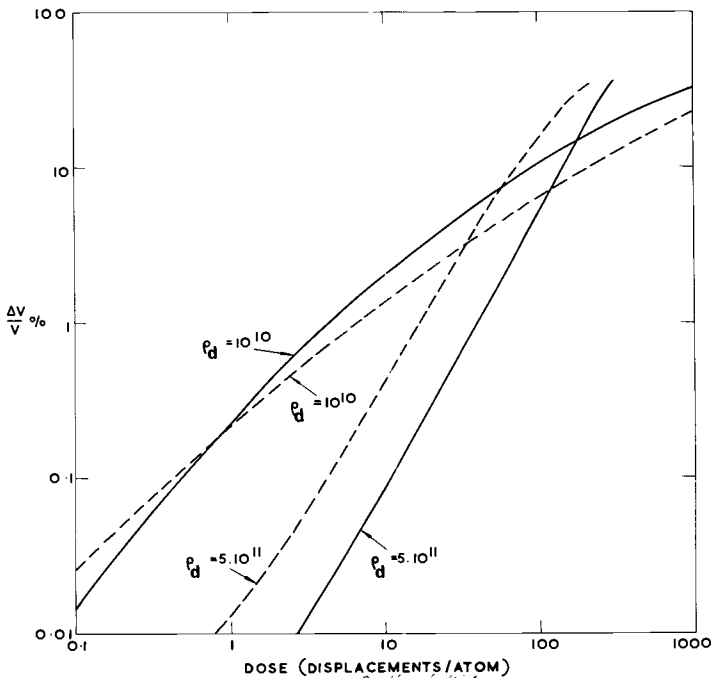


FIG. 2—The kinetics of void swelling when $Z_v=1.00$ and $Z_i=1.01$ for various void and dislocation densities. The solid line denotes a void density $\rho_v=10^{15}$ /cm³, the dashed line denotes a void density $\rho_v=5 \times 10^{15}$ /cm³, and ρ_d is the dislocation density in lines/cm².

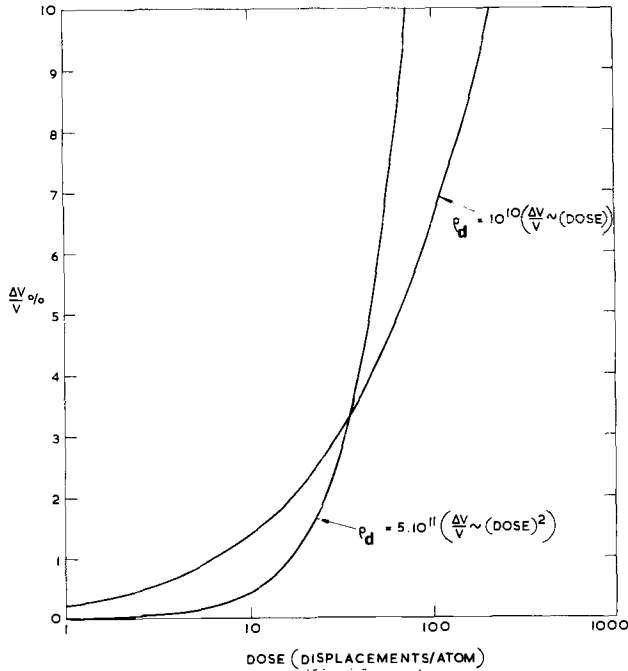


FIG. 3—The kinetics of void swelling for $Z_v=1.00$, $Z_i=1.0\%$, and $\rho_v=5 \times 10^{15}/\text{cm}^3$. Curves for two values of P_d are given.

is high, the fivefold increase in void density causes the swelling also to increase by approximately a factor of five over most of the dose range.

3. At low dislocation densities the swelling is reduced by *increasing* the void density, whereas at high dislocation densities the swelling is reduced by *decreasing* the void density.

4. No matter what the values of ρ_d and ρ_v , the curves all tend to bunch together at about 10 percent swelling.

5. All the theoretical kinetics are independent of dose rate.

6. If the void concentration is increasing continuously, then at high dislocation densities the swelling kinetics could increase even faster than (dose)².

Finally, we have found that when the dislocation density is high the void growth kinetics can be very rapid ($\Delta V/V \simeq (\text{dose})^2$) and that this rapid increase in volume can persist right up to saturation; the curves in Figs. 1 and 2 confirm the analytic asymptotic form of the approach to saturation (Eq 27), where we see that the higher the dislocation density the lower will be the saturation dose and therefore the more sudden must be the saturation effect. Similarly, Eq 27 indicates that the lower ρ_v the quicker the eventual saturation—a trend which is again clear in Figs. 1 and 2 (explicitly when $\rho_d = 10^{10}$). The basic reason for such a rapid growth

regime when ρ_d is large is simply that a high dislocation density obscures the spherical geometry of the domain around each void and the effects of the finite curvature of the void $r=r_v$ are soon lost. The flow kinetics then become identical to migration to a planar sink at $x=x_v$, which has an associated velocity varying linearly with dose. The higher the dislocation density the sooner the spheroidicity of the void has a negligible effect on the flow process. In low dislocation density situations this effect will tend to happen, but, because it only occurs later, saturation will take over before it becomes manifest.

References

- [1] Bullough, R. and Perrin, R. C., *Radiation Damage in Reactor Materials*, Vol. II, International Atomic Energy Agency, Vienna, 1969, pp. 233–251.
- [2] Bullough, R., “The Kinetics of Void Growth During Neutron Irradiation,” AERE Report TP. 375, Atomic Energy Research Establishment, Harwell, 1969.
- [3] Bullough, R., Eyre, B. L., and Perrin, R. C., “The Growth and Stability of Voids in Irradiated Metals,” AERE Report R. 6284, Atomic Energy Research Establishment, 1969.
- [4] Harkness, S. D. and Li, Che-Yu, *Radiation Damage in Reactor Materials*, Vol. II, International Atomic Energy Agency, Vienna, 1969.
- [5] Harkness, S. D., Tesk, J. A., and Li, Che-Yu, *Nuclear Applications*, NUAPA, Vol. 9, No. 1., 1970, p. 24.
- [6] Bullough, R., Newman, R. C., and Wakefield, J., *Proceedings of the Physical Society (London)*, PPSAA, Vol. 72, 1958, pp. 369–379.

DISCUSSION

*G. L. Kulcinski*¹—You stated that gases are necessary for void nucleation. Certainly we are all concerned about neutron produced gases such as helium and hydrogen, but could you say a few words about the importance of residual gases such as oxygen and nitrogen on the nucleation phenomena.

R. Bullough (authors' closure)—We believe that such residual gases could assist in the nucleation process. Also, the vacancies clearly can aggregate as voids around small incoherent precipitate particles.

*J. W. Corbett*²—Would those who spoke on theories please comment on the difference between the theories.³

R. Bullough (authors' closure)—This is a rather difficult question to answer at all briefly, and from the oral presentations alone it is not really possible to assess all the detailed assumptions in the various theories. It will, however, perhaps help if I mention an important feature of the Bullough and Perrin model of the void growth process which seems to be absent from the other theories.

The special feature of our approach is that we consider the actual flow process in the geometrically defined neighborhood of a void. That is, we actually solve a spatial migration problem and do not resort to a completely "kinetic" model with *all* the sinks smeared out into a continuous distribution. The void is a well defined, large geometrical defect and can be defined explicitly.

The importance of including the geometrical shape of the void in the theory can be seen by our predictions concerning the effects of cold work. Thus at low doses cold work will cause an immediate reduction in the volume swelling but this decrease, below the solution treated (low dislocation density) material, is not sustained, and at high doses the volume swelling for the cold-worked material can exceed that of the solution treated material. This relatively rapid swelling when the dislocation density is high occurs because the spherical nature of the region in the neighborhood of each void is essentially obscured by the high dislocation sink density.

¹ Senior research scientist, Pacific Northwest Laboratories, Battelle Memorial Institute, Richland, Wash. 99352.

² Professor, Physics Department, State University of New York at Albany, Albany, N.Y. 12203.

³ See also discussion by Li et al, pp. 347-361.

This is an important effect and can hardly be expected in models in which the voids are themselves smeared out.

The possibility of premature saturation, though not explicitly discussed in our present paper, can also be conveniently included in the present model. We believe this will occur when the void concentration and the size of the individual voids reach a critical value and cause a sudden drop in the dislocation density. This can be included by simply including a spherical shell of varying thickness around each void, inside which there are no dislocations; dislocations inside such a domain would be pulled into the adjacent void by the image forces. Swelling will terminate when these dislocation free regions begin to overlap. A precise, quantitative estimate of this effect is under way at present.

*D. W. Keefer,¹ H. H. Neely,¹ J. C. Robinson,¹ A. G. Pard,¹
and D. Kramer¹*

Void Formation in Proton Irradiated Stainless Steel*

REFERENCE: Keefer, D. W., Neely, H. H., Robinson, J. C., Pard, A. G., and Kramer, D., "Void Formation in Proton Irradiated Stainless Steel," *Irradiation Effects on Structural Alloys for Nuclear Reactor Applications, ASTM STP 484*, American Society for Testing and Materials, 1970, pp. 332-346.

ABSTRACT: Voids have been produced by 1.2-MeV proton irradiation at 500 C in Type 316 stainless steel containing 2 appm helium. The proton fluence was 6×10^{18} p/cm². Observations of electron microscope foils obtained at various positions along the proton path length have shown that the volume swelling increased with increasing number of atom displacements. Calculated volume swelling ranged from 0.2 to 5 percent. In addition to voids, irradiation produced dislocation loops and small precipitate particles on dislocations have been observed.

KEY WORDS: irradiation, proton irradiation, radiation effects, stainless steel, microstructure, vacancies (crystal defects), voids, dislocations (materials), precipitates, helium, swelling, electron microscopes, foils (materials), nuclear reactors

The first observation, in an irradiated metal, of what are now known to be voids was reported by Cawthorne and Fulton [1].² Other such observations followed, and it quickly became apparent that the occurrence of voids presented a significant practical problem relating to the dimensional stability of various reactor components, notably fuel cladding [2]. The formation of voids also presents a tantalizing subject for basic studies of

¹ Atomics International, a division of North American Rockwell, Canoga Park, Calif. 91304.

* Based on work supported by the U. S. Atomic Energy Commission under Contract AT(04-3)-701.

² Italic numbers in brackets refer to the list of references at the end of this paper.

the behavior of radiation produced point defects in metals, and some work on irradiated pure metals has been reported [3].

Progress in achieving a detailed understanding of void formation has been relatively slow. The complexity of the process whereby voids nucleate and grow certainly accounts in part for this. Also, most studies have been performed on complex alloys, and control of important material properties has not always been possible. Perhaps most important, the majority of irradiations have been performed in reactors. Such irradiations necessitate long times, and control and monitoring of specimen temperature and neutron flux and fluence are difficult. Further, helium and hydrogen are produced in significant quantities in many metals during reactor irradiations, and the importance of the presence of these impurities on void formation is difficult to establish by such irradiations.

As has already been demonstrated at Harwell [4], irradiation with heavy charged particles can also be used to form voids. The British have successfully produced voids in stainless steel with protons as well as with iron and carbon ions. There are a number of advantages to studying void formation in this way. All experimental conditions are far more easily controlled and monitored than in a reactor. Furthermore, heavy charged particles, because of their higher displacement cross sections, compress the experimental time from the several years required in a reactor to a few hours in an accelerator. An additional advantage to the use of charged particles comes about because of the inverse relationship (for Rutherford scattering) between the displacement cross section and particle energy. As the particles slow down in their traversal of a specimen, the displacement rate and total number of displacements increase. Thus, information on voids produced under effectively different irradiation conditions at the same temperature can be obtained from electron microscope foils taken from various positions within the thickness of a single specimen.

Although the production of voids by heavy charged particle irradiation undoubtedly will be of great value in void studies, the precise correlation between void arrays created by neutrons and those produced by charged particles may require careful study. The difference in time scale of the two experimental techniques and variations in the nature of damage created by the different particles will have to be taken into account in such a correlation.

The present proton irradiation experiments are intended to study the effects of atom displacement rate, total number of displacements, temperature, helium content, and microstructure on void formation and the attendant volume swelling in Type 316 stainless steel. It is also hoped that out of this program a correlation with reactor irradiations will be developed. Thus far, only preliminary irradiations have been made. Although voids have been produced, the results reported here must be viewed in the context of their preliminary nature.

Experimental Procedure

Specimen Preparation

The specimens used in this work are 0.0127-mm-thick foils having cross-sectional dimensions of 1.78 by 0.88 cm. Following an appropriate heat treatment, the specimens are diffusion bonded under pressure to thick copper plates. These plates serve as a heat transfer medium between the specimens and the temperature control apparatus. The bonding time and temperature are chosen so that no copper is allowed to diffuse into the front portion of the specimen, approximately 0.008 mm thick, which is to be irradiated.

Prior to irradiation, the specimens are injected with helium by means of a cyclotron. The procedure used here is similar to that used previously by members of our laboratory [5]. The technique results in an even distribution of helium throughout the specimen volume. This has been verified by analysis of injected "sandwiches" of 0.0025-mm-thick foils. The helium content is determined by mass spectrometry [6]. The temperature of specimens undergoing helium injection does not rise significantly above ambience.

Following irradiation, the copper plate is removed from each specimen by immersion in nitric acid. Each specimen is then cut into at least six sections for electron microscope examination. Microscope foils are obtained from selected positions within the specimen thickness by means of careful electropolishing of a section. The polishing procedure is periodically interrupted so that X-ray absorption measurements can be made to monitor the material thickness and hence the ultimate position from which the foil is obtained. It is estimated that the foil position determined in this way is accurate within ± 1000 Å. This accuracy will be improved upon in future experiments.

Target Assembly

The target assembly is shown in Fig. 1. The main body of the assembly serves as a reservoir for cooling water. The three support posts of the specimen heater block are soft soldered to this reservoir. The block contains a coiled heater element. Bolting of the specimen plate to the heater block completes the heat transfer system.

Temperature Control

During irradiation, the specimen temperature is monitored by an infrared detector which has previously been calibrated against a thermocouple attached to the heater block. The output of the detector is also used in the programming circuit of an electronic temperature control system. During an irradiation at 500 C with a 1.2-MeV beam of approximately 1.6×10^{15}

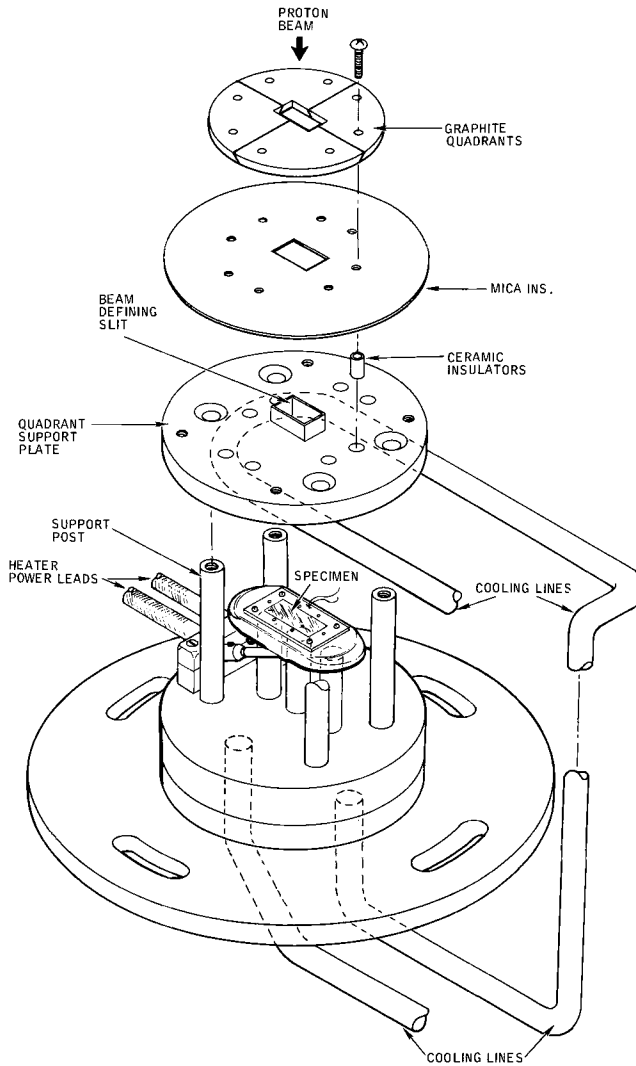


FIG. 1—Exploded view of proton irradiation target assembly.

p/cm²-s, the control system was able to keep the temperature typically within ± 10 C. Extreme beam instability led to periodic downward fluctuations of approximately 20 C.

Proton Beam

The proton beam is delivered by a 3-MeV Dynamitron. The beam is magnetically analyzed, shaped, and steered prior to its entry into the target chamber. The shape and homogeneity of the beam is continuously

observed by means of a High Voltage Engineering Corp. beam profile monitor. The particles emerging from the Dynamitron source are preponderantly mass II particles, that is, two protons with a shared electron. In order to achieve high proton beam currents, it is these mass II particles which are made to impinge on the target. The energy required to separate each pair of protons from the electron is only a few electron volts, and the separation occurs at the specimen surface; thus, no significant error in proton energy occurs with this technique. In this report, proton energies and currents are stated directly, for example, a mass II energy of 2.0 MeV and current of 1×10^{15} particles/cm²-s will be given as a proton energy of 1.0 MeV and a current of 2×10^{15} p/cm²-s.

The proton beam is defined, by a graphite quadrant system, to an area of 2.0 cm² (see Fig. 1). This system is attached to a water cooled support plate; this plate further defines the beam on the specimen to an area of 1.3 cm². Each quadrant is electrically biased with respect to the target chamber to minimize backscattered electrons. The proton current which is integrated is the sum of the currents measured on the specimen and the target chamber.

Displacement Calculations

The total number of displacements per atom, N , created by a flux of protons, ϕ , in time t was calculated by means of the expression

$$N = \phi t \int_{E_d}^{T_m} d\sigma(T) \nu(T) \dots \dots \dots (1)$$

where T_m is the maximum transfer energy, E_d is the threshold energy, and

$$d\sigma(T) = 4\pi a_B^2 Z_1^2 Z_2^2 \frac{M_1}{M_2} \frac{E_R^2}{E} \frac{dT}{T^2} \dots \dots \dots (2)$$

is the differential cross section for transferring energy T to $T+dT$ in Rutherford collisions. a_B is the Bohr radius for hydrogen, Z_1 , Z_2 , and M_1 , M_2 are the charge numbers and masses of the incident and target particles, respectively, $E_R=13.6$ eV is the Rydberg energy, and E is the energy of the moving particle. In Eq 1, $\nu(T)$ is the number of displacements per primary recoil of energy T . In this work, the Kinchin-Pease [γ] expression $\nu(T) = T/2E_d$, with $E_d=25$ eV, has been used. With appropriate values of ϕ and t , Eq 1 has been used in calculating the number of displacements per atom and the displacement rate as a function of proton penetration into a specimen. Proton energy loss as a function of energy, in other words, the depth of penetration, was obtained from Ref 8.

The calculations discussed above are admittedly approximate, particularly because of the use of the Kinchin-Pease model. More refined calculations are to be made in the near future.

Determination of Void Number and Size

The number of voids and the distribution of void diameters in electron photomicrographs were determined by means of a particle size analyzer. The void densities were calculated with an assumed foil thickness of 1000 \AA . Contributions to the swelling (increase in volume per unit volume) for each size interval on the analyzer were determined and summed to give the total swelling. The diameter of a void can be determined within plus or minus one interval on the analyzer. Depending on the magnification of the photomicrograph, this amounts to some $\pm 10 \text{ \AA}$ of uncertainty in the diameter of each void.

Experimental Results

The data presented here were obtained from a single specimen of Type 316 stainless steel. Prior to bonding to its copper plate, the specimen was solution annealed at 980 C in vacuum for 1 h. This was followed by an 8-h precipitation anneal at 760 C . This treatment resulted in the formation of $M_{23}C_6$ carbides at the austenite grain boundaries [9], with an average

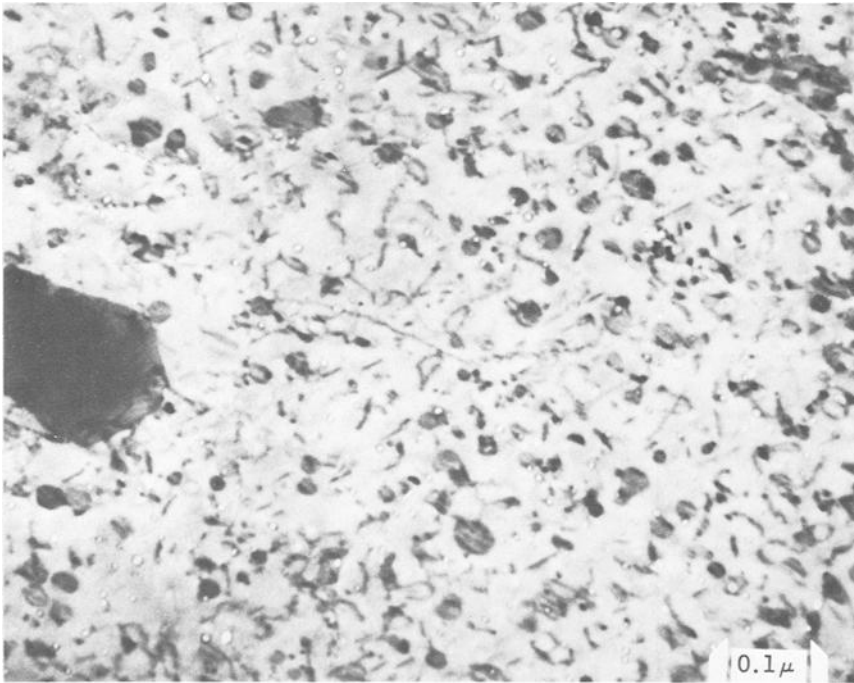


FIG. 2—Transmission electron micrograph showing voids obtained in Type 316 stainless steel containing 2 appm helium and irradiated at 500 C . The proton penetration depth is 0.0025 mm . Note the presence of faulted dislocation loops and dislocations decorated with small precipitate particles.

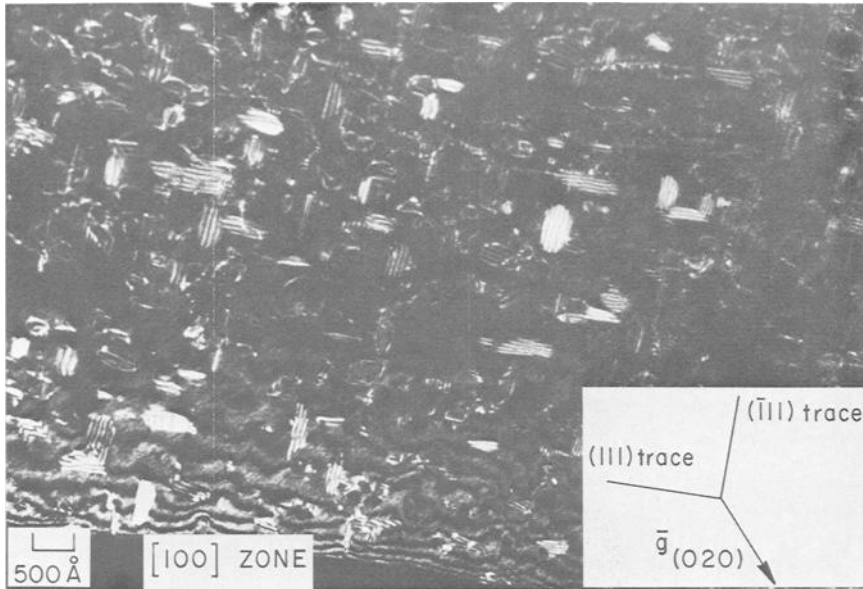


FIG. 3—Transmission electron micrograph showing details of dislocation loops as seen in dark-field contrast. Proton penetration depth is 0.0025 mm.

grain size of between 20 and 30 μm . After the annealing treatment, the specimen was bonded to a copper plate and subsequently injected with helium to a level of 2 ppm (atomic).

During irradiation, the specimen temperature was maintained at 500 ± 10 C with periodic downward fluctuations greater than 10 C. The 1.2-MeV proton flux was nominally 1.6×10^{15} p/cm²-s, but due to beam instability the average flux was approximately half this value. The average flux has been used in all calculations. The fluence was approximately 6×10^{18} p/cm².

The range of a 1.2-MeV proton in stainless steel is 0.0084 mm [8]. Foils for electron microscope analysis were taken at proton penetration distances of 0.0025, 0.0051, and 0.0076 mm by the technique described in a preceding paragraph. Results from a foil produced prior to development of the X-ray absorption technique will also be discussed. Although the exact position of this foil is not known, the results clearly indicate that it was taken from a depth slightly beyond the 0.0076-mm level.

At the 0.0025-mm position, the energy of a 1.2-MeV incident proton has been reduced to 0.93 MeV. The displacement rate at the 0.0025-mm position is, from Eq 1 with $\phi \approx 8 \times 10^{14}$ p/cm²-s, about 1×10^{-4} atom fraction per second. The total number of displacements per atom is about 0.8.

Figure 2 shows the disposition of voids obtained at the 0.0025-mm position. Also visible in the photograph are faulted dislocation loops and other

dislocation structures. Careful examination of the foil has revealed the presence of small precipitates on dislocations; these can be detected in the figure. These precipitates are not present in unirradiated material.

A more detailed photograph showing the orientation of the loops is given in Fig. 3. These loops were found to be extrinsic in nature. The nature of the loops was determined for the case of $\mathbf{g} \cdot \mathbf{b} \neq 1$. Tunstall [10] has shown that, for the case of $|\mathbf{g} \cdot \mathbf{b}| = \frac{2}{3}$, a strongly visible image occurs for $\mathbf{g} \cdot \mathbf{b} = +\frac{2}{3}$, whereas $\mathbf{g} \cdot \mathbf{b} = -\frac{2}{3}$ gives a weak, or even invisible image (with $S > 0$).

At the 0.0025-mm position, the void density was approximately 3×10^{15} voids/cm³. The size distribution is shown as a histogram in Fig. 4; the average void size in this distribution is about 110 Å. The swelling due to void formation is calculated to be 0.2 percent.

At the 0.0051-mm position, the proton energy has been reduced to 0.61 MeV. The displacement rate is approximately 1.6×10^{-4} atom fraction per second, and the total number of displacements per atom is about 1.2. The voids obtained at the 0.0051-mm level are shown in Fig. 5. Faulted dislocation loops and dislocations decorated with small precipitates are

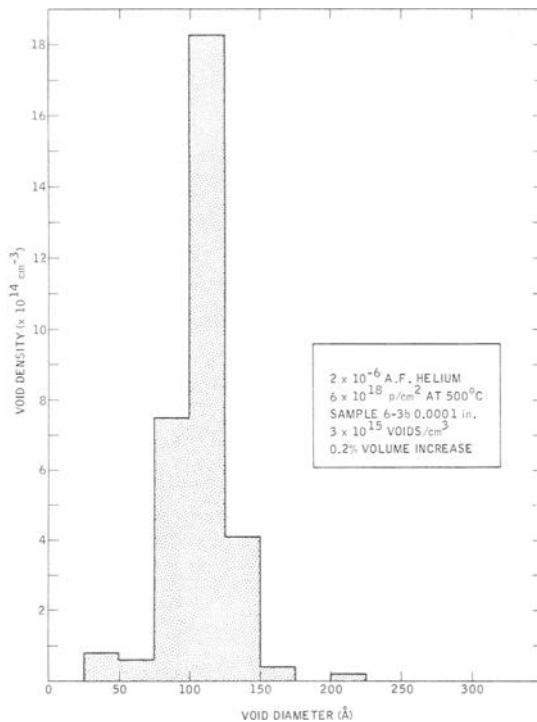


FIG. 4—Histogram showing void size distribution at the 0.0025-mm level. The average void size is about 110 Å.

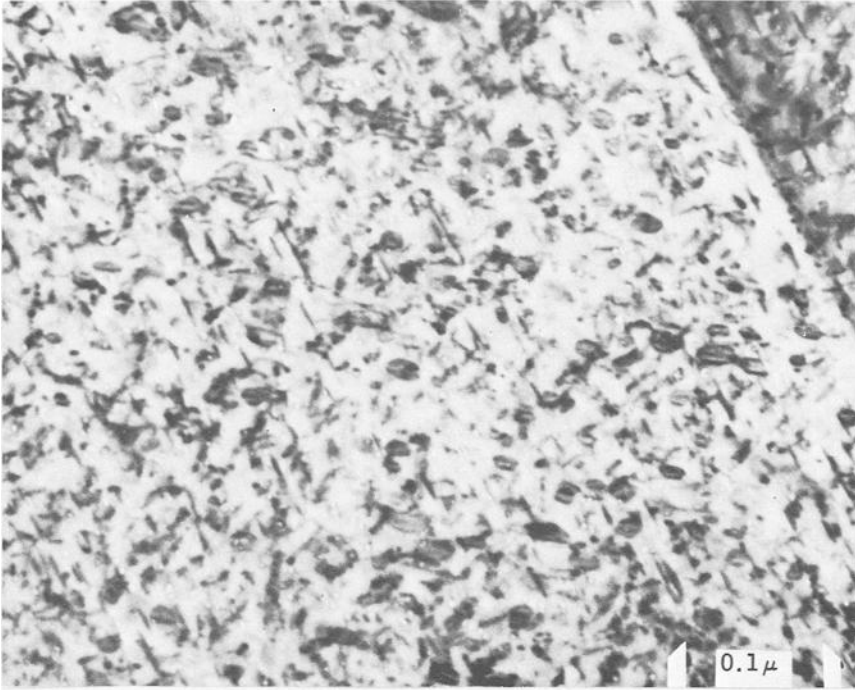


FIG. 5—Transmission electron micrograph showing voids obtained at a proton penetration depth of 0.0051 mm in Type 316 stainless steel containing 2 appm helium.

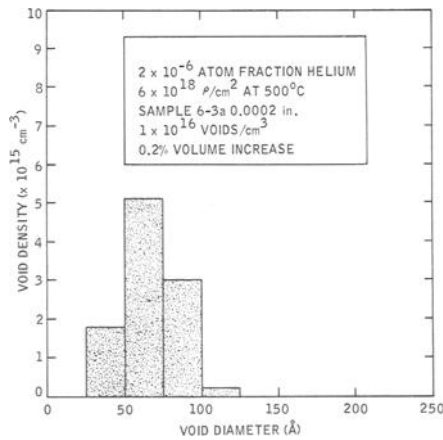


FIG. 6—Histogram showing void size distribution at the 0.0051-mm level. The average void size is about 70 Å.

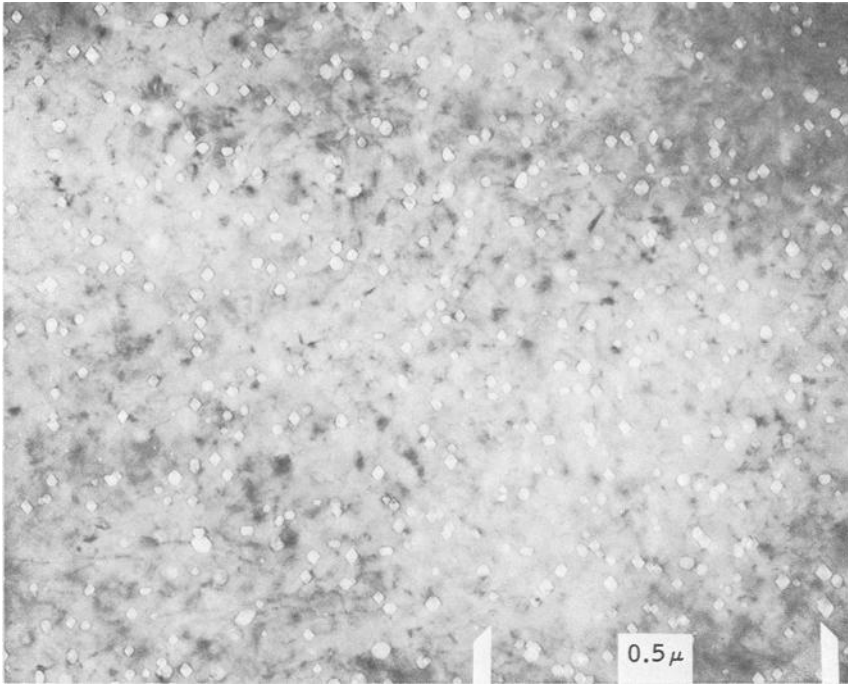


FIG. 7—Transmission electron micrograph showing voids obtained at a proton penetration depth of 0.0076 mm in Type 316 stainless steel containing 2 appm helium.

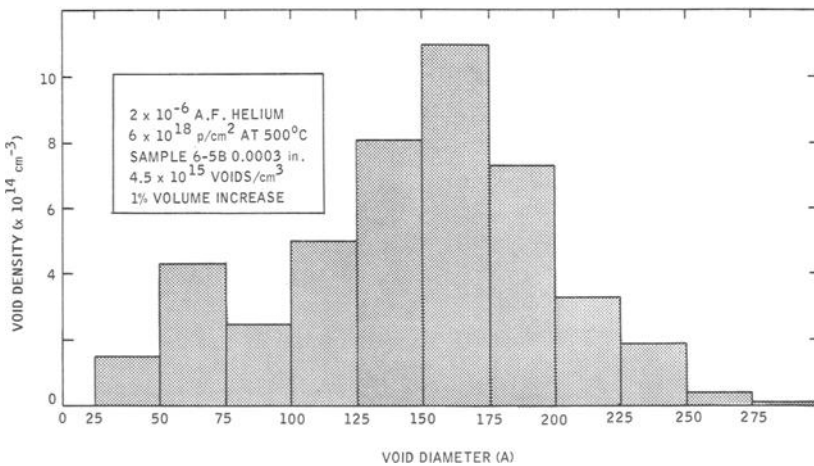


FIG. 8—Histogram showing void size distribution at the 0.0076-mm level. The average void size is about 150 Å.

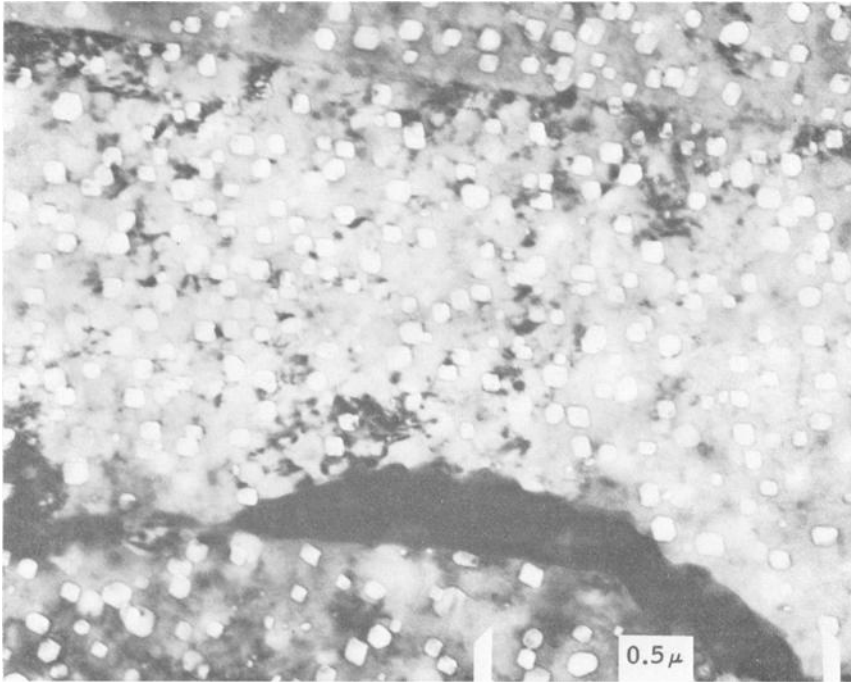


FIG. 9—Transmission electron micrograph showing voids obtained at a proton penetration depth greater than 0.0076 mm. Note the homogeneous void distribution throughout the microstructure.

also visible in the figure. The density of voids observed at this level was $10^{16}/\text{cm}^3$. The size distribution is shown in Fig. 6; the average void diameter in this distribution is 70 Å. The calculated volume swelling is 0.2 percent.

At the 0.0076-mm penetration distance, the proton energy has been reduced to about 0.14 MeV. The displacement rate is about 5.6×10^{-4} atom fraction per second, and the total number of displacements per atom is about 4. The voids observed at the 0.0076-mm level are shown in Fig. 7. The density of voids obtained from this photograph was about $4.5 \times 10^{15}/\text{cm}^3$. The average void diameter from the size distribution shown in Fig. 8 is about 150 Å. The volume swelling is calculated to be about 1 percent.

As mentioned in a preceding paragraph, the exact position of the fourth foil is not known; therefore, the defect production rate and total number of displacements cannot be calculated. However, because of the large amount of damage observed in this foil (see Fig. 9), it appears that the foil position was beyond the 0.0076-mm depth. Note that the void density is homogeneous throughout the microstructure. Similar results have been obtained at the other specimen positions. This observation differs from those made following reactor irradiations, where along grain boundary zones denuded of voids have frequently been observed. From Fig. 9, the

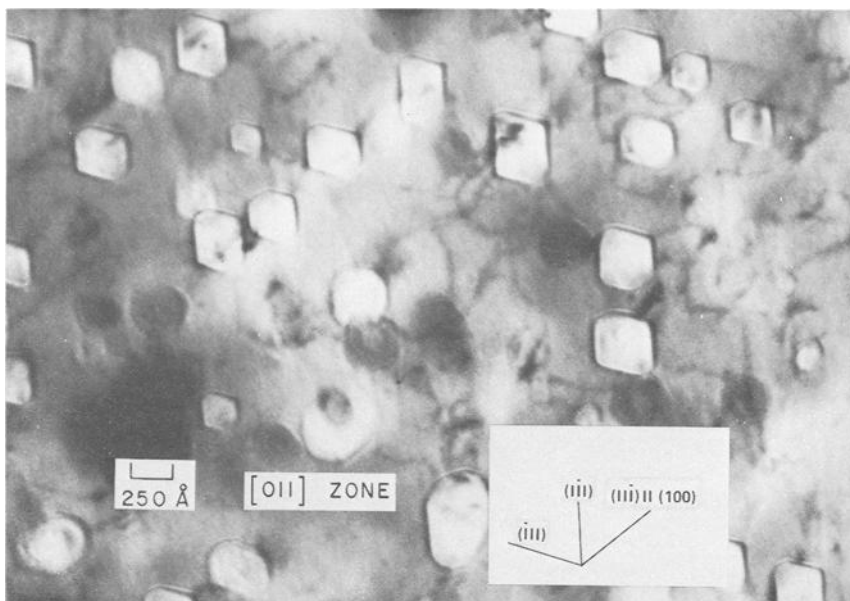


FIG. 10—Transmission electron micrograph showing voids to be octahedra bounded by $\{111\}$ planes. The proton penetration depth is greater than 0.0076 mm.

void density is $3 \times 10^{15}/\text{cm}^3$. Trace analyses of the voids at this level in three orientations, $[100]$, $[110]$, $[211]$, have shown that the voids are octahedra bounded by $\{111\}$ planes. Occasional truncation by $\{100\}$ planes was observed. This is shown in Fig. 10. The void size distribution is shown in Fig. 11, where the average void diameter is 290 Å. The volume swelling in this final foil is then about 5 percent.

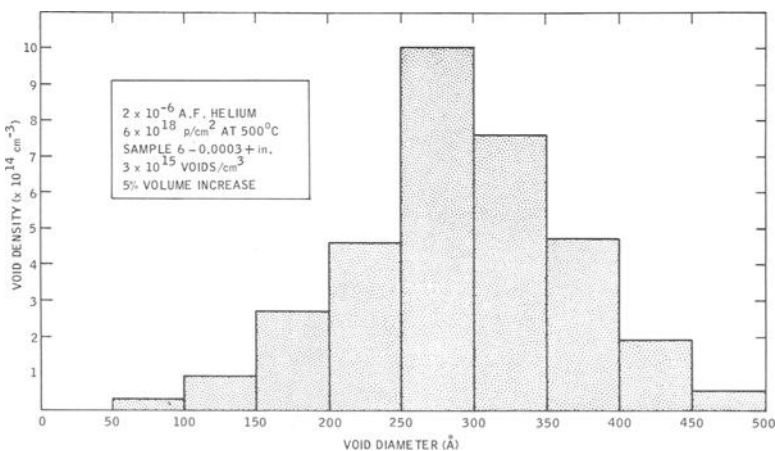


FIG. 11—Histogram showing void size distribution at a depth beyond 0.0076 mm. The average void size is about 290 Å.

Discussion

The production of voids in Type 316 stainless steel by proton irradiation has been amply demonstrated in this work. Although the results are preliminary, some interesting features have already emerged. In addition to voids, faulted dislocation loops of the interstitial type were observed. Also formed during the irradiation were small precipitates which are evidently associated with dislocations in every case. The particles are too small to be identified by means of electron diffraction. The volume swelling increased generally with increasing depth into the specimen. This increase is attributable to the increase in vacancy production, by approximately a factor of ten, over the proton range investigated here. The absence of a zone denuded of voids about grain boundaries in this work may be due to a higher displacement rate than is the case in reactor irradiations.

Acknowledgments

We express our sincere thanks to R. M. Kniefel and K. R. Garr for their able assistance in the initial phases of these experiments and for performing the helium injections. We also wish to acknowledge the contribution of C. G. Rhodes, of the North American Rockwell Science Center, whose work led to Figs. 3 and 10 of this paper and identification of the type of loop created during irradiation.

References

- [1] Cawthorne, C. and Fulton, E. J., *Nature*, NATUA, Vol. 216, 1967, p. 575.
- [2] Holmes, J. J., *Journal of Nuclear Materials*, JNUMA, Vol. 29, 1969, p. 241.
- [3] Brimhall, J. L. and Mastel, B., *Journal of Nuclear Materials*, JNUMA, Vol. 29, 1969, p. 123.
- [4] Nelson, R. S. and Mazey, D. J. in *Proceedings of the IAEA Symposium on Radiation Damage in Reactor Materials*, Vol. 2, International Atomic Energy Agency, Vienna, 1969, p. 157.
- [5] Kramer, D., Brager, H. R., Rhodes, C. G., and Pard, A. G., *Journal of Nuclear Materials*, JNUMA Vol. 25, 1968, p. 121.
- [6] Farrar, H., IV, and Knox, C. H., *Transactions*, American Nuclear Society, TANSAs, Vol. 11, 1968, p. 503.
- [7] Kinchin, G. H. and Pease, R. S., *Reports on Progress in Physics*, RPPHA, Vol. 18, 1955, p. 1.
- [8] Janni, J. F., "Calculations of Energy Loss, Range Pathlength, Straggling, Multiple Scattering, and the Probability of Inelastic Nuclear Collisions for 0.1 to 1000 MeV Protons," AFWL-TR-65-150, Air Force Weapons Laboratory, Sept. 1966.
- [9] Kramer, D., Garr, K. R., Rhodes, C. G., and Pard, A. G., *Journal of the Iron and Steel Institute*, JISIA, Vol. 207, 1969, p. 1141.
- [10] Tunstall, W. J., *Philosophical Magazine*, PHMMA, Vol. 20, 1969, p. 701.

DISCUSSION

*G. L. Kulcinski*¹—Have you noticed a change in the degree of truncation as you examine areas in the foil closer to the end of path for the protons? Recent work at Pacific Northwest Laboratories by Dr. Laidler has shown that hydrogen can change the morphology of voids in quenched nickel, in general reducing the degree of truncation in the (100) planes.

D. W. Keefer (authors' closure)—We have observed no change in the degree of truncation of voids produced at different positions along the proton pathlength, nor have we noted changes in truncation with increasing proton fluence.

*G. J. C. Carpenter*²—In studies of void formation under neutron irradiation, the zones adjacent to grain boundaries are normally denuded with respect to voids and dislocation loops. This implies that the boundaries act as sinks for the irradiation induced defects. Your observation that there is no denuded region after proton irradiation seems to suggest that the grain boundaries are not acting as sinks. Strictly, for there to be no denuded region, voids must be situated *on* the grain boundaries. If no voids occur on the boundaries, there is of necessity a “denuded region,” although it may be small. This could be due either to slow diffusion kinetics (a low irradiation temperature) or to a restriction on the ability of the grain boundaries to absorb point defects. Is there any reason to suppose that in your ion bombardment experiments the denuded region was smaller than observed for neutron irradiation at a comparable temperature? If there is a large difference, perhaps account should be taken of the stresses that must build up in the region of maximum swelling, where the ions stop, resulting from the constraint imposed by the surrounding material.

D. W. Keefer (authors' closure)—I disagree with your statement that, in the absence of a “denuded region,” voids should be found on grain boundaries. I feel that the absence of such a region is defined by the average void-boundary distance being no greater than the average void-void separation. As I mentioned, in our experiments no such denuded region was observed. I feel this observation, compared to the neutron results,

¹ Senior research scientist, Battelle Memorial Institute, Pacific Northwest Laboratories, Richland, Wash. 99352.

² Chalk River Nuclear Laboratories, Atomic Energy of Canada Limited, Chalk River, Ontario, Canada.

most likely can be attributed to the higher defect production rate in our experiments.

*D. J. Mazey*³—The concentration of hydrogen is expected to be high near the end of the protons range in the steel. Do you think this hydrogen is influencing void formation?

D. W. Keefe (*authors' closure*)—In the absence of preinjected helium, we find that the void concentration is lower by several orders of magnitude. We infer from this that hydrogen does not have a significant influence on void nucleation. The possible influence of hydrogen on void growth has yet to be determined.

³Solid State Division, Atomic Energy Research Establishment, Harwell, Didcot, Berkshire, United Kingdom.

Che-Yu Li,¹ D. G. Franklin,¹ and S. D. Harkness¹

Considerations of Metal Swelling and Related Phenomena Caused by Fast Neutron Irradiation

REFERENCE: Li, Che-Yu, Franklin, D. G., and Harkness, S. D., “**Considerations of Metal Swelling and Related Phenomena Caused by Fast Neutron Irradiation,**” *Irradiation Effects on Structural Alloys for Nuclear Reactor Applications*, ASTM STP 484, American Society for Testing and Materials, 1970, pp. 347–361.

ABSTRACT: The existing analytical model that describes metal swelling under fast neutron irradiation is reviewed. The assumption of quasi-steady state and uniform point defect generation used in the present model is partially justified. Possible effects, due to microstructural defect interactions, that may occur at high fluences are discussed. The effect of stress field on point defect migration and its consequences on metal swelling and creep are considered.

KEY WORDS: irradiation, neutron irradiation, ion irradiation, neutron flux, fluence, fast neutrons, radiation damage, swelling, bias, point defects, vacancies (crystal defects), voids, dislocations (materials), interstitials, creep properties, stresses, metals, stainless steels, fast reactors (nuclear)

In recent papers [1–3]² analytical models have been proposed for the irradiation induced swelling and in-reactor creep observed in metals. These models are basically quasi-steady state approaches that calculate the magnitude of point defect supersaturation under the assumption of uniform point defect generation. Knowing the concentration of vacancies and interstitials, the rate of nucleation and growth of voids can be estimated. A by-product of these considerations [1] is the rate of enhanced dislocation climb, which could be an important mechanism for in-reactor creep. We [1, 3] have been able to use this model to rationalize the existing

¹ Materials Science Division, Argonne National Laboratory, Argonne, Ill. 60439.

² Italic numbers in brackets refer to the list of references at the end of this paper.

stainless steel swelling data. However, the existing data are obtained at lower flux levels and smaller fluences than those of interest to commercial liquid metal fast breeder reactor design. Efforts are being made experimentally in several laboratories [4, 5] to use high-flux (effective neutron flux $>10^{18}$ n/cm²-s) ion bombardment to simulate fast neutron damage and thus achieve high fluences ($>10^{23}$ n/cm²) in a shorter time than is possible with present reactors. It is not clear at this time how to extrapolate directly the ion bombardment results obtained at high flux levels to the lower flux levels pertinent to fast breeder reactor design.

In order to make this extrapolation, a clear understanding of the effects of flux and fluence levels is required. The first part of this paper is intended to contribute to this understanding. The question of the applicability of a uniform point defect generation, quasi-steady state approach to high-temperature radiation damage will be examined, and its limitations on flux level noted. Possible effects that may limit void growth at high fluences will also be discussed.

In addition to the effects of high flux and high fluence, the effects of applied stress on metal swelling has been of current interest and will be discussed in the second part of the paper. The discussion will be based on an extension of the concept developed in the present model [1-3] of stress gradient biased, point defect migration. Another consequence of this type of biased diffusion is a diffusional mechanism based on the Kirkendall effect for in-reactor creep.

At present, the analytical work in this general area is limited, because many important physical parameters are poorly known and very little experimental data are available. It is, therefore, not the purpose of this paper to give a detailed analytical description of the phenomena of interest but, rather, to point out possible effects and areas where future research is required.

Review of the Metal Swelling Model

In the present swelling model [1, 3] the concentrations of point defects (vacancies and interstitials) are assumed to be distributed uniformly throughout the system. Concentration gradients exist only around various point defect sinks (voids, loops, grain boundaries, dislocations, etc.). The form of the concentration gradient is obtained by solving the steady state diffusion equation, with appropriate simplifying geometrical assumptions. The steady state is achieved through a balance between the point defect generation rate, the rate of migration to sinks, and the rate of recombination,

$$G_v - K_v N_v - [v_i N_i N_0] N_{v\rho} / M = 0 \dots\dots\dots (1a)$$

$$G_i - K_i N_i - [v_i N_i N_0] N_{v\rho} / M = 0 \dots\dots\dots (1b)$$

where

G = the rate of point defect generation,
 K = the kinetics constant for point defect migration to various sinks,
 that is,

$$K_v = \sum \left(\frac{Q_{v,\text{sink}}}{N_v} \right) \text{ where } Q_{v,\text{sink}} \text{ is defined in Ref } \mathcal{B}$$

N = the point defect concentration in atomic fraction,
 N_0 = Avogadro's number,
 ρ = density of the metal, and
 M = the effective molecular weight.

Physically these equations imply that point defects are generated uniformly throughout the system. This assumption will be discussed further in the next section. As can be noted from the above equations, the point defect concentration depends on its generation rate G , which, in turn, depends on the flux level. Since the void nucleation and growth is a function of time and point defect concentration, care should be exercised, when reporting experimental data, to separate the flux effect and the fluence effect. The fluence dependence should be different depending on whether the data are obtained for a given exposure time with varied flux levels or for a given flux level with varied exposure times [3].

The kinetics constant K [1, 3, 6] includes all of the physical processes that govern the point defect annihilation at various sinks. Voids and interstitial loops are both good sinks for point defects. The importance of these sinks in controlling the steady state, point defect concentrations will depend on size and number density. The values of both these parameters will change with time as the nucleation and growth process proceeds and thus result in kinetics constants and in point defect concentrations that vary with time. This is the reason that the model discussed here is a quasi-steady state approach. An important consideration, in the calculation of the K 's, is the effects [7-10] caused by the interaction between the misfit strain of a point defect and the stress field around a sink.

The misfit strain of an interstitial in a crystal lattice is greater than that of a vacancy. In the case of a dislocation, the migration of interstitials to a dislocation is favored because of its stress field; consequently, excess vacancies flow to the voids. It is believed, at the present time [1-3], that the biased point defect migration is the reason swelling will occur in metals under fast neutron irradiation.

A Consideration of the Uniform Point Defect Generation, Steady State Approach

As pointed out in the previous section, the point defects are assumed to be generated uniformly throughout the system. In fact, displacement

spikes are formed in a discrete fashion. In the immediate vicinity of the displacement spike, the point defect concentration will be high initially and will decay with time. The concentration of the interstitials will decay at a much faster rate when compared with the vacancies. As a result, the concentration relaxation process is both time and position dependent. Therefore, the most that can be expected from a quasi-steady state approach to point defect concentrations is a reliable estimate of the concentration averaged over time and position. To determine whether or not a quasi-steady state, uniform defect generation approach is appropriate for estimating the averaged point defect concentrations, the approximation must be examined in two ways.

First, if one assumes that a uniform point defect distribution does exist, one must decide whether a quasi-steady state approach is applicable by comparing the time required to establish the steady state point defect concentrations with times required for significant changes in the sink number density and size. The approach is invalid if the times required to achieve steady state point defect concentrations are long compared with those required to significantly change the microstructure by void and loop formation. Sharp and Foreman [6] have discussed this problem and derived the time to achieve steady state conditions for a given point defect generation rate, temperature, and sink number density and size. By using their treatment, the time to achieve steady state for fast breeder reactor conditions (generation rate = 10^{-7} atom fraction point defect per second, irradiation temperature = 500 C, void number density = $10^{15}/\text{cm}^3$, loop number density = $10^{15}/\text{cm}^3$) is of the order of 1 s. This time is too short for significant changes in microstructure and, thus, is consistent with the use of a steady state approach.

The second question concerns the assumption that the point defects are generated uniformly throughout the system, although in reality the concentration profile of point defects will fluctuate in time and position because of the discreteness of spike formation. The situation for the interstitials is worse than that for a vacancy because of their high mobility [1, 3]. The lifetime of the interstitials τ_i can be calculated from the ratio of interstitial concentration, as calculated from Eqs 1a and 1b, and the interstitial generation rate. For a typical interstitial concentration of 10^{-15} atomic fraction and a generation rate of 2×10^{-7} atomic fraction per second, τ_i has the value of 5×10^{-9} s. During this period, the interstitial will travel a distance \bar{X} of 10^4 Å, where $\bar{X} = 2\sqrt{D_i\tau_i}$ with D_i the diffusivity of the interstitial. Within a spherical volume of 10,000 Å radius, there will be on the average 2×10^3 displacement spikes formed per second. In this calculation the number of displacement spikes formed is equal to $\frac{4}{3}\pi\bar{X}^3(\phi\sigma N_L)$, where ϕ is the flux (2×10^{15} n/cm²-s), σ is the cross section (3 barns), and N_L is the number of atoms per cubic centimeter (8×10^{22} atoms/cm³). The time between spike formations $\tau_{\text{s spike}}$ in a volume of $\frac{4}{3}\pi\bar{X}^3$ is, therefore,

much larger than a typical interstitial lifetime. This confirms the previous statement that the concentrations of the interstitial in Eqs 1a and 1b represent only the time and position average. Furthermore, the use of Eqs 1a and 1b to obtain this average must be seriously questioned, since the equations include a recombination term that is a function of the product of the interstitial and vacancy concentrations. This term will become impossible to calculate when the vacancy population is also time and position dependent. Thus, Eqs 1a and 1b are useful only either when the vacancy concentration is nearly time and position independent or when the amount of recombination is small compared with the amount of point defect annihilation at sinks. When recombination is not an important mechanism of point defect annihilation, the time and position dependence of the vacancy population become irrelevant to the use of Eqs 1a and 1b, since the migration terms are linear [11] with both vacancy and interstitial concentration. In Fig. 1 (for the conditions given in the figure), the relative amounts of point defects that are annihilated by recombination and migration to the sinks have been estimated as a function of fluence by using the program in Ref 3. As seen in the figure, the recombination term becomes insignificant at higher fluences and the use of Eqs 1a and 1b is justified.

In the fluence region where the recombination term is important, it is essential to establish the time and position dependence of the vacancy concentration. For the vacancy concentration to behave as a uniform sea, two conditions must be satisfied. First, the average vacancy lifetime τ_v

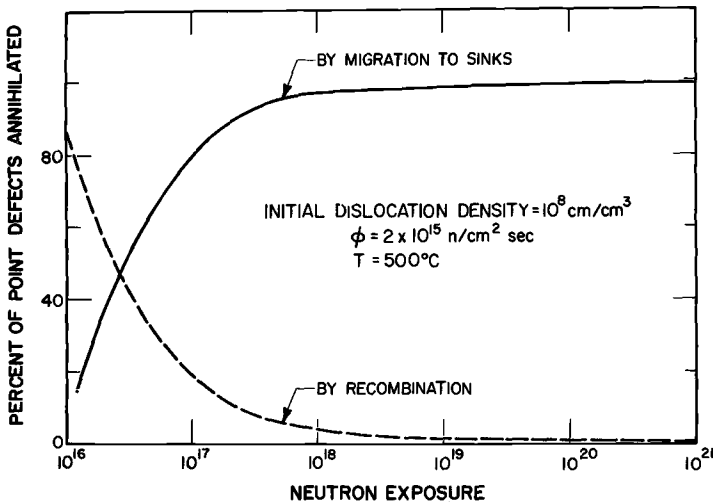


FIG. 1—The relative amounts of point defect annihilation by migration to sinks and by recombination.

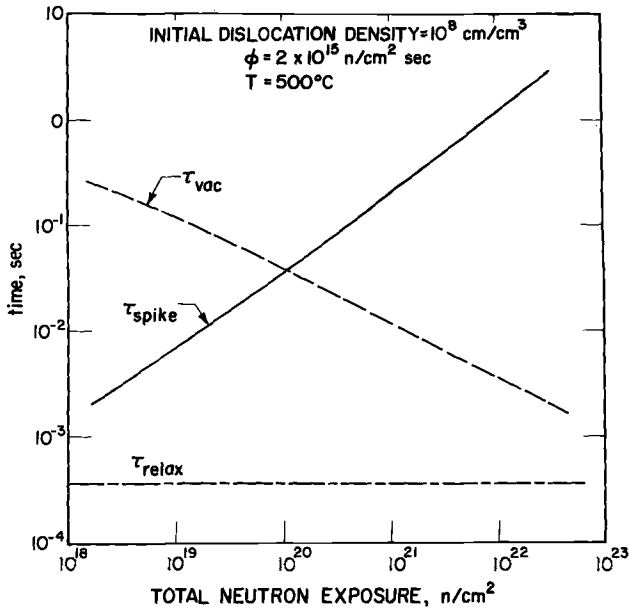


FIG. 2—The effect of neutron exposure on decay times pertinent to the use of a quasi-steady state model.

must be long with regard to the time τ_{spike} between spikes that occur in a volume defined by the average migration distance of the vacancy. This condition ensures that the vacancy sea will remain at about the same level at steady state. As can be seen in Fig. 2, this condition is satisfied for the low fluences where recombination is important.

The second condition ensures that the concentration peaks of vacancies resulting from spike formation decay quickly into a broad profile relative to the rate of injection of displacement spikes τ_{spike} . The decay time τ_{relax} (to the e^{-1} value) for a vacancy peak can be estimated from $r_c^2/3D_v$ [12], where r_c is the radius of a displacement spike (~ 200 Å) and D_v is the vacancy diffusivity ($\sim e^{-30,000/RT}$ cm²/s). For these conditions, τ_{relax} is of the order of 10^{-4} s and, as seen in Fig. 2, much smaller than τ_{spike} . It can be argued, for this situation, that the recombination terms will be linearly proportional essentially to the concentration of the interstitials and the average values used are acceptable. At high fluences, τ_v will be less than τ_{spike} but the recombination will also become unimportant.

The interest in the use of the analytical model [1, 3], developed to interpret the ion bombardment data, requires the examination of whether or not the assumption discussed in this section can be applied at high flux levels. Similar calculations have been performed for the case where the flux is 10^{18} n/cm²-s. From these results it can be concluded that the as-

sumption of uniform point defect generation applies also. The discussion given here demonstrates the possibility of using the present analytical model for translating the ion bombardment data to useful design information.

It should be noted that the nucleation rate of voids and interstitial loops is not linearly proportional to the concentration of vacancies and interstitials, respectively [1, 3]. The average values used will not, therefore, be a good approximation. In the calculation of the nucleation rate given in Ref 3, the approach is essentially an empirical fit of the observed experimental data on void nucleation. It has been emphasized in this paper that experimental data on loop nucleation also are required, since it is just as important as void nucleation. From this viewpoint it is essential that good experimental data on nucleation also be obtained in the ion bombardment experiments to avoid the difficulty in the analysis.

High-Fluence Effects

As the fluences increase, the void volume and dislocation density become larger and various complicated interactions will occur among the microstructural defects. The present model [1, 3] requires further modifications to account for these interactions. It is reasonable to state that existing theoretical capability in the field probably will not be sufficient to analyze all the possible interactions. A qualitative discussion will be given on the possible interactions. Some of the useful experimental approaches will be mentioned so that necessary data can be generated to aid in the development of the model and to extend its predictive capabilities.

Based on the present model [1, 3] calculations, as the fluences increase, ignoring dislocation-dislocation interactions, dislocation-void interactions, etc., the void growth rate actually accelerates. This is because at high fluences dislocation density will reach a value of 10^{11} and higher resulting from the interstitial loop growth. The dislocation is a biased sink; thus, when the dislocation density becomes large, the biasing effect will increase and cause a larger excess of vacancies to flow to the voids. Physically, from electron microscopy observations [13], the dislocation structure becomes very complicated even at moderate fluences (5×10^{22} m/cm²) and the identity of individual loops and the measurement of dislocation density become difficult in stainless steel. It is possible that various interactions will occur so that the dislocation density cannot increase indefinitely, thereby limiting the accelerated growth at high fluences mentioned above. There are three possible interactions.

1. Dislocation-Dislocation Annihilation—Interstitial loops of smaller sizes cannot glide because of the low stacking fault energy of stainless steel. If they are in the same atomic plane, they can grow into each other and annihilate a portion of each loop. As the loop size becomes large, the

prismatic form will be favored. Since prismatic loops can glide, this will increase the chance of mutual loop annihilation.

2. Dislocation-Dislocation Interactions—When dislocation density increases, dislocation locking and the development of cell structure may occur. When the dislocation becomes less free to climb, the efficiency of a dislocation as a sink will decrease, which will reduce the biasing effect for point defect migration. Dislocation-precipitate and dislocation-void interactions [14] will also tend to decrease the efficiency of the dislocation.

3. Dislocation-Void Annihilation—This possibility has been pointed out by several investigators [11, 15]; however, the kinetics of this process, when dislocation and voids are in contact, have not been worked out in detail.

As the supersaturation of point defects becomes less at high fluences, diffusional flow between vacancy-rich (voids) and interstitial-rich (loops) structures may become as important as the migration term given in Eqs 1a and 1b. As previously mentioned, analytical capabilities are limited at present, and it will be difficult to model all the interactions of interest.

Quantitative experimental measurements of the dependence of dislocation structure on fluence, with special attention to possible saturation effects, are particularly needed. This information can be used to estimate the effectiveness of the dislocation as a sink, as well as its effect on biased diffusion. This application will be in the same spirit as using experimentally measured voids and interstitial loop number density to calculate parameters for estimating void and loop nucleation rates [3].

Effects of Applied Stress on Metal Swelling

The effect of applied stress on metal swelling due to fast neutron irradiation is a subject of engineering importance. At present, little information is available on this effect from well characterized experiments. An obvious consequence of applied stress is the creation of a stress field around a point defect sink where no stress field exists in the absence of an applied field, for example, around a void or some precipitate under unidirectional tension [16]. The existing stress field around some of the point defect sinks can also be altered under an applied stress, for example, piled up dislocation. The concept developed so far, for the excess vacancy flux over that of the interstitial arriving at the void, in the unstressed system results from the biased diffusion caused by the stress field around the dislocation. It is conceivable that the stress field produced by the applied stress around various sinks could become effective in altering the point defect migration, which would change the excess vacancy flux to the void and, therefore, the rate of void growth.

In the present models [1–3], the diffusion equation, including the influence of a stress field, is the one used by Ham [7]. This equation is based on the concept that the stress field creates an additional driving force in

the form of a potential gradient. There is another effect that should be included. This subject has been discussed in detail by Girifalco and Welch [8], Koehler [9], and Johnson [10]. Physically the latter effect is caused by the change in motion energy due to lattice distortion in a stress field. Johnson's formulation is phenomenological and will be reproduced here. Under the influence of an applied stress field, the diffusion flux J can be expressed as

$$J = -D(P) \left[\nabla C + \frac{C}{kT} \bar{V} \nabla P \right] \dots \dots \dots (2)$$

where

- $D(P)$ = the diffusion coefficient in a stress field,
- C = the concentration of point defects,
- P = pressure, and
- \bar{V} = the partial atomic volume of a point defect.

The diffusion coefficient in the stress field is defined as $D(0)e^{-PV_m/kT}$, where $D(0)$ is the diffusion coefficient in the absence of a stress field and V_m is the activation volume.

The partial atomic volume of an interstitial corresponds to its relaxation volume, which is the volume change of the crystal resulting from the relaxation of atoms around an interstitial. For the vacancy, the partial atomic volume is not equal to the relaxation volume. For the purpose of Eq 2 the relaxation volume should be used. This is due to the fact that the motions of a vacancy and an atom are always coupled [17, 18]. The physical significance of the activation volume has been discussed [8, 9]. According to the reasoning given by Johnson and Brown [19] and Li et al [20] for a nonhydrostatic stress field, only the gradient of the hydrostatic component is important in affecting the point defect migration. Therefore, in this case, the pressure P in Eq 2 should be replaced by the hydrostatic component of the stresses. The conservation equation, including the influence of a stress field, is

$$\frac{\partial C}{\partial t} = D(P) \left[\nabla^2 C + \frac{(\bar{V} - V_m)}{kT} \nabla P \nabla C - V_m \bar{V} \left(\frac{\nabla P}{kT} \right)^2 C \right] \dots \dots \dots (3)$$

In Koehler's derivation [9] it is assumed that, under the influence of a stress gradient, the forward jump and the backward jump experience the same activation energy and, therefore, the last term on the right-hand side of Eq 3 is absent in his expression. It will be of interest to compare the results using Ham's equation [7] and those using Eq 3 for the effect of an edge dislocation in biasing the point defect migration.

The biasing effect due to the applied stress can be illustrated for the case of a void. When a unidirectional tension is applied, the hydrostatic component of the stress is [16]

$$\sigma_H = -\frac{2\mu}{3} \frac{1+\nu}{1-2\nu} \frac{c}{r^3} (2+6 \cos 2\theta) \dots\dots\dots (4)$$

where

- μ = the modulus,
- ν = Poisson's ratio,
- r = distance from the center of the void, and

$$c = \frac{TR^3}{8\mu} \frac{5(1-2\nu)}{8-10\nu} \quad (T = \text{the applied stress and } R = \text{the radius of the void}).$$

Goodier [16] has also calculated the stress field around a precipitate. Of course, in some cases, a stress field will occur around a precipitate in the absence of an applied stress due to the misfit strain. As is evident from Eq 4, the stress field depends on the magnitude of the applied stress and the size of the void and the precipitate. In general, the stress gradient around the void probably will be smaller than that around an edge dislocation [21]. The total effect due to the void and the precipitate will be a function of their number density and size distribution. The latter parameters vary with the fluence. It will be difficult to predict the effect of applied stress, based on the concept given here, without a detailed calculation, which will be reported in a future publication.

A sample calculation for the interstitial migration has been performed to demonstrate the biasing effect due to the applied stress field around a void. In this calculation, applied tension is 10,000 psi, void size is 100 Å, temperature is 700 K, Poisson's ratio is 0.3, V_m is set as zero, and \bar{V} is taken to be $0.1a^3$, with $a = 4$ Å. The boundary condition is such that at the void surface the concentration of the interstitial is zero, and at a distance ten times the void diameter the concentration is that calculated from Eqs 1a and 1b. From Eqs 3 and 4, the concentration profile can be calculated by a numerical method. The results of the calculation can be expressed in terms of an effective radius of the void such that the flux arriving at the void is $4\pi D_i (R_v + \Delta R_v) C_i$ [3], where R_v is the radius of the void and ΔR_v is the effective change in void radius due to the applied stress. In this particular case, ΔR_v is found to be approximately 0.3 Å and causes an enhanced interstitial flow to the void. If the calculation is carried out for the vacancy migration, care must be taken to account for the effect of applied stress and capillarity on the thermal equilibrium values of vacancy concentrations at the void surface. These considerations have been analyzed by Nolfi [18]. However, boundary conditions alone will not account for

the effect of stress on swelling, and the stress biased diffusion should be included in the calculation.

The stress field around the void also depends on the shape of the void. Recently Nolfi [18] has discussed the shape change of a void in the absence of neutron irradiation due to the effect of capillarity and applied stress, and Tien and Copley [22] observed that aging under unidirectional stresses produced a shape change of the precipitate that depended on the direction of the stress. This effect will become important when the void size becomes large and the supersaturation of point defects becomes small, that is at high fluences. On the other hand, under fast neutron bombardment and with the applied stress field, the point defect flux arriving at the void surface will not be uniform, which will also lead to a shape change. In the detailed calculation, the shape change of voids should also be considered. Some experimental observation of this phenomenon will be very useful.

Irradiation Enhanced Diffusional Creep

An extension of the present metal swelling model also provides a method of estimating the irradiation enhanced dislocation climb rate, which could be an important mechanism for irradiation creep in metals. There are other mechanisms that can contribute to in-reactor creep. The possibility of irradiation enhanced diffusional creep has been discussed in the literature [23]. The conclusion made by Hesketh that, under a uniform applied stress field, irradiation will not alter diffusion creep to the first order is reasonable. Under a nondivergent and nonuniform stress field, he concludes that irradiation will also not cause enhanced diffusional creep but will increase the transfer of matter from one surface of the specimen to the opposite surface, in other words, the Kirkendall effect. Actually, the latter effect will cause a shape change of interest to the reactor application and can be considered a form of diffusional creep. This type of shape change will be the subject of discussion of this section.

Consider a cylinder made of a single-crystal material, which could be fuel element cladding or a section of ceramic fuel with a center void formed by bubble or cavity migration or both. If matter can be transferred from the inside surface to the outside surface, a change in diameter of the cylinder will result. This process can be caused by an applied stress gradient. For example, when the outer surface is in tension and the inner surface is in compression, atoms will move toward the outer surface and the vacancy will move in the opposite direction. Under neutron bombardment, following Hesketh's argument, it can be shown that the rate of matter transport will be altered. The above example will be used to illustrate this effect, with the further assumptions that there is no sink of point defects in the crystal and that the irradiation induced point defects are generated uniformly throughout the specimen. The conservation equations for the one-

dimensional case are

$$D_i(P) \nabla \left(\nabla C_i + \frac{C_i}{kT} \bar{V}_i \nabla P \right) + G_i - \nu_i C_i C_v \frac{M}{\rho N_0} = 0 \dots \dots \dots (4a)$$

$$D_v(P) \nabla \left(\nabla C_v + \frac{C_v}{kT} \bar{V}_v \nabla P \right) + G_v - \nu_i C_i C_v \frac{M}{\rho N_0} = 0 \dots \dots \dots (4b)$$

where $V_m = 0$ and $G_i = G_v$. Subtracting Eq 4b from Eq 4a we obtain

$$D_i(P) \nabla \left(\nabla C_i + \frac{C_i}{kT} \bar{V}_i \nabla P \right) - D_v(P) \nabla \left(\nabla C_v + \frac{C_v}{kT} \bar{V}_v \nabla P \right) = 0 \dots (5)$$

Integrating Eq 5,

$$D_i(P) \left(\nabla C_i + \frac{C_i}{kT} \bar{V}_i \nabla P \right) - D_v(P) \left(\nabla C_v + \frac{C_v}{kT} \bar{V}_v \nabla P \right) = \text{constant} \dots \dots (6)$$

This equation represents the difference of the interstitial flux and the vacancy at any point in the crystal. Integrating again between the inside surface and the outside surface,

$$D_i(P) \left(C_i \Big|_{r_1}^{r_2} + \int_{r_1}^{r_2} \frac{C_i}{kT} \bar{V}_i \nabla P \, dr \right) - D_v(P) \left(C_v \Big|_{r_1}^{r_2} + \int_{r_1}^{r_2} \frac{C_v}{kT} \bar{V}_v \nabla P \, dr \right) = \text{constant} (r_2 - r_1) \dots (7)$$

As is noted from Eq 7, the value of the constant will be different depending on the neutron flux because C_i and C_v in the bulk depend on irradiation. Consequently, from Eq 6 the difference between the interstitial flux and the vacancy flux will be altered by irradiation and, therefore, the rate of diameter change. Physically this effect is another consequence of stress biased diffusion, because the interaction between the interstitial and the stress field differs from that between the vacancy and the stress field. For a pressurized tube made of a single-crystal material, the hydrostatic component of the applied stress is constant across the thickness of the tube [24]; therefore, the diffusional creep discussed here will not occur. On the other hand, when a temperature gradient occurs across the thickness of the cylinder, the hydrostatic component of the thermal stress will vary with thickness [25]. The magnitude of thermal stress could be significant in the ceramic fuel. This type of creep process should be considered in the modeling of the behavior of a fuel element.

In the previous discussion a section of cylinder made of a single-crystal material without any internal sinks was considered. With the grown-in dislocations and grain boundaries, the conservation equation must be

modified to account for the effect of these point defect sinks. For polycrystalline materials, the shape change of each individual grain controls the shape of the specimen. There are two additional effects that should be considered. (1) If grain boundary sliding cannot occur and the tangential stresses at the grain boundary are not relaxed, the stress distribution within each grain will be identical to the macroscopic stress distribution. However, there will be an additional stress distribution created as a result of atomic motion in order to maintain compatibility at the grain boundary. This is similar to the problem discussed by Herring [26] concerning the diffusional creep under tension of a wire with bamboo structure. (2) If the tangential stresses at the grain boundary can be relaxed, the stress distribution within each grain will be different from the macroscopic stress distribution. This has also been discussed by Herring [26] and probably will be important in the high-temperature regions of the ceramic fuel. Further work is required to estimate the consequences of these additional effects. Furthermore, the rate of grain boundary sliding could also be affected by irradiation and by the stress field. Ashby and Raj [27] have analyzed the diffusion controlled grain boundary sliding in the absence of irradiation.

From the previous discussion, stress biased diffusion plays an important role in controlling irradiation induced metal swelling and creep deformation both by the dislocation process and by diffusional processes. At present, the parameters in Eq 3 are not known precisely. The capability of model analysis is, therefore, limited and depends on a semiempirical approach by fitting various parameters to experimental data. It will be desirable to obtain some of the important parameters by independent experiments in order to improve the applicability of the model analysis.

Summary

In this paper the possible flux and fluence effects on metal swelling due to fast neutron irradiation and ion bombardment were discussed. These considerations are important in extrapolating ion bombardment data to generate design information on metal swelling. The effects of stress field in biasing point defect migration also were considered. A sample calculation has been performed to show that the applied stress field around a void can produce biasing, with possible implications on the effect of stress on swelling. The stress biased point defect migration can also cause shape changes, which could be of interest in the behavior of fuel elements.

Acknowledgments

We wish to express our appreciation to R. W. Balluffi of Cornell University for providing many of the ideas in this paper and also to H. H. Johnson of Cornell University for helpful discussions on stress biased diffusion.

References

- [1] Harkness, S. D., Tesk, J. A., and Li, Che-Yu, "An Analysis of Fast Neutron Effects on Void Formation and Creep in Metals," presented at American Nuclear Society Winter Meeting, 1969, to be published in *Nuclear Applications and Technology*.
- [2] Bullough, R., Eyre, B. L., and Perrin, R. C., "The Growth and Stability of Voids in Irradiated Metal," presented at ANS Winter Meeting, 1969, to be published in *Nuclear Applications and Technology*.
- [3] Harkness, S. D. and Li, Che-Yu, "A Study of Void Formation in Fast Neutron Irradiated Metals," submitted to *Metallurgical Transactions*.
- [4] Mazey, D. J., Hudson, J. A., and Nelson, R. S., "Void Formation in Metals During Accelerator Irradiation," presented at the Symposium on Effects of Radiation on Structural Metals, Annual Meeting, American Society for Testing and Materials, Toronto, Ontario, 21-26 June 1970.
- [5] Keefer, D. W., Neely, H. H., Robinson, J. C., and Kramer, D., "Void Formation in Stainless Steel by Proton Irradiation," presented at this symposium, ASTM Annual Meeting, Toronto, Ontario, 21-26 June 1970 (see pp. 332-345, this volume).
- [6] Sharp, J. V. and Foreman, A. J. E., "Calculation of Build-up Times for Radiation Enhanced Diffusion," AERE-R-5786, Atomic Energy Research Establishment, Harwell, England, 1968.
- [7] Ham, F. S., *Journal of Applied Physics*, JAPIA, Vol. 30, 1959, p. 915.
- [8] Girifalco, L. A. and Welch, D. O., *Point Defects and Diffusion in Strained Metals*, Gordon and Breach, 1967.
- [9] Koehler, J. S., *Physical Review*, PHRVA, Vol. 181, 1969, p. 1015.
- [10] Johnson, H. H. and Koliwad, K., "Interstitial and Vacancy Transport in Pressure Gradients," presented at Spring Meeting, Metallurgical Society, Las Vegas, 1970.
- [11] Flynn, C. P., *Physical Review*, PHRVA, Vol. 133, 1964, p. A587.
- [12] Carslaw, H. S. and Jaeger, J. C., *Conduction of Heat in Solids*, Clarendon Press, Oxford, 1959.
- [13] Holmes, J. J., Robbins, R. E., Brimball, T. E., and Mastel, B., *Acta Metallurgica*, AMETA, Vol. 16, 1968, p. 955.
- [14] Weeks, R. W., Pati, S. R., Ashby, M. F., and Barrand, P., *Acta Metallurgica*, AMETA, Vol. 17, 1969, p. 1403.
- [15] Straalsund, J. L. and Holmes, J. J., *Transactions of the American Nuclear Society*, TANSa, Vol. 12, 1969, p. 115.
- [16] Goodier, J. N., *Transactions*, American Society of Mechanical Engineers, TASMA, Vol. 55, 1933, p. 39.
- [17] Herring, C. in *The Physics of Powder Metallurgy*, W. E. Kingston, Ed., McGraw-Hill, New York, 1951.
- [18] Nolfi, F. V., Jr., "Capillarity and Stress Effects in Solids," submitted to *Metallurgical Transactions*.
- [19] Johnson, R. A. and Brown, E., *Physical Review*, PHRVA, Vol. 127, 1962, p. 446.
- [20] Li, J. C. M., Oriani, R. A., and Darken, L. S., *Zeitschrift fuer Physikalische Chemie Neu Folge*, ZPYFA, Vol. 47, 1966, p. 271.
- [21] Cottrell, A. H., *Dislocations and Plastic Flow in Crystals*, Clarendon Press, Oxford, 1953.
- [22] Tien, J. K. and Copley, S. M., "The Effect of Uniaxial Stress on the Coarsening of Coherent γ' Precipitates in Monocrystalline Nickel Based Alloys," presented at Spring Meeting, Metallurgical Society, Las Vegas, 1970.
- [23] Hesketh, R. V., *Journal of Nuclear Materials*, JNUMA, Vol. 29, 1969, p. 217.
- [24] Honsner, G. W. and Vreeland, T., Jr., *The Analysis of Stress and Deformation*, MacMillan, 1966.
- [25] Timoshenko, S. and Goodier, J. N., *Theory of Elasticity*, McGraw-Hill, New York, 1951.
- [26] Herring, C., *Journal of Applied Physics*, JAPIA, Vol. 21, 1950, p. 437.
- [27] Ashby, M. F. and Raj, R., "The Rate of Diffusion-Controlled Grain Boundary Sliding," presented at Spring Meeting, Metallurgical Society, Las Vegas, 1970.

DISCUSSION

*J. W. Corbett*¹—Would those who spoke on theories please comment on the differences between the theories.²

Che-Yu Li (authors' closure)—The physical principles on which these models are developed are the same for all the models. They differ only in the mathematical approaches and in the assumptions for nucleation processes and for the boundary conditions for the growth processes.

¹ Professor, Physics Department, State University of New York at Albany, Albany, N.Y. 12203.

² See also Bullough and Perrin, pp. 317–331.

P. J. Barton¹ and P. R. B. Higgins¹

Some Observations on the Structure and Tensile Properties of AISI Type 316 Steel as a Function of Fast Reactor Irradiation Temperature

REFERENCE: Barton, P. J. and Higgins, P. R. B., "Some Observations on the Structure and Tensile Properties of AISI Type 316 Steel as a Function of Fast Reactor Irradiation Temperature," *Irradiation Effects on Structural Alloys for Nuclear Reactor Applications*, ASTM STP 484, American Society for Testing and Materials, 1970, pp. 362–374.

ABSTRACT: Solution treated AISI Type 316 steel strip specimens were irradiated in the Dounreay fast reactor to doses of 1.0 to 1.3×10^{22} n/cm² (total), 1.7 to 2.6×10^{21} n/cm² (fission) within the following measured temperature ranges: 420 to 440, 500 to 513, 520 to 533, 560 to 570, and 645 to 650 C.

Transmission electron microscopy reveals the presence of voids after irradiation at all these temperatures. Distribution is uniform after irradiation at 420 to 440, 500 to 513, and 520 to 533 C. At higher temperatures it is uneven and concentration is so low that probably helium bubbles and not voids are being observed. From the temperature dependence of void concentration and average diameter it is deduced that the consequent density decrease is maximal after irradiation at 500 to 513 C.

Dislocation loops are present for irradiation at all but the highest temperature. They are interstitial and lie on {111} planes with Burgers vectors of the type $a/3 \langle 111 \rangle$. At 420 to 440 C all loops are faulted. As irradiation temperature increases, loop concentration decreases, and at 520 to 533 C a few unfaulted loops are observed. Yield stress increases estimated from loop and void concentrations are found to be in fair agreement with measured values.

KEY WORDS: irradiation, neutron irradiation, radiation effects, tensile properties, voids, dislocations (materials), yield strength, temperature, structural steels, alloy steels, nuclear reactors, fast reactors (nuclear)

Certain general conclusions have been drawn [1, 2, 3]² from the many published observations of voids and dislocation loops in neutron irradiated

¹ United Kingdom Atomic Energy Authority, Atomic Energy Research Establishment, Harwell, Didcot, Berkshire, England.

² Italic numbers in brackets refer to the list of references at the end of this paper.

metals and alloys. First, the Frenkel pair creation rate has to be sufficiently great for void growth. Intuitively one expects this to have to exceed some critical value dependent on the concentration of point defect sinks in the material. The concentration of these will depend in turn on dislocation density and the material purity, the importance of the latter being borne out by observations on void formation in nickel [4]. Secondly, it appears that irradiation temperature must lie very roughly between one third and two thirds of the absolute melting point. Below this temperature range the diffusion rate of vacancies is too slow and cluster formation may be preferred instead, while above it the diffusion coefficient is large and there is a greater probability that a void will lose a vacancy rather than capture one. Thirdly, the transmutation product helium plays a part in void nucleation. The concept has been advanced that helium bubbles are formed by clustering of vacancies and helium atoms and that if the Frenkel pair creation rate is sufficiently high the vacancy supersaturation in the structure is adequate for bubbles to grow by vacancy accumulation [2, 5, 6].

The displacement rate required for void growth during neutron irradiation of alloys of engineering use such as stainless steels is attained in fast reactors. The temperature dependence of the void growth process needs to be established for technological and fundamental reasons. This paper describes the results of an experiment in which the structure of AISI Type 316 steel has been studied after fast reactor irradiation at measured temperatures in the range from 420 to 650 C.

Experimental Details

The composition of the steel is given in Table 1. The material was obtained as 0.028-in. (0.7-mm)-thick softened and descaled strip. This was cold reduced to 0.020 in. (0.5 mm). Tension specimens die stamped with their gage lengths parallel with the rolling direction were solution treated in vacuum at 1050 C for 30 min followed by rapid cooling. The resultant structure consisted of equiaxed grains of 25- μ m diameter.

Specimens were irradiated in the core of the Dounreay fast reactor, Caithness, Scotland. Heating was by gamma ray absorption. Temperatures were controlled by surrounding the cylindrical specimen containers with accurately dimensioned annular gas gaps to regulate the rate of heat loss to the reactor coolant [7]. Specimen temperatures measured during irradiation by means of chromel-alumel thermocouples varied between the follow-

TABLE 1—*Composition of AISI Type 316 steel (weight percent).*

Fe	Cr	Ni	C	Mo	Si	Mn	B	N	Co
Bal	17.3	11.4	0.039	2.5	0.32	1.54	0.0018	0.023	0.037

ing limits: 420 to 440, 500 to 513, 520 to 533, 560 to 570, and 645 to 650 C. The fission and total neutron doses received by the specimens were 1.7 to 2.6×10^{21} n/cm² and 1.0 to 1.3×10^{22} n/cm², respectively. The displacement dose, calculated according to the Kinchin and Pease model [8], is 8 to 11 per atom and the concentration of transmutation product helium in the steel is 3×10^{-6} atoms/atom.

The dependence of the steel structure upon irradiation temperature has been established by transmission electron microscopy. Disks of 2.3-mm diameter were cut from tension specimens using a remotely operated ultrasonic drill. They were prepared for the microscope by a two-stage electrolytic process,³ first by jetting at room temperature with 1:3 *v/v* concentrated nitric acid:methanol mixture at 90 V and 60 mA. When the disk center was approximately 0.002 in. (50 μm) thick, polishing was continued until perforation in 34:56:10 *v/v* concentrated sulphuric acid:phosphoric acid:methanol mixture at a potential of 14 V.

Specimens were examined using a Siemens Elmiskop I microscope fitted with a Valdré double tilt stage and operated at 100 kV. Magnifications were checked using a diffraction grating replica, and correction was made for the slight variations in specimen height in the microscope from one disk to another. Postirradiation uniaxial tension tests were performed at various temperatures and a strain rate of 2×10^{-4} s⁻¹ using shielded and remotely operated tension machines.

Results

The void distribution in the structure is uniform after irradiation at 420 to 440, 500 to 513, and 520 to 533 C (Figs. 1, 2, 3). After irradiation at 560 to 570 and 645 to 650 C the voids are nonuniformly distributed and are present in very low concentration (Figs. 4 and 5).

Faulted dislocation loops are present after irradiation at all temperatures except 645 to 650 C. They are interstitial in character, lie on {111} planes, and have Burgers vectors of the type $\mathbf{a}/3 \langle 111 \rangle$. As irradiation temperature is increased their concentration decreases and becomes very low after irradiation at 560 to 570 C, when they are more regular in outline than at the lower temperatures. Evidence of unfaulting and growth is detected after irradiation at 520 to 533 and 560 to 570 C (Figs. 4 and 6). Since no loops are seen after irradiation at 645 to 650 C, it is inferred that helium bubbles rather than voids are produced at this temperature.

Selected area electron diffraction after irradiation at 420 to 440 C has been claimed to reveal double diffraction and streaking effects which may be evidence for a very early stage of carbide precipitation.⁴ This temperature is much lower than that at which the steel exhibits precipitation on

³ Private communication with G. P. Wlaters, UKAEA, Harwell.

⁴ Private communication with P. R. B. Higgins, UKAEA, Harwell.

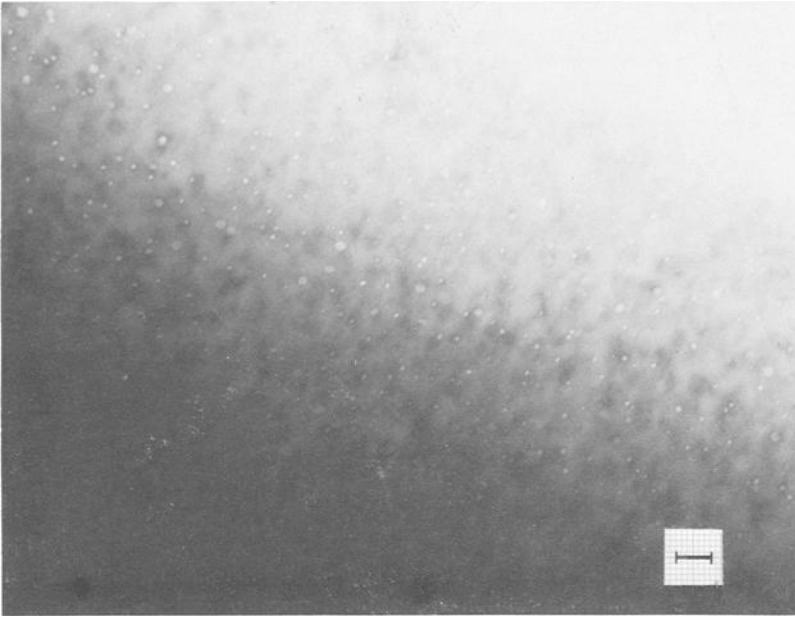


FIG. 1—*Variation of structure with fast reactor irradiation temperature. Scale length in photographs is equivalent to 0.1 μm . Irradiation temperature, 420 to 440 C.*

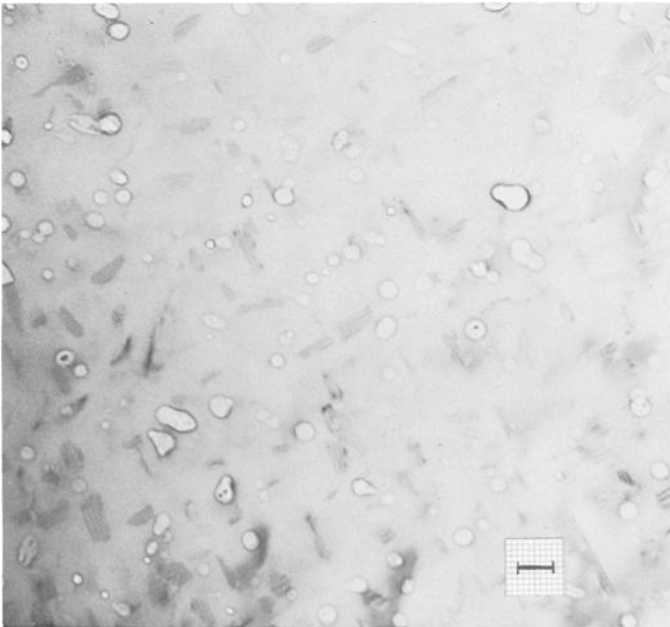


FIG. 2—*Variation of structure with fast reactor irradiation temperature. Scale length in photographs is equivalent to 0.1 μm . Irradiation temperature, 500 to 513 C.*

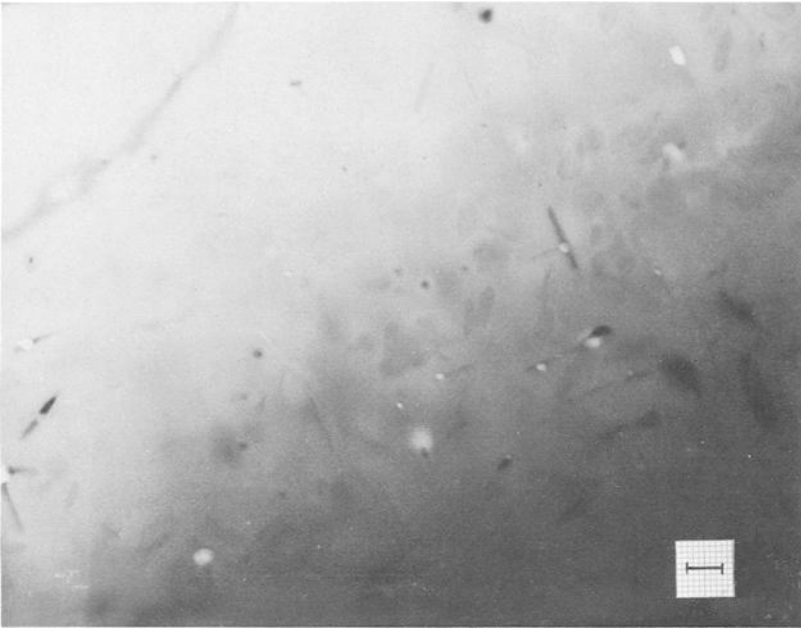


FIG. 3—Variation of structure with fast reactor irradiation temperature. Scale length in photographs is equivalent to 0.1 μm . Irradiation temperature, 520 to 533 C.

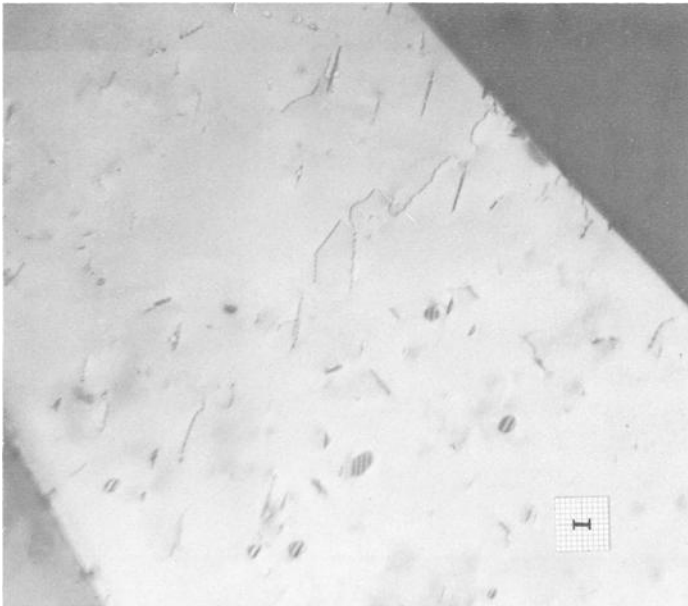


FIG. 4—Variation of structure with fast reactor irradiation temperature. Scale length in photographs is equivalent to 0.1 μm . Irradiation temperature, 560 to 570 C.

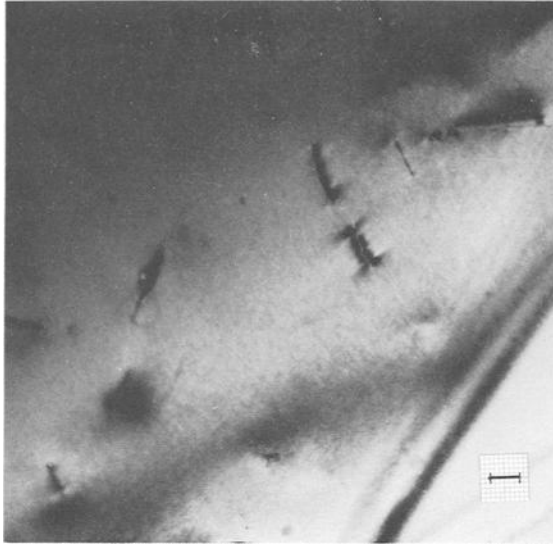


FIG. 5—Variation of structure with fast reactor irradiation temperature. Scale length in photographs is equivalent to 0.1 μm . Irradiation temperature, 645 to 650 C.

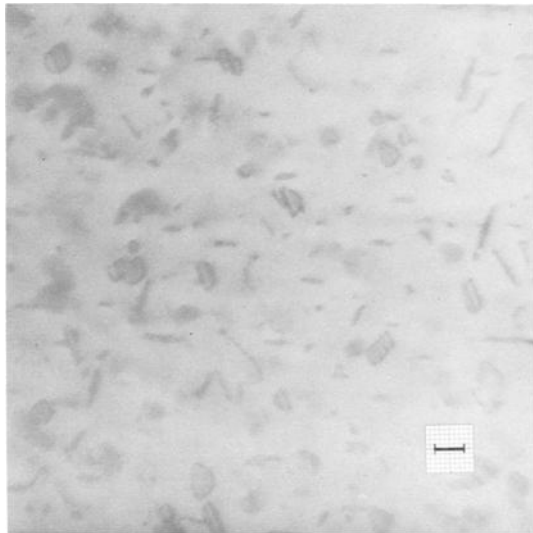


FIG. 6—Variation of structure with fast reactor irradiation temperature. Scale length in photographs is equivalent to 0.1 μm . Irradiation temperature, 520 to 533 C.

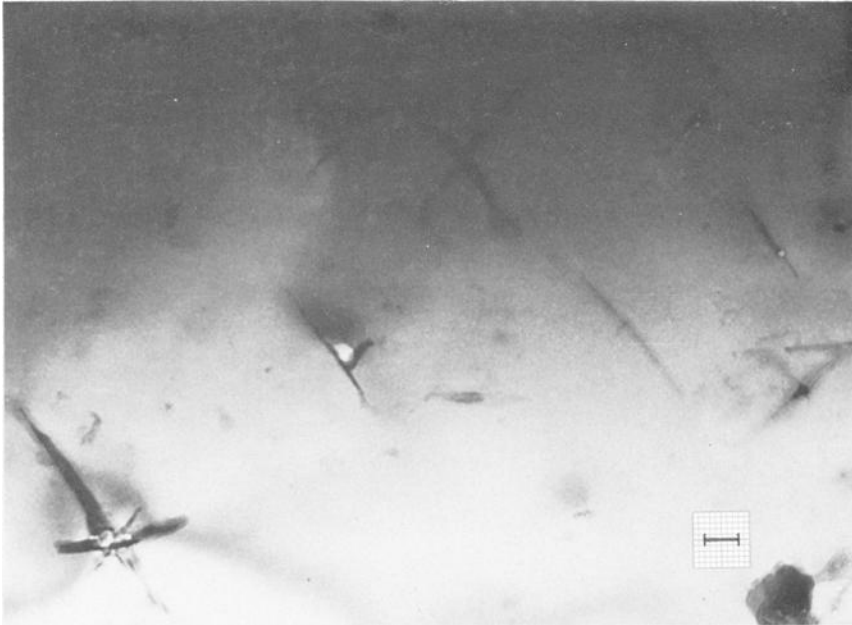


FIG. 7—Variation of structure with fast reactor irradiation temperature. Scale length in photographs is equivalent to $0.1 \mu\text{m}$. Irradiation temperature, 645 to 650 C.

heating out of pile. Alternatively, since these effects are not observed at higher temperatures, including those at which precipitate particles are resolved, these effects may arise from the presence of a high concentration of interstitial loops.

The precipitate particles are observed after irradiation at 520 to 533 C and higher temperatures. They have a rodlike habit and appear to lie on $\{111\}$ planes. At 560 to 570 and 645 to 650 C (Figs. 5 and 7) most of the voids or bubbles are of irregular shape and are associated with the particles which are assumed to be M_{23}C_6 .

A sufficient number of voids was counted in material irradiated at 500 to 513 and 520 to 533 C to allow plotting of size distributions (Figs. 8 and 9). Loop concentrations have been estimated for those irradiations yielding a uniform distribution, and an attempt has been made to estimate loop diameter by measuring the lengths of the images of those viewed edge on. Loop and void sizes and concentrations as a function of irradiation temperature are collated in Table 2.

Discussion

From these structural studies it is clear that the upper limit for void formation in this steel when subject to the above displacement rate is close

TABLE 2—Void and loop size and concentration as a function of irradiation temperature.

Irradiation Temperature, deg C	Voids				Loops				
	Number Measured	Average Diameter, nm	Most Probable Diameter, nm	Concentration, n/cm ³ for t = 100 nm	Concentration, n/cm ³ for t = 150 nm	Number Measured	Average Diameter, nm	Concentration, n/cm ³ for t = 100 nm	Concentration, n/cm ³ for t = 150 nm
420 to 440.....	603	13.4	9.9	1.8 × 10 ¹⁵	1.2 × 10 ¹⁵	11	37.4	2.2 × 10 ¹⁵	1.5 × 10 ¹⁵
500 to 513.....	990	32.8	18.6	0.6	0.4	80	87.6	0.8	0.5
520 to 533.....	103	21.8	18.8	0.2	0.1	37	83.4	0.4	0.3
560 to 570.....	25	31.1	33.0
645 to 650.....	17	24.0	18.7

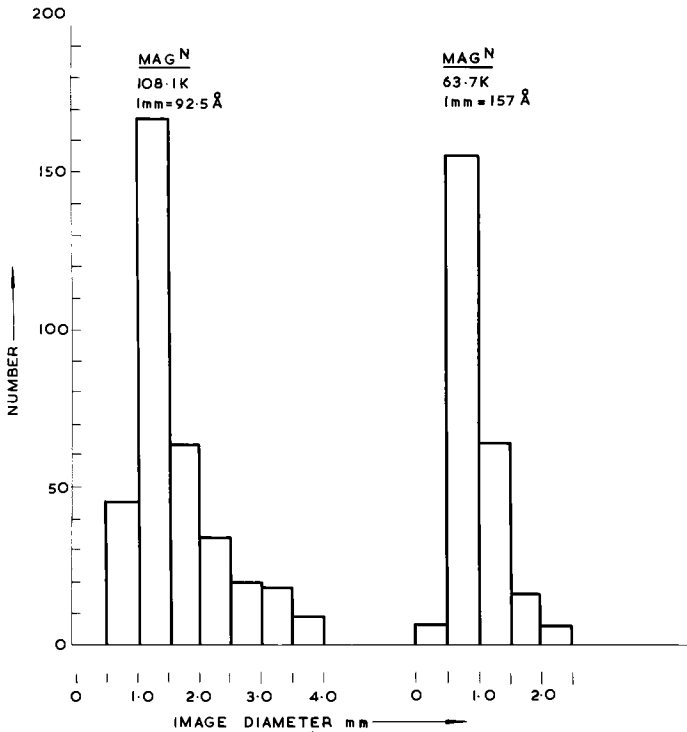


FIG. 8—Void size distribution after irradiation at 420 to 440 C to 1.0 to 1.3×10^{22} n/cm^2 (total).

to 560 to 570 C. Reference to Fig. 4 shows that an occasional faulted loop and void is present after irradiation at this temperature. This upper temperature limit for void formation agrees rather well with that predicted by Bullough and Perrin [2, 5]. Their model allows prediction of a void growth rate in terms of the probability of a void capturing a vacancy, capturing an interstitial, and boiling off a vacancy. These three probabilities vary quite differently with temperature, the last probability becoming dominant at high temperatures so that the predicted growth rate drops rapidly to zero. To quantify the growth rate one has to assume a recombination constant for vacancies and interstitials, a dislocation density, and a Frenkel pair creation rate. Putting in what are considered to be realistic values, Bullough and Perrin predict an upper temperature limit of 540 to 580 C for fast reactor irradiated AISI 316 steel, which is in good agreement with experiment. A lower temperature limit for void formation may be inferred from this model by noting the temperature below which growth becomes negligibly slow. For stainless steel this would be about 300 C.

The volume increase due to voidage has been estimated for those irradiation temperatures yielding a uniform void distribution. Here mean void diameters have been used and, as will be seen by reference to Table 3, the density decrease is a maximum at 500 to 513 C and becomes vanishingly small at 560 to 570 C. Estimated density decreases have been calculated

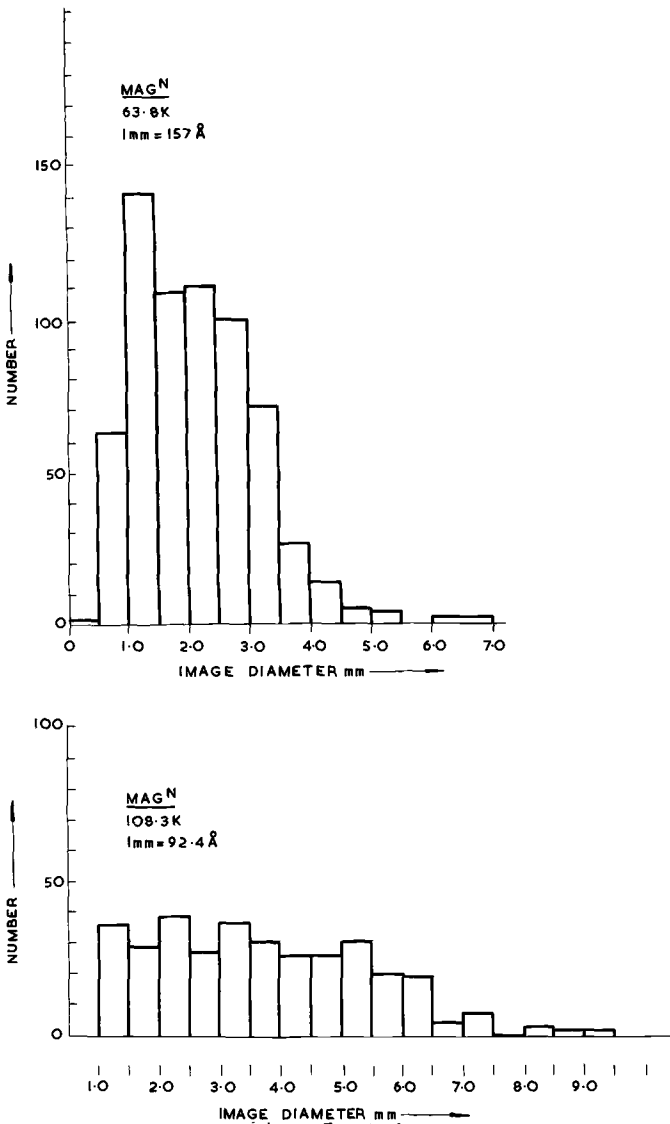


FIG. 9—Void size distribution after irradiation at 500 to 513 C to 1.0 to 1.3×10^{22} n/cm² (total).

TABLE 3—Volume change due to voidage as a function of irradiation temperature.

Irradiation Temperature, deg C	Volume Change, %	
	for $t = 100$ nm	for $t = 150$ nm
420 to 440.....	0.2	0.13
500 to 513.....	1.1	0.7
520 to 533.....	0.07	0.05

for assumed foil thicknesses of 100 and 150 nm, which are reasonable values.

Various attempts have been made to estimate yield stress increases due to the presence of voids in metals and alloys [9]. Coulomb quantifies this increase as follows [10]:

$$\Delta\sigma_v = \frac{Gb}{2\beta L}$$

where

G = the shear modulus,

β = approximately unity,

b = the slip dislocation Burgers vector, and

L = the mean nearest neighbor spacing of voids on a slip plane.

L is given by

$$L = 0.5(nd)^{-1/2}$$

where n is the concentration per unit volume and d is the void diameter. The yield stress increases in shear and in uniaxial tension due to the voids in the DFR irradiated steel have been calculated using these expressions and are given in Table 4.

Attempts have been made also to calculate the hardening due to the presence of loops resulting from quenching [11] or from neutron irradiation.

TABLE 4—Increase in yield stress due to loops and voids.

Irradiation Temperature, deg C	$\Delta\sigma_{\text{voids}}$		$\Delta\sigma_{\text{loops}}$		$\Delta\sigma_{\text{shear}}$		$\Delta\sigma_{\text{tensile}}$	
	ksi	MN/m ²	ksi	MN/m ²	ksi	MN/m ²	ksi	MN/m ²
420 to 440.....	4.8	33.1	10.5	72.4	11.5	79.9	23	160
500 to 513.....	4.1	28.3	8.8	60.7	9.7	66.9	19	130
520 to 533.....	2.0	13.8	6.4	44.1	6.7	46.2	13	90

NOTE—The value of shear modulus, G , taken is 9.5×10^6 psi (65.5×10^3 MN/m²) at 430 C and 9.0×10^6 psi (62.1×10^3 MN/m²) at 510 C [15].

tion [12]. Although the Fleischer model [13] assumes that the defects causing hardening are relatively small, it is reported that it predicts quite well the increase in yield stress of fast quenched aluminium which contains loops of 300 to 1000-Å diameter [11]. Because the loops observed in the DFR irradiated AISI Type 316 steel are of a similar size, the model is applied to the present results. The yield stress increase is given by

$$\Delta\sigma_{L_1} = \frac{Gb}{2L} \text{ for edge dislocations}$$

$$\Delta\sigma_{L_2} = \frac{Gb}{3L} \text{ for screw dislocations}$$

Yield stress increase for both types of dislocation is given by

$$\Delta\sigma_L = \frac{Gb}{2.5L}$$

It is assumed that half the loops have noninteracting Burgers vectors and that the true loop diameters are two thirds of their measured image lengths. Calculated shear stress increases arising from the presence of loops are given in Table 4, which includes the combined effect on yield stress of both loops and voids calculated by taking the square root of the sum of the squares of the two contributions [14]. The tensile yield stress is taken as twice that in shear.

Limit of proportionality values have been measured by postirradiation tension testing at the irradiation temperatures. To minimize postirradiation annealing, straining was commenced as soon as the machine furnace returned to thermal equilibrium, about half an hour after completion of specimen loading. Measured values are compared with estimated yield stress increases in the table below.

Irradiation Temperature, deg C	Measured,		Estimated,	
	ksi	MN/m ²	ksi	MN/cm ²
420 to 440	37	255	23	160
500 to 513	17	117	19	130
520 to 533	17	117	13	90

The discrepancy between estimated and measured values at 420 to 440 C may arise because the treatment of Fleischer oversimplifies the hardening mechanism. It is possible that dislocation loops are thrown round obstacles at this temperature, in the manner suggested by Orowan, while at higher

temperatures glissile dislocations are cutting obstacles. Experiments are in hand to examine this point. Apparently, relatively little hardening arises from the presence of the carbide precipitate observed after irradiation at 520 to 533 C.

Summary

1. The upper temperature limit for void formation in solution treated AISI Type 316 steel irradiated in this experiment is close to 560 to 570 C, which is in good agreement with the theoretical predictions of Bullough and Perrin.

2. The volume increase due to voidage is a maximum after irradiation at 500 to 513 C.

3. Interstitial dislocation loops are present after irradiation at temperatures up to 560 to 570 C. Their disappearance from the structure coincides with the disappearance of the voids. Loop unfaulting and growth is noted at 520 to 533 C and 560 to 570 C.

4. Precipitation, presumably of $M_{23}C_6$, is observed after irradiation at 520 to 533 C and higher temperatures.

5. Increased yield stresses in uniaxial tension calculated from loop and void concentrations are in fair agreement with measured values.

References

- [1] Cawthorne, C. and Fulton, E. J., *Nature*, NATUA, Vol. 216, 1967, p. 575.
- [2] Bullough, R., Eyre, B. L., and Perrin, R. C., AERE-R 6284, Atomic Energy Research Establishment, Harwell, 1969.
- [3] Mastel, B. and Brimhall, J. L., *Journal of Nuclear Materials*, JNUMA, Vol. 18, 1968, p. 115.
- [4] Holmes, J. J., *Transactions*, American Nuclear Society, TANSAS, Vol. 12, 1969, p. 114.
- [5] Bullough, R. and Perrin, R. C., to be published in Proceedings of the Symposium on Radiation Damage in Reactor Materials, Vienna, 1969.
- [6] Li, Che-Yu and Harkness, S. D., to be published in Proceedings of the Symposium on Radiation Damage in Reactor Materials, Vienna, 1969.
- [7] Pounder, J. O. et al, Paper 4/5, International Conference on Fast Reactor Irradiation Testing, Thurso, Scotland, 1969.
- [8] Kinchin, G. H. and Pease, R. S., *Reports on Progress in Physics*, RPPHA, Vol. 18, 1955, p. 1.
- [9] Holmes, J. J., Robbins, R. E., Brimhall, J. L., and Mastel, B., *Acta Metallurgica*, AMETA, Vol. 16, 1968, p. 955.
- [10] Coulomb, P., *Acta Metallurgica*, AMETA, Vol. 7, 1959, p. 556.
- [11] Westmacott, K. H., *Philosophical Magazine*, PHMAA, Series B, Vol. 14, 1966, p. 239.
- [12] Kroupa, F. and Hirsch, P. R. B., *Discussions of the Faraday Society*, DFSA, Vol. 38, 1964, p. 49.
- [13] Fleischer, R. L., *Acta Metallurgica*, AMETA, Vol. 10, 1962a, p. 835.
- [14] Kopenaal, T. J. and Kuhlmann-Wilsdorf, D., *Applied Phys. Letters*, APPLA, Vol. 4, 1964, p. 59.
- [15] Woolman, J. and Mottram, R. A., *Properties of the EN Steels*, Vol. III, Pergamon Press, Oxford, 1969.

W. N. McElroy¹ and R. E. Dahl, Jr.¹

Neutron Dosimetry for Fast Reactor Applications*

REFERENCE: McElroy, W. N. and Dahl, R. E., Jr., "Neutron Dosimetry for Fast Reactor Applications," *Irradiation Effects on Structural Alloys for Nuclear Reactor Applications, ASTM STP 484*, American Society for Testing and Materials, 1970, pp. 375-399.

ABSTRACT: The status of fast reactor dosimetry is reviewed in terms of the results of recent studies in fast test reactors. Fast reactor dosimetry must provide proper spectral, flux, and fluence information for material and fuel irradiation effects programs and surveillance studies. In this review consideration is given to (1) monitor materials in current use and information needed in the data reduction of reaction product measurements to neutron interaction rates, (2) neutron flux-spectral definition from multiple foil interaction rates and comparison with results based on other methods of analysis, and (3) application of the flux-spectral data to determination of flux levels and fluences. These dosimetry techniques are applied to determine flux spectra and fluence for material irradiation programs. Such information is needed in the determination of damage functions, which relate the damage producing effectiveness of neutrons to their energy. These damage functions permit correlation of irradiation effects data in different thermal and fast reactor irradiation facilities and therefore provide a basis for setting dosimetry accuracy requirements.

KEY WORDS: radiation effects, radiation damage, neutron irradiation, dosimetry, neutron flux, particle fluence, spectral determination fast reactors (nuclear), thermal reactors, fission, monitors, computers, tests, evaluation

The technology associated with fast reactor dosimetry for materials irradiation studies has progressed significantly within the last three years. This is largely a result of research and development programs established by the Fuels and Materials Branch of the Reactor Development and Technology Division of the United States Atomic Energy Commission.

¹ Research associates, Metallurgy and Ceramics Department, Pacific Northwest Laboratory, operated by Battelle Memorial Institute for the United States Atomic Energy Commission, Richland, Wash. 99352.

* This paper is based on work performed under United States Atomic Energy Commission Contract AT(45-1)-1830.

As a result of such programs, dosimetry requirements for most fuels and materials experiments can now be met.

In this paper the status of fast reactor dosimetry, reviewed earlier [1],² is updated in terms of the results of recent studies in fast reactors, in particular the experimental breeder reactor II (EBR-II) [2-13], and the requirements of damage analysis techniques for materials irradiation experiments. Problems are encountered in the subsequent application and correlation of data to other test and liquid metal fast breeder reactor (LMFBR) environments. To cope with these problems dosimetry must provide for the acquisition of proper spectral, flux, and fluence information for material and fuel irradiation effects programs and surveillance studies.

This information is needed in such applications as the generation of semiempirical damage functions from reactor test data [14-17]. These damage functions, which are experimental modifications of theoretical forms, are used in assessing radiation conditions in design studies of LMFBR's. In developing damage functions it became clear that the total neutron fluence and the corresponding integral flux energy spectrum for all neutrons must be defined to an accuracy (approximately within 10 to 30 percent) consistent with expected uncertainties in neutron induced material property change data.

For proper dosimetry a combination of fission and nonfission flux/fluence monitors are used for materials irradiation in fast and thermal test reactors. These monitors are sensitive to all neutron energy ranges, but their number can be varied depending on the accuracy required in the irradiation experiments. The basic reference data and information needed for converting from measured activities to reaction rates (saturated monitor activities) to flux/fluence values have been compiled for these monitors. EBR-II flux/fluence results from these monitors are used to generate damage functions for a specified material property change. The damage functions then permit the subsequent engineering application of correlated irradiation effects data.

Dosimetry

Monitor Selection and Reference Data

Monitor reactions are generated by neutrons in different energy ranges. Better accuracy in integral flux and fluence determinations can be achieved by the use of monitors that are sensitive to the energy regions comprising the major portion of the spectrum. While this is the primary criterion, selection of a set of monitors must also be based on the following additional criteria.

1. The monitor materials must have melting points above the temperatures anticipated for the environment (up to 1000 to 1500 F) and be en-

² *Italic numbers in brackets refer to the list of references at the end of this paper.*

capsulated suitably to prevent cross contamination or loss of reaction products or both.

2. The half-life of a product isotope must be long enough to allow ample time for removal from the reactor and counting.

3. The activation cross sections for the materials (and fission yields for fission foils) must be well defined.

4. High-purity materials must be used to reduce analytical problems caused by the interference from activation of contaminants. Flux perturbation and self-shielding effects that could affect the accuracy of dosimetry must be eliminated through proper selection of the mass and geometry of monitors (for example, foil thickness).

An optimum set of ten monitor materials (up to 14 reactions) has been selected for future fast reactor irradiations based on experience gained in previous EBR-II dosimetry tests [2, 4-7] using the stated criteria. For this set Table 1 lists the reactions, product isotopes, and suggested half-lives, fission yields, and target abundances that have been found to give consistent results in fast and thermal reactor irradiations [6, 7, 18, 19]. Because of its wide use, the $^{58}\text{Ni}(n, p)^{58}\text{Co}$ reaction, which duplicates the $^{54}\text{Fe}(n, p)^{54}\text{Mn}$ reaction in energy response, is also given. For the fission foils, the abundances were selected so that a bare foil thermal reactor irradiation (with approximately equal thermal and fast components) would not require more than ~ 10 percent reaction rate correction for the impurity isotopes. Values of fission yields for ^{238}Pu and ^{237}Np are still required and will be determined in comparative interlaboratory irradiations in different fast reactor environments.

For the longer half-life products ($t_{1/2}$ greater than ~ 1 month), which can be measured after most irradiations and decay periods, the energy response ranges of neutrons that produce 90 percent of the product isotope activity at an EBR-II central core position are indicated by the bars in Fig. 1. That all of the spectrum is covered is evident from the overlapping of the bars. The response of these same monitors is shown in Fig. 2 for the fast test reactor (FTR) driver fuel spectrum, which is more typical of an LMFBR core. In this case the energy dependence of each monitor's response is shown. Note that the $^{45}\text{Sc}(n, \gamma)^{46}\text{Sc}$ reaction has a broad and much desired $1/v$ type response as compared with the other n, γ reactions—a difference the bars in Fig. 1 do not show.³ Further, since the cross section $\sigma(E)$ times the differential flux $\phi(E)$ response is plotted versus lethargy in Fig. 2 (only the corresponding neutron energies are shown on the abscissa), the relative distribution of the area under each curve indicates the relative fractional energy response of each monitor. Thus, except for

³ The $^{45}\text{Sc}(n, \gamma)$ response is very similar in shape to that of the $^6\text{Li}(n, \alpha)$ or $^{10}\text{B}(n, \alpha)$ reactions, which have no significant major resonances; and this makes the ^{45}Sc an excellent broad spectrum detector.

TABLE 1—Monitor reactions and associated parameters.

Fission Reaction	Half-Life of Products [7] ^a			Fission Yields, ^b % [7, 20, 21]			Required Target Isotope Abundance, ^c %		
	⁹⁹ Mo	¹⁴⁰ Ba	¹³⁷ Cs	¹⁴⁸ Nd	¹⁴⁰ Ba	¹³⁷ Cs		¹⁴⁸ Nd	
²³⁹ Pu (n, f) F.P.	66.7 h	12.8 d	30.1 y	Stable	5.9	5.1	6.5	1.71	≥99.0
²³⁵ U (n, f) F.P.					6.1	6.1	6.2	1.75	≥93.0
²³⁷ Np (n, f) F.P.	5.8	6.4	...	≥99.98
²³⁸ U (n, f) F.P.					6.3	6.0	6.3	1.93	≥99.995
²³⁹ Pu (n, f) F.P.	≥99.8
Nonfission Reaction									
			Half-Life of Products			Fission Yields			Target Isotope Abundance, %
⁴⁶ Sc (n, γ) ⁴⁶ Sc.			84.0 d			...			100.0
⁵⁹ Co (n, γ) ⁵⁹ Co.			5.268 y			...			100.0
⁵⁸ Fe (n, γ) ⁵⁸ Fe.			44.5 d			...			0.33
⁵⁴ Fe (n, p) ⁵⁴ Mn.			313.5 d			...			5.84
⁶² Cu (n, γ) ⁶² Cu.			12.84 h			...			69.09
⁶⁵ Cu (n, α) ⁶⁰ Co.			5.268 y			...			69.09
⁵⁸ Ni (n, p) ⁵⁸ Co.			71.3 d			...			67.88
⁴⁶ Ti (n, p) ⁴⁶ Sc.			84.0 d			...			7.99
⁴⁷ Ti (n, p) ⁴⁷ Sc.			3.43 d			...			7.32
⁴⁹ Ti (n, p) ⁴⁸ Sc.			44.0 h			...			73.99

^a h = hours, d = days, y = years.
^b The uncertainty associated with these values of fission yield are estimated to be about 5 to 10 percent (1 standard error) depending on the isotope. Additional yield information for some of these reaction products will be available in the near future from program work now in progress at Argonne National Laboratory and Idaho Nuclear Corp.
^c Except for the ²³⁹Pu, fission foils meeting these requirements are available through the Isotope Target Center, Oak Ridge National Laboratory [22].

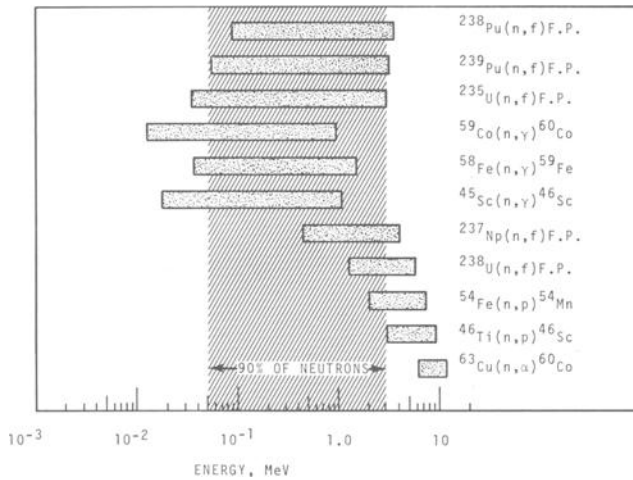


FIG. 1—Ninety percent response range for 2DB calculated spectrum—EBR-II core ($r=5.2$ cm, $z=0.0$).

$^{58}\text{Fe}(n, \gamma)$ and $^{59}\text{Co}(n, \gamma)$, this set of monitors provides a well spaced step function type of response down to energies of $\sim 10^{-3}$ MeV. Below this the $^{58}\text{Fe}(n, \gamma)$ and $^{59}\text{Co}(n, \gamma)$ reactions provide both broad spectrum- and resonance-type coverage down to $\sim 10^{-4}$ MeV. Consequently, for most fast reactor spectra, these monitors should provide an independent and reliable empirical definition of integral flux spectra and fluence.

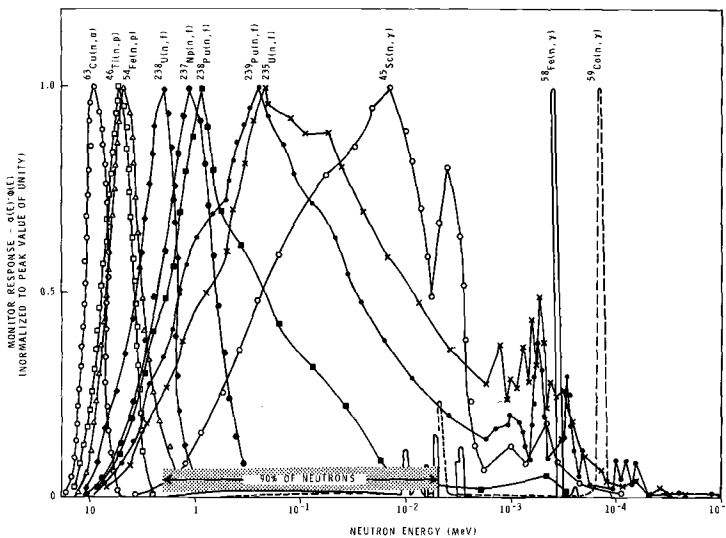


FIG. 2—Monitor response in the FTR driver spectrum.

Depending on how well the spectrum has been defined by reactor physics calculations, and the needs and economics of a particular materials experiment, fewer monitors may be used; as a minimum, perhaps Fe, ^{237}Np , and ^{235}U . If the production of helium from n, α reactions is considered important in a materials experiment, then the $^{63}\text{Cu}(n, \alpha)$ reaction should also be included. Use of single monitors such as Fe or Ni will generally not suffice unless the spectrum is already well defined [6].

The radioactive counting of foils and conversion from measured activity to reaction rates (saturated activities) is not discussed in this report. Kellogg and Zimmer have discussed this aspect for an EBR-II dosimetry test, and their results indicate an estimated accuracy of approximately ± 7 percent (1 standard deviation) or better for most measurements of a single-foil reaction rate in EBR-II [5, 7]. Repeated measurements for a single reaction give estimated accuracies as low as ± 1 to 2 percent (1 standard error). These results are consistent with previous experience gained in other fast and thermal test reactors [18, 19, 23-25].

High-purity vanadium (<10 ppm of impurities) is now being used for the encapsulation of fission and other foils that might be adversely affected by the extreme environmental conditions in fast reactors. Milligram and lesser quantities of fission and nonfission foils are sealed by welding in 50-mil-outside diameter by 30-mil-inside diameter by $\frac{1}{8}$ -in.-long vanadium capsules.⁴ The vanadium permits the direct counting of these foils with a minimum of interference. The encapsulation of fission and other foils in stainless steel and assembly of a typical foil set for a short irradiation in EBR-II are described in Ref 6.

An optimum foil set has been selected for fast reactor dosimetry, but experimental requirements and economic considerations may dictate use of a smaller set. To achieve a proper balance between dosimetry requirements and costs, all factors must be carefully considered in relation to the intended needs and anticipated use of irradiation effects data obtained from materials irradiation experiments. This balance has not, in general, been achieved in the past.

Monitor Cross Sections

Determination of flux and fluence from the measured reaction rates of the eleven monitors requires the use of a consistent set of evaluated energy-dependent cross sections, $\sigma(E)$. Reported indications [19, 26, 27] of inconsistencies in energy-dependent cross sections motivated the revision of the SAND-II reference cross section library [28], which is used to translate reaction rates to flux and fluence with the SAND-II code [18, 29].

⁴ These encapsulated foils can be obtained from the Isotope Target Center, Oak Ridge National Laboratory [22].

Twelve cross section revisions (or additions) came from literature review and eleven more were readjusted by an iterative unfolding procedure [30]. Five reference spectra were used together with three reference fission and one reference activation reaction to readjust the cross sections by the unfolding technique. (The five spectra were the FISSION [19, 27], APFA-III-Godiva [19], EBR-II core center [6], and ECEL Cores 14 and 16 [18]. The four reference reactions were $^{235}\text{U}(n, f)$, $^{238}\text{U}(n, f)$, $^{237}\text{Np}(n, f)$, and $^{27}\text{Al}(n, \alpha)$.) Results of the unfolding for the $^{54}\text{Fe}(n, p)$ ^{54}Mn reaction, which has been of prime interest in fast reactor dosimetry, are presented in Ref 6. Additional results for this and the 22 remaining reactions are given in Ref 28.

The basic requirement placed on the acceptance of the current SAND-II $\sigma(E)$'s was that calculated values of thermal averaged cross sections, resonance integrals, and fission averaged cross sections (Table 2) should agree with measured values.⁵ While most calculated and measured values agree well within 10 percent, not all agree within this range because of limitations in experimental data. For example, for the threshold reactions, a single form of the fission spectrum has not been defined that is consistent with photo plate/time-of-flight and multiple-foil measurements. In presenting the status of fast reactor dosimetry, therefore, this problem cannot be ignored. The degree of this inconsistency, as indicated in Table 2, is

TABLE 2—Monitor reaction cross section data (barns).

Reaction	Thermal Averaged ^a	Resonance Integral ^a	Fission Averaged ^a		Ratio (SAND-II/Watt)
			Watt Form	SAND-II Form	
$^{238}\text{Pu}(n, f)\text{F.P.}$	14.6	19.5	2.50	2.56	1.02
$^{239}\text{Pu}(n, f)\text{F.P.}$	757	345	1.76	1.77	1.01
$^{235}\text{U}(n, f)\text{F.P.}$	563	290	1.23	1.22	0.99
$^{237}\text{Np}(n, f)\text{F.P.}$	0.0187	6.12	1.29	1.34	1.04
$^{238}\text{U}(n, f)\text{F.P.}$	0.287	0.314	1.09
$^{45}\text{Sc}(n, \gamma)^{46}\text{Sc}$	25.3	10.1	0.00624	0.00565	0.91
$^{59}\text{Co}(n, \gamma)^{60}\text{Co}$	37.1	70.0	0.00532	0.00473	0.89
$^{58}\text{Fe}(n, \gamma)^{59}\text{Fe}$	1.19	1.38	0.00286	0.00267	0.93
$^{54}\text{Fe}(n, p)^{54}\text{Mn}$	0.0763	0.0874	1.15
$^{63}\text{Cu}(n, \gamma)^{64}\text{Cu}$	4.53	4.64	0.0109	0.0103	0.95
$^{65}\text{Cu}(n, \alpha)^{60}\text{Co}$	0.000356	0.000384	1.08
$^{58}\text{Ni}(n, p)^{58}\text{Co}$	0.102	0.117	1.15
$^{46}\text{Ti}(n, p)^{46}\text{Sc}$	0.0113	0.0130	1.15
$^{47}\text{Ti}(n, p)^{47}\text{Sc}$	0.0172	0.0195	1.13
$^{48}\text{Ti}(n, p)^{48}\text{Sc}$	0.000236	0.000260	1.10

^a Calculated values, see Appendix.

⁵ These quantities are defined in the Appendix, and suggested measured values are given in Refs 28 and 31.

seen to be larger than 10 percent by considering the ratio of the fission averaged cross sections based on multiple foils (SAND-II form) and on photo plate/time-of-flight (Watt form) measurements.⁶ The Watt and SAND-II forms of the fission spectrum are compared in Table 4 in the Appendix.

It is concluded that on an integral averaged basis, the current measured and calculated detector cross sections are accurate to within ± 10 percent (1σ).⁷

Flux-Spectral Determination

In developing damage functions and in correlating irradiation effects data for the LMFBR program, it is necessary to define the neutron spectrum and total values of integral flux and fluence to an accuracy such that their contribution to the total error is not larger than the contribution from the measurement of irradiation induced property changes. In terms of total values of integral flux and fluence, the current accuracy requirement is between 10 and 30 percent.

Prior to the EBR-II Run 31F dosimetry test [6], this accuracy was not being achieved. As an example, for in-core irradiations the high-power flux measured with iron and nickel was ~ 60 percent of the flux value based on reactor physics, power level, and burnup analyses. This discrepancy was reduced to within 10 and 15 percent as a result of interlaboratory cooperative studies of multiple- and single-foil response in EBR-II and other fast reactor spectra as well as the fission spectrum.

The most important results of these latter studies were (1) the change of energy-dependent cross sections of nonfission reactions to produce consistency with fission reactions [28], (2) the selection of a consistent set of fission yields for the fission reactions [7, 19, 21], (3) the realization that iron- and nickel-measured fluxes and fluences based on the new cross sections were still subject to large uncertainties in fast reactors because of local flux perturbations between fuel and structural subassemblies [6, 11, 12], and (4) experimental verification that reactor physics calculations intended to describe core conditions cannot be used for out-of-core and boundary regions [6].

The results of analytical studies illustrate the variety of spectra encountered in the cores of reactors. Figure 3 includes lethargy plots of the spectrum at the core center of the FTR, ETR, and EBR-II. As is evident, there is substantial difference between thermal and fast reactors. In addition, the figure includes the fission spectrum to illustrate the modification

⁶ If the Cranberg instead of the Watt form had been used, the differences would be even larger [19, 27].

⁷ Requests for additional energy-dependent cross section measurements for a number of reactions of interest for fast reactor dosimetry are listed in the current WASH document [32].

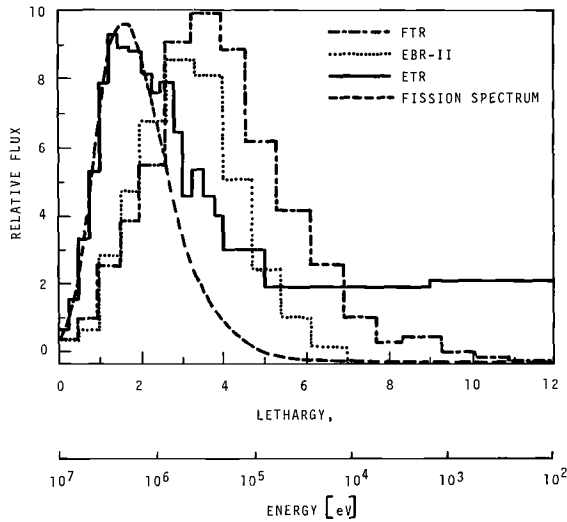


FIG. 3—Comparison of core spectra in *FTR*, *ETR*, and *EBR-II* to the Watt fission spectrum.

which occurs even in the core of a fast reactor. Both the shape and the position of the maximum of the distribution change from one reactor to another. Substantial spectrum changes are encountered even in a single reactor. In thermal reactors the spectrum becomes more moderated by water away from the core. Spectral changes of a different nature are just as pronounced in a fast reactor.

Among the experimental methods, the multiple-foil activation method lends itself to the determination of spectra in operating high-power reactors [6]. In this method a set of activation monitors of varying energy response are irradiated. The activities are considered as coefficients of the functional expansion of the spectrum in terms of the response curves. The mathematical problem is that of unfolding the spectrum from the coefficients.

The SAND-II computer code, one of several available, performs that unfolding [29, 33-35]. The code accepts as input the activities and a trial solution for the spectrum. While the trial solution may be a calculated spectrum, it may even be a constant. The code then uses the energy-dependent activation cross sections and the trial spectrum to calculate the expected activations for the materials comprising the monitor set. These numbers are compared with the actual activations and the spectrum is readjusted by an iterative process. When the calculated and experimental activities agree within specified limits, the process ends and yields the solution spectrum.

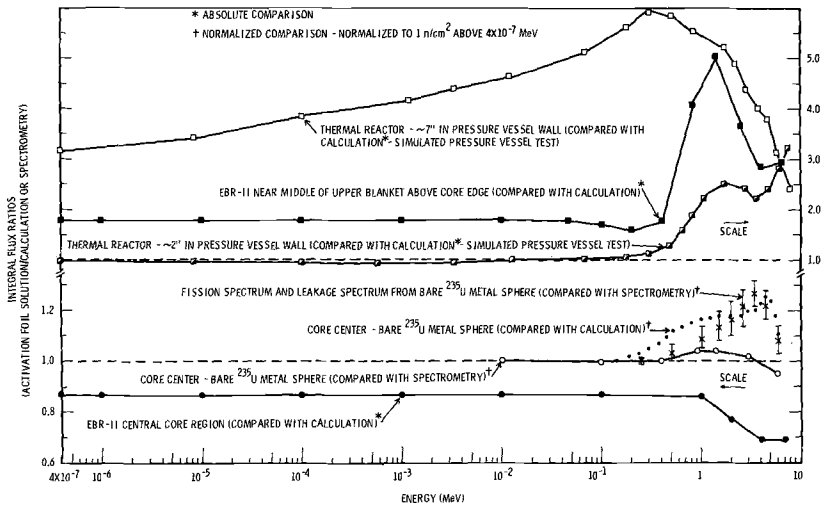


FIG. 4—Activation foil versus calculation and spectrometry integral flux comparison.

Experiments have been performed to compare this method with spectrometer measurements and analytical methods [6, 18, 19, 26, 27]. The comparison of differential flux results is considered elsewhere [1, 18, 27]; here the results of comparing the energy-dependent integral fluxes (integrals of the area under the differential flux curves, such as those shown in Fig. 3) for a number of spectra will be considered.

In Fig. 4, taken from Ref 36, the results of multiple-foil measurements (based on the use of up to 15 to 20 foil reactions) are compared with reactor physics calculations or T-O-F and proton recoil measurements or both for five fast and two thermal reactor spectra, as well as for the fission spectrum. Values of integral flux versus neutron energy from multiple-foil activation measurements are compared with similar results from other methods of analysis. The degree of disagreement at any energy between the results is indicated by the value of the ratio—a ratio of unity indicating exact agreement for the integral flux above that energy.

The results presented in Fig. 4 and Refs 6, 18, 19, 26, and 27 indicate, with current technology and for the energy range from 10^{-10} to 18 MeV, that

1. The foil activation method is capable of yielding integral flux values as a function of neutron energy that are accurate to within about 10 to 30 percent, depending on the number of foils used and their energy response ranges.

2. The foil activation method provides more accurate results than reactor physics calculations, which may be uncertain by large factors (about 2 to 6 for the spectra shown in Fig. 4) at out-of-core positions. This is to

be expected, since the reactor physics calculations were not designed to give accurate results at such positions.

3. For the fission spectrum and the bare ²³⁵U sphere leakage spectrum, differences of up to ~30 percent exist between the results of the three methods of analysis. For instance, for the bare U²³⁵ sphere core center position, the multiple-foil and T-O-F results (circles) agree within ~5 percent, but both disagree with calculations (dots) by up to ~25 percent at 4 to 5 MeV.

The reason or reasons for the up to ~30 percent differences for the fission and bare ²³⁵U sphere spectra must be found if further improvements in the accuracy of activation foil spectrometry (and other methods) are to be achieved.

Fluence Determination

The spectrum defined either analytically or experimentally and the energy-dependent activation cross section are used to define the effective cross section for individual flux/fluence monitor materials. The effective cross section is defined empirically by the formula

$$\bar{\sigma}_{\text{eff}}(E_L) = A/\Phi(E_L) \dots \dots \dots (1)$$

or calculated by the formula

$$\bar{\sigma}_{\text{eff}}(E_L) = \int_0^\infty \sigma(E)\phi(E) dE / \int_{E_L}^\infty \phi(E) dE \dots \dots \dots (2)$$

where

- A = a measured reaction rate (saturated activity),
- Φ(E_L) = a measured value of integral flux,
- σ(E) = the energy-dependent activation cross section,
- φ(E) = the differential flux distribution, and
- E_L = the lower limit for the reported flux.

The effective cross section will change with the spectrum, as indicated previously [1]. Hence, an effective cross section value must be defined not only for different reactors but also for different reactor positions. Further, it has been determined that calculated values, Eq 2, are subject to considerably more error than measured values, Eq 1 [6].

Having defined a value of σ_{eff}(E_L), the fluence is determined by obtaining a suitable approximate solution to an activation integral equation of the form [29]

$$n = \left\{ m_0 \exp \left[-\lambda_n t - \int_0^t \bar{\sigma}_n(t') \Phi(t') dt' \right] \right\} \\ \times \left\{ \int_0^t \bar{\sigma}_{\text{eff}}(t') \Phi(t') \times \exp \left[\lambda_n t' + \int_0^{t'} \{ \bar{\sigma}_n(t'') - \bar{\sigma}_m(t'') \} \Phi(t'') dt'' \right] dt' \right\} \dots (3)$$

where

- n = the number of reaction product atoms at time t ,
- m_0 = the initial number of target atoms,
- λ_n = the reaction product atom decay constant,
- $\bar{\sigma}_{\text{eff}}(t)$ = the effective cross section at time t ,
- $\bar{\sigma}_n(t)$ = the effective cross section for the burnout of product atoms n at time t ,
- $\bar{\sigma}_m(t)$ = the effective cross section for the burnout of target atoms m_0 at time t , and

$$\Phi(E_L) \times t \equiv \int_0^t \Phi(t) dt \dots \dots \dots (4)$$

is the required value of fluence.⁸

Most EBR-II irradiations have not exceeded fluences of $\sim 5 \times 10^{22}$ n/cm² and burnout of target atoms has not been a problem. Values of $\bar{\sigma}_m(t)$ and $\bar{\sigma}_n(t)$ are generally less than $\sim 2 \times 10^{-24}$ cm² for the EBR-II central core region for most monitor materials. Therefore, values of the target and product atom burnout integrals

$$\int_0^t \bar{\sigma}_m(t') \Phi(t') dt' \quad \text{and} \quad \int_0^t \bar{\sigma}_n(t') \Phi(t') dt'$$

in Eq 3 have generally been less than 0.1 at the end of exposure for past EBR-II irradiations. A value of 0.1 is approximately equivalent to a 10 percent burnout of target atoms.

In the future, however, fluences of 10^{23} n/cm² or greater will be encountered in EBR-II and in FTR. These higher fluences, coupled with larger values of $\bar{\sigma}_m(t)$ and $\bar{\sigma}_n(t)$ for FTR because of the softer LMFBR-type spectra, will make these burnout corrections more significant. Thus, approximate solutions for equations such as 3 will have to be provided and must include burnout corrections for individual flux/fluence monitors to maintain the accuracy requirements of about 10 to 30 percent.⁹

For present EBR-II dosimetry, burnout of target and product atoms can be neglected and it is assumed that $\phi(E)$ does not change significantly. Equation 3 then reduces to the form

$$n = \bar{\sigma}_{\text{eff}}(E_L) m_0 e^{-\lambda_n t} \int_0^t \Phi(t') e^{\lambda_n t'} dt' \dots \dots \dots (5)$$

Assuming that $\Phi(t')$ is constant over each day of operation and that the

⁸ The argument E_L , Eq 1, has been dropped in the integrals of Eqs 3 and 4 as a matter of convenience. Inclusion of a time dependence for $\bar{\sigma}_{\text{eff}}$ accounts for changes in the spectrum $\phi(E)$ during irradiation, which may be significant for some high-flux test reactor irradiations.

⁹ For fission foils, both burnout and burnin of reaction products must be considered.

core configuration is reasonably constant, Eq 5 has been approximated by a summation of one-day constant flux (or power level) runs. The relative flux or power level for each day, which is obtained from EBR-II operations, together with measured values of n and $\bar{\sigma}_{eff}(E_L)$ are used to obtain flux and fluence values using the equations

$$\Phi(E_L) = n\lambda_n e^{\lambda_n t} \left/ \left[\bar{\sigma}_{eff}(E_L) \times \sum_{i=1}^q P_i (e^{\lambda_n t_{i+1}} - e^{\lambda_n t_i}) \right] \right. \dots \dots \dots (6)$$

and

$$\Phi(E_L) \times t = \Phi(E_L) \sum_{i=1}^q P_i (t_{i+1} - t_i) \dots \dots \dots (7)$$

where

- t = the total time of irradiation, including shutdowns;
- t_i and t_{i+1} = the total times of irradiation, including shutdowns, through the i th and i th+1 days of irradiation;
- P_i = the relative reactor power level for the i th day of irradiation or shutdown;
- q = the total number of days of irradiation; and
- $\Phi(E_L)$ = the maximum flux level achieved during any of the q days of operation.

A computer program, TIMH [37], has been written to perform the computations represented by Eqs 6 and 7.¹⁰ This program contains the necessary values of P_i (dating back to the startup of EBR-II) and requires as input only the calendar dates of the insertion and removal of a monitor material and the values of the time of removal activity ($n\lambda_n$) and $\bar{\sigma}_{eff}(E_L)$ to obtain flux and fluence values. For fission foils, $n\lambda_n$ must be divided by the fission yield before insertion into the program.

If the reaction product has a very long half-life (¹³⁷Cs for fission foils) or is stable (¹⁴⁸Nd for fission foils and helium for n, α reactions), and again burnout of target and product atoms and changes in $\phi(E)$ can be neglected, Eq 3 reduces to the simple form

$$n = m_0 \bar{\sigma}_{eff}(E_L) \int_0^t \Phi(t') dt' \dots \dots \dots (8)$$

In this case the fluence is obtained directly from the relationship

$$\Phi(E_L) \times t = \int_0^t \Phi(t') dt' = n/m_0 \bar{\sigma}_{eff}(E_L) \dots \dots \dots (9)$$

¹⁰ A similar computer program (EBR-II history program) has been prepared by the EBR-II Project, Argonne, Ill. [66].

TABLE 3—Spectral averaged cross sections of materials irradiated in EBR-II row 4 center.

Reaction	Helium Concentration and Estimated 2σ Standard Deviation, atom fraction	Measured Values of $\bar{\sigma}_{\text{eff}}(E_L)$, ^a mbarn ($E_L = 10^{-10}$ MeV)
B (n, α)	$220 \pm 10 \times 10^{-6}$	171
Ti (n, α)	<0.077	<0.060
Cr (n, α)	0.10 ± 0.03	0.076
Mn (n, α)	0.11 ± 0.01	0.085
Fe (n, α)	0.100 ± 0.004^b	0.077
Ni (n, α)	1.35 ± 0.06^b	1.05
N (n, α)		23 ^c
304 SS (n, α) ^d	0.32 ± 0.01	0.25

^a Calculated from column 2 using Eq 8 and

$$\int_0^t \Phi(t') dt' = 1.29 \times 10^{21} \text{ n/cm}^2.$$

An estimated 10 percent (1σ) absolute uncertainty is assigned to these measured cross sections, which is due mainly to the uncertainty in the absolute value of fluence.

^b The measured nitrogen content of the nickel before and the iron after the irradiation in EBR-II were <14 ppma and ~22 ppma, respectively; consequently, nitrogen appears to contribute less than 0.001 ppma to the total helium content of these iron and nickel specimens.

^c Calculated value, using Eq 2 [40].

^d The atom fractions of the main constituents of the 304 stainless steel specimen were Fe 0.72, Cr 0.20, Ni 0.085, B 2.6×10^{-6} , and N 5.5×10^{-3} .

independent of the time variation of the flux $\Phi(t)$. For fission foils n must be divided by the fission yield.

Thus, using Eqs 6 and 7, the shorter half-life reaction products give a measurement of the flux level and fluence only if the time history of irradiation is known. For very long or stable products, however, Eq 9 provides a direct measurement of fluence.

Values of $\bar{\sigma}_{\text{eff}}(E_L)$ for most of the monitor reactions listed in Table 1 for EBR-II in- and out-of-core positions for reactor run 31F are available from the Fast Reactor Materials Dosimetry Center.¹¹ Values for n, α reactions for a number of materials, including stainless steel, for EBR-II central core-positions have been reported [38-40] and selected values taken from Ref 40 are presented in Table 3. The measurement of the amount of stable helium reaction product is obtained by using a high-sensitivity gas mass spectrometer system designed and calibrated for this purpose by Farrar and Knox [41, 42]. Helium levels as low as 10^{-10} atom fraction can be measured in specimens no larger than 10 mg. Assuming no significant loss of helium by diffusion,¹² the helium content of an irradiated

¹¹ At WADCO Corp., Richland, Wash.

¹² Available experimental results support this assumption [40].

piece of stainless steel, iron, nickel, or chromium could be used to obtain an approximate value of fluence. If the nitrogen content (or certain other impurities with high n, α cross sections) of any of these materials is very high, however, a correction may be required. The measured approximate 5.5×10^{-3} atom fraction of nitrogen is estimated to have caused an increase of up to ~ 38 percent in the total helium content and the value of $\bar{\sigma}_{\text{eff}}(E_L)$ for the stainless steel specimen, see Table 3, irradiated in run 31F.

Damage Analysis

Damage¹³ is caused by complex interaction of the thermal, nuclear environment, the state of stress during irradiation, and the initial state of the material. These are defined as follows: the *thermal* conditions of interest are the temperature and temperature gradients within the material; the *nuclear environment* is the flux and spectra of neutrons bombarding the material and the fluence (which is simply the flux integrated over the time of irradiation); and the parameters which define the *initial state of the material* include the concentration and type of impurities, grain size distribution, and dislocation density.

An apparent axiom of irradiation testing is that the nuclear environment in one reactor or irradiation facility is not duplicated in another because of variations between designs and modes of operation. Thus, detailed analyses must be performed to relate and compare effects observed in one test to those observed in another and to use all available test data in the design of reactors. Such analyses must include consideration of all of the variables described in the preceding paragraph. An accurate determination of the nuclear environment and a clear definition of its effects upon property changes of interest is required. Damage analyses consist primarily of determining a function that describes the relative effectiveness of neutrons producing damage as a function of their energy. Two types of approaches have been used to derive these functions. These are the analytical approach, based on theoretical physics considerations [1, 43–55], and the experimental or empirical approach, which utilizes radiation effects results [14–17].

Analytical Approach

The theoretical or analytical approach, which has been used exclusively until quite recently, has been described [1, 50, 55], so only a brief review is appropriate here. A number of damage functions have been derived from calculations that estimate the number of displaced atoms caused by

¹³ As used here the term “damage” describes any mechanical or physical property change induced in a material by neutron irradiation. The term “damage analysis” relates to the determination of the effectiveness of neutrons in causing damage as a function of their energy.

neutrons of particular energies in various materials. The dissipation of the energy of an atom struck by a neutron—either through ionization or transfer of kinetic energy to other atoms with the formation of a displacement spike—has been calculated with varying degrees of sophistication. In most cases, the number of atom displacements as a function of neutron energy is estimated. This function, $\nu(E)$, is calculated on the basis of the physics of atomic interactions. From this function the total displacement production rate N_d is calculated by the equation

$$N_d \equiv N \int_0^\infty \sigma_s(E) \nu(E) \phi(E) dE \dots \dots \dots (10)$$

where

- N = the nuclear density of the matrix atoms,
- $\sigma_s(E)$ = the neutron scattering cross section of these atoms, and
- $\phi(E)$ = the differential flux.

The product $\sigma_s(E)\nu(E)$ represents an energy-dependent damage cross section [51–55]. Jenkins [56] has recently developed a computerized method for calculating this damage cross section using a Kinchin and Pease secondary displacement model and ENDF/B data file. The function $\nu(E)$ gives an estimate of the number of displacements caused by secondary collisions (that is, atom-atom) during the formation of a spike. The mechanism is simply the transfer of kinetic energy through hard sphere, or Rutherford, collisions. Effects such as stability of defects and nucleation of complexes have not been included in the damage cross sections but have been studied by Doran [57] and Beeler [46–48].

The damage function (or cross section) which is developed from theoretical considerations is, then,

$$G(E) \equiv \sigma_s(E) \nu(E) \dots \dots \dots (11)$$

These functions have been used to correlate irradiation effects data in a variety of neutron spectra [51–55], and they provide a good reference for assessing “what is physically reasonable”; however, there are fundamental limitations that must be recognized in the use of damage functions based only on theory to develop engineering design criteria. These are

1. For a specified material the $\nu(E)$ functions are based upon only one mechanism (the transfer of kinetic energy of a neutron to lattice atoms in a perfect crystal). Yet other nuclear processes such as transmutations and gas formation [50, 58–61] can affect the physical and mechanical properties of metals. For a model which is based upon theory alone it is virtually impossible to quantitatively relate the effects of different mechanisms with sufficient accuracy to satisfy the requirements of the materials scientist or the reactor designer.
2. The fundamental assumption has been made that damage, whatever

property change it may be, will be proportional to the number of displacements produced during the irradiation. Thus, having chosen a displacement model (Kinchin and Pease or other), only one function could be used to describe damage in a material (such as steel, carbon, zirconium) for all temperatures and at all levels of fluence. Although reasonable data correlation has been achieved in spectra which were not too dissimilar by this method, its use for obtaining reliable estimates of damage and for correlating radiation effects data from fast and thermal reactors is questionable.

3. The strictly theoretical approach to damage correlation provides no direct way for refinement or modification of the damage functions using experimental observations.

Empirical Damage Function

The correlation and engineering application of irradiation effects data can be improved if all experience, both experimental and theoretical, is used. The empirical approach for determining damage functions was developed to help satisfy this need. The empirical approach is used to derive a damage function, $G(E)$, through the solution of a set of integral equations of the form [14]

$$S_j = t \int_0^\infty G(E) \phi_j(E) dE \quad (j=1, \dots, m) \dots \dots \dots (12)$$

where the right-hand side of Eq 12 is a calculated integral property change for a specified material, irradiated for a time t in the j th neutron environment at constant temperature, and $\phi_j(E)$ is the corresponding j th neutron differential flux spectrum; the left-hand side of Eq 12 is the measured value. The SAND-II method of obtaining a solution, $G(E)$, for Eq 12 is explained in Ref 14; the unfolding procedure is essentially the same as explained in an earlier section of this paper for $\phi(E)$.

In this method the "best" theoretical damage function for a selected property change can be used as a starting point (that is, as an initial input, $G^0(E)$, where the superscript zero represents the initial index in an iterative procedure). It is then adjusted by the unfolding procedure to minimize the difference between measured and calculated fluences required to cause the same change in property in each of a number of different spectra. The $G(E)$ function so derived, now representing other damage mechanisms as well as displacements, can be used to determine the fluence required to cause this property change for any reactor spectrum of interest for design or testing purposes. Using a reactor physics group structure, Eq 12 may be rewritten in the form

$$\Phi t = S \left[\sum_{i=1}^m \Phi_i G_i \right]^{-1} \dots \dots \dots (13)$$

where S is a designated property change, the subscript i refers to the neutron energy group for a particular reactor physics group representation of $\phi(E)$ and $G(E)$, and Φ_i is normalized such that

$$\sum_{i=1}^m \Phi_i = 1 \dots \dots \dots (14)$$

Spectral data Φ_i are available from multigroup reactor physics calculations or dosimetry measurements or both. The fluence, Φt , will be in absolute units, since G_i is defined in absolute units and is therefore directly applicable for reactor design and irradiation test planning.

The demands upon materials and the limitation of time and money impose the requirement that all pertinent data be used in developing materials for fast reactors. Much of the experience and data on the irradiation behavior of materials has been obtained in thermal reactors. These data can be extremely valuable and should be used in fast reactor development. However, in order to do so, the nuclear environment and the energy dependence of damage must be well defined and understood. This type of application of irradiation effects data has necessitated the measurement and consideration of the damaging effect of the total flux, that is, neutrons of all energies. As yet this is not a widely used concept, since most data correlation studies are still based on the use of a damaging "fast flux," such as the flux greater than 0.1 or 1 MeV.

Damage Analysis Applications

Semiempirical damage functions have been defined for several property changes to allow correlation and prediction of neutron induced property changes. A damage function for a 200 F increase in ductile-brittle transition temperature ($\Delta T T$) for pressure vessel steels (irradiated at temperatures <450 F) has been defined [14, 15]. It was used to calculate the range of damaging neutrons and fluence required to produce a 200 F $\Delta T T$ change in fast and thermal reactor environments. The energy bounds of neutrons responsible for 90 percent of the damage for the metal fueled EBR-II central core and out-of-core blanket regions proved to be between about 0.1 and 5 MeV and between about 0.1 and 1 MeV, respectively. The range for locations within light and heavy water-moderated thermal reactors with high thermal to fast neutron ratios was between about 10^{-8} and 5 MeV. These results indicate that lower energy neutrons (less than ~ 1 MeV) can contribute significantly to damage in ferritic steels.

The relative importance of low- and high-energy neutrons in causing damage to austenitic steels is being studied [16, 17]. A damage function, $G(E)$, for a change in yield strength to a level of $S=60$ ksi for an irradiation and test temperature of 450 C (842 F) for 304 stainless steel has been

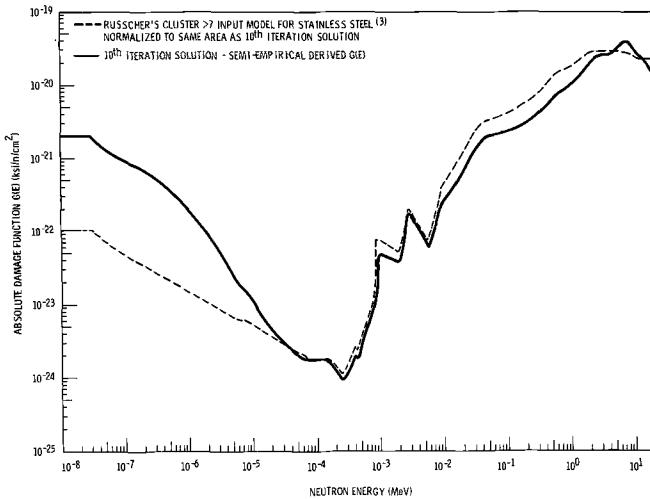


FIG. 5—Absolute damage function for a change in yield strength to 60 ksi for 304 stainless steel for a 450 C irradiation and test temperature.

generated, the solid line in Fig. 5¹⁴ [17]. In both the high- and low-energy regions the departure of its shape from that of an input model developed by Russcher [49] for stainless steel (for the production rate of clusters containing more than seven vacancies) is also shown. Damage from low-energy thermal neutrons appears to be more important than indicated by Russcher's input model. The derived damage function for a 200 F ΔTT shift for ferritic steel also showed this effect—relative to a gross defect production rate based on eight displacements per n, γ reaction in iron.

The $G(E)$ presented in Fig. 5 was used in conjunction with Eq 13 to estimate the total fluence¹⁵ required to cause a change in yield strength to the 60-ksi level for 304 stainless steel irradiated at 450 C in different reactor spectra, as well as in the fission spectrum. In Fig. 6 the energy limits of neutrons responsible for 90 percent of the change in yield strength are indicated by the ends of the bars. The spectra are listed from top to bottom in order of decreasing fluence. For instance, it takes ten times as much fluence to cause the same damage in the FTR grid plate spectrum as in the FTR driver fuel spectrum. Similarly, it takes about three times as

¹⁴ The property change data at the $S_j=60$ ksi level were obtained from the study of yield strength measurements at the 0.2 percent yield point for 304 stainless steel irradiated in EBR-II and ETR. The multiple-foil method, coupled with reactor physics calculations, provided absolute values of differential flux, $\phi_i(E)$, and fluence,

$$t \int_0^S \phi_i(E) dE,$$

for defining the $G(E)$ with Eq 12.

¹⁵ For neutrons of all energies, including thermal, intermediate, and fast.

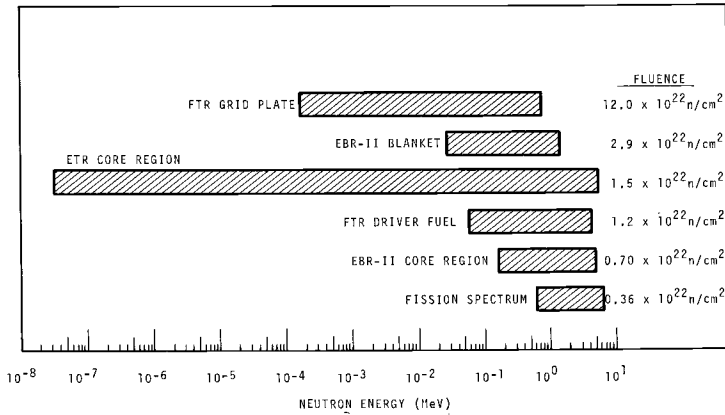


FIG. 6—Prediction of fluence and energy response necessary to produce a change in yield strength to 60 ksi for 304 stainless steel for an irradiation and test temperature of 450 C.

much exposure in the FTR driver fuel spectrum as in the fission spectrum to create the same damage.

In addition to differences in fluence, Fig. 6 shows that neutrons of different energies cause damage in different spectra. For the fast reactor cases the upper and lower energy limits for 90 percent of the damage move down in energy when going from the fission spectrum to the FTR grid plate spectrum. Whereas 90 percent of the damage results from neutrons with energies greater than 0.7 MeV in the fission spectrum, about 90 percent of the damage results from neutrons below this energy in the FTR grid plate spectrum.

The form of the semiempirically derived damage function, Fig. 5, between 10^{-8} and 10^{-2} MeV is not well established because of limitations in Russcher's input model for $G(E)$ and a lack of experimental data from irradiations that produce damage from neutrons with these energies. Nevertheless, the derived $G(E)$ does effect a correlation of all available thermal and fast reactor experimental data, reveals inconsistencies in the data, and extracts a maximum of information from test reactor data. The derived information on the damaging effectiveness of different energy neutrons also helps to provide an improved understanding of radiation damage mechanisms.

Damage functions for other property changes in austenitic steels, such as creep strain [16], have been developed. Comparisons of similarities and differences in these damage functions will help establish the validity of individual damage functions, pinpoint areas of excessive uncertainty in the experimental measured property change and flux-spectral/fluence data, and select irradiation facilities for subsequent experimental programs.

It is concluded that the correlation of irradiation effects data obtained in thermal reactors and present hard spectrum, metal fueled fast test reactor environments, and the application of such data to estimate damage in softer spectrum LMFBR's, will require careful assessment of the damaging potential of neutrons of all energies.

Conclusions

The current status and requirements of fast reactor dosimetry as applied to materials damage analysis programs sponsored by the Division of Reactor Development and Technology of the U. S. Atomic Energy Commission is reviewed. The methods and data recommended for fast reactor applications are presented. The most significant developments are given below:

1. The neutron fluence and integral spectrum can be determined within ± 10 to 30 percent in most fast and thermal reactors using the monitors and analytical methods presented.

2. An optimum set of fission and nonfission monitors has been selected to achieve the accuracy described in 1. The need for accuracy and minimal cost and requirements of long-term materials irradiation tests were considered in selecting this set. Reduced dosimetry efforts are defined for experiments in which the nuclear environment is known or where cost prohibits more completely definitive dosimetry.

3. A dosimetry center has been established to interpret, store, and provide detailed information on neutron flux, fluence, and spectra in fast test reactors. The availability of suitable suppliers of monitor materials and necessary interlaboratory calibration of radioactivity counting facilities will be maintained through the activities of the dosimetry center.

4. Theoretically based damage functions are expected to be inadequate in themselves for meeting the requirements of materials technology for advanced fast breeder reactors.

5. Empirical damage functions are expected to include the effects of all damaging mechanisms and can be used to help identify these processes. The empirical damage function method should, therefore, help to satisfy some of the immediate requirements of designers of fast reactors.

6. The applications of empirical damage functions have been demonstrated in the correlation of irradiation data on yield strength and creep for austenitic stainless steels and for loss of ductility data for ferritic steels.

APPENDIX

The SAND-II code [29] was used to obtain the calculated values of thermal averaged, fission averaged, and resonance integrals. Except for $^{238}\text{Pu}(n, f)$, the current SAND-II energy-dependent cross sections, $\sigma(E)$, were used [28]. The

²³⁸Pu(n, f) cross section was obtained from the Battelle master library tape [62] and was added to the SAND-II library tape.

Thermal averaged cross section is defined by the relation

$$\sigma_{2200} \equiv \frac{2}{\sqrt{\pi}} \int_{10^{-10} \text{ MeV}}^{18 \text{ MeV}} \sigma(E) \phi^M(E) dE$$

where $\phi^M(E)$ is defined as

$$\phi^M(E) = E e^{-E/KT} / (KT)^2$$

and $KT = 2.52 \times 10^{-8}$ MeV, corresponding to a Maxwell temperature of 20 C.

The fission averaged cross section is defined by the relation

$$\bar{\sigma}^f \equiv \int_{10^{-10} \text{ MeV}}^{18 \text{ MeV}} \sigma(E) \phi^f(E) dE / \int_{10^{-10} \text{ MeV}}^{18 \text{ MeV}} \tilde{\phi}^f(E) dE$$

using two forms of the fission spectrum $\phi^f(E)$. The two forms are the Watt [63] and SAND-II [19] forms, and on an integral flux basis they are compared in Table

TABLE 4—Watt and SAND-II fission spectrum representations.

Neutron Energy, MeV	Integral Flux Above Specified Neutron Energies ^a		Ratio (SAND-II/Watt)
	Watt [63]	SAND-II	
1 × 10 ⁻²	9.995 × 10 ⁻¹	9.996 × 10 ⁻¹	1.00
2	9.987	9.989	1.00
4	9.964	9.970	1.00
7	9.917	9.932	1.00
1 × 10 ⁻¹	9.86	9.89	1.00
2	9.62	9.69	1.01
4	9.02	9.20	1.02
7	7.97	8.30	1.04
1 × 10 ⁰	6.92	7.36	1.06
1.5	5.31	5.82	1.10
2	3.98	4.48	1.13
3	2.12	2.47	1.17
4	1.09	1.26	1.16
5	5.38 × 10 ⁻²	6.06 × 10 ⁻²	1.13
6	2.60	2.78	1.07
7	1.24	1.30	1.05
8	5.78 × 10 ⁻³	6.24 × 10 ⁻³	1.08
9	2.67	3.03	1.13
10	1.22	1.45	1.19
Mean energy, MeV	2.00	2.16	

^a Normalized to 1 n/cm² between 10⁻¹⁰ and 18 MeV.

4.¹⁶ The two forms are required because there is some uncertainty associated with the true form of the ²³⁵U fission spectrum [19, 26, 27, 65].

The resonance integral is defined by the relation [28, 29, 31]

$$RI = \int_{10^{-10} \text{ MeV}}^{18 \text{ MeV}} \frac{\sigma(E)}{E} e^{-\Sigma_a(E)X} dE$$

where the exponential term accounts for the neutron absorption of a 40-mil cadmium cover.

References

- [1] Yoshikawa, H. H. and McElroy, W. N. in *Irradiation Effects in Structural Alloys for Thermal and Fast Reactors*, ASTM STP 457, American Society for Testing and Materials, 1969, pp. 342-351.
- [2] Jackson, J. L. and Ulseth, J. A., *Nuclear Applications*, NUAPA, Vol. 5, 1968, p. 275.
- [3] Dudey, N. D. et al, *Nuclear Applications*, NUAPA, Vol. 7, 1969, p. 35.
- [4] McElroy, W. N., Jackson, J. L., and Ulseth, J. A., *Transactions of the American Nuclear Society*, TANSAS, Vol. 12, 1969, p. 937.
- [5] Kellogg, L. S., Zimmer, W. H., and Ulseth, J. A., *Transactions of the American Nuclear Society*, TANSAS, Vol. 12, 1969, p. 938.
- [6] McElroy, W. N., Jackson, J. L., Ulseth, J. A., and Simons, R. L., "EBR-II Dosimetry Test Data Analysis," BNWL-1402, Battelle-Northwest, Richland, Wash., 1970.
- [7] Kellogg, L. S. and Zimmer, W. H., "EBR-II Dosimetry Test Reaction Rate Measurements," BNWL-1403, Battelle-Northwest, Richland, Wash., 1970.
- [8] Kamphouse, J. L., Stuart, R. L., and Moteff, J., *Transactions of the American Nuclear Society*, TANSAS, Vol. 12, 1969, p. 223.
- [9] Kamphouse, J. L., Stuart, R. L., and Moteff, J., "Theoretical Spectrum-Threshold Detector Data Correlation in EBR-II," GEMP-720, General Electric, NSP, 1969.
- [10] Withop, A., Hutchins, B. A., and Martin, G. C., "Analytical Procedures and Applications of Fluence Determinations from EBR-II Flux Wires," GEAP-5744, General Electric Co., San Jose, Calif., 1969.
- [11] Dudey, N. D. and Heinrich, R. R., "Flux Characterization and Neutron Cross Section Studies in EBR-II," ANL-7629, Argonne National Laboratory, Argonne, Ill., 1969.
- [12] Miller, L. B. and Jarka, R. E., *Transactions of the American Nuclear Society*, TANSAS, Vol. 12, 1969, p. 772.
- [13] Kirn, F. S., *Nuclear News*, NUNWA, Vol. 13, 1970, pp. 62-68.
- [14] McElroy, W. N., Dahl, R. E., Jr., and Serpan, C. Z., Jr., *Nuclear Applications*, NUAPA, Vol. 7, No. 6, Dec. 1969, pp. 561-571.
- [15] Serpan, C. Z., Jr., and McElroy, W. N., "Damage-Function Analysis of Neutron-Energy and Spectrum Effects Upon the Radiation Embrittlement of Steels," NRL Report 6925 (1969), presented at IAEA Symposium, Vienna, Austria, June 1969.
- [16] McElroy, W. N., Dahl, R. E., Jr., and Gilbert, E. R., "Neutron-Energy-Dependent Damage Function for Analysis of Austenitic Steel Creep Data," BNWL-SA-3186, Battelle-Northwest, Richland, Wash., 1970.

¹⁶ If the Cranberg [64] form had been used instead of the Watt form, there would be a larger difference between it and the SAND-II form. The mean energies for the SAND-II, Watt, and Cranberg forms are 2.16, 2.00, and 1.95 MeV, respectively. The Grundl multiple-foil form has a mean energy of 2.20 MeV [26].

- [17] McElroy, W. N., Simons, R. L., and Blackburn, L. D., *Transactions of the American Nuclear Society*, TANSAs, Vol. 13, 1970, p. 144.
- [18] McElroy, W. N. et al, *Nuclear Science and Engineering*, NSENA, Vol. 36, 1969, p. 15.
- [19] McElroy, W. N., Armani, R. J., and Tochilin, E., *Transactions of the American Nuclear Society*, TANSAs, Vol. 12, 1969, pp. 757-759.
- [20] Meek, M. E. and Rider, B. F., "Summary of Fission Product Yields for U^{235} , U^{238} , Pu^{239} , and Pu^{241} at Thermal, Fission Spectrum and 14 MeV Neutron Energies," APED-5398-A, Class 1, Revised, General Electric, Cincinnati, Ohio, Oct. 1968.
- [21] McElroy, W. N., Kellogg, L. S., Armani, R. J., Tochilin, E., and Zimmer, W. H., "Selection of Fission Yields," to be presented at Winter Meeting, American Nuclear Society, Washington, D.C., Nov. 1970, WADCO, Westinghouse, Richland, Wash.
- [22] Private communications with E. Kobisk and D. Box, Oak Ridge National Laboratory, Oak Ridge, Tenn., 1970.
- [23] Yoshikawa, H. H. and Zimmer, W. H., "Fast Neutron Dosimetry: Intercalibration of Counting Facilities," USAEC Report HW-81871, General Electric Company, Richland, Wash., April 1964.
- [24] Ulseth, J. A., "Intercalibration of Counting Laboratories," BNWL-1096, Battelle-Northwest, Richland, Wash., June 1969.
- [25] Personal communication with M. S. Wechsler, ASTM-ORNL Intercomparison Program on Neptunium-237 Fission Threshold Neutron Dosimetry, 1969.
- [26] Grundl, J. A., *Nuclear Science and Engineering*, NSENA, Vol. 31, 1968, pp. 191-206.
- [27] McElroy, W. N., *Nuclear Science and Engineering*, NSENA, Vol. 36, 1969, p. 109.
- [28] Simons, R. L. and McElroy, W. N., "Evaluated Reference Cross Section Library," BNWL-1312, Battelle-Northwest, Richland, Wash., 1970.
- [29] McElroy, W. N. et al, "A Computer Automated Iterative Method for Neutron Flux Spectra Determination by Foil Activation," Vols. I-IV, AFWL-TR-67-41, Air Force Weapons Laboratory, Albuquerque, N.M., 1967.
- [30] McElroy, W. N. et al, "Neutron Differential Cross Section Evaluation by a Multiple Foil Activation Iterative Method," NBS 299, Vol. 1, National Bureau of Standards, Special Publications, 1968, p. 235.
- [31] Barrall, R. C. and McElroy, W. N., "Experimental and Evaluated Cross Section Library of Selected Reactions," AFWL-TR-65-34, Vol. II, Air Force Weapons Laboratory, Albuquerque, N.M., 1965.
- [32] Stewart, L., Motz, H. T., and Moore, M. S., "Compilation of Requests for Nuclear Cross Section Measurements," WASH-1144, Los Alamos Scientific Laboratory, Los Alamos, N.M., 1970.
- [33] Greer, C. R., Halbleib, J. A., and Walker, J. V., "A Technique for Unfolding Neutron Spectra from Activation Measurements," SC-RR-67-746, Sandia, Albuquerque, N.M., 1967.
- [34] DiCola, G. and Rota, A., "RDMM—A Code for Fast Neutron Spectra Determination by Activation Analysis," EUR-2985.e, Joint Nuclear Research Center, Ispra Establishment, Italy, 1966.
- [35] *ASTM Discussion of Computer Codes for Determining Neutron Flux Spectra by Multiple Foil Measurements*, Tentative Computer Code Information Document, to be published, American Society for Testing and Materials, 1970.
- [36] McElroy, W. N., *Transactions of the American Nuclear Society*, TANSAs, Vol. 13, 1970, p. 422.
- [37] Bourquin, R. D., "TIMH—A Computer Program for the Determination of Fluence with a Time-Varying Flux," BNWL-1492, Battelle-Northwest, Richland, Wash., 1970.
- [38] Hutchins, B. A., Turner, J. E., Busboom, H., and Comprelli, F. A., *Transactions of the American Nuclear Society*, TANSAs, Vol. 12, 1969, p. 587.
- [39] Scherrer, J. F. and Moteff, J., "The Use of Spectrum Averaged Cross Sections in the Calculation of Helium Generated in Stainless Steel During Reactor Irradiations," GEMP-721, General Electric, NSP, 1969.
- [40] McElroy, W. N., Farrar, H., IV, and Knox, C. H., *Transactions of the American Nuclear Society*, TANSAs, Vol. 13, 1970, p. 314.

- [41] Farrar, H., IV, and Knox, C. H., *Transactions of the American Nuclear Society*, TANSAs, Vol. 11, 1968, p. 503.
- [42] Private communication with H. Farrar, IV, Atomics International, Canoga Park, Calif., 1970.
- [43] Dienes, G. J. and Vineyard, G. H., *Radiation Effects in Solids*, Vol. II, Interscience Publishers, New York, 1957.
- [44] Chadderton, L. T., *Radiation Damage in Crystals*, John Wiley and Sons, New York, 1965.
- [45] Kinchin, G. H. and Pease, R. S., *Reports of Progress in Physics*, RPPHA, Vol. 18, No. 1, 1955.
- [46] Beeler, J. R., Jr., *Journal of Applied Physics*, JAPIA, Vol. 37, 1966, pp. 3000-3009.
- [47] Beeler, J. R., Jr., *Physical Review*, PHRVA, Vol. 150, 1966, pp. 470-487.
- [48] Beeler, J. R., Jr., in *Lattice Defects and Their Interactions*, R. R. Hasiguti, Ed., Gordon and Breach Science Publishers, New York, 1967.
- [49] Russcher, G. E., "Calculated Damage Functions for Determining Irradiation Effectiveness," BNWL-1093, Battelle-Northwest, Richland, Wash., Sept. 1969.
- [50] Wechsler, M. S. in *Symposium on Radiation Effects on Metals and Neutron Dosimetry*, ASTM STP 341, American Society for Testing and Materials, 1963, p. 86.
- [51] Harries, D. R., Barton, P. J., and Wright, S. B. in *Symposium on Radiation Effects on Metals and Neutron Dosimetry*, ASTM STP 341, American Society for Testing and Materials, 1963, p. 276.
- [52] Rossin, A. D., *Nuclear Structural Engineering*, NSTEA, Vol. 1, 1965, p. 76.
- [53] Dahl, R. E., Jr., and Yoshikawa, H. H., *Nuclear Science and Engineering*, NSENA, Vol. 21, 1965, pp. 312-318.
- [54] Shely, W. F., *Nuclear Science and Engineering*, NSENA, Vol. 29, 1967, p. 165.
- [55] Shure, K., *Nuclear Applications*, NUAPA, Vol. 2, 1966, p. 106.
- [56] Jenkins, J. D., *Transactions of the American Nuclear Society*, TANSAs, Vol. 12, 1969, p. 139.
- [57] Doran, D. G., *Radiation Effects*, Vol. 2, 1970, p. 249.
- [58] Harries, D. R., *Journal of the British Nuclear Energy Society*, JBNSA, Vol. 5, 1966, p. 74.
- [59] Lindhagen, P., "Observations on Helium Bubbles in an Irradiated 18Cr-27Ni Austenitic Stainless Steel," to be published as part of the Symposium on Radiation Damage in Reactor Materials, Vienna, 1969.
- [60] Kramer, D., Brager, H. R., Rhodes, C. G., and Pard, A. G., *Journal of Nuclear Materials*, JNUMA, Vol. 25, 1968, p. 121.
- [61] Kangilaski, M., Perrin, J. S., and Wullaert, R. A. in *Irradiation Effects in Structural Alloys for Thermal and Fast Reactors*, ASTM STP 457, American Society for Testing and Materials, 1969, p. 67.
- [62] Private communication with J. Carter, Battelle-Northwest, Richland, Wash., 1970.
- [63] Watt, B. E., *Physical Review*, PHRVA, Vol. 83, 1952, p. 1037.
- [64] Cranberg, L. et al, *Physical Review*, PHRVA, Vol. 103, 1956, p. 662.
- [65] Fabry, A., *Nukleonik*, NUKKA, Vol. 10, 1967, p. 280.
- [66] Private communication with A. D. Rossin, Argonne National Laboratory, Argonne, Ill., 1969.

AGENDA DISCUSSION SESSION

How Do We Solve the Void Problem?

*T. T. Claudson*¹—The effect of metal swelling on the design, operation, and safety of fast reactors has only recently become apparent through the design efforts associated with the Fast Flux Test Facility (FFTF) and LMFBR demonstration plants. Extrapolation of current swelling data to high burnup indicates that swelling of cladding and structural materials will limit the reactor core performance. Core performance limitations due to materials behavior during the early stages of the development of a new reactor concept is not new. In the past metallurgical solutions to these problems have been possible, such as the development of corrosion-resistant zirconium alloys for water reactor systems. There are data at present which indicate again that there may be metallurgical solutions to the problems associated with metal swelling.

Swelling has been observed in several metals including aluminum, molybdenum, nickel, as well as in stainless steel. Through the comparison of the response of different metals and alloys, it is possible to gain some indication of several approaches to the solution of the problem. In the case of nickel it has been determined that impurity content and cold work are important. Figure 1 shows the change in volume as a function of fluence for nickel 200 and nickel 270 irradiated in the EBR-II. The response to swelling of Inconel 600 is also shown for comparison. One can see that annealed nickel 200 swells less than annealed nickel 270. Furthermore 50 percent cold-worked nickel 200 swells less than the same material in the annealed material. Inconel 600, a high nickel content alloy, did not swell although irradiated under the same conditions. The major difference between nickel 270 and nickel 200 was impurity content, the nickel 200 having about 1600 ppm of silicon.

Further indication of the effect of alloy content on swelling response is shown in Fig. 2. Specimens of AISI 316 and 348 were irradiated under identical conditions in the EBR-II. As temperature and fluence were increased the swelling response of the two alloys varied. Whereas the 348

¹ WADCO Corp., Richland, Wash. 99352.

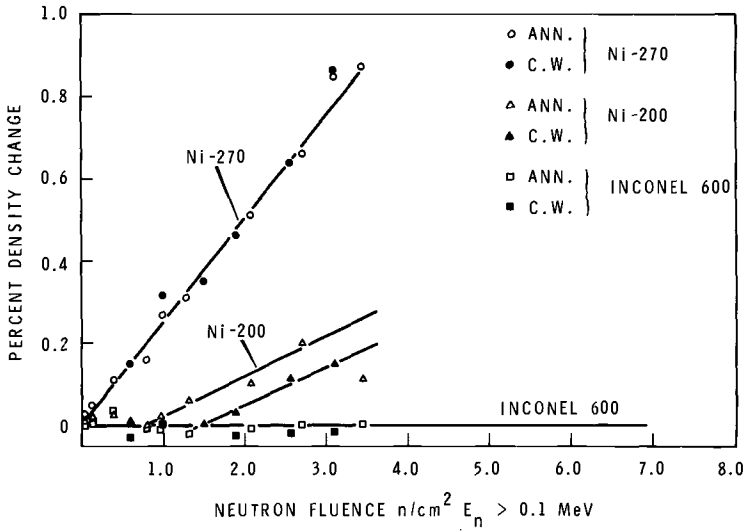


FIG. 1—Swelling in nickel irradiated in the EBR-II at 480 C.

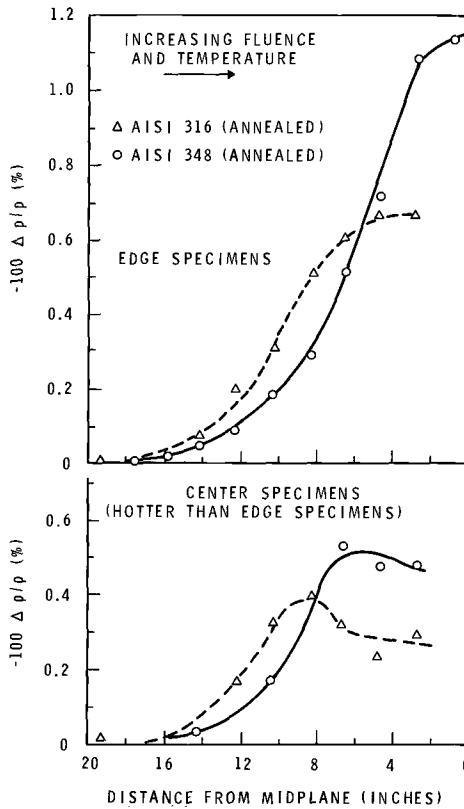


FIG. 2—Effect of temperature and fluence on swelling of AISI 316 and 347.

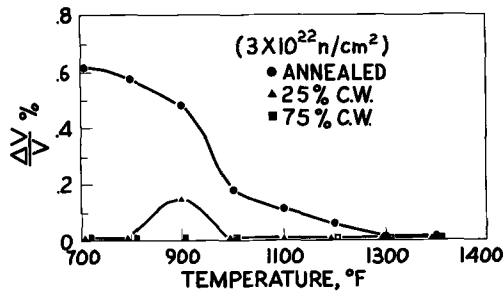


FIG. 3—Effect of cold work on the swelling response of austenitic stainless steel.

alloy had superior properties (lower swelling) at lower temperature and fluences, the 316 alloy was better as temperature and fluence were increased.

Metallurgical structure appears to have a significant effect on the swelling of metals. It has already been mentioned that cold-worked nickel swells less than the same material in the annealed condition. Figure 3 shows the effect of cold-working AISI 316 on swelling, at low temperatures the effect is marked. As irradiation temperatures increase the benefit of cold work becomes less apparent because of recovery.

From the above discussion it appears that swelling in engineering alloys may be affected by several metallurgical variables including structure and composition. This indicates that the solution to the problem may involve alloy composition modifications, heat treatment, mechanical working, or a combination of them, all of which are within present commercial capability.

The role of the designer and other related metallurgical phenomena must not be forgotten. While swelling will promote high bending stresses in core components such as ducts, it is anticipated that irradiation induced creep will aid in the relaxation of these stresses. Also, as designers become more acquainted with the problem and better means of predicting the actual swelling values as a function of stress, temperature, and fluence become available, improved designs can be effected. No doubt the true solution will involve a combination of these factors.

*H. W. Wiedersich*²—With regard to the differences in the various theories on void formation, I would like to make some comments. The theories are still in a state of flux. Even though the basic models used are similar and the gross features of swelling emerge from any one of the theories, their quantitative predictions do vary significantly. Swelling is a very complicated phenomenon, and, therefore, approximations which simplify the complexity must be made. The differences in theories and, hence, in

² Member of technical staff, Science Center, North American Rockwell Corp., Thousand Oaks, Calif. 91360.

results lie mainly in the differences between the approximations used. With improvements in the understanding of the subtleties of the phenomenon, a more realistic assessment of the consequences of the various simplifying assumptions will be possible and appropriate modifications will be made. On the request of Dr. Bullough, I give just one example of the differences.

The assumptions that voids grow during the early stages in a point defect environment essentially determined by dislocation sinks and recombination and that there exists *no* concentration gradient of defects in the vicinity of a void yield a void volume growth proportional to the cube of time, t^3 , as suggested by Bullough and co-workers. If, however, the concentration gradient resulting from the defect loss to the void is assumed not to be negligible, one obtains a $3/2$ power dependence in time for otherwise unchanged conditions. The latter assumption is contained in the treatment of Harkness and Li. Of course, their result on the time dependence is more complicated, because they allow the point defect environment to change as nucleation and growth proceeds.

Gases which dissolve in metals and have reasonably high diffusion coefficients at temperatures of void formation, such as hydrogen and nitrogen, may ease the nucleation of voids by virtue of lowering of the surface energy by absorption. However, they will not reduce the barrier to nucleation to any significant extent by the internal pressure in the nuclei in equilibrium with the dissolved gas. The internal pressure may build up to a sufficiently large magnitude only when gases with very low solubilities and, hence, very high equilibrium pressures are trapped and low diffusion coefficients prevent their escape to surfaces in the temperature range of interest. Aside from noble gases, notably helium, so-called "residual hydrogen" could be of importance to void nucleation. As H. H. Podgurski [1]³ has shown, hydrogen can be trapped in steel in the form of CH_4 , which is rather insoluble and immobile.

A fine dispersion of precipitates may reduce the swelling by providing additional sinks for point defects. Precipitates in the matrix are expected to act as self-compensating sinks for interstitials and vacancies, because any excess annihilation of interstitials will produce a compressive strain field around the precipitate which attracts vacancies and repels interstitials. Excess vacancy annihilation will reverse the situation. Grain boundaries, precipitates in boundaries, and dislocation networks are not self-compensating sinks. The precipitates have to be highly dispersed to be effective; their number density should be higher than typical observed void densities, that is, greater than 10^{15} cm^{-3} .

*J. D. Elen*⁴—Concerning the regime for void formation in body centered cubic metals, I would like to show the influence of chemical interstitial

³ *Italic numbers in brackets refer to the list of references at the end of this paper.*

⁴ PETTEN, Reactor Centrum Nederland, Netherlands.

impurity on the damage structure in vanadium. A series of three purities of recrystallized vanadium was irradiated in the high flux reactor at Petten to a fast neutron dose of $1.6 \times 10^{20} \text{n/cm}^2$ in a flux of $1.1 \times 10^{14} \text{n/cm}^2\text{-s}$, $E > 0.1 \text{ MeV}$. The carbon, oxygen, and nitrogen contamination is given below.

Chemical Impurity, ppm			Interstitial Damage, μm		Voids		
N	C	O	l	d	N, cm^{-3}	$\bar{a}, \text{\AA}$	$V, \text{deg}/100$
310	355	255	0.2	0.4	9.4×10^{14}	68	0.3
610	330	2030	0.4	0.8	5.0×10^{14}	110	0.9
340	385	700	0.6	1.1	3.5×10^{13}	283	1.4

The as-irradiated damage structure is essentially different from the small cluster type observed by Elen [2] and Rau et al [3] in pure vanadium after similar irradiations. The irradiation capsule here, not being instrumented, might have been different in temperature. From postirradiation annealing the irradiation temperature was estimated to be about 200 C. A uniform distribution is observed of large dislocation tangles (Fig. 1), centered at second-phase particles. The original impurity determined structure is swept out. The tangles consist of large interstitial $\{111\} 1/2\mathbf{a}$ $\langle 111 \rangle$ dislocation loops.

The vacancy damage shows up in multiple-beam condition as a population of perfect cubic voids (Fig. 2). Considering the various purities, there seems to be a relation between the number N , the average size \bar{a} ,

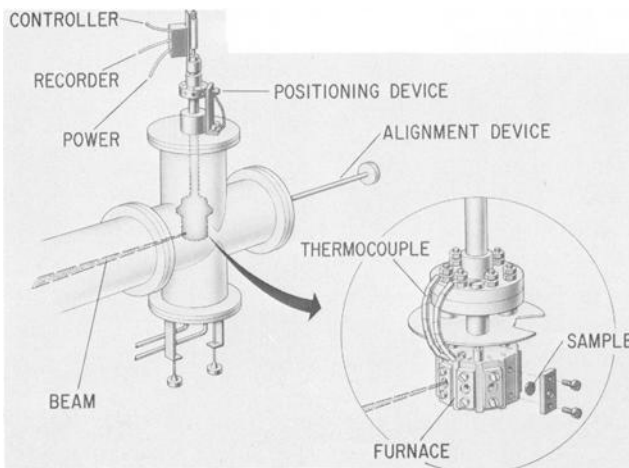


FIG. 4—Specimen chamber for ion bombardment studies.

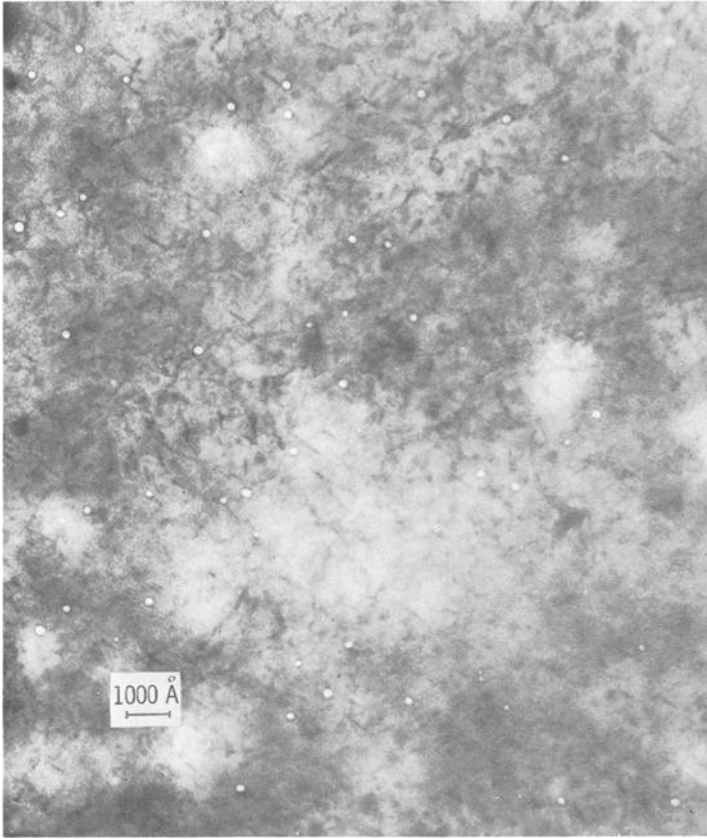


FIG. 5—Voids in 20 percent cold-worked 316 stainless steel after irradiation with 5-MeV Ni^{++} at 565 C to 3×10^{16} ions/cm².

and the total volume fraction V of the voids and the size l and interspacing d of the interstitial loop tangles. There is no systematic change with purity. The observations are tabulated for brevity. They might be considered in terms of the influence of the interstitial damage nucleation, which seems to be determined by impurity, on the supersaturation of vacancies.

*G. L. Kulcinski, H. R. Brager, and J. J. Laidler*⁵—The use of charged particle irradiation to produce voids in stainless steel was first demonstrated by Nelson and Mazey [4] in 1969. These authors initially used 100-keV protons and carbon ions, but later 22-MeV carbon and 100-keV nickel ions were used [5, 6]. High-temperature bombardment with these ions resulted in a microstructure very similar to the voids and faulted loops observed after high-temperature neutron irradiation. More recently,

⁵ Pacific Northwest Laboratories, Battelle Memorial Institute, Richland, Wash. 99352.

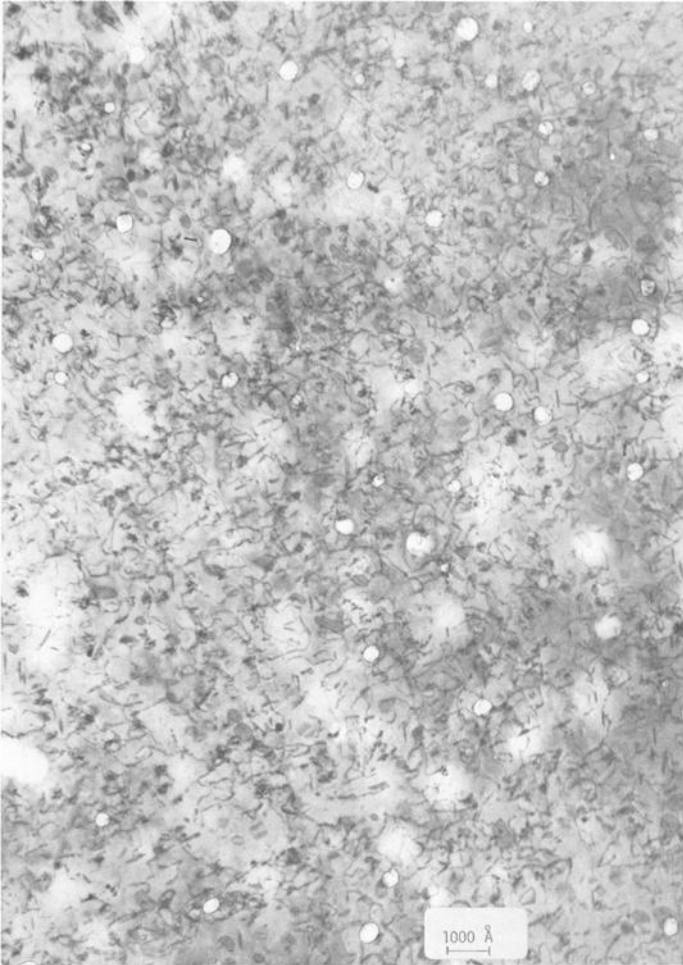


FIG. 6—Voids in solution treated 316 stainless steel irradiated with 5-MeV Ni^{++} at 585 C to 3×10^{16} ions/cm².

Keefer et al [7] have used 1.2-MeV protons and Kulcinski et al [8] have used 5-MeV Cu ions to produce voids in Type 316 stainless steel.

Ideally, one would like to use bombarding ions which will not substantially alter the chemistry of the metal or alloy bombarded. This requirement in stainless steels would dictate the use of iron, chromium, or nickel and in some special cases molybdenum, columbium, or titanium. Furthermore, to make meaningful correlations between ion and neutron fluences and to eliminate surface effects, the incident ion should penetrate at least a few thousand angstroms. The latter requirement means that heavy ion energies ≥ 1 MeV must be achieved.

This note describes an experiment designed to fulfill the above require-

ments by using 5-MeV Ni⁺⁺ ions to produce voids in 316 stainless steel at 565 to 585 C. The void size and density in the ion bombarded material is consistent with that which would be observed after an equivalent neutron fluence of 4×10^{22} n/cm², $E > 0.1$ MeV, at the temperature.

Experimentally, the specimens were irradiated at temperatures from 565 to 585 C while in intimate contact with a resistance heated stainless steel furnace (Fig. 4). Beam currents of up to $9 \mu\text{A}/\text{cm}^2$ (5.4×10^{13} ions/cm²/s) were used in this study.

The specimen material was certified Type 316 stainless steel which was solution treated for 10 min in hydrogen at 1040 C. Some of this material underwent a 20 percent reduction in area after this treatment. The actual specimens were 3-mm-diameter disks 0.2 to 0.22 mm thick. The preparation of the specimens for microscopy is described elsewhere [9].

Typical microstructures of the solution treated and 20 percent cold-worked material after irradiation with 5-MeV Ni⁺⁺ to a fluence of 3×10^{16} ions/cm² are shown in Figs. 5 and 6. In both materials voids and faulted loops were present. The void density is somewhat lower in the solution treated specimens (3×10^{13} cm⁻³ versus 6×10^{13} cm⁻³) and the void size is somewhat larger (400 Å versus 250 Å) than the cold-worked specimens. The calculated volume increase is approximately 0.1 percent for the solution treated specimen and approximately 0.05 percent for the cold-worked steel.

Calculations of the equivalent neutron fluence to be expected as a result of irradiation with 3×10^{16} ions/cm² were made from the theory of Lindhard et al [10] in a manner described elsewhere [8]. The results of the calculations indicate that the equivalent neutron fluence should be in the range of 2 to 5×10^{22} n/cm². For the specific specimens of this study, 4×10^{22} n/cm² is a reasonable estimate.

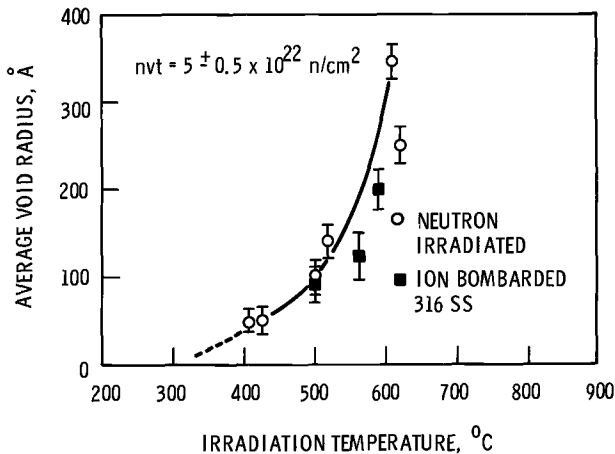


FIG. 7—Effect of irradiation temperature on the void size in austenitic stainless steel.

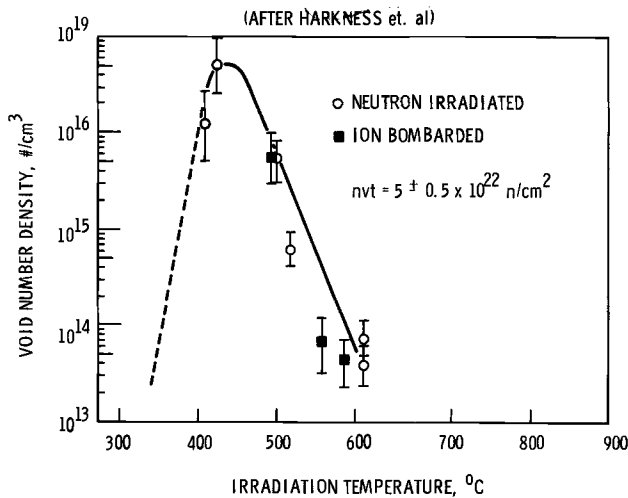


FIG. 8—Effect of irradiation temperature on void number density in austenitic stainless steel.

Figures 7 and 8, taken from the data of Harkness et al [11], show how the void size and density (open circles) vary with temperature at a constant neutron fluence of approximately $5 \times 10^{22} \text{ n/cm}^2$. The closed circles are the data from this study and one datum point from a previous experiment [8] using 5-MeV copper ions. It is obvious that the agreement between the neutron irradiated and ion bombarded specimens is quite good, at least in this temperature and fluence range. These results also point out the insensitivity of the resulting microstructure to the rate at which the atoms are displaced. For a typical neutron irradiation in EBR-II the displacement rate is $2 \times 10^{-6} \text{ s}^{-1}$, whereas in the present experiments it is in the neighborhood of 10^{-2} s^{-1} .

References

- [1] Podgurski, H. H., *Transactions of the American Institute of Mining, Metallurgical and Petroleum Engineers*, TAIMA, Vol. 221, 1961, p. 389.
- [2] Elen, J. D., "Direct Observation of Damage in Neutron Irradiated Vanadium," RCN-96, Reactor Centrum Nederland, 1967.
- [3] Rau, R. C. and Ladd, R. L., *Journal of Nuclear Materials*, JNUMA, Vol. 30, 1969, p. 297.
- [4] Nelson, R. A. and Mazey, D. J., *Symposium on Radiation Damage in Reactor Materials*, Vol. I, International Atomic Energy Agency, Vienna, 1969, p. 157.
- [5] Nelson, R. S., AERE-R-6151, Atomic Energy Research Establishment, Harwell, England, 1969.
- [6] Mazey, D. J., *Journal of Nuclear Materials*, JNUMA, Vol. 35, 1970, p. 55.
- [7] Keefer, D. W., Neely, H. H., Robinson, J. C., and Kramer, D., "Void Formation in Stainless Steel by Proton Irradiation," presented at this symposium, see pp. 332-346.
- [8] Kulcinski, G. L., Laidler, J. J., and Doran, D. G., to be published.
- [9] Brager, H. R., Kissinger, H. E., and Kulcinski, G. L., to be published.
- [10] Lindhard, J., Scharff, M., and Schiott, H. E., *Matematiks-Fysiske Meddelelser*, Danske Videnskabernes Selskab, MFYMA, Vol. 33, No. 14, 1963.
- [11] Harkness, S. D. and Ki, C. Y., to be published.

R. A. Moen,¹ J. C. Tobin,¹ and K. C. Thomas²

Neutron Fluence Limit Determinations for Some Fast Flux Test Facility Components*

REFERENCE: Moen, R. A., Tobin, J. C., and Thomas, K. C., "Neutron Fluence Limit Determinations for Some Fast Flux Test Facility Components," *Irradiation Effects on Structural Alloys for Nuclear Reactor Applications*, ASTM STP 484, American Society for Testing and Materials, 1970, pp. 409–418.

ABSTRACT: This paper describes the analytical procedures that have been developed at Battelle-Northwest Laboratory (BNWL) and Westinghouse Advanced Reactors Division (ARD) to determine neutron fluence limits for certain components of the Fast Flux Test Facility (FFTF), namely the core barrel, core support structure, and the reactor vessel.

KEY WORDS: irradiation, neutron flux, radiation effects, fast reactors (nuclear), degradation, mechanical properties, crystal lattices, helium, grain boundaries, deformation, ductility, nuclear reactor materials, stainless steels, temperature, tests

The degradation of the mechanical properties of materials by neutron irradiation is of major concern to the reactor designer because of its effect in reducing component life and jeopardizing the safety of a reactor system. There are three main types of neutron induced damage which deleteriously affect materials:

1. Displacement-type damage [*I*]³ in which interstitial atoms and vacant lattice sites are created.

¹ Research engineer and manager, respectively, Materials and Codes, Pacific Northwest Laboratory, Battelle Memorial Institute, Richland, Wash. 99352.

² Manager, Materials Engineering, Advanced Reactors Division, Westinghouse Electric Corp., Madison, Pa. 15663.

* Study carried out under U. S. Atomic Energy Commission Prime Contract AT(45-1)-1830 and WARD/BNWL Contract BDR-362. Note—many of the decisions made in the FFTF design and many of the data used in the evaluation are contained in internal memoranda that cannot be referenced.

³ Italic numbers in brackets refer to the list of references at the end of this paper.

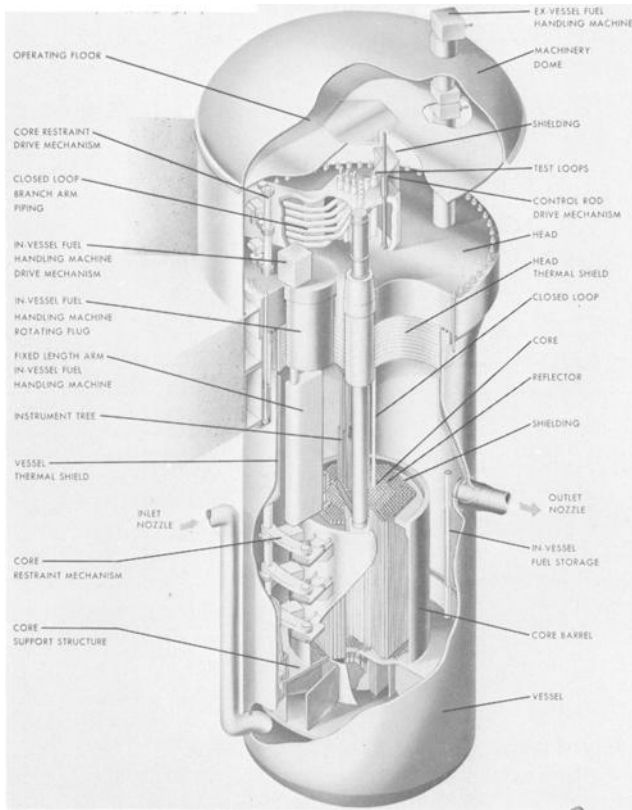


FIG. 1—FFTF reactor separated function: IVHM fixed length arm, rotating plug; instrument tree fixed plug.

2. Helium bubble generation [2] in which α particles, formed by nuclear transmutation, agglomerate into bubbles at grain boundaries and within the grains themselves.

3. Void formation [3] in which vacancies condense into three-dimensional defects within the grains.

These three types of lattice damage present different degrees of severity depending on factors such as the irradiation temperature, irradiation dosage, incident neutron energy, testing temperature, and material composition. It is, therefore, of paramount importance to assess the effects of these damage processes on materials subjected to typical reactor environments. This is achieved by testing specimens which have been irradiated in test reactors under conditions which simulate, as closely as possible, anticipated conditions in the reactor being designed. When the effects of neutron irradiation have been ascertained to a sufficient degree of confi-

dence, it becomes possible to design for optimum reactor performance, economy, and safety.

When completed in mid 1974, the Fast Flux Test Facility (FFTF) will be a 400-MWt⁴ sodium cooled fast breeder reactor. It will utilize a fuel of uranium and plutonium oxides and will have a design flux level of 7×10^{15} n/cm², $E > 0.1$ MeV. The cladding material will be AISI Type 316 stainless steel, and most of the structural components will be of AISI Type 304 stainless steel. Figure 1 gives a general description of the FFTF. The anticipated neutron spectrum at the vessel wall is given in Fig. 2. Note that it peaks at approximately 0.1 KeV, compared to the EBR-II and ETR spectra which peak between 0.1 and 0.5 MeV.

Development of Fluence Limit Criteria

During the conceptual design of the FFTF it became obvious that efficient component design depended on defining realistic limits beyond which materials in nuclear environments could not be subjected without seriously compromising the safety and efficiency of the reactor. Prior to 1968 the only known reference to fluence limits for fast reactor components was that found in the design criteria for the Fermi reactor vessel [4]. This was simply described as a fluence of 1×10^{22} n/cm², $E > 0.1$ MeV, over the 20-year plant life at an operating power level of 430 MWt. It

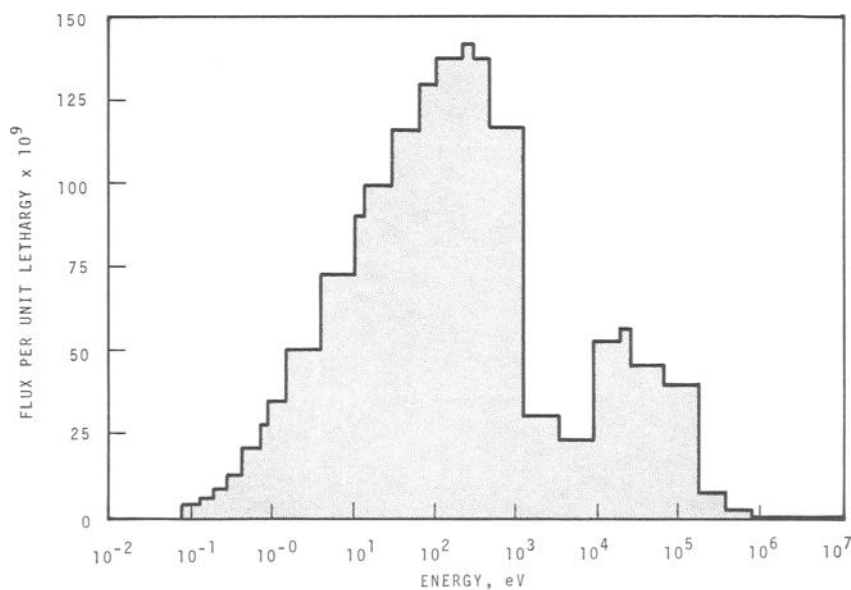


FIG. 2—Spectrum at inner surface of ETR vessel wall.

MWT = megawatts (thermal).

was an overall limit which did not consider the degradation of individual mechanical properties. At the inception of FFTF, BNWL adopted a criterion which specified that the maximum permissible fluence level would be governed by the time it took a reactor component to attain a "significant" (>10 percent) deterioration at 400 to 1200 F⁵ in any critical mechanical property such as ductility or creep rupture strength. It soon became clear that this was overly cautious and would lead to restrictive amounts of shielding to protect vital structural components; therefore, revised fluence limits based on more liberal values of 30 and 50 percent degradation in mechanical properties were defined. However, with a permissible degradation of 50 percent, concern developed that certain critical properties such as the ductility could fall below acceptable safety margins. It was decided by the BNWL/ARD that a more reasonable approach would be to define a limit based upon the residual mechanical properties at the end of life of a component.

Since all mechanical properties are not equally susceptible to neutron induced degradation it is unnecessary from a design standpoint to assign specific reliability limits to each property. The approach presently used jointly by BNWL and ARD is to determine the one critical mechanical property which is most sensitive to neutron exposure and use it as a guide to define the maximum permissible fluence level. The data in Table 1 show typical effects of neutron irradiation on the main mechanical properties of 304 stainless steel. It can be seen that the ductility generally is affected most severely, and this parameter has, therefore, been adopted by BNWL and ARD in determining fluence limits. A limit based on ductility degradation would ensure that all other deteriorations in mechanical properties would fall within the overall safety envelope. At the present time BNWL and ARD have defined an arbitrary fluence limit for the core barrel, core support structure, and reactor vessel based on a 10 percent residual ductility at end of life.

Selection of Representative Elongation Data

Before fluence limits based on the ductility criteria can be ascertained, available data have to be screened so that only the most representative are used. Such a procedure is important since it increases the level of confidence in the projected life of a component. Listed below are the most important guidelines which have been used here in the selection of appropriate ductility data.

1. Specimens irradiated in different reactors may yield data which are functions of the neutron spectrum. Frequently, cutoff energies of 0.1 and 1 MeV have been used to correlate data from different sources, that is, irradiation damage caused by neutrons with energies below 0.1 and 1 MeV

⁵ At that time the vessel design temperature was 1200 F.

TABLE 1—Effects of neutron irradiation on the mechanical properties of AISI Type 304 stainless steel.

Property	Test Temperature, deg F	Irradiation Conditions	Irradiated Specimen	Unirradiated Specimen	% Change	Reference
0.2% Offset Yield Stress	1100	1.4×10^{22} n/cm ² , $E > 0.1$ MeV, 1004 F	36 ksi	15 ksi	+140	10
Ultimate Tensile Strength	1100		46 ksi	47 ksi	-2	10
Total Elongation	1100		8%	55%	-85	Irradiated specimens, 10 Unirradiated control, 11
Rupture Time for 30-ksi Stress	1100	1×10^{22} n/cm ²	72 h	110 h	-35	12
Minimum Creep Rate for 30-ksi Stress	1100	1.6×10^{22} n/cm ² , $E > 0$ MeV, 1100 F	1×10^{-4} h ⁻¹	4.8×10^{-4} h ⁻¹	-72	13

has been ignored. However, recent work has shown that low-energy neutrons ($E < 0.1$ MeV) contribute significantly to the overall damage level in ferritic steels [5]. Since this could also be true for Type 304 stainless steel, it was decided, where possible, to quote total fluences with respect to irradiation damage.

2. Data from specimens irradiated in fast reactors should be given priority over those from thermal reactors, since fast fluxes more closely simulate anticipated FFTF service conditions.

3. Fluence levels assigned to each datum point should, where possible, be measured values obtained from flux monitors placed in close proximity to the specimen undergoing irradiation. This would eliminate errors which might occur in calculated fluences which depend, for example, on specimen geometry and the precision with which the specimen can be positioned within the reactor. Calculated fluence data should only be used when measured fluence data are scarce. In this case they should be used on an interim basis until more accurate data become available.

4. Fluence limits for a particular component should be determined, where possible, from specimens made from the same material as the component. If the data are limited, and meaningful property trends cannot be established, it is permissible to use data from materials belonging to the same family. In the case of Type 304 stainless steel estimates of property trends may be made using data for 304L, 316, 316L, 347, and 348 stainless steels. In this work no distinction has been made between 304 and 304L stainless steels, since within commercial limits the chemical compositions of the two alloys may overlap.

5. The fluence limit for a particular component should be governed by that section of the structure which exhibits the greatest susceptibility to neutron induced degradation of properties. Since weldments usually have the lowest starting ductility [6], they will undoubtedly exhibit very low end-of-life fracture strains and, therefore, control the lifetime of the component.

6. In cases where the 10 percent residual ductility values lie in a scatterband, the ductility trend line should be drawn through minimum value points. This ensures that at end of life the material will not violate the criterion of 10 percent residual ductility.

7. All data should be obtained from specimens which have been tested at temperatures within ± 50 F of the irradiation temperature. This limitation is imposed because testing at temperatures substantially different from the irradiation temperature may not yield data representative of actual service conditions. This is clear from experiments which show that different processes may control deformation in different ranges of temperature [7]; hence, if care is not taken the incorrect selection of a test temperature may mask the true state of damage. However, when few data falling within the ± 50 F specification are obtainable, it is permissible to extend

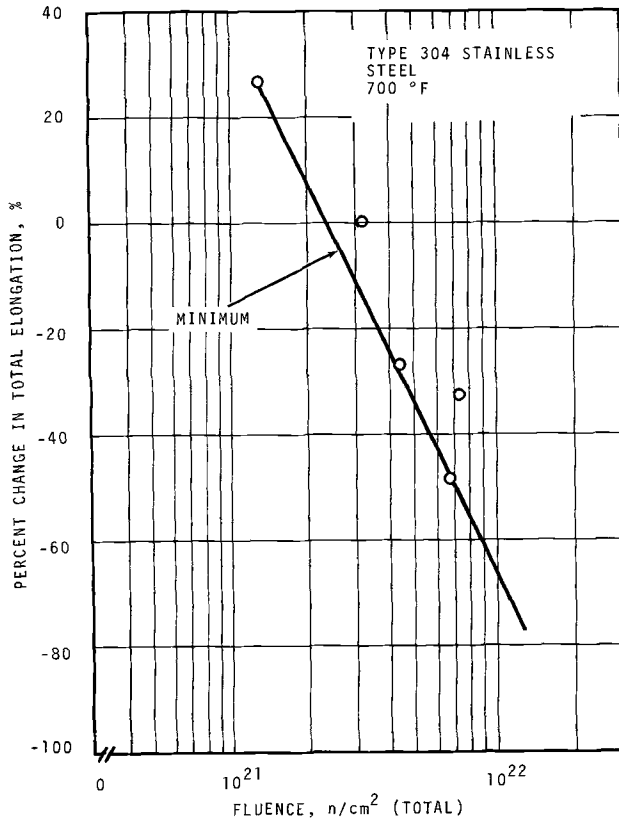


FIG. 3—Typical plot of irradiation effects data for Type 304 base metal at 700 F.

this range to ± 200 F so that a general idea of property trends may be obtained.

Fluence Limit Evaluations

Once representative data have been selected by the above guidelines, the fluence limits for the core barrel, core support structure, and reactor vessel may be evaluated. Since this paper was primarily intended to describe the general procedure for obtaining these limits, no attempt has been made to include plots of all of the data used. Below is a list of the procedures being used at BNWL and ARD to determine neutron fluence limits.

1. Data from irradiated specimens are matched against those for unirradiated control specimens to obtain percentage changes in ductility as a function of test temperature and total neutron fluence.

2. Master plots are constructed, for a given temperature, of the percentage change in the total elongation versus the neutron fluence. The use of percentage changes in elongation values compensates for differences in unirradiated elongation values for the various specimens. Figure 3 shows a typical master plot for specimens tested at 700 F. Other plots, not given here, have been made for 600, 800, 900, 1000, 1100, and 1200 F. The line in Fig. 3 has been drawn through points of minimum ductility as specified in the last section.

3. In order to determine the permissible change in elongation at 700 F necessary to leave a residual ductility of 10 percent, an average value for the ductility of Type 304 stainless steel has been obtained from the comprehensive data compiled in the *Report on Elevated-Temperature Properties of Stainless Steels, ASTM DS 5 S1* (1965). From this report the ductility of average Type 304 stainless steel plate at 700 F in the unirradiated condition is 38 percent. For a residual elongation of 10 percent, therefore,

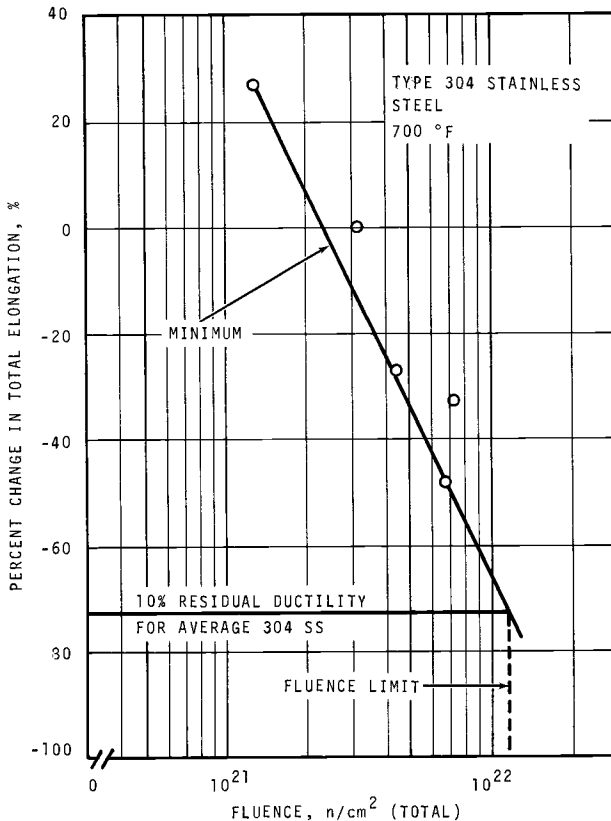


FIG. 4—Determination of the fluence limit for average Type 304 base metal at 700 F.

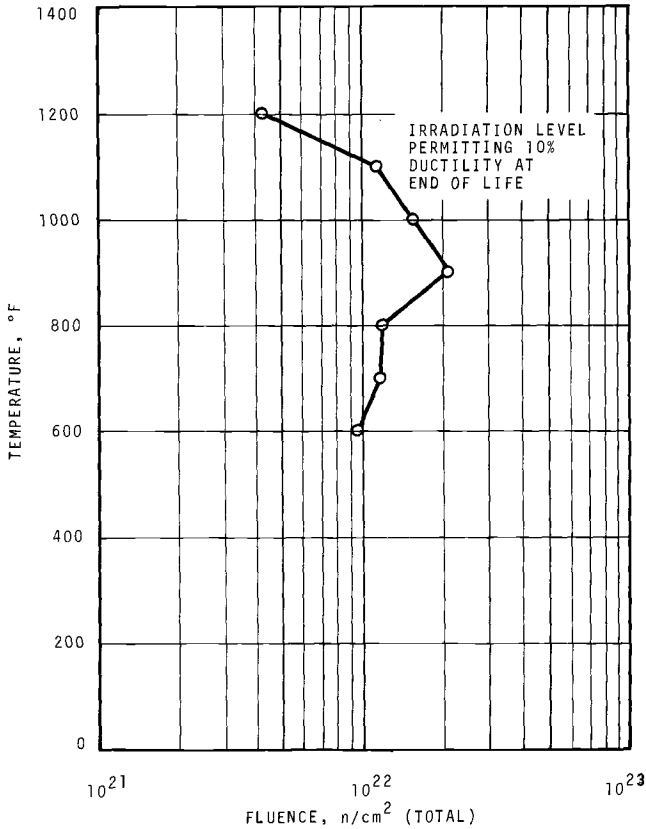


FIG. 5—Fluence limit for Type 304 stainless steel base metal.

the percentage change is 28 ÷ 38 percent, or 74 percent. This value when plotted in Fig. 4 gives a fluence limit of approximately 1.1×10^{22} n/cm² (total). The results of this and other test temperatures are given in Fig. 5. A similar study for Type 304 stainless steel weldments has also been conducted at BNWL but, at present, this information is restricted.

Conclusions

The form of the temperature-neutron fluence limit curve in Fig. 5 suggests that two deformation processes limit ductility in irradiated specimens for $T < 900$ F and $T > 900$ F. In the lower temperature range it is possible that displacement-type damage is responsible for the restricted ductility [8]. At elevated temperatures the agglomeration of helium at the grain boundaries possibly is responsible [9]. The relatively low fluence limit below 700 F is particularly significant with respect to the core barrel,

core support structure, and reactor vessel since all three were exposed to liquid sodium at a temperature of 600 F. This problem is being minimized by the use of designs which effectively shield these components from excessive neutron doses.

It should be emphasized that the data presented in Fig. 5 are tentative and are likely to change as more data become available. The results are considered to be conservative primarily because of the assumption that neutrons of all energy levels are equally damaging and because of the use of minimum values in the master plots. It seems possible that, with the advent of more comprehensive and more representative data, the neutron fluence limits will approach average values rather than the minimum values reported here.

References

- [1] Kelly, B. T., *Irradiation Damage to Solids*, Chapter 1, Pergamon Press, 1966.
- [2] Broomfield, G. H., Harries, D. R., and Roberts, A. C., *Journal of the Iron and Steel Institute*, JISIA, Vol. 203, 1965, p. 502.
- [3] Cawthorne, C. and Fulton, E. J., AERE-R5269, Vol. 2, Atomic Energy Research Establishment, Harwell, England, 1966, p. 446.
- [4] Yevick, J. G., *Fast Reactor Technology: Plant Design*, MIT Press, 1966, p. 158.
- [5] McElroy, W. N., Dahl, R. E., and Serpan, C. Z., *Nuclear Applications and Technology*, NUATA, Vol. 7, 1969, p. 561.
- [6] Ward, A. L., Lovell, A. J., and Blackburn, L. D., FFTF Quarterly Tech. Rept. BNWL-1328, Dec. 1969–Feb. 1970, p. 7.21.
- [7] Makin, M. J., *Radiation Effects*, Gordon and Breach, 1967, p. 627.
- [8] Martin, W. R. and Weir, J. R. in *The Effects of Irradiation on Structural Materials*, ASTM STP 426, American Society for Testing and Materials, 1967, p. 440.
- [9] Kramer, D., Brager, H. R., Rhodes, C. G., and Pard, A. G., Atomic International Report No. Naa-SR-12601, 1967.
- [10] Holmes, J. J., Robbins, R. E., and Lovell, A. J. in *Irradiation Effects in Structural Alloys for Thermal and Fast Reactors*, ASTM STP 457, American Society for Testing and Materials, 1969, p. 371.
- [11] Simmons, W. F. and Van Echo, J. A., *Report on the Elevated-Temperature Properties of Stainless Steels*, ASTM DS 5, American Society for Testing and Materials, 1965.
- [12] FFTF Monthly Tech. Prog. Rept. BNWL-1062, April 1969, p. 434.
- [13] FFTF Monthly Tech. Prog. Rept. BNWL-1282, Dec. 1969, p. 7.11.

J. M. Beeston¹ and C. R. Brinkman¹

Axial Fatigue of Irradiated Stainless Steels Tested at Elevated Temperatures*

REFERENCE: Beeston, J. M. and Brinkman, C. R., "Axial Fatigue of Irradiated Stainless Steels Tested at Elevated Temperatures," *Irradiation Effects on Structural Alloys for Nuclear Reactor Applications, ASTM STP 484*, American Society for Testing and Materials, 1970, pp. 419-450.

ABSTRACT: Uniaxial fatigue properties from tests at 400, 500, 600, and 700 C on Type 304, 304L (Ti modified), and 316 stainless steel specimens irradiated at 450 C in sodium and 750 C in argon at fluences of 0.03 to 9.3×10^{21} n/cm², $E > 0.1$ MeV, are given and compared with control specimens. Material was tested in the annealed, cold-worked, and chilled-swaged-tempered condition, while primary controls received a pretest anneal of 1500 h at 750 C. The data at 400, 500, and 600 C are compared with proposed design curves for 18-8 steels. Some data on microstructural changes due to irradiation are given. A reduction in the fatigue life by a factor of less than 2.5 was found in the annealed material, which was attributed to irradiation damage. A beneficial effect on fatigue life of pretreatment by swaging was found after irradiation at 450 and 750 C for 2550 h.

KEY WORDS: neutron irradiation, radiation effects, liquid metal cooled reactors, fast reactors (nuclear), stainless steels, helium, carbides, voids, microstructure, ductility, embrittlement, fatigue (materials), cold working, axial strains, mechanical properties, fatigue tests, high-temperature tests

Low-cycle high-strain fatigue is important to liquid metal fast breeder reactor (LMFBR) vessels and components operating at local temperatures of 300 to 650 C, since nozzle angles and other discontinuities can result in stress concentrations requiring local plastic flow to allow for redistribution of stresses. During operation, irradiation may reduce the ductility of the materials, enhancing the possibility of localized failure. The fast

¹ Materials Research Section, Idaho Nuclear Corp., Idaho Falls, Idaho 83401.

* The work described in this paper was performed under the auspices of the United States Atomic Energy Commission under Contract AT(10-1)-1230.

test reactor (FTR) has components, for example, vessel, instrument tree, and in-vessel fuel handling machine, for which the design irradiation fluences are less than 10^{22} n/cm², $E > 0.1$ MeV, and the temperatures are between 320 and 600 C [1].² Although postirradiation testing is less relevant to reactor stress conditions than in-reactor testing, many more tests are conducted in this manner because of difficulties and costs involved with the latter, and only limited fatigue tests on irradiated materials [2, 3, 4, 5] have been conducted.

The interplay of the irradiated strength and ductility of stainless steels upon the fatigue properties is a question of major interest. Whether the source of the high-temperature embrittlement resides in the behavior of voids, carbides, helium, or other complex defects has not been established, nor has the action of alternating stresses on these defects in the nucleation and growth of cracks. At temperatures above one half the melting point (> 580 C) the void density is predicted to be greatly reduced, and at these temperatures the diffusivity is high enough that carbide or second-phase precipitates and helium behavior could be important. At fluences of about 10^{21} n/cm², $E > 1$ MeV, Martin and Weir [6] showed that strength properties were unaffected by irradiation at temperatures above 600 C. Holmes et al [7] point out that the subject is controversial at this fluence level, but that at higher fluence levels strengthening (yield increase) occurs at temperatures approaching 750 C. Agreement appears to exist that high-temperature ductility losses are due to embrittlement processes apart from strengthening processes, although the ductility above $T_m/2$ is strain rate sensitive.

It was also noted by Martin and Weir that 10 percent cold work in an irradiated austenitic steel appeared to have a beneficial effect. Plastic deformation below the martensite induced deformation temperature in low-carbon metastable austenitic steels has been shown [8] to result in an improved combination of strength and ductility. The apparent relationship between tensile and fatigue properties and the presence of some cold work in fabricated vessel components point to the need for an examination of the effect on high strain fatigue in stainless steels. No studies of microstructural effects on irradiated stainless steel fatigue properties are known, although some work on effects of microstructure in pressure vessel steels has been accomplished [9].

In the present paper, uniaxial fatigue properties from tests at 400, 500, 600, and 700 C on Type 304, 304L (Ti modified), and 316 stainless steel specimens irradiated at 450 and 750 C (maximum temperatures) at fluences of 0.03 to 9.3×10^{21} n/cm², $E > 0.1$ MeV, are given and compared with control specimens. Some tests on cold-worked and pretreatment (chill-swaged-tempered) specimens are also presented. A summary of the

² Italic numbers in brackets refer to the list of references at the end of this paper.

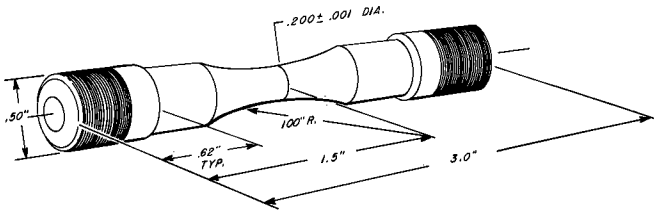


FIG. 1—Fatigue hourglass shaped specimen details.

data at 400, 500, and 600 C for the stainless steels is compared with proposed design curves. The identification of important factors affecting the irradiated fatigue life is attempted.

Procedure

Fatigue tests were conducted using electrohydraulic test frames in an argon enclosure (atmosphere checked at less than 3 ppm oxygen) by con-



FIG. 2—Typical specimen surface at failure defined as a 10 to 20 percent decrease in steady state stress amplitude (X10).

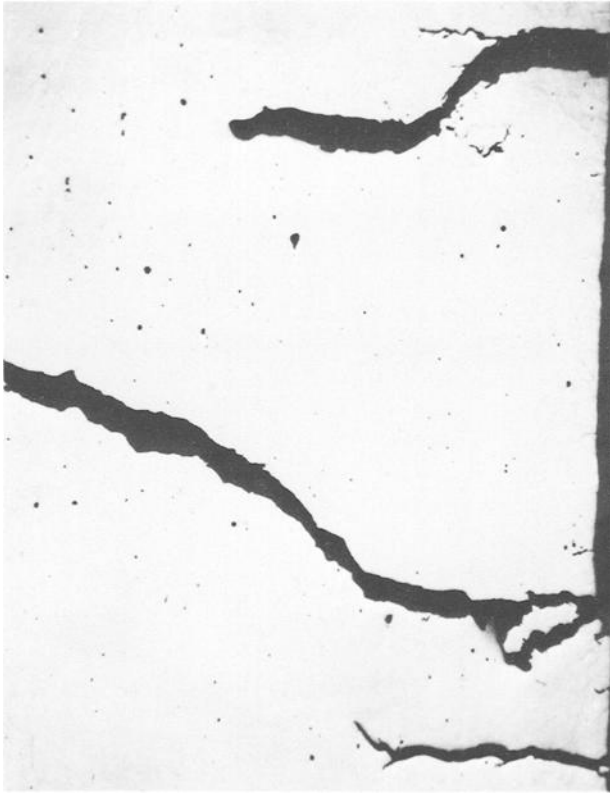


FIG. 3—Cross section of failed specimen showing typical multiple cracks emanating from specimen surface ($\times 50$).

stant strain range and frequency control. Strain ranges were varied from approximately 0.7 to 3.5 percent, and the testing strain rate was either 4 or 8×10^{-4} in./in./s. The loading was axial (push-pull) completely reversed, that is zero mean strain, on specimens of hourglass shape as shown in Fig. 1. The mass of the specimens was kept low to reduce radioactivity from irradiation. Specimens were polished longitudinally to an 8- μ in. finish. After irradiation the specimens were ultrasonically cleaned and the specimen surface generally had no film or only a thin film on it. Tests were run to failure, defined as a 10 to 20 percent drop in tensile load carrying capacity, and verified by the presence of a crack, Fig. 2. Multiple crack nucleation and growth were common, as seen in Fig. 3. Thermocouple controlled induction heating with temperature verification from a second thermocouple in the gage region was used. Both thermocouples were attached in the same region for each test. Calibration of the extensometer and load cell was made by comparison with NBS standards at room

temperature with adjustment at elevated temperature. Continuous monitoring of strain, load, and temperature with periodic recording of hysteresis loops was accomplished. Irradiation was conducted in reactor grid position 7C3 in two subassemblies, X037 and X060, in EBR-II in flowing or static sodium at 450 C (max) or in argon at 750 C (max). The total time at power for X037 and X060 was about 1500 and 2550 h, respectively. The temperatures were determined from encapsulated melt wire and SiC monitors placed in the hollow ends of the specimens [10]. Flux wire monitors of iron, nickel, aluminum-cobalt, and titanium were attached alongside the gage length from which the fluence, $E > 1$ MeV, was determined for the fission averaged cross section. The reported total [11] fluence was obtained from the values ($E > 1$ MeV) by multiplying them by correction factors of 1.58, to convert to the cross section obtained from the integral equations, and 8.4, for position 7C3 in EBR-II. The fluence greater than 0.1 MeV was then obtained by correcting for the specimen vertical distance from the core midplane.

Materials

Specimens were fabricated from $\frac{5}{8}$ -in.-diameter Type 304 and 316 stainless steel rods obtained from the AEC standard heats stockpile at Pacific Northwest Laboratory [12] and from Type 304L (Ti modified) rods obtained from Oak Ridge National Laboratory and were of the following compositions and heat treatment.

Composition, %	304 Stainless Steel Heat 55697	304L Stainless Steel Heat 3756 (Ti modified) ^a	316 Stainless Steel Heat 65808
C	0.053	0.019	0.06
Mn	0.87	1.05	1.72
P	0.018	...	0.012
S	0.012	0.017	0.009
Si	0.49	...	0.40
Cr	18.41	19.23	17.30
Ni	9.71	11.22	13.30
Mo	0.18	...	2.33
Cu	0.21	...	0.065
Al	0.012
Ti	<0.01	0.22	0.003
Pb	<0.001	...	0.0014
Sn	0.008	...	0.013
Co	0.030
B	0.0005
Fe	...	balance	...
N ₂	0.032	27 ppm	0.048
Total rare earths	<0.001	...	0.001

^a Special heat made at Oak Ridge National Laboratory. Titanium, a carbide and complex boride former, was added to produce a more uniform distribution of boron and to improve the elevated-temperature ductility of the irradiated material.

Irradiation Pretreatment

Type 304L (Ti Modified)—Four-inch-diameter billet was extruded to rod and rolled with two intermediate 16-h anneals in argon at 1200 C. Final rod anneal for 1 h in argon at 929 C. Hardness HRB 66.

Type 304—Hot rolled at 1175 C to $\frac{5}{8}$ -in.-diameter rod and coiled. The coils were annealed at 1070 C for 1 h, WQ. Cut to 5-ft-length rods; to eliminate straightening effects the rods were annealed at 1010 C for $\frac{1}{2}$ h, WQ. Hardness HRB 77.

CW—Some cold-worked specimens were prepared from annealed rods after swaging 11 percent reduction in area at room temperature. Hardness HRB 92.

CST—Some specimens were prepared from chilled-swaged-tempered rods (27 percent reduction) in two steps: (1) chill in liquid nitrogen, swage 11 percent reduction in area, anneal 16 h at 700 C; (2) chill in liquid nitrogen, swage 16 percent reduction, anneal 16 h at 760 C. Hardness HRB 88.

Type 316—Hot rolled at 1200 C, final roll to coil for 0.650-in. rod stock. Coils annealed at 1065 C 1 h, WQ, pickled and straightened, cut to 5-ft lengths. Hardness HRB 84.

CW—Some cold-worked specimens were prepared from annealed rods after swaging 11 percent reduction in area at room temperature. Hardness HRB 98.

CST—Some specimens were prepared from chilled-swaged-tempered rods (27 percent reduction) in two steps as with the Type 304. Hardness HRB 98.

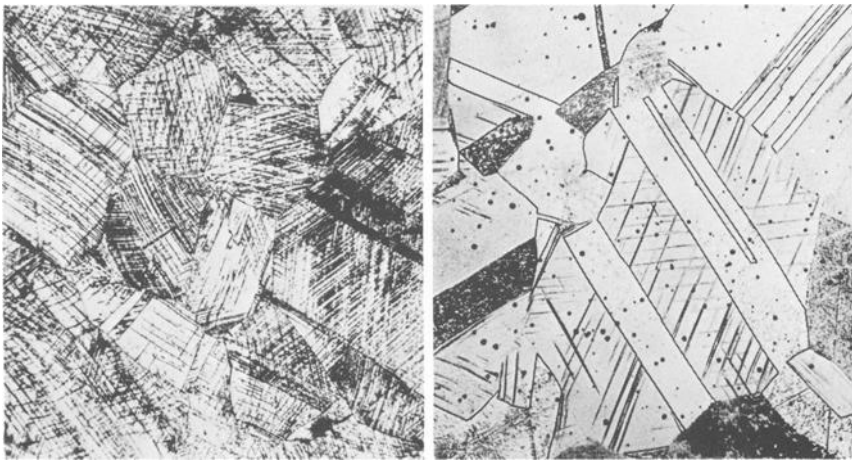


FIG. 4—Photomicrographs of unirradiated Type 316 stainless showing modified microstructure ($\times 270$): left, chilled-swaged-tempered 27 percent; right, cold-worked 11 percent.

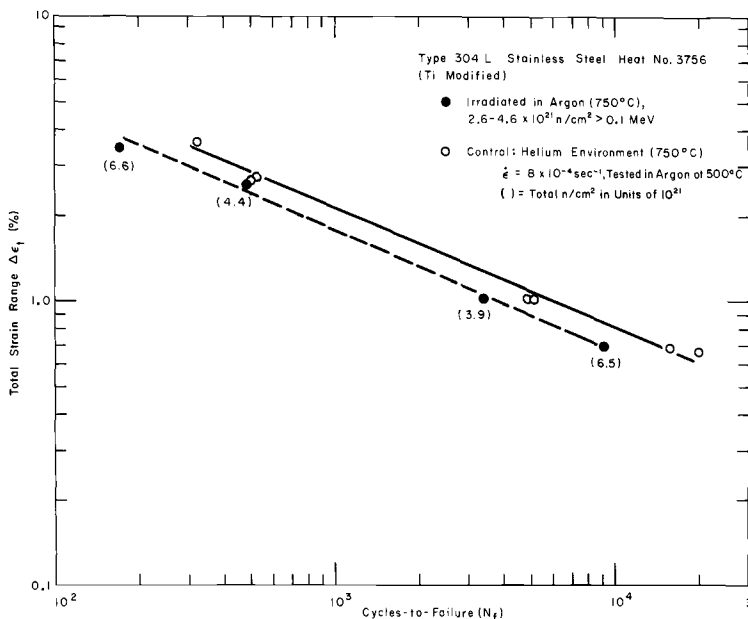


FIG. 5—Effect of irradiation on the fatigue life of Type 304L stainless steel, tested at 500 C.

Microstructures of the chilled-swaged-tempered treatment and the cold work for Type 316 are shown in Fig. 4; those for Type 304 are similar to these treatments.

Results

The effects of irradiation at 750 C on the fatigue lives of these materials appear to be slightly less than the effects after 450 C irradiation as indicated by tests conducted at similar temperatures. The 750 C irradiations will be considered first.

A slight reduction in the fatigue life of Type 304L (Ti modified), 304, and 316 stainless steel irradiated at 750 C is indicated in Figs. 5, 6, and 7. At test temperatures of 500 C for Type 304L, Fig. 5, the reduction is a factor of about 1.5 from the controls heated at 750 C for 1500 h after fabrication. This treatment was given to the controls used for comparison in Figs. 5–10, 13. In Fig. 6 for Type 304, the reduction from the Type 304 controls amounts to a factor of about 1.8. An interesting point in Fig. 6 is indicated by the addition of the line for the 304L controls, whereby it is shown that the fatigue life for the Type 304L is slightly greater than for Type 304 for equivalent conditions (unirradiated and irradiated). At test temperatures of 600 C for Type 316, Fig. 7, the reduction in irradiated fatigue life is about 1.4. The rise in test temperature toward the irradiation temperature of 750 C has, thus, not enhanced the effect of irradiation on the fatigue life.

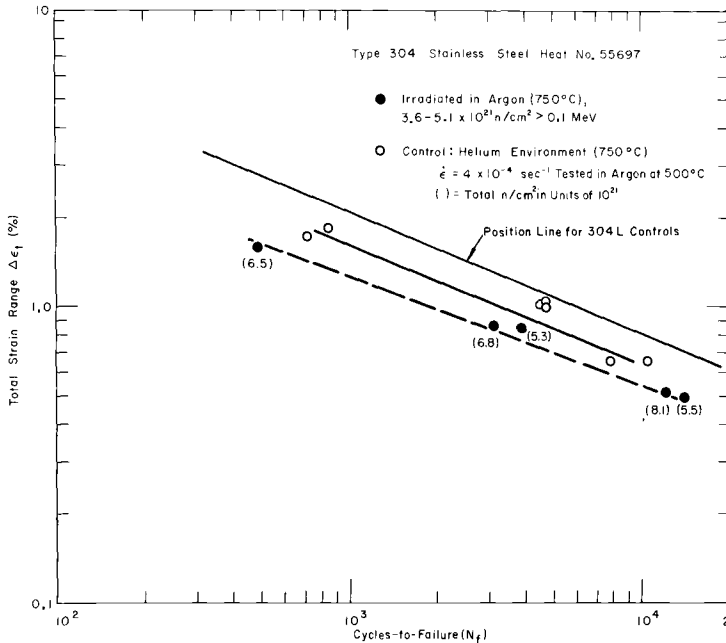


FIG. 6—Effect of irradiation on the fatigue life of Type 304 stainless steel, tested at 500 C.

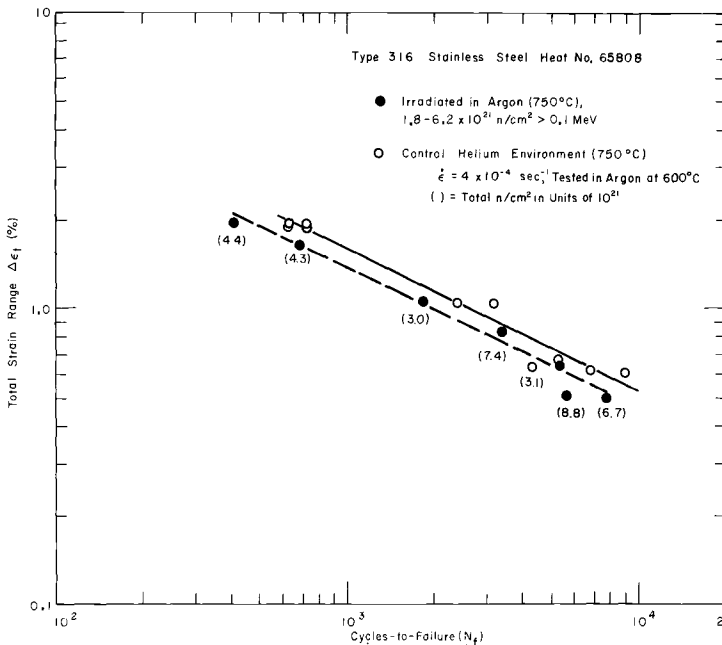


FIG. 7—Effect of irradiation on the fatigue life of Type 316 stainless steel, tested at 600 C.

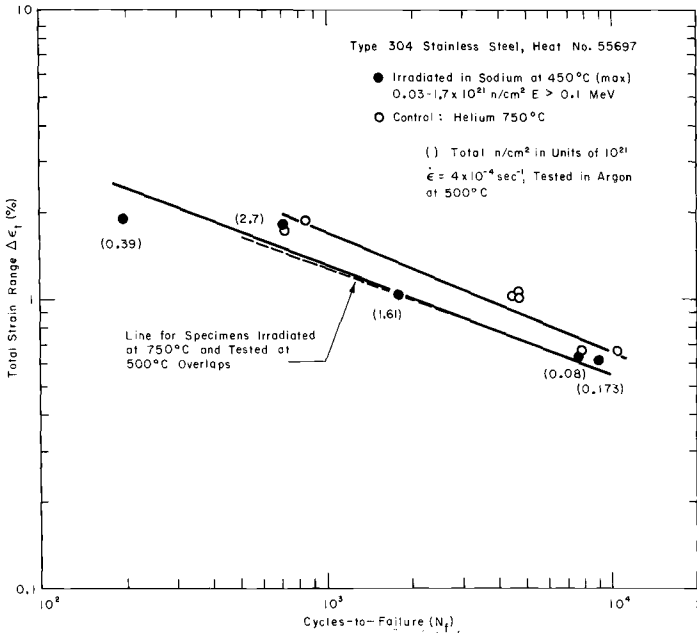


FIG. 8—Effect of irradiation at 450 C on the fatigue life of Type 304 stainless steel, tested at 500 C.

The data from the tests are given in Tables 1 through 6 for the various steels and test temperatures.

Type 304 stainless steel specimens irradiated in sodium at a temperature of 450 C and tested at 500 C have about the same reduction in fatigue life, Fig. 8, from the controls as those irradiated at 750 C. Type 316 specimens irradiated at 450 C in sodium and tested at 600 C, however, have a larger reduction in fatigue life than those irradiated at 750 C, as indicated in Fig. 9 by redrawing the line for the irradiated specimens from Fig. 6, and a 2.5 reduction from the controls. The increase in test temperature from 500 to 600 C thus enhances the irradiation effect on the fatigue life in specimens irradiated at lower temperatures than the test temperature.

The total strain range, $\Delta\epsilon_t$, is the sum of a plastic, $\Delta\epsilon_p$, and an elastic, $\Delta\epsilon_e$, component. In the low-cycle region, log-log plots of plastic strain range versus cycles to failure are linear and can be approximated by the relation $\Delta\epsilon_p N_f^\alpha = D/2$, where D is the fracture ductility and α is a material- and temperature-dependent constant. In Fig. 10 it is seen that for a given $\Delta\epsilon_t$ and $\Delta\epsilon_p$ irradiation has effected a decrease in the fatigue life; whence, for a given plastic strain range, $\Delta\epsilon_p$, and from equations for the unirradiated (u) and irradiated (i) data, a relationship exists between cycles to failure

TABLE 1—Fatigue properties of Type 304L (Ti modified) stainless steel, heat 3756, tested at 500 C.

Specimen No.	Pretest Treatment	Environment	Fluence, $E > 0.1$ MeV	Axial Strain Range			Cycles to Failure, N_f	Stress Range, $\Delta\sigma$, kg/mm ²	Strain Rate, $\dot{\epsilon}$, s ⁻¹
				Total, $\Delta\epsilon_t$, %	Plastic, $\Delta\epsilon_{pr}$, %	Elastic, $\Delta\epsilon_e$, %			
8F.....	Control ^a	He-750	0	0.66	0.42	0.24	19 857	38	8×10^{-4}
10F.....	Control	He-750	0	0.68	0.44	0.24	15 906	40	8
3F.....	Control	He-750	0	1.01	0.72	0.29	5 051	50	8
6F.....	Control	He-750	0	1.02	0.73	0.29	4 958	48	8
7F.....	Control	He-750	0	2.64	2.18	0.46	500	72	8
9F.....	Control	He-750	0	2.73	2.34	0.39	538	62	8
25F.....	Control	He-750	0	3.64	3.18	0.46	322	72	8
ID-3-19.....	Anneal	A-750	4.70×10^{21}	0.68	0.39	0.29	9 165	47	8
ID-3-21.....	Anneal	A-750	2.72	1.02	0.71	0.31	3 364	50	8
ID-3-17.....	Anneal	A-750	2.82	2.50	2.05	0.45	499	72	8
ID-3-20.....	Anneal	A-750	4.80	3.42	2.97	0.45	171	72	8

^a Control—heated at 750 C, 1500 h in helium.

TABLE 2—Fatigue properties of Type 304 stainless steel, heat 55697, tested at 400 C.

Specimen No.	Pretest Treatment	Environment ^a	Fluence, E > 0.1 MeV	Axial Strain Range			Cycles to Failure, N _f	Stress Range, Δσ, kg/mm ²	Strain Rate, ε̇, s ⁻¹
				Total, Δε _t , %	Plastic, Δε _{sp} , %	Elastic, Δε _e , %			
1E.....	Anneal	He	0	1.02	0.73	0.29	7 580	49	8 × 10 ⁻⁴
3E.....	Anneal	He	0	2.03	1.53	0.50	1 099	85	8
A46.....	Anneal	He	0	3.03	2.46	0.57	357	95.6	8
3-C-1-10.....	Anneal	S-450	0.05 × 10 ²¹	0.63	0.33	0.30	30 200	50	4
3-C-1-10.....	Anneal	S-450	0.13	2.06	1.47	0.59	483	98	4
3-E-2-14.....	CW-11%	F-450	0.07	0.72	0.33	0.39	25 277	65	8
3-C-2-9.....	CW-11%	S-450	1.24	0.72	0.30	0.42	15 041	70	8
3-E-2-11.....	CW-11%	F-450	1.63	1.48	0.98	0.50	2 883	82	8
3-E-2-13.....	CW-11%	F-450	0.20	1.52	1.04	0.48	3 005	80	8
3-C-2-8.....	CW-11%	S-450	0.42	2.56	1.98	0.58	657	96	8
3-E-2-12.....	CW-11%	F-450	0.58	2.94	2.32	0.62	396	102	8
3-C-2-6.....	CW-11%	S-450	0.07	3.47	2.83	0.64	231	108	8
3-C-2-7.....	CW-11%	S-450	0.17	3.70	3.03	0.67	195	112	8
3-C-3-7.....	CST	S-450	0.13	0.66	0.29	0.37	54 794	64	8
3-E-3-13.....	CST	F-450	0.18	0.73	0.42	0.31	13 012	53	8
3-E-3-14.....	CST	F-450	0.07	1.10	0.76	0.34	11 000	56	8
3-C-3-6.....	CST	S-450	0.06	2.10	1.62	0.48	788	80	8
3-C-3-9.....	CST	S-450	0.85	2.15	1.65	0.50	786	84	8
3-E-3-12.....	CST	F-450	0.46	2.65	2.15	0.50	610	82	8
3-E-3-11.....	CST	F-450	1.37	2.97	2.43	0.54	566	90	8
B46.....	CW-13%	As fabricated	0	1.95	1.26	0.69	1 070	114	8
B47.....	CW-13%	As fabricated	0	2.67	1.93	0.74	685	123	8

^a S = static sodium.

F = flowing sodium.

^b Annealed at 1075 C for ½ h, cooled in helium stream at 100 C/min.

TABLE 3—Fatigue properties of Type 304 stainless steel, heat 55697, tested at 500 C.

Specimen No.	Pretest Treatment	Environment	Fluence, $E > 0.1$ MeV	Axial Strain Range			Cycles to Failure, N_f	Stress Range, $\Delta\sigma$, kg/mm ²	Strain Rate, $\dot{\epsilon}$, s ⁻¹
				Total, $\Delta\epsilon_t$, %	Plastic, $\Delta\epsilon_p$, %	Elastic, $\Delta\epsilon_e$, %			
23E.....	Control	He-750	0	1.03	0.71	0.32	4 803	51	4×10^{-4}
26E.....	Control	He-750	0	1.06	0.72	0.34	4 666	54	4
27E.....	Control	He-750	0	1.71	1.25	0.46	714	72	4
32E.....	Control	He-750	0	0.63	0.34	0.29	10 407	48	4
38E.....	Control	He-750	0	1.00	0.67	0.33	4 698	54	4
39E.....	Control	He-750	0	0.65	0.34	0.31	7 969	50	4
40E.....	Control	He-750	0	1.88	1.45	0.43	832	72	4
3-C-1-6.....	Anneal	S-450	1.70×10^{21}	1.80	1.32	0.48	717	77	4
3-C-1-7.....	Anneal	S-450	0.93	1.05	0.67	0.38	1 797	60	4
3-E-1-14.....	Anneal	F-450	0.07	0.62	0.33	0.29	9 000	46	4
3-E-1-13.....	Anneal	F-450	0.18	1.94	1.41	0.53	197	86	4
3-E-1-15.....	Anneal	F-450	0.03	0.63	0.32	0.31	7 690	48	4
1-D-7-68.....	Anneal	A-740	4.00	0.49	0.23	0.26	14 025	42	4
1-D-2-70.....	Anneal	A-750	5.20	0.51	0.20	0.31	12 194	50	4
1-D-7-66.....	Anneal	A-750	3.60	0.84	0.50	0.34	3 912	54	4
1-D-7-67.....	Anneal	A-750	4.90	0.86	0.51	0.35	3 162	56	4
1-D-2-74.....	Anneal	A-750	4.50	1.60	1.17	0.43	490	68	4

TABLE 4—Fatigue properties of Type 316 stainless steel, heat 65808, tested at 400 C.

Specimen No.	Pretest Treatment	Environment	Fluence, $E > 0.1$ MeV	Axial Strain Range			Cycles to Failure, N_f	Stress Range, $\Delta\sigma$, kg/mm ²	Strain Rate, $\dot{\epsilon}$, s ⁻¹
				Total, $\Delta\epsilon_t$, %	Plastic, $\Delta\epsilon_p$, %	Elastic, $\Delta\epsilon_e$, %			
3-C-4-8	Anneal	S-450	0.38×10^{21}	0.72	0.35	0.37	23 835	64	4×10^{-4}
3-C-4-9	Anneal	S-450	0.86	1.09	0.69	0.40	11 000	70	4
3-E-4-11	Anneal	F-450	0.03	1.99	1.45	0.54	1 350	94	4
3-C-5-8	CW-11%	S-450	0.4	0.76	0.26	0.50	23 956	86	8
3-E-5-12	CW-11%	F-450	0.55	1.52	0.99	0.53	3 112	92	8
3-E-5-13	CW-11%	F-450	0.19	2.53	1.85	0.68	521	116	8
3-C-5-7	CW-11%	S-450	0.16	3.01	2.29	0.72	249	123	8
3-E-5-15	CW-11%	F-450	0.03	3.45	2.71	0.74	198	127	8
3-C-5-10	CW-11%	S-450	2.12	4.15	3.30	0.85	88	145	8
D-47	Anneal	He	0	2.05	1.54	0.51	1 537	87	8
D-51	Anneal	He	0	2.87	2.21	0.68	235	116	8
E-47	CW-13%	As fabricated	0	2.05	1.33	0.72	1 568	124	8
E-48	CW-13%	As fabricated	0	2.59	1.87	0.72	875	124	8

TABLE 5—Fatigue properties of Type 316 stainless steel, heat 65808, tested at 600 C.

Specimen No.	Pretest Treatment	Environment	Fluence, $E > 0.1$ MeV	Axial Strain Range			Cycles to Failure, N_f	Stress Range, $\Delta\sigma$, kg/mm ²	Strain Rate, $\dot{\epsilon}$, s ⁻¹
				Total, $\Delta\epsilon_t$, %	Plastic, $\Delta\epsilon_p$, %	Elastic, $\Delta\epsilon_e$, %			
18D	Control	He-750	0	0.60	0.28	0.32	8 844	50	4 × 10 ⁻⁴
19D	Control	He-750	0	0.62	0.30	0.32	6 922	50	4
38D	Control	He-750	0	0.63	0.27	0.36	4 333	56	4
39D	Control	He-750	0	0.66	0.28	0.38	5 270	60	4
17D	Control	He-750	0	1.02	0.62	0.40	3 181	62	4
16D	Control	He-750	0	1.04	0.65	0.39	2 383	62	4
36D	Control	He-750	0	1.92	1.43	0.49	702	78	4
40D	Control	He-750	0	1.92	1.45	0.47	607	74	4
41D	Control	He-750	0	1.96	1.55	0.39	703	64	4
31D	Control	He-750	0	1.99	1.49	0.50	621	78	4
3-E-4-14	Anneal	F-450	0.71 × 10 ²¹	0.66	0.25	0.41	7 390	65	4
3-C-4-7	Anneal	S-450	0.14	0.68	0.28	0.40	3 429	62	4
3-E-4-12	Anneal	F-450	0.09	0.71	0.34	0.37	3 008	58	8
3-E-4-15	Anneal	F-450	1.98	1.08	0.63	0.45	765	71	4
3-C-4-6	Anneal	S-450	0.06	1.91	1.42	0.49	248	74	4
3-E-4-13	Anneal	F-450	0.24	2.46	1.91	0.55	111	87	8
1-D-1-71	Anneal	A-750	4.3	0.49	0.22	0.27	7 788	42	4
3-E-4-17	Anneal	A-750	6.3	0.51	0.20	0.31	5 683	50	4
1-D-6-80	Anneal	A-750	2.15	0.64	0.24	0.40	5 440	63	4
1-D-1-74	Anneal	A-750	5.4	0.82	0.46	0.36	3 389	55	4
1-D-6-76	Anneal	A-750	1.94	1.06	0.57	0.49	1 831	76	4
1-D-1-75	Anneal	A-750	3.0	1.61	1.14	0.47	682	74	4
1-D-6-79	Anneal	A-750	3.22	1.95	1.45	0.50	403	78	4
3-C-6-6	CST	S-450	0.06	0.65	0.26	0.39	8 942	60	8
3-C-6-10	CST	S-450	1.42	0.71	0.27	0.44	6 937	70	8
3-E-5-12	CST	F-450	0.44	0.72	0.28	0.44	5 304	70	8

3-E-5-14.....	CST	F-450	0.07	1.07	0.59	0.48	1 464	76	8
3-C-6-7.....	CST	S-450	0.13	1.05	0.55	0.50	1 326	80	8
3-C-6-9.....	CST	S-450	0.71	2.23	1.69	0.54	316	86	8
3-E-6-11.....	CST	F-450	1.31	2.41	1.84	0.57	283	91	8
3-E-6-15.....	CST	F-450	0.03	2.98	2.31	0.67	115	106	8

TABLE 6—Fatigue properties of Type 316 stainless steel, heat 65808, tested at 700 C.

Specimen No.	Pretest Treatment	Environment	Fluence, $E > 0.1$ MeV	Axial Strain Range				Stress Range, $\Delta\sigma$, kg/mm ²	Strain Rate, $\dot{\epsilon}$, s ⁻¹
				Total, $\Delta\epsilon_t$, %	Plastic, $\Delta\epsilon_p$, %	Elastic, $\Delta\epsilon_e$, %	Cycles to Failure, N_f		
3-D-4-2	Anneal	A-750	8.52×10^{21}	0.56	0.25	0.31	1 975	46	8×10^{-4}
3-D-4-3	Anneal	A-750	9.27	1.02	0.66	0.36	220	54	8
3-D-4-1	Anneal	A-750	5.65	2.43	2.00	0.43	87	65	8
3-D-5-2	CW-11%	A-750	8.5	0.56	0.26	0.30	1 603	44	8
3-D-5-5	CW-11%	A-750	6.23	1.03	0.63	0.40	495	60	8
3-D-5-1	CW-11%	A-750	6.2	2.43	1.98	0.45	134	68	8
3-D-6-4	CST	A-750	5.1	0.54	0.16	0.38	6 600	58	8
3-D-6-3	CST	A-750	7.14	1.14	0.75	0.39	565	60	8
3-D-6-2	CST	A-750	5.42	2.44	1.97	0.47	114	70	8
D-50	Anneal	He-1075	0	2.56	2.11	0.44	141	66	8

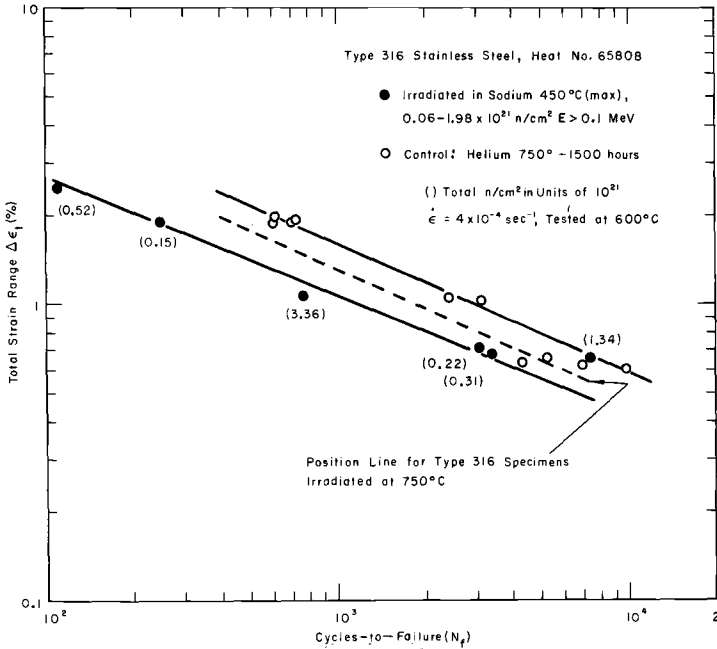


FIG. 9—Effect of irradiation at 450 C on the fatigue life of Type 316 stainless steel, tested at 600 C.

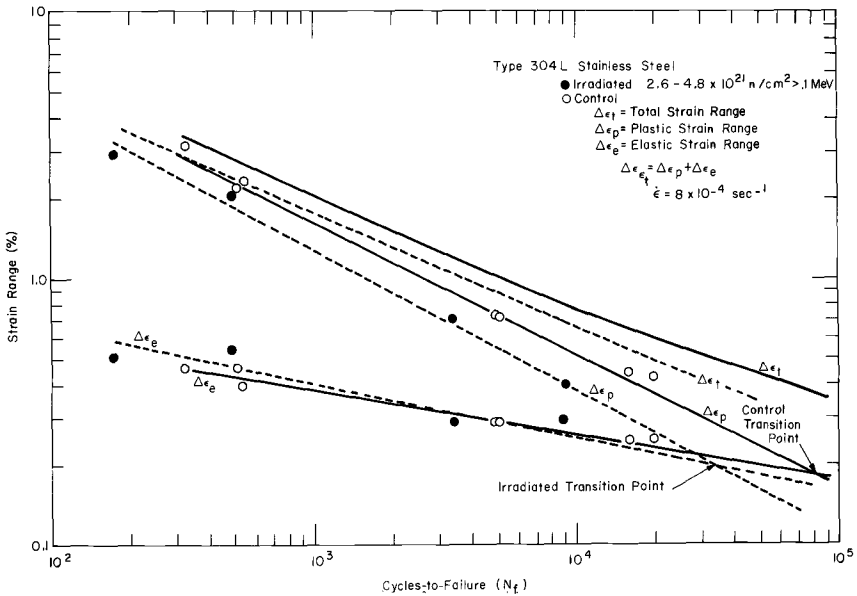


FIG. 10—Comparison of strain range components for Type 304L stainless steel, tested at 500 C.

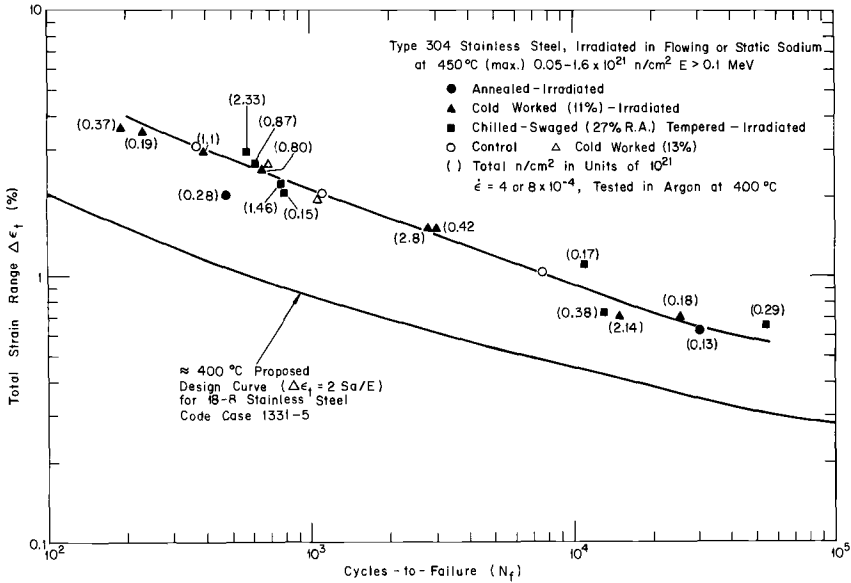


FIG. 11—Summary of the irradiation effects on the fatigue life of Type 304 stainless steel, tested at 400 C.

and fracture ductility in the form $(N_f)_i = (N_f)u(Di/Du)^{1/\alpha}$. Thus, changes in fracture ductility are indicated to be a dominant factor in the decrease in fatigue life after irradiation. Coffin [13] examined the relationship between fatigue ductility and tensile ductility and found that surface oxidation and cyclic specimen shape changes, in addition to the strong ductility effects, influenced the fatigue life. The fatigue ductility is an equivalent ductility defined by the equation when $\alpha = 1/2$. Further, Fig. 10 shows a shift in the transition point (intersection of the $\Delta\epsilon_p$ and $\Delta\epsilon_e$ curves) to the left for the irradiated material. At the left of the transition point, $\Delta\epsilon_p$ is the major component of the total strain range which affects the fatigue life.

It is noted that in the figures a straight line fit is used to represent the data when the plastic strain range is the principal or dominant strain variable, for example, the $\Delta\epsilon_p$ curve in Fig. 10, but that a curve is used to fit the data when the sum of the plastic and elastic components are representative, for example, the upper curve in Fig. 10, and the curves in Figs. 11, 12, and 14.

Fatigue tests were conducted at 400 C (approximately reactor nozzle inlet temperatures) on Type 304 and 316 specimens that had been irradiated at 450 C in flowing or static sodium. The material had received the cold work (CW) or the chilled-swaged-tempered (CST) treatment prior to irradiation. A few tests on annealed-irradiated specimens were also con-

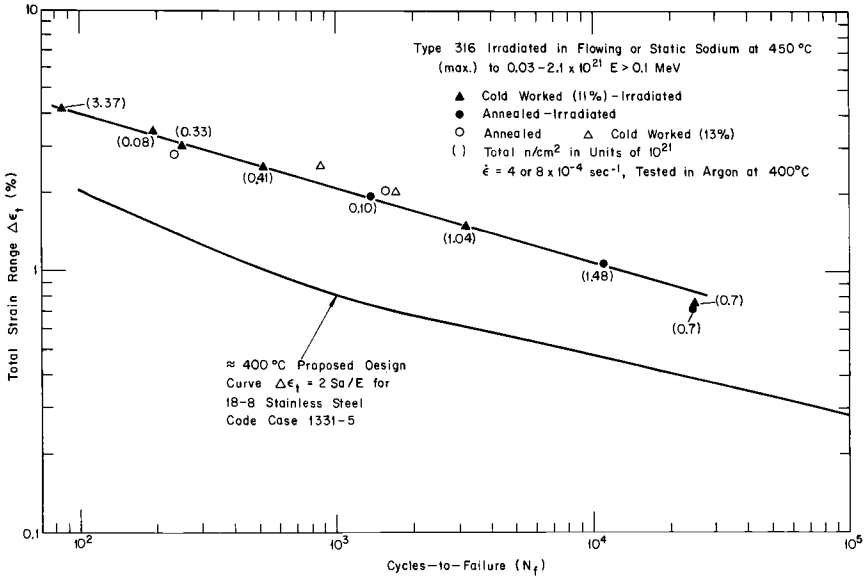


FIG. 12—Summary of the irradiation effects on the fatigue life of Type 316 stainless steel, tested at 400 C.

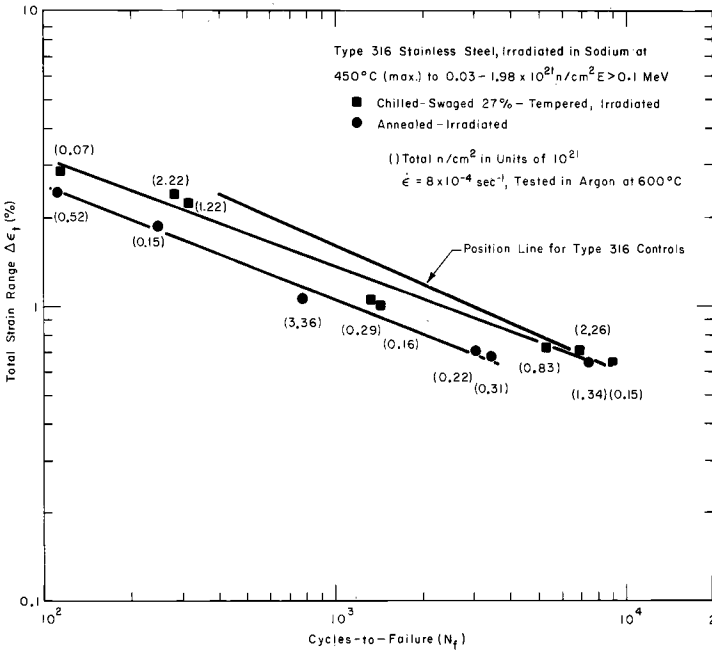


FIG. 13—Effect of pretreatment on the fatigue life of irradiated Type 316 stainless steel, tested at 600 C.

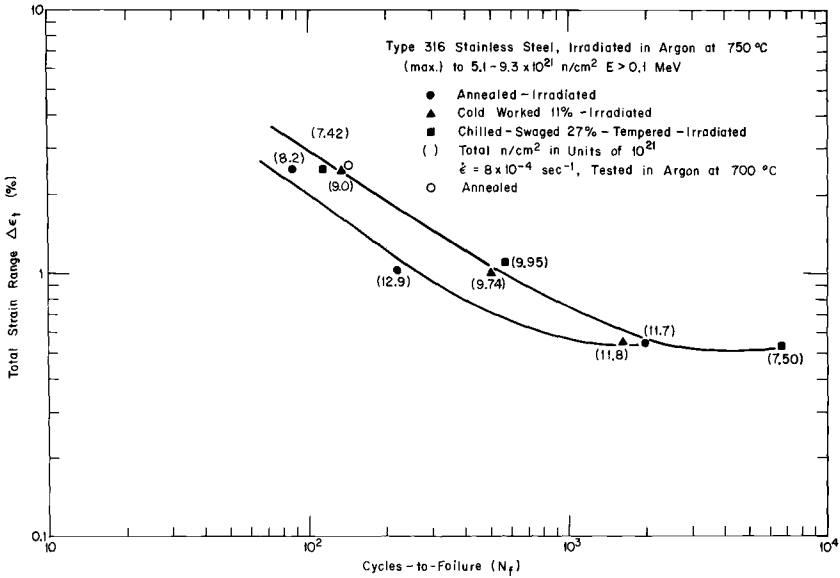


FIG. 14—Effect of cold work and pretreatment on the irradiated fatigue life of Type 316 stainless steel, tested at 700 C.

ducted. No difference in the fatigue behavior of specimens irradiated in flowing or static sodium could be discerned. The data are compared with a proposed design curve for 18-8 stainless steel in Figs. 11 and 12. The proposed design curves in Figs. 11, 12, 16, and 17 were prepared by the American Society of Mechanical Engineers (ASME) Committee-Subgroup on Elevated Temperature Design and are referred to as ASME Code Case 1331-5.

The CW or CST treatment appeared to improve the irradiated fatigue life, and the effect seemed to increase with increase in test temperature from 400 to 600 and 700 C, Figs. 11, 12, 13, and 14. This tendency to improve with temperature is contrary to what is usually found in unirradiated material where cold work at elevated temperature tends to strain soften, with resultant little or no effect on overall fatigue life. At 400 C CW or CST treatments appear to be beneficial to the fatigue behavior of irradiated Type 304 (limited data), Fig. 11; however, no effect was found for Type 316, Fig. 12. At 600 C (Fig. 13) and 700 C (Fig. 14) there is a factor of two improvement in the fatigue life of the CW-irradiated and the CST-irradiated specimens when compared with the annealed-irradiated specimens at the same temperatures. The line for the Type 316 controls is

drawn in Fig. 13, which indicates that at 600 C the fatigue life of the pretreatment (CST) specimens is not as great as that of the controls.

Hardness values taken from the shoulders of several irradiated specimens of Type 316 stainless in the various pretreatment conditions are given in Table 7. It can be concluded that (1) all the values decreased from the un-irradiated hardness, (2) the hardness of the cold-worked and the chilled-swaged-tempered irradiated specimens is greater than that of the annealed-irradiated specimens, and (3) the hardness of the chilled-swaged-tempered is slightly greater than the cold-worked and irradiated material, although the initial hardness was the same.

It is seen that the hardness values of the specimens subjected to the 750 C irradiations are about the same as those subjected to the 450 C irradiations even though the irradiation time in both cases was 2550 h but the fluences were not the same. The irradiation, and not the test temperature, controls hardness, since the shoulder was always colder. It might be argued that the beneficial effect of pretreatment was due to compressive surface strains introduced by swaging. However, while no diametral hardness measurements were made, specimen machining reduced the gage section by 86 percent; therefore, the increase in fatigue life of the worked material is mostly due to bulk rather than to a surface property.

Boron monitors were strategically placed in the ends of specimens after the irradiations were analyzed for ^{10}B burnup and lithium production, from which it was determined that the transmutation of the boron in the steel should be a small fraction (0.1 to 0.2 percent) of the original boron. Any helium production should thus come principally from fast nuclear reactions with constituents of the stainless steel. Table 8 gives helium determinations from sections of several Type 304 specimens after fatigue testing. Helium contents obtained after 750 C irradiations were similar to those obtained after 450 C irradiation to lower fluence. No evidence of helium bubbles was found in electron microscopy investigations.

In order to evaluate further the nature of changes in the cold-worked and pretreatment specimens after irradiation, the plastic and elastic components are replotted in Fig. 15 from Fig. 13 for Type 316 irradiated at 450 C and tested at 600 C. Similar plots were obtained for the data in Figs. 11 and 14, which are not presented. Although there is some scatter in the data, especially at strain ranges in the region of the transition from plastic to elastic dominated fatigue behavior, it is seen for a given number of cycles to failure that the amount of plastic strain that can be tolerated by the CST treatment is greater than that tolerated by the annealed condition, again illustrating the beneficial effect of the pretreatment. The scatter in the data, inherent in fatigue testing, increases with decreasing strain [14] and can be due to a number of factors, including a variation in surface finish resulting from irradiation.

A summary of the data for Types 304 and 304L at the 500 C test temper-

TABLE 7—Hardness of Type 316 pretreated irradiated specimens.

Pretreatment	Specimen No.	Fluence, n/cm ² (total)	Test Temperature, deg C	Irradiation Temperature, deg C	Hardness, ^b HRB
Annealed-straightened. hardness HRB 84	3-D-4-1	8.2 × 10 ²¹	700	750	81.9
	3-D-4-3	12.9	700	750	82.5
	3-C-4-6	0.15	600	450	81.9
Swaged, 11% reduction in area. hardness HRB 98	3-E-4-15	3.36	600	450	82.5
	3-D-5-1	9.0	700	750	88.4
	3-D-5-5	9.74	700	750	88.9
Chilled-swaged-tempered, 27% reduction in area... hardness HRB 98	3-D-6-2	7.42	700	750	92.6
	3-D-6-3	9.95	700	750	91.7
	3-C-6-9	1.22	600	450	90.9
	3-E-6-11	2.22	600	450	91.3

^a At temperature for 2550 h.

^b Average of three readings.

TABLE 8—Helium determinations for Type 304 stainless steel.

Specimen No.	Fluence, n/cm ² , E > 1 Mev	Irradiation Temperature, deg C	Helium Content		Ratio of Determined to Calculated ^a
			ppm wt	Atomic Fraction	
I-D-7-69	2.72 × 10 ²⁰	750	0.03	4.1 × 10 ⁻⁷	1.9
I-D-2-70	6.07	750	0.03	4.1	0.8
III-C-1-9	0.21	450	0.03	4.1	24
III-C-3-7	0.22	450	0.02	2.8	19
^b	6 × 10 ²¹	290	17	2.37 × 10 ⁻⁴	45

^a Alter, H. and Weber, C. E., *Journal of Nuclear Materials*, JNUMA, Vol. 161, 1965, p. 68.

^b Robbins, R. E., *Journal of Nuclear Materials*, JNUMA, Vol. 33, 1969, pp. 101-102.

ature is presented in Fig. 16 and for Type 316 at 600 C test temperature in Fig. 17. A proposed design curve for 18-8 stainless steel (ASME Code Case 1331-5) also has been drawn on the figures, from which it is seen that at fluences less than 10²² n/cm², E > 0.1 MeV, the proposed design curves are conservative.

The cyclic hardening (or softening) behavior for these materials in the annealed condition is typified by the data presented in Fig. 18 for Type

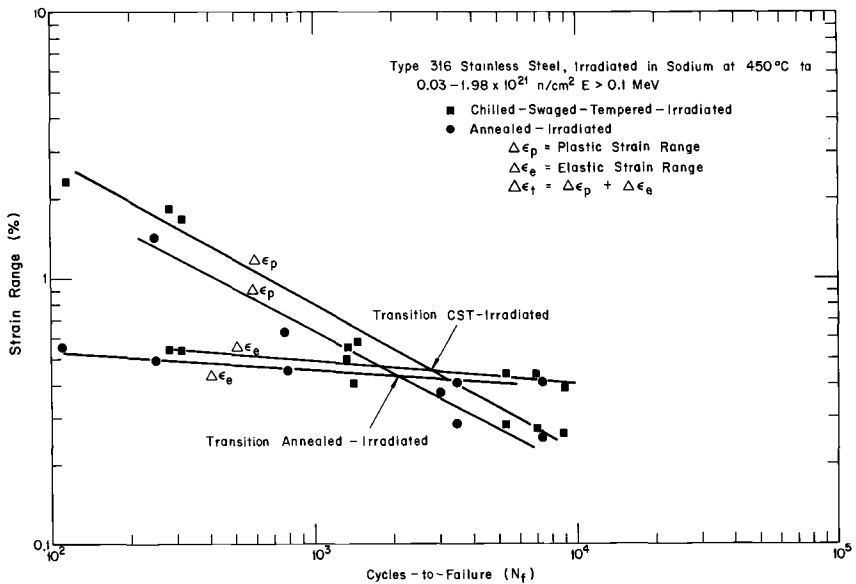


FIG. 15—Comparison of strain range components for Type 316 stainless steel, tested at 600 C. Total strain range is given in Fig. 13.

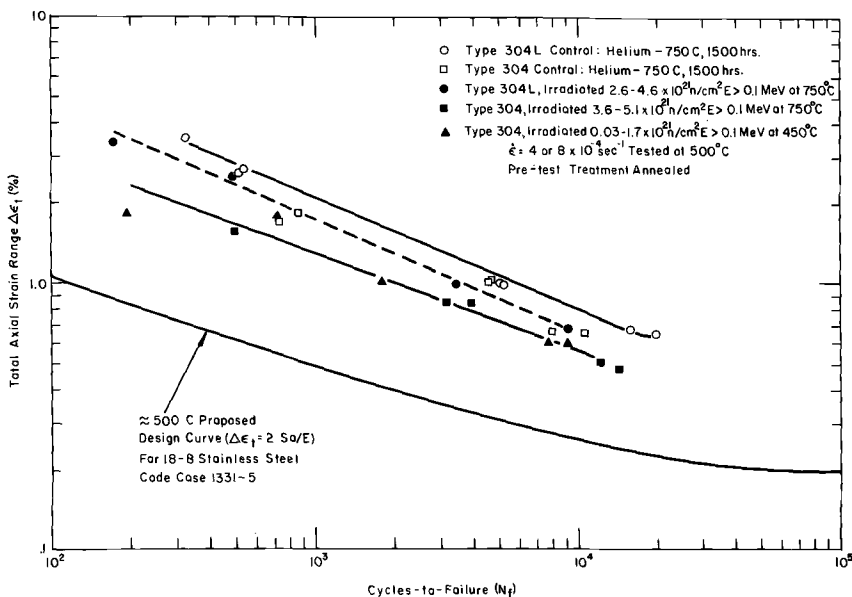


FIG. 16—Summary of fatigue data compared with proposed design curve for 18-8 stainless steel for 500 C.

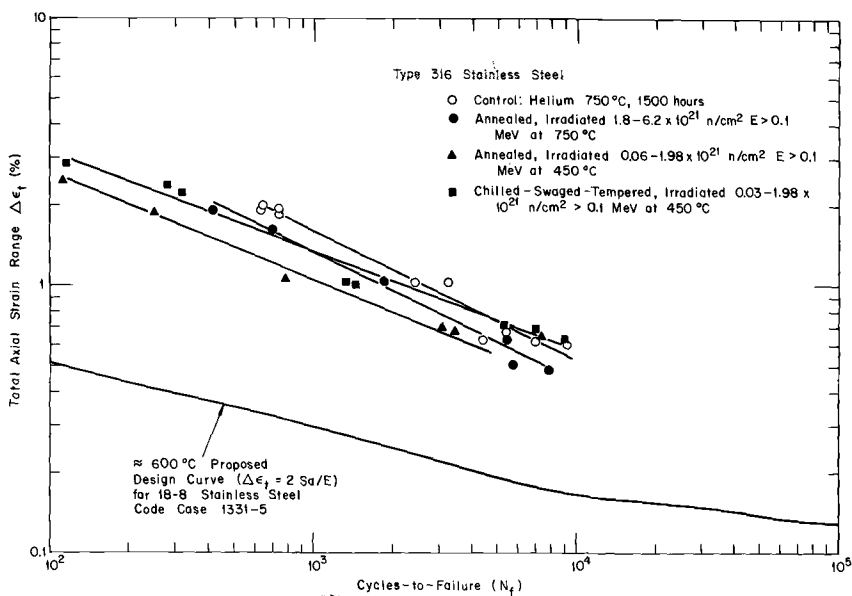


FIG. 17—Summary of fatigue data compared with proposed design curve for 18-8 stainless steel for 600 C.

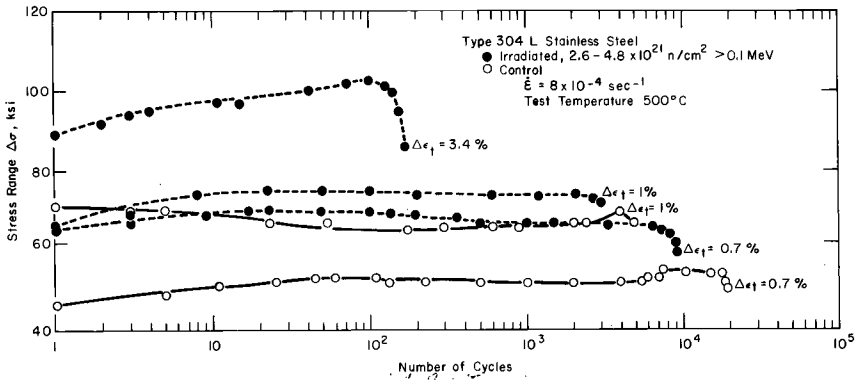


FIG. 18—Comparison of cyclic hardening (softening) behavior for Type 304L stainless steel in the pre and postirradiated conditions.

304L. Generally, it was found that the stress range required to produce a given strain range in irradiated material was slightly greater than that required to produce the same in the unirradiated material, which is indicative of a small yield increase.

A change from a primarily transgranular crack propagation to mixed mode crack propagation between 500 and 600 C (Fig. 19) occurred for the irradiated specimens. Electron transmission micrographs are presented in Fig. 20 from which the following can be seen: (1) Fatigue induced plastic

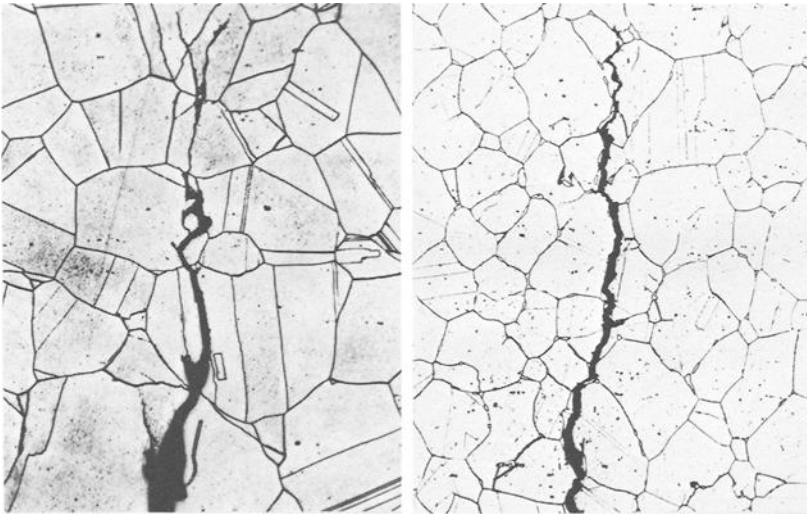


FIG. 19—Photomicrographs showing modes of crack propagation in irradiated stainless steels, tested at 500 and 600 C ($\times 195$). On the left, primarily transgranular crack propagation in Type 304 stainless steel tested at 500 C (specimen 7-69); on the right, mixed mode crack propagation in Type 316 stainless steel tested at 600 C (specimen 1-73).

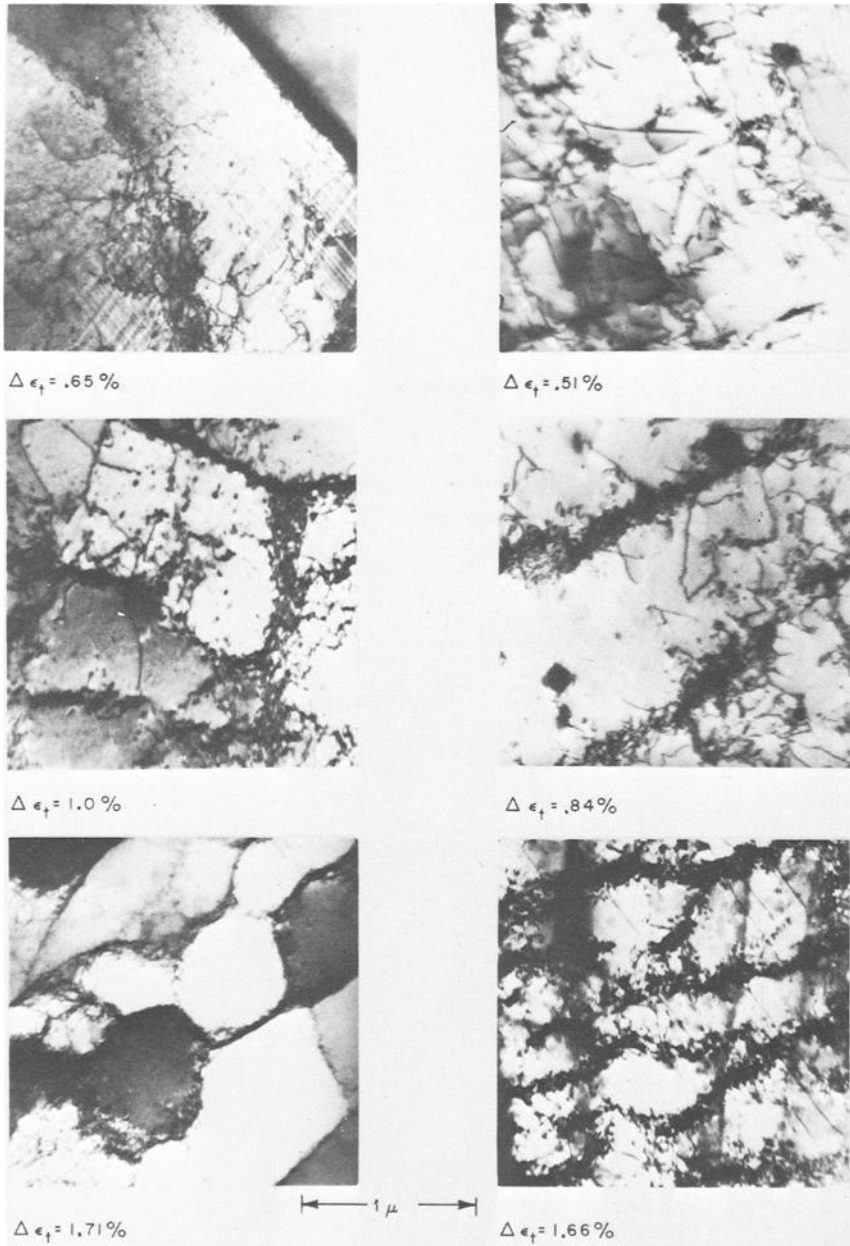


FIG. 20—Comparison of fatigue induced substructure in Type 304 stainless steel, tested at 500 C at various strain ranges: left, unirradiated control; right, irradiated 2 to 5×10^{21} n/cm², E > 1 MeV, 750 C.

deformation results in the formation of many dislocations which arrange themselves into clusters and cell walls or subboundaries as the amount of plastic deformation is increased. The effect is a function of strain and temperature and would perhaps be more pronounced if the strains occurred during equal time at temperature. A longer time is required to produce failure at lower strain ranges. (2) Differences exist in fatigue induced dislocation cell substructure between the irradiated specimens and the controls at equivalent strain ranges, temperatures, and time. The cell structure in the former is less closed, with dislocations in a more open or pinned arrangement.

Discussion

Although the irradiation induced reductions in fatigue life are small, the trends are believed to be significant. Ductility is believed to be the property which controls the high-strain fatigue life of irradiated as well as unirradiated stainless steels. Factors which affect the ductility in these tests should, therefore, be the cause of the reported reductions in fatigue lives of the irradiated specimens. Three chief elements influencing ductility [15] in austenitic steels are (1) metallurgical: grain size, crystal orientation, solutes, second phases including voids and helium; (2) environmental: temperature and strain rate; and (3) external geometry: specimen size and shape, stress state, and surface conditions. In tension tests of irradiated steels at temperatures above 500 C the major metallurgical factor is believed to be changes in second-phase content and morphology.

Reasons for changes in fatigue life from the 750 and 450 C irradiations are of principal concern. In consideration of the fatigue properties of specimens irradiated at 750 C, it was noted previously that above 600 C ductility was independent of irradiation temperature and dependent upon deformation temperature. The grain size (43 to 61 μm) did not change measurably during irradiation at 750 C for 1500 h. The environmental and external geometry were fixed by the test conditions and voids were not seen; hence, carbide precipitates or helium are thought to be influencing any changes that occur in the irradiated fatigue lives.

The greater high-strain fatigue life of the Type 304L (Ti modified) irradiated and control specimens as compared with the Type 304 is consistent with the lower strength and higher ductility associated with this low-carbon stainless steel. The addition of titanium—a complex boride and carbide former—which nucleates precipitation throughout the grains may contribute to a greater ductility and, hence, high-strain fatigue life by reduction of the carbon in solution.

Austenitic stainless steels when heated at 430 to 800 C are known to become sensitized by the precipitation of chromium carbides at the grain

boundaries. This sensitization generally has a negligible effect [16] on mechanical properties but has been shown to decrease the high-cycle fatigue life [17]. At the low-temperature end of the region, the precipitates are fine and closely spaced, and chromium depleted regions at the grain boundaries occur. At the high-temperature end the precipitates are relatively coarse, and dispersed chromium diffuses into depleted areas and sensitization does not occur. Upon prolonged heating at temperatures of 750 C, it has been reported [18] that measurable changes in the mechanical properties occur. For instance, heating of Type 316 stainless steel at 750 C for 1300 h resulted in a decrease in ductility, reported as reduction in area, of 29 percent; little further change occurred up to 3000 h. At 650 C or lower, however, longer times were required to effect a small change in the resultant properties; for example, at 650 C, 3000 h were required for measurable change. In an electron microprobe analysis of a Type 304 control specimen heated at 750 C for 1500 h, the grain boundary appeared rich in chromium with little evidence of a depleted zone. Measurements by electron microscopy of the carbide precipitate size in the controls and irradiated material indicated that compared with the controls at 750 C the precipitate decreased in density and increased in size as a function of irradiation fluence.

The similar reductions in irradiated fatigue life of the three stainless grades irradiated at 750 C suggest the possibility of a single responsible mechanism. As was pointed out above, carbide behavior can be important; however, the low carbon content of 304L indicates that an irradiation induced defect rather than carbide behavior is responsible for decreased fatigue life. Further, the similar fatigue life of Type 304 irradiated at 750 or 450 C, with resultant differences in carbide content and distribution but with a near identical helium content, indicates again an irradiation effect. The greater fatigue life of the pretreated material is indicative of a beneficial microstructure effect at elevated test temperatures, since as was previously pointed out residual stresses tend to relax out in cyclic tests. The differences in fatigue induced substructure shown in Fig. 20 suggest the presence of an irradiation induced defect which effectively impedes cell formation. Pretreatment which introduces a complex substructure prior to irradiation evidently helps to negate the irradiation effect by substructure-defect interaction. However, the possibility of other factors such as cold work induced sigma phase [18, 20] precipitation with possible grain boundary strengthening at elevated temperatures cannot be discounted.

Although the fatigue behavior at those fluences is believed to be defined by the irradiation temperatures, at fluences where voids are abundant an intermediate irradiation temperature may produce a greater loss in ductility and fatigue life.

Conclusions

From the results of the low-cycle fatigue tests conducted on Types 304, 304L, and 316 stainless steel, the following conclusions were drawn:

1. Irradiations at temperatures of 450 or 750 C to fluences less than 10^{22} n/cm², $E > 0.1$ MeV, resulted in a reduction in fatigue life by at most a factor of 2.5, which was attributed to an irradiation produced defect.
2. Material pretreatment consisting of either cold work by swaging or a chill-swage-temper treatment was found to be beneficial when the post-irradiation fatigue tests were conducted at 600 and 700 C.
3. Generally, a given strain range required the stress range to be greater in the irradiated material, indicative of a small yield increase.
4. Changes in fracture ductility are indicated to be a dominant factor in the decrease in fatigue life after irradiation.

Acknowledgments

We gratefully acknowledge the support of the Fuels and Materials Branch, USAEC, and express our appreciation to M. D. Harper, G. A. Rigby, and W. O. Williams, who helped in the experimental work.

References

- [1] Roake, W. E. and Tobin, J. C., *Nuclear News*, NUNWA, Vol. 13, March 1970, pp. 56-61.
- [2] Reynolds, M. B. in *Flow and Fracture of Metals and Alloys in Nuclear Environment*, ASTM STP 380, American Society for Testing and Materials, 1965, p. 323.
- [3] Gibbons, W. G., Mikoleit, A. E., and O'Donnel, W. J. in *The Effects of Radiation on Structural Metals*, ASTM STP 426, American Society for Testing and Materials, 1967, p. 408.
- [4] Conway, J. B., Berling, J. T., and Stenz, R. H., "New Correlations Involving the Low-Cycle Fatigue and Short-Term Behavior of Irradiated and Unirradiated 304 and 316 Stainless Steel," GEMP-726, December 1969.
- [5] Kangilaski, M. and Shoher, F. R., *Nuclear Applications*, NUAPA, Vol. 5, Oct. 1968, pp. 283-285.
- [6] Martin, W. R. and Weir, J. R. in *ASTM STP 380*, American Society for Testing and Materials, 1965, pp. 251-268.
- [7] Holmes, J. J., Robbins, R. E., and Lovell, A. J. in *Irradiation Effects in Structural Alloys for Thermal and Fast Reactors*, ASTM STP 457, American Society for Testing and Materials, 1969, pp. 371-389.
- [8] Zackay, V. F., Parker, E. R., Fahr, D., and Busch, R., *Transactions*, American Society for Metals, TASEA, Vol. 60, 1967, pp. 252-259.
- [9] DePaul, R. A. and Pense, A. W. in *Fatigue at High Temperature*, ASTM STP 459, American Society for Testing and Materials, 1969, pp. 130-143.
- [10] Beeston, J. M., Ellingford, M. W., and Brinkman, C. R., "Fatigue Specimen Capsules, EBR-II MARK B-7 Subassembly," CONF-690910, 9-10 Sept. 1969, pp. 24-37.
- [11] Personal communication with John Jackson, Battelle Memorial Institute, Pacific Northwest Laboratory, Richland, Wash., 23 Sept. 1969.
- [12] T. T. Claudson, "Fabrication History of Alloys Used in the Irradiation Effects on Reactor Structural Materials Program," BNWL-CC-236, Oct. 1965.
- [13] Coffin, L. F., Jr., *Thermal and High Strain Fatigue*, Metals and Metallurgy Trust, 1967, pp. 171-197.

- [14] Raske, D. T. and Morrow, J. in *Manual on Low Cycle Fatigue Testing, ASTM STP 465*, American Society for Testing and Materials, 1969, p. 3.
- [15] *Ductility*, ASM Seminar, 14–15 Oct. 1967, American Society for Metals, Metals Park, Ohio, 1968: (a) Dieter, G. E., pp. 1–30; (b) Rogers, H. C., pp. 31–62.
- [16] *ASM Metals Handbook*, 8th ed., American Society for Metals, Metals Park, Ohio, 1961, p. 422.
- [17] Ueda, J. and Yamane, T., “The Relationship Between Carbide Precipitation and Fatigue Strength of an 18-8 Stainless Steel,” Proceedings of the International Conference on the Strength of Metals and Alloys, Japan Institute of Metals, Tokyo, 1967, pp. 1020–1022.
- [18] Edwards, A. M. and Nicholson, A., *Journal of the Iron and Steel Institute, JISIA*, Vol. 207, Aug. 1969, p. 1067.
- [19] Tisinai, G. F., Stanley, J. K., and Samans, C. H., *Journal of Metals, JOMTA*, Vol. 206, May 1956, pp. 600–604.
- [20] Blenkinsop, P. A. and Nutting, J., *Journal of the Iron and Steel Institute, JISIA*, Sept. 1967, pp. 953–958.

DISCUSSION

*A. L. Bement*¹—The development of alpha and epsilon phases in austenitic stainless steel is of interest as a possible metallurgical approach for reducing radiation induced swelling. The volume percent of alpha phase formed per unit cold work should increase with decreasing temperature and with decreasing carbon content in order of 316, 304, and 304L stainless steels. Is it possible that the favorable fatigue resistance of 304L and chilled-swaged material can be attributed to either the presence of alpha phase prior to fatigue testing or the formation of alpha phase at the fatigue crack root during fatigue testing?

J. M. Beeston (authors' closure)—Phase transformations that can occur in the metastable austenitic steels of the 18-8 variety due to deformation and aging temperatures are of importance to the structure and properties of these steels. Although the question as to whether the α phase in 18-8 steels can be produced by quenching may be controversial,^{2,3} its increased formation with percent cold work as some function of temperature appears to be established.⁴ Mangonon and Thomas conclude that further thermal nucleation of α phase is achieved by aging up to 400 C but that softening occurs by aging at 500 C and above due to a decrease in percent α phase. The ϵ phase could not be detected above 400 C.

By X-ray diffraction of a specimen, cold-worked and irradiated at 450 C and fatigue tested at 400 C, we could see evidence of the α phase. X-ray line broadening of the (111) γ peak due to irradiation obscured the (110) α peak so that the evidence is based on the (211) α and the (200) α peaks which have the next highest intensity. X-ray diffraction of a chill-swage-temper specimen at the same irradiation and test temperature yielded negative indications of α phase. It is noted that the CST specimens were given a final temper at 760 C before irradiation and testing to stabilize the structure which would remove the α phase. We showed that the beneficial effect of cold work and the chill-swage-temper treatment were about the same at 700 C and present in the 600 C tests. The cyclic hardening behavior at

¹ Battelle-Northwest, Richland, Wash. 99352.

² Mangonon, P. L., Jr., and Thomas, Gareth, *Metallurgical Transactions*, MTG7B, Vol. 1, June 1970, pp. 1577-1588.

³ Gullberg, R. and Lagneborg, R., *Transactions*, AIME, TAIMA, Vol. 236, Oct. 1966, pp. 1482-1485.

⁴ Mangonon, P. L., Jr., and Thomas, Gareth, *Metallurgical Transactions*, MTG7B, Vol. 1, June 1970, pp. 1587-1594.

test temperatures of 500 C and above did not indicate significant strain hardening behavior, which could be attributed to the production of the higher strength α phase (see Fig. 18).

These observations appear to rule out the presence of α phase prior to fatigue testing or its formation at the crack root during fatigue testing as the principal agent producing the beneficial effect. This is an interesting subject and needs further attention to determine the nature of the defect-substructure interaction which produces the higher fatigue life.

E. E. Bloom¹ and J. O. Stiegler¹

Effect of Fast Neutron Irradiation on the Creep Rupture Properties of Type 304 Stainless Steel at 600 C*

REFERENCE: Bloom, E. E. and Stiegler, J. O., "Effect of Fast Neutron Irradiation on the Creep Rupture Properties of Type 304 Stainless Steel at 600 C," *Irradiation Effects on Structural Alloys for Nuclear Reactor Applications, ASTM STP 484*, American Society for Testing and Materials, 1970, pp. 451-467.

ABSTRACT: The creep rupture properties of Type 304 stainless steel have been determined at 600 C after irradiation at temperatures in the range from 370 to 600 C to fast neutron fluences of 1×10^{21} to 6.7×10^{22} n/cm², $E > 0.1$ MeV. The microstructures were characterized by electron microscopy. Irradiation at 370 to 470 C caused a decrease in ductility and rupture life which became larger with increasing fast neutron fluence. The irradiated specimens fractured along the grain boundaries with no evidence of deformation within the matrix. A specimen irradiated at 410 C to 6.7×10^{22} n/cm² ruptured in 0.5 h with 0.1 percent elongation, as compared to a rupture life of 185 h and elongation of 19.7 percent for the unirradiated material tested at the same stress. Specimens irradiated at 600 C to fluences from 2.5 to 3.5×10^{22} n/cm² exhibited decreased ductilities and creep rates and essentially the same rupture lives as unirradiated specimens.

The increased tendency for grain boundary fracture, and thus reduced ductility and rupture life, appears to result from the effects of the irradiation produced voids and dislocations upon deformation processes, which effects would be inoperative in an unirradiated specimen. The voids and dislocations prevent dislocation motion within the matrix. Regions along grain boundaries are denuded of these defects and grain boundary sliding occurs, leading to stress concentrations and the initiation of grain boundary cracks. The presence of helium at the boundaries may increase the rate of crack propagation.

KEY WORDS: neutron irradiation, neutron flux, fast neutrons, radiation effects, cracking (fracturing), crack propagation, deformation, ductility, microstructure, crystal lattices, crystal dislocations, voids, grain boundaries, creep rupture strength, creep rupture tests, austenitic stainless steels, fast reactors (nuclear), nuclear fuel cladding

¹Metals and Ceramics Division, Oak Ridge National Laboratory, Oak Ridge, Tenn. 37830.

* Research sponsored by the United States Atomic Energy Commission under contract with the Union Carbide Corp.

Austenitic stainless steels have several properties which make them attractive for use as fuel cladding and structural components in liquid metal fast breeder reactors (LMFBR). These alloys possess adequate high-temperature strength, are resistant to corrosion by liquid sodium (the reactor coolant), and are compatible with uranium-plutonium oxides (the proposed reactor fuel) at the projected operating temperatures of 350 to 650 C. Changes in mechanical and physical properties do occur, however, as a result of neutron irradiation. It is important that these changes do not endanger the safe or economical operation of the reactor system.

Changes in properties are a sensitive function of the irradiation temperature, the neutron fluence, and energy spectrum as well as the post-irradiation test variables. It now appears that the irradiation damage as characterized by electron microscopy can be classified into three forms, depending on the irradiation temperature [1].² At low temperatures ($<0.37T_m$, 350 C, where T_m is the absolute melting temperature), the visible damage has the form of small defect clusters, a few tens of angstroms in diameter. Such damage is observed at fast neutron fluences as low as 1×10^{20} n/cm² and does not change in form at least for fluences up to 3×10^{22} n/cm² [2, 3]. At intermediate temperatures (0.37 to $0.55T_m$, that is 350 to 650 C) the damage structure consists of voids (ranging up to a few hundred angstroms in diameter) and interstitial dislocation loops. The changes in this structure with increasing fast neutron fluence and irradiation temperature have been discussed in detail elsewhere [2-7]. At high temperatures, above approximately 650 C, the primary form of damage is helium bubbles formed by precipitation of helium produced by n, α transmutations. For LMFBR applications, irradiation damage at temperatures above approximately 350 C is of concern. For specimens irradiated and tested at intermediate temperatures, where the damage structure consists of voids and dislocation loops, the tensile yield strength is increased and the uniform elongation is reduced [8-10]. Holmes et al [8, 9] have investigated the postirradiation tensile properties of Type 304 stainless steel irradiated at 540 ± 50 C to 1.1×10^{22} n/cm², $E > 0.1$ MeV. At test temperatures below $0.5T_m$, the ductility loss was caused by the onset of the plastic instability (local necking) induced by the increased flow stress and reduced work hardening rates. Above $0.5T_m$, helium embrittlement was thought to control ductility. Carlander et al [10] have investigated the change in tensile properties as a function of fast neutron fluence and postirradiation test temperature. For specimens irradiated at temperatures in the range from 370 to 470 C and tension tested at 450 C, the changes in yield strength and uniform elongation were found to saturate at about 2×10^{22} n/cm², $E > 0.1$ MeV.

Previous investigations in which specimens were irradiated in thermal

² Italic numbers in brackets refer to the list of references at the end of this paper.

reactors have shown that at test temperatures above about 550 C the transmutation produced helium caused a significant reduction in the ductility, particularly at the low strain rates encountered in creep rupture tests [11, 12]. This loss of ductility results from the increased rate of grain boundary crack initiation and propagation due to helium at the grain boundaries. The effect of irradiation to high fast neutron fluences on the creep rupture properties has not been investigated. Of particular interest are the changes in properties which occur when the specimen contains the void and dislocation loop structure formed at irradiation temperatures below about 650 C and when the test is conducted at a temperature where helium embrittlement is an important factor (above 550 C). The objective of this work was to study the postirradiation creep rupture properties in specimens which were irradiated under different conditions in order to relate the changes in creep rupture properties to the irradiation produced microstructure.

Experimental Procedure

Sheet specimens of Type 304 stainless steel, having the dimensions shown in Fig. 1, were machined from a safety rod thimble irradiated in the experimental breeder reactor II (EBR-II). The thimble, which was a hexagonal tube measuring about 3.2 cm across each flat, 0.10 cm in thickness, and 116.6 cm in length, was placed in the reactor in the annealed condition and had an average grain diameter of 0.045 mm. It was irradiated in a row 3 position of the reactor to a peak fluence of 6.7×10^{22} n/cm², $E > 0.1$ MeV. There was a gradient in both neutron fluence and irradiation temperature along the length of the thimble, shown in Fig. 2. Because of the small dimensions, only two specimens at a given irradiation temperature and fluence condition were obtained. By removing specimens from those segments of the thimble which were located below and above the reactor core, the effect of varying fast neutron fluence at constant irradiation temperatures of 370 or 462 C was investigated.

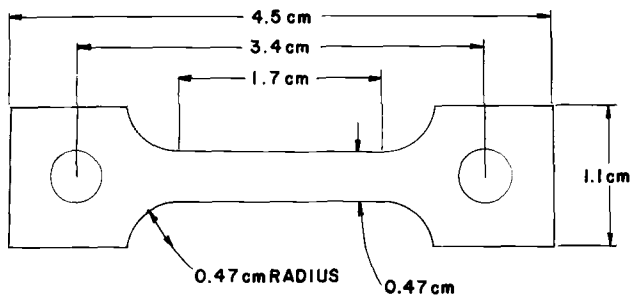


FIG. 1—Sheet specimen used for postirradiation creep rupture testing of EBR-II safety rod thimble.

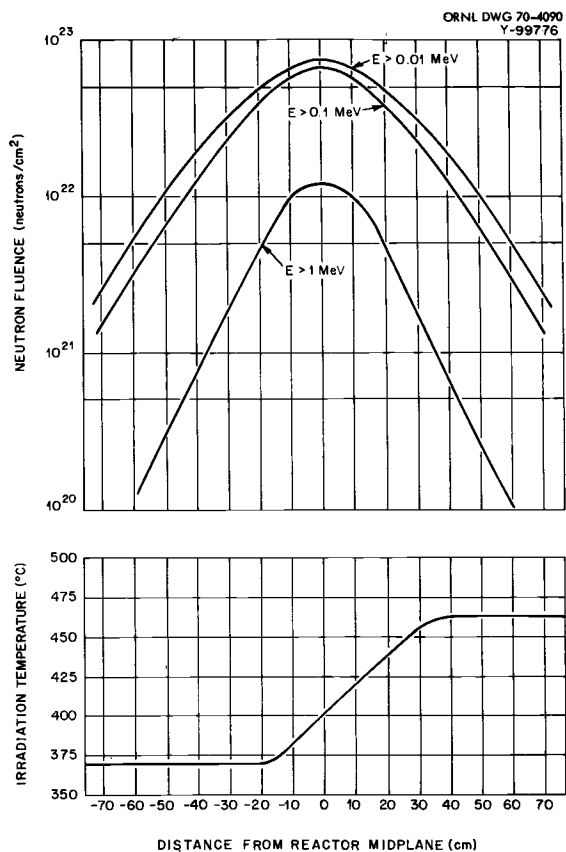


FIG. 2—Fast neutron fluence and irradiation temperature for EBR-II safety rod thimble.

The microstructure of the material in the as-irradiated condition was characterized by transmission electron microscopy of specimens removed from various positions along the length of the thimble. The details of this portion of the experimental procedure have been discussed elsewhere [7].

In order to expand the range of irradiation temperature beyond that available through an examination of the safety rod thimble, specimens of Type 304 stainless steel were irradiated in an experimental subassembly located in row 2 of the reactor. The specimens were irradiated in specimen holders such as the one shown schematically in Fig. 3. A gas gap between the holder surface and the inside surface of the tube element provided a barrier to radial heat flow and allowed temperatures above the reactor coolant temperature to be obtained. The experiment was designed and calibrated on the basis of nuclear heating rates as a function of position within the reactor, as determined in a previous experiment. The calculated

irradiation temperature was 600 C for a peak gamma heating rate of 3.5 W/g. Gamma heating rates of 3.0 and 4.0 W/g would give irradiation temperatures of 570 and 630 C, respectively.

Postirradiation creep rupture tests were performed in air at 600 ± 5 C in lever arm creep machines located in hot cells. Specimen elongation as a function of time was determined by a linear differential transformer which measured the relative movement of the upper and lower specimen grips. Creep rupture tests on specimens machined from an unirradiated EBR-II safety rod thimble were run to determine the change in properties due to irradiation. Posttest examination of specimens included optical metallography, transmission microscopy, and scanning electron microscopy.

Results

As-Irradiated Microstructures

Specimens irradiated to fast neutron fluences in the range 2×10^{21} to 6.7×10^{22} n/cm² at temperatures between 370 and 470 C contained voids and faulted interstitial dislocation loops. The details of the microstructures have been reported elsewhere [7]. At low fast neutron fluences (below 10^{22} n/cm²) the damage was distributed heterogeneously. Dislocation loops were clustered around grown-in dislocation lines, and voids were often located on dislocation lines. For specimens irradiated to a constant fast neutron fluence, the void and dislocation loop concentrations decreased and the size of these defects increased with increasing temperature. Examples of the dislocation loop structure and void structure for specimens irradiated at 370 to 380 and 460 to 470 C are shown in Figs. 4 and 5. Regions on the order of 1000 Å wide adjacent to grain boundaries were denuded of these defects. At fluences in excess of about 1×10^{22} n/cm²

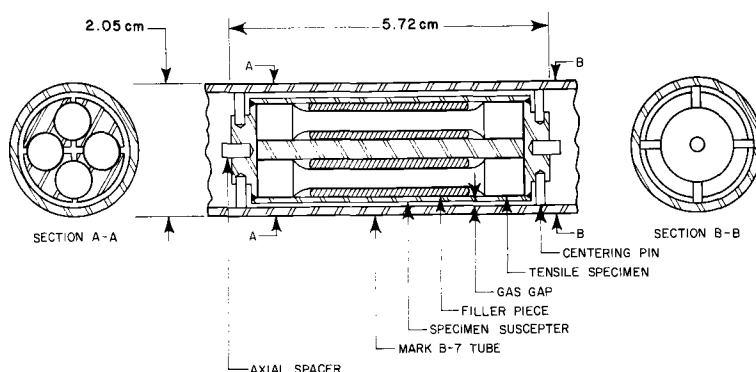


FIG. 3—Schematic drawing of specimen holder used in EBR-II materials irradiation experiments.

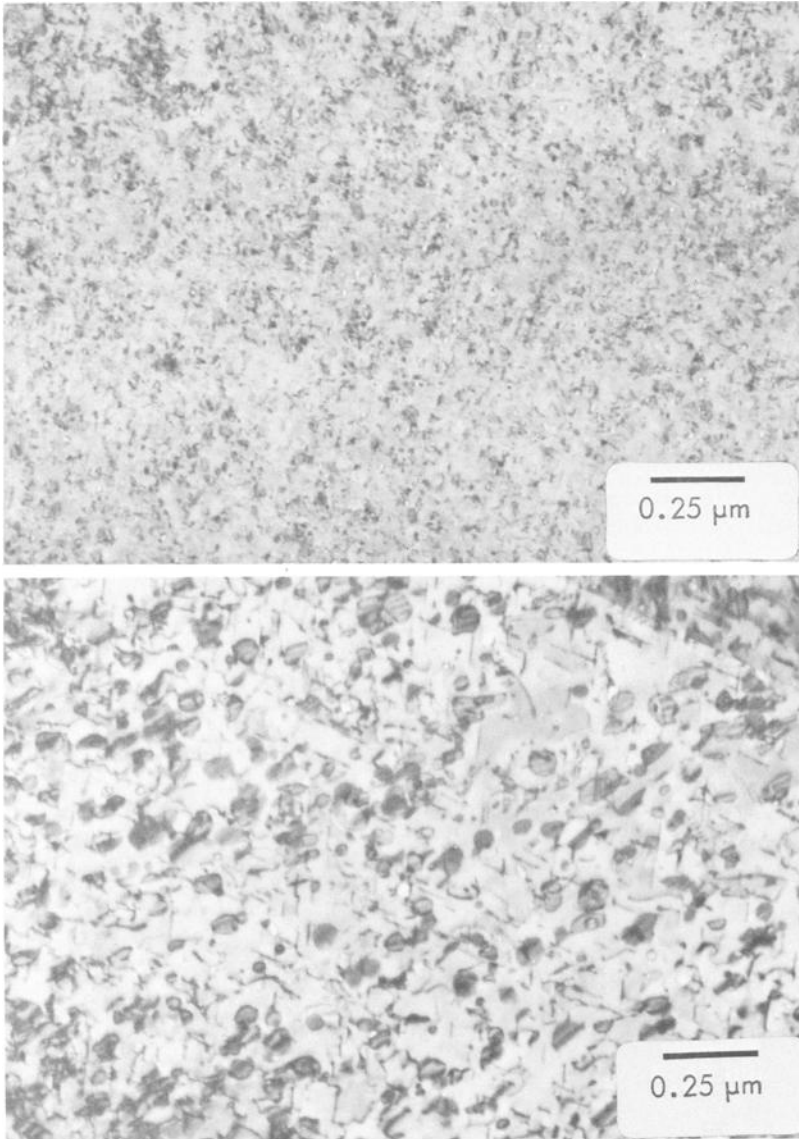


FIG. 4—Dislocation loops in Type 304 stainless steel irradiated at (top) 370 C to $0.8 \times 10^{22} \text{ n/cm}^2$ and (bottom) 460 C to $0.9 \times 10^{22} \text{ n/cm}^2$.

the loop concentration was so high that quantitative microscopy measurements were impossible. The void concentration increased monotonically as a function of fluence, as shown in Fig. 6.³ After irradiation at about 600 C

³ See Ref 7 for a discussion of the errors involved in determining the void concentration.

to fluences of 2.5 to 3.5×10^{22} n/cm², the damage structure consisted of a dislocation network, a few unfaulted dislocation loops, and voids ranging up to about 600 \AA in diameter. A typical microstructure is shown in Fig. 7. The dark, rectangular particle is a thin sheet precipitate.

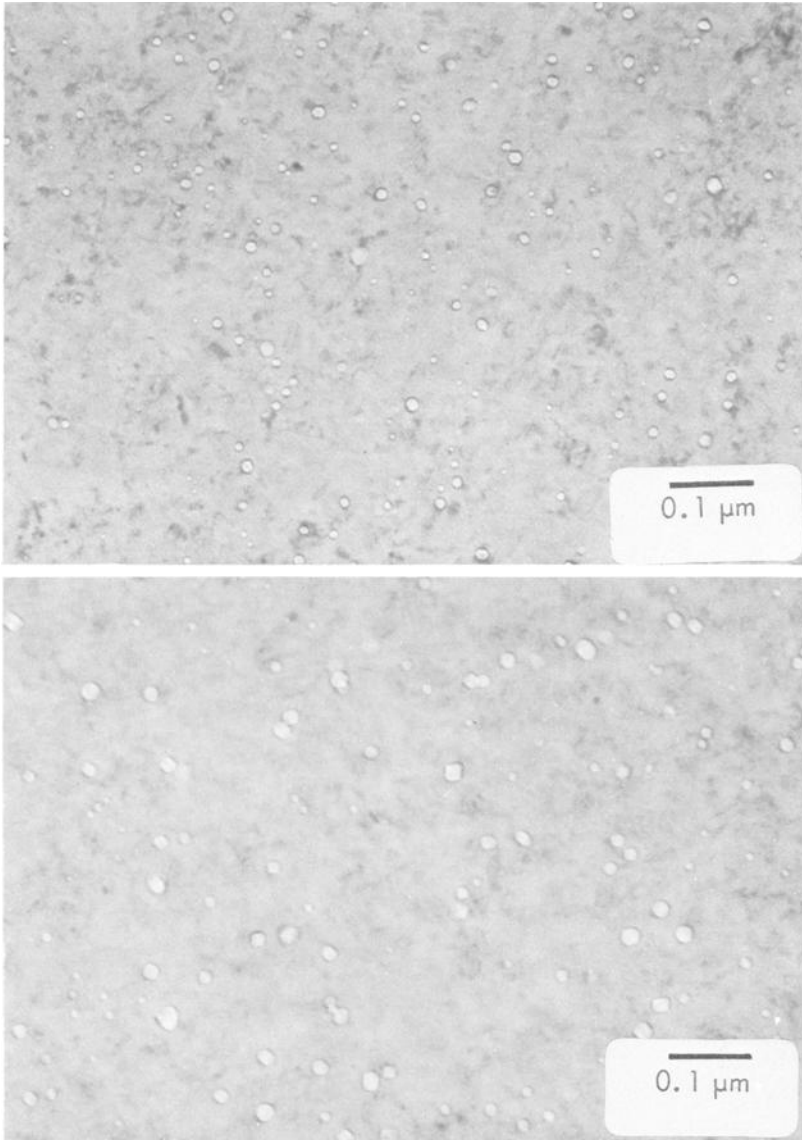


FIG. 5—Voids in Type 304 stainless steel irradiated at (top) 370 C to 1.2×10^{22} n/cm² and (bottom) 460 C to 2.1×10^{22} n/cm².

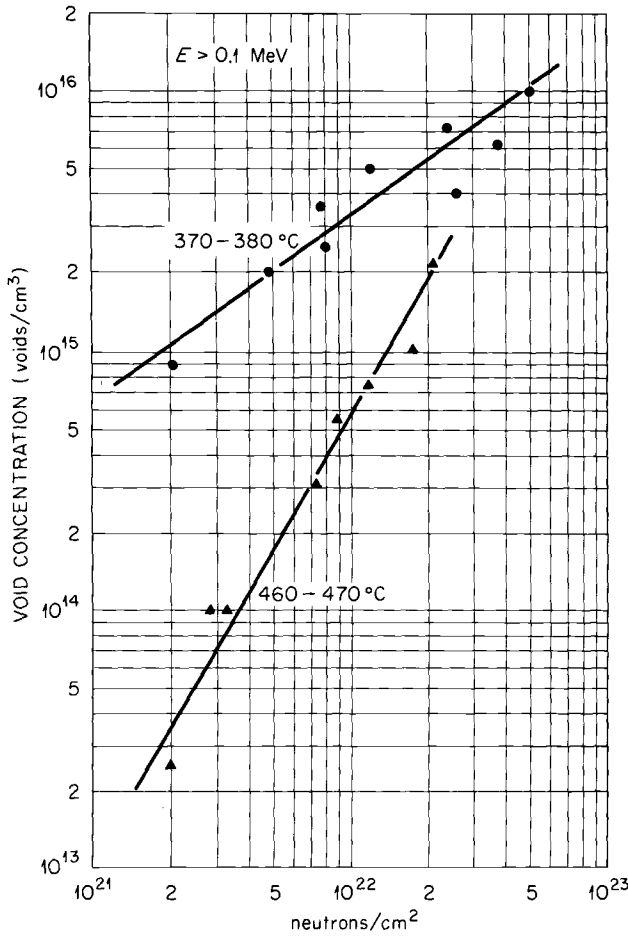


FIG. 6—Variation of void concentration with fast neutron fluence in Type 304 stainless steel irradiated at 370 to 380 and 460 to 470 C.

Creep Rupture Properties

The creep rupture properties at 600 C of sheet specimens removed from an unirradiated safety rod thimble (SRT) and of rod specimens of the same heat as was irradiated in the experimental subassembly (heat BO) are shown in Fig. 8. The strength properties of these two heats of Type 304 stainless steel are typical for this alloy, and the variation in properties between these two heats is well within the heat-to-heat variation as discussed by Smith [13]. Ductility, as measured by total elongation, ranged from 16 to 40 percent for the SRT specimens and from 9 to 25 percent for specimens from heat BO.

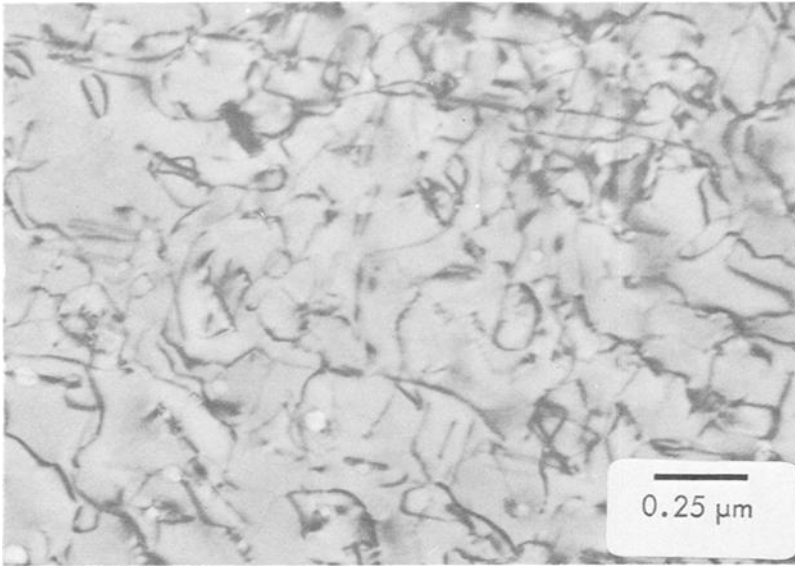


FIG. 7—Dislocation network and voids in Type 304 stainless steel irradiated at 600 C to 3.5×10^{22} n/cm².

The effect of fast neutron fluence on the rupture life of SRT specimens which were irradiated at temperatures in the range from 370 to 470 C and tested at 600 C and 27,500 psi is shown in Fig. 9. The rupture life of the unirradiated SRT at this temperature and stress was 185 h. Specimens irradiated at 370 C exhibited shorter rupture lives than did specimens

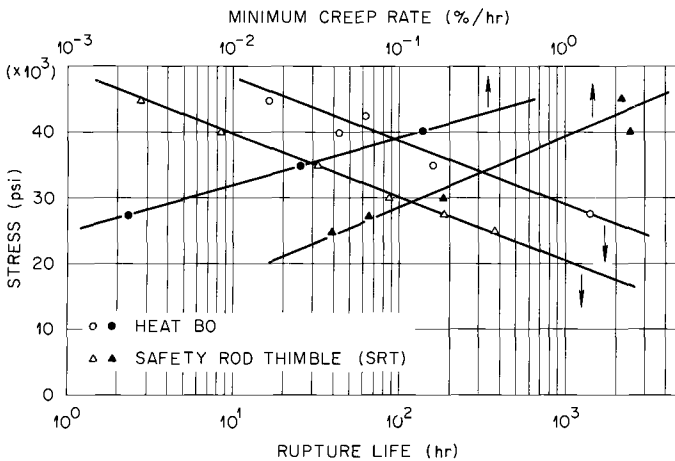


FIG. 8—Creep rupture properties of two heats of Type 304 stainless steel at 600 C.

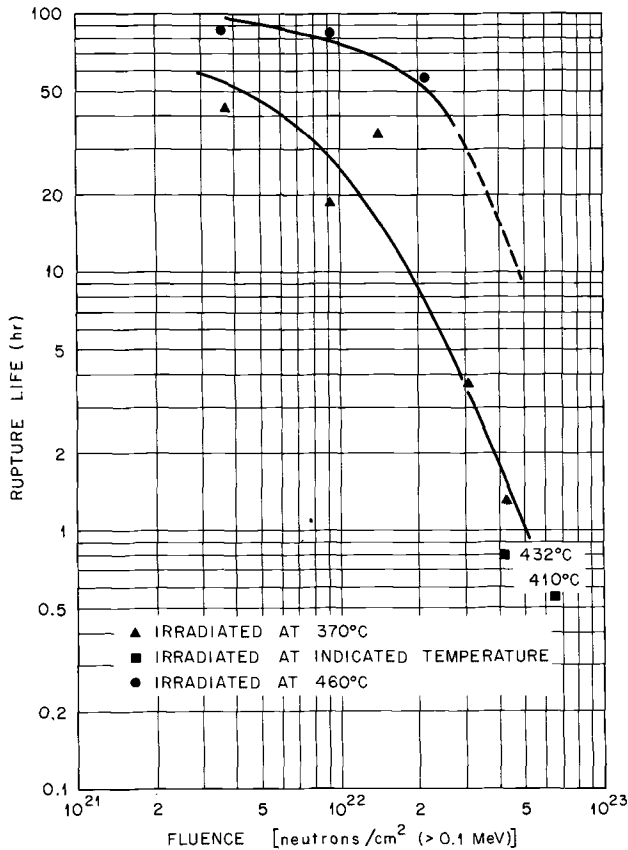


FIG. 9—Postirradiation rupture life of Type 304 stainless steel at 600 C and 27,500 psi. The rupture life of an unirradiated specimen tested at this temperature and stress was 185 h.

irradiated at 470 C. For each irradiation temperature, the rupture life decreased sharply with increasing fast neutron fluence. A specimen irradiated at 410 C to about 6.5×10^{22} n/cm² had a rupture life of 0.55 h, a factor of 330 less than the unirradiated material. The total elongation as a function of fluence for these specimens is shown in Fig. 10. The total elongation was reduced from values in the range of 15 to 25 percent for unirradiated specimens tested at these conditions to values in the range of 2 to 3 percent for specimens irradiated to fluences of 4×10^{21} n/cm². The ductility decreased continuously with increasing fast neutron fluence and was essentially independent of irradiation temperature over the range from 370 to 470 C.

Typical strain-time curves for specimens irradiated at 370 C are shown in Fig. 11. Irradiated specimens exhibited a very short primary creep

stage, usually less than 1 h, as compared to 12 h for an unirradiated specimen. Secondary creep rates were reduced by the irradiation, but for specimens irradiated to fluences greater than about 1×10^{22} n/cm² fracture occurred in such short times that the creep rates have little significance. None of the irradiated specimens exhibited tertiary creep.

Creep rupture properties of specimens irradiated at 600 C to fast neutron fluences of from 2.5 to 3.5×10^{22} n/cm² are shown in Fig. 12. For these irradiation conditions, little or no change in the rupture life was observed; however, the ductility was significantly reduced. For example, an annealed specimen tested at 27,500 psi exhibited about 5 percent elongation at the onset of tertiary creep and about 9 percent total elongation at fracture as compared to an irradiated specimen tested at the same stress, which exhibited 2.1 percent total elongation with no tertiary creep. Minimum creep

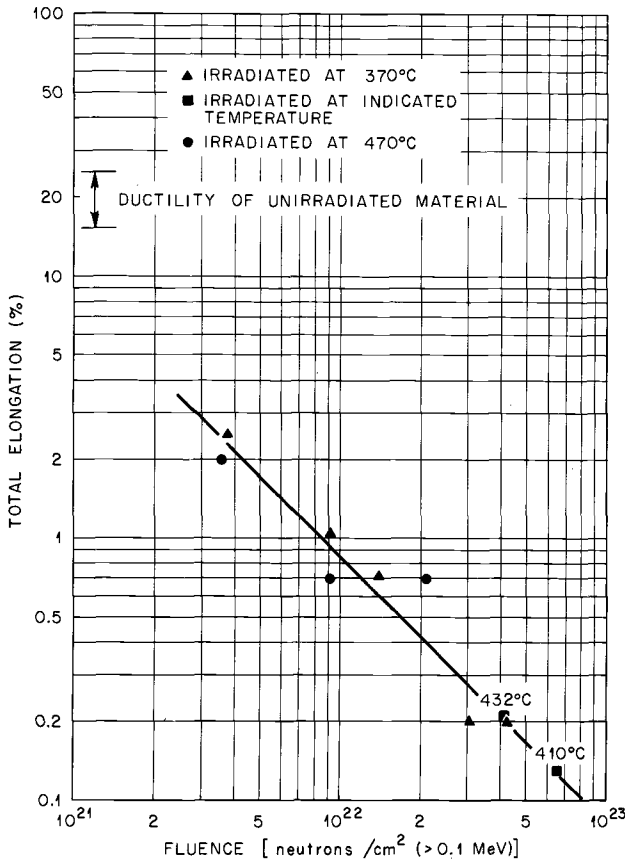


FIG. 10—Postirradiation ductility of Type 304 stainless steel tested at 600 C and 27,500 psi.

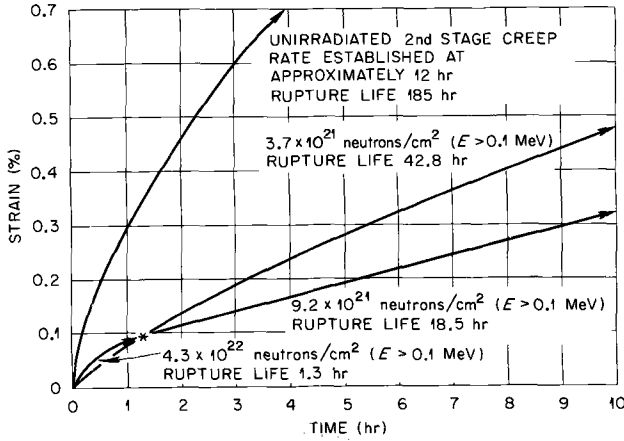


FIG. 11—Effect of irradiation at 370 C on the creep curves of Type 304 stainless steel tested at 600 C and 27,500 psi.

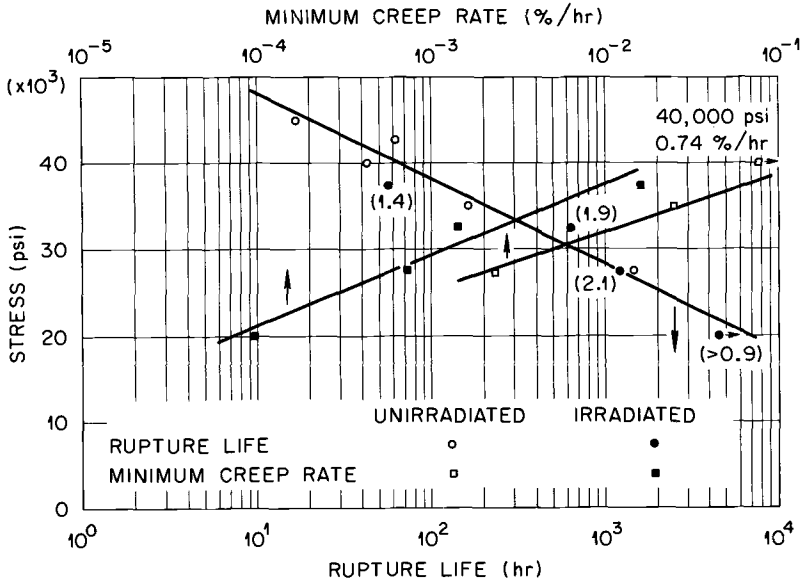


FIG. 12—Effect of irradiation at 600 C to 2.5 to 3.5×10^{22} n/cm² on the creep rupture properties of Type 304 stainless steel at 600 C.

rates of irradiated specimens were about a factor of 4 less than the unirradiated material. The net result of the reduced minimum creep rates and reduced ductilities was that irradiation did not change the rupture life.

Metallography of Test Specimens

The fractures of all irradiated specimens were intergranular. Figure 13 is a scanning electron micrograph of a specimen irradiated at 410 C to 6.7×10^{22} n/cm² and tested at 600 C and 27,500 psi stress. The intergranular fracture was initiated on the left-hand side of the specimen and propagated to the right. The right-hand portion failed last in a shear mode, presumably at a very high stress level and high strain rate. Optical metallography confirmed that even in those specimens irradiated to relatively low fluences the fractures were intergranular, with no evidence of deformation within the matrix and little or no grain boundary cracking in the region adjacent to the fracture. It thus appears that a grain boundary crack, once initiated, propagates rapidly to cause failure.

For those specimens which were removed from the EBR-II safety rod thimble, the irradiation temperature was lower than the test temperature. It was thus important to determine the changes in microstructure which occurred during the test. Figure 14 shows a transmission micrograph of the area near the fracture of the same specimen as shown in Fig. 13. The specimen had been at 600 C for approximately 4 h before failure occurred. Prior to testing, the structure consisted of voids and faulted dislocation loops. During the test, the dislocation loops unfaulted to produce the dislocation structure shown in Fig. 14. Previous results [6] have shown that unfaulting of the dislocation loops can occur during annealing 1 h at 600 C. It thus is probable that the dislocation loops had unfaulted during the 3-h hold time at 600 C prior to application of the stress. The dislocation density and configurations were very similar to those observed in a specimen irradiated under the same conditions and then annealed for 2 h at 600 C. The lack of dislocation tangles and the similarity of microstructures between stressed and unstressed specimens are evidence that little deformation occurred within the matrix. The void concentration and size distri-

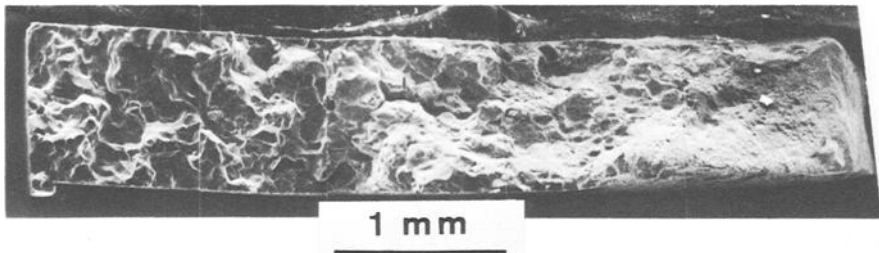


FIG. 13—Fracture of Type 304 stainless steel irradiated at 410 C to 6.7×10^{22} n/cm² and tested at 600 C and 27,500 psi.

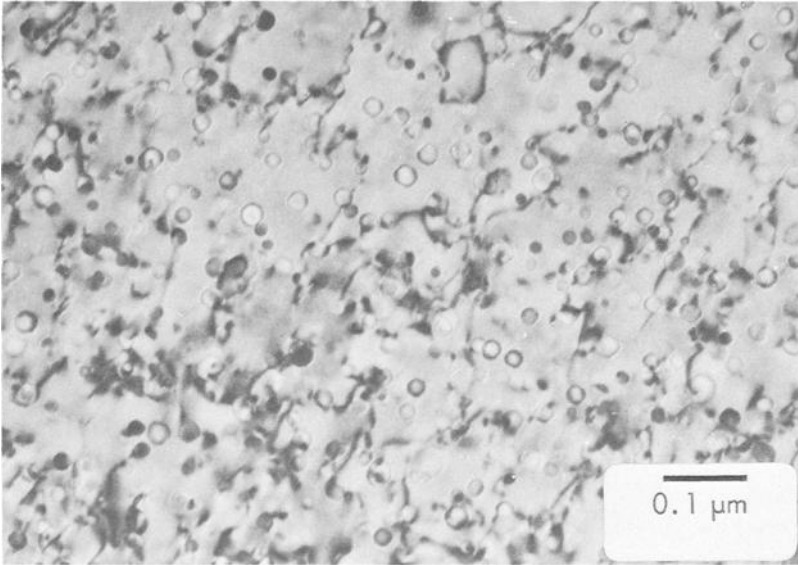


FIG. 14—Dislocation structure of Type 304 stainless steel irradiated at 410 C to 6.7×10^{22} n/cm² and tested at 600 C and 27,500 psi.

bution in the tested specimen were approximately the same as in the as-irradiated condition.

Summary of Results and Discussion

Specimens of Type 304 stainless steel were irradiated at temperatures in the range from 370 to 600 C to fast neutron fluences in the range from 2×10^{21} to 6.7×10^{22} n/cm², $E > 0.1$ MeV, and then creep rupture tested at 600 C. For irradiation at temperatures from 370 to 470 C, the as-irradiated microstructure consisted of voids and faulted interstitial dislocation loops. The void concentration increased with increasing fluence at constant irradiation temperature and decreased with increasing irradiation temperature at constant fluence.

Characterization of the dislocation loop structure in a quantitative manner was impossible owing to the complexity and density of the structure. It was apparent, nonetheless, that the loop concentration decreased and the loop size increased with increasing irradiation temperature. Specimens irradiated at 600 C contained a dislocation network, a few unfaulted dislocation loops, and voids which were nearly always associated with either dislocations or precipitate particles.

The rupture life, ductility, and creep rate were all affected by the irradiation. For a given fast neutron fluence, the reduction in rupture life was

larger for specimens irradiated at 370 C than for specimens irradiated at 470 C. For these irradiation conditions the reduction in rupture life is a result of the increased tendency of the material to fracture along the grain boundaries. Scanning electron microscopy of the fracture surfaces and optical metallography of the gage section of tested specimens indicated that the fractures were intergranular and that there were essentially no grain boundary cracks along the gage section. It thus appears that a crack, once initiated, propagates very rapidly to cause failure. It is well documented [11, 12, 14] that the helium produced during the irradiation causes a reduction in ductility and rupture life due to its effects on grain boundary fracture processes. The specimen which was irradiated at 410 C to 6.7×10^{22} n/cm² contained about 12 atomic ppm.⁴ This specimen exhibited about 0.1 percent total elongation and ruptured in 0.5 h, a factor of 330 less than the unirradiated material. King [14] has shown that a uniform concentration of 20 atomic ppm helium reduced the rupture life of annealed Type 304 stainless steel from 900 to 40 h at 600 C and 30,000 psi. The reduction in rupture life and ductility of the fast neutron irradiated specimens may not be entirely due to the irradiation produced helium. The intergranular fracture which is observed at elevated temperatures is initiated by grain boundary sliding [15]. In the irradiated specimens the regions adjacent to the grain boundaries are denuded of the damage structure. Deformation along the boundaries probably occurs in a similar fashion in unirradiated and irradiated specimens. When this deformation occurs, stresses are concentrated at constraints such as jogs and grain boundary junctions. In an unirradiated specimen, these stresses can be reduced by deformation within the matrix. For irradiated specimens, deformation in the matrix is impeded by the defect structure, and cracks are thus nucleated in high-stress regions. The propagation of these cracks along grain boundaries is likely to be enhanced by the presence of helium.

In specimens irradiated at 600 C to 2 to 3×10^{22} n/cm² the concentration of irradiation produced voids and dislocations was much lower than in the specimens irradiated at lower temperatures; thus, some deformation within the matrix (and relaxation of stresses) could occur. The observation of no effect of irradiation on the rupture life in these specimens was a consequence of the reduced creep rate and reduced ductility. If the damage mechanism does depend upon the concentration of defects present in the matrix, the rupture life of specimens irradiated at 600 C and tested at 600 C would be expected to exhibit a fluence dependence similar to that for specimens irradiated at lower temperatures. This curve would be displaced to higher fluences because of the higher fluences required to establish a given defect concentration.

⁴ Helium analysis was conducted by H. Farrar, Atomic International, Canoga Park, Calif.

Acknowledgments

We would like to acknowledge the assistance of the following people in connection with this work: F. L. Beeler and L. G. Rardon for performing the mechanical properties tests; G. D. Stohler and C. Jones for preparing the optical and electron microscopy specimens; and J. R. Weir, C. J. McHargue, C. E. Sessions, and H. E. McCoy for reviewing the manuscript.

References

- [1] Weir, J. R., Stiegler, J. O., and Bloom, E. E. in *Proceedings of the National Topical Meeting on Fast Reactor Systems, Materials and Components*, CONF-680419, Cincinnati, Ohio, 2-4 April 1968, pp. 189-224.
- [2] Cawthorne, C. and Fulton, E. J. in *The Nature of Small Defect Cluster*, Vol. 2, M. J. Makin, Ed., Atomic Energy Research Establishment, Harwell, Report AERE-R5269, H. M. Stationery Office, London, 1966, p. 446.
- [3] Cawthorne, C. and Fulton, E. J., *Nature*, NATUA, Vol. 216, 1967, p. 515.
- [4] Harkness, S. D. and Li, Che-Yu in *Radiation Damage in Reactor Materials*, Vol. 2, International Atomic Energy Agency, Vienna, 1969, p. 189.
- [5] Claudson, T. T., Holmes, J. J., Straalsund, J. L., and Brager, H. R. in *Radiation Damage in Reactor Materials*, Vol. 2, International Atomic Energy Agency, Vienna, 1969, p. 165.
- [6] Stiegler, J. O. and Bloom, E. E., *Journal of Nuclear Materials*, JNUMA, Vol. 33, 1969, p. 33.
- [7] Bloom, E. E., "An Investigation of Fast Neutron Radiation Damage in an Austenitic Stainless Steel," ORNL-4580, Oak Ridge National Laboratory, Aug. 1970.
- [8] Holmes, J. J., Robbins, R. E., Brimhall, J. L., and Mastel, B., *Acta Metallurgica*, AMETA, Vol. 16, 1968, p. 955.
- [9] Holmes, J. J., Robbins, R. E., and Brimhall, J. L., *Journal of Nuclear Materials*, JNUMA, Vol. 32, 1969, p. 330.
- [10] Carlander, R., Harkness, S. D., and Yaggee, F. L., *Nuclear Applications*, NUAPA, Vol. 7, 1969, p. 67.
- [11] Harries, D. R., *Journal of the British Nuclear Energy Society*, JBNSA, Vol. 5, 1966, p. 74.
- [12] Bloom, E. E. and Weir, J. R. in *Irradiation Effects in Structural Alloys for Thermal and Fast Reactors*, ASTM STP 457, American Society for Testing and Materials, 1969, pp. 261-289.
- [13] Smith, G. V., *An Evaluation of the Yield, Tensile, Creep, and Rupture Strengths of Wrought 304, 316, 321, and 347 Stainless Steels at Elevated Temperatures*, ASTM DS 5S2, American Society for Testing and Materials, 1969.
- [14] King, R. T., "Cyclotron Simulation of Neutron Transmutation Produced Gases in Reactor Cladding and Structural Materials," presented at the International Conference on the Use of Cyclotrons in Chemistry, Metallurgy, and Biology, Oxford, England, Sept. 1969 (to be published in the proceedings).
- [15] Grant, N. J., *Fracture*, B. L. Averbach, D. K. Felbeck, G. T. Hahn, and D. A. Thomas, Eds., Wiley, New York, 1959, p. 562.

DISCUSSION

*A. L. Bement*¹—Your last figure demonstrates a strong interaction of dislocations with voids, which is a subject requiring more fundamental study. In particular, the following aspects should be pursued:

1. Do dislocations always end at the void surface normal to the surface?
2. What types of void interactions occur with prior dislocations as compared with dislocations resulting from loop defaulting, especially with regard to network formation during elevated-temperature deformation?
3. What effects do dislocation pileups at voids have on the stress field around a void? How does this stress field affect void growth and dislocation bypassing of the void?
4. What effect does a polyhedral geometry as compared with a spherical geometry have on the interaction force (Orowan force) involved in a planar barrier model for void strengthening?

E. E. Bloom (authors' closure)—We agree that the interaction of the dislocations with radiation produced voids and dislocations is an area in which additional fundamental study is needed.

¹ Battelle-Northwest, Richland, Wash. 99352.

A. J. Lovell¹ and R. W. Barker¹

Uniaxial and Biaxial Creep Rupture of Type 316 Stainless Steel After Fast Reactor Irradiation*

REFERENCE: Lovell, A. J. and Barker, R. W., "Uniaxial and Biaxial Creep Rupture of Type 316 Stainless Steel After Fast Reactor Irradiation," *Irradiation Effects on Structural Alloys for Nuclear Reactor Applications, ASTM STP 484*, American Society for Testing and Materials, 1970, pp. 468-483.

ABSTRACT: The degradation in creep rupture properties of Type 316 stainless steel after fast reactor irradiation has been determined for both uniaxial and biaxial loading conditions. Uniaxial specimens (rod type) and biaxial specimens (tube type) were irradiated in the 7C4 position of the EBR-II to a total fluence of 1.2×10^{22} n/cm² (1×10^{22} n/cm², $E > 0.1$ MeV) at ~ 480 C. Postirradiation tests were performed over a temperature range of 538 to 760 C.

The results from both uniaxial and biaxial tests at 538 C show significant losses in rupture life relative to unirradiated specimens when compared on the basis of initial true stress. Rupture life was reduced by factors down to 1/20 for uniaxial and 1/40 for biaxial tests. The substantial loss in rupture life at 538 C was primarily a result of high creep rates, and the contribution from ductility loss was relatively small. Uniaxial test results at 593 C show reductions in rupture life to a factor of $\frac{1}{2}$ at high stresses and only small reductions at low stresses. The rupture life for both uniaxial and biaxial tests at 649 C show only a decrease of $\frac{1}{2}$ after irradiation. The decrease becomes more substantial again at 760 C, with a reduction in life to 1/10 to 1/7. The rupture life reductions at 593, 649, and 760 C were the results of reduced ductility, with no significant contributions from creep rate differences. The underlying cause of the low ductility at these higher temperatures is associated with helium embrittlement and defect structure.

KEY WORDS: irradiation, neutron irradiation, degradation, fast neutrons, axial stress, bursting, creep properties, creep rate, creep rupture strength, creep tests, ductility, embrittlement, structural steels, austenitic stainless steels, fast reactors (nuclear), liquid metal cooled reactors

¹ Senior research engineer, Metallurgy and Ceramics Dept., and engineer, FTF Fuels Dept., Pacific Northwest Laboratory, Battelle Memorial Institute, Richland, Wash. 99352.

* This paper is based on work performed under U. S. Atomic Energy Commission Contract AT(45-1)-1830.

The selection of AISI Type 316 stainless steel as a prime alloy for application in liquid metal fast breeder reactor systems has prompted a need to know how this alloy is affected by fast neutron irradiation at elevated temperatures. Only limited data on the postirradiation mechanical properties obtained from fast reactor experiments are available for this alloy. This limitation is particularly acute for the time-dependent creep and creep rupture properties. To obtain such information, creep tests have been made on Type 316 stainless steel after fast reactor irradiation in the experimental breeder reactor II (EBR-II). These tests were designed to determine empirically the stress dependence of minimum creep rate and rupture life and the ductility of this irradiated alloy over the temperature range of 538 to 760 C. Both a uniaxial loading condition on conventional tension specimens and a biaxial loading condition on pressurized tube specimens were included in this investigation. The study shows that creep and creep rupture properties were changed significantly as a result of irradiation and discusses possible explanations for the observed property changes.

Experimental Procedure

Materials

The chemical compositions of the two AISI Type 316 stainless steels used for the uniaxial and biaxial specimens are shown in Table 1. The

TABLE 1—Chemical composition of AISI Type 316 stainless steels used in uniaxial and biaxial creep rupture studies.

Element	Composition, wt%		
	Specimen Type		
	Uniaxial		Biaxial
V	I		
C.....	0.057	0.052	0.081
Mn.....	1.80	1.72	1.51
P.....	0.024	0.012	0.016
S.....	0.014	0.020	0.023
Si.....	0.36	0.38	0.50
Ni.....	13.39	13.55	13.25
Cr.....	17.71	17.80	17.84
Mo.....	2.26	2.33	2.32
Cu.....	0.18	0.20	0.05
Co.....	0.13	0.14	0.071
N ₂	0.041	0.039
V.....	...	0.04	<0.005
Ti.....	...	0.003	<0.005
Al.....	...	0.026	<0.005
B.....	...	<0.005	0.0006
O ₂	0.0178	N.A.

NOTE—V = vendor analysis; I = independent analysis.

only significant differences in chemical composition between the two materials were in the carbon and manganese contents.

The material for uniaxial specimens was received as 15.9-mm rod; this rod was reduced to a diameter of 7.75 mm by cold swaging with intermediate anneals at 1065 C. In the final cold swaging, the diameter was reduced from 7.75 mm to 6.86 mm. The rod was given a final anneal at 1065 C for 1 h followed by a rapid air cool. The grain size of this material was ASTM 5–6. Tension specimens with a gage section diameter of 3.18 mm and a gage section length of 26.5 mm were then machined from the rod.

The test material for biaxial specimens was 5.3-mm-diameter by 0.2-mm-wall AISI Type 316 stainless steel tubing in the as-received condition. The as-received condition contains a small amount of cold work, which is shown by the following room temperature yield strength values for as-received and annealed (1065 C, 1 h) tube specimens:

Material Condition	0.2% Offset Yield Strength, psi
As-received	38 000
	39 000
Annealed	33 400
	33 800

The grain size of the as-received material is about ASTM 7–8. Biaxial stress rupture specimens were composed of a section of the tubing to which appropriate fittings had been attached, resulting in a test specimen having a length diameter ratio of about 6.

Irradiation

The uniaxial and biaxial test specimens were sealed in Type 316 stainless steel capsules in an environment of pure sodium containing 12 to 15 ppm O₂, 29 ppm carbon, 25 ppm silicon, 110 ppm potassium, and 10 ppm calcium. Boron, magnesium, manganese, and other elements were identified as being present in trace quantities. These capsules were placed in Mk B-7 type tubes normally used for structural materials irradiation in EBR-II. An annular gas gap filled with a 30 percent helium-70 percent argon mixture was used in conjunction with nuclear heating to achieve an irradiation temperature estimated to be ~482 C. This estimate was based on heat transfer calculations using the best available information on reactor sodium temperature for the assembly, experiment geometry, and reactor gamma heat (~0.84 W/g). However, the observed microstructure and the post-irradiation tensile properties of the rod specimens, when compared with other irradiated materials, would indicate that the irradiation temperature

could have been 540 C or higher. Irradiations were conducted in position 7C4 of EBR-II within the core region. Both sets of specimens were irradiated to a fluence of $1.2 \times 10^{22} \pm 15$ percent (total) (1.0×10^{22} n/cm², $E > 0.1$ MeV). The irradiation period was equivalent to 127 full power days (3045 h). After irradiation the sodium environment was removed by dissolving and rinsing with water, followed by rinsing with ethyl alcohol for drying purposes.

Test Methods

The basic test procedure was the ASTM Tentative Recommended Practice for Conducting Creep and Time-for-Rupture Tension Tests of Materials (ASTM E 139 – 66 T (1966)). Uniaxial and biaxial stress tests were conducted within these recommended ASTM specifications for temperature and stress, and uniaxial tests were conducted within these ASTM recommendations for alignment.

All uniaxial tests were conducted in an inert gas (helium or argon) environment. The test procedure allowed 20 h for heatup and thermal stabilization prior to applying the creep load. Specimen extension was monitored during the test by measuring pull-rod motion with a dial indicator. Total elongations were obtained in two ways. One value was obtained by posttest measurement of specimen length and a second value was estimated from the strain-time curves.

Biaxial stress rupture tests were conducted in an argon atmosphere by internally pressurizing unrestrained thin wall tubes with argon gas and holding pressure constant until rupture occurred. Under these conditions, the initial hoop stress to axial stress ratio is 2. Maximum engineering hoop stress was determined using the formula for thin wall cylinders:

$$\sigma = \frac{PD}{2t}$$

where

P = internal gas pressure,

D = original inside diameter of tube, and

t = original minimum wall thickness of tube.

Tests were conducted by attaching the tubular cladding specimen to a test rig through the use of standard tube fittings, placing the assembled specimen-test rig in a heated furnace, and applying the desired pressure after the specimen had stabilized (~ 4 h) at the desired test temperature.

Diametral strain for biaxial stress rupture tests was not measured at the point of maximum strain on fragmented test pieces to avoid confusing uniform strain with strain which is related to sudden gas expulsion at the time of failure. It was determined empirically that a diameter measurement taken halfway between the ruptured area and the end fitting, using the

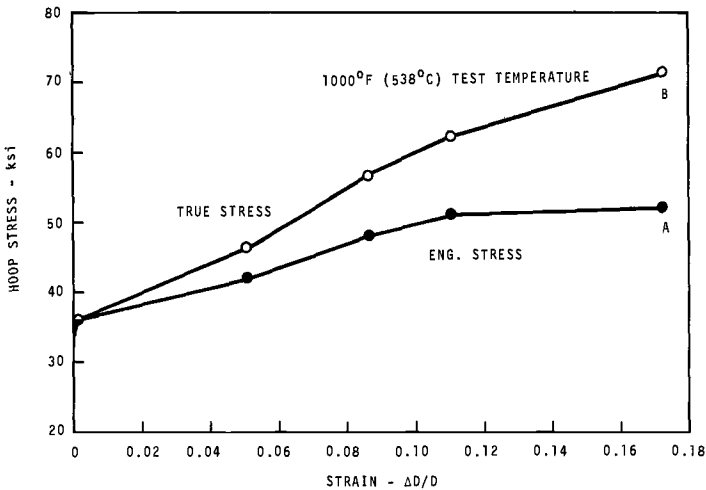


FIG. 1—Hoop stress-strain curve for 5.3-mm-diameter by 0.2-mm-wall Type 316 stainless steel subjected to internal pressure.

longest part of the fragmented specimen, gave a reasonably good value of uniform strain.

The uniaxial and biaxial tests were conducted at constant load and pressure, respectively. At particular test temperatures and stresses, substantial plastic straining occurred during initial application of load (pressure). The increased flow stress of irradiated material reduced the initial strain on loading with respect to the strain obtained on loading an unirradiated specimen. This difference in initial strain resulted in a lower true stress in irradiated specimens than in unirradiated specimens with identical loads (pressure). All comparisons were therefore based on true initial stress.

True initial stress values for uniaxial tests were calculated as $\sigma_0(1 + \epsilon_L)$, where σ_0 is the engineering creep stress and ϵ_L is the engineering strain in a fully loaded creep specimen. Values of ϵ_L were determined from tension tests at each temperature on both irradiated and unirradiated specimens.

The relationship of strain in the biaxially loaded specimen to the internal gas pressure during loading was determined by subjecting a specimen to an ascending series of test pressures, holding for a 1-min period, and measuring the strain produced. A stress-strain curve was constructed, as shown in Fig. 1. Curve *A* is the engineering stress, σ_0 , based on original dimensions, and curve *B* is the true stress, calculated as $\sigma_0(1 + \epsilon)^2$, where ϵ is the engineering diametral strain. In each test the instantaneous strain is obtained from line *A* and the true stress is obtained from line *B* for that strain.

Attempts to establish curves *A* and *B* at 538 C on irradiated tubes which show low initial strain indicated there was very little difference between

true and engineering hoop stress, thus engineering initial hoop stress was used for all biaxial tests on irradiated tubes.

The average creep rate of biaxial test specimens was evaluated by separating the strain caused by creep and the strains associated with initial loadup and with the geometric changes during creep. The creep component of the total strain was obtained by first determining the final true hoop stress, $\sigma_0(1+\epsilon_r)^2$, from the rupture strain, ϵ_r , and using this stress in conjunction with line *B* of Fig. 1 to determine the tensile strain, ϵ_t . Then ϵ_t was subtracted from ϵ_r to obtain ϵ_c , the creep strain. For the low strain obtained in the irradiated tubes, ϵ_c was assumed to be equal to ϵ_r . Average creep rate values were then calculated by dividing the creep strain, ϵ_c , by the rupture time.

Results

Rupture Life

The uniaxial creep and creep rupture results for tests determined at 538, 593, 649, and 760 C are given in Table 2. The stress dependence of rupture life is shown on a conventional log stress-log rupture time plot in Fig. 2. In general, the curve plotted for the irradiated specimens is parallel, or nearly parallel, to the curve for unirradiated specimens, except at 593 C where the rupture life of irradiated specimens exhibits a somewhat higher stress dependence than does the rupture life of unirradiated speci-

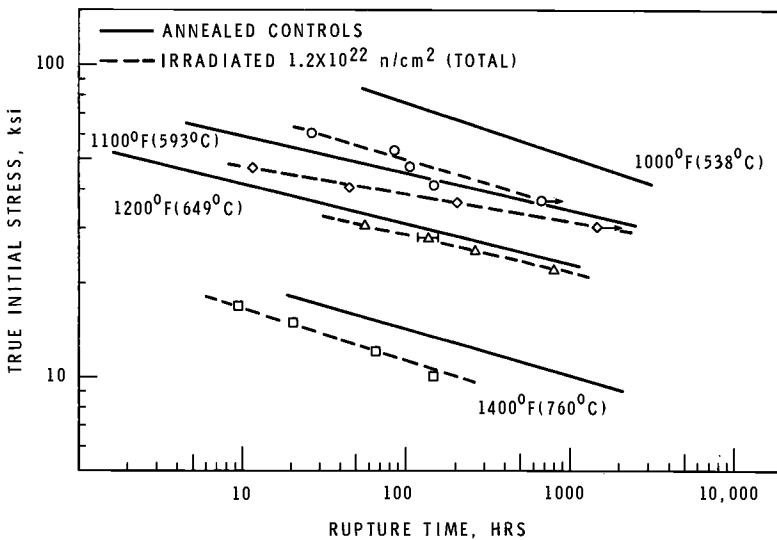


FIG. 2—Effect of EBR-II irradiation on the rupture life of AISI Type 316 stainless steel determined in uniaxial tests.

TABLE 2—Uniaxial creep rupture data for 316 stainless steel irradiated in EBR-II^a to 1.2×10^{22} n/cm² (total) at ~900 F (482 C).

Test Temperature, deg C	Engineering Stress, ksi	True Initial Stress, ksi		Minimum Creep Rate, in./in./h		Rupture Time, h		Total % Elongation	
		Irradiated	Control	Irradiated	Control	Irradiated	Control	Irradiated	Control
538	55	60.2	64.2	107.0×10^6	9.3×10^6	26.7	263	17.6	38.9
	50	53.0	56.5	31.9	3.3	85.2	433	12.3	18.2
	45	47.1	49.5	24.2	1.4/2.7	107.8	1032	5.8	15.4
	40	41.1	43.1	6.3	0.8	149.6	2795	3.7 ^b	14
	36	36.7	38.1	1.0	~0.27	>673.5 ^c
	30	30.5	30.6	~0.1	~0.06 ^d	on test
593	45	46.8	50.0	489.0	250.0	11.5	23	14.1	~25.1
	40	40.6	43.3	68.6	4.4/34.2	45.5	~200	7.9	25
	36	36.6	38.4	23.2	~26.7	202.8	236	8.0	20.9
	30	30.2	31.3	4.7	~5.2 ^d	>1489 ^c
	26	26.1	26.7	0.9	~1.5 ^d	on test
	30	30.3	31.1	~84.5	212.0	56.8	95	...	~50
649	28	28.1	28.8	~42.8	94.4	~130	168	~13 ^b	51
	25	25.1	25.5	~25.0	63.8	262	375	...	66
	22	22.1	22.2	10.1	15.9	~800	1295	~19 ^b	35
	17	17	17.1	948	878	9.3	28	~8.8 ^b	72
	15	15	15	~222.0	460/412	20.1	72	7.2	70
	12	12	12	66	90.4	55.1	246	~4.5 ^b	64
760	10	10	10	23.2	28.5	146.5	1050	5.3	59

^a All tests in inert gas.
^b Estimated from creep curve.
^c Test stopped before rupture.
^d Extrapolated value.

TABLE 3—*Biaxial stress rupture data for AISI Type 316 stainless steel.*

Test Temperature, deg C	Hoop Stress, ksi		Rupture Time, h	Ductility ($\Delta D/D$), %	Average Creep Rate, in./in./h
	Engineering	True Initial			
538	52.0	71.0	0.1	N.A.	N.A.
	51.0	62.0	6.0	17.0	117 × 10 ⁶
	49.0	58.7	79	21.0	46.8
	48.0	56.7	55	14.0	54.6
	42.0	46.7	545	13.0	10.1
	38.0	44.8	1681	8.7	2.56
649	38.5	44.0	0.5	16.5	1120
	31.5	33.0	5.8	6.2	450
	30.0	31.4	12	5.8	225
	29.0	30.0	15	8.6	370
	25.5	26.0	70	4.8	46
	23.5	24.0	875	13.0	127
	20.0	20.0	385	1.9	3.6
	18.0	18.0	3470	6.7	1.93
	17.0	17.0	1230	14.3	115
	26.0	27.0	0.4	24.0	4350
760	19.8	20.0	6.8	19.2	2000
	18.0	18.0	10.0	15.0	1400
	17.0	17.0	16	13.9	800
	13.9	13.9	42	21.5	512
	9.6	9.6	300	9.1	31
	6.5	6.5	1981	9.6	4.8

mens. The rupture life of all irradiated specimens was reduced when compared to unirradiated control material. The reduction at 538 C was to a factor of about 1/20. Losses in rupture life at 593 and 649 C were less severe, with reductions to 1/5 to 1/2 and 1/2, respectively. At 760 C, the reduction in rupture life was to about 1/7.

Biaxial stress rupture results on the as-received material determined at 538, 649, and 760 C are given in Table 3. These results are in reasonable agreement with stress rupture data published by other experimenters [1, 2].² The results determined at the same temperatures for irradiated material are given in Table 4.

The biaxial stress rupture data are plotted as log stress against log rupture time in Fig. 3. It was found that irradiation reduced the rupture life of the 316 stainless steel, when tested under biaxial stress conditions, at each of the test temperatures. At 538 C the reduction in rupture life is to about 1/40. The decrease in rupture life at 649 C was only 1/2, while at 760 C the reduction in rupture life was to about 1/10.

² Italic numbers in brackets refer to the list of references at the end of this paper.

TABLE 4—Biaxial stress rupture data for AISI Type 316 stainless steel irradiated in EBR-II to 1.2×10^{22} n/cm² (total) at ~ 900 F (482 C).

Test Temperature deg C	Engineering Hoop Stress, ^a ksi	Rupture Time, h	Ductility ($\Delta D/D$), %	Average Creep Rate, in./in./h
538.....	58.3	0.1	3.3	...
	54.0	2.2	N.A.	N.A.
	50.0	4.1	4.3	1000×10^5
	50.0	9.6	3.8	397
	49.0	29	N.A.	N.A.
649.....	46.0	22	2.9	132
	40.0	140	1.0	10
	36.0	0.6	9.7	9744
	36.0	2.1	1.9	905
	30.0	32	2.4	75
760.....	25.2	20	0.5	25
	23.5	70	1.9	27
	18.0	739	5.7	7.7
	16.0	820	0.9	1.0
	23.5	0.3	N.A.	N.A.
760.....	17.5	1.4	N.A.	N.A.
	12.0	8.2	5.3	646
	7.8	330	5.3	16

^a Engineering and true stress assumed to be the same for irradiated tubes.

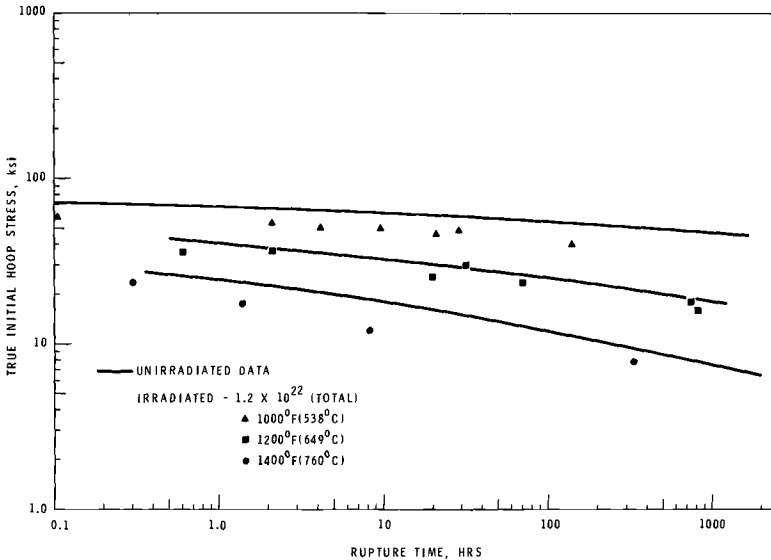


FIG. 3—Effect of EBR-II irradiation on the rupture life of AISI Type 316 stainless steel determined in biaxial tests.

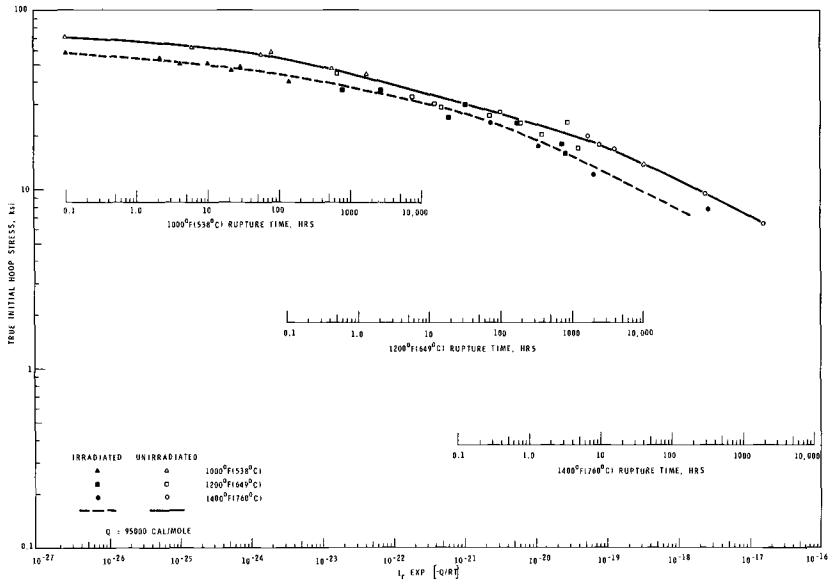


FIG. 4—Effect of EBR-II irradiation on the theta correlation of uniaxial test results for AISI Type 316 stainless steel.

Temperature-Compensated Rupture Life

The uniaxial data and the biaxial data are presented in Figs. 4 and 5 on log stress-log θ plots, where θ is defined as

$$\theta = t_r \exp \left(-\frac{Q}{RT} \right)$$

where

- t_r = rupture life,
- Q = activation energy, cal/mole,
- T = absolute temperature, deg K, and
- R = gas constant, cal/mole-deg.

Results from preirradiation and postirradiation tests correlate well with a Q value of 95,000 cal/mole in both the uniaxial and biaxial tests. Since only two of the 538 C uniaxial tests (at engineering stresses of 45 and 40 ksi) on irradiated specimens fall short of the curve, even within the 538 C test series, it appears that these specimens failed prematurely. The temperature-compensated rupture life plots in Figs. 4 and 5 clearly show the large reduction in rupture life at 538 C, the lesser reductions at 593 and 649 C, and the larger losses again at 760 C.

Creep Rates

The minimum creep rates determined in uniaxial tests on both irradiated and unirradiated material are given in Table 2. The results are plotted as log creep rate against log stress in Fig. 6. The creep rate was found to increase significantly (that is, by up to a factor of 10) after irradiation for tests at 538 C. The stress dependence of minimum creep rate appeared to be higher for irradiated material at this temperature. The magnitude and stress dependence of minimum creep rate do not appear to be changed significantly at test temperatures of 593, 649, and 760 C.

Average creep rates determined from biaxial tests are presented graphically in Fig. 7. These results also showed higher creep rates in irradiated material at a test temperature of 538 C. The creep rates of irradiated specimens at 649 C were virtually the same as the unirradiated values. Although the data at 760 C were quite limited, it appeared that irradiated creep rate values were again higher than unirradiated values.

Ductility

Strain at rupture in both uniaxial tests (see Table 2) and biaxial tests (see Tables 3 and 4) was reduced by irradiation. The lowest strains observed

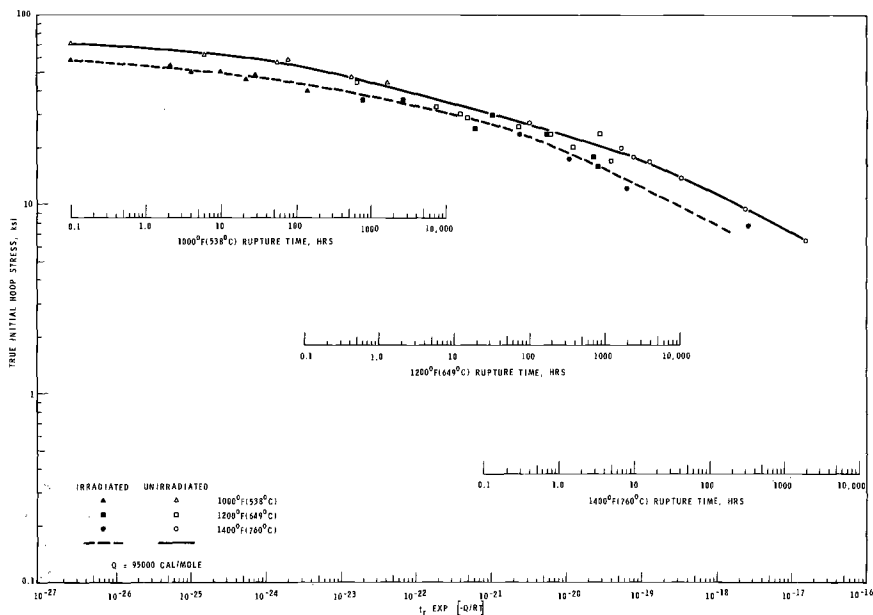


FIG. 5—Effect of EBR-II irradiation on the theta correlation of biaxial test results for AISI Type 316 stainless steel.

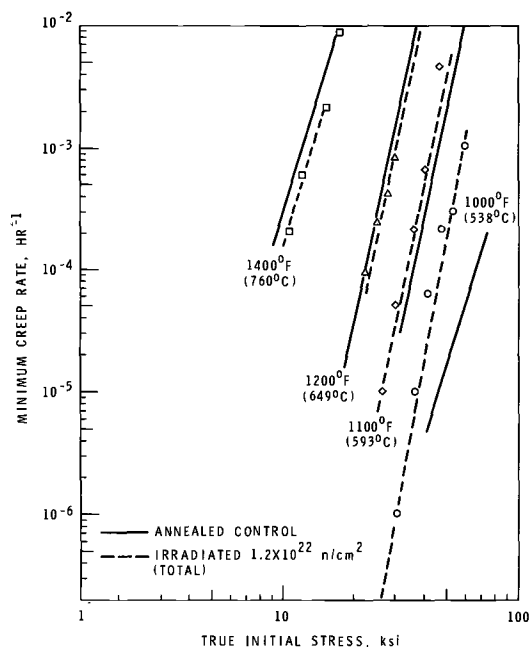


FIG. 6—Effect of EBR-II irradiation on the minimum creep rate of AISI Type 316 stainless steel determined in uniaxial tests.

were about 5 percent for uniaxial tests and about 1 percent for biaxial tests. Comparison of the uniaxial strain-time curves revealed that both second- and third-stage creep strain are reduced in irradiated material at temperatures of 593 C and above. Although the creep strains may be somewhat lower in irradiated material tested at 538 C, the major factor affecting ductility at this temperature was reduced plastic strain on loading.

Discussion

The results of this investigation show that fast reactor irradiation produces nearly the same changes in rupture life in both uniaxial and biaxial tests. This agreement between the two sets of test results shows that the basic material behavior is similar in both types of tests. However, it is important to emphasize that this conclusion is based on the use of initial true stress in comparing results from unirradiated specimens with results from irradiated specimens. If comparisons are based on engineering stress, then uniaxial tests and biaxial tests do not show the same losses in rupture life at high stresses. For example, it was found that the reduction in rupture life at 538 C, based on initial true stress, was to about $\frac{1}{40}$ in biaxial tests.

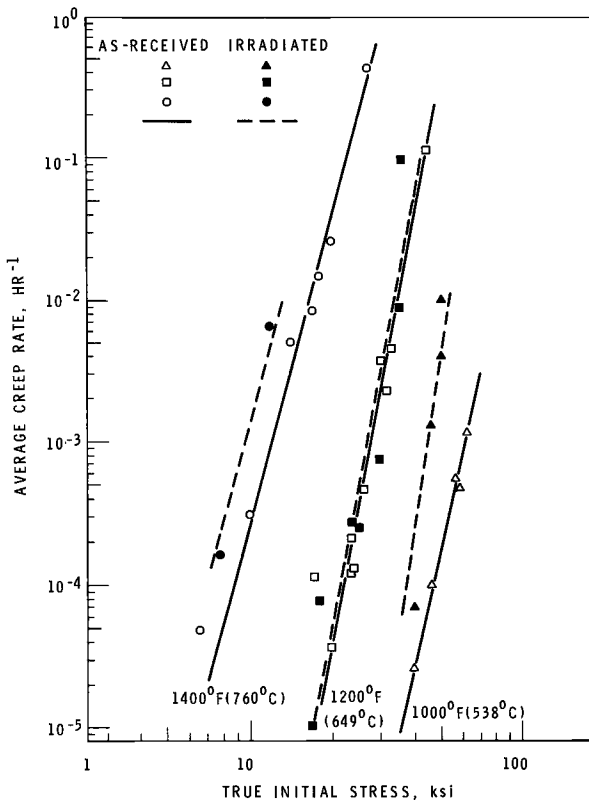


FIG. 7—Effect of EBR-II irradiation on average creep rate of AISI Type 316 stainless steel tube determined in biaxial tests.

If results for tests are compared on the basis of engineering stress, it is found that there is essentially no difference in rupture life at 538 C. On the other hand, the reduction in rupture life in 538 C uniaxial tests changes from a value of $1/20$ to a value of $1/10$ when the basis of comparison changes from initial true stress to engineering stress. Thus the differences in initial plastic strain between irradiated and unirradiated specimens are significant in evaluating rupture life losses, particularly in the case of high-stress biaxial tests. The use of engineering stress results in a significant apparent difference between uniaxial and biaxial test results; however, the use of initial true stress provides a precise correlation for the data.

Fast reactor irradiation can also affect the creep properties of Type 316 stainless steel, as evidenced by the increased creep rates measured in irradiated specimens at 538 C. Both the minimum creep rate values determined in uniaxial tests and the average creep rate values determined in

biaxial tests show the increased creep rate. At a temperature of 538 C there was very little primary or tertiary creep strain, so the average creep rate in biaxial tests should be a good approximation of the actual minimum creep rate. Minimum creep rates at 593, 649, and 760 C were apparently not significantly affected by irradiation; the average creep rate values indicate that irradiation does not affect creep rates in 649 C tests but does lead to increased creep rates in 760 C tests. The apparent discrepancy between the uniaxial test and the biaxial test in reflecting creep rate changes at 760 C probably is due to the fact that the average creep rate is no longer a good approximation of the actual minimum creep rate. Uniaxial tests on the unirradiated tubular material at 760 C indicated there was substantial primary creep strain; however, this primary creep strain is included as linear creep strain in computing average creep rates from the diametral strains. When primary creep becomes significant, it is quite possible to obtain higher average creep rate values for irradiated specimens, even though the actual minimum creep rate is the same in both irradiated specimens and unirradiated specimens.

Standring et al [1] have reported results on tubes irradiated in DFR and tested in a biaxial stress mode. They observed decreased rupture life for a given effective initial hoop stress, decreased ductility, and no change in average creep rate for tests at 650 C. The results observed in biaxial tests in the present study at 649 C are in qualitative agreement with these results. Creep rupture tests on uniaxial specimens after fast reactor irradiation in DFR have been reported by Weisz et al [3]. These observations indicated testing at 700 C after irradiation at 600 C to a total fluence of 1.6×10^{22} n/cm² resulted in increased minimum creep rates. The results in the present study for uniaxial tests at 649 and 760 C indicated little if any change in the minimum creep rate. The exact cause of the variance between the two sets of data is not clear, but quite possibly was related to differences in the irradiation temperature, alloy composition, fluence, or any combination of them.

A clear picture of the mechanism responsible for the increased creep rates at 538 C has not yet emerged, but several possible explanations are being evaluated currently. One consideration is that the increased creep rate is a result of irradiation induced precipitation that has been observed in the as-irradiated uniaxial material [4]. A current investigation [5] of unirradiated, thermally aged specimens of the uniaxial test material does indeed indicate that for aging temperatures above 600 C extensive precipitation can lead to increased creep rates similar to those observed in irradiated specimens. Although the relationship between the structure and the creep rate in material which has undergone extensive second-phase precipitation is not yet established, the present evidence identifies irradiation induced precipitation as one explanation of the increased creep rates.

Another possible explanation for the creep behavior centers on the irradiation induced defect structure. Transmission electron microscopy observations showed a low density of voids and dislocations in the as-irradiated uniaxial test material. Increased creep rates could result if this substructure somehow leads to an increased density or increased velocity of mobile dislocations during creep. At higher test temperatures, increased creep rates may not be observed if the substructure annealed out prior to beginning the creep test. At the present time there is no direct evidence or detailed theory to support these hypotheses. However, several irradiated specimens have been annealed for 50 h at 649 C prior to creep testing at 538 C. These specimens still exhibited higher creep rates than unirradiated specimens, so a simple picture of radiation damage annealing is apparently an inadequate explanation of the observed effects. Also, current studies by A. J. Lovell and L. D. Blackburn of this same alloy continue to show increased creep rates at 538 C over a wide range of irradiation temperatures and fluences. Therefore, if the observed creep behavior is directly related to the irradiation induced defect structure, the relationship is apparently a complex one.

The magnitude of rupture life loss after irradiation depends on test temperature and is related to the changes in creep rates and to reduced ductility. At 538 C the substantial loss in rupture life was primarily a result of the high creep rates, and the contribution from any ductility loss was relatively small. However, at temperatures of 593, 649, and 760 C, the losses in rupture life resulted from reduced ductility (reduced second- and third-stage creep strains), with no significant contribution from creep rate differences. The ductility loss was most severe at 760 C, and, correspondingly, a larger reduction in rupture life was observed at this temperature. The underlying cause of the low ductility at these higher temperatures was undoubtedly associated with a helium embrittlement mechanism, perhaps operating in conjunction with effects produced by the defect structure and second-phase precipitations.

Summary

Fast reactor irradiation to a total fluence of 1×10^{22} n/cm² at a temperature of 482 C resulted in a significant degradation of the creep rupture properties of Type 316 stainless steel. High creep rates, possibly resulting from irradiation induced precipitation, led to a substantial loss in rupture life at a test temperature of 538 C. Low ductility, probably attributable to helium embrittlement, was responsible for reduced rupture life in the temperature range from 593 to 760 C.

Results from both uniaxial and biaxial tests showed similar changes in rupture life when comparisons were based on initial true stress. Changes in rupture life measured in high-stress biaxial tests were substantially

smaller when the comparison was made on the basis of engineering stress because of substantial differences in initial plastic strain between unirradiated and irradiated specimens.

References

- [1] Standring, J., Bell, I. P., Tickel, H., and Glendinning, A. in *Irradiation Effects in Structural Alloys for Thermal and Fast Reactors*, ASTM STP 457, American Society for Testing Materials, 1969, pp. 414–428.
- [2] Lee, W. T., “Biaxial Stress-Rupture Properties of Austenitic Stainless Steels in Static Sodium”, A-1-AEC-12694, U. S. Atomic Energy Commission, June 1968.
- [3] Weisz, M., Malkin, J., Erler, J., and Andre, J. P. in *Irradiation Effects in Structural Alloys for Thermal and Fast Reactors*, ASTM STP 457, American Society for Testing and Materials, 1969, pp. 352–370.
- [4] Brager, H. R. and Kissinger, H. E., *Transactions*, American Nuclear Society, TANSAS, Vol. 12, 1969, p. 118.

A. L. Lowe, Jr.,¹ and C. J. Baroch¹

Effect of Irradiation on the Mechanical Properties of 19-9DL Alloy

REFERENCE: Lowe, A. L., Jr., and Baroch, C. J., "Effect of Irradiation on the Mechanical Properties of 19-9DL Alloy," *Irradiation Effects on Structural Alloys for Nuclear Reactor Applications*, ASTM STP 484, American Society for Testing and Materials, 1970, pp. 484-494.

ABSTRACT: Austenitic stainless steels, which are used extensively in water cooled nuclear reactors, are presently being considered for use in fast reactors; however, these steels are susceptible to irradiation embrittlement and irradiation induced swelling. The modified austenitic stainless steel 19-9DL alloy, on the other hand, exhibits good creep strength at high temperatures. Babcock & Wilcox conducted an exploratory program to determine the effects of irradiation on 19-9DL alloy at temperatures of 55 C (130 F), 343 C (650 F), and 413 C (775 F). The maximum fluence in this program (9.2×10^{20} n/cm², $E > 1$ MeV) was too low to prove the suitability of the alloy's potential for fast reactor applications but did show that additional evaluation of the alloy for fast reactors was warranted. The results indicate that the alloy is suitable for use in thermal reactors, since the ductility at 413 C was greater than 10 percent at a fluence approaching 1×10^{21} n/cm², $E > 1$ MeV.

KEY WORDS: irradiation, neutron irradiation, water cooled reactors, fast reactors (nuclear), thermal reactors, nuclear fuel cladding, creep properties, mechanical properties, yield strength, ultimate strength, ductility, elongation, annealing, solid solutions, austenitic stainless steels

The U.S. Atomic Energy Commission and reactor manufacturers are conducting extensive programs to select a suitable cladding material for use in fast reactors. The requirements are stringent because the cladding must have a relatively low neutron capture cross section and resist attack by sodium. In addition, it must have a high creep strength at 700 C (1300 F) to contain the fission gases, must withstand plastic deformation caused by swelling of the fuel, and must not swell excessively because of fast neutron irradiation damage.

¹ Senior materials engineer, Nuclear Power Generation Dept., Power Generation Div., and chief, Ceramics and Metallurgy Section, Research and Development Div., respectively, Babcock & Wilcox Co., Lynchburg, Va. 24505.

19-9DL alloy has been considered for use in fast reactors because its creep strength at temperatures from 649 C (1200 F) to 760 C (1400 F) may be as much as 2.5 times that of Type 316 stainless steel, the current reference cladding [1, 2].² This modified 18-8 austenitic stainless steel contains small additions of molybdenum, tungsten, and carbon which serve as solid solution strengtheners. The long-term corrosion behavior of 19-9DL in sodium and water and its behavior under irradiation are relatively unknown.

In 1965 Babcock & Wilcox (B&W) initiated a program to determine the effects of irradiation on the mechanical properties of core materials [3]. Since there was unused space in the irradiation capsules, positions in five capsules were filled with 19-9DL alloy specimens. A total of 210 tension specimens were irradiated at 55 C (130 F), 343 C (650 F), or 413 C (775 F) to fast fluences ranging from about 2×10^{17} to 9.2×10^{20} n/cm², $E > 1$ MeV. Irradiated and unirradiated specimens were tested at 20 C (70 F), 413 C (775 F), and 700 C (1300 F). This paper describes the results of these tests and their significance.

Program and Materials

Program Description

The capsules were irradiated in the Babcock & Wilcox test reactor (BAWTR) for periods ranging from 60 h to 300 effective full power days. Fluences ranged from about 2×10^{17} to 9.2×10^{20} n/cm², $E > 1$ MeV. Each capsule was divided into three sections, one operating at 55 C (130 F), one at 343 C (650 F), and one at 413 C (775 F), each of which contained 12 specimens of 19-9DL. The variables for the irradiation program are shown in Table 1. Unirradiated specimens were aged for 60 h and 45 days at 343 and 400 C and for 340 days at 343 C. The aged specimens were

TABLE 1—*Irradiation program variables.*

Variable	Limits
Fast flux, n/cm ² -s, $E > 1$ MeV.....	7×10^{12} and 3×10^{13}
Peak fast fluence, n/cm ² , $E > 1$ MeV.....	1.5×10^{18} , 2.7×10^{19} , 1.2×10^{20} , 1.8×10^{20} , 8×10^{20}
Exposure time, days.....	2, 45, 300
Irradiation temperature,	
deg C.....	55, 343, 413
deg F.....	130, 650, 775
Tension test temperature,	
deg C.....	20, 413, 700
deg F.....	70, 775, 1300

² Italic numbers in brackets refer to the list of references at the end of this paper.

tested at 20 and 413 C. The as-received, aged, and irradiated specimens were tested at 20, 413, and 700 C (1300 F).

The tension specimens were prepared from tubing having an outside diameter of 1.27 cm (0.500 in.) and a wall thickness of 0.051 cm (0.020 in.). The tubing was annealed at 982 C (1800 F) after the final reduction and thus did not possess necessarily the highest creep strength. Tubing was flattened in a hydraulic press and cut into strips 0.762 cm (0.300 in.) wide and 6.98 cm (2.75 in.) long. A Tensile Kut machine was used to prepare the reduced gage section, which was 2.54 cm long with a cross section of 0.0508 ± 0.0025 cm by 0.508 ± 0.05 cm. The specified and actual compositions of the tubing are shown in Table 2.

The as-received, aged, and irradiated specimens were tested at 20, 413, and 700 C (1300 F). Some specimens tested at 700 C were annealed for 1 h at 1000 C (1832 F) before testing to remove radiation induced damage. Irradiation programs on austenitic stainless steels have shown that at test temperatures below 538 C (1000 F), irradiation produces displacement defects that harden the lattice, increase the strength, and reduce the ductility. At test temperatures above 538 C, displacement defects are removed very rapidly; as a result, strength is not affected, but ductility is considerably reduced. The loss of ductility at the higher temperatures cannot be restored even by solution annealing. The 19-9DL annealed

TABLE 2—19-9DL composition.

Element	Percentage			
	Specification ^a		Nominal	Mill Test Report
	Range			
Nickel	8.0	to 11.0	9.0	8.79
Iron	Balance		Balance	Balance
Chromium	18.0	to 20.0	18.5	18.85
Molybdenum	1.0	to 1.75	1.4	1.44
Columbium	0.25	to 0.60	0.40	0.38
Tungsten	1.0	to 1.75	1.35	1.12
Titanium	0.1	to 0.35	0.25	0.32
Carbon	0.28	to 0.35	0.32	0.32
Manganese	0.75	to 1.50	1.15	1.20
Silicon	0.30	to 0.80	0.55	0.70
Phosphorus	0.040	max	0.025	0.027
Sulfur	0.030	max	0.01	0.004
Copper	0.5	max	0.15	0.12
Boron		^b	^b	^c
Nitrogen		^b	^b	^c
Rare earths		^b	^b	^c

^a Aeronautical Material Specification 5526.

^b Not applicable.

^c Not available.

specimens were used to determine whether similar behavior was observed in this program.

Irradiation Capsule

Each irradiation capsule had three sections: one maintained at 775 F, one at 650 F, and one at ambient reactor temperature, about 130 F. A helium or helium-argon atmosphere in the capsule prevents contamination of the specimens during irradiation and provides the desired insulating properties. The elevated temperatures are maintained in the capsule with electric heaters spirally wrapped around the specimen housing unit. Iron and nickel flux wires are placed in the capsule at various locations to determine the integrated fast neutron flux.

The assembled capsules, approximately 30 in. long and 1.75 in. in diameter, are irradiated in a reflector or a center position of the BAWTR. The peak instantaneous fast fluxes ($E > 1$ MeV) in the reflector and center positions are approximately 7×10^{12} and 3×10^{13} n/cm²-s, respectively. The thermal flux is 4×10^{13} n/cm²-s in the reflector and 1×10^{14} n/cm²-s in the center positions.

Test Procedure

A specially designed compensating extensometer that could be used at all test temperatures was attached to the specimens using a special fixture suitable for remote operation. The specimens were tested at a crosshead speed of 0.02/min. The elevated temperature specimens were allowed to reach the desired temperature and then soaked an additional 10 min before testing. In all elevated-temperature tests, a thermocouple to monitor temperature was attached to the specimen's grips. The temperature measured by the thermocouple was compared with that measured by thermocouples in a dummy specimen used in the daily calibration of the equipment. Based on this calibration, it was possible to maintain the temperature of the grips so that the specimens were also at the desired temperature. The test procedures and the temperatures of the specimen were within the allowable limits of ASTM recommended practices.

Standard tension test procedures are used to determine yield strength and ultimate tensile strength. The uniform elongation and total elongation are obtained directly from the load-elongation plot obtained from the extensometer. Tests have shown that the total plastic strain recorded on the chart is very similar to that obtained by measuring the gage length before and after fracture.

Results

Properties at 20 C (70 F)

The results of tests conducted at 20 C are plotted in Figs. 1 and 2. Irradiation at 55 C (130 F) significantly increases the yield and ultimate

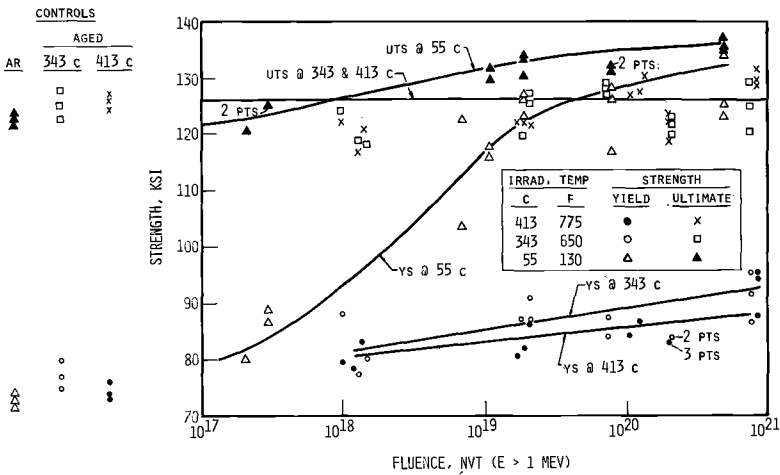


FIG. 1—Effect of irradiation on strength of 19-9DL at 20 C (70 F).

strengths and decreases uniform and total elongations; the changes are more pronounced at the higher fluences. Irradiation at 343 C (650 F) and 413 C (775 F) did not affect the ultimate strength but did cause a minor increase in the yield strength and a minor decrease in elongation. Apparently there were no significant differences in the properties of the 19-9DL irradiated at 343 C and of that irradiated at 413 C. Aging the specimens at 343 and 413 C had essentially no effect on the properties of 19-9DL at 70 F.

Properties at 413 C (775 F)

The results of the tests conducted at 413 C are shown in Figs. 3 and 4. These results are similar to those observed at 20 C. The only differences are in the absolute values for strength and elongation, both of which are

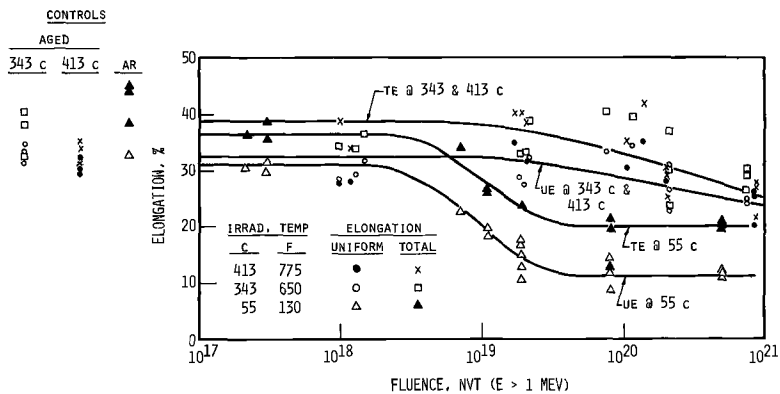


FIG. 2—Effect of irradiation on elongation of 19-9DL at 20 C (70 F).

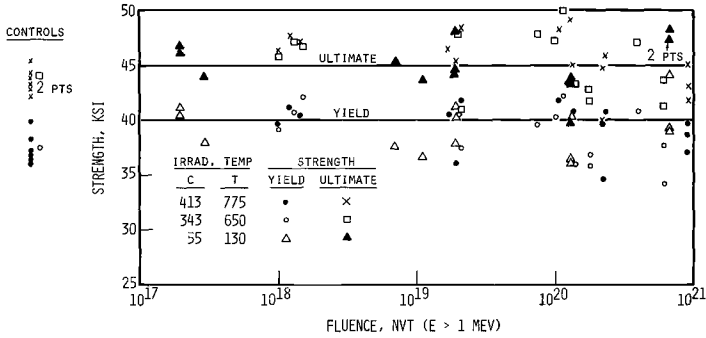


FIG. 5—Effect of irradiation of strength of 19-9DL at 700 C (1300 F).

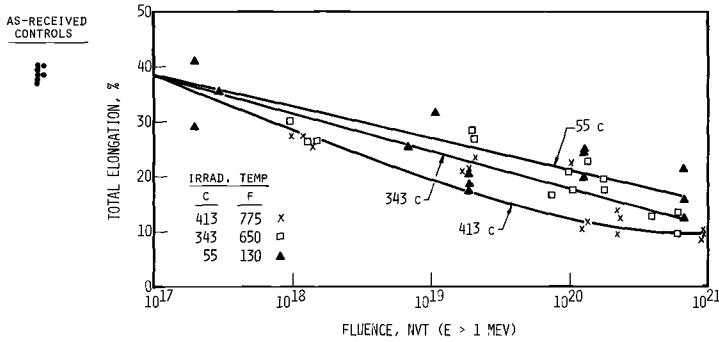


FIG. 6—Effect of irradiation on total elongation of 19-9DL at 700 C (1300 F).

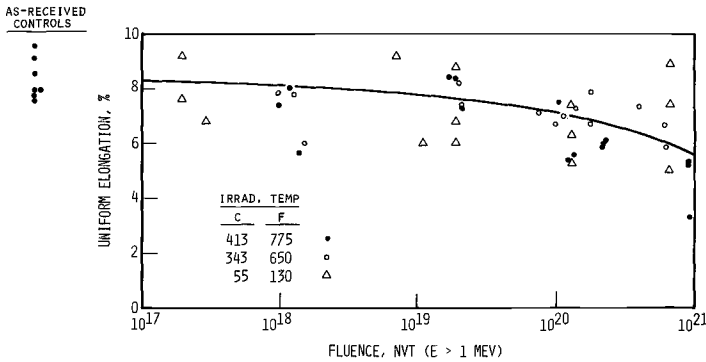


FIG. 7—Effect of irradiation on uniform elongation of 19-9DL at 700 C (1300 F).

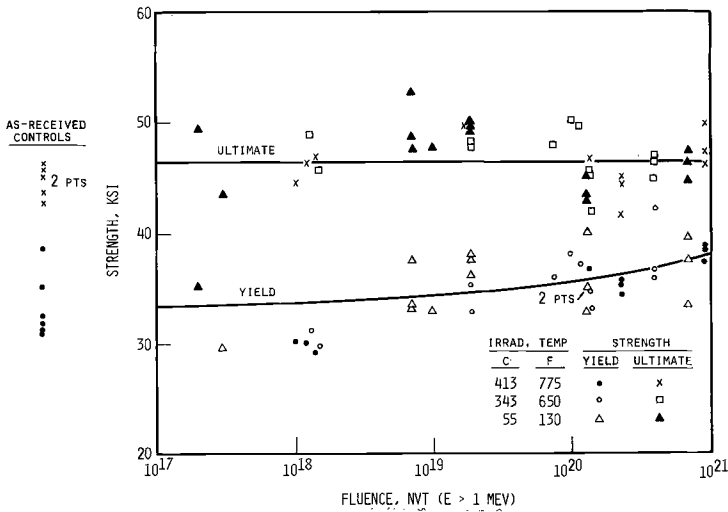


FIG. 8—Strength of irradiated 19-9DL at 700 C (1300 F) after annealing for 1 h at 1000 C (1832 F).

elongation. The uniform elongation did not seem to be related to the irradiation temperature. At 700 C the uniform and total elongations were not identical, as they were at 413 C; in fact, the uniform and total elongations at 700 C were significantly different.

Properties at 700 C (1300 F) After Annealing at 1000 C (1832 F)

Some of the irradiated and unirradiated 19-9DL specimens were annealed at 1000 C for 1 h before testing to determine the contribution of radiation induced damage to the changes in properties at elevated temperatures. The results are presented in Figs. 8 and 9. These data indicate that some of the effects of irradiation remain after annealing.

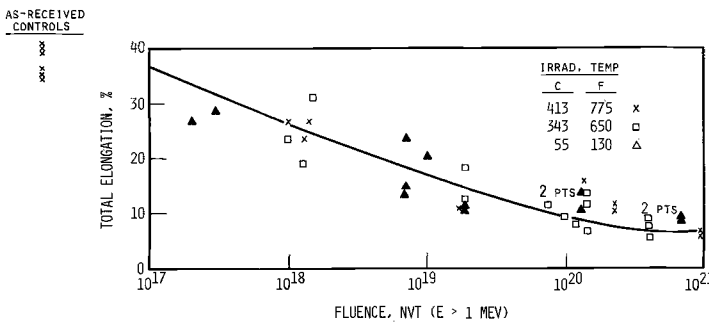


FIG. 9—Total elongation of irradiated 19-9DL at 700 C (1300 F) after annealing for 1 h at 1000 C (1832 F).

The effectiveness of the annealing operation can be assessed better by comparing Figs. 5, 6, and 7 with Figs. 8 and 9. Irradiation does not affect the ultimate strength, and annealing does not affect the ultimate strength of the unirradiated or the irradiated material. Annealing does not reduce the yield strength of both the irradiated and the unirradiated material because the annealing operation is less effective at fluences exceeding 10^{20} n/cm². At fluences of about 10^{21} n/cm², the yield strength is essentially unaffected by annealing.

Annealing has only a minor effect on total elongation. However, annealing does eliminate any difference in total elongation because of differences in the irradiation temperature. At fluences of less than 10^{20} n/cm², the uniform elongation is increased by annealing; at fluences of more than 10^{20} n/cm², the annealing operation becomes less effective; and, at fluences of about 10^{21} n/cm², annealing has no effect on uniform elongation.

Evaluation of Data

Many data are available on the effects of irradiation on the properties of ferrous metals. It is difficult to compare the various data precisely because many factors determine the behavior of the materials during irradiation. It has been shown that irradiation temperature, test temperature, strain rate, alloy composition, crystallographic structure, grain size, heat treatment, fluence, and flux spectrum are important variables.

The fluence received by the 19-9DL specimens in this program was too low to permit assessment of the potential of the material for use in fast reactors. However, the data at 1300 F indicate that the material is not extremely sensitive to irradiation embrittlement because the uniform elongation does not appear to be sensitive to fluence. These results, coupled with the work of Kramer [4] showing that 19-9DL was still ductile after being injected with helium particles, indicate that the material may indeed be suitable for fast reactor application. However, the properties at higher fluences and higher irradiation temperatures must be determined before the full potential of the material is known.

At the test temperature of 413 C (775 F), the 19-9DL was very ductile after receiving fluences as high as 10^{21} n/cm². Extrapolation of these data indicate that the elongation will be about 10 percent at a fluence of 10^{22} n/cm². This is in contrast to the Irvin and Bement [5] data on annealed Type 304 stainless steel, which indicated that the elongation of Type 304 stainless steel at all test temperatures is less than 3 percent at a fluence of 6×10^{21} n/cm².

Conclusions

Several conclusions can be made based on the results of this program.

1. The tensile properties of 19-9DL were affected by irradiation regardless of irradiation and test temperatures. In some instances there was an

increase in strength accompanied by a decrease in ductility, and in other instances there was only a decrease in ductility. The effects were most pronounced at a test temperature of 20 C (70 F) and an irradiation temperature of 55 C. Although the alloy is susceptible to the elevated-temperature (700 C) embrittlement, it is less susceptible to embrittlement than is Type 304 stainless steel irradiated under similar conditions.

2. At the test temperature of 413 C (775 F), only minor changes in the tensile properties were observed after irradiation at 343 and 413 C. The uniform elongations exceeded 10 percent at a fluence of 10^{21} , and extrapolation of the data to 10^{22} indicated that the elongations would range from about 8 to 10 percent. Because of this resistance to embrittlement, 19-9DL appears to be more suitable for thermal reactors than Type 304 stainless steel.

3. Thermal aging at 343 and 413 C has essentially no effect on the tensile properties at 20 and 413 C.

References

- [1] Lowe, A. L., Jr., "Steam-Cooled Breeder Reactor—Mechanical and Physical Properties of Selected High-Temperature Materials," BAW-237, Babcock & Wilcox, Lynchburg, Va., July 1965.
- [2] AEC Fuels and Materials Development Program, Progress Report No. 78, GEMP-1010, General Electric Co., Cincinnati, Ohio, Dec. 1968.
- [3] Harbinson, E. N. and Baroch, C. J., *Journal of Materials*, JMLSA, Vol. 3, No. 1, March 1968, pp. 107–115.
- [4] Kramer, D., unpublished work on helium embrittlement studies, Atomic International, Canoga Park, Calif., May 1969.
- [5] Irvin, J. E. and Bement, A. L. in *The Effects of Radiation on Structural Metals*, ASTM STP 426, American Society for Testing and Materials, 1967, pp. 278–327.

DISCUSSION

*Ph.B. van Asbroeck*¹—Irradiation experiments carried out at C.E.N./S.C.K., Mol, Belgium, under higher fast fluences than those reported by A. L. Lowe, Jr., and C. J. Baroch show that 19-9DL is still less susceptible to elevated-temperature embrittlement than austenitic stainless steel.

19-9DL solution annealed 15 min at 1050 C and aged 1 h at 760 C, AISI 316 solution annealed 15 min at 1050 C, and Incoloy-800 annealed 15 min at 980 C in the form of tension plate specimens (0.5 mm thick) have been neutron irradiated at 60 C in BR2 up to a fast fluence of 2.65 n/cm², $E > 0.1$ MeV, 1.30 n/cm², $E > 1$ MeV, and a thermal fluence of 2.4 n/cm². Total elongation at 700 C (Table 1 of the discussion) has been measured by postirradiation tension testing at a strain rate of 5×10^{-3} min⁻¹. The analysis of the table indicates a levelling of the total elongation decrease between a fast fluence of 1.2 and 1.9×10^{21} n/cm², $E > 0.1$ MeV. Tension tests on specimens irradiated at a fast fluence greater than 10^{22} n/cm² are under way and will check this levelling.

Furthermore if the ratio of the total elongation before irradiation to the total elongation after irradiation is taken as a measure of the susceptibility to high-temperature embrittlement, statistical testing leads to the conclusion that this susceptibility is different for the three alloys at a 5 percent level of significance. The value of this susceptibility to high-temperature (700 C) embrittlement is about 2.6 for 19-9DL, 4.3 for AISI 316, and 9.0 for Incoloy-800.

TABLE 1—Total elongation at 700 C (strain rate = 5×10^{-3} min⁻¹; irradiation temperature = 60 C).

Fast Fluence, $E > 0.1$ MeV, n/cm ²	Total Elongation, %		
	19-9DL	AISI 316	Incoloy-800
0	58.5, 63.5, 68.0	68.0, 70.0, 72.5	71.0, 72.5, 77.6
1.20×10^{21}	26.7, 28.6, 35.5	19.0, 19.1, 22.0	10.0, 11.4, 11.4
1.90	22.4	20.5	7.1
2.30	23.4	16.9	7.6
2.50	20.0, 24.8	15.3, 22.9	8.1, 9.1
2.65	19.6, 24.9, 26.3, 27.7	10.5, 11.9, 11.9, 17.6	7.2, 9.3, 10.2

¹ Ingénieur civil, U.I.Lv., section head, C.E.N.-S.C.K., B-2400 Mol, Belgium.

K. Ehrlich,¹ H. Böhm,¹ and C. Wassilew¹

Influence of Neutron Irradiation on the Creep Rupture Properties of a 16Cr-13Ni Steel

REFERENCES: Ehrlich, K., Böhm, H., and Wassilew, C., "Influence of Neutron Irradiation on the Creep Rupture Properties of a 16Cr-13Ni Steel," *Irradiation Effects on Structural Alloys for Nuclear Reactor Applications*, ASTM STP 484, American Society for Testing and Materials, 1970, pp. 495-508.

ABSTRACT: The influence of neutron irradiation (up to 1.1×10^{22} n/cm², $E > 0.1$ MeV) on the creep rupture properties of a Cb stabilized 16Cr-13Ni steel was studied in this paper. Different heat treatments and cold work conditions and several irradiation temperatures were investigated.

Low-temperature irradiation causes an increase in time to rupture at 650 and 750 C, whereas creep rate is reduced by more than a factor of ten. The creep ductility decreased to less than 1 percent. High-temperature irradiation does not cause a substantial change in rupture time at 650 C for the aged condition and the 50 percent cold work and 50 percent cold work + 1 h 850 C conditions.

The rupture life of specimens which were cold-worked 10 percent is strongly decreased by irradiation. Only slight changes in creep rate could be observed after high-temperature irradiation. Electron microscopy investigations indicate that the increase in rupture life and reduction in creep rate after low-temperature irradiation is due to a large number of dislocation loops. In the specimens irradiated at 650 C and above only He bubbles could be detected.

KEY WORDS: irradiation, neutron irradiation, radiation effects, bursting, creep rate, creep rupture strength, creep tests, ductility, embrittlement, dislocations, cold working, hardening (materials), heat treatment, austenitic stainless steels, precipitation hardening steels, nickel-chromium steels

The influence of neutron irradiation upon the creep rupture properties of austenitic stainless steel is one of the most important factors which governs the behavior of fuel element cladding for fast breeder reactors. A large number of papers have been published about the creep rupture behavior of austenitic steels during and after irradiation [1-8].² Most of these investigations have been carried out on AISI Type 316 and 304 stainless steels.

¹ Institut für Material- und Festkörperforschung, Kernforschungszentrum Karlsruhe, Germany.

² Italic numbers in brackets refer to the list of references at the end of this paper.

All results show that neutron irradiation leads to a remarkable reduction in rupture life and ductility, when tested above $T_M/2$, independent of irradiation temperature. In contrast to the change of rupture life by irradiation the creep rate is influenced in a nonuniform manner. The effect of irradiation has been found to cause faster creep rates [5], slower creep rates [1], and no change in creep rate [1, 2, 3, 5]. A comparison of the in-reactor and postirradiation creep rupture properties of 304 stainless steel shows no difference in rupture life and creep rate [2]. This result, as well as other in-pile creep experiments [1, 3] which show no change in creep rate, indicates that neutron irradiation, at least at low fluxes ($<10^{14}$ n/cm²-s), does not change the mechanism of the deformation process by irradiation induced point defects. Further in-pile creep tests must show whether this is also true in high, fast neutron fluxes.

The formation of stable dislocation loops and voids, which appear in austenitic stainless steel at high fluences ($>10^{22}$ n/cm²), can reduce the creep rate at temperatures at about $T_M/2$, as A. J. Lovell [7] has shown. The observed changes in creep rate at lower neutron fluxes and fluences may be attributed to irradiation induced precipitation processes [5] or perhaps to pinning of dislocations by helium bubbles [9]. The published results indicate that the reduction in rupture life after irradiation at low fluences is mainly due to high-temperature embrittlement induced by n,α reactions and only in some cases influenced by a change in creep rate. It is to be expected that the influence of irradiation induced defects upon creep rate and rupture life is increasing with higher fast neutron fluxes and fluences.

Because high-temperature embrittlement and changes in creep rate due to irradiation influenced precipitation processes should be dependent on the structure of the steel, it seemed important to study the postirradiation behavior of a 16Cr-13Ni steel (steel number 1.4988) in different conditions and after different neutron irradiations.

Experimental Procedure

The chemical composition by weight percent of the commercial chromium-nickel steel used in this investigation was 0.08 C, 0.27 Si, 1.1 Mn, 0.019 P, 0.009 S, 16.1 Cr, 13.6 Ni, 1.28 Mo, 0.7 V, 0.87 Nb, 0.0002 B, and balance Fe. Sheet specimens (thickness 0.5 mm, gage length 25 mm) of this steel in the normal heat-treated condition (1 h 1050 C + 3 h 750 C) were irradiated in the BR 2 reactor Mol and in the DIDO reactor at Jülich. Other specimens were irradiated in four different heat-treated and cold-worked conditions in the BR 2. The data of irradiation and the conditions of the material are compiled in Table 1.

Postirradiation creep rupture tests were performed at 650 C and in some cases at 750 C in lever arm machines. The accuracy of the strain measurement is about 5×10^{-3} percent strain.

TABLE 1—Irradiation conditions and thermomechanical treatments of a 16Cr-13Ni steel.

Reactor	Irradiation Temperature, deg C	Thermal Neutron Dose, n/cm ²	Fast Neutron Dose, n/cm ² , E > 0.1 MeV	Heat Treatment and Cold Working
BR 2.....	50	0.6×10 ²²	0.8×10 ²²	1 h 1050 C+3 h 750 C
DIDO.....	650	1.0×10 ²¹	4.5×10 ²⁰	1 h 1050 C+3 h 750 C
BR 2.....	650 to 750	0.7×10 ²²	1.1×10 ²²	Solution anneal+10% cold work; solution anneal+10% cold work+1 h 850C; solution anneal+50% cold work; solution anneal+50% cold work +1 h 850 C

The nature of the substructure was revealed by thin film electron microscopy with the use of a Siemens Elmiskop I A. Sheet specimens were prethinned to about 0.2 to 0.3-mm thickness by electropolishing in a solution of 90 percent nitric acid, 5 percent hydrofluoric acid, and 5 percent water at 10 to 15 V and 0.9 A/cm². Afterwards small disks of 3-mm diameter were punched from the unstrained heads of the creep specimens or from the gage lengths. The final electropolishing was done in an automatic jet polishing cell with a solution of 80 percent methanol and 20 percent sulfuric acid at 12 V and 0.6 A/cm².

Results

The results of the creep rupture tests of the specimens irradiated at 50 C and up to 0.8×10²² n/cm² are summarized in Figs. 1 and 2. As can be seen from these figures, the low-temperature irradiation causes a strong increase in rupture life at 650 and even 750 C and a reduction in minimum creep rate by a factor of more than ten. The creep ductility is reduced by irradiation to less than 1 percent compared with about 10 percent for the unirradiated specimens. Tension tests of the irradiated specimens have shown an increase in yield strength of about 15 kg/mm² at 650 C and of about 8 kg/mm² at 750 C, whereas the ultimate tensile strength remains nearly unchanged at both test temperatures.

It seemed to be of interest to study the influence of postirradiation heat treatment on the creep rupture properties. Because annealing above 750 C would cause a change not only of the irradiation induced defects but also of the prior carbide distribution, a postirradiation heat treatment (1050 C+3 h 750 C) which led to prior structure was carried out. The rupture life and ductility of the specimens, treated in this manner, is slightly reduced

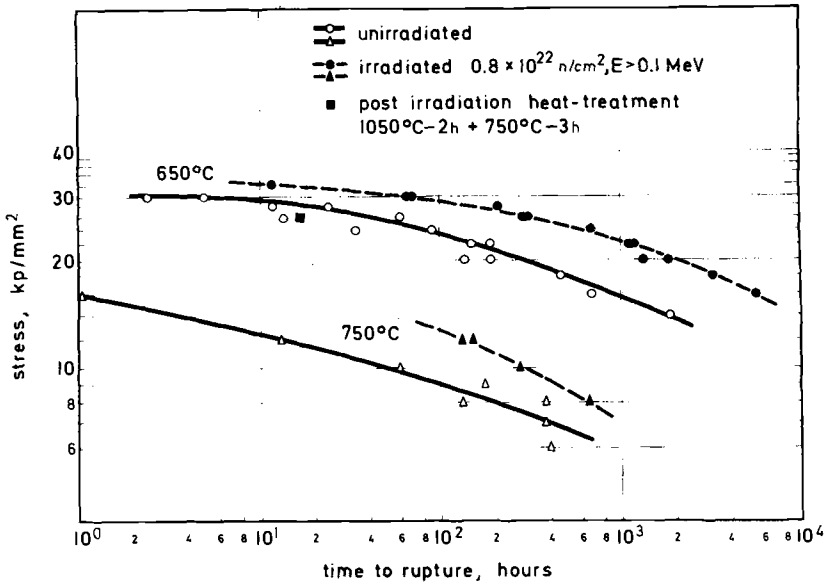


FIG. 1—Effect of neutron irradiation on the rupture life of 16Cr-13Ni steel at 650 and 750 C. Irradiation temperature 50 C; preirradiation heat treatment 1050 C/1 h + 750 C/3 h.

compared with the unirradiated materials, whereas the creep rate has the same value as in the unirradiated condition (Figs. 1 and 2). Compared with the properties of the as-irradiated specimens, strain at fracture is strongly increased (to about 8 percent) by the postirradiation treatment.

The rupture life, creep rate, and total elongation at 650 C of the normally

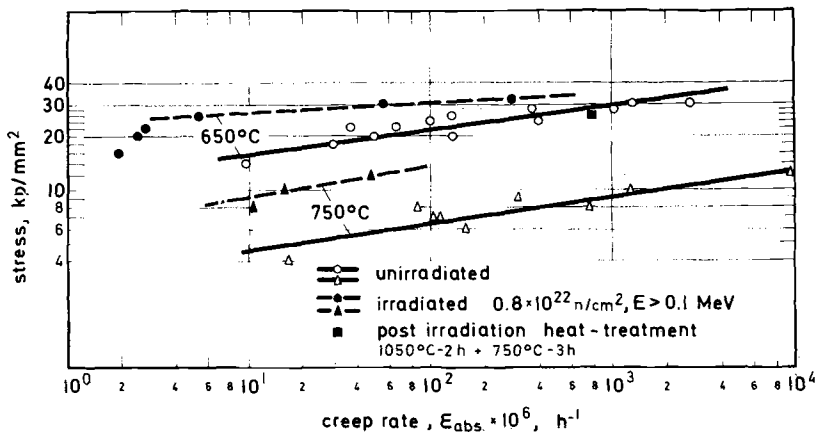


FIG. 2—Minimum creep rate of irradiated and unirradiated 16Cr-13Ni steel at 650 and 750 C. Irradiation temperature 50 C.

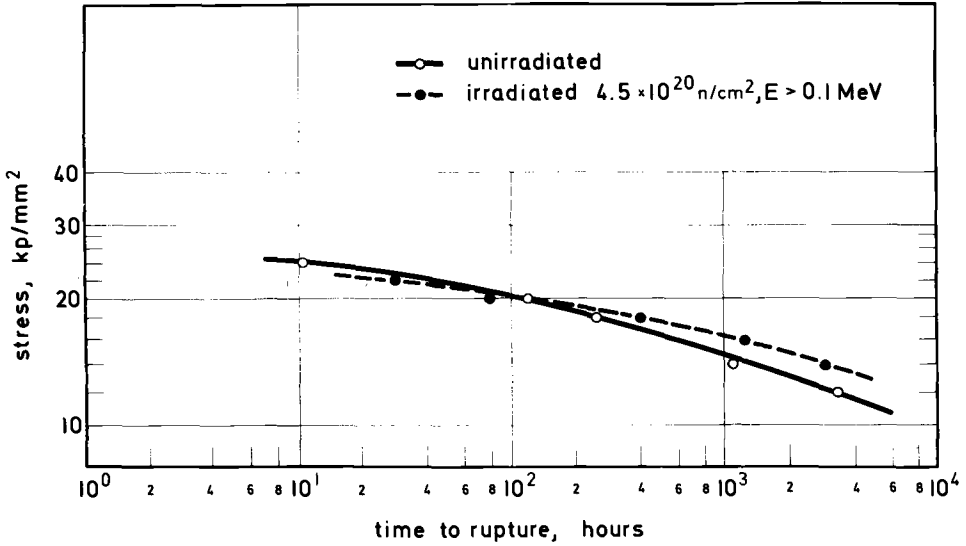


FIG. 3—Effect of neutron irradiation on the rupture life of 16Cr-13Ni steel at 650 C. Irradiation temperature 650 C; preirradiation heat treatment 1050 C/1 h+750 C/1 h.

heat-treated specimens after irradiation at 650 C to a fast neutron fluence of 4.5×10^{20} n/cm² are given in Figs. 3, 4, and 5. In order to get comparable results the unirradiated specimens were aged at 650 C for the irradiation time, so differences between the irradiated and unirradiated condition are due only to irradiation influence and not to annealing affects. As indicated by the figures, stress rupture strength remains nearly unaffected by this irradiation, while creep rate and ductility are reduced.

The influence of different thermomechanical treatments upon the post-irradiation creep rupture properties can be seen from Figs. 6–11. As

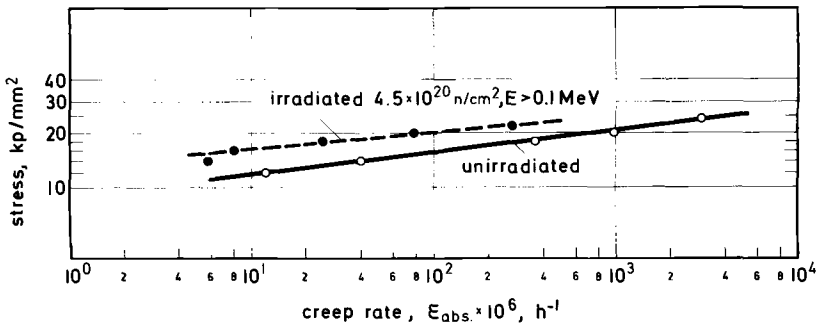


FIG. 4—Minimum creep rate of irradiated and unirradiated 16Cr-13Ni steel at 650 C. Irradiation temperature 650 C.

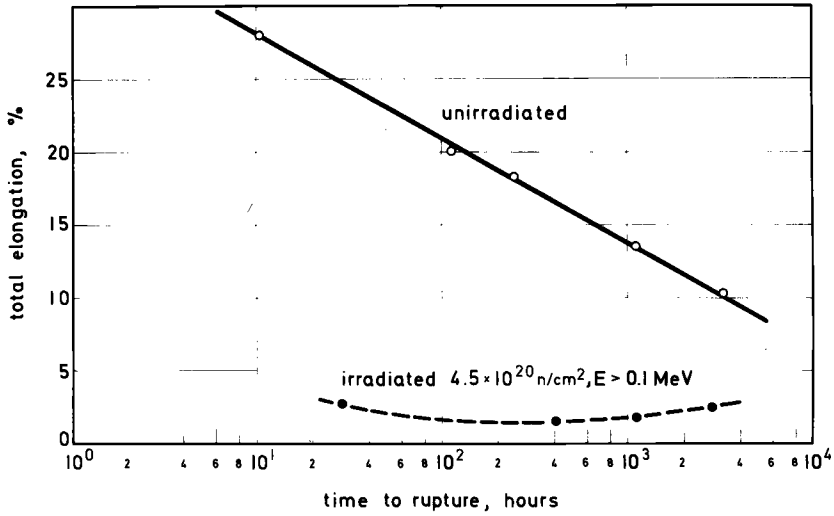


FIG. 5—Total elongation versus rupture time for unirradiated and irradiated 16Cr-13Ni steel tested at 650 C. Irradiation temperature 650 C.

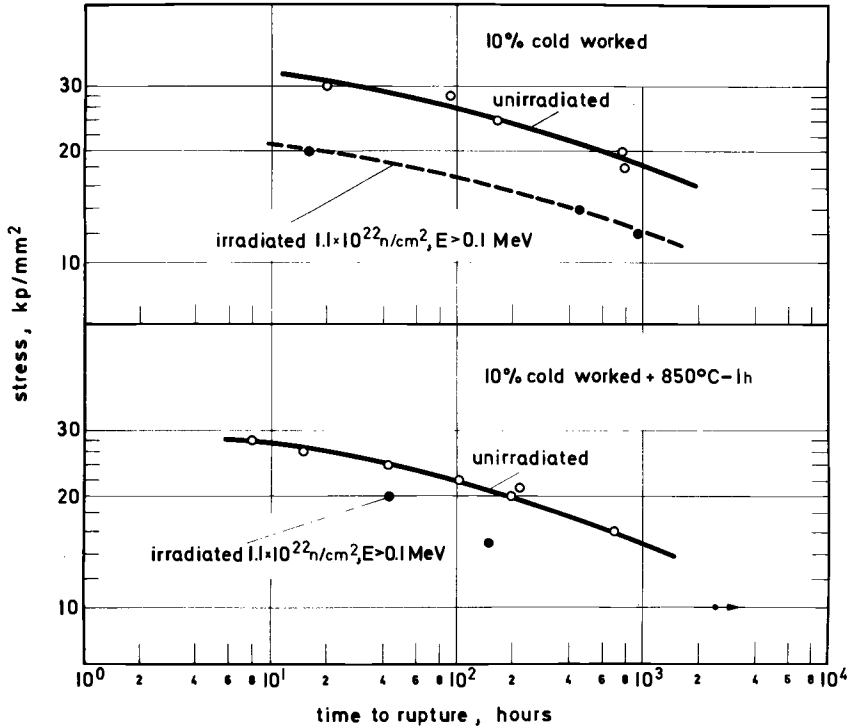


FIG. 6—Rupture life of irradiated and unirradiated 16Cr-13Ni steel in different conditions at 650 C. Irradiation temperature 650 to 750 C.

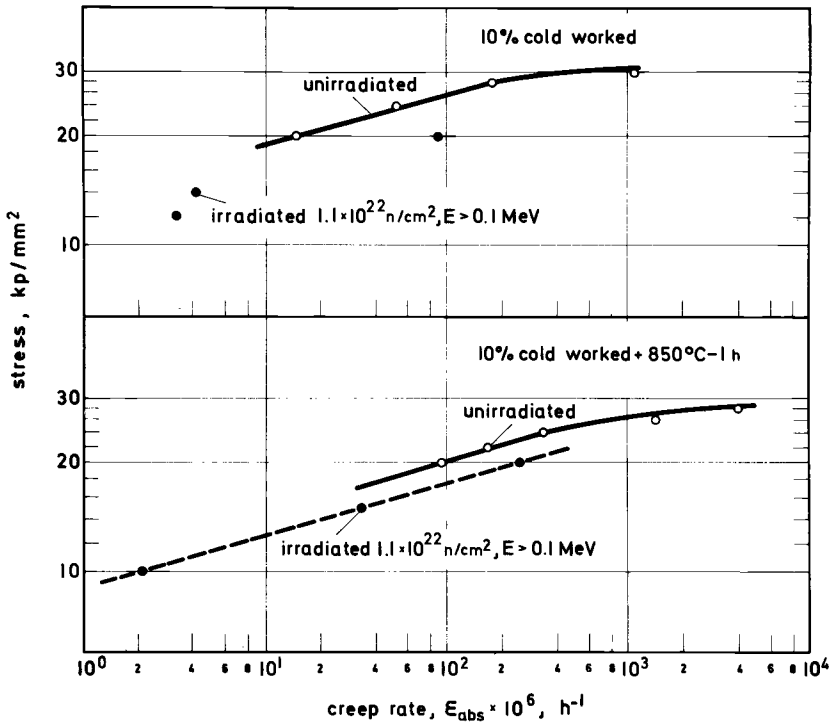


FIG. 7—Minimum creep rate versus stress for $^{16}\text{Cr}\text{-}^{13}\text{Ni}$ steel in different conditions. Irradiation temperature 650 to 750 C.

pointed out earlier, the unirradiated conditions have been aged at about the irradiation temperature for the corresponding time. Figures 6, 7, and 8 show that the rupture life and strain at fracture of the 10 percent cold work and 10 percent cold work + 1 h 850 C anneal conditions are severely reduced by the high-temperature irradiation, while the creep rate remains nearly unchanged. This result is in agreement with earlier investigations [6] on in-pile stress rupture properties of this steel, where thin walled tubes in the as-received condition (which is similar to 10 percent cold working) exhibit a substantial decrease in time to rupture due to irradiation. The metallographic investigation shows that no recrystallization occurred during irradiation.

As can be seen from Figs. 9, 10, and 11 the 50 percent cold work and 50 percent cold work + 1 h at 850 C anneal conditions are much less affected by irradiation than the 10 percent cold work condition. It should be mentioned that the 1-h anneal at 850 C led to recrystallization, while the specimens which were cold-worked to only 50 percent recrystallized at the irradiation temperature after several hours. The grain size after irradiation

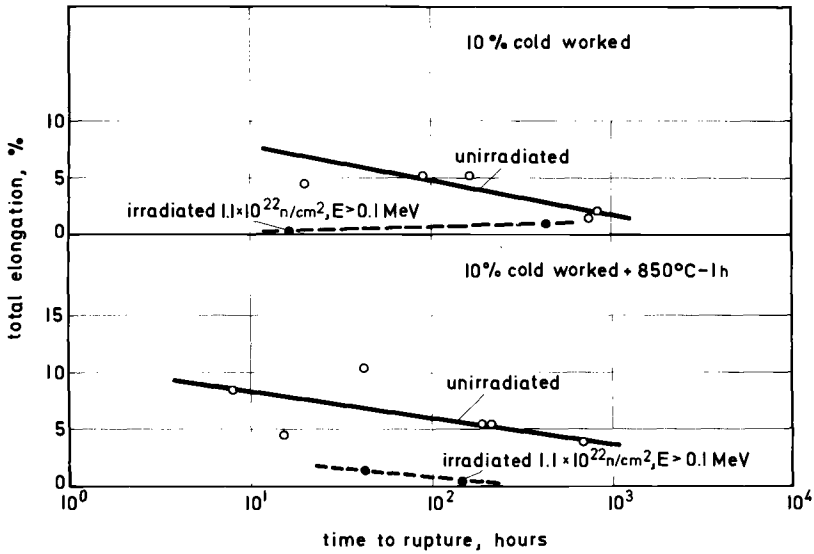


FIG. 8—Total elongation versus rupture time for unirradiated and irradiated 16Cr-13Ni steel tested at 650 C. Irradiation temperature 650 to 750 C.

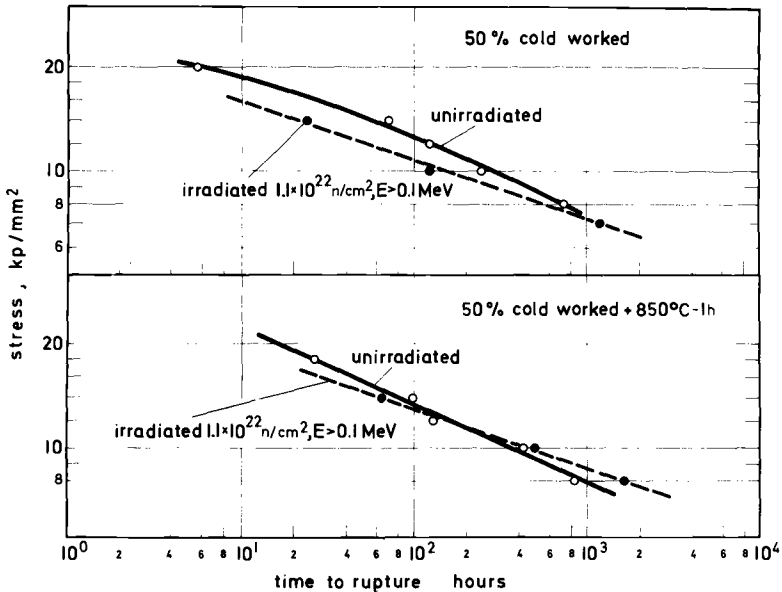


FIG. 9—Rupture life of irradiated and unirradiated 16Cr-13Ni steel in different conditions at 650 C. Irradiation temperature 650 to 750 C.

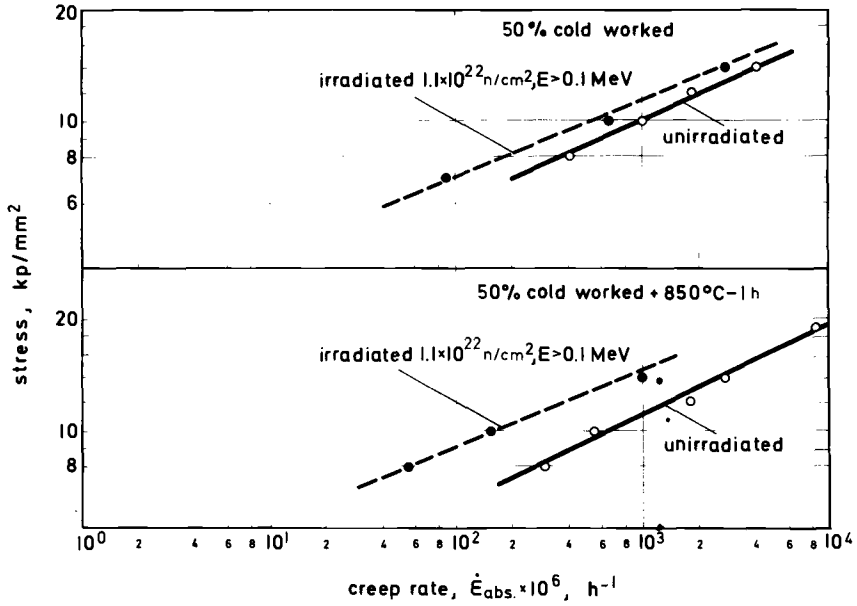


FIG. 10—Minimum creep rate versus stress for 16Cr-13Ni steel in different conditions. Irradiation temperature 650 to 750 C.

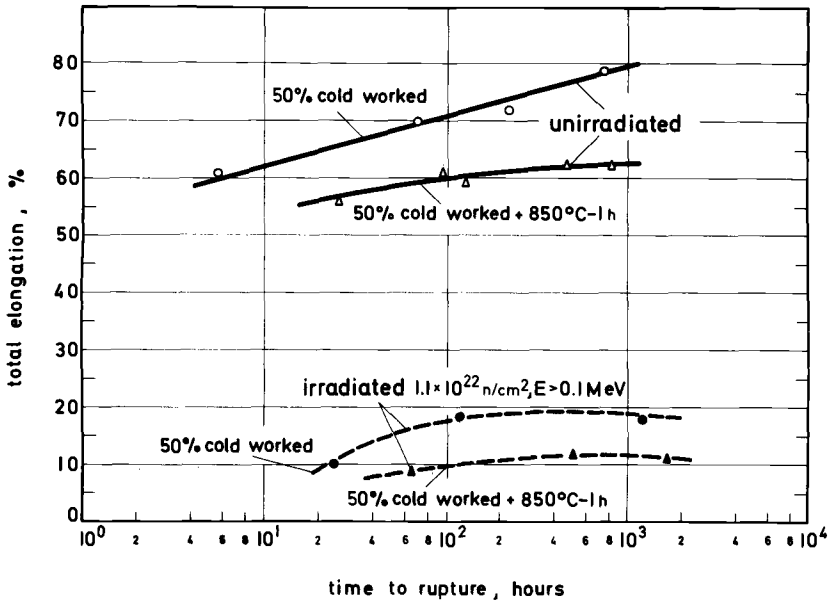


FIG. 11—Total elongation versus rupture time for unirradiated and irradiated 16Cr-13Ni steel tested at 650 C. Irradiation temperature 650 to 750 C.

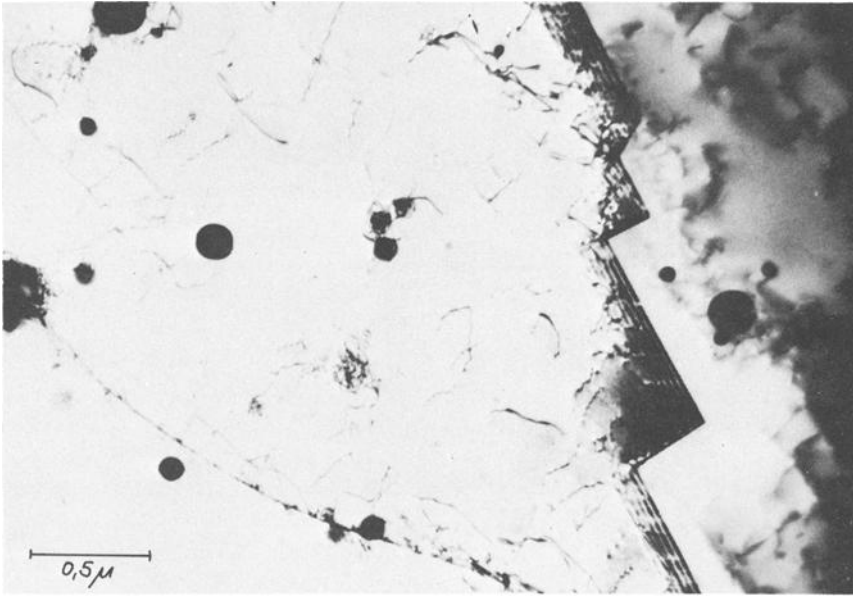


FIG. 12—Transmission electron micrographs of 16Cr-13Ni steel: top, unirradiated; bottom, irradiated at 50 C to 0.8×10^{22} n/cm².

of both conditions is very small ($<10 \mu\text{m}$). This explains the low stress rupture strength of the steel in the 50 percent cold work and 50 percent cold work + 1 h 850 C heat treat conditions. Rupture life at 650 C does not show a marked change due to irradiation (Fig. 9), while the creep rate

seems to be slightly reduced (Fig. 10). The creep ductility is reduced, though a strain at fracture greater than 10 percent after a neutron irradiation of up to 1.1×10^{22} n/cm² is higher than in other conditions.

To achieve a better understanding of the above mentioned results a number of specimens were investigated by transmission electron microscopy. The substructure of the material after an irradiation at about 50 C of up to 0.8×10^{22} n/cm², $E > 0.1$ MeV, consists of a very high concentration of unresolvable black dots as well as of small dislocation loops, the concentration of which is about 2×10^{15} cm⁻³. The average diameter of these loops is about 100 Å. Because of the high number of defects an analysis could not be done. No denudation of defects could be observed near grain boundaries or precipitation. Figure 12 shows a comparison of the microstructure between the unirradiated and irradiated material.

After annealing at 650 C for 1 h the black dots disappeared (Fig. 13). The concentration of loops is about 2×10^{15} cm⁻³. Their average diameter was determined to be 200 ± 100 Å. Less than 10 percent of the loops are larger than 300 Å. They lie mainly on (111) planes. The loop density is reduced to 7.5×10^{14} cm⁻³ or 1×10^{14} cm⁻³ after heat treatment at 750 C for 1 or 264 h, respectively. The average diameter increases to ~ 300 Å. This annealing also leads to the precipitation of very fine particles which seem to be carbides (Fig. 14). A large number of loops are still to be found

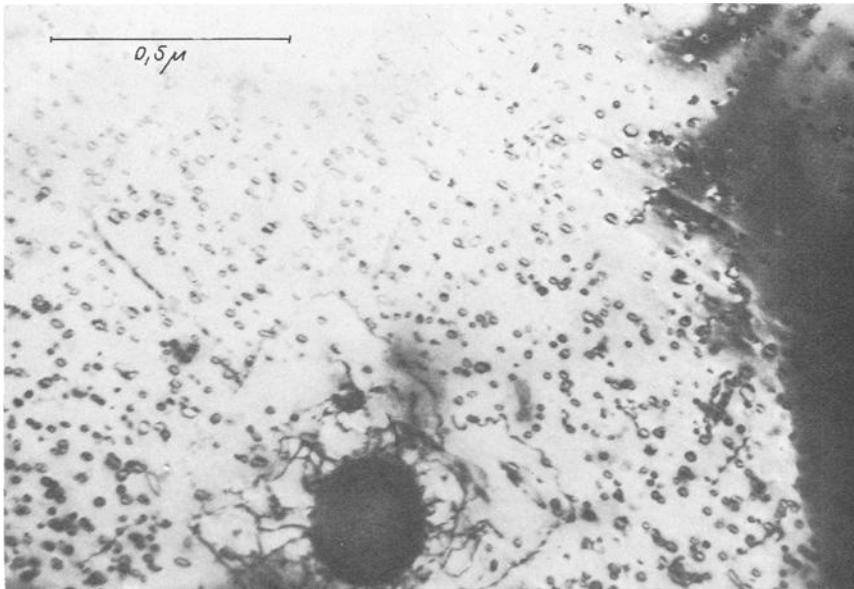


FIG. 13—Transmission electron micrograph of irradiated 16Cr-13Ni steel after 1-h anneal at 650 C.

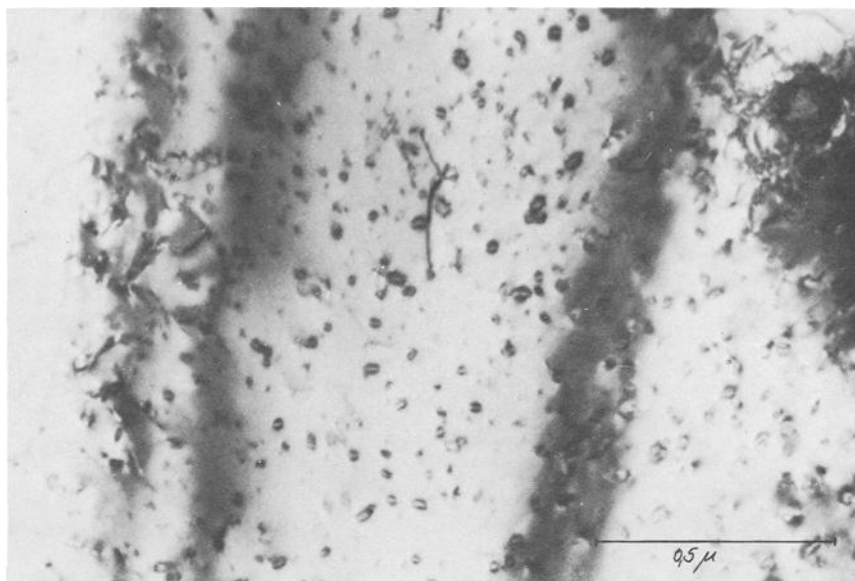


FIG. 14—Transmission electron micrograph of irradiated 16Cr-13Ni steel after 1-h anneal at 750 C.

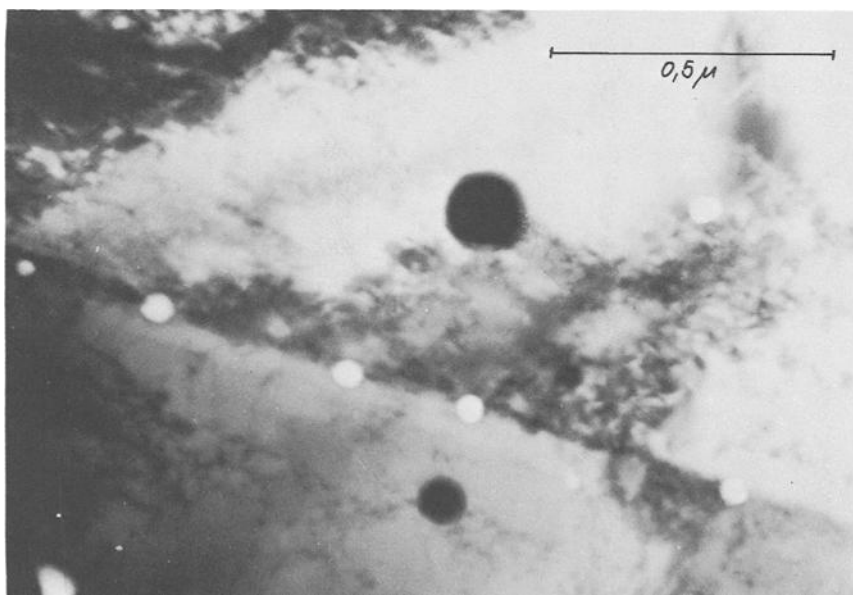


FIG. 15—Helium bubbles in irradiated 16Cr-13Ni steel after annealing at 1050 C.

after creep testing at 650 C. Annealing at 900 C leads to a complete recovery of the irradiation induced dislocation loops.

At annealing temperatures up to 750 C no helium bubbles were observed, whereas at heat treatments in the region of 900 to 1050 C bubbles could be detected in the grain boundaries as well as in the grains (Fig. 15). The transmission electron microscope (TEM) investigation of specimens which were irradiated at 650 C in the DIDO reactor to a neutron fluence of 4.5×10^{20} n/cm², $E > 0.1$ MeV, indicated no evidence of irradiation damage. This is in agreement with earlier observations by Rowcliffe [10], who could not find any displacement damage after a neutron exposure (1×10^{20} n/cm²) at 650 C. High neutron exposure (1.1×10^{22} , $E > 0.1$ MeV) at temperatures between 650 and 750 C did not produce observable displacement damage. Neither dislocation loops nor black dots were observed in the undeformed heads of specimens, which were creep tested at 650 C, but a high concentration of helium bubbles with a mean size of ~ 250 Å was detected. The number of the bubbles corresponds to the helium generated by n, α reactions in the same order of magnitude.

Discussion

The results of the electron microscopic investigations indicate that the reduction in creep rate and increase in rupture life after low-temperature irradiation are due to irradiation induced dislocation loops. The increase in yield strength at 650 and 750 C after irradiation can be explained semi-quantitatively by dislocation loop hardening. The remarkable result is that these loops are still stable at 750 C for a long time; J. J. Holmes and co-workers [11] have found that dislocation loops, produced in Type 304 stainless steel by irradiation at 532 C to 1.4×10^{22} n/cm², disappeared entirely after annealing at 650 C. It is possible that the stability of the loops at high temperatures is due to very fine carbide precipitation on the dislocation loops.

Irradiation at up to 1.1×10^{22} n/cm² at temperatures between 650 and 750 C does not cause the formation of dislocation loops or voids, so the observed changes in creep rupture properties are only based on high-temperature embrittlement (due to helium formation) and possibly on changes in precipitation processes. Specifically, the small changes in creep rate may be contributed to irradiation influenced precipitations.

The results clearly indicate that the irradiation induced embrittlement as characterized by reduction in time to rupture and strain at fracture is strongly dependent upon the pretreatment of the steel. In agreement with earlier results, cold-worked conditions of a material, which do not recrystallize during irradiation or testing, exhibit the highest reduction in rupture life. One reason for this behavior may be that in the cold-worked condition the dislocation hardening within the grain favors grain boundary sliding,

which may promote embrittlement. As the results have shown, the 50 percent cold work conditions are less affected by neutron irradiation. This can be attributed to the very small grain size, which is known to reduce irradiation induced embrittlement [12].

References

- [1] Williams, J. A. and Carter, J. W. in *The Effects of Radiation on Structure Metals*, ASTM STP 426, American Society for Testing and Materials, 1967, p. 149.
- [2] Bloom, E. E., "In Reactor and Postirradiation Creep Rupture Properties of Type 304 Stainless Steel at 650 C," ORNL-TM 2130, 1968.
- [3] André, J. P., Beaufrère, J., Valibus, L., and Weisz, A., "Influence of Sodium and of Irradiation on the High-Temperature Creep Behavior of Certain Stainless Steels," ANL-7520, Part I, 1968, p. 55.
- [4] Gilbert, E. R. and Harding, N. E. in *Irradiation Effects in Structural Alloys for Thermal and Fast Reactors*, ASTM STP 457, American Society for Testing and Materials, 1969, p. 17.
- [5] Standring, J., Bell, I. P., Tickle, H., and Glendinning, A. in *ASTM STP 457*, American Society for Testing and Materials, 1969, p. 414.
- [6] Laue, H. J., Böhm, H., and Hauck, H. in *ASTM STP 457*, American Society for Testing and Materials, 1969, p. 390.
- [7] Lovell, A. J., *Transactions of the American Nuclear Society*, TANSAs, Vol. 12, 1969, p. 127.
- [8] Bloom, E. E., *Transactions of the American Nuclear Society*, TANSAs, Vol. 12, 1969, p. 129.
- [9] Woodford, D. A., Smith, J. P., and Moteff, J., "Effect of Helium Gas Bubbles on the Creep Ductility of an Austenitic Alloy," GEMP-607, 1968.
- [10] Rowcliffe, A. F., *Journal of Nuclear Materials*, JNUMA, Vol. 18, 1966, p. 60.
- [11] Holmes, J. J., Robbins, R. E., Brimhall, J. L., and Mastel, B., *Acta Metallurgica*, AMETA, Vol. 16, 1968, p. 955.
- [12] Martin, W. R. and Weir, J. R., *Journal of Nuclear Materials*, JNUMA, Vol. 18, 1966, p. 108.

D. Kramer,¹ K. R. Garr,¹ C. G. Rhodes,² and A. G. Pard¹

The Effects of Helium on the High-Temperature Ductility of Sandvik 12R72HV and Inco IN-744X*

REFERENCE: Kramer, D., Garr, K. R., Rhodes, C. G., and Pard, A. G., "The Effects of Helium on the High-Temperature Ductility of Sandvik 12R72HV and Inco IN-744X," *Irradiation Effects on Structural Alloys for Nuclear Reactor Applications, ASTM STP 484*, American Society for Testing and Materials, 1970, pp. 509-520.

ABSTRACT: Small tension specimens of Sandvik 12R72HV and Inco IN-744X were injected with helium by means of α particle irradiation from a cyclotron to produce approximately uniform concentrations of from 1×10^{-6} to 2.5×10^{-5} atom fraction. The specimens subsequently were tension tested in vacuum between 500 and 800 C. Sandvik 12R72HV is significantly more resistant to helium embrittlement than Type 304 or 316 stainless steel. Helium in Inco IN-744X has little effect on the superplastic behavior of this alloy.

KEY WORDS: irradiation, alpha irradiation, radiation effects, helium, ductility, elongation, microstructure, embrittlement, grain boundaries, grain size, cracking (fracturing), failure, carbides, precipitates, creep tests, tension tests, alloys, stainless steels

Helium causes a loss of ductility in many alloys during high-temperature tension or creep testing, because it accumulates at grain boundaries where it has a strong positive influence on intergranular cracking. This has been observed in reactor irradiated specimens [1, 2]³ and in specimens that have been injected with helium by cyclotron irradiation [3-5].

Premature intergranular failure may be due either to the joining of grain boundary helium bubbles that have grown with the assistance of

¹ Physical Metallurgy, Atomics International Division, North American Rockwell Corp., Canoga Park, Calif. 91304.

² Physical Metallurgy, Science Center, North America Rockwell Corp., Thousand Oaks, Calif. 91360.

* This work was performed under the auspices of the U. S. Atomic Energy Commission under Contract AT(04-3)-701.

³ Italic numbers in brackets refer to the list of references at the end of this paper.

TABLE 1—Compositions of alloys in weight percent.

Alloy	C	N	Ni	Cr	Mo	Ti	Mn	Si	Fe
12R72HV	0.1	...	15	15	1.2	0.5	1.8	0.5	balance
IN-744X	0.06	0.03	6.6	27	...	0.2	0.4	0.5	balance

stress [6] or to the formation of grain boundary cracks by grain boundary sliding, as promoted by helium bubbles in the grain boundary [7]. Test temperature, strain rate, and the degree of grain boundary sliding will determine which mechanism is favored during testing. The alloys that are the subject of this paper, Sandvik 12R72HV and Inco IN-744X, are of interest because of the nature of their microstructures. Finely dispersed precipitates in the grain boundaries may be developed in 12R72HV, whereas the superplastic IN-744X has an extraordinarily high amount of grain boundary area per unit volume—the alloy has a grain size of only a few micrometers [8, 9]. Both of these features may be expected to mitigate the effects of helium, and some confirmatory evidence has been reported in the case of IN-744X [10].

Experimental Procedure

The compositions of 12R72HV and IN-744X are given in Table 1. Small sheet tension specimens with a cross section of 0.20 by 1.02 mm and a gage length of 12.7 mm were punched from strip and annealed as shown in Table 2. The anneal of 12R72HV was used to produce fine carbides whereas the anneal of IN-744X merely removed cold work without grain growth. The specimens then were injected with helium by means of alpha particle irradiation from a cyclotron [6], and the resulting helium contents were determined analytically [3].

Tension tests were performed in vacuum at a strain rate of 0.02/min; yield strengths were measured at 0.2 percent elongation; and specimens were held at the test temperature for 1 h before the load was applied.

Results

12R72HV

Tension test results are presented in Table 3, where the values shown are the averages of two specimens. The yield strengths of the specimens

TABLE 2—Alloy anneals before testing.

Alloy	Anneal
12R72HV	1 h at 1100 C+8 h at 825 C
IN-744X	10 min at 870 C

TABLE 3—Tension test results for 12R72HV.

Test Temperature, deg C	Atom Fraction Helium	Yield Strength, kg/mm ²	Tensile Strength, kg/mm ²	Elongation, %	
				Uniform	Total
500	0	13.1	43.1	26	27
	1×10 ⁻⁶	13.1	41.8	25	26
	5×10 ⁻⁵	15.0	43.1	25	27
600	0	12.0	37.7	28	29
	1×10 ⁻⁶	11.7	38.5	28	30
	5×10 ⁻⁵	14.1	38.4	27	29
700	0	11.8	25.7	22	41
	1×10 ⁻⁶	11.2	25.0	21	37
	2.5×10 ⁻⁵	11.7	24.9	20	34
800	0	9.9	15.2	13	57
	1×10 ⁻⁶	10.1	15.4	14	46
	5×10 ⁻⁵	10.0	15.5	13	27

that have received the higher helium dose showed an increase at 500 and 600 C, which is probably due to the displacement damage caused by the irradiation. The principal effect of helium was to reduce the total elongation at 700 C and 800 C; the uniform elongation remained essentially unchanged at all test temperatures.

The microstructure of this alloy prior to testing consisted of austenite grains, with an average size of 35 μm , with both fine and coarse M_{23}C_6 precipitates (as determined by electron diffraction) in the grain boundaries. The fine precipitates ranged between 100 and 200 \AA in size whereas the coarser ones were about 1 μm .

Figure 1 shows these fine precipitates in a specimen tested at 700 C. At this temperature, specimens without helium failed transgranularly, those with the lower helium content failed in a predominantly transgranular mode, and those with the higher helium content experienced a mixed transgranular-intergranular failure. A few small helium bubbles, 20 \AA in diameter, were found attached to some of the coarse grain boundary carbides.

At 800 C the presence of 5×10^{-5} atom fraction helium caused the failure mode to change from transgranular to intergranular. Voids were observed in grain boundaries in the high helium content specimens, but they were not adjacent to the coarse carbide particles as shown in Fig. 2. Very large helium bubbles, up to 1500 \AA in size, were observed in grain boundaries (Fig. 3a) and occasionally in the matrix. These large bubbles were not generally attached to carbide particles. Smaller bubbles were found throughout the matrix averaging about 50 \AA in size (Fig. 3b).

IN-744X

The total elongation of this superplastic alloy rises rapidly with increasing temperature, with a concomitant fall in strength. The presence of helium causes the rise in total elongation to be less steep but has no effect on strength. The small increases in yield and tensile strength at 500 C are probably the residual effect of displacement damage. The uniform elongations appear merely as a formality in Table 4, since necking, in the usual sense, was absent; rather, the entire gage length may be considered as the neck.

The microstructure of this alloy prior to testing was a mixture of austenite and ferrite grains whose size averaged between 1 and 2 μm (Fig. 4). Testing at 700 C resulted in intergranular failures for all specimens with no increase in grain size. Voids and cracks were observed in grain boundaries and they were more numerous in specimens with helium. Figure 5a shows the appearance of voids and cracks in the region close to the failure surface. Helium bubbles, 50 to 150 \AA , were seen on ferrite-ferrite grain boundaries and within the ferrite grains (Fig. 5b). These grains had a very low dis-

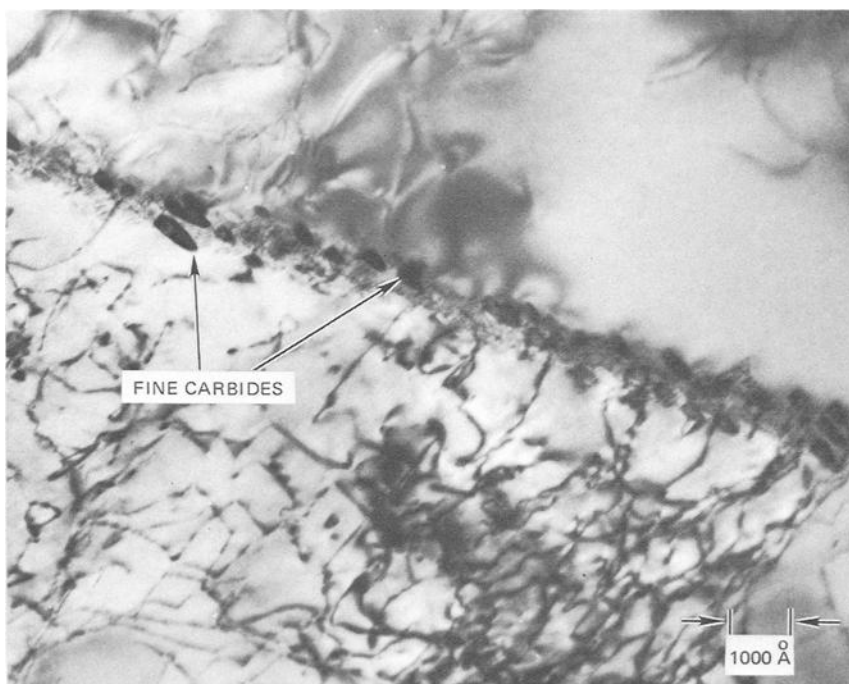


FIG. 1—Transmission electron micrograph of Sandvik 12R72HV, with 2.5×10^{-5} atom fraction helium, tested at 700 C. Fine precipitates of $M_{23}C_6$ are present in the grain boundary.

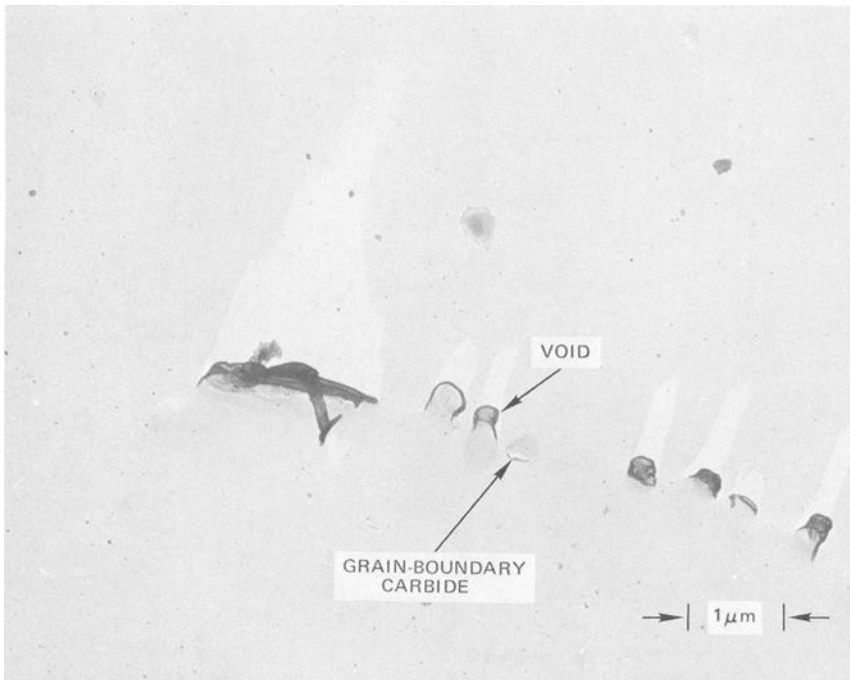


FIG. 2—Replica electron micrograph of Sandvik 12R72HV, with 5×10^{-5} atom fraction helium, tested at 800 C. Voids in the grain boundary are not adjacent to the coarse carbide particles.

TABLE 4—Tension test results for Inco IN-744X.

Test Temperature, deg C	Atom Fraction Helium	Yield Strength, kg/mm ²	Tensile Strength, kg/mm ²	Elongation, %	
				Uniform	Total
500.....	0	52.8	56.0	2.1	18
	1×10^{-6}	57.7	57.7	2.0	15
	2×10^{-6}	55.1	57.9	2.0	16
600.....	0	26.9	28.3	2.0	53
	1×10^{-6}	26.3	28.3	1.8	44
	2×10^{-6}	27.1	28.4	2.0	32
700.....	0	11.5	14.5	3.4	205
	1×10^{-6}	10.6	13.1	3.5	114
	2×10^{-6}	11.5	13.8	3.2	94
800.....	0	3.8	4.4	3.9	>300
	2×10^{-6}	3.5	4.2	3.5	>300

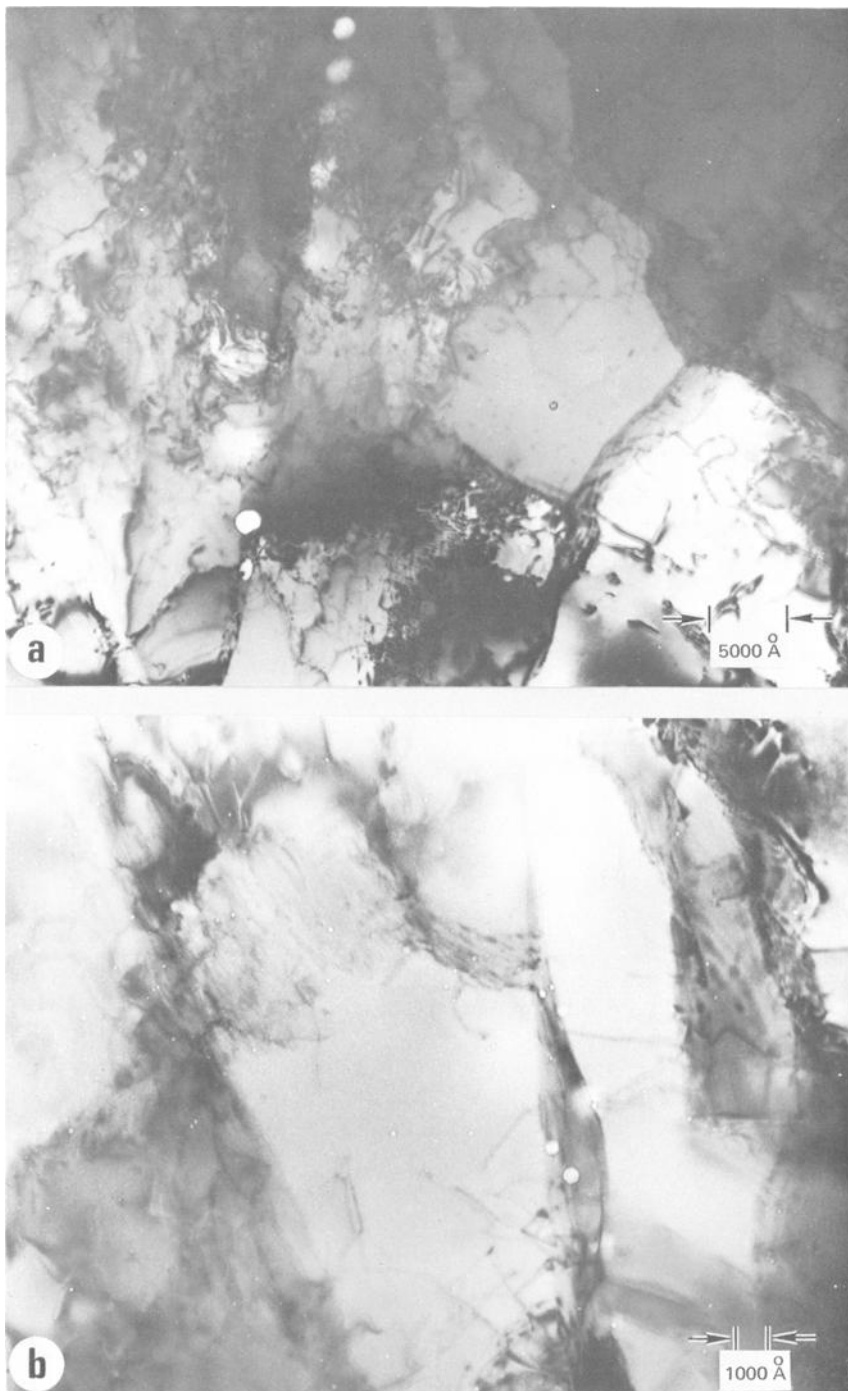


FIG. 3—Transmission electron micrographs of Sandvik 12R72HV, with 5×10^{-5} atom % helium, irradiated at 800°C. Large helium bubbles are seen in (a) the grain boundary and (b) in the grain boundary, with smaller bubbles in the matrix.

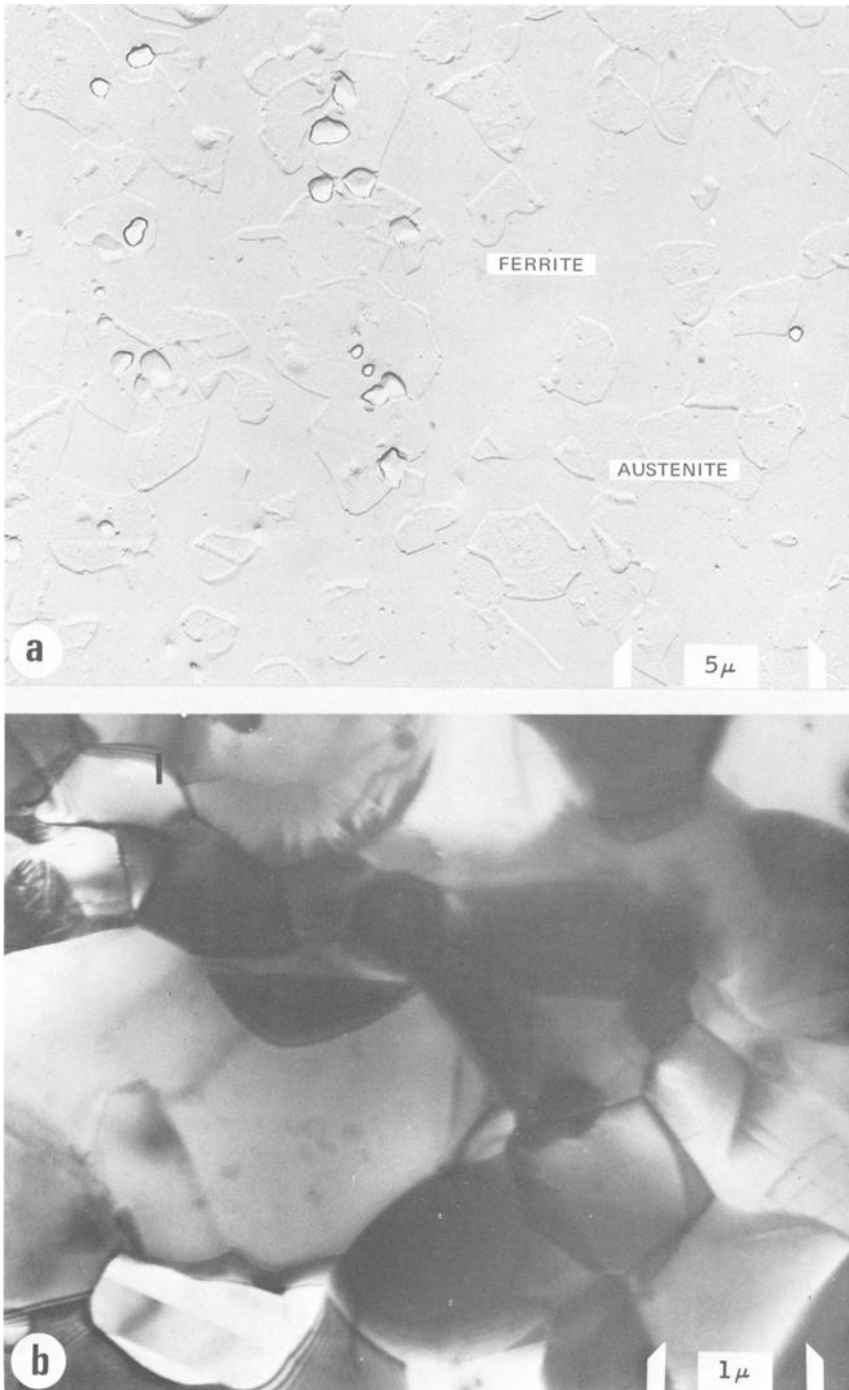


FIG. 4—Microstructure of IN-744X prior to testing: (a) replica electron micrograph, (b) transmission electron micrograph.

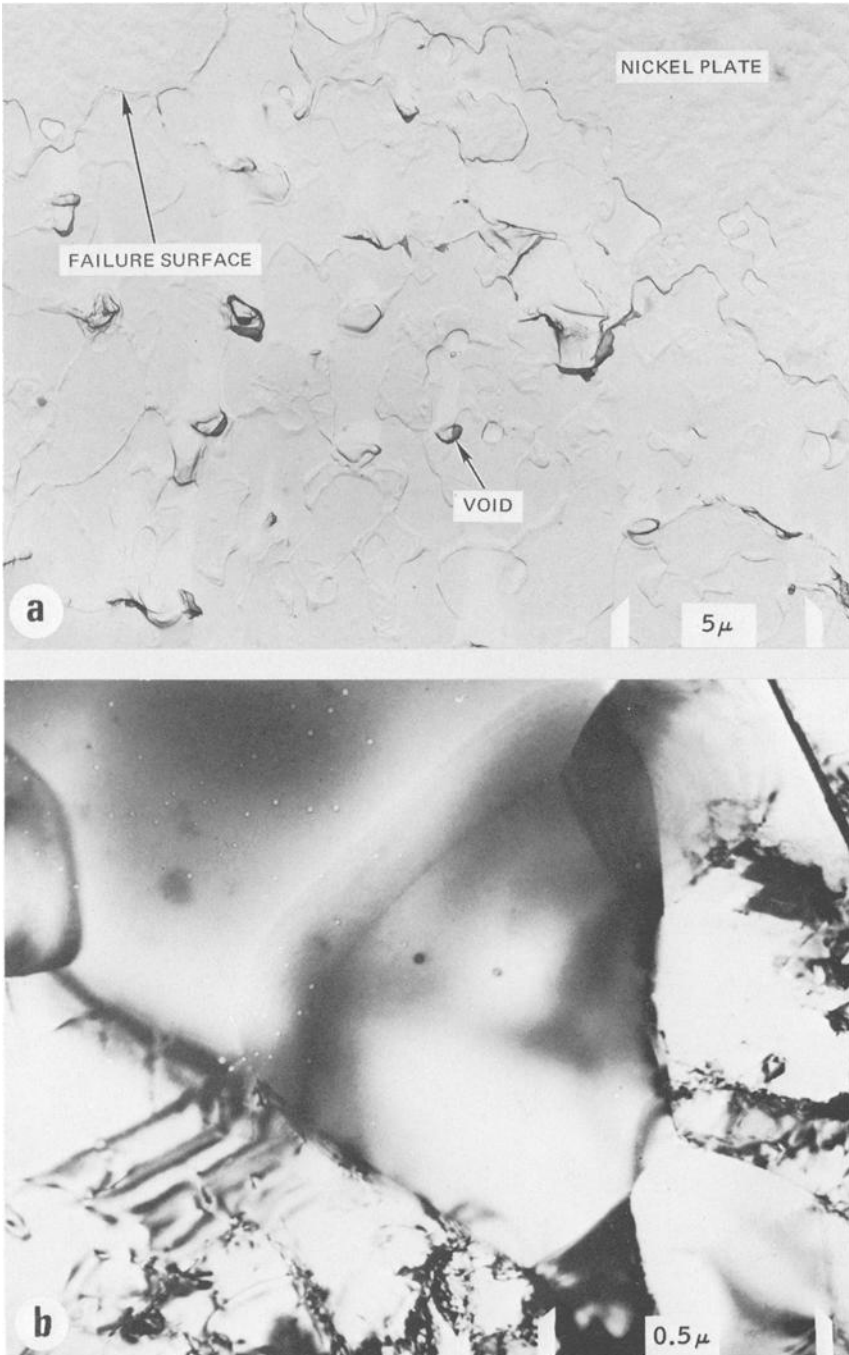


FIG. 5—Microstructure of IN-744X, with 2×10^{-5} atom fraction helium, tested at 700 C: (a) replica electron micrograph showing intergranular voids and cracks near failure surface; (b) transmission electron micrograph showing helium bubbles in the ferrite phase..

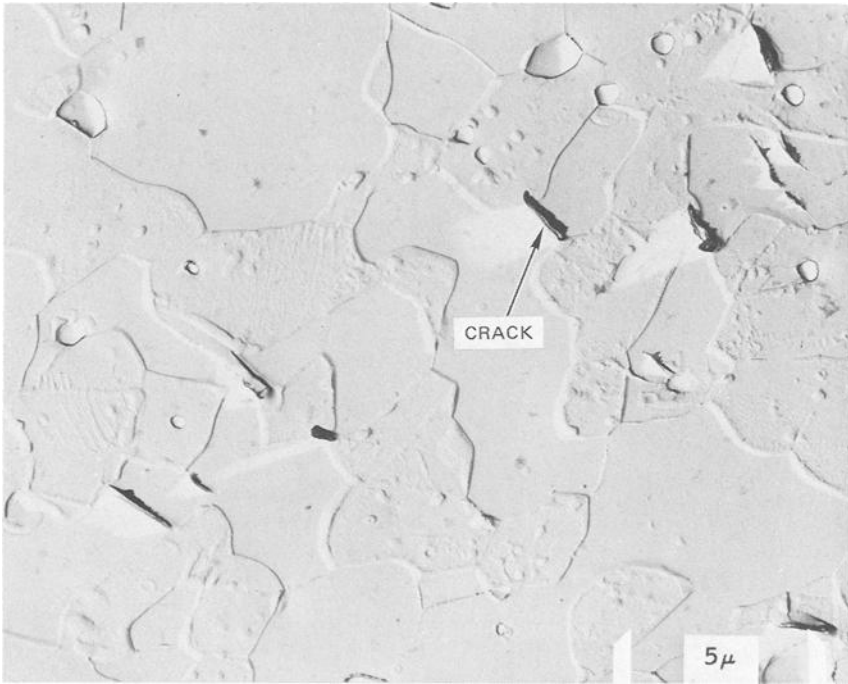


FIG. 6—Replica electron micrograph of IN-744X, containing no helium, elongated 300 percent without failure at 800 C. Cracks are seen at ferrite-ferrite boundaries.

location density, as contrasted with the austenite grains in which no bubbles were detected.

Specimens tested at 800 C did not fail after 300 percent elongation, the limit of the apparatus. The average grain size increased to between 2 and 4 μm , and intergranular cracks were present mostly at ferrite-ferrite boundaries in specimens with or without helium, as shown in Fig. 6. Helium bubbles ranged from 50 to 450 \AA in size and, again, were predominantly associated with the ferrite phase.

Discussion

The reduction of total elongation by helium in 12R72HV is significantly less than in Type 316 or 304 stainless steel [5, 6]. The presence of titanium in 12R72HV makes it possible to produce a fine dispersion of M_{23}C_6 carbides in the grain boundaries. These precipitates would be expected to impede grain boundary sliding, an essential part of the intergranular failure mechanism in 316 and 304. In these alloys, intergranular failure was initiated by the formation of voids at grain boundary carbide particles through the action of grain boundary sliding; this process is aided by the presence of helium bubbles on the particles. The voids observed in 12R72HV

were isolated in the grain boundaries, not usually associated with the coarse carbide particles (Fig. 2). It is therefore likely that grain boundary sliding was inconsequential and that these voids grew from helium bubbles under the influence of the applied stress [7]. Additional evidence for the reduced grain boundary sliding in 12R72HV as compared to 316 is given in the Appendix.

The extremely fine grain size and the superplastic nature of IN-744X put this alloy in a class by itself. Since the mechanism of deformation is uncertain, one is unable to explain the effect of helium in detail; nevertheless, the extraordinarily high amount of grain boundary area per unit volume will severely limit locally high concentrations of helium. This is evidenced by the relative scarcity of bubbles seen after testing as compared to 12R72HV.

Summary

1. Sandvik 12R72HV is significantly more resistant to helium embrittlement than Type 316 or 304 stainless steel.
2. The improved resistance is due to a fine dispersion of $M_{23}C_6$ grain boundary carbide particles.
3. The presence of helium in IN-744X merely moderates the rapid rise of total elongation with increasing temperature that occurs above 500 C.

Acknowledgments

We are pleased to acknowledge the assistance of R. M. Kniefel and K. G. Clody with the cyclotron irradiations and testing and the contributions of R. A. Spurling and D. R. Warner to the metallography. Helium analyses were performed by H. Farrar on the mass spectrometer.

APPENDIX

The expression we have used for elongation due to grain boundary sliding, ϵ_{gb} , relating the various parameters which can be measured experimentally, as taken from Stevens [11], is

$$\epsilon_{gb} = (1 + \epsilon_t)[1 - (1 + N_T \bar{v}_T)^{-2}]$$

where

- ϵ_t = total elongation,
- N_T = number of grain boundaries per unit length, transverse to the stress axis, after elongation, and
- \bar{v}_T = average value of grain displacement perpendicular to the stress axis, normal to the surface, transverse traverse.

The equation is valid providing $\theta_1 = \theta_2$, where θ_1 is the angle between the stress axis and the grain boundary trace on the surface of the specimen and θ_2 is the angle between the stress axis and the grain boundary trace on a section perpendicular to the surface.

TABLE 5—Grain boundary sliding data for Sandvik 12R72HV and 316 SS.

Alloy	Test Temperature, deg C	Total Elongation, %	Elongation due to Grain Boundary Sliding, %	γ , %
12R72HV.....	800	15	0.62±0.27	4.1±1.8
316.....	800	9.1	0.89±0.23	9.78±2.5

Prior to tension testing, 0.025 mm was electropolished from each surface of the specimen. This provided a polished surface for displacement measurements and also assured that $\theta_1 = \theta_2$ prior to test (determined experimentally). The grain displacements were measured by means of a Zeiss two-beam interference microscope, Carl Zeiss, Inc., Burbank, Calif., with approximately 200 measurements made to determine \bar{v}_T . The specimens were then sectioned and examined to assure that $\theta_1 = \theta_2$ after testing.

The results for 12R72HV and 316 without helium are presented in Table 5. The specimens were tested to their maximum uniform elongations. The parameter γ is $(\epsilon_{gb}/\epsilon_t)$ (100), which is a measure of the relative contribution of grain boundary sliding to the total elongation. The error limits are the 95 percent confidence intervals based on the 95 percent confidence intervals for the \bar{v}_T of each specimen.

References

- [1] Rowcliffe, A. F., Carpenter, G. J. C., Merrick, H. F., and Nicholson, R. B. in *The Effects of Radiation on Structural Metals*, ASTM STP 426, American Society for Testing and Materials, 1967, p. 21.
- [2] Carpenter, G. J. C. and Nicholson, R. B. in *Radiation Damage in Reactor Materials*, Vol. II, International Atomic Energy Agency, Vienna, 1969, p. 383.
- [3] Kramer, D., Garr, K. R., Rhodes, C. G., and Pard, A. G. in *Radiation Damage in Reactor Materials*, Vol. 1, International Atomic Energy Agency, Vienna, 1969, p. 303.
- [4] Kramer, D., Garr, K. R., and Pard, A. G., *Transactions of the American Institute of Mining, Metallurgical and Petroleum Engineers*, TAIMA, Vol. 245, Sept. 1969, p. 1909.
- [5] Kramer, D., Garr, K. R., Rhodes, C. G., and Pard, A. G., *Journal of the Iron and Steel Institute*, JISIA, Vol. 207, Aug. 1969, p. 1141.
- [6] Kramer, D., Brager, H. R., Rhodes, C. G., and Pard, A. G., *Journal of Nuclear Materials*, JNUMA, Vol. 25, Feb. 1968, p. 121.
- [7] Barnes, R. S., *Nature*, NATUA, Vol. 206, June 1965, p. 1307.
- [8] Hayden, H. W. and Floreen, S., *Transactions Quarterly*, American Society for Metals, ASMQA, Vol. 61, Sept. 1968, p. 474.
- [9] Hayden, H. W. and Floreen, S., *Transactions Quarterly*, American Society for Metals, ASMQA, Vol. 61, Sept. 1968, p. 489.
- [10] Weinstein, D., *Transactions of the American Institute of Mining, Metallurgical and Petroleum Engineers*, TAIMA, Vol. 245, Sept. 1969, p. 2041.
- [11] Stevens, R. N., *Metallurgical Reviews*, MREVA, Vol. 11, 1966, p. 169.

DISCUSSION

*G. J. C. Carpenter*¹—From your results there seems to be no doubt that there is less grain boundary sliding in the 12R72HV alloy than in 304 stainless steel and that this is related to the carbides at the grain boundaries. However, the inference of a direct correlation between reduced grain boundary sliding and improved postirradiation ductility seems less well founded. An alternative explanation could be advanced on the basis of the small size of the helium bubbles which probably nucleate on the fine carbide particles and would require a larger stress in order to grow. Is there any reason to reject this possibility?

C. G. Rhodes (authors' closure)—While it is probably true that the presence of fine carbides on the grain boundaries of 12R72HV will keep the accumulated helium dispersed as small bubbles, thereby inhibiting their stress induced growth, the comment presumes that this mechanism of helium embrittlement is also operating in Types 304 and 316 stainless steel, which is not the case. It is proper to point out that the fine carbides can mitigate helium embrittlement by inhibiting bubble growth as well as by restricting grain boundary sliding.

¹ Associate research officer, Atomic Energy of Canada Limited, Chalk River, Ontario, Canada.

V. M. Stefanović¹ and N. Lj. Milašin¹

Correlation Between the Mechanical Properties and Microstructure of Irradiated Iron and Low-Carbon Steel

REFERENCE: Stefanović, V. M. and Milašin, N. Lj., “Correlation Between the Mechanical Properties and Microstructure of Irradiated Iron and Low-Carbon Steel,” *Irradiation Effects on Structural Alloys for Nuclear Reactor Applications*, ASTM STP 484, American Society for Testing and Materials, 1970, pp. 521–536.

ABSTRACT: The radiation hardening of iron and low-carbon steel was studied on the basis of transmission electron microscopy and tension test data. No visible defects were observed in the iron specimens after irradiation to 3.5×10^{19} n/cm², $E > 1$ MeV, at 35 C, as well as after postirradiation annealing at 150 C. Marked microstructural changes occurred in steel irradiated to 2.5×10^{18} n/cm² both at 320 C and 450 C. In the former case a 5.1×10^8 cm⁻² increase in dislocation density was found, while in the latter the presence of small dislocation loops of average diameter 200 Å and density 2.4×10^{14} cm⁻³ was observed.

The approximative theoretical values of yield stress increment were calculated using the models for hardening by small dislocation loops and by a dislocation forest and were compared with the experimental values of the yield stress increment. A satisfactory agreement was obtained.

KEY WORDS: Neutron irradiation, radiation effects, mechanical properties, yield stress, microstructure, crystal defects, crystal structure, dislocations (materials), lattices (mathematics), tension tests, electron microscopy, hardening, iron, carbon steels, metal foils

Studies of the relationship between lattice defects and metal strength have revealed that the yield stress is determined by the nature of the interaction between free dislocations and crystal lattice atoms, defects, and impurities. This has led to attempts to formulate quantitative relations between a given mechanical property (mostly yield stress) and some of the measurable characteristics of defects, such as diameter and density (distance) [1, 2, 3].² However, very few experimental data exist allowing

¹ Associate research metallurgists, Boris Kidric Institute of Nuclear Sciences, Vinca, Yugoslavia. Mr. Milasin was formerly with CEN Saclay, France.

² Italic numbers in brackets refer to the list of references at the end of this paper.

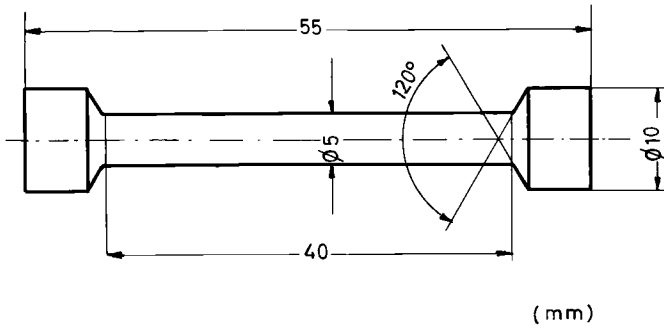


FIG. 1—*Tension specimen.*

the comparison of the calculated and measured values, particularly for metals with body centered cubic lattices.

In this work we shall report direct observations of irradiated iron and steel obtained using the electron microscope, together with tension test results before and after irradiation. Data on the diameter and density of the defects provided by electron microscopy and existing theoretical relations were used to estimate the corresponding yield stress increments, which were then compared with our experimental results. The concentration of invisible defects was calculated approximately on the basis of the integrated neutron exposure.

Experimental Methods

Materials and Irradiation Conditions

Details of the chemical analysis, thermal treatment, and irradiation conditions of the materials used in this study are given in Table 1.

The iron specimens were irradiated in the reactor OSIRIS-CEN Saclay, in hermetic aluminium capsules filled with helium. Plate specimens 10 by 6 by 0.9 mm were used for transmission electron microscopy (TEM), and wires 0.6 mm in diameter and 80 mm in length were irradiated in the tension tests. The steel specimens, Fig. 1, were irradiated in a TVRF reactor at Vinca, in hermetic aluminium and stainless steel capsules filled with argon. The TEM specimens were 3 mm in diameter and 0.7 mm thick.

Preparation of Thin Foils

The iron foils were prepared by grinding to 0.1 mm and chemical thinning to a final thickness suitable for electron microscopic observation. The chemical thinning was carried out by a 2.5 percent solution of hydrofluoric acid in hydrogen peroxide with intensive stirring. This method has proved extremely suitable for work in hot cells.

TABLE 1—Chemical composition, thermal treatment, and irradiation conditions.

Material	Chemical Composition, wt %	Thermal Treatment	Irradiation Conditions	
			Integrated Neutron Exposure, n/cm ² , E > 1 MeV	Temperature, deg C
Iron.....	C 0.027, Mn 0.05, 5 ppm N, 35 ppm O	Annealed 24 h at 700 C + 27 h at 300 C; furnace cooled; grain size 20 μm	3.47 × 10 ^{19a}	35
Low-carbon steel.....	C 0.007, Mn 0.005, 1 ppm N, 100 ppm O C 0.11, Si 0.02, Mn 0.35, Cr 0.15, Ni 0.08, Cu 0.06, V 0.012, Mo 0.03, Al 0.03, Si 0.011, P 0.016, 80 ppm N, 25 ppm O	Same as above; grain size 22 μm Annealed 2 h at 1050 C, furnace cooled; annealed 3 h at 680 C, furnace cooled; grain size 170 μm	1.1 × 10 ^{19b} 2.5 × 10 ¹⁸	320 ^a 345 ^b 450 ^a 475 ^b

^a Transmission electron microscopy.

^b Tensile properties.

The thin foils of steel were also prepared by grinding to 0.2 mm, preliminary electropolishing to 0.1 mm, and final electropolishing to perforation, according to the PTFE holder method [4]. The polishing was done with a solution of 133 cm³ acetic acid + 25 g chromic acid + 20 cm³ water, at 20 V and 0.1 A/cm² current density.

Estimate of Defect Density

Invisible Defects—According to the calculation of Beeler [5], the probability of the formation of “zones” containing more than ten vacancies³ amounts to 0.5 for neutrons of energy $E > 1$ MeV. Thus, the number of effective zones, N_z , is

$$N_z = \frac{n_p}{2} = \frac{\phi \bar{\sigma}_{el} n_{Fe}}{2} \dots \dots \dots (1)$$

where

- ϕ = integrated neutron exposure, n/cm²,
- n_{Fe} = number of iron atoms per cm³, and
- $\bar{\sigma}_{el}$ = average elastic scattering cross section of iron causing displacement, cm².

Dislocations—The density of Frank network dislocations was estimated according to the formula [7]

$$\rho = \frac{2n}{st} \dots \dots \dots (2)$$

where

- n = number of intersections along s ,
- s = total length of the set of parallel lines, cm, and
- t = foil thickness (approximately 2000 Å, as estimated by counting the number of thickness fringes from the edge of the foil, Ref 7, p. 496).

Visible Loops—The density of visible loops, N_F (Frank-type loops), was estimated from

$$N_F = \frac{n_0}{At} \dots \dots \dots (3)$$

where

- n_0 = number of loops on the surface A and
- A = surface area, cm².

³ By analyzing data for face centered cubic metals, Thomas and Washburn [6] concluded that only aggregates containing more than ten vacancies are effective in the hardening.

The determination of dislocation density was based on the examination of nine micrographs.

Measurements of Mechanical Properties

The measurements of the tensile properties of iron were made on an Instron hard tension testing machine, at a strain rate of $2.8 \times 10^{-4} \text{ s}^{-1}$. The tensile properties of steel were measured on the remotely controlled Amsler machine at a strain rate of $1.5 \times 10^{-4} \text{ s}^{-1}$. Test temperature was 20 C.

Results and Discussion

Typical microstructures of iron obtained by electron microscopy are presented in Fig. 2 for (a) an as-irradiated specimen and (b) a specimen annealed after irradiation at 150 C. As seen from the micrographs, irradiation at $3.47 \times 10^{19} \text{ n/cm}^2$ did not result in the appearance of visible defects, in agreement with Bryner's results [8] for 0.003 wt % iron and a similar neutron dose. The bowed-out form of slip dislocations in b indicates the existence of invisible obstacles interacting with mobile dislocations. (These dislocations are probably produced by the deformation of the foil during manipulation. The heating of the foil in the electron beam caused many of the dislocations to move.) A similar effect was observed by Tucker [9] in irradiated columbium after annealing at 600 C and 1.1 percent deformation.

Micrographs in Fig. 3 show the microstructure of steel specimens: (a) and (b) before irradiation (for coarse and fine grain size, respectively), (c) after irradiation at 320 C, and (d) after irradiation at 450 C.

The increase of dislocation density did occur in the coarse-grained specimens irradiated at 320 C, while in the case of fine-grained material it was not observed. Analogously, the component σ_2 of the yield stress increment (obtained by the method described in the Ref 10) has a much higher value for the coarse-grained than for fine-grained specimens (Fig. 4), suggesting a close connection between the two phenomena. One can try to understand this by comparing the microstructures of nonirradiated coarse- and fine-grained specimens, Figs. 3a and 3b, respectively. In the first case, the grain boundaries, having a continuous layer of cementite, are expected to repel dislocations by virtue of the image force, as the "free surface" is small; while in the second, showing the isolated lenslike carbides at the grain boundaries, the dislocations will migrate to the grain boundaries and annihilate there owing to the greater free surface which may attract them.

The specimen irradiated at 450 C contains a number of small dislocation loops with an average diameter of 200 Å. Since the radiation damage in steel is completely annealed out at 450 C, these loops are probably the

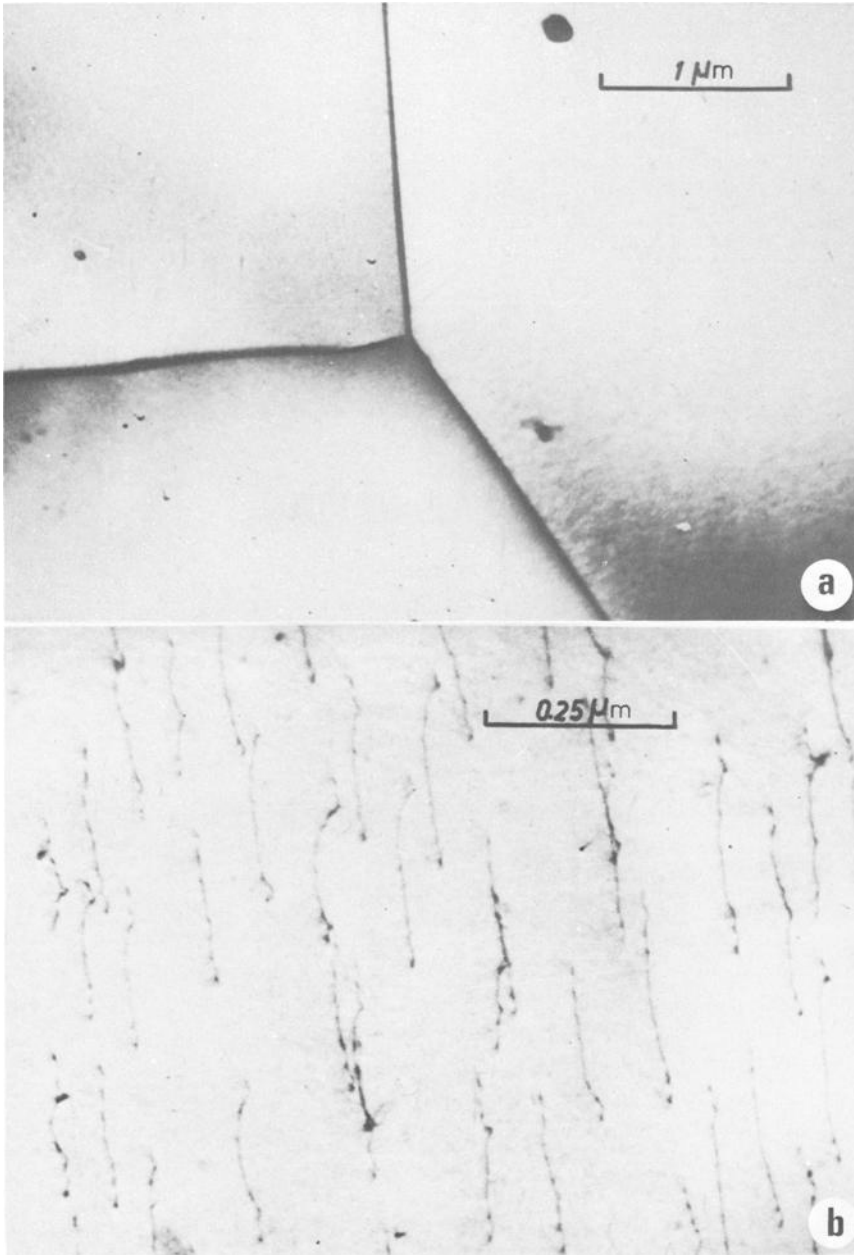


FIG. 2—Pure iron after irradiation to 3.5×10^{19} n/cm^2 , $E > 1$ MeV: (a) as irradiated at 35 C; (b) irradiated and annealed 1 h at 150 C, slip dislocations are bowed out between invisible obstacles.

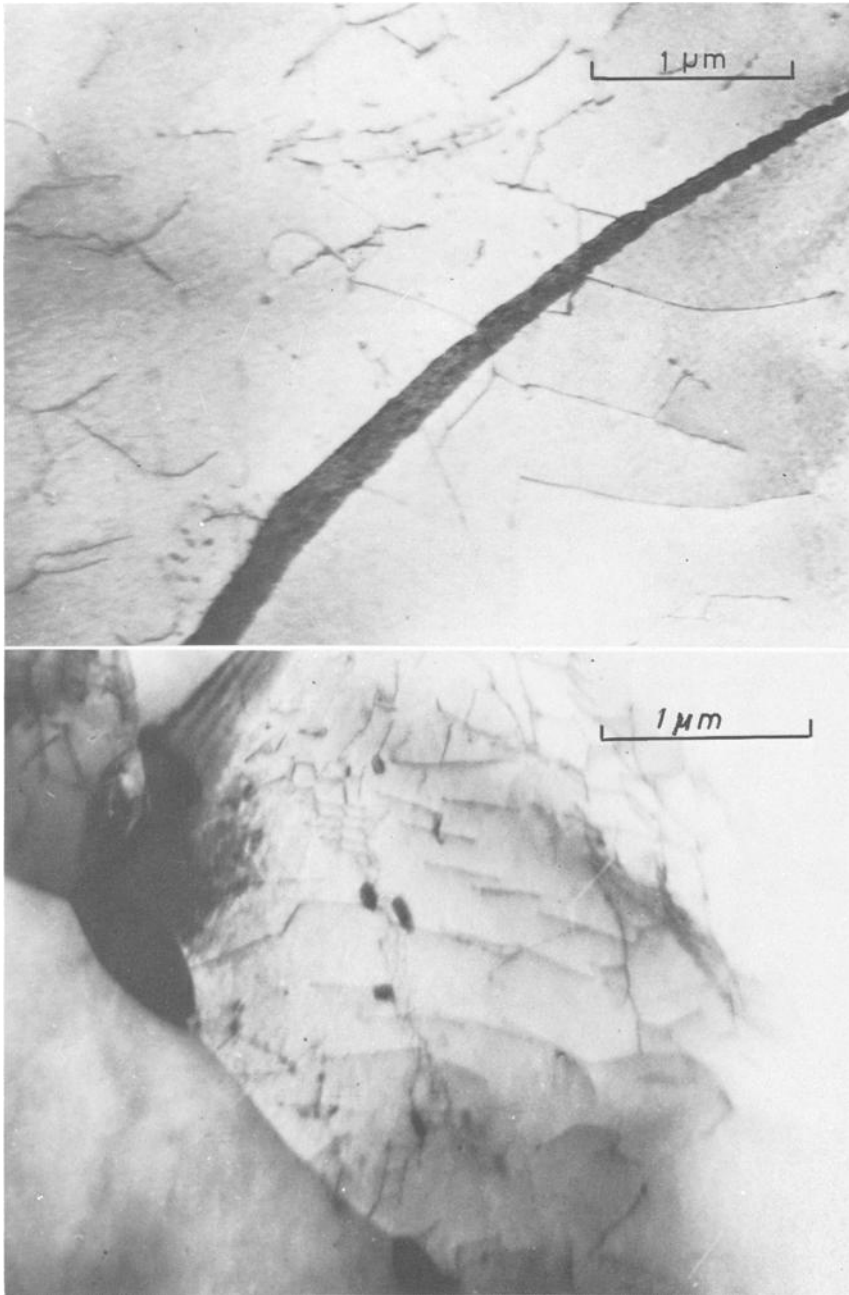


FIG. 3—Low-carbon steel before irradiation and after irradiation to 2.5×10^{18} n/cm², $E > 1$ MeV: (a) unirradiated (coarse grain, 170 μm); (b) unirradiated (fine grain, 30 μm).

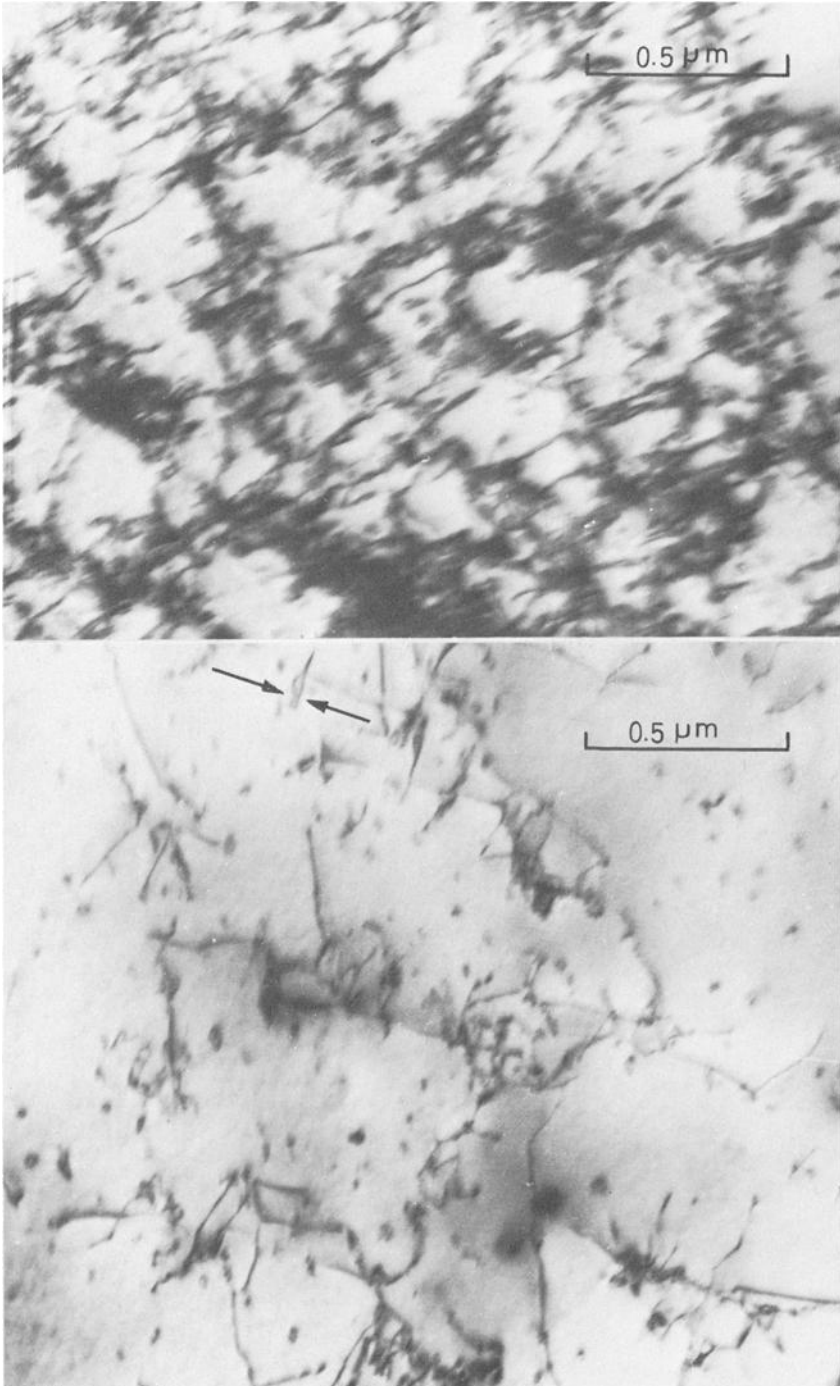


FIG. 3—Continued: (c) irradiated at 320 C, tangled dislocations are observed; (d) irradiated at 450 C, disappearance of long dislocations and formation of small loops.

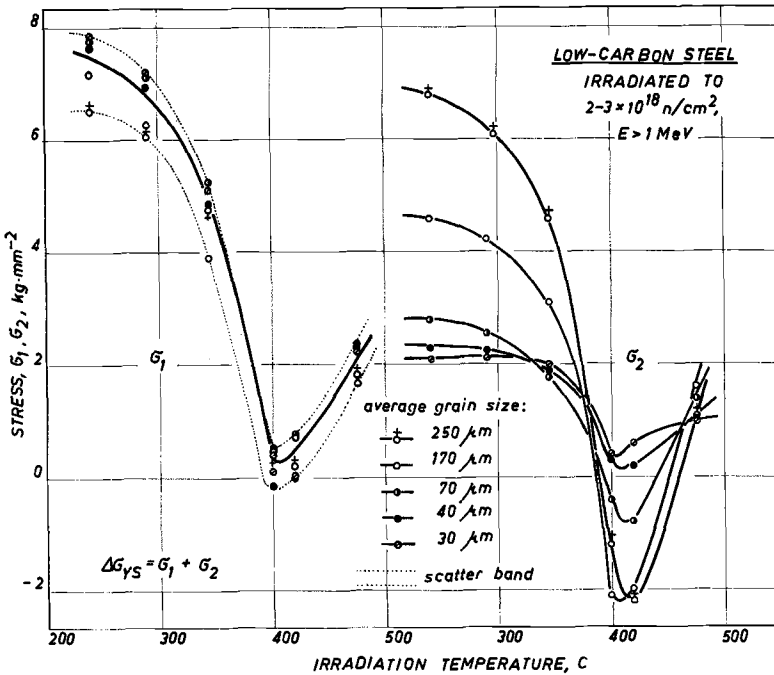


FIG. 4—Effect of irradiation temperature on the yield stress increments, $\sigma_2(T, I)$ and $\sigma_1(T)$, for different grain sizes of a low-carbon steel.

consequence of the breakup of remaining long dislocation loops by one of the cross-slip mechanisms [11]. The arrows in Fig. 3d indicate the area in which the formation of a small dislocation loop can be seen.

The absence of dislocations after 450 C irradiation is in agreement with the Birkle and Rall [12] experiments with A212B steel: after annealing of irradiated specimens in the 340 to 450 C temperature range, radiation induced dislocation density increase disappeared. At the same time, the cold-worked specimens did not noticeably decrease in dislocation density after annealing at 450 C. The interpretation of these findings will remain difficult until more detailed studies of the subject have been made.

That the defect responsible for the radiation hardening of iron cannot be observed by electron microscopy suggests that its size must be $\leq 20 \text{ \AA}$. In his theory Seeger [13] proposed the notion that the hardening was caused by "depleted zones." According to Nichols [5], in ferritic steels irradiated at normal reactor temperatures the Seeger zones become small spherical or spheroidal voids. Bullough and Perrin [14] concluded that platelike voids containing more than 21 vacancies will collapse into stable vacancy loops. Since we, in our estimate of the number of defects effective in hardening, took into account only those aggregates containing more than ten vacancies, it will be assumed that the main part of these is in the

form of vacancy loops $\sim 20 \text{ \AA}$ in diameter. The literature on steel [12, 15-18] and iron [19] indicates that these defects are stable up to around 300 C. Our results on the effect of irradiation temperature are in agreement with the above data (Fig. 5).

The estimate of hardening defect concentrations has been done on the basis of Eq 1 for iron and for steel irradiated at 320 C, and the results are given in Table 2. The increase in the dislocation density of steel irradiated at 320 C (Eq 2) and the density of small dislocation loops in steel irradiated at 450 C (Eq 3) are also given in Table 2.

Yield stress increments were calculated on the basis of our experimental data for defect diameters and densities according to following relations:

1. For small loop hardening:

The relation proposed by Kimura and Maddin [3],

$$\tau_i = \frac{GbdN^{2/3}}{8} \dots \dots \dots (4)$$

where

- G = shear modulus, kg/mm^2 ,
- b = Burger's vector, cm ,
- d = loop diameter, cm , and
- N = loop density, cm^{-3} .

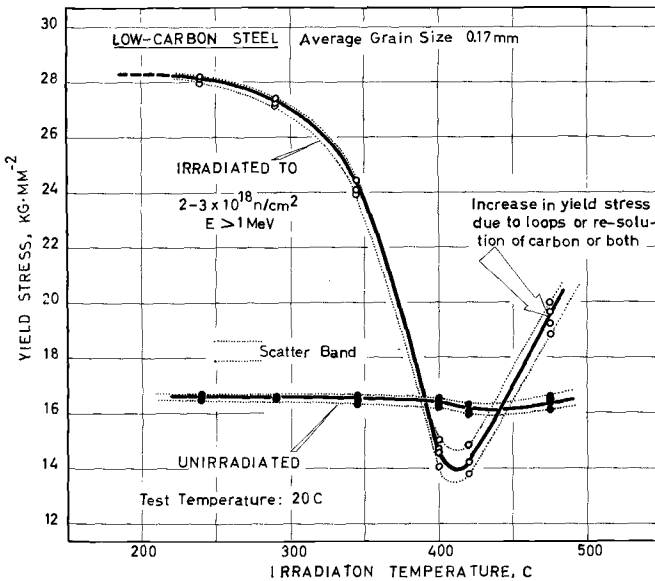


FIG. 5—Effect of irradiation temperature on the yield stress of a low-carbon steel.

TABLE 2—Defect diameters and densities in irradiated iron (1.1×10^{19} n/cm²) and low-carbon steel (2.5×10^{18} n/cm²).^a

Material	Invisible Defects ^b		Visible Dislocation Loops			Dislocation Network, ^c $\rho = \frac{2n}{sl}, \text{ cm}^{-2}$
	Diameter, $d, \text{ \AA}$	Density, $N_i = \frac{\phi \cdot n_{Fe} \cdot \bar{\sigma}_{el}}{2}, \text{ cm}^{-3}$	Diameter, $d, \text{ \AA}$	Density, $N_F = \frac{n_0}{Al}, \text{ cm}^{-3}$	Density, $\frac{n_0}{Al}, \text{ cm}^{-3}$	
Iron (irradiated at 35 C)	20	9.3×10^{17}	None found	None found	None found	None found
Steel (irradiated at 320 C)	20	2.5×10^{17}	A small number	A small number	$5.4 \times 10^8 \pm 11$ (percent)	$5.4 \times 10^8 \pm 11$ (percent)
Steel (irradiated at 450 C)	No contribution	No contribution	ave. 200	ave. 2.4×10^{14d}	A small number	A small number

^a Constants used in calculating the values: $n_{Fe} = 0.846 \times 10^{23}$ atoms/cm³; $\bar{\sigma}_{el} = 2 \times 10^{-24}$ cm²; $l = 2000 \text{ \AA}$.
^b The diameter of invisible defects was adopted on the basis of the evaluation of the size of the Seeger zone [5, 13].
^c Dislocation density in nonirradiated steel $\rho_0 = 3 \times 10^8 \text{ cm}^{-2} \pm 15$ (percent).
^d Average value only of four photographs.

2. For dislocation network hardening:

a. By long-range interaction due to the Frank network [2],

$$\tau_i = \frac{Gb}{2\pi} \times \rho^{1/2} \dots \dots \dots (5)$$

where ρ is the mean density of dislocation in the Frank network, cm^{-2} .

b. By elastic interactions with "trees,"

$$\tau_i = \frac{Gb}{\beta} \times \rho^{1/2} \dots \dots \dots (6)$$

where β is a numerical constant on the order of 3 to 4.

These relations assume an athermal hardening mechanism.⁴ In view of the recent analysis of the effect of radiation damage on thermally activated flow by Smidt and Bement [20], one has to keep in mind that the included processes are more complex and may be added by the thermal activation. The results obtained using Eqs 4, 5, and 6 are quoted in Table 3, together with the experimental values of the yield stress obtained by tension tests.

The correlation of calculated values with experimental ones indicates that radiation hardening in α iron for exposures on the order of 10^{19} n/cm² might be explained as due to small dislocation loops approximately 20 Å in diameter. As yet the exact nature of these loops is not known. In addition to considering vacancy aggregates responsible for hardening, we found experimental evidence provided by Eyre and Bartlett [21] in favor of interstitial loops in irradiated α iron.

A rough comparison of the calculated and experimental values of the yield stress increment for low-carbon steel (Table 3) tentatively suggests the existence of two different hardening components: (1) the hardening due to increased dislocation density (amounting to about one half of the total value) and (2) the hardening due to invisible loops according to Eq 4. The sum of these two values comes close to the experimentally found hardening, the agreement being better if the dislocation contribution is determined according to Eq 6 for the interaction with trees. One analysis based on the stress-strain curves [10] also indicated two hardening components in steel, and the values obtained were in good agreement with the data in the present work. Of course, the results of the simple addition of two types of barrier contribution to the shear stress must be taken with precaution, particularly in view of the more recent considerations of Diehl and Seidel [22] concerning the additivity of barriers. Birkle and Rall [12]

⁴ Except crossing of trees, which may be thermally activated.

TABLE 3—Comparison of theoretical and experimental values of the yield stress increments in irradiated iron (1.1×10^{19} n/cm²) and low-carbon steel (2.5×10^{19} n/cm²).^a

Material	D I S L O C A T I O N L O O P S		T H E O R E T I C A L		EXPERIMENT Yield Stress Increment ($\tau_y = 0.5\sigma_y$), $\Delta\tau_y$
	Invisible $\Delta\tau = \frac{Gb^2N^{2/3}}{8}$, kg/mm ²	Visible $\frac{Gb^2N^{2/3}}{8}$, kg/mm ²	Long-range Interaction, $\Delta\tau_i = \frac{Gb^2}{2\pi}(\rho^{1/2} - \rho_0^{1/2})$, kg/mm ²	Dislocations Interaction with trees, $\Delta\tau_i = \frac{Gb^2}{4}(\rho^{1/2} - \rho_0^{1/2})$, kg/mm ²	
Iron (irradiated at 35 C).....	4.6	4.2
Steel (irradiated at 320 C).....	2.1	...	1.9	2.9	4.9
Steel (irradiated at 450 C).....	...	0.2	0.5

^a Constants used in calculations: G (iron) = 7.7×10^8 kg/mm²; G (steel) = 8.45×10^8 kg/mm²; $b = 2.5 \text{ \AA}$.

also found a dislocation density increase amounting to $3 \times 10^{10} \text{ cm}^{-2}$ in a steel irradiated at 93 C to $5 \times 10^{19} \text{ n/cm}^2$. The corresponding yield stress increments, according to Eqs 5 and 6, would be 5.3 and 8.3 kg/mm², respectively, while the value of hardening due to invisible defects (Eq 5) would be 13.7 kg/mm². Since the experimental value (from the hardness measurements) is 17.6 kg/mm², in this case the sum of the hardening due to long-range interaction (Eq 5) and to invisible defects yields a value closer to the experimental data. It should be pointed out that in the Birkle and Rall experiments the irradiation temperature was considerably lower than in the present investigation, which could have affected the configuration of dislocations.

The calculated value of the hardening of steel irradiated at 450 C due to the presence of dislocation loops with an average diameter of 200 Å (Eq 4) amounts to 0.2 kg/mm², while the value obtained by experiment was 0.5 kg/mm². As seen, both values are of the same order of magnitude; the difference might be explained by the presence of carbon, which redissolves to a considerable amount at this temperature⁵ [22].

A good agreement between the calculated and experimental values obtained in the present investigation could be fortuitous, in view of the approximate nature of defect density calculations and certain simplifications in the use of theoretical relations. Nevertheless, these results tentatively suggest a possible approach in the study of the correlation between the size and the number of defects responsible for radiation hardening and the magnitude of that hardening.

Summary

1. Radiation hardening due to invisible defects in iron and low-carbon steel in the conditions of the present experiment may be expressed as hardening by small dislocation loops $\sim 20 \text{ Å}$ in diameter.
2. For iron irradiated at 35 C to $1.1 \times 10^{19} \text{ n/cm}^2$, the total amount of hardening seems to be due to invisible defects.
3. For coarse-grained steel irradiated at 320 C to $2.5 \times 10^{18} \text{ n/cm}^2$, part of the hardening is caused by an increase in dislocation density.

Acknowledgments

We are indebted to P. Lacombe, Faculty of Sciences in Orsay, and B. Božić, Faculty of Technology and Metallurgy in Belgrade, for their con-

⁵ The resolution of carbon probably is related to the cooling rate of specimens from the reactor (being 50 deg C/min down to 300 C).

tinuous interest in this work. Thanks are also due to M. Weisz, head of the Applied Metallurgical Research Dept. of CEN Saclay, and to M. Rogulić, Faculty of Technology and Metallurgy in Belgrade, for many useful suggestions. We are grateful to the staff of the reactors OSIRIS (CEN Saclay) and TVRF (Vinca) for performing irradiations and to the personnel of the hot cells (LEMI, CEN Saclay) for their help in the experiments on irradiated materials.

References

- [1] Kroupa, F. and Hirsch, P. B. in *Dislocations in Solids*, the Faraday Society, London, 1964, p. 49; Kroupa, F., *Philosophical Magazine*, PHMAA, Vol. 7, No. 77, May 1962, pp. 783–801.
- [2] Friedel, J. in *Electron Microscopy and Strength of Crystals*, Interscience Publishers, Wiley, New York, 1963, p. 605; Friedel, *Journal of Dislocations*, Pergamon Press, New York, 1964, p. 211.
- [3] Kimura, H. and Maddin, R. in *Lattice Defects in Quenched Metals*, Academic Press, New York, 1965, p. 319; Maddin, R. and Kimura, H., in "The Nature of Small Defect Clusters," Report AERE-T5269, Vol. I of Report of a Consultants Symposium held at Atomic Energy Research Establishment, Harwell, 4–6 July 1966, p. 503.
- [4] Briers, G. W., Dawe, D. W., Dewey, M. A. P., and Brammar, I. S., *Journal of the Institute of Metals*, JIMEA, Vol. 93, Part 3, 1964–65, pp. 77–80.
- [5] Referenced in Nichols, F. A., *Philosophical Magazine*, PHMAA, Vol. 14, No. 128, Aug. 1966, pp. 335–342.
- [6] Thomas, G. and Washburn, J., *Reviews of Modern Physics*, RMPHA, Vol. 35, No. 4, Oct. 1963, pp. 992–1011.
- [7] Hirsch, P. B., Howie, A., Nicholson, R. B., Pashley, D. W., and Whelan, M. Y., *Electron Microscopy of Thin Crystals*, Butterworths, London, 1965, p. 422.
- [8] Bryner, J. S., *Acta Metallurgica*, AMETA, Vol. 14, No. 3, March 1966, pp. 323–336.
- [9] Tucker, R. P., "Transmission Electron Microscopy and Plastic Deformation in Neutron Irradiated Niobium," thesis, ORNL-TM-2480, Oak Ridge National Laboratory, March 1969.
- [10] Stefanović, V. M., *Journal of the Iron and Steel Institute*, JISIA, Vol. 204, Part 10, Oct. 1966, pp. 987–990.
- [11] Price, P. B. in *Electron Microscopy and Strength of Crystals*, Interscience Publishers, Wiley, New York, 1963, p. 73.
- [12] Birkle, A. J. and Rall, W., *Transactions*, Metallurgical Society of AIME, TMSAA, Vol. 230, No. 1, Feb. 1964, pp. 156–163.
- [13] Seeger, A. in *Proceedings of the Second International Conference on Peaceful Uses of Atomic Energy*, Vol. 6, United Nations, New York, 1958, p. 250.
- [14] Bullough, R. and Perrin, R. C. in *Radiation Damage in Reactor Materials*, Vol. II, International Atomic Energy Agency, Vienna, 1969, p. 233.
- [15] Berggren, R. G., "Steels for Reactor Pressure Circuits," Special Report No. 69, the Iron and Steel Institute, London, 1961, p. 370.
- [16] Amaev, A. D., Platonov, P. A., and Pravdyuk, N. F. in *Proceedings of the Third International Conference on the Peaceful Uses of Atomic Energy*, Vol. 9, United Nations, New York, 1964, p. 240.
- [17] Nichols, R. W. and Harries, D. R. in *Symposium on Radiation Effects on Metals and Neutron Dosimetry*, ASTM STP 341, American Society for Testing and Materials, 1963, p. 162.
- [18] Milasin, N., *Bulletin of the Boris Kidric Institute of Nuclear Science*, BKNSA, Vol. 17, No. 4, Oct. 1966, pp. 256–273.

- [19] Hinkle, N. E., Ohr, S. M., and Weshsler, M. S. in *The Effects of Radiation on Structural Metals*, ASTM STP 426, American Society for Testing and Materials, 1968, pp. 573-591.
- [20] Smidt, F. A. and Bement, A. L. in *Dislocation Dynamics*, Rosenfield et al, Eds., McGraw-Hill, 1968, p. 409.
- [21] Eyre, B. L. and Bartlett, A. F., *Philosophical Magazine*, PHMAA, Vol. 12, No. 116, Aug. 1965, pp. 261-272.
- [22] Diehl, J. and Seidel, G. P. in *Radiation Damage in Reactor Materials*, Vol. I, International Atomic Energy Agency, Vienna, 1969, p. 187.
- [23] Gouzou, J., *Acta Metallurgica*, AMETA, Vol. 12, No. 7, July 1964, pp. 785-795.

C. L. Younger¹ and F. A. Haley¹

Irradiation Effects at Cryogenic Temperature on Tensile Properties of Titanium and Titanium-Base Alloys

REFERENCE: Younger, C. L. and Haley, F. A., "Irradiation Effects at Cryogenic Temperature on Tensile Properties of Titanium and Titanium-Base Alloys," *Irradiation Effects on Structural Alloys for Nuclear Reactor Applications, ASTM STP 484*, American Society for Testing and Materials, 1970, pp. 537-563.

ABSTRACT: Significant increases in tensile strength and slight decreases in ductility occur when titanium and titanium-base alloys are irradiated at 17 K to 1 to 10×10^{17} fast neutrons per square centimeter. The magnitude of the irradiation effect appears to depend on total alloy content and, over the fluence range investigated, does not reveal a significant dependence on impurity content or initial heat treat condition. These results were obtained using commercially pure titanium, Ti-5Al-2.5Sn (normal impurity and extralow impurity contents), Ti-6Al-4V (annealed and age hardened conditions), and Ti-8Al-1Mo-1V alloys. Test specimens were exposed to irradiations at 17 K and then tension tested at 17 K without intervening warmup using test loops specially designed and fabricated for cryogenic irradiation testing. Additional results, using commercially pure titanium, show recovery of about 50 percent of the irradiation induced increase in yield strength following heat treatment at 178 K. For the ultimate strength, 50 percent recovery occurred following heat treatment at 78 K.

KEY WORDS: irradiation, neutron irradiation, radiation damage, radiation effects, cryogenics, titanium, titanium alloys, tensile properties, yield strength, brittleness, nuclear propelled rockets

The titanium-base alloys are finding wide acceptance for use at liquid hydrogen temperature (20 K). These alloys are also candidate materials for nuclear rocket applications where the nuclear environment is imposed on a structural material which is at the cryogenic temperature.

The tensile behavior of the various titanium-base alloys as a function of cryogenic temperature is now fairly well established [1].² In general, most titanium-base alloys experience a marked decrease in elongation and

¹ Nuclear engineers, Reactor Irradiation Branch, Nuclear Systems Div., Lewis Research Center, National Aeronautics and Space Administration, Cleveland, Ohio 44135.

² Italic numbers in brackets refer to the list of references at the end of this paper.

reduction of area as the temperature is reduced to 20 K. At temperatures below about 78 K only a few alloys experience plastic deformation prior to failure. The tensile behavior of titanium alloys as a function of irradiation [2-12], however, has received only minor attention. There is some evidence [2, 8-11] that cryogenic temperatures accelerate the onset of brittle behavior for irradiated commercially pure titanium and the Ti-5Al-2.5Sn alloy.

To further investigate the effect of nuclear irradiation on embrittlement of titanium and titanium alloys at cryogenic temperature, an experimental program was undertaken at NASA's Plum Brook reactor facility, Sandusky, Ohio. Test materials included in the program were selected to be representative of the various titanium-base alloys suitable for use at cryogenic temperatures. Tests were conducted using specially designed test equipment capable of maintaining the test specimen at 17 K throughout irradiation exposure and postirradiation tension testing. The objectives of this test program were to determine the radiation damage threshold, that is, the fluence at which changes in tensile properties became significant for each alloy, and to investigate the effects of impurities and heat treatment on this threshold.

Experimental Procedures

Tension test data for various titanium alloys were obtained using miniature round tension test specimens and specially designed test equipment installed at the Plum Brook reactor facility. The program was conducted in accordance with the provisions of ASTM Tentative Method for Measuring Neutron Flux by Radioactivation Techniques (E 261 - 65 T), Standard Methods for Tension Testing of Metallic Materials (E 8 - 68), and Recommended Practice for Effects of High-Energy Radiation on the Mechanical Properties of Metallic Materials (E 184 - 62(1968)). Unirradiated control tests were conducted in a test loop under the same test conditions as their irradiated counterparts. For each of the test materials in the program at least three specimens were tested for each exposure condition.

Test Materials

Test materials were commercially pure titanium (CP Ti); Ti-5Al-2.5Sn, NI (normal impurity content); Ti-5Al-2.5Sn, ELI (extralow impurity content); Ti-6Al-4V, annealed; Ti-6Al-4V, aged; and Ti-8Al-1Mo-1V. All test materials were obtained as 0.5-in. (1.27-cm)-diameter round bar stock. Stock materials were prepared by consumable electrode vacuum arc melting, forging to 1.5-in. (3.81-cm)-square bar at 1200 to 1422 K, rolling to 0.5-in. (1.27-cm)-diameter round bar at 978 to 1256 K, and then heat treating. Material compositions and heat treat conditions are given in Table 1.

TABLE 1—Chemical composition and fabrication history of test materials.

Test Material	Temper- Treatment ^a	Chemical Composition, wt % ^b										
		Titanium	Alumi- num	Tin	Vanadium	Molyb- denum	Iron	Carbon	Nitrogen	Oxygen	Hy- drogen	
CP Ti	Annealed	Balance	0.190	0.032	0.023	0.218	0.006	
Ti-5Al-2.5Sn, NI.	Annealed	...	5.10	2.47	0.110	0.032	0.019	0.116	0.012	
Ti-5Al-2.5Sn, ELI.	Annealed	...	5.36	2.35	0.025	0.022	0.010	0.059	0.006	
Ti-6Al-4V	Annealed	...	5.95	...	4.00	...	0.170	0.010	0.022	0.065	0.006	
Ti-6Al-4V	Aged	...	5.80	...	3.90	...	0.150	0.010	0.035	0.102	0.010	
Ti-8Al-1Mo-1V	Duplex annealed	...	8.02	...	1.14	1.00	0.120	0.030	0.013	0.091	0.009	

^a Heat treatment:

A = annealed at 978 K for 2 h, air cooled.

B = annealed at 1033 K for 2 h, air cooled.

C = solution treated at 1214 K for 0.5 h, water quenched; aged at 811 K for 4 h, air cooled.

D = annealed at 1172 K for 1 h, air cooled; annealed at 867 K for 8 h, air cooled.

^b Actual analyses on as-received bar.

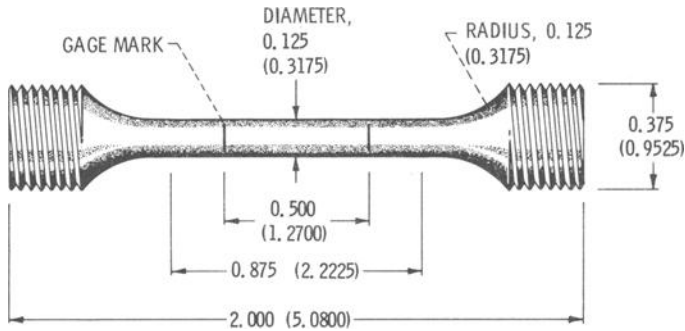


FIG. 1—Miniature, round tension test specimen.

Test Specimens

The tension test specimen (Fig. 1) was a geometrically similar miniaturization of the standard 0.5-in. (1.27-cm) round tension specimen of ASTM E 8. This specimen had a gage uniform section of 0.125-in. (0.3175-cm) diameter by 0.875-in. (2.2225-cm) length. Gage marks were inscribed by light sandblasting to delineate a 0.5-in. (1.27-cm) gage length. Ratios of significant dimensions were the same as for the standard ASTM specimen.

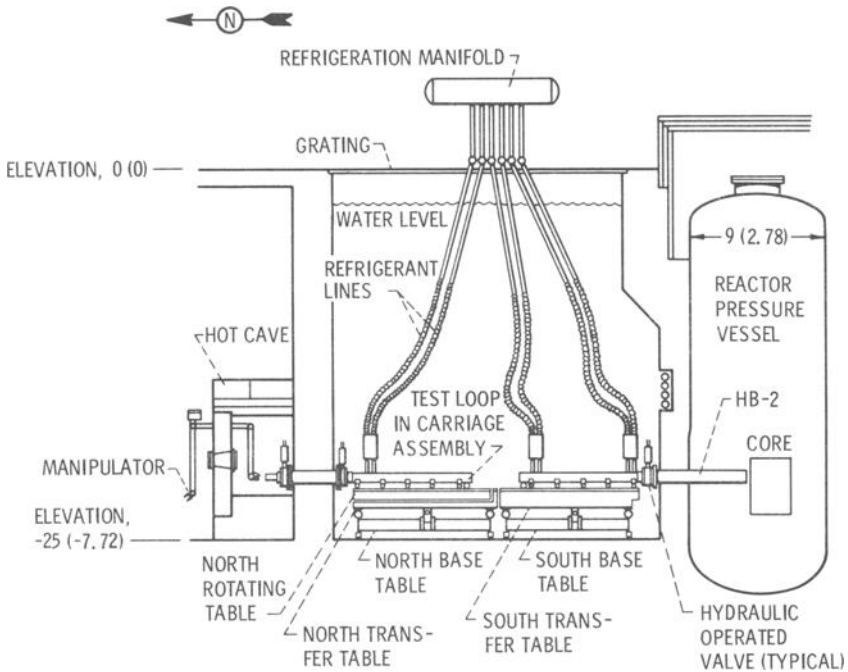


FIG. 2—Cryogenic irradiation test equipment.

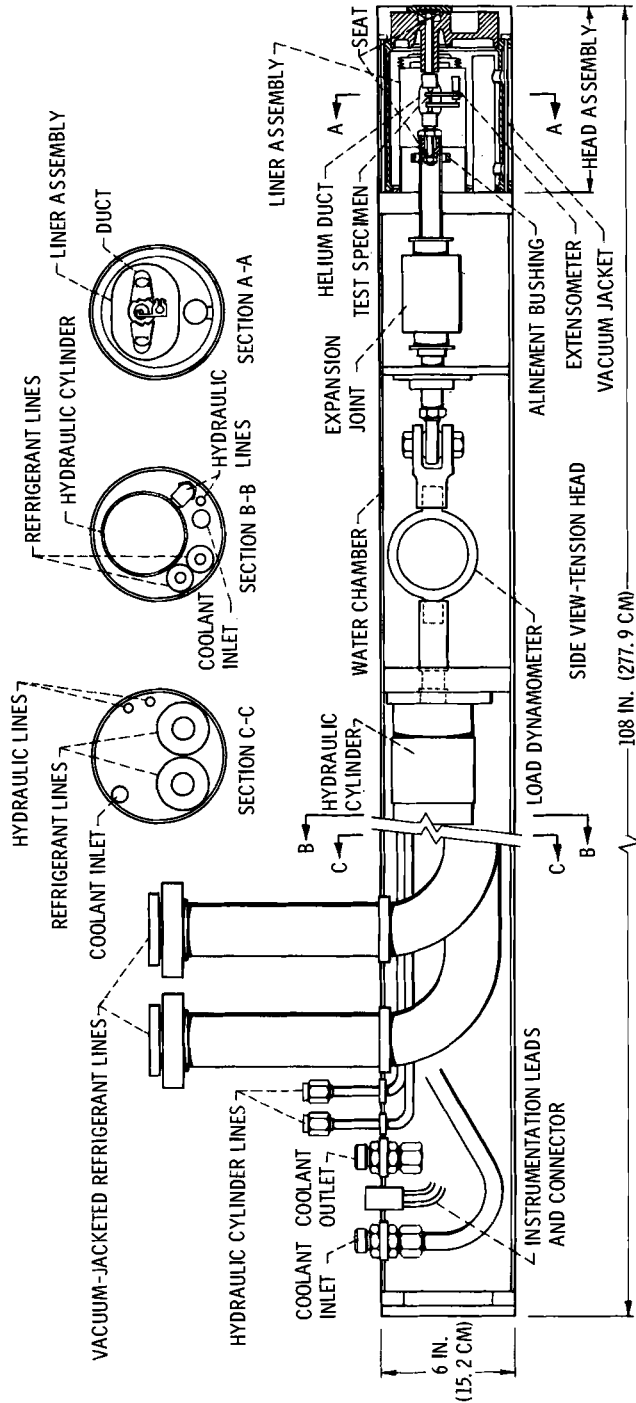


FIG. 3—Cryogenic irradiation test loop.

Test Equipment

The major components of the test equipment are shown in Fig. 2 and include a helium refrigeration system, test loops, and transfer tables. The test loop body (Fig. 3) contained a horizontally placed 5000-lb (22,241-N)-capacity test machine together with the necessary load actuation components, stress-strain monitoring instrumentation, and vacuum insulated refrigerant transfer lines. The forward section, or head assembly, served as both a fixed crosshead of the test machine and a cryostat for temperature control. The head assembly was removable by remote handling methods to allow specimen change. Detailed discussions of the test equipment and its operation are given elsewhere [13-16].

Test Procedure

The typical testing sequence can readily be followed by reference to Fig. 2. A test loop was inserted into the hot cave for specimen installation. After specimen installation, the loop was withdrawn from the hot cave to the north table in quadrant D. Refrigerant flow was started and the table holding the loop was rotated 180 deg. The loop was then transferred to the south table and positioned in line with HB-2 and, after stabilization of specimen temperature at 17 K, inserted into HB-2. The loop was held in this position with the specimen maintained at 17 K until the required fast neutron fluence was attained. The test loop was then retracted approximately 4 ft (1.2 m) and an axial tensile load was applied to the specimen. After specimen failure the loop was returned to the hot cave for specimen replacement.

Specimen Temperature Control—Direct measurement of the specimen temperature was not feasible. Platinum resistance thermometers positioned in inlet and return gas streams at the refrigerator manifold were calibrated to provide specimen temperature control within ± 0.5 K.

Measurement of Neutron Fluence—The fast neutron spectrum in the test location in HB-2 was determined using foil measurement techniques. Sets of foils, as shown in Table 2, were irradiated and then counted and evaluated by standard techniques. From these data and the reactor operating conditions at the time of foil exposure, the fast neutron fluence, with energy greater than 0.5 MeV ($E > 0.5$ MeV (80 fJ)), was determined. Periodic measurements throughout the life of a reactor power cycle were performed to establish the neutron flux as a function of control rod position. During test program performance, the exposure rate for test specimens varied from about 2.0×10^{12} to 2.5×10^{12} n/cm²/s. (The ratio of the fluence with neutron energy greater than E to the fluences with energies greater than 0.5 MeV (80 fJ) is given in Fig. 4. This figure is based on 27 sets of foils irradiated during the test program.)

Stress-Strain Recording—The load applied to the test specimen was monitored by a proving ring type dynamometer using a linear variable

TABLE 2—Foils used for spectral measurements of fast neutron fluence in HB-2.

Type of Foil	Nuclear Reaction	Threshold Energy,		Cross Section, cm ²
		MeV	fJ	
Indium	¹¹⁵ In (neutron, neutron) ^{115m} In	0.45	72	0.20 × 10 ⁻²⁴
Neptunium	²³⁷ Np (neutron, fission) ¹⁴⁰ Ba	0.75	120	1.52
Uranium	²³⁸ U (neutron, fission) ¹⁴⁰ Ba	1.45	232	0.54
Thorium	²³² Th (neutron, fission) ¹⁴⁰ Ba	1.75	280	0.10 ^a
Sulfur	³² S (neutron, proton) ³² P	2.9	464	0.284
Nickel	⁵⁸ Ni (neutron, proton) ⁵⁸ Co	5.0	800	1.67
Magnesium	²⁴ Mg (neutron, proton) ²⁴ Na	6.3	1008	0.0715
Aluminum ^b	²⁷ Al (neutron, alpha) ²⁴ Na	8.1	1296	0.110
Aluminum	²⁷ Al (neutron, alpha) ²⁴ Na	8.6	1376	0.23

^a Cross section for thorium is not considered reliable.

^b ²⁷Al (neutron, proton) ²⁷Mg reaction with a threshold energy of 5.3 MeV (848 fJ) is not included because of short (9.8 min) half-life of product.

differential transformer (LVDT) to measure the ring deflection resulting from loading. Dynamometers in each test loop were calibrated to within 2 percent of a National Bureau of Standards certified reed-type proving ring. Strain was measured using an extensometer which measured the increase of the separation between two knife edges initially 0.5 in. (1.27 cm) apart. The measurement was accomplished through the use of a LVDT specially constructed to be resistant to radiation effects. This extensometer had a range of reliable accuracy of approximately 0.01 in. (0.025 cm), which was sufficient to record strains to well beyond the yield strength (0.2 percent offset method). The extensometer was verified in accordance with ASTM Tentative Method for Verification and Classification of Extensometers (E 83 - 57 T), and the error in indicated strain was less than 0.0001. Installation of the extensometer by remote means, however, introduces the possibility for increased error in the indicated strain. An X-Y recorder was employed to automatically plot the load-strain curve to approximately 0.02 total strain. The *x* axis was then switched to time travel and a load-time curve through fracture was obtained.

Ductility Measurements—After removal from the test loop the fractured gage length and minimum diameter were measured. The broken halves of the test specimens were fit together and measurements were obtained by means of a micrometer stage and hairline apparatus accurate to ±0.0001 in. (0.00025 cm).

Data Reduction and Analysis—The load-strain/load-time curve developed by the X-Y recorder during testing and the initial specimen dimensions provided data for the determination of the ultimate tensile strength and the tensile yield strength (0.2 percent offset method). The modulus of elasticity was also approximated from these curves. Elongation and re-

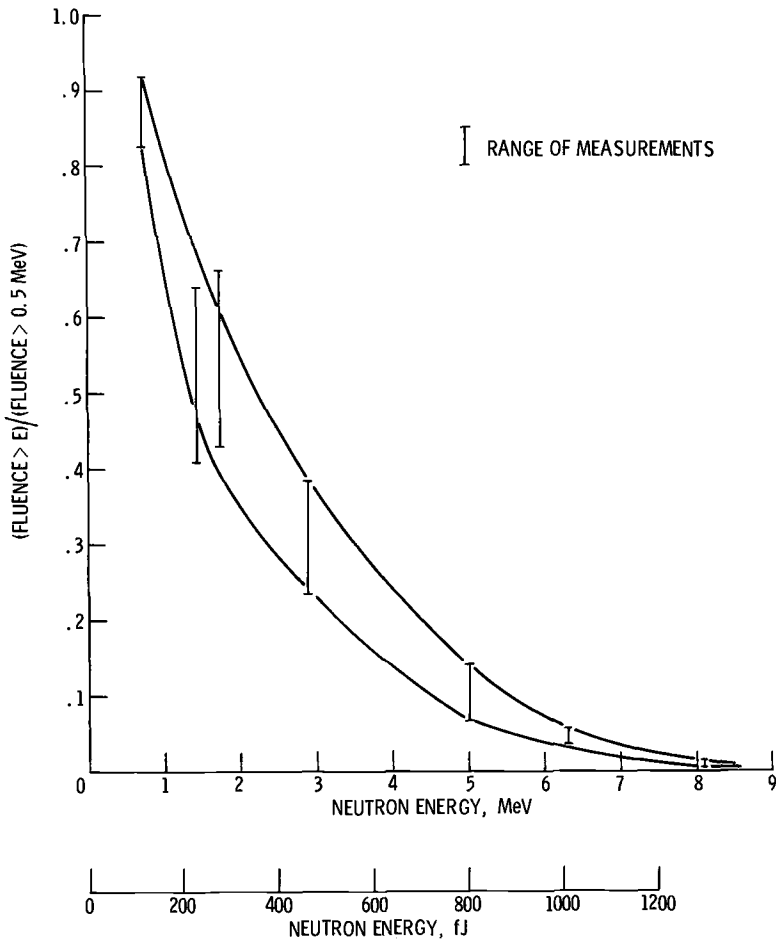


FIG. 4—Ratio of fluence greater than E to fluence greater than 0.5 MeV (80 fJ).

duction of area values were calculated from the original specimen dimensions and the dimensions following fracture. The test data were compiled and subjected to statistical analysis in accordance with various methods given by Natrella [17]. These analyses included determination of (1) average values and estimated standard deviations for each material and test condition, (2) the differences between values for irradiated and unirradiated test conditions, and (3) the 95 percent confidence interval associated with these differences and estimation of the following irradiation.

Test Results

Tension test data obtained during performance of the data acquisition phase of the test program are compiled in Tables 3-10 of the Appendix.

Summaries of the statistical analyses performed in connection with data analyses are also included in the tables.

Commercially Pure Titanium

Some CP Ti was used as test material for investigating the synergistic effect of reactor irradiation and cryogenic temperature on the tensile properties. The objective of this investigation was to determine the radiation damage threshold, that is, the fluence level at which significant changes in tensile properties occurred, and to study the reduction of this damage during postirradiation annealing.

Radiation Damage Threshold—The radiation damage threshold was determined from tests conducted at 17 K following reactor irradiation at 17 K to fluence levels of 1×10^{17} , 6×10^{17} , and 10×10^{17} n/cm², $E > 0.5$ MeV (80 fJ). Tests conducted at 17 K on unirradiated material were used as base line control data. Results of the data analyses are shown in Fig. 5, where it can be seen that the irradiation increased strength parameters, decreased ductility parameters, but did not alter the tensile modulus of elasticity. The increases in yield and ultimate strengths are approximately

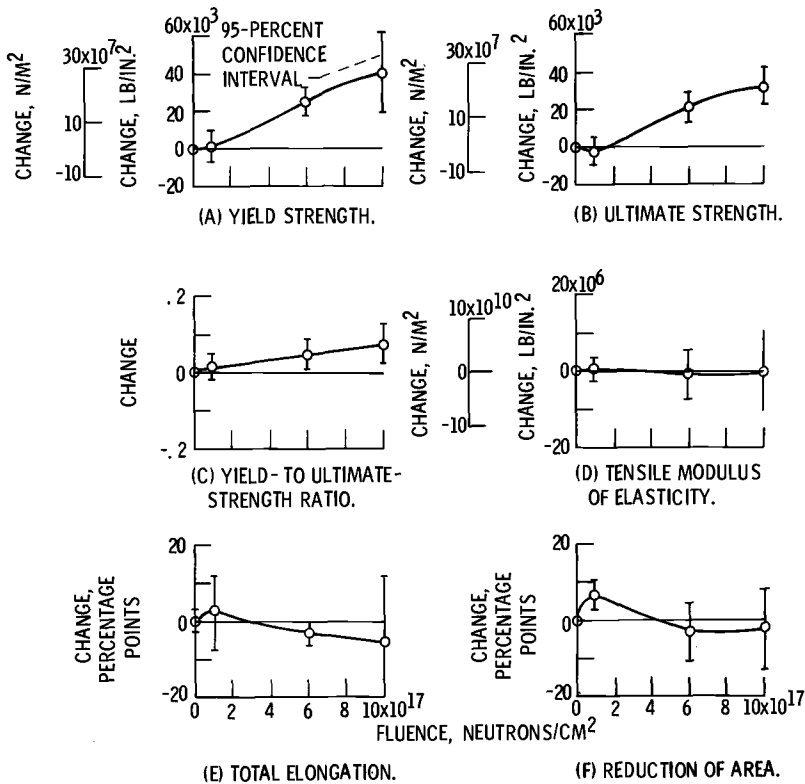


FIG. 5—Effect of reactor irradiation at 17 K on 17 K tensile properties of commercially pure titanium. Neutron energy > 0.5 MeV (80 fJ).

linear with increasing fluence, with the yield strength increasing more rapidly than the ultimate strength, as may be observed from the plot of yield to ultimate strength ratio. The changes in total elongation and reduction of area are small and in most cases are not statistically significant at the 0.05 level of significance. (In order for the difference to be statistically significant at the 0.05 level of significance, the 95 percent confidence interval must not include zero.) Only the increase in the reduction of area following 1×10^{17} -n/cm² exposure and the decrease in total elongation following 6×10^{17} -n/cm² exposure are statistically significant.

The general data trend for irradiations to 10×10^{17} n/cm² at 17 K indicates that the radiation damage threshold occurs in the region between 1×10^{17} and 6×10^{17} n/cm². This threshold is defined by a significant increase in both yield strength and ultimate strength and possibly a small decrease in ductility. The increase in reduction of area following irradiation to 1×10^{17} n/cm² appears to be anomalous.

Reduction of Radiation Damage—The reduction of radiation damage was investigated using heat treatments following irradiation at 17 K to 6×10^{17} n/cm². Unirradiated specimens were subjected to the same heat treatment conditions except for the time of initial 17 K exposure. The unirradiated specimens were held for 1 h at 17 K prior to heat treatment, whereas the irradiated specimens were held approximately 40 h (irradiation time) at 17 K prior to heat treatment.

Two cases are considered to be pertinent to the reduction of radiation damage. The first case consists of simply warming the specimen from 17 K to a higher temperature and then testing at this higher temperature. This provides information relative to the reduction of the irradiation induced defects influence on the metal lattice, but does not separate the annihilation of defects from the reduction in lattice friction due to higher thermal oscillation of lattice ions. The second case, defined as annealing, duplicated the previous warming condition, but specimen temperatures were subsequently reduced to 17 K and held for 1 h prior to testing at 17 K. The combination of these two cases permits a separation of defect annihilation from defect resistance. Results of data analyses are shown in Fig. 6.

As can be seen from the dashed curves of the figure, warming the specimens from 17 to 178 K resulted in a recovery of approximately one half of the radiation damage for the yield strength and three fourths for the ultimate strength. The greater portion of this recovery occurred between 17 and 78 K. The reduction of area and tensile modulus of elasticity are not significantly different at 178 K than at 17 K, although the trend for the reduction of area does indicate some damage at 17 K which has fully recovered at 178 K. The total elongation indicates further damage at 78 K; however, the 95 percent confidence intervals for this property overlap at all temperatures, suggesting an equal probability that the indicated trend is within material variability limits.

Annealing the test material resulted in essentially the same recovery

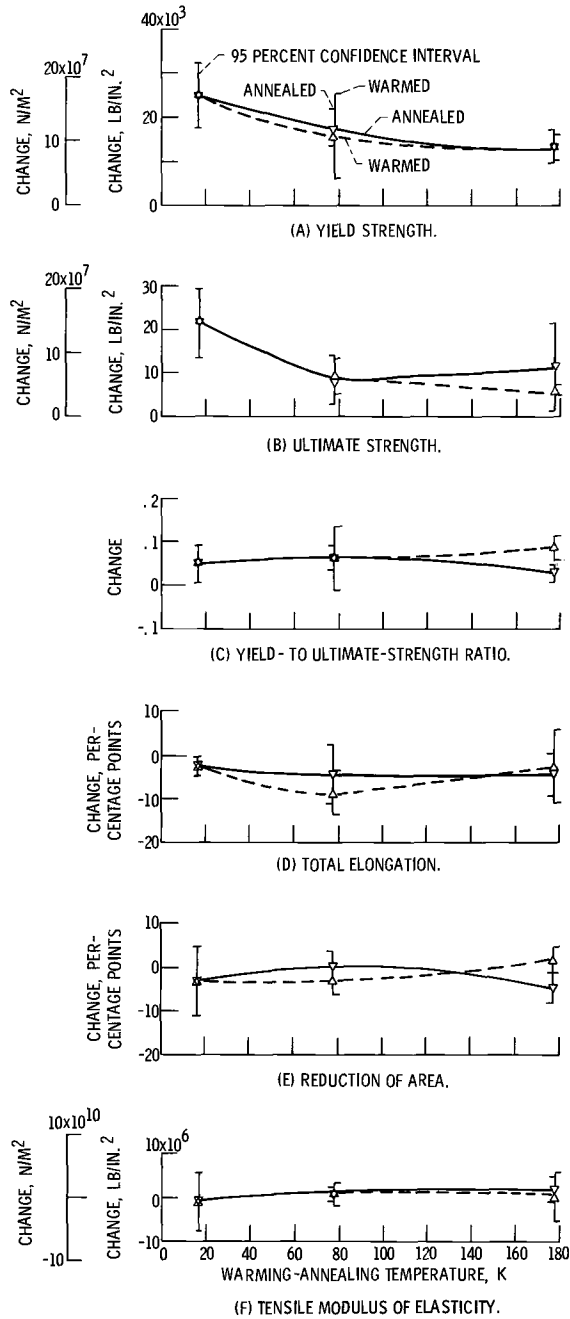


FIG. 6—Effect of postirradiation warming and annealing on tensile properties of commercially pure titanium irradiated at 17 K to 6×10^{17} n/cm². Energy > 0.5 MeV (80 fJ).

Copyright by ASTM Int'l (all rights reserved); Thu Aug 27 10:12:15 EDT 2020

Downloaded/printed by

(USP) Universidade de Sao Paulo ((USP) Universidade de Sao Paulo) pursuant to License Agreement. No further reproductions authorized.

as observed for the warming case, as may be noted from the solid curves of Fig. 6. The ultimate strength following 178 K annealing appears somewhat higher than the corresponding 178 K warming case; however, the 95 percent confidence interval is also greater and includes the confidence interval for the warming case. Such a condition suggests that there is no difference between the two thermally cycled conditions. This conclusion is somewhat shadowed, however, by the distinct separation of the confidence intervals for the yield to ultimate strength ratio following thermal treatment at 178 K. The results for total elongation following the 78 K treatment and the reduction of area following the 78 and 178 K treatments show some deviations; however, for each case there is an overlap of the 95 percent confidence intervals, which indicates no significant differences.

The data compared in Fig. 6 lead to the conclusion that thermally cycling CP Ti to 178 K following irradiation at 17 K to 6×10^{17} n/cm² reduces the irradiation damage by annihilation of irradiation induced defects. As a result of this annihilation the irradiation damage to the yield and ultimate strengths is reduced by about 50 percent. Furthermore, for the ultimate strength, there is an indication that additional recovery, attributable to reduced lattice resistance, occurs between 78 and 178 K.

Titanium-5 Aluminum-2.5 Tin Alloy

The titanium alloy containing 5 weight percent aluminum and 2.5 weight percent tin (Ti-5Al-2.5Sn) was used as test material for investigating the influence of impurity elements on radiation damage at cryogenic temperature. Two heats of the alloy (Table 1), one having the normal level of impurity content and one having an extralow level of impurity content, were used.

Tests using each material were conducted at 17 K following reactor irradiation at 17 K to 1×10^{17} and 10×10^{17} n/cm². Tests conducted at 17 K on unirradiated materials were used as base line control data. Results of the data analyses are shown in Fig. 7.

Radiation Damage Threshold—As may be seen from the solid curves of the figure, irradiation of the normal impurity material at 17 K to 10×10^{17} n/cm² increased the yield and ultimate strengths, with the yield strength increasing more rapidly than the ultimate strength, as evidenced by the plot of yield to ultimate strength ratio. The total elongation was decreased slightly by the irradiation, while the reduction of area and tensile modulus of elasticity remained unchanged. These data indicate that the threshold for radiation damage at 17 K occurs prior to 1×10^{17} n/cm², as evidenced by the marked increases in yield and ultimate strengths.

Irradiation of the extralow impurity material at 17 K to 10×10^{17} n/cm² caused essentially the same changes in 17 K tensile properties (dashed curves shown in Fig. 7) with the exception of the reduction of area. The reduction of area shows a significant decrease following irradiation to

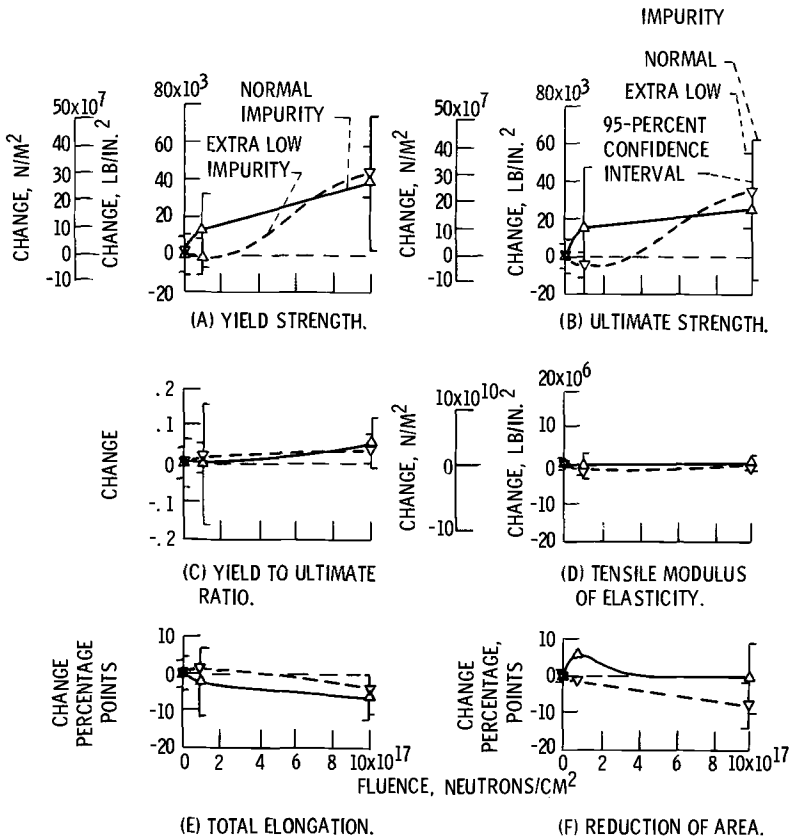


FIG. 7—Effect of reactor irradiation at 17 K on 17 K tensile properties of titanium-5 aluminum-2.5 tin alloy. Neutron energy >0.5 MeV (80 fJ).

10×10^{17} n/cm². It should be noted also that following irradiation to 1×10^{17} n/cm² the tensile modulus of elasticity decreased. The decrease is small, but it is statistically significant at the 0.05 level of significance. The threshold for radiation damage is higher than the normal impurity material and occurs in the interval between 1×10^{17} and 10×10^{17} n/cm².

Influence of Impurity Elements on Radiation Damage—As for the effects of impurity elements on radiation damage, Fig. 7 shows that in every case there is an overlap of the 95 percent confidence intervals and in most cases the overlapped regions include the mean values for both normal impurity and extralow impurity materials. Notable exceptions occur for yield and ultimate strengths following 1×10^{17} n/cm². Here the 95 percent confidence intervals do overlap, but the difference in mean values of the yield and ultimate strengths for the two materials do not fall within the overlapped intervals. It would be presumptuous to conclude from these data that there is a difference in the radiation damage attributable to

impurity content except possibly for the yield and ultimate strengths following 1×10^{17} -n/cm² exposure.

Titanium-6 Aluminum-4 Vanadium Alloy

Two heats of the titanium alloy containing 6 weight percent aluminum and 4 weight percent vanadium (Ti-6Al-4V) were used for cryogenic irradiation studies. One heat of the material was in the annealed condition, while the second heat of material was solution treated then aged.

Tests using each heat of material were conducted at 17 K following reactor irradiation at 17 K to 1×10^{17} and 10×10^{17} n/cm². Tests conducted at 17 K on unirradiated materials were used as base line control data. Results of data analyses are shown on Fig. 8.

Radiation Damage Threshold—As may be seen from the figure, with the exception of the reduction of area, there is little difference in the irradiation effect on annealed material and aged material. For both material conditions the radiation damage threshold occurs for exposures of less than 1×10^{17} n/cm², as evidenced by increases in yield and ultimate strengths, a decrease in total elongation, and changes in the reduction of area. The decreases in total elongation are small; yet, they are statistically significant at the 0.05 level of significance.

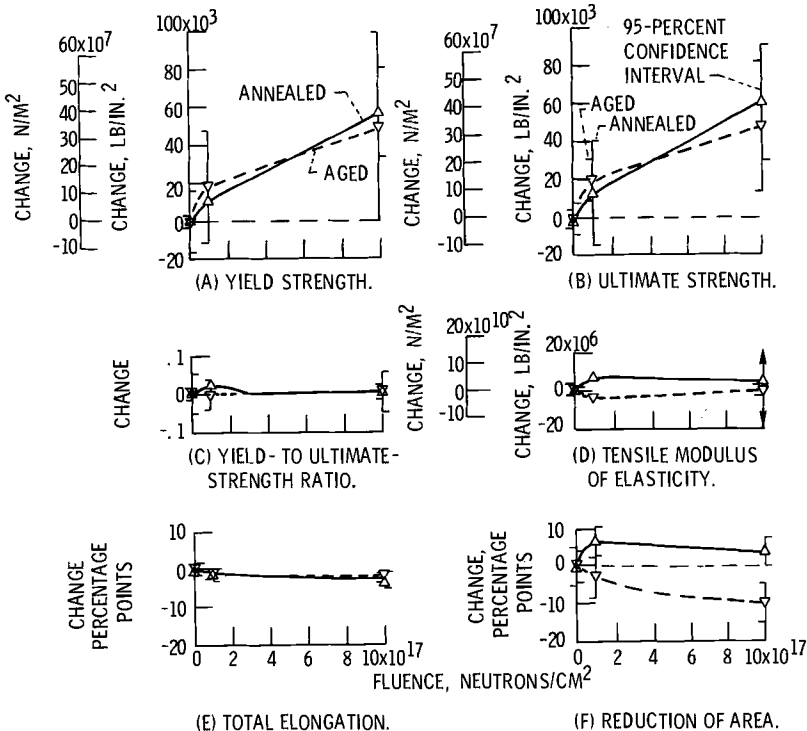


FIG. 8—Effect of reactor irradiation at 17 K on 17 K tensile properties of titanium-6 aluminum-4 vanadium alloy. Neutron energy >0.5 MeV (80 fJ).

The reduction of area shows the irradiation of annealed material causes an increase, whereas irradiation of the aged material causes a decrease. The 95 percent confidence intervals are approximately equal for all differences. Following irradiation to 1×10^{17} and 10×10^{17} n/cm², these confidence intervals do not overlap, which indicates that there is a difference in the effect of irradiation at 17 K on annealed material and aged material. The difference indicated by the tensile modulus of elasticity is probably exaggerated, since the variability of the annealed material following irradiation to the latter fluence is unusually large and data from only one specimen for each temper condition were obtained following irradiation to the former.

From these data, the only indication that metallurgical condition influences radiation damage at 17 K is a small difference in the reduction of area following exposure to 10×10^{17} n/cm². This difference represents a decrease in the ductility of aged material which is not evident in the annealed material.

Titanium-8 Aluminum-1 Molybdenum-1 Vanadium Alloy

The titanium alloy containing 8 weight percent aluminum, 1 weight percent molybdenum, and 1 weight percent vanadium (Ti-8Al-1Mo-1V) was irradiated at 17 K to a fluence of 1×10^{17} n/cm² to determine the threshold for radiation damage. Tests conducted at 17 K on unirradiated material were used as base line control data. Results of data analyses are shown in Fig. 9, where it can be seen that the threshold for radiation damage at 17 K occurs for exposures of less than 1×10^{17} n/cm², as evidenced by the increase in both yield and ultimate strengths. The total elongation following this exposure appears to decrease; however, the decrease is small and not statistically significant at the 0.05 level of significance. The indicated increase in the tensile modulus of elasticity is subject to considerable uncertainty, since it is based on only two irradiated specimen values, both of which appear to be unusually high. The irradiated values and the unusually large 95 percent confidence interval are due most probably to test techniques rather than irradiation.

Comparison of Radiation Damage to Titanium-Base Alloys

The effect of reactor irradiation at 17 K on 17 K tensile properties of CP Ti and the three titanium-base alloys is shown in Fig. 10. The points plotted on this figure are the differences in the mean values of each tensile property for each alloy and alloy condition. The curves for Ti-5Al-2.5Sn are the average for normal impurity and extralow impurity heats of material. The curves for Ti-6Al-4V are the average for annealed and aged conditions (with the exception of reduction of area, where curves representing the two material conditions are shown).

The comparisons of the figure show that irradiation at 17 K to 10×10^{17} n/cm² causes similar changes in the 17 K tensile properties of all alloys.

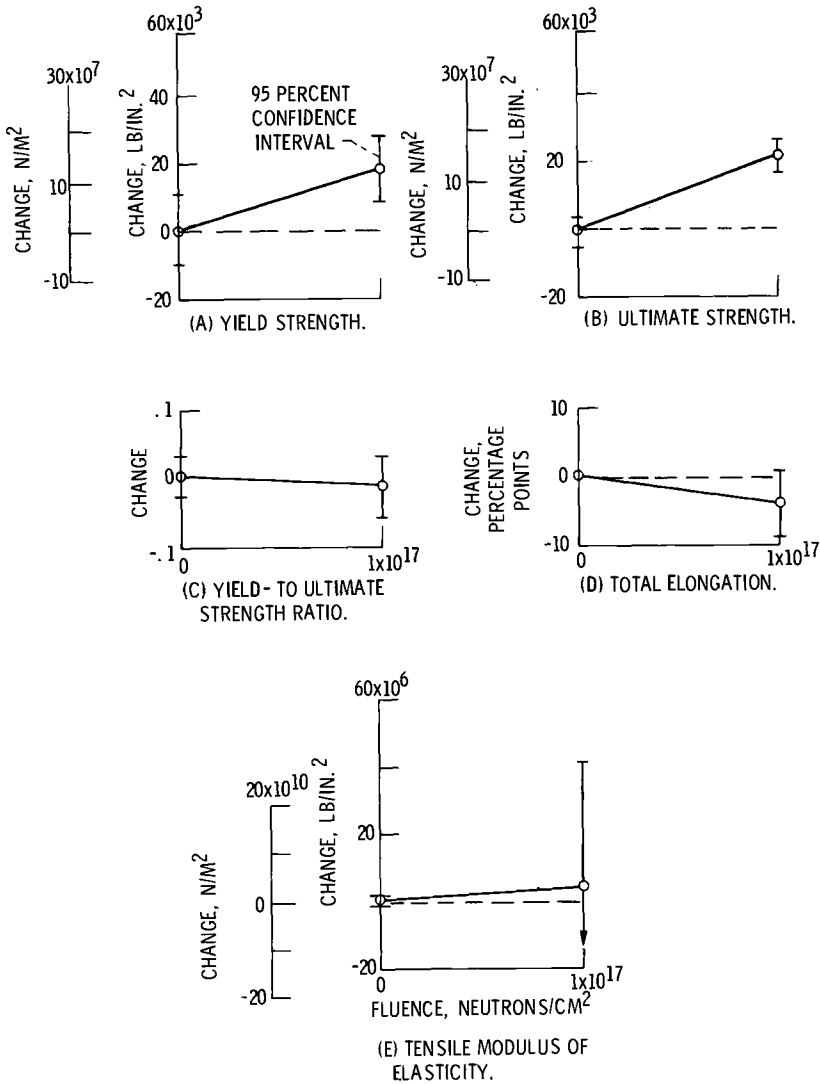


FIG. 9—Effect of reactor irradiation at 17 K on 17 K tensile properties of titanium-8 aluminum-1 molybdenum-1 vanadium alloy. Neutron energy >0.5 MeV (80 fJ).

Tensile strengths increase (with the yield strength increasing more than the ultimate strength) and ductilities decrease slightly. There is also an indication that the magnitude of the change due to irradiation depends on total alloy content or metallurgical structure.

Summary of Results and Conclusions

Commercially pure titanium and three titanium-base alloys have been subjected to reactor irradiation at 17 K for fluence levels of up to 10×10^{17}

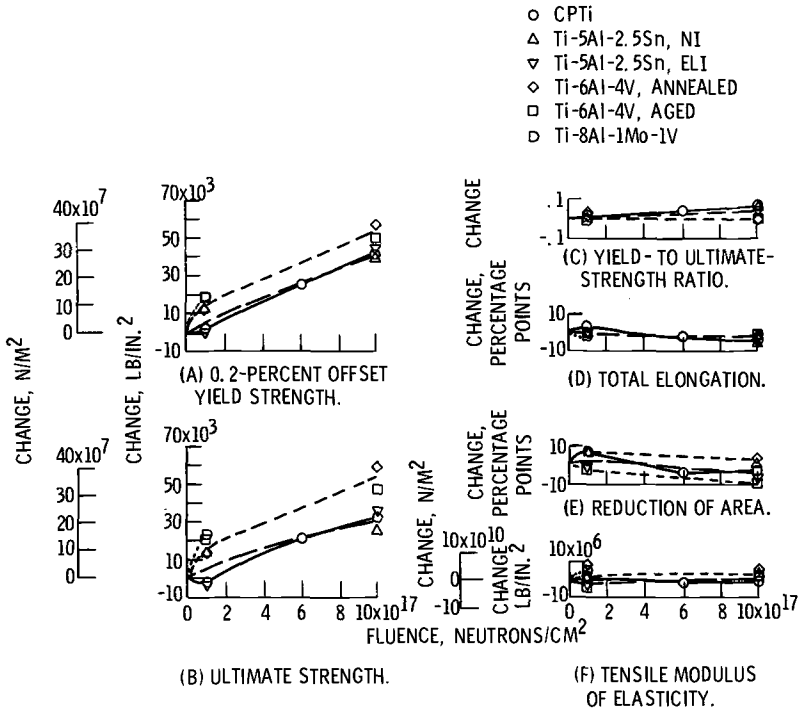


FIG. 10—Effect of reactor irradiation at 17 K on 17 K tensile properties of titanium and titanium-base alloys. Neutron energy >0.5 MeV (80 fJ).

n/cm², *E*>0.5 MeV (80 fJ). Postirradiation tension tests were conducted at 17 K without intervening warmup, except for a few tests using CP Ti. Test results show the following:

1. The irradiation damage threshold at 17 K for CP Ti occurs in the region between 1×10^{17} and 6×10^{17} n/cm². This threshold is defined by a significant increase in both yield and ultimate strengths and possibly a small decrease in ductility.

2. Thermally cycling CP Ti to 178 K following irradiation at 17 K to 6×10^{17} n/cm² reduces the irradiation damage by annihilation of irradiation induced defects. As a result of this annihilation the irradiation damage to the yield and ultimate strengths is reduced by about 50 percent. Furthermore, for the ultimate strength, there is an indication that additional recovery, attributable to reduced lattice resistance, occurs between 78 and 178 K.

3. The threshold for radiation damage at 17 K of Ti-5Al-2.5Sn alloy with normal impurity content occurs for exposures less than 1×10^{17} n/cm². For the same alloy with extralow impurity content, the threshold for radiation damage at 17 K is higher than the normal impurity material and

occurs in the interval between 1×10^{17} and 10×10^{17} n/cm². These thresholds are indicated by significant increases in both yield and ultimate strengths and decreases in ductility. The differences in radiation damage thresholds shown by the Ti-5Al-2.5Sn alloys may be due to material variability.

4. The irradiation damage threshold at 17 K for Ti-6Al-4V alloy occurs for exposures of less than 1×10^{17} n/cm². The threshold is evidenced by significant increases in yield and ultimate strengths and decreases in ductility parameters. Differences in the reduction of area following irradiation are the only indications that the heat treat condition influences the irradiation effect.

5. The irradiation damage threshold at 17 K for the Ti-8Al-1Mo-1V alloy occurs for exposures of less than 1×10^{17} n/cm². This threshold is indicated by significant increases in both the yield and ultimate strengths and probable decrease in ductility.

6. The effect of reactor irradiation at 17 K on 17 K tensile properties of CP Ti and the three titanium-base alloys investigated are similar. Irradiation damage is evidenced by significant increases in strength parameters and probable decreases in ductility parameters. The magnitude of radiation damage appears to depend on the total alloy content or metallurgical structure.

APPENDIX

Tabulated Test Data and Summary of Statistical Analyses

Tension test data obtained during performance of the data acquisition phase of the program are compiled in Tables 3 to 10. Summaries of the statistical analyses performed in connection with data analyses are also included in the tables. Symbols used on the tables for statistical analysis are defined as follows:

$$X_A = \frac{1}{n_A} \sum_{i=1}^n X_i$$

arithmetic mean of n_A measurements yielding property values of X_1, X_2, \dots, X_n

$$s_A = \sqrt{\frac{\sum_{i=1}^n (X_i - \bar{X}_A)^2}{n_A - 1}}$$

estimated standard deviation of n_A measurements yielding property values of X_1, X_2, \dots, X_n

$$X_L = (\bar{X}_A - \bar{X}_B) - u_A$$

lower limit of the 95 percent confidence interval of the difference between arithmetic means

$$\text{or}$$

$$(\bar{X}_B - \bar{X}_A) - u_{BA}$$

$$X_U = (\bar{X}_A - \bar{X}_B) + u_A$$

upper limit of 95 percent confidence interval of difference between arithmetic means

or

$$(\bar{X}_B - \bar{X}_A) + u_{BA}$$

$$u_A = t_{0.975} \frac{s_A}{\sqrt{n_A}}$$

for $n_A - 1$ degrees of freedom

TABLE 3—Effect of reactor irradiation at 17 K on 17 K tensile properties of commercially pure titanium.^a

Specimen	Fast Fluence, ^b n/cm ²	Statistical Analysis ^c	Tensile Modulus of Elasticity,		Yield Strength (0.2 percent offset)		Ultimate Strength,		Yield to Ultimate Strength Ratio	Total Elongation, ^d %	Reduction of Area, %
			lb/in. ²	N/m ²	lb/in. ²	N/m ²	lb/in. ²	N/m ²			
1Aa211.....	0	...	19.0×10 ⁶	13.1×10 ¹⁰	126.0×10 ³	86.8×10 ⁷	185.0×10 ³	127.5×10 ⁷	0.681	32.0	44.0
1Aa3.....	0	...	18.0	12.4	131.0	90.3	182.0	125.4	0.719	31.0	48.0
1Aa2.....	0	...	19.0	13.1	134.0	92.3	188.0	129.5	0.712	30.0	47.0
1Aa138.....	1×10 ¹⁷	\bar{X}_A	18.7×10 ⁶	12.9×10 ¹⁰	130.3×10 ³	89.8×10 ⁷	185.0×10 ³	127.5×10 ⁷	0.704	31.0	46.3
1Aa148.....	1	\bar{X}_A	0.6	0.4	4.1	2.8	3.0	2.1	0.020	1.0	2.1
1Aa144.....	1	$\bar{X}_A, \bar{S}_A, \bar{Y}_A$	0	0	0	0	0	0	0	0	0
1Aa138.....	1×10 ¹⁷	\bar{X}_U	-1.5	-1.0	-10.2	-7.0	-7.4	-5.1	-0.050	-2.5	-5.2
1Aa148.....	1	...	1.5	1.0	10.2	7.0	7.4	5.1	0.050	2.5	5.2
1Aa144.....	1	...	18.4×10 ⁶	12.7×10 ¹⁰	128.0×10 ³	88.2×10 ⁷	181.0×10 ³	124.7×10 ⁷	0.706	36.0	54.0
1Aa152.....	6×10 ¹⁷	...	18.5	12.7	131.0	90.3	180.0	124.0	0.728	32.0	52.0
1Aa153.....	6	...	21.4	14.7	136.0	93.7	187.0	128.8	0.736	34.0	53.0
1Aa205.....	10	\bar{X}_B	19.4×10 ⁶	13.4×10 ¹⁰	131.7×10 ³	90.7×10 ⁷	182.7×10 ³	125.9×10 ⁷	0.730	34.0	53.0
1Aa203.....	6	\bar{X}_B	1.7	1.2	4.0	2.8	3.7	2.6	0.012	2.8	1.4
1Aa206.....	10	\bar{X}_B	0.7	0.5	1.4	0.9	-2.3	-1.6	0.016	3.0	6.7
1Aa152.....	10×10 ¹⁷	\bar{X}_B, \bar{Y}_A	-2.6	-1.8	-6.7	-4.6	-9.4	-6.5	-0.020	-5.9	2.7
1Aa153.....	6	\bar{X}_L	4.0	2.8	9.5	6.5	4.8	3.3	0.052	11.9	10.7
1Aa205.....	10	\bar{X}_D	8.03	9.00	9.5	6.5	4.8	3.3	0.052	11.9	10.7
1Aa203.....	6	\bar{S}_B^2/\bar{S}_A^2	90.0×10 ⁶	13.8×10 ¹⁰	154.0×10 ³	106.1×10 ⁷	203.0×10 ³	139.9×10 ⁷	0.757	29.0	45.0
1Aa152.....	10×10 ¹⁷	...	15.0	10.3	154.0	106.1	211.0	145.4	0.729	27.0	38.0
1Aa153.....	6	...	19.0	13.1	158.0	108.9	204.0	140.6	0.773	29.0	46.0
1Aa203.....	6	\bar{X}_C	18.0×10 ⁶	12.4×10 ¹⁰	155.3×10 ³	107.0×10 ⁷	206.0×10 ³	142.0×10 ⁷	0.753	28.3	43.0
1Aa152.....	10×10 ¹⁷	\bar{X}_C	9.9	1.8	2.3	1.6	4.4	3.0	0.022	2.2	4.4
1Aa205.....	10	\bar{X}_C	-7.5	-5.1	-17.5	-12.7	21.0	14.5	0.049	-2.7	-3.3
1Aa206.....	10	\bar{X}_C, \bar{Y}_A	5.9	4.1	32.3	22.4	13.4	9.2	0.007	-11.1	-9.5
1Aa152.....	10×10 ¹⁷	\bar{X}_L	18.78	22.56	0.31	0.32	29.2	20.2	0.091	-0.5	4.5
1Aa205.....	10	\bar{S}_C^2/\bar{S}_A^2	14.2×10 ⁶	9.8×10 ¹⁰	159.0×10 ³	109.6×10 ⁷	213.0×10 ³	146.8×10 ⁷	0.746	30.0	49.0
1Aa206.....	10	...	22.2	15.3	171.0	117.8	216.0	148.8	0.701	29.0	44.0
1Aa152.....	10×10 ¹⁷	\bar{X}_D	18.2×10 ⁶	12.5×10 ¹⁰	170.3×10 ³	117.4×10 ⁷	217.3×10 ³	149.7×10 ⁷	0.783	26.0	43.7
1Aa205.....	10	\bar{X}_D	5.7	3.9	11.0	7.6	5.1	3.5	0.033	6.1	5.6
1Aa206.....	10	\bar{X}_D	-0.5	-0.4	40.0	27.6	32.3	22.2	0.079	-2.6	-1.6
1Aa152.....	10×10 ¹⁷	\bar{X}_D, \bar{Y}_A	-52.0	-35.9	18.4	12.7	23.1	15.9	0.022	-20.4	-18.4
1Aa205.....	10	\bar{X}_L	51.0	35.1	61.6	42.4	42.1	29.0	0.136	8.2	8.2
1Aa206.....	10	\bar{S}_D^2/\bar{S}_A^2	90.25	95.06	7.19	7.36	2.89	2.78	2.72	37.21	6.55

^a Specimen exposed in gaseous helium and maintained at 17 K throughout test.
^b Fast fluence is for E=0.5 MeV (80 fJ).
^c Arithmetic mean \bar{X} , estimated standard deviation s ; lower and upper limits of 95 percent confidence interval of the difference, X_L, X_U .
^d Total elongation in 0.5-in. (1.27-cm) gage length.
^e Values for tensile modulus of elasticity, yield strength, and ultimate strength differ because of significant figures maintained in comparative calculations between the two systems of units.
^f Value exceeds lower limit of possible change.

TABLE 4—Effect of warming following reactor irradiation at 17 K on tensile properties of commercially pure titanium.^a

Specimen	Fluence, ^b n/cm ²	Test Temperature, ^c deg K	Statistical Analysis ^d	Tensile Modulus of Elasticity,		Yield Strength (0.2 percent offset),		Ultimate Strength,		Yield to Ultimate Strength Ratio	Total Elongation, ^e %	Reduction of Area, %
				lb/in. ²	N/m ²	lb/in. ²	N/m ²	lb/in. ²	N/m ²			
1Aa201.....	0	78	...	20.0×10 ⁶	13.8×10 ¹⁰	103.0×10 ⁸	71.0×10 ⁷	134.0×10 ⁸	92.3×10 ⁷	0.768	52.0	66.0
1Aa195.....	0	78	...	17.0	11.7	106.0	73.0	137.0	94.4	0.773	51.0	68.0
1Aa11.....	0	78	...	18.3×10 ⁶	12.4×10 ¹⁰	106.0	73.0	138.0	95.1	0.767	47.0	67.0
			\bar{X}_E	1.5	1.0	105.0×10 ⁸	72.3×10 ⁷	136.4×10 ⁸	93.9×10 ⁷	0.769	50.0	67.0
			s_E	18.0×10 ⁶	12.4×10 ¹⁰	1.7	1.2	2.1	1.5	0.003	2.6	1.0
1Aa212.....	6×10 ¹⁷	78	...	18.0×10 ⁶	12.4×10 ¹⁰	116.0×10 ⁸	79.9×10 ⁷	145.0×10 ⁸	99.9×10 ⁷	0.800	43.0	63.0
1Aa1.....	6	78	...	19.0	13.1	120.0	82.7	145.0	99.9	0.827	39.0	66.0
1Aa42.....	6	78	...	19.0×10 ⁶	13.1×10 ¹⁰	126.0	86.8	147.0	101.3	0.857	41.0	63.0
			\bar{X}_F	1.0	0.7	120.6×10 ⁸	83.1×10 ⁷	145.7×10 ⁸	100.4×10 ⁷	0.828	41.0	64.0
			s_F	0.7	0.5	15.6	10.7	1.2	0.8	0.029	2.0	1.7
			\bar{X}_L	-2.0	-1.4	15.6	10.7	9.3	6.5	0.059	-9.0	-3.0
			s_L	3.4	2.3	5.9	4.1	5.4	3.7	-0.014	-13.6	-6.2
			s_F^2/s_E^2	0.44	0.49	25.3	17.4	13.2	9.1	0.132	-4.4	0.2
1Aa59.....	0	178	...	17.0×10 ⁶	11.7×10 ¹⁰	8.64	8.02	0.33	0.27	93.44	0.59	2.89
1Aa51.....	0	178	...	21.0	14.5	76.9×10 ⁸	53.0×10 ⁷	94.2×10 ⁸	64.9×10 ⁷	0.817	30.0	64.0
1Aa17.....	0	178	...	15.0	10.3	78.9	54.4	94.3	65.0	0.836	26.0	62.0
			\bar{X}_G	17.7×10 ⁶	12.2×10 ¹⁰	79.9	55.1	95.2	65.6	0.839	35.0	61.0
			s_G	3.1	2.1	78.6×10 ⁸	54.2×10 ⁷	94.6×10 ⁸	62.2×10 ⁷	0.831	30.3	62.3
			\bar{X}_H	17.0×10 ⁶	11.7×10 ¹⁰	1.5	1.5	0.6	0.4	0.012	4.5	1.5
			s_H	18.3×10 ⁶	12.6×10 ¹⁰	90.7×10 ⁸	62.5×10 ⁷	101.0×10 ⁸	69.6×10 ⁷	0.807	25.0	64.0
1Aa23.....	6×10 ¹⁷	178	...	18.0	12.4	92.0	63.8	100.0	68.9	0.826	30.0	64.0
1Aa45.....	6	178	...	20.0	13.8	92.7	63.9	101.0	68.6	0.817	29.0	63.0
1Aa35.....	6	178	...	18.3×10 ⁶	12.6×10 ¹⁰	92.0×10 ⁸	63.4×10 ⁷	100.7×10 ⁸	68.4×10 ⁷	0.813	28.0	63.7
			\bar{X}_I	1.5	1.0	1.1	0.8	0.9	0.4	0.015	2.6	0.6
			s_I	0.6	0.4	13.4	9.2	6.1	4.2	0.082	-2.3	1.4
			\bar{X}_J	-4.9	-3.4	10.6	7.3	4.9	3.4	0.055	-10.8	-4.3
			s_J	6.1	4.2	16.2	11.2	7.3	5.0	0.109	6.0	4.3
			s_I^2/s_G^2	0.23	0.23	0.54	0.53	1.00	1.00	1.56	0.33	0.16

^a Specimen exposed in gaseous helium throughout test.
^b Unirradiated specimen cooled to 17 K and held for 1 h prior to warming and testing. Irradiated specimen cooled to and held at 17 K throughout irradiation exposure.
^c Fast fluence is for neutron energies greater than 0.5 MeV (80 fJ).
^d Specimen warmed to and held for 1 h at test temperature, then fractured at test temperature.
^e Arithmetic mean, \bar{X} ; estimated standard deviation, s ; lower and upper limits of 95 percent confidence interval of the difference, X_L , X_U .
^f Total elongation in 0.5-in. (1.27-cm) gage length.
^g Values for tensile modulus of elasticity, yield strength, and ultimate strength differ because of significant figures maintained in comparative calculations between the two systems of units.

TABLE 5—Effect of annealing following reactor irradiation at 17°K on tensile properties of commercially pure titanium.^a

Specimen	Fast Fluence, ^b n/cm ²	Annealing Temperature, ^c deg K	Statistical Analysis ^d	Tensile Modulus of Elasticity,		Yield Strength (0.2 percent offset),		Ultimate Strength,		Yield to Ultimate Strength Ratio	Total Elongation, ^e %	Reduction of Area, ^f %
				lb/in. ²	N/m ²	lb/in. ²	N/m ²	lb/in. ²	N/m ²			
1Aa34.....	0	78	...	19.0×10 ⁶	13.1×10 ¹⁰	131.0×10 ⁸	90.3×10 ⁷	184.0×10 ⁸	126.8×10 ⁷	0.711	30.0	46.0
1Aa16.....	0	78	...	18.0	12.4	135.0	93.0	188.0	129.5	0.718	35.0	44.0
1Aa19.....	0	78	\bar{X}_I	18.7×10 ⁶	12.9×10 ¹⁰	136.0	93.7	185.3×10 ⁸	127.7×10 ⁷	0.738	28.0	48.0
			<i>s</i> / <i>I</i>	0.6	0.4	2.6	1.8	2.3	1.6	0.014	3.6	2.0
1Aa47.....	6×10 ¹⁷	78	...	19.0×10 ⁶	13.1×10 ¹⁰	151.0×10 ⁸	104.0×10 ⁷	196.0×10 ⁸	135.0×10 ⁷	0.770	30.0	47.0
1Aa4.....	6	78	...	20.0	13.8	152.0	104.7	190.0	130.9	0.799	24.0	47.0
1Aa14.....	6	78	\bar{X}_J	19.5×10 ⁶	13.4×10 ¹⁰	152.0	104.7	195.0	134.4	0.779	26.0	44.0
			<i>s</i> / <i>J</i>	0.7	0.5	0.6	0.4	3.2	2.2	0.015	3.1	1.7
			$\bar{X}_I - \bar{X}_J$	-0.9	0.5	17.7	12.2	8.4	5.7	0.061	-4.3	0
			$\frac{\bar{X}_I}{\bar{X}_J}$	-0.9	0.5	11.1	7.6	2.6	1.8	0.032	-11.0	-3.7
			<i>s</i> / <i>J</i>	2.5	1.7	24.3	16.8	14.2	9.8	0.090	2.4	3.7
			<i>s</i> / <i>J</i> ² / <i>s</i> / <i>J</i>	1.36	1.56	0.05	0.05	1.94	1.89	1.15	0.74	0.74
1Aa25.....	0	178	...	18.0×10 ⁶	12.4×10 ¹⁰	131.0×10 ⁸	90.3×10 ⁷	176.0×10 ⁸	121.3×10 ⁷	0.744	32.0	52.0
1Aa53.....	0	178	...	19.0	13.1	134.0	92.3	184.0	126.8	0.728	31.0	54.0
1Aa24.....	0	178	\bar{X}_K	18.0	12.4	134.0	92.3	186.0	128.2	0.720	36.0	50.0
			<i>s</i> / <i>K</i>	0.6	0.4	1.7	1.2	5.3	3.7	0.012	2.6	2.0
			\bar{X}_L	19.0×10 ⁶	13.1×10 ¹⁰	145.0×10 ⁸	99.9×10 ⁷	192.0×10 ⁸	132.3×10 ⁷	0.755	29.0	48.0
1Aa28.....	6×10 ¹⁷	178	...	20.0	13.8	146.0	100.6	194.0	133.7	0.752	30.0	47.0
1Aa50.....	6	178	...	22.0	15.2	149.0	102.7	195.0	134.4	0.764	27.0	46.0
1Aa41.....	6	178	\bar{X}_L	20.3×10 ⁶	14.0×10 ¹⁰	146.7×10 ⁸	101.1×10 ⁷	193.7×10 ⁸	133.5×10 ⁷	0.757	28.7	47.0
			<i>s</i> / <i>L</i>	1.5	1.0	2.1	1.5	1.5	1.1	0.006	1.5	1.0
			$\bar{X}_I - \bar{X}_K$	-2.0	1.4	13.7	9.5	11.7	8.1	0.026	-4.3	-5.0
			$\frac{\bar{X}_I}{\bar{X}_L}$	-0.9	0.6	9.9	6.9	1.6	1.1	0.004	-9.1	-8.6
			<i>s</i> / <i>L</i>	4.9	3.4	17.5	12.1	21.8	15.1	0.048	0.5	-1.4
			<i>s</i> / <i>L</i> ² / <i>s</i> / <i>L</i>	6.25	6.25	1.52	1.56	0.08	0.09	0.25	0.33	0.25

^a Specimen exposed in gaseous helium throughout test.
^b Unirradiated specimen cooled to 17°K and held for 1 h prior to annealing. Irradiated specimen cooled to and held at 17°K throughout irradiation exposure. Fast fluence is for *E*>0.5 Me V (80 *I*/*J*).
^c Specimen warmed from 17°K to annealing temperature, held 1 h at annealing temperature, cooled to 17°K, held 1 h at 17°K.
^d Arithmetic mean, \bar{X} ; estimated standard deviation, *s*; lower and upper limits of 95 percent confidence interval of the difference, *X*_L, *X*_U.
^e Total elongation in 0.5-in. (1.27-cm) gage length.
^f Values for tensile modulus of elasticity, yield strength, and ultimate strength differ because of significant figures maintained in comparative calculations between the two systems of units.

TABLE 6—Effect of reactor irradiation at 17 K on 17 K tensile properties of normal impurity titanium-5 aluminum-2.5 tin alloy.

Specimen	Fast Fluence, ^a n/cm ²	Statistical Analysis ^b	Tensile Modulus of Elasticity,		Yield Strength (0.2 percent offset),		Ultimate Strength,		Yield to Ultimate Strength Ratio	Total Elongation, ^c %	Reduction of Area, %
			lb/in. ²	N/m ²	lb/in. ²	N/m ²	lb/in. ²	N/m ²			
3Aa55.....	0	...	18.0×10 ⁶	12.4×10 ⁸	200.0×10 ³	137.8×10 ⁷	231.0×10 ³	159.2×10 ⁷	0.865	18.0	21.0
3Aa54.....	0	...	17.5	12.1	201.0	138.5	213.0	146.8	0.943	12.0	30.0
3Aa30.....	0	...	18.2	12.5	225.0	155.0	0.895	13.0	35.0
3Aa21.....	0	...	18.4	12.7	205.0	141.2	229.0	157.8	0.895	13.0	34.0
3Aa29.....	0	...	18.2	12.5	215.0	148.1	226.0	155.7	0.951	13.8	30.0
...	18.1×10 ⁶	12.5×10 ⁸	205.3×10 ³	141.1×10 ⁷	224.8×10 ³	154.9×10 ⁷	0.914	13.8	30.0
...	0.3	0.2	6.9	4.7	0	0	0.041	2.9	6.4
...	0	0	0	0	0	0	0	0	0
...	0.4	-0.3	-11.0	-7.5	-8.7	-6.0	-0.065	4.6	-10.2
...	0.4	0.3	11.0	7.5	8.7	6.0	0.065	4.6	10.2
3Aa58.....	1×10 ¹⁷	...	14.8×10 ⁶	10.2×10 ⁸	211.0×10 ³	145.4×10 ⁷	257.0×10 ³	177.0×10 ⁷	0.821	9.0	...
3Aa52.....	1	...	18.1	12.5	212.0	146.1	222.0	153.0	0.955	14.0	36.0
3Aa57.....	1	...	20.5	14.1	231.0	159.2	238.0	164.0	0.970	11.2	36.0
...	17.8×10 ⁶	12.3×10 ⁸	218.0×10 ³	150.2×10 ⁷	239.0×10 ³	164.7×10 ⁷	0.915	11.2	36.0
...	2.0	2.0	11.3	7.8	17.5	12.0	0.082	3.2	6.0
...	-0.3	-0.2	12.7	8.8	14.2	9.8	0.001	-2.3	6.0
...	-7.5	-5.2	-17.8	-9.8	-19.5	-13.4	-0.164	-1.3	...
...	6.0	4.8	33.2	22.0	47.9	33.0	0.166	6.3	...
...	93.44	100.00	27.68	27.6	6.25	6.24	4.00	1.66	...
3Aa73.....	10×10 ¹⁷	...	20.0×10 ⁶	13.8×10 ⁸	205.3×10 ³	141.5×10 ⁷	211.8×10 ³	145.9×10 ⁷	0.969	8.0	34.0
3Aa168.....	10	...	20.0	13.8	220.6	152.0	226.8	156.3	0.971	8.0	34.0
3Aa167.....	10	...	16.0	11.9	248.2	171.0	250.8	172.8	0.900	7.0	37.0
3Aa160.....	10	...	22.0	15.9	262.8	181.0	270.8	186.6	0.970	8.0	33.0
3Aa66.....	10	...	23.0	17.2	273.9	192.0	289.2	199.3	0.967	7.0	29.8
...	20.0×10 ⁶	14.2×10 ⁸	243.4×10 ³	167.7×10 ⁷	249.9×10 ³	172.2×10 ⁷	0.973	7.4	29.8
...	3.5	2.5	30.4	21.0	31.5	21.7	0.009	0.9	5.3
...	2.5	1.7	38.1	26.3	25.1	17.3	0.059	-6.4	-0.2
...	4.6	3.1	88.1	61.4	82.0	58.3	-0.008	-9.7	-9.7
...	6.6	4.5	74.2	51.2	62.2	42.9	0.126	-2.2	9.3
...	121.00	132.52	19.39	19.96	20.25	20.42	0.05	0.10	0.68

^a Specimen exposed in gaseous helium at 17 K throughout test. Fast fluence is for E>0.5 MeV (80 EJ).
^b Arithmetic mean, \bar{X} ; estimated standard deviation, s ; lower and upper limits of 95 percent confidence interval of the difference, $\bar{X}L$, $\bar{X}U$.
^c Total elongation in 0.5-in. (1.27-cm) gage length.
^d Values for tensile modulus of elasticity, yield strength, and ultimate strength differ because of significant figures maintained in comparative calculations between the two systems of units.

TABLE 7—Effect of reactor irradiation at 17 K on 17 K tensile properties of extralow impurity titanium-5 aluminum-2.5 tin alloy.

Specimen	Fast Fluence, ϕ n/cm ²	Tensile Modulus of Elasticity,		Yield Strength (0.2 percent offset),		Ultimate Strength,		Yield to Ultimate Strength Ratio	Total Elongation, ^c %	Reduction of Area, %
		lb/in. ²	N/m ²	lb/in. ²	N/m ²	lb/in. ²	N/m ²			
8Aa18.....	0	...	15.5 × 10 ¹⁰	203.0 × 10 ⁸	139.9 × 10 ⁷	231.0 × 10 ⁸	159.2 × 10 ⁷	0.879	8.0	33.0
8Aa32.....	0	213.0	146.8	223.0	153.6	0.955	11.0	32.0
8Aa35.....	0	...	14.3	213.0	146.8	225.0	155.0	0.947	10.0	32.0
8Aa34.....	0	...	20.8	217.0	149.5	227.0	156.4	0.956	9.7	32.3
8Aa27.....	0	...	22.4	225.0	155.0	236.0	162.6	0.954	1.5	0.6
		\bar{X}_D	15.1 × 10 ¹⁰	214.2 × 10 ⁸	147.6 × 10 ⁷	228.4 × 10 ⁸	157.4 × 10 ⁷	0.938	0	0
		$\bar{X}_D - \bar{X}$	0	8.0	5.5	5.2	3.6	0.033	0	0
		\bar{X}_U	-1.7	-9.9	0	-6.4	-4.4	-0.041	-3.7	-1.5
		\bar{X}_L	1.7	9.9	6.8	6.4	4.4	0.041	3.7	1.5
		\bar{X}_E	12.9 × 10 ¹⁰	211.0 × 10 ⁸	145.4 × 10 ⁷	222.0 × 10 ⁸	153.0 × 10 ⁷	0.950	11.0	31.0
8Aa25.....	1 × 10 ¹⁷	...	12.7	213.0	146.8	225.0	155.0	0.947
8Aa24.....	1	...	12.9	215.0	148.1	223.0	153.6	0.964
8Aa12.....	1	...	12.8 × 10 ¹⁰	213.0 × 10 ⁸	146.8 × 10 ⁷	223.3 × 10 ⁸	153.9 × 10 ⁷	0.953	11.0	31.0
		\bar{X}_E	0.1	2.0	1.4	1.5	1.0	0.009	1.3	-1.3
		$\bar{X}_E - \bar{X}_D$	-2.3	-1.2	-0.8	-0.8	-3.5	0.015
		\bar{X}_L	-3.8	-10.7	-7.4	-7.4	-7.7	-0.026
		\bar{X}_U	-1.1	8.3	5.7	1.0	0.7	0.056
		$\bar{X}_E^2 / \bar{S}_D^{2d}$	0.01	0.06	0.06	0.08	0.09	0.07
8Aa60.....	10 × 10 ¹⁷	...	15.2 × 10 ¹⁰	250.0 × 10 ⁸	172.3 × 10 ⁷	252.6 × 10 ⁸	174.0 × 10 ⁷	0.990	6.0	27.0
8Aa49.....	10	...	15.2	262.1	180.6	268.0	184.7	0.978	6.0	22.0
8Aa55.....	10	...	15.3	263.1	181.3	270.9	186.7	0.971	6.0	25.0
		\bar{X}_E	15.4 × 10 ¹⁰	252.4 × 10 ⁸	178.1 × 10 ⁷	263.8 × 10 ⁸	181.8 × 10 ⁷	0.980	6.0	24.7
		\bar{X}_F	0.6	7.3	5.1	3.8	6.3	0.010	0	2.5
		$\bar{X}_F - \bar{X}_D$	-0.4	44.2	30.5	24.3	24.3	0.042	0	-7.6
		\bar{X}_L	-1.2	31.7	21.3	15.7	10.3	0.003	-7.4	-14.0
		\bar{X}_U	2.0	57.2	39.3	55.1	38.1	0.081	0	-1.9
		$\bar{S}_E^2 / \bar{S}_D^{2d}$	0.44	0.83	0.83	3.55	3.57	0.09	0	17.36

^a Specimen exposed in gaseous helium at 17 K throughout test. Fast fluence is for $E > 0.5$ MeV (80 eV).
^b Arithmetic mean, \bar{X} ; estimated standard deviation, s ; lower and upper limits of 95 percent confidence interval of the difference, \bar{X}_L , \bar{X}_U .
^c Total elongation in 0.5-in. (1.27-cm) gage length.
^d Values for tensile modulus of elasticity, yield strength, and ultimate strength differ because of significant figures maintained in comparative calculations between the two systems of units.

TABLE 8—Effect of reactor irradiation at 17°K on 17°K tensile properties of annealed titanium-6 aluminum-4 vanadium alloy.

Specimen	Fast Fluence, ^a n/cm ²	Statistical Analysis ^b	Tensile Modulus of Elasticity,		Yield Strength (0.2 percent offset)		Ultimate Strength,		Yield to Ultimate Strength Ratio	Total Elongation, ^c %	Reduction of Area, %
			lb/in. ²	N/m ²	lb/in. ²	N/m ²	lb/in. ²	N/m ²			
2Ac1.....	0	...	17.6×10 ⁶	12.1×10 ¹⁰	228.0×10 ³	157.1×10 ⁷	249.0×10 ³	171.6×10 ⁷	0.915	10.0	30.0
2Ac9.....	0	...	16.3	11.2	230.0	158.5	264.0	181.9	0.871	7.0	30.0
2Ac71.....	0	...	17.7	12.2	250.0	172.3	265.0	182.6	0.843	7.0	36.0
2Ac10.....	0	...	17.9	12.3	253.0	174.3	261.0	179.8	0.869	7.0	27.0
2Ac12.....	0	...	16.8	11.6	255.0	175.7	263.0	181.2	0.869	7.0	29.0
		\bar{X}_A	17.3×10 ⁶	11.9×10 ¹⁰	243.2×10 ³	167.6×10 ⁷	260.4×10 ³	179.4×10 ⁷	0.833	7.6	30.4
		$\bar{X}_A - \bar{X}_A$	0	0	13.1	9.0	6.5	4.5	0.041	1.3	3.4
		\bar{X}_L	-0.9	-0.6	16.2	11.2	8.1	5.6	-0.051	-1.5	-4.2
		\bar{X}_U	0.9	0.6	16.2	11.2	8.1	5.6	0.051	1.5	4.2
2Ac59.....	1×10 ¹⁷	...	24.8×10 ⁶	17.1×10 ¹⁰	154.0×10 ³	175.0×10 ⁷	265.0×10 ³	182.6×10 ⁷	0.955	6.0	37.0
2Ac61.....	1	...	24.8×10 ⁶	17.1×10 ¹⁰	154.0×10 ³	175.0×10 ⁷	266.0	183.3	0.955	6.0	37.0
2Ac72.....	1	...	24.8×10 ⁶	17.1×10 ¹⁰	254.0×10 ³	175.0×10 ⁷	273.7×10 ³	188.6×10 ⁷	0.955	5.7	37.3
		\bar{X}_B	7.5	5.2	10.8	7.4	13.3	9.2	0.022	-1.9	6.9
		\bar{X}_L	14.2	9.7	...	-3.5	10.9
		\bar{X}_U	14.4	9.9	...	-3.5	10.9
		s_B^2/s_A^2	41.0	28.2	...	-0.3	10.9
2Ac54.....	10×10 ¹⁷	...	20.0×10 ⁶	13.8×10 ¹⁰	289.4×10 ³	199.4×10 ⁷	4.76	4.64	0.956	4.0	0.03
2Ac56.....	10	...	25.0	17.2	294.7	203.0	302.7×10 ³	208.6×10 ⁷	0.907	6.0	34.0
2Ac55.....	10	...	22.5×10 ⁶	15.5×10 ¹⁰	314.5	216.7	325.0	233.9	0.945	4.0	34.0
		\bar{X}_C	3.5	2.4	56.3	38.8	332.9	230.6×10 ⁷	0.936	4.7	34.0
		$\bar{X}_C - \bar{X}_A$	5.2	3.6	13.2	9.1	15.7	10.8	0.026	1.2	0
		\bar{X}_L	-26.6 ^d	-17.8 ^d	79.8	55.0	59.8	41.2	0.003	-2.9	3.6
		\bar{X}_U	37.0	25.0	79.8	55.0	29.6	20.3	-0.052	-0.7	7.8
		s_C^2/s_A^2	25.00	23.03	1.02	1.02	90.1	62.1	0.058	-0.7	7.8
							5.83	5.75	0.40	0.85	0

^a Specimen exposed in gaseous helium at 17°K throughout test. Fast fluence is for $E > 0.5$ MeV (80 eV).
^b Arithmetic mean, \bar{X} ; estimated standard deviation, s ; lower and upper limits of 95 percent confidence interval of the difference, \bar{X}_L , \bar{X}_U .
^c Total elongation in 0.5-in. (1.27-cm) gage length.
^d Values for tensile modulus of elasticity, yield strength, and ultimate strength differ because of significant figures maintained in comparative calculations between the two systems of units.
^e Value exceeds lower limit of possible change.

TABLE 9—Effect of reactor irradiation at 17 K on 17 K tensile properties of aged titanium-6 aluminum-4 vanadium alloy.

Specimen	Fast Fluence, ^a n/cm ²	Tensile Modulus of Elasticity,		Yield Strength (0.2 percent offset),		Ultimate Strength,		Yield to Ultimate Strength Ratio	Total Elongation ^c %	Reduction of Area, %
		lb/in. ²	N/m ²	lb/in. ²	N/m ²	lb/in. ²	N/m ²			
2Aa30.....	0	20.4 × 10 ⁶	14.1 × 10 ¹⁰	273.0 × 10 ³	188.1 × 10 ⁷	286.0 × 10 ³	197.1 × 10 ⁷	0.954	6.0	22.0
2Aa11.....	0	19.7	13.6	274.0	188.8	277.0	190.9	0.989	7.0	28.0
2Aa29.....	0	17.1	11.8	274.0	188.8	281.0	193.6	0.975	7.0	24.0
2Aa10.....	0	17.4	12.0	275.0	189.5	284.0	195.7	0.969	7.0	31.0
2Aa13.....	0	18.1	12.5	279.0	192.2	283.0	195.0	0.986	5.0	22.0
		18.5 × 10 ⁶	12.8 × 10 ¹⁰	275.0 × 10 ³	189.5 × 10 ⁷	282.2 × 10 ³	194.5 × 10 ⁷	0.975	6.4	25.4
		1.5	1.0	2.4	1.6	3.4	2.4	0.014	0.9	4.0
		$\bar{X}D$	$\bar{X}D/\bar{X}D$	0	-2.0	0	-2.9	-0.017	0	0
		$\bar{X}L$	$\bar{X}L$	-3.0	2.0	-4.2	2.9	0.017	-1.1	-5.0
		$\bar{X}U$	1.3	3.0	5.0	4.2	2.9	0.017	1.1	5.0
2Aa43.....	1 × 10 ¹⁷	14.6 × 10 ⁶	10.1 × 10 ¹⁰	281.0 × 10 ³	192.6 × 10 ⁷	296.0 × 10 ³	203.9 × 10 ⁷	0.949	5.0	24.0
2Aa44.....	1	204.0	202.6	303.0	208.8	308.0	212.3	0.870	5.0	21.0
2Aa77.....	1	14.6 × 10 ⁶	10.1 × 10 ¹⁰	293.3 × 10 ³	202.1 × 10 ⁷	302.3 × 10 ³	203.3 × 10 ⁷	0.890	5.0	22.5
		$\bar{X}E$	$\bar{X}E$	12.9	8.3	6.0	4.1	0.021	0	2.1
		$\bar{X}E/\bar{X}D$	-2.7	18.3	12.6	20.1	13.8	-0.005	-1.4	-2.9
		$\bar{X}L$...	-11.9	-8.2	9.6	6.6	-0.044	-2.5	-8.4
		$\bar{X}U$...	48.5	33.4	30.6	21.1	0.034	-0.3	2.6
		$sf^2/\bar{X}D^{2d}$...	25.00	26.85	3.11	2.92	2.25	0	0.28
2Aa78.....	10 × 10 ¹⁷	20.0 × 10 ⁶	13.8 × 10 ¹⁰	289.5 × 10 ³	199.5 × 10 ⁷	296.1 × 10 ³	204.0 × 10 ⁷	0.978	5.0	21.0
2Aa87.....	10	15.0	10.3	324.8	223.8	324.8	223.8	0.980	4.0	13.0
2Aa89.....	10	19.0	13.1	319.0	219.8	325.2	224.1	0.980	5.0	16.0
2Aa82.....	10	20.0	13.8	322.1	221.9	328.3	226.2	0.981	5.0	14.0
2Aa81.....	10	22.0	15.2	365.5	251.8	373.2	257.1	0.979	3.0	13.0
		$\bar{X}F$	19.2 × 10 ⁶	324.0 × 10 ³	233.3 × 10 ⁷	329.5 × 10 ³	227.0 × 10 ⁷	0.979	4.4	15.4
		sf	2.6	31.3	21.5	27.7	19.1	0.002	0.9	3.4
		$\bar{X}F/\bar{X}D$	0.7	49.0	33.8	47.3	32.5	0.004	2.0	-10.0
		$\bar{X}L$	-2.4	-0.9	-0.6	12.7	8.7	-0.013	-3.3	-15.3
		$\bar{X}U$	3.8	98.9	68.2	81.9	56.3	0.021	-0.7	-4.7
		$sf^2/\bar{X}D^{2d}$	3.00	170.09	180.57	66.37	63.34	0.02	1.00	0.72

^a Specimen exposed in gaseous helium at 17 K throughout test. Fast fluence is $E > 0.5$ MeV (80 fJ).
^b Arithmetic mean, \bar{X} ; estimated standard deviation, s ; lower and upper limits of 95 percent confidence interval of the difference, XL , XU .
^c Total elongation in 0.5-in. (1.27-cm) gage length.
^d Values for tensile modulus of elasticity, yield strength, and ultimate strength differ because of significant figures maintained in comparative calculations between the two system of units.

TABLE 10—Effect of reactor irradiation at 17 K on 17 K tensile properties of titanium-8 aluminum-1 molybdenum-4 vanadium alloy.

Specimen	Fast Fluence, ^a n/cm ²	Statistical Analysis ^b	Tensile Modulus of Elasticity,		Yield Strength (0.2 percent offset)		Ultimate Strength,		Yield to Ultimate Strength Ratio	Total Elongation, ^c %	Reduction of Area, %
			lb/in. ²	N/m ²	lb/in. ²	N/m ²	lb/in. ²	N/m ²			
4Aa3.....	0	...	19.2×10 ⁶	13.2×10 ¹⁰	217.0×10 ³	149.5×10 ⁷	236.0×10 ³	162.6×10 ⁷	0.920	12.1	...
4Aa1.....	0	...	18.3	11.6	220.0	151.6	242.0	166.7	0.909	5.8	...
4Aa4.....	0	...	16.4	12.3	224.0	154.3	236.0	162.6	0.950	7.8	...
4Aa5.....	0	...	18.5	12.7	224.0	154.3	238.0	164.0	0.940	7.8	...
4Aa2.....	0	...	18.9	13.0	236.0	162.6	243.0	167.4	0.970	15.2	...
		\bar{X}_A	18.3×10 ⁶	12.6×10 ¹⁰	224.2×10 ³	154.5×10 ⁷	239.0×10 ³	164.7×10 ⁷	0.938	9.5	...
		s_A	1.1	0.7	7.2	5.0	3.3	2.3	0.024	3.8	...
		$\bar{X}_A - \bar{X}_A$	0	0	0	0	0	0	0	0	...
		\bar{X}_L	-1.4	-1.0	-8.9	-6.1	-4.2	-2.9	-0.030	-4.7	...
		\bar{X}_U	1.4	1.0	8.9	6.1	4.2	2.9	0.030	4.7	...
4Aa34.....	1×10 ¹⁷	...	19.6×10 ⁶	13.5×10 ¹⁰	238.0×10 ³	164.0×10 ⁷	264.0×10 ³	181.9×10 ⁷	0.630	6.0	31.0
4Aa43.....	1	...	25.4	17.5	243.0	167.4	262.0	180.5	0.627	6.0	30.0
4Aa38.....	1	...	22.5×10 ⁶	15.5×10 ¹⁰	247.0	170.2	259.0	178.5	0.657	6.0	30.0
		\bar{X}_B	4.1	2.8	4.5	3.7	2.7	1.7	0.027	5.7	29.0
		s_B	4.2	2.9	18.5	12.7	22.7	15.6	-0.011	-3.8	...
		$\bar{X}_B - \bar{X}_A$	-35.2 ^e	-22.9 ^e	0.0	6.2	17.9	12.3	-0.037	-3.8	...
		\bar{X}_U	41.6	28.7	28.0	19.3	27.5	18.9	0.035	1.0	...
		s_B/s_A ^d	13.90	16.00	0.39	0.38	0.57	0.55	1.26	0.02	...

^a Specimen exposed in gaseous helium at 17 K throughout test. Fast fluence is for $E > 0.5$ MeV (80 eV).
^b Arithmetic mean, \bar{X} ; estimated standard deviation, s ; lower and upper limits of 95 percent confidence interval of the difference, X_L , X_U .
^c Total elongation on 0.5-in. (1.27-cm) gage length.
^d Values for tensile modulus of elasticity, yield strength, and ultimate strength differ because of significant figures maintained in comparative calculations between the two system of units.
^e Value exceeds lower limit of possible change.

$$u_{BA} = t_{0.975} \sqrt{\frac{s_A^2}{n_A} + \frac{s_B^2}{n_B}} \quad \text{for } \frac{\left(\frac{s_A^2}{n_A} + \frac{s_B^2}{n_B}\right)^2}{\frac{(s_A^2/n_A)^2}{n_A+1} + \frac{(s_B^2/n_B)^2}{n_B+1}} - 2$$

effective number of degrees of freedom

$t_{0.975}$ distribution value for t test of significance (see Ref 21, Table A-4)

References

- [1] Schwartzberg, F. R., Osgood, S. H., Keys, R. D., and Kiefer, T. F., "Cryogenic Materials Data Handbook," AFML-TDR-64-280, DDC No. AD-609562, Martin Co., 1964.
- [2] Makin, M. J. and Minter, F. J., *Journal of the Institute of Metals*, JIMEA, Vol. 85, 1956-1957, pp. 397-402.
- [3] Eckel, J. F., Bruch, C. A., Levy, A., Willis, A. H., and Seymour, W. E., AEC Report TID-7515 (Part 2) (Del.), Radiation Effects Review Meeting, Congress Hotel, Chicago, Ill., 31 July-1 Aug. 1956, pp. 170-221.
- [4] Bruch, C. A., McHugh, W. E., and Hockenbury, R. W., *Transactions*, AIME, TAIMA, Vol. 206, 1956, pp. 1362-1372.
- [5] Anderson, W. K., Beck, C. J., Kephart, A. R., and Theilacker, J. S. in *Reactor Structural Materials: Engineering Properties as Affected by Nuclear Reactor Service*, ASTM STP 314, American Society for Testing Materials, 1962.
- [6] Bomar, E. S., Cooke, F. W., Leonard, W. J., Prislinger, J. J., and Wodtke, C. H., "Engineering Metallurgy," Metallurgy Division Annual Progress Report for Period Ending September 1, 1959, ORNL-2839, Union Carbide Corp., 1959, pp. 127-143.
- [7] Adamson, G. M., "Metallurgy—Mechanical Metallurgy—Tensile Properties of Irradiated Titanium Alloys," Homogeneous Reactor Program Quarterly Progress Report for Period Ending October 31, 1957, ORNL-2432, Union Carbide Corp., 1958, pp. 135-136.
- [8] Lombardo, J. J., Dixon, C. E., and Begley, J. A. in *Effects of Radiation on Structural Metals*, ASTM STP 426, American Society for Testing and Materials, 1967, pp. 625-652.
- [9] Watson, J. F., Christian, J. L., and Allen, J. W., "A Study of the Effects of Nuclear Radiation on High-Strength Aerospace Vehicle Materials at the Boiling Point of Hydrogen (-423°F)," ERR-AN-085, General Dynamics/Astronautics, 1961.
- [10] Shogan, R. P., "Tensile Properties of Irradiated Ti-5 Al-2.5Sn ELI at Cryogenic Temperatures," WANL-TME-1860, Westinghouse Astronuclear Lab., 1968.
- [11] Drennan, J. E. and Hamman, D. J., "Supplemental Analysis of GTR-19 Data," BMI-NRE-10, Battelle Memorial Institute, 1968.
- [12] Wallack, S., "The Effect of Radiation on the Physical and Mechanical Properties of Metals and Alloys," WADC TR 58-605, DDC No. AD-215540, Universal Winding Co., Inc., 1959.
- [13] Younger, C. L. and Haley, F. A., "Effect of Nuclear Radiation at Cryogenic Temperatures on the Tensile Properties of Titanium and Titanium-Base Alloys," NASA TN D-5442, National Aeronautics and Space Administration, 1969.
- [14] Bridges, W. L. and Liebschutz, A. M. in *Advances in Cryogenic Engineering*, Vol. 7, K. D. Timmerhaus, Ed., Plenum Press, New York, 1962, pp. 440-447.
- [15] Aseff, G. V., Sr., Callaway, R. F., and Liebschutz, A. M. in *Advances in Cryogenic Engineering*, Vol. 8, K. D. Timmerhaus, Ed., Plenum Press, New York, 1963, pp. 624-630.
- [16] Liebschutz, A. M. and Schulte, C. A. in *Advances in Cryogenic Engineering*, Vol. 7, K. D. Timmerhaus, Ed., Plenum Press, New York, 1962, pp. 181-188.
- [17] Natrella, M. G., *Experimental Statistics*, Handbook 91, National Bureau of Standards, 1963.